Transactions of the ASME

EDITORIAL STAFF
Director, Technical Publishing,
JOSEPH SANSONE
Managing Editor,
CORNELIA MONAHAN
Production Editor,
JACK RUMMEL
Editorial Production Asst.
BETH DARCHI
Associate Editors
Air Pollution Control
H. E. HESKETH
Diesel and Gas Engine Power
F. PEKAR
Gas Turbine
R. A. HARMON
Power
D. T. BERUBE
Solar Energy
H. M. CURRAN
Energetics
J. B. COMLY
Fuels
R. E. BARRETT
Nuclear Engineering
M. S. OZKER

BOARD ON COMMUNICATIONS
Chairman and Vice-President
M. J. RABINS

Members-at-Large
W. BEGELL
J. CALLAHAN
D. KOENIG
M. KUTZ
F. LANDIS
J. W. LOCKE
J. E. ORTLOFF
C. PHILLIPS
K. REID

Business Staff
345 E. 47th St.
New York, N.Y. 10017
(212) 644-7789
Mng. Dir., Publ., J. J. FREY

OFFICERS OF THE ASME
President, ROBERT B. GAITHER
Exec. Dir. & Sec'y,
BURKE E. NELSON
Treasurer, ROBERT A. BENNETT

Journal of Engineering for Power (ISSN 0022-0825) is edited and published quarterly at the offices of The American Society of Mechanical Engineers, United Engineering Center, 345 E. 47th St., New York, N. Y. 10017. ASME-TWX No. 710-581-5267. New York. Second Class postage paid at New York, N.Y., and at additional mailing offices.

CHANGES OF ADDRESS must be received at Society headquarters seven weeks before they are to be effective. Please send old label and new address.

PRICES: To members, $30.00, annually; to nonmembers, $60.00. Single copies, $20.00 each. Add $5.00 for postage to countries outside the United States and Canada.

INDEXED by the Engineering Index, Inc.

Journal of Engineering for Power

Published Quarterly by The American Society of Mechanical Engineers
VOLUME 103 • NUMBER 4 • OCTOBER 1981

LMFBR Loss of Flow Simulations in the Sodium Loop Safety Facility[1]

W. A. Ragland
Assistant Nuclear Engineer,
Sodium Loop Safety Facility,
Reactor Analysis and Safety Div.
Argonne National Laboratory,
Argonne, Ill.

A series of three LMFBR unprotected loss of flow (LOF) accidents has been simulated in the Sodium Loop Safety Facility (SLSF). The results of these in-reactor experiments verify that the dynamics of sodium voiding are, in general, well represented by current single channel slug expulsion models. Some refinement in the models in the very early stages of voiding would be desirable to account for minor two dimensional effects. However, cladding motion is not as well understood and current modeling does not accurately predict all of the aspects of blockage formation. Two of the three experiments produced partial rather than complete upper blockages as had been predicted. Predictions of time of fuel melting appear relatively accurate. In general, the sequence of events is correctly predicted and the timing of these events is relatively accurate. Reactivity measurements and post-test examinations indicate that no significant fuel compaction occurred. This behavior would prevent an energetic recriticality in an LOF accident.

Introduction

Automatic safety systems inherent to LMFBR design preclude a loss of flow (LOF) without reactor shutdown (scram). However, certain hypothetical accidents have been postulated in which a LOF is accompanied by a delay or failure of the reactor shutdown system. In such a scenario the extent and nature of cladding melting and movement may play a critical role in determining the extent of fuel migration. Subsequently, the fuel disruption impacts the accident energetics.

The objective of all three SLSF experiments was to investigate cladding and fuel behavior during the early stages of a hypothetical, unprotected LMFBR LOF accident under prototypic thermal-hydraulic and fuel conditions. In addition the experiments provided data to check current sodium boiling and expultion models. Items of interest included: mode of fuel element failure; extent of fuel coolant interaction, if any; coolant response; and fuel motion (either dispersion or compaction). In particular, dispersive fuel motion during the initiation of a LOF may reduce the accident energetics. Proposed models of fuel disruptions include: buckling of a stack of pellets; large scale swelling of solid fuel; melting and draining of fuel inside a solid shell; melting and falling of molten fuel with breakup of the outer shell; and breakup of solid fuel into small particles. Prior to the SLSF tests, no conclusive evidence existed to identify one single mode as a dominant effect of fuel disruption. In addition to information regarding accident energetics, the SLSF LOF tests provide vital information regarding the coolability of post accident reactor subassemblies.

Experiment Design

All of the LOF experiments were conducted in a SLSF loop which was inserted into the Engineering Test Reactor (ETR) at the Idaho National Engineering Laboratory. The SLSF loop includes: primary and secondary containment vessels; an annular linear induction pump; a sodium to helium heat exchanger; control and protection instrumentation; and a removable test train containing the experiment test section and instrumentation. Although the ETR is a thermal reactor, a hard neutron spectrum more prototypic of LMFBR's is provided by a cadmium filter located on the secondary containment vessel. Figure 1 is an axial schematic view of the major components of the loop.

After consideration of experimental objectives, it was determined that a series of tests would be required in order to define both the accident sequence and possible scale effects due to test section size. Starting with a 19-pin test (P2), the series then concluded with two 37-pin tests (P3A and P3). SLSF experiment P2 was performed first because the smaller 19-pin test would be a natural extension of 7-pin LOF TREAT R-series experiments. In addition, P2 allowed for evaluation of the SLSF loop performance for LOF experiments prior to the use of the larger 37-pin test sections in P3A and P3. Comparison of the results as the experiment size increased was intended to determine the nature and magnitude of any scale effects. This information could therefore be used to infer the applicability of a 37-pin experiment to a full scale

[1] The submitted manuscript has been authored by a contractor of the U. S. Government under contract No. W-31-109-ENG-38. Accordingly, the U. S. Government retains a nonexclusive, royalty-free license to publish or reproduce the published form of this contribution, or allow others to do so, for U. S. Government purposes.

Contributed by the Nuclear Engineering Division of the AMERICAN SOCIETY OF MECHANICAL ENGINEERS and presented at the Century 2 Nuclear Engineering Conference, San Francisco, Calif., August 19-21, 1980. Manuscript received at ASME Headquarters April 21, 1980.

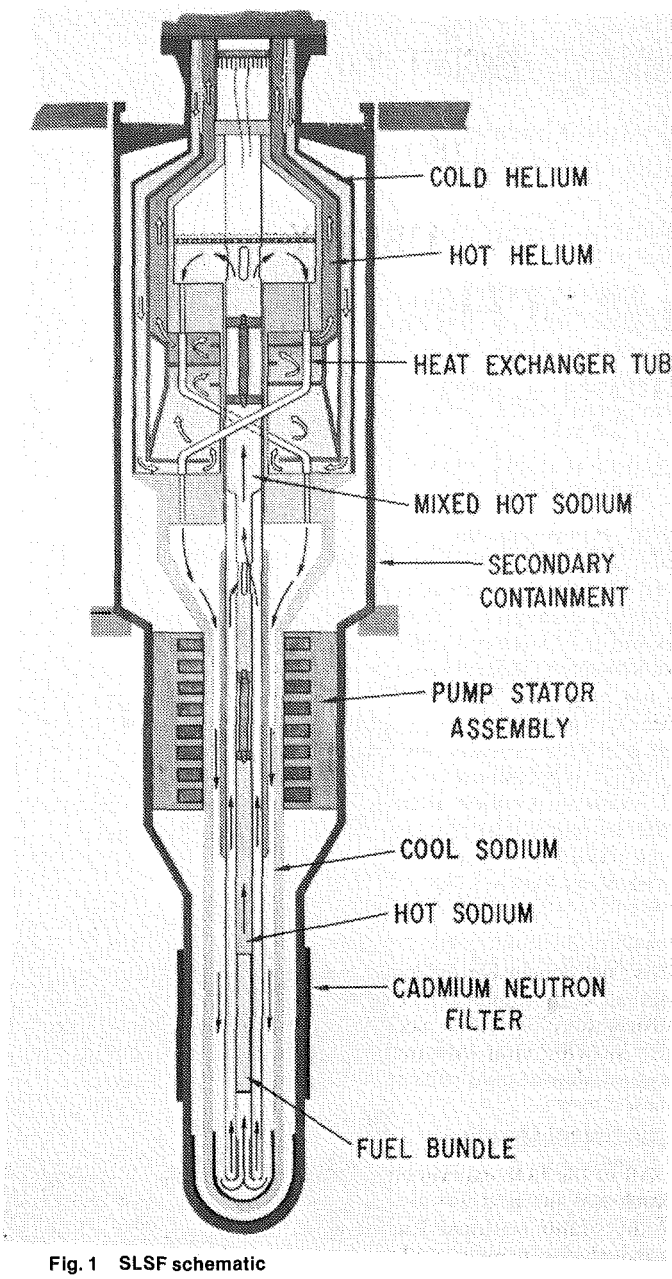

Fig. 1 SLSF schematic

(217-pin) LMFBR subassembly. Also, the smaller 19-pin test section would allow operation at hot channel conditions rather than nominal power. The P3A experiment was identical to the final P3 test except that it was planned to terminate at the moment of initial fuel motion. With such an early termination, P3A would preserve a "snap shot" of the very early stage of fuel disruption.

All tests were operated at steady-state conditions which simulated the central portion of a fast test reactor (FTR) subassembly at beginning of life (<0.8 percent b.u.). To obtain a structurally acceptable sodium temperature at the loop heat exchanger inlet, some of the sodium was bypassed around the test section. A set of ribbed tubes was used in the test section inlet and the bypass inlet to provide proper flow split and duplicate the FTR pressure drop. The use of these tubes in lieu of orifices eliminated cavitation and assured that the test section would duplicate FTR voiding characteristics. In order to prevent excessive heat loss from the test section to the bypass an insulator consisting of an inner hexcan, ceramic

Table 1 Operating conditions

	P2	P3A	P3
Scram time, s	21.0	12.9	15.3
Average power per fuel pin, kW/m	41.2	36.4	36.7
Inlet temperature, K	695	696	707
Outlet temperature, K	981	931	936
Test section sodium flow, Ks/s	1.95	4.2	4.3
Loop sodium flow, Kg/s	5.4	8.8	9.2
Test section power, kW	730	1240	1250
Total irradiation (full-power-days)	24	26	21

insulator and outer duct was constructed. Figure 2 shows a cross section of the SLSF loop with the 37-pin test subassembly.

In contrast with the two 37-pin tests to follow, P2 contained 19 pins operating at a higher specific power. The insulator surrounding the fuel was a sandwich of Inconel X-750, alumina, and 316 stainless steel. To improve the ability of the loop to safely contain the larger 37-pin P3 and P3A experiments, zirconia and Inconel 625 were substituted for the last two layers.

Experimental Observations

All LOF experiments followed the same general sequence of events, but the timing in P2 differed significantly from P3A and P3. Table 2 gives a comparison of the steady state conditions just prior to the beginning of each LOF while Table 3 shows the predicted and actual timing of subsequent events. Note that the P2 higher specific power would lead one to expect earlier cladding dryout. The P2 pretest analysis predicted boiling initiation at 6.7 s into the transient, and flow reversal at 7.5 s. The onset of boiling occurred in P2 at 6.3 s based on acoustic sensor and flowmeter data. The sudden expulsion of coolant from the bundle which had been expected did not occur, rather there was a slow boil out of sodium. In both the P3 and P3A experiments sodium boiling occurred at 8.8 s. Boiling then proceeded in both radial and axial directions requiring ~1 s for boiling to reach the edge subchannels. At this time the pressure buildup in the bundle is of sufficient magnitude to reverse the inlet flow (Figs 3, 4). Both the P3A and P3 test sections voided within 2.5 s after boiling.

P2 Experiment. While adjusting loop parameters in preparation for the P2 LOF transient, a change was noted in the overall loop heat balance. Closer examination of all sensor data showed a simultaneous decrease in loop sodium level and increase in insulator region pressure. From this it was concluded that sodium leaked into the hexcan insulator region. The reduction of insulator efficiency due to sodium logging therefore caused a increased heat loss from the test section to the bypass. This is thought to be responsible for increased radial voiding incoherencies and abnormally slow boil out of the P2 test section.

As a result of the slow boil out, the remaining P2 events were significantly delayed. The first pin failure occurred at 9.5 s. Most of the test section instrumentation failed between 10.5 and 11.5 s indicating gross cladding melting and motion. The flow was very low with small oscillations which damped between 17 and 19 s indicating the formation of a lower blockage. Flowmeter signals indicated a small net positive flow. This suggests some porosity in the blockage (later found to be impervious). ETR negative reactivity changes due to fuel dispersal occurred at 14.5 s.

Unlike the other experiments, P2 was programed for a

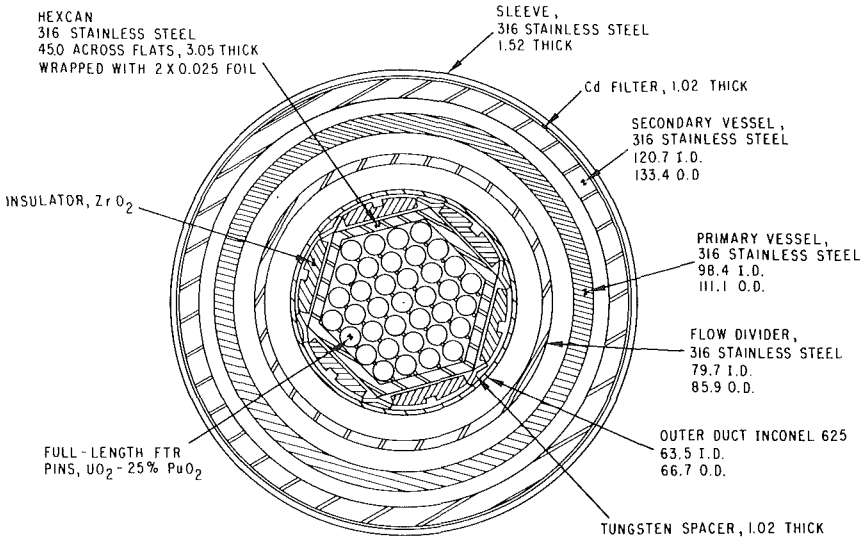

Fig. 2 P3 cross section

Table 2 Experiment design parameters

	P2	P3A	P3	FTR
Number of pins	19	37	37	--
Fuel pin length, m	2.36	2.36	2.36	2.36
Heat section length, m	0.91	0.91	0.91	0.91
Cladding o.d., mm	5.84	5.84	5.84	5.84
Cladding thickness, mm	0.381	0.381	0.381	0.381
Spacer wire diameter				
Interior channels, mm	1.42	1.42	1.42	1.42
Exterior channels, mm	0.71	0.71	0.71	--
Hexcan material	In-X750	Nb-1%Zr	SS316	SS316
Insulator material	AlO_2	ZrO_2	ZrO_2	--
Outer duct material	SS316	IN-625	IN-625	--

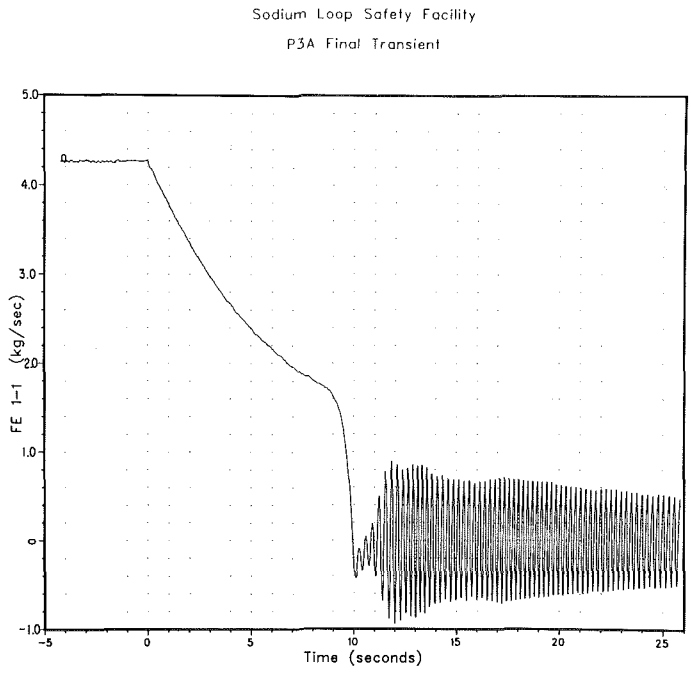

Fig. 3 P3A inlet flow

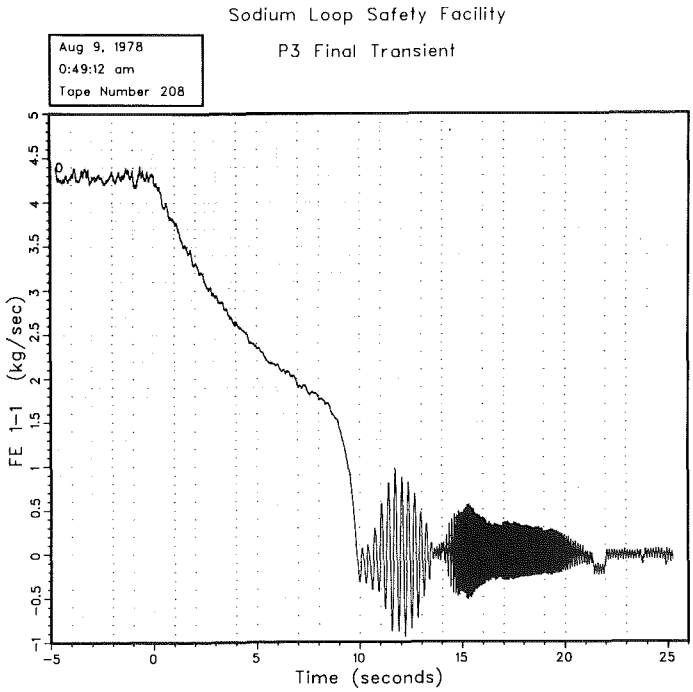

Fig. 4 P3 inlet flow

partial restoration of pump power to coincide with reactor scram at 21 s. At ~1 s following scram the pressure rose within the test section. This event coupled with possible melting of the hex assembly outer duct caused the ejection of ~1/3 of the P2 molten fuel inventory into the bypass. Other indications of this event were simultaneous failure of bundle inlet and outlet thermocouples indicating severence of the

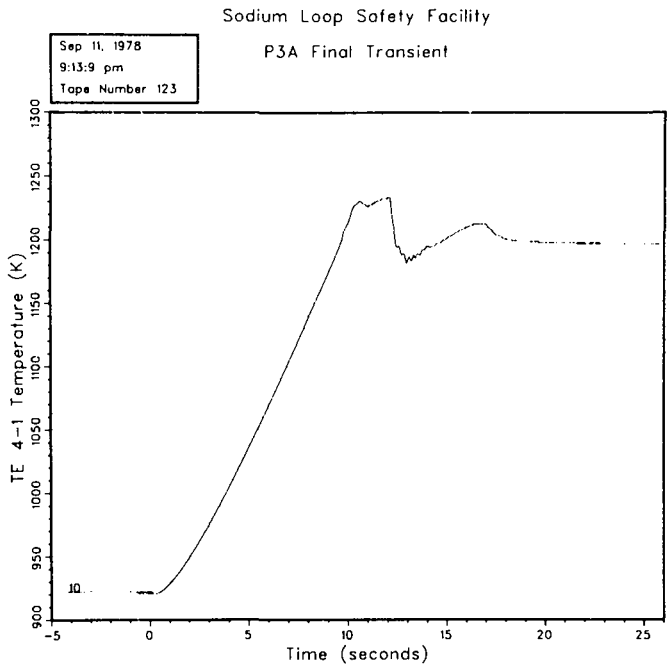

Fig. 5 P3A sodium exit temperature

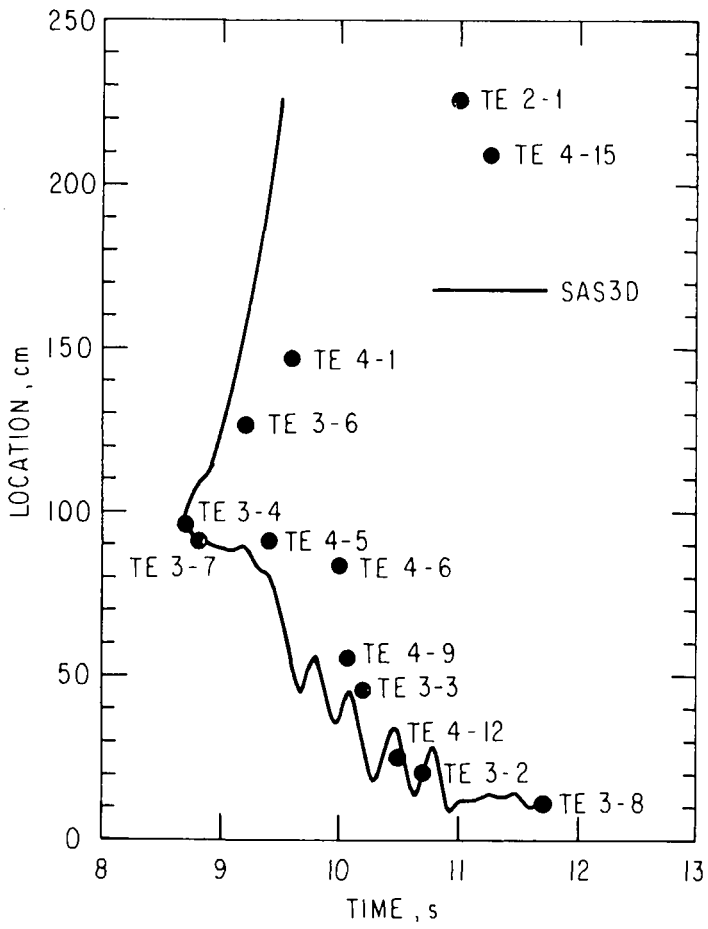

Fig. 6 P3 voiding profile

sheath containing these sensor leads. Distrubances were observed in the bundle inlet and total loop flowmeters, some pressure sensors, and the sodium reservoir level. These disturbances were accompanied by pops in the acoustic sensors and interpreted as a voiding of the bypass. Posttest examination of the P2 experiment revealed that part of the insulator had broken away, the outer duct was ruptured, and the flow divider was cracked. In addition, a small amount of molten material had been deposited on the interior walls of the primary vessel. Both primary and secondary vessels were intact with no significant damage to the primary vessel.

P3A Experiment. From wire wrap thermocouple temperatures it was possible to estimate a time required for dryout of 1 to 1.5 s. Radial expansion of the sodium void to the edge subchannel coincided with the inlet reversal which occurred 1.2 s after boiling inception.

The data for P3A show a continued rise in bundle coolant temperature for about 1 s after the onset of boiling. This agrees with predictions that indicate upper bundle voiding causes an increasing back pressure manifesting itself as a brief ramp in saturation temperature (Fig. 5).

The complete flow coastdown curve as shown in Fig. 4 exhibits a very characteristic ring as predicted by the SAS code. This ringing is identical in frequency to predictions but different in phase and amptitude. By adjusting data and SAS predictions such that flow reversal occurs at the same time, the two curves come in phase. Following ETR scram, the hex duct temperature climbed and at 16 s there was a general increase in heat transfer from the test section to the bypass. Acoustic and flowmeter data gave indications of fission gas release. The exit and loop flowmeters showed free passage of this gas.

P3 Experiment. The P3 experiment was conducted at a slightly higher inlet temperature of 707K. This increase in was dictated by heat transfer limits for the SLSF heat exchanger and the secondary coolant system atmospheric heat sink. This inlet temperature was 12K above the value assumed in the pretest analysis. Because the increase tends to accelerate the preboiling phase of the transient, it was necessary to reduce the scram time from 15.6 to 15.3 s. Full power operating experience, including inlet flowmeter data, indicated that the selected flow coastdown profile would produce a slightly higher test section flow than planned, but within the desired operational envelop. The measured P3 voiding shown in Fig. 6 was in very good agreement with the SAS3D predictions.

Following flow reversal at 10 s, a 3 Hz inlet flowmeter oscillation gradually increased in magnitude until ~12 s and then decreased becoming very nearly zero at 13.6 s (Fig. 4). The flowmeter oscillation then increased in magnitude but the frequency of the oscillation was 8 to 12 Hz. These oscillations built to a maximum amplitude at ~15.3 s then gradually decreased to near zero.

Analysis of Data

Although general agreement of pretest predictions and experimental data were good particularly in the P3A and P3 experiment, extensive posttest analyses sought to determine possible causes for some differences between data and prediction. In addition, this analysis explained some of the nonprototypic behavior of the P2 experiment.

P2 Experiment. To explain the difference in SAS predictions and the P2 data, the effect of bypass heat loss was simulated by a thick steel heat sink around the test section. The results of these modifications showed little change from the pretest analysis. The posttest analysis suggests that nothing is basically wrong with SAS which would effect the validity of previous reactor safety analysis. Rather the problem appears to be that SAS does not adequately simulate the nonprototypic thermal boundary conditions of the P2 test subassembly.

The P2 test was also modeled using COBRA-3M which models thermal-hydraulic behavior of multichannel reactor

Table 3 LOF Events

	P2	P3A	P3
Start flow coastdown†	0.0 (0.0)	0.0 (0.0)	0.0 (0.0)
Initial boiling	6.3 (6.7)	8.8 (8.0)	8.8 (8.8)
Flow reversal	None (7.5)	10.0 (9.8)	9.8 (9.9)
Local dryout	10.5	9.8-10.3	9.8 – 10.3
Cladding failure	9.5 (8.0)	10.8 (9.4)	< 11.5 (10.5)
Cladding motion	10.5-11.5 (9.0)	11.9-12.2 (11.0-12.0)	11.5-11.8 (10.9)
Top blockage formation	* (9.0)	12.0-13.0** (11.1-12.8)	13.0** (11.2)
Bottom blockage formation	* (11.6)	* (12.8)	13.3 (11.9-13.3)
Fuel motion	14.5 (11.5)	*	14.7 (13.9)
Reactor scram	21.0	12.9	15.3

† all times in seconds, predictions in parenthesis
*occurred after scram
**incomplete blockage

Table 4 Effects of flux tilt on boiling

	COBRA-3M		Data
Radial power profile	Uniform	Flux Tilt	--
Boiling inception, s	8.40	8.80	8.8
Boiling (edge channel, .83 m above fuel bottom), s	9.85	9.75	10.0
Boiling (interior channel, .90 m above fuel bottom), s	9.20	9.46	10.0

subassemblies. Using the nonuniform radial temperature distribution in the P2 subassembly it was possible to predict boiling inception which agreed well with P2. Because COBRA-3M did not model flow reversal, a simple computer model of a boiling subassembled channel called LIMBO (Liquid Metal Boiling) (1, 2) was developed to conduct parametric studies and evaluate heat transfer correlations. The model is capable of analyzing both quasi-stable boiling and rapid vapor expulsion. By assuming an insulated hexcan assembly and a uniform radial liquid distribution, the LIMBO results were in qualitative agreement with SAS when large radial heat loss from the bundle to the bypass were included. The calculations predicted that approximately half of the vapor entering the upper bundle condensed and the rate of coolant expulsion was significantly reduced. By accounting for both radial heat loss and radial two phase sodium inhomogenity, this model predicted an inlet flow in agreement with P2 test results. In addition LIMBO predicted a partially voided upper test section in agreement with the observed subcooled discharge. It is likely, therefore, that the nonprototypic voiding behavior observed in the P2 experiment is due to a combination of the effects of bundle heat loss and radial inhomogenuity.

P3A Experiment. The rapid flow decay following boiling in the P3A test indicated dynamic coolant behavior different from P2. An obvious difference between P2 and P3A experiments is that the P3A experiment test section remained well insulated throughout the experiment. Another explanation for different coolant response is an interconnected channel effect due to an decrease in the ratio of edge subchannel area to total area as the bundle size increases. Therefore, the effect of flow diversion from voiding subchannel to edge subchannels becomes less significant.

During the P3A experiment there was possible ETR neutron flux tilt. To investigate the effects of the flux tilt on boiling inception, COBRA-3M calculations were performed for both uniform and skewed radial power distribution. The uniform power distribution calculations predicted boiling at 8.4 s versus 8.8 s for the skewed case (identical with experimental

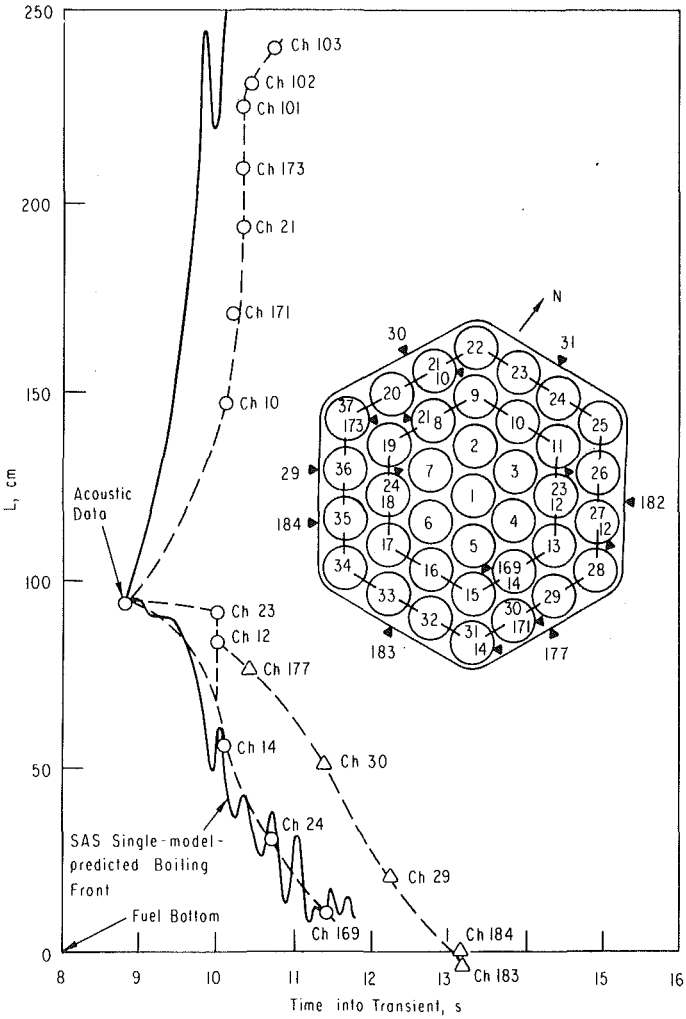

Fig. 7 P3A voiding profile

data). This compares with SAS boiling initiation time of 8.83 s for the single channel model. Table 4 compares boiling times at several additional locations. During the early part of the voiding the calculational and experimental results show rapid flow decay with a time difference of 0.2 s. To explain this difference it is postulated that the bubble grew both axially and radially so that it took 0.2 s for the bubble to develop a sufficient cross section to fill the entire test section. After this boiling dynamics became single channel phenomena as modeled by SAS (Fig. 7).

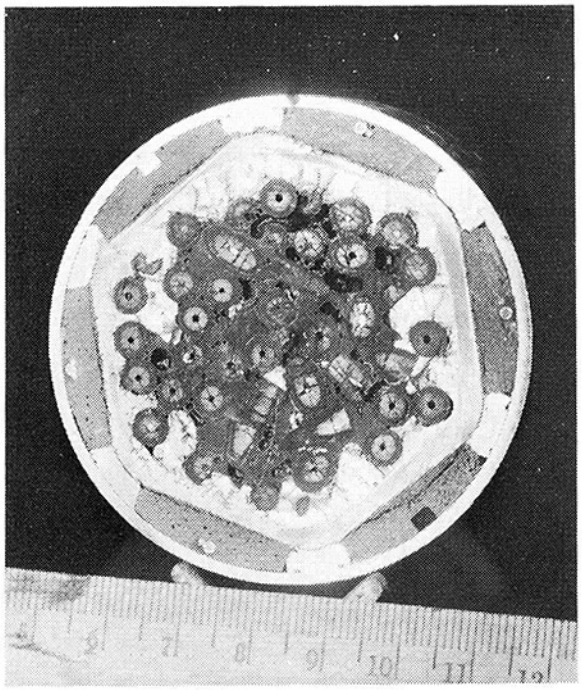

Fig. 8 P3A posttest cross section

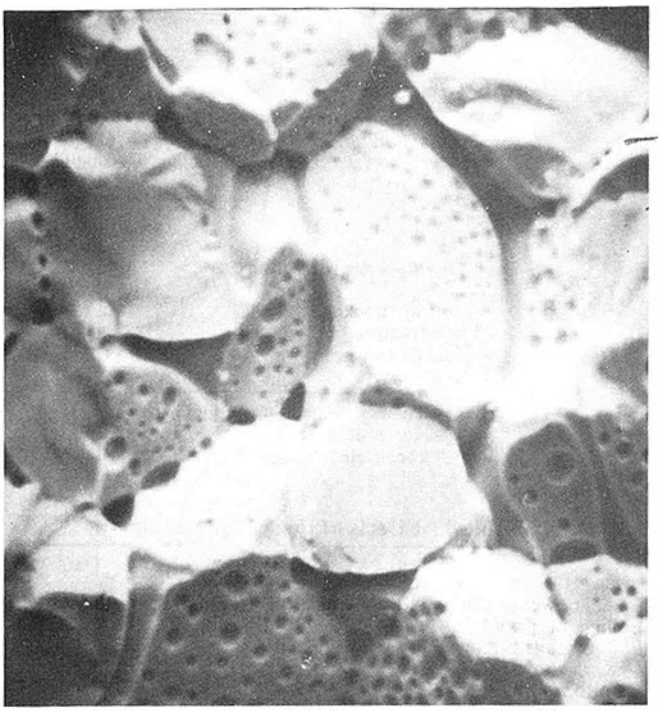

Fig. 9 P3A fuel scanning electron micrograph

Cladding failure was indicated by fission gas passing through outlet and total loop flowmeters at 10.8 and 11.6 s respectively. Extensive cladding melting occurred in the period 11.9 to 12.2 s as indicated by the wire-wrap thermocouple temperatures. Molten cladding was carried upward by sodium vapor streaming to form a partial blockage at the top. As this blockage started to form it increased the vapor pressure drop thereby reducing saturation pressure and temperature in the region above the blockage. This is confirmed by a temperature drop of 50K between 12 and 13 s as indicated by wire-wrap thermocouple located 55 cm above the heated region (Fig. 5). Other indications of the incomplete blockage were the passage of fission gas through both the outlet and total loop flowmeter throughout the transient. Also, after the reactor was scrammed and liquid sodium reentered the upper portion of the bundle, the upper void interface was maintained 146 cm above the bottom of the fuel. This indicates there was decay heat transfer from the test section. The major portion of molten cladding which then drained downward reached fuel midplane at 12.7 s and reached a location 20 cm above the bottom of the fuel at 13 s. The inlet flowmeter was showing flow oscillations around zero for ~60 s that eventually stopped at zero. This shows that the bottom blockage was complete but there is no clear indication of the time of formation.

The inner hexcan was heated extensively during and following the transient. Locally the hexcan was probably above the melting point of stainless steel and Inconel and perhaps near the solidus temperature of the niobium alloy (2675K). After reactor scram, there was a general increase in heat transfer from the bundle to the bypass beginning at 16 s. The two most probable causes for this increase in heat transfer were melting of the hexcan or melting of the Inconel spacer pieces with formation of a bridge from hexcan to outer duct. Posttest examination of the test section reveals melting of both the insulator spacer pieces and portions of the inner hexduct.

Posttest disassembly of the P3A test section shows limited fuel disruption and only slight relocation of the fuel. Figure 8 shows a cross sectional cut of the P3A test train at an elevation 0.6 m above the fuel bottom. The remains of the fuel pins form a bed of individual pellets in which the central voids are clearly visible and the fuel is severely swollen. It is not certain whether the collapse of the stack of pellets occurred before or after scram. Detailed metallography showed that the fission gas had moved to the grain boundaries (Fig. 9). These results support buckling of a stack of pellets and large scale swelling as modes of fuel disruption. Draining of fuel within a solid shell appears to be ruled out.

P3 Experiment. The P3 experiment continued to operate at full power up to 15.3 s as compared to 12.9 s for the P3A experiment. Pretest calculations indicated that termination at this time would allow dispersive mechanisms to develop but would stop the test prior to gross meltdown. Therefore, it was expected that P3 would reproduce and go beyond the early events observed in P3A although differences in hexcan material would have a minor effect on the sequence. Figure 6 compares the SAS3 predicted void front and thermocouple data, with a void front estimate based on the data shown for both central and edge channels. The two-dimensional effects are very evident during the first second of voiding, then they converge rapidly to one-dimensional voiding. These effects are more pronounced in the P3 experiment than P3A due to the higher heat capacity of the stainless steel hexcan.

SAS3D calculations predict cladding motion at 10.9 s, and a complete upper blockage formed by 11.2 s. At 11.9 s a complete lower blockage is forecast. The P3 data does not completely support this scenario. Initial cladding melting may be established based on time of thermocouple failure because cladding material and thermocouple sheath material melt at approximately the same temperature. Using these data, the failures occurred between 11.5 and 11.8 s. Furthermore, at 11.7 s a series of closely spaced spikes on the upper total flowmeter indicated the presence of noncondensible gas. Outlet thermocouple response agrees with SAS. The temperature rise slowed at 9.5 s and showed a small drop at 10.4 s. This drop was not the result of blockage formation but indicated momentary equilibrium between vapor formation in the bundle and vapor condensation at the liquid interface and at the hexcan walls. At 13.3 s, however, there was a dramatic

drop in temperature (similar to P3A, Fig. 5) as a result of blockage formation which significantly reduced vapor flow from the heated region. The formation of the lower blockage is readily observed in Fig. 4 as the frequency of flow oscillations changed from 3 Hz to 8 to 12 Hz at 13.3 s. The inlet flow oscillations can be modeled as a simple harmonic oscillator with a steady-state vapor bubble acting as a spring. For small displacements, the equation of motion is:

$$m\frac{d^2x}{dt^2}+\frac{C\times P}{L}=0$$

where m = the mass of the piston, x = piston displacement from equilibrium, c = piston area, P = local pressure, and L = bubble length.

The solution to this equation is a simple harmonic motion with frequency:

$$\omega=\sqrt{\frac{Cp}{2\pi ml}}$$

If the frequency is to change from 3 Hz to 8 Hz it is necessary for the length of the bubble to reduce by a factor of $(3/8)^2$. Assuming the original length of the bubble is 215 cm (length of the region from the bottom of the fuel to the top of the pin), the calculation leads to a reduced bubble length of 30 cm. Within one second the frequency had increased form 8 Hz to 12 Hz and a similar calculation reveals a bubble length of 13 cm, a factor of 7 smaller then the fuel region. If one assumes a lower vapor liquid interface constant during these frequency changes it is highly unlikely that the characteristics of the bubble formed by blockage at the top of the fuel could produce the observed frequencies. However, the calculated bubble dimensions are consistent with the blockage near the bottom of the fuel. This supports the hypothesis that a complete or nearly complete blockage formed at the bundle inlet at 13.3 s.

Posttest analysis (3) based in part on P3 thermocouple data show that it is probable that 30 percent of fuel at average power melted and that it is possible 100 percent of the fuel at peak power melted. Although ETR reactivity feedback indicated that fuel dispersed without slumping, the data from the developmental fuel motion monitors are inconclusive. By the time of the transient, only 8 of the original 35 detectors were operating and those had a very high noise level. Post experiment studies have shown that these difficulties may have arisen from fabrication techniques. A new set of detectors is being fabricated with modifications to improve lifetime and response for future SLSF tests.

Posttest examination of the P3 experiment is still in very early stages. However, radiographs of the test section do show significant fuel melting and some fuel motion. Disassembly of P3 is in progress.

Conclusions

- Sodium voiding during an LOF is relatively well understood and modeled using one dimensional expulsion models. There are some two dimensional effects in the early stages of voiding which are enhanced by radial heat loss. In particular, an extreme radial heat loss will cause an unprototypically slow boilout. (This phenomena would not occur in an LMFBR).
- Cladding motion and blockage formation occurs somewhat slower than had been originally predicted. In addition the blockage porosity predicted may be incorrect. An imprevious upper blockage is predicted and the data from both P3A and P3 suggest only a partial blockage. This partial blockage, however, is sufficient to cause cladding drainage and the formation of the lower blockage. The lower blockage appears to be complete and accurately timed.
- Some fuel disruption, although limited in nature, may occur due to falling stacks of pellets without the presence of large scale melting as observed in the P3A experiment. The presence of fission gas at grain boundaries may be a precursor to large scale swelling breakup. With large scale fuel melting and bundle disruption, the fuel tends to disperse monotonicaly upward as observed in P2 and P3. Although there are insufficient data to describe fuel motion exactly, a clear picture of macroscopic behavior emerges. From this, it is indicated that an energetic recriticality after an LOF accident is unlikely with oxide fuel.
- Agreement between SAS3D predictions and observed data is excellent for sodium voiding. SAS also correctly predicts the majority of the LOF sequence. However, it is not as accurate in clad predictions as in sodium voiding. In particular, the SAS model conservatively overpredicts the speed of formation of upper and lower blockages.

Acknowledgments

This work was performed under the auspices of the U.S. Department of Energy. The author wish to acknowledge contributions of the SLSF In-Reactor Experiments Section under the direction of J. H. Tessier and SLSF Technical Support Section under the direction of D. R. Pedersen in conducting these experiments. In particular I wish to thank G. L. Bordner, D. H. Thompson, and T. E. Kraft for individual experiment summaries, S. D. Thompson and K. J. Miles for data reduction, J. W. Holland and Larry Kelman for posttest disassembly, T. T. Anderson and T. A. McDonald for analog data reduction, SLSF Project Manager, D. H. Lennox, for editorial comments, and M. E. Reinke for manuscript preparation.

References

1 Bordner, G. L., "LIMBO Model for Interpreting and Predicting Voiding Dynamics in LMFBR Safety Tests," *Proceedings of the International Meeting on Fast Reactor Safety Technology*, Seattle, Wash., Aug. 1979

2 Bordner, G. L., "LIMBO Computer Code for Analyzing Coolant-Voiding Dynamics in LMFBR Safety Tests," ANL-79-91, Oct. 1979.

3 Kraft, T. E., et al., "Simulations of an Unprotected Loss-of-Flow Accident with a 37-pin Bundle in the Sodium Loop Safety Facility," *Proceedings of the International Meeting on Fast Reactor Safety Technology*, Seattle, Wash., Aug. 1979.

EBR-II Metallic Driver Fuel—A Live Option[1,2]

B. R. Seidel

L. C. Walters

EBR-II Project,
Argonne National Laboratory,
Idaho Falls, Idaho

The exceptional performance of metallic driver fuel has been demonstrated by the irradiation of a large number of Experimental Breeder Reactor II (EBR-II) driver-fuel elements of uranium-5 wt percent fissium clad in austenitic stainless steel. High burnup with high reliability has been achieved by a close coupling of element design and materials selection. The irradiation performance has been improved by decreasing the fuel smear density, increasing the plenum volume, increasing the cladding thickness, and selecting a higher-strength, lower-swelling cladding alloy which exhibits less fuel-cladding chemical interaction. Quantification of reliability has allowed full utilization of the element lifetime. Lifetimes much greater than 10 at. percent could be achieved by a design change of the restrainer, which currently limits life. Use of U-Pu-Zr fuel alloy with current cladding material would provide higher-temperature capability, as demonstrated by test elements. Metallic fuel systems with their inherently superior breeding and irradiation performance are capable and attractive next-generation power systems.

Introduction

Metal fuels were first used in LMFBR's (EBR-I, EBR-II, DFR, and Fermi) because of their superior breeding performance. With the technology of that time, a peak burnup of about 1 at. percent of the heavy-metal atoms was considered to be a reasonable objective for fuel-element design.

The next generation of LMFBR's (FFTF, CRBR, Phenix, and PFR) had as early design objectives the attainment of high sodium-outlet temperatures of the order of 600-650° C and high fuel burnups in the range of 10 at. percent. These designs began to evolve in 1966 and attention turned toward oxide and carbide fuels to satisfy these objectives, with oxide fuels emerging as the leading contender. As the designs matured in later years, the outlet temperatures were lowered to about 550°C. Although it was known that the breeding performance of oxide and carbide systems was inferior to that of metal fuels, the doubling times calculated for oxide and carbide systems were considered adequate. Metal fuels were not considered for two reasons. The high outlet temperatures of the early designs imposed fuel-cladding interface temperatures high enough to cause concern about excessive metallurgical interactions between fuel and cladding. In addition, the high burnup potential of metal fuels had not yet been demonstrated. Many believed that the performance of metal fuels would be limited by fuel swelling at a relatively low burnup.

While the rest of the LMFBR community turned its attention toward oxide and carbide fuels, Argonne National Laboratory (ANL) continued a developmental effort on metal fuels, as well as active participation in the oxide and carbide fuel programs. The original mission of EBR-II was to demonstrate the concept of an integrated plant in which fuel could be irradiated, reprocessed, and returned to the reactor. Although the first fuel used in EBR-II had a relatively low burnup potential, it was adequate to fulfill the fuel-performance requirements for this first mission. The goal of the first mission was successfully achieved when by 1969 a large number of fuel elements had been reprocessed and refabricated remotely in a facility adjacent to the reactor for further irradiation in the reactor. This feat has not been duplicated for any other fuel-element type.

The reason that ANL continued to develop metal fuels was directly related to the change in mission of EBR-II. The EBR-II facility became the nation's fuels and materials test reactor in development of LMFBR base technology. To minimize the cost of operating EBR-II as an irradiation test facility and to achieve a high plant availability to expeditiously gain irradiation data, it was necessary to extend the burnup capability through redesign of the driver-fuel elements.

A discovery by ANL personnel and the successful conversion of this discovery into a practical fuel-element design yielded a dramatic increase in the burnup potential of metal fuels. The early EBR-II driver-fuel design (Mark-IA) allowed only a 17 percent volume increase of the fuel before fuel-cladding contact [1]. The fission gas was retained in the fuel and although the cladding offered some restraint to fuel swelling, the cladding would eventually breach at a low burnup when the available cladding ductility was exceeded.

The early design philosophy was to attempt to limit the fuel swelling with the addition of suitable alloy elements and heat treatment. Parallel experimental irradiations of metal fuels

[1] Work supported by the U.S. Department of Energy.

Contributed by the Nuclear Engineering Division of THE AMERICAN SOCIETY OF MECHANICAL ENGINEERS presented at the Century 2 Nuclear Engineering Conference, San Francisco, Calif., August 9-21, 1980. Manuscript received at ASME Headquarters April 4, 1980. Paper No. 80-C2/NE-23.

were being carried out in the ANL-CP-5 reactor [2]. These irradiations showed that when swelling from fission-gas bubble growth was allowed to exceed ~25 percent, the larger gas bubbles began to interconnect among themselves and with the fuel surface. Most of the fission gas was released from the fuel if it was permitted to swell more than 30 percent. It was reasoned that the fuel element would exhibit higher burnup capability if the designs permitted interconnected porosity with consequent gas release to occur before the fuel contacted the cladding. Fuel with interconnected porosity was thought to be relatively weak and it should, therefore, be easily restrained by the cladding. The porosity would also be available to accommodate the inexorable swelling from solid fission products.

The EBR-II Mark-II fuel element was designed to take advantage of the phenomenon of interconnected porosity. The smear density of the fuel was 75 percent, which allowed 33 percent volume swelling of the fuel before fuel-cladding contact. This magnitude of swelling was well beyond the extent required to produce interconnected porosity and gas release. The gas plenum was designed with sufficient volume to keep the plenum pressure, due to the released gas, reasonably low over the life of the element.

The final step required to realize the full benefit of the improved driver fuel came with the development of a means to establish the optimum burnup limit for the fuel. Early methods utilized a "bootstrapping" technique whereby if lead subassemblies performed adequately, then the remainder of the core would be allowed to achieve a burnup near that of the examined lead subassemblies. The technique was deficient in many respects, particularly the expense of examining the lead subassemblies at a given burnup increment and the uncertainty as to whether enough lead subassemblies had been examined to justified an increase in burnup for the entire core.

A disciplined method for core qualification evolved at EBR-II that serves as a benchmark for future LMFBR core qualifications [3]. A small number of subassemblies containing xenon-tagged elements are intentionally run to cladding breach. The location of breach is determined through post irradiation examination and this information is further utilized for safety analyses. The burnups at breach for these subassemblies are then analyzed with Weibull statistical methods to give a quantitative assessment of the likelihood of breach, at any given burnup, in an entire core loading of fuel.

Following qualification, a surveillance activity must be maintained whereby a small number of subassemblies are subjected to examination after the burnup limit is achieved, to insure that the fuel is performing in a manner representative of fuel intentionally operated to cladding breach. If the performance is not as expected, then further qualification may prove necessary. The combination of a disciplined qualification effort followed by the surveillance activity has resulted in negligible plant downtime due to unanticipated fuel-element breach and, at the same time, has resulted in the optimum burnup for economic utilization of fuel.

The purpose of the present paper is to briefly review the EBR-II experience with design and fabrication of metallic driver fuel and then discuss the performance of the driver fuel to high burnup. The experience gained with EBR-II driver fuel when coupled with the results from limited testing of advanced metallic fuel systems will then be used as a basis to discuss the direction for potential utilization of metallic fuels in future LMFBR's.

Element Design and Fabrication

The EBR-II driver-fuel-element design has been changed from the initial Mark-I to the Mark-IA, and finally to the Mark-II. The important design features of the element types are compared in Table 1 and Fig. 1. With the small plenum of the Mark-I design, it was calculated that, for fuel-swelling volume changes in excess of 8 percent, the pressure inside the element would begin to approach the postirradiated burst strength of the cladding [4]. Since an 8 percent volume-swelling change of the Mark-I fuel was attained at a fuel burnup of 1.2 at. percent, this burnup was established as the initial limit. Then it was reasoned that if the gas-plenum volume could be increased relative to a given fuel-volume change due to swelling, the internal pressure would be less and the burnup limit could be extended. The Mark-IA was therefore designed with a shorter pin to increase the plenum volume and the ^{235}U enrichment was increased to compensate for the shorter pin. However, at the same time the design change was instituted, the fuel used for the Mark-IA exhibited a higher swelling rate, and this led to a plenum-volume decrease that almost exactly canceled the potential benefit of the design change.

The Mark-II design was instituted to take advantage of the interconnected-porosity phenomenon, which has been described earlier, so that by the time of fuel-cladding contact, interconnected porosity had occurred. Several design variations that included the type of fuel-pin restrainer, the magnitude of the plenum volume, and the cladding alloy were explored prior to the choice of the reference Mark-II design [3]. The important design changes of the Mark-II compared to the Mark-IA were the lower smear density, the larger plenum volume, the thicker cladding, and the cladding material.

The composition of the EBR-II driver fuel has always been uranium-5 wt percent fissium, with the 5 wt percent fissium being 2.4 wt percent molybdenum, 1.9 wt percent ruthenium, 0.3 wt percent rhodium, 0.2 wt percent palladium, 0.1 wt

Table 1 Design features of the Mark I, Mark-IA, and Mark-II driver-fuel elements

	Mark I	Mark-IA	Mark-II
Fuel Alloy, wt percent	U-5 Fs	U-5 Fs	U-5 Fs
Enrichment, (at. percent ^{235}U)	48.4	52.5	67.0
Fuel Pin Length, mm	361	343	343
Fuel Pin Diameter, mm	3.65	3.65	3.30
Fuel Volume, m^3	3.8×10^{-6}	3.6×10^{-6}	2.9×10^{-6}
Fuel Smear Density, percent	85	85	75
Fuel/Clad Radial Gap, mm	0.152	0.152	0.254
Cladding Wall Thickness, mm	0.23	0.23	0.30
Cladding, o.d., mm	4.42	4.42	4.42
Cladding Material	304L (SA)	304L (SA)	316 (SA)[1]
Element Length, mm	460	460	612
Plenum Volume,[2] m^3	0.50×10^{-6}	0.67×10^{-6}	2.41×10^{-6}

[1] Solution-annealed Type 316 stainless steel is presently the reference cladding material. Some experimental Mark-II elements were clad with solution-annealed Type 304L stainless steel.

[2] At room temperature.

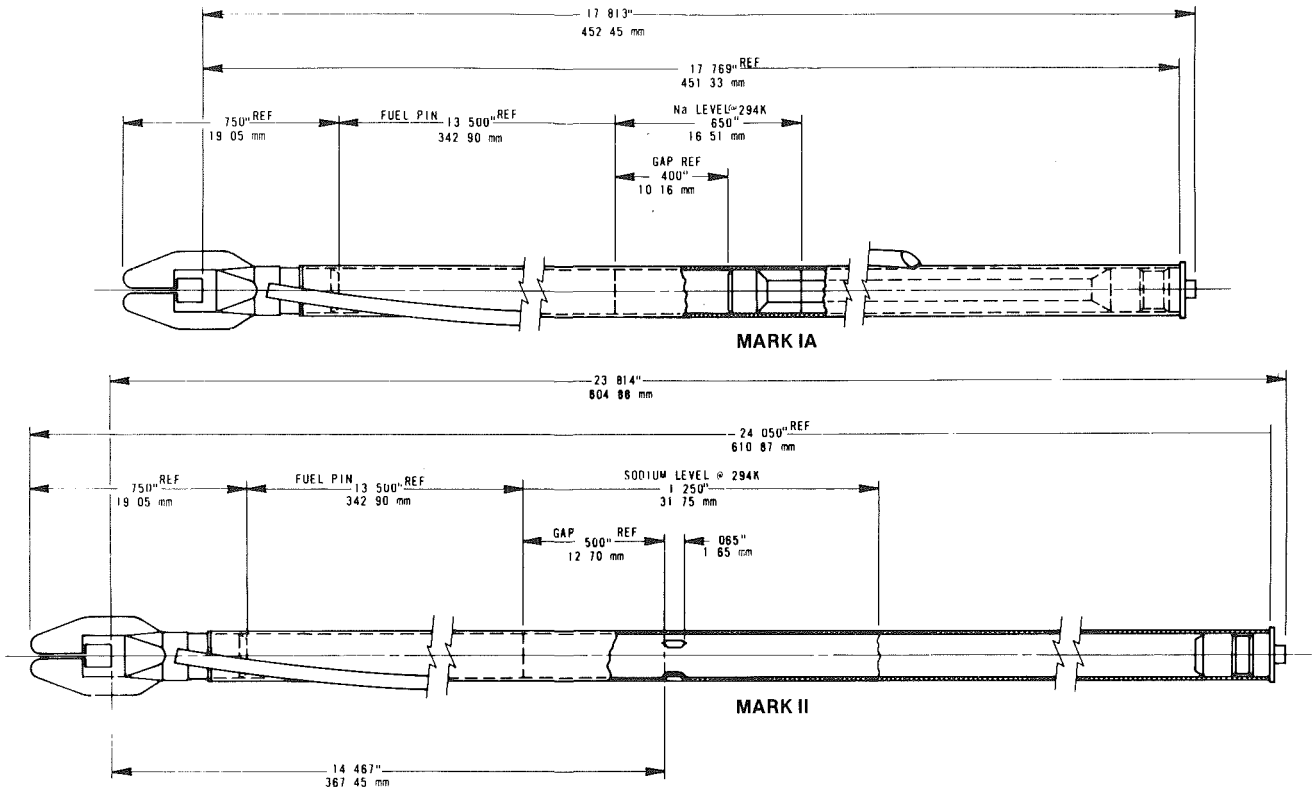

Fig. 1 EBR-II driver-fuel designs

percent zirconium, and 0.01 wt percent niobium. This particular composition arises in the following way. During pyrometallurgical reprocessing, the EBR-II fuel was melted in a zirconia crucible [5-9]. The fission-product gases (xenon and krypton) and the condensable fission products (cesium and iodine) were almost entirely released from the melt, and the electropositive fission products (alkaline-earth and rare-earth elements) reacted with the zirconia crucible to form oxides. Molybdenum, ruthenium, rhodium, palladium, niobium, and technetium were not removed as a result of the melting, and some zirconium remained with the melt as well. During irradiation, the concentration of the elements increased at the rate of about 0.35 wt percent per at. percent burnup of the heavy metals. Thus, if the fuel burnup were 1 at. percent prior to reprocessing, then each time the fuel was refabricated, irradiated, and reprocessed, the fissium content would increase by 0.35 wt percent. However, in the actual reprocessing, a skull formed in the zirconia crucible that contained the oxided fission products, as well as some unpoured uranium metal. The skull represented about 5-10 percent of the original furnace charge and, thus, the uranium metal that was removed with the skull was replaced with pure uranium of the proper enrichment. This addition of pure uranium eventually resulted in a steady-state value for the fissium content, because as much fissium was removed with the skull as was generated during irradiation to 1 at. percent burnup. If the original fuel were pure uranium, after many reprocessing cycles of fuel with a burnup of 1 at. percent the fissium would reach the equilibrium value of 5 wt percent. The selected alternative was to simply start with a fuel containing 5 wt percent simulated fissium and, in this way, the irradiation performance did not change appreciably after each reprocessing cycle. In addition, the 5-wt-percent-fissium alloy was beneficially found to have a much lower swelling rate than pure uranium.

The first step in the manufacture of fuel elements was the injection casting of enriched uranium-5 wt percent fissium pins from a melted prealloyed ingot into Vycor[3] molds [10]. The pins were cast to final diameter and were sheared to length upon removal from the molds. The pins were subsequently inserted into wire-wrapped stainless steel jackets with an extruded mass of sodium. After heat was applied to settle the sodium, an end plug was capacitance-discharge welded to the top end of the element. This entire process was carried out in an inert-atmosphere hot cell, for reprocessed fuel – or in a glovebox, for cold fuel.

Batches of elements were heated in a bonding furnace at 500°C for one hour to transform the metastable gamma phase

Table 2 Production and procurement history of EBR-II driver fuel

Dates	Quantity	Manufacturing Source
	Mark-IA Elements	
6/60-2/61	10,781	ANL Cold line (East)
10/67-12/69	14,457	ANL Cold line (West)
9/64-4/69	34,976	ANL Hot Line (West)*
1/67-8/71	22,358	Procured from Vendor
7/73-2/74	11,241	ANL Cold line (West)
4/75-9/75	3,586	ANL Cold line (West)
Total	97,399	
	Mark-II Elements	
8/69-9/69	780	ANL Cold line (West) (Preliminary Production)
11/72-6/73	4,492	ANL Cold line (West) (1st Production)
3/74-2/75	16,945	ANL Cold line (West) (2nd Production)
11/75-8/76	6,749	ANL Cold line (West) (2nd Production)
5/73-9/76	24,200	Procured from Vendor
Total	53,166	

*Remotely reprocessed and refabricated in EBR-II Fuel Cycle Facility.

[3] Vycor is a trade name for high-silica glasses from Corning Glass Works.

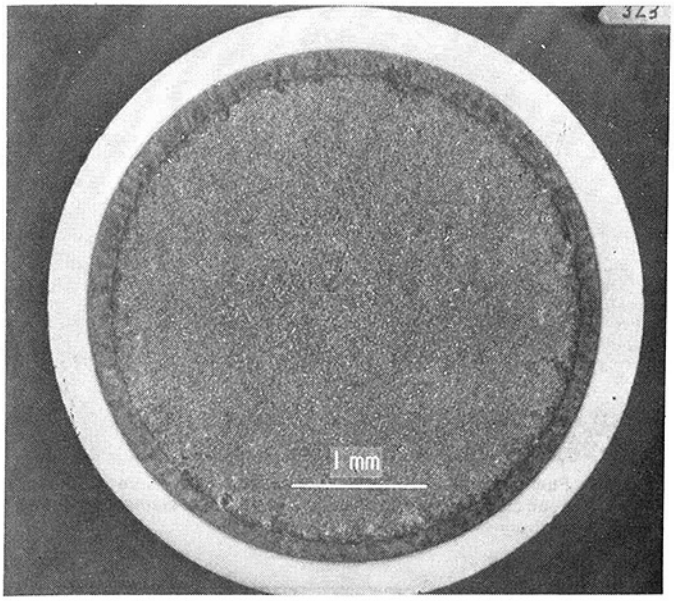

Fig. 2 Fuel structure of Mark-II driver-fuel element near top of fuel column (~575°C peak cladding temperature) at 7.9 at. percent burnup

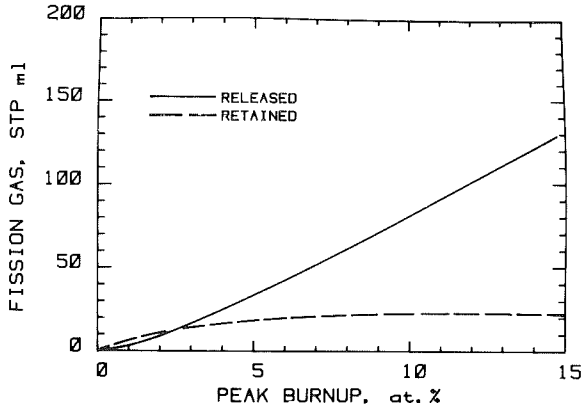

Fig. 3 Released and retained fission gas in Mark-II fuel elements

to the alpha phase. The elements were then repeatedly impacted to insure a uniform bubble-free bond of sodium around the fuel pin. The elements were leak-tested and inspected for bond quality before release for reactor use.

This fuel-fabrication process was successfully applied by ANL for both fabrication of cold fuel and remote fabrication of fuel elements that were reprocessed in a hot cell. Additionally, the process was used by two vendors for supply of EBR-II driver fuel. Table 2 summarizes the procurement history of EBR-II driver fuel.

EBR-II Driver-Fuel Performance

The current exceptional performance of EBR-II driver fuel has been due to successes with both design and materials.

The element design, as described earlier, was modified to take advantage of the observed fuel swelling and subsequent fission-gas release in metallic fuels. The stresses within the cladding were decreased by increasing the plenum volume and the cladding thickness. Replacement of the Type 304L cladding material with Type 316 material increased the strength, decreased the irradiation swelling rates, and decreased the fuel-cladding chemical interaction rates.

At present, the Mark-IA design is limited to 3 at. percent burnup at a peak cladding temperature of 550°C, and the Mark-II design is limited to 10 at. percent at 590°C peak cladding temperature. Since the dimple restrainer of the Mark-II element has been the preferred site for end-of-life breaches, an alternative design would be expected to exhibit even longer life. If more fuel were needed for EBR-II operation, a new design based on current experience would unquestionably surpass 15 at. percent burnup.

The key to this success and to development of its future potential lies in an understanding of the proven consistent behavior of the EBR-II driver fuel. The significant materials-related, steady-state performance characteristics of metallic EBR-II driver fuel are related to fuel swelling, fission-product distribution, fuel-cladding chemical interaction, diameter increase, cladding breach, and resultant lifetime.

Fuel Swelling. Fuel deformation is due primarily to retained fission gas and solid-fission-product accumulation within the matrix. Early irradiations indicated that the swelling rate of uranium-5 wt percent fissium was reduced with increased minor amounts of impurities, silicon in particular [11]. Although the rate determined the exposure at which the fuel contacted the cladding, the significant issue was whether the fuel smear density was sufficiently low to allow release of fission gas via interconnected porosity. In a Mark-IA fuel element with a smear density of 85 percent, the fuel contacted the cladding over the full extent of the fuel column by 1.8 at. percent burnup [11]. Within an additional 1.5 at. percent burnup, the loading on the cladding by the deforming fuel in addition to the high plenum pressure caused breach in the fuel-column region [1]. In contrast, in the Mark-II fuel element with a smear density of 75 percent, the fuel came into full contact with the cladding by 3.2 at. percent burnup and the element proceeded an additional 7 at. percent burnup before breach occurred in the dimple restrainer at the top of the fuel column [12].

The fuel swelled at equivalent rates for equal temperatures in both designs, but the low-smear-density design allowed dynamic and repeated swelling of the matrix fuel into the continually developing and decaying interconnected porosity (Fig. 2). This dynamic process of closed fission-gas porosity growing and interconnecting and then being eliminated by additional fuel swelling never occurred in the Mark-IA element, whereas several complete cycles were achieved in the Mark-II element.

The fuel deformation was primarily radial and was readily restrained when interconnected porosity was allowed. Axial deformation also could be restrained, but apparently was self-limiting [13]. Axial restraint may be necessary, however, to limit fuel-pin liftoff. (Liftoff is a term describing the observation of fuel being displaced above the lower fuel-pin support.) The mechanisms of fuel-pin liftoff are currently being investigated.

Fission-Product Distribution. About 11.5 cm^3 of fission gas were generated for each at. percent burnup in the driver-fuel elements [14]. Because of the restrained fuel swelling in the Mark-IA element, only 7 percent of the fission gas was released. In the Mark-II element, however, once interconnected porosity began to develop, most of the subsequently formed fission gas was released, as shown in Fig. 3. The retained-fission-gas curve demonstrates that fission gas was released at the same rate that it was generated in the matrix. At the Mark-II operating temperatures, the stresses generated within the fuel by about 20 cm^3 of retained fission gas were sufficient to deform the fuel into the open porosity and available free space.

The fission gas that had accumulated in the plenum and the gas-plenum volume were measured during postirradiation examination of the elements. The plenum pressure of Mark-II elements at operating temperatures of 527 ± 100°C increased

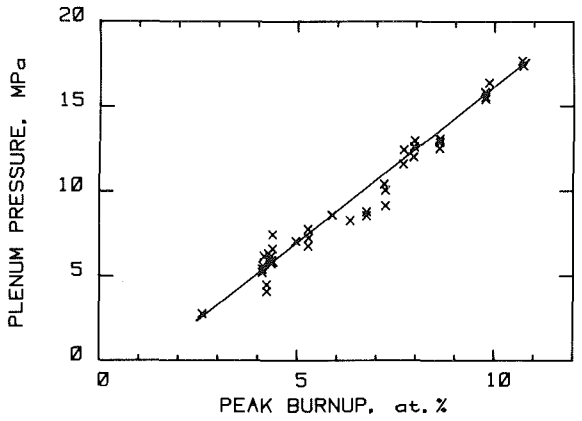

Fig. 4 Plenum pressure in Mark-II fuel elements

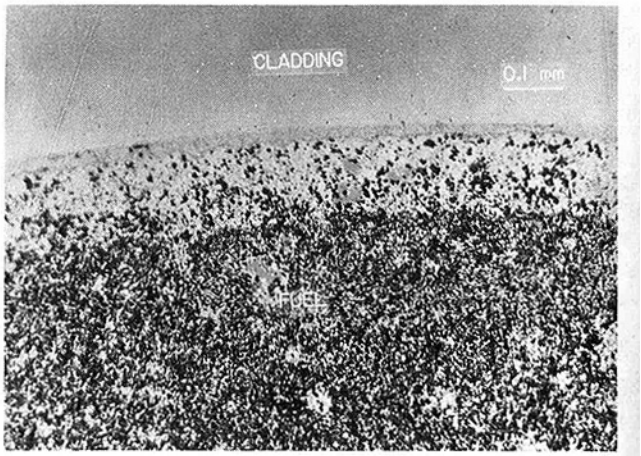

Fig. 5 Fuel-cladding chemical interaction near core midplane (~480°C peak cladding temperature) in a Mark-II fuel element at 10.3 at. percent burnup

linearly with increasing burnup in the range of 4–10 at. percent, as shown in Fig. 4 [15]. The plenum volume and pressure of Mark-IA elements were difficult to assess since the fuel swelled and displaced the bond sodium to the plenum, essentially reducing the gas volume in the plenum to zero.

The liquid fission products, primarily cesium with a 16 percent fast-fission yield [14], were distributed between the fuel and the bond sodium. Cesium was distributed within the bond sodium, in the interconnected porosity in the fuel column, and in the bond sodium above the fuel column in Mark-II elements. Very little cesium was observed in the bond sodium of Mark-IA elements. Recent gamma scanning of several elements has shown that the amount of cesium released to the bond sodium in the plenum region increased with burnup, and that up to 40 percent had been transported above the fuel at 5.5 at. percent burnup. The ^{133}Cs species as detected by the ^{134}Cs activation product was more concentrated in the plenum than the ^{137}Cs species, since the longer-lived gaseous precursors of ^{133}Cs were partially or fully transported to the plenum before decaying to cesium.

The solid fission products remained in the fuel matrix either in solid solution or as intermetallic-compound precipitates. Since the subsequent volume increase was limited (~2 vol. percent per at. percent burnup), the accumulation only becomes significant for high-smear-density designs. The fuel-element diameter increase due to irradiation swelling and creep may wholly offset the accumulation of solid fission products at high burnup. Since the Mark-IA burnup was limited to 3 at. percent, solid-fission-product accumulation was minimal. At 10 at. percent burnup in the Mark-II element, the solid-fission-product accumulation may have increased the smear density sufficiently to retard the interconnection of porosity.

Fuel-Cladding Chemical Interaction (FCCI). Primarily, nickel diffused from the Mark-II Type 316 stainless steel cladding into the fuel, leaving a nickel-depleted zone in the cladding and an enriched zone in the fuel [13, 15]. Only limited diffusion of the uranium into the cladding occurred. The interaction zone exhibited uniform fronts at both the fuel and the cladding interfaces (Fig. 5). Only 5 percent of the cladding wall thickness was consumed at more than 10 at. percent burnup at peak cladding temperatures of 590°C. The penetration into the fuel was found to be 3–10 times greater than penetration into the cladding.

Because of the limited exposure of the Mark-IA elements, no FCCI was observed. Irradiation of Mark-II elements clad with Type 304L stainless steel, however, indicated that interpenetration was much greater than that observed with 316 stainless steel [13].

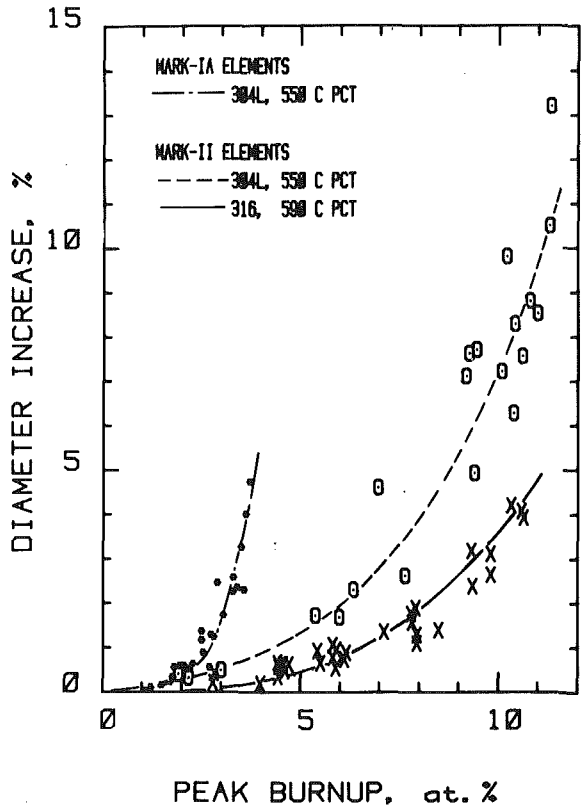

Fig. 6 Diameter increase of Mark-IA and Mark-II fuel elements with increasing burnup

Diameter Increase. The peak diameter increases observed for the two element designs with increasing burnup were significantly different. As shown in Fig. 6, the increase at equivalent burnup for the 304L-clad Mark-IA elements was greater than observed for Mark-II elements clad with 304L stainless steel, and much greater than that exhibited by the reference-design 316 stainless steel cladding.

The diametral increase along the axis of a representative Mark-IA element is shown in Fig. 7. The peak diameters were observed between the midplane and the top of the fuel column, where the convolutions of flux and temperature were maximum. The peak diameter increase of the Mark-II elements was located above the core midplane also. Large diameter increases were observed at the top of the fuel column near the dimple restrainer (Fig. 8).

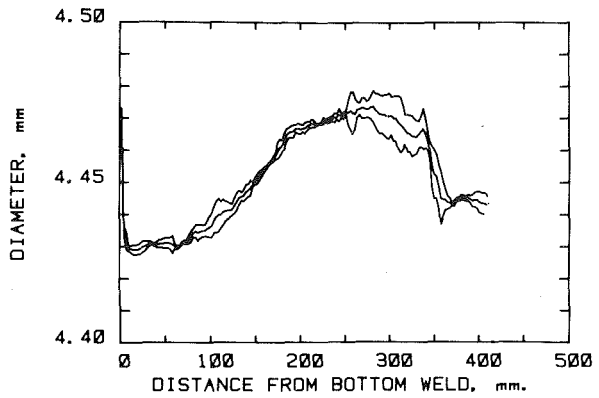

Fig. 7 Major, minor, and equivalent circular diameters of a Mark-IA fuel element at 2.5 at. percent burnup

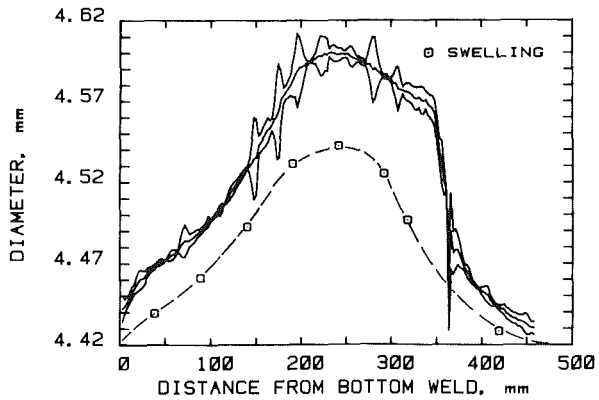

Fig. 8 Major, minor, and equivalent circular diameters of a Mark-II fuel element at 10.5 at. percent burnup and the contribution of irradiation swelling to diameter increase

The increases in diameter resulted from irradiation swelling and creep. About 50 percent of the peak diameter increase of the Mark-IA elements was due to swelling as measured by immersion-density techniques [1]. The resolution of diameter increase into creep and swelling components, as shown in Fig. 8 for a representative element, has indicated that the swelling component typically comprises 67–85 percent of the total increase in a Mark-II element.

Interaction between each element and its spacer wire developed with increasing burnup. Since the temperature of the spacer wire was below that of the cladding, the swelling rate of the wire was less also. The spacer wire became tighter and tighter with increasing burnup. Elements examined after 11.5 at. percent burnup exhibited a helical aspect due to constraint by the wire. The diametral profile of the Mark-II element as shown in Fig. 8 is representative of the periodic ovality due to element/spacer-wire interaction at the elevations of contact between the element, its spacer wire, and adjacent spacer wires. In general, the orientation of the ovality in cross section had no correspondence with the spacer wire until the diameter increase of the elements in the bundle was sufficient to cause interaction. Above 1 percent dia increase, the interaction caused the ovality to be oriented in relationship with the spacer-wire position, as illustrated in Fig. 9.

Interaction between the 61 Mark-IA elements in control- and safety-rod subassemblies and the hexagonal subassembly duct with a nominal flat-to-flat outer dimension of 46.6 mm was predicted to begin at a diameter increase of 0.5 percent, based on nominal minimum tolerances. At that average diameter increase, the elements along the hexagonal diagonals would just contact each other.

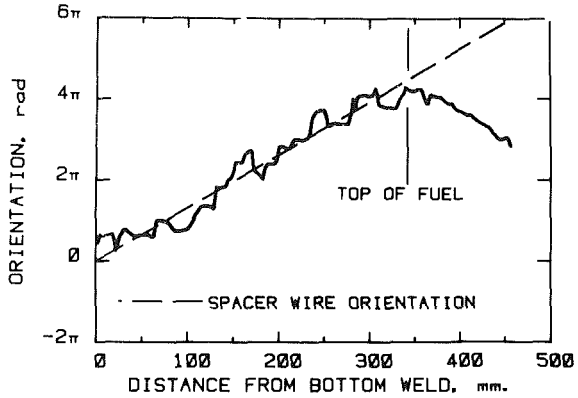

Fig. 9 Orientation of the minor diameter of the ovality exhibited by a Mark-II fuel element and the position of the spacer wire

Contact with the hexagonal duct initially occurs at elevations periodic with the pitch of the spacer wire. Additional diameter increases of the elements and the spacer wire of each can only be accommodated by bending of the element in the direction opposite the spacer wire until the diameter increase consumes the initial clearance of one spacer-wire diameter. With no increase in the dimensions of the hexagonal duct, the elements can only increase 3.6 percent in dia before rearrangement of the elements within the bundle is required.

The driver-fuel subassembly with a nominal hexagonal flat-to-flat outer dimension of 58.2 mm contains 91 elements. Interaction between the elements occurs at a 0.4 percent dia increase, based on nominal minimum tolerances. Element bending allows accommodation of diameter increases to 3 percent.

Swelling and creep of the hexagonal duct of the control and safety rods is constrained by a guide ring near the core midplane. However, the driver-fuel hexagonal duct is only constrained by its neighbors. Known increases in the driver-fuel duct [16] allow clearance to accommodate additional element diameter increases of 1.8 percent before the elements and spacer wires must either rearrange within the bundle or begin to stress the duct.

The burnup at which each of the types of interaction for the fueled subassemblies began can be estimated from the known diameter increases (Fig. 6). Since the elements in the outermost row of the subassembly operated at lower temperatures and therefore exhibited less diameter increase, the average diameter increase of all the elements in a subassembly would be slightly less than described by the curves in Fig. 6.

Subassemblies of each type are currently being impregnated with a low-melting eutectic alloy in preparation for transverse sectioning and subsequent analysis of interactions within the whole bundle of elements.

Cladding Breach and Element Lifetime. Breach of Mark-IA cladding has always occurred in the fuel-column region. The defects were intergranular in nature and originated on the outer cladding surface. Olson [1] has described the breach characteristics and statistically determined that the threshold for breach was 3 at. percent burnup for nominal 550°C beginning-of-life peak cladding temperatures. Subsequent irradiations have shown that the lifetime was decreased to 2.7 at. percent burnup for slightly higher operating temperatures.

Breach of Mark-II driver-fuel elements has been at substantially higher burnups. Weibull statistical analysis of lifetime based on measured lifetimes obtained from run-to-cladding-breach subassemblies has permitted an increase in exposure limit from less than 1 to 8 at. percent burnup. Early

information was obtained from experimental elements irradiated in capsules to breach. The elements were clad with 304L stainless steel and were either 610 or 660 mm in length; they also incorporated several other new design features [13]. The additional plenum length of 50 mm provided an additional 1.5 at. percent burnup of life over the minimum life of 8.9 at. percent burnup. All the breaches occurred in the fuel-column region. One element has surpassed 16.4 at. percent burnup without breach.

Reference-design Mark-II elements clad with 316 stainless steel have consistently breached in the dimple restrainer above 10 at. percent burnup [12]. The defects (Fig. 10) originated on the outer surface, were intergranular and about 3 mm long, and appeared to have resulted from bending of the dimple due to high stresses at the inner cladding surface. Defects have been observed in all the dimples of breached elements as shown in Fig. 11. No defects have been observed at lower burnups.

Weibull statistical analysis of the dimple breaches has shown that no breaches could be expected below 10 at. percent burnup and that the breach rate was very high once that burnup was surpassed. Several breaches since the early analysis have verified the validity of the lifetime correlation for Mark-II elements exhibiting dimple breach.

Recently, breach was observed between 9 and 12 at. percent burnup in the plenum region of one element each from two subassemblies irradiated at a slightly lower cladding temperature but higher heat rating. One breach was located near the upper spacer-wire-to-tubing weld. The defect was very small and intergranular in nature. Further analysis is expected to determine if the defect was due to interaction between the element and the spacer wire. The defect in the other breached element was too small to detect, even by internal pressurization to 38.6 MPa; but from fission-gas release data, weight measurement, and activity smears of the outer element surface, the position of the defect was limited to the plenum region. The implications of these results are that an additional mode of breach was in competition with the dimple mode under certain conditions. Further irradiations are in progress to verify the reality of the plenum breach mode. One driver-fuel subassembly has surpassed 16.5 at. percent burnup under these conditions without breach.

In addition to RTCB experiments, irradiation of large numbers of driver-fuel elements to high burnup without breach has shown the reliability of the element. Figure 12 graphically illustrates the reliability proven by irradiating the driver fuel to the increased burnup limits of 4.7, 6, and 8 at. percent. The RTCB irradiations have defined the region of proven unreliability. A significant margin of reliability exists between the current 8 at. percent burnup limit and the initiation of dimple breach. The margin of reliability appears to be less for elements limited by plenum breach – but this conclusion is tentative since it was based on only two end-of-life events.

The lifetime of Mark-II elements was also decreased by irradiation at higher temperature. Dimple breach has been observed at 9.2 at. percent burnup in an element operated at 615°C peak cladding temperature. A second experimental irradiation at higher temperature has surpassed 10 at. percent burnup without breach; sibling elements at normal temperature have breached in the dimple at 11.5 at. percent burnup.

Performance Summary. In summary, the Mark-IA element has performed adequately to end of life. Useful life was limited because the high-smear-density design did not allow significant fission-gas release and because of a very limited plenum volume. Had the design been improved, the life would have been limited by the materials performance of the 304L cladding.

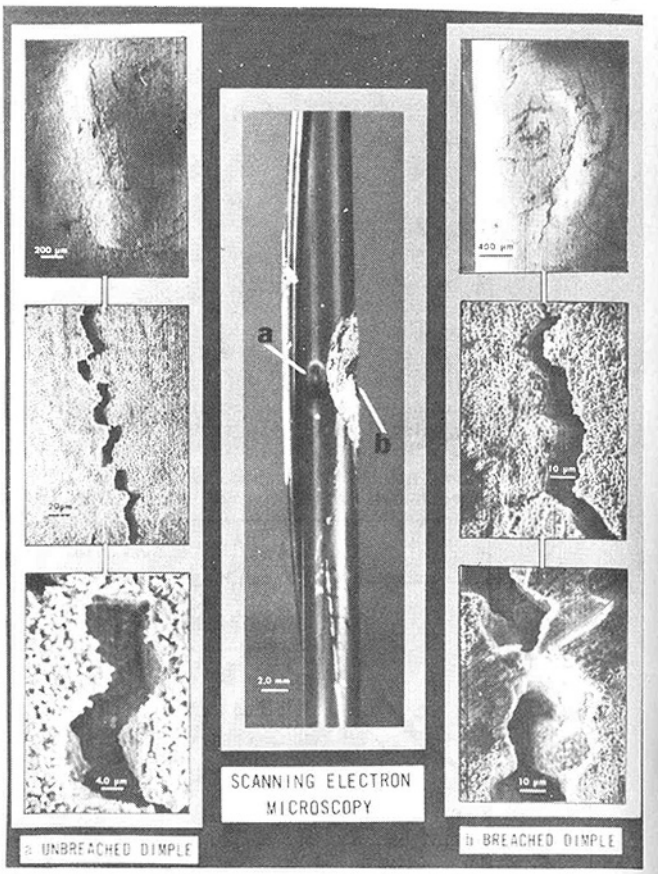

Fig. 10 Scanning-electron micrographs of the outer cladding surface in the dimple region of a breached Mark-II fuel element at 10.7 at. percent burnup

The Mark-II element has performed beyond all expectations because of the low smear density and the fuel-to-plenum ratio of 1.2. The 316 stainless steel cladding material exhibited less swelling, creep, and FCCI. Lifetime was limited by breach in the dimple restrainer at burnups greater than 10 at. percent. The life could be extended by a design change. The high reliability of the Mark-II element has been verified by lead RTCB irradiations and the irradiation of several thousand elements to high burnup without breach.

Advanced Metal Fuels

The two early objections to the use of metal fuels are no longer valid. As described in the previous section of this paper, the high-burnup capability of metal fuels has been demonstrated through the performance of EBR-II driver fuel. Furthermore, current designs of LMFBR's have revealed a trend toward lowering sodium-outlet temperatures to a range where metal fuels have adequate compatibility with cladding materials.

A U-Pu-Zr fuel alloy clad with stainless steel is a promising fuel system for future LMFBR applications where temperatures greater than those generated in EBR-II are required [17, 18]. The burnup potential of this fuel system is expected to parallel the experience gained from the EBR-II Mark-II driver fuel for a design with a low smear density to take advantage of the phenomenon of interconnected porosity. Figure 13 shows that interconnected porosity and gas release are independent of the fuel composition and that significant release occurs at about 25 percent volume swelling [2].

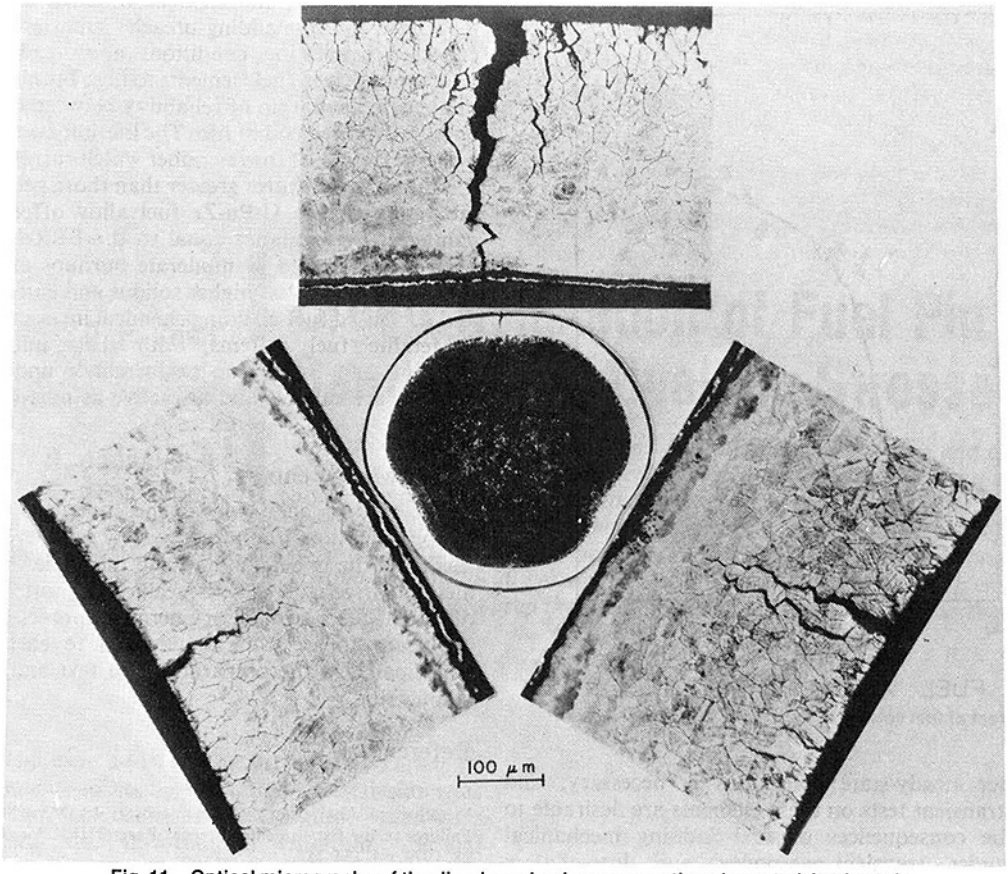

Fig. 11 Optical micrographs of the dimple region in cross-section characterizing breach

Although high-burnup information does not exist for the U-Pu-Zr system, a significant number of elements were irradiated to moderate burnups. A maximum burnup of 5.6 at. percent was achieved by 33 elements that contained metal fuel pins of U-15 wt percent Pu-X at. percent Zr (X ranged from 9-12) with several different cladding materials, without any performance degradation. Small cladding-diameter changes and high fission-gas release were observed, which supported the interconnected-porosity weak-fuel concept. The peak cladding temperature of these elements was 640°C.

Metallurgical compatibility of the U-Pu-Zr fuel with stainless steel cladding materials is expected to be comparable and perhaps superior to that observed for uranium-5 wt percent fissium fuel [17, 18]. Eutectic formation under transient overtemperature conditions and, as well, fuel penetration into the cladding during steady-state irradiation conditions are issues that must be addressed when assessing the reliability of a metal-fuel-element design. Zirconium additions to metal fuel alloys are not only effective in elevating the fuel-cladding eutectic temperature and the solidus temperature of the alloy, but tend also to decrease fuel-cladding penetration rates. For example, the eutectic temperature of 825°C for U-15 wt percent Pu-10 wt percent Zr and Type 304 stainless steel is higher than the eutectic temperature of 705°C for U-5 wt percent fissium and Type 304 stainless steel and well above the 640°C peak cladding temperature projected for a 1000-MWe LMFBR. Lidkewise, it has been shown that the interaction zone that develops between the fuel and cladding during normal operation by chemical interdiffusion is only about 0.4 mm for a one-year in-reactor exposure of U-Pu-Zr fuel clad with Type 316 stainles steel operating at a peak cladding temperature of 650°C.

Although the U-Pu-Zr fuel alloy system is a promising

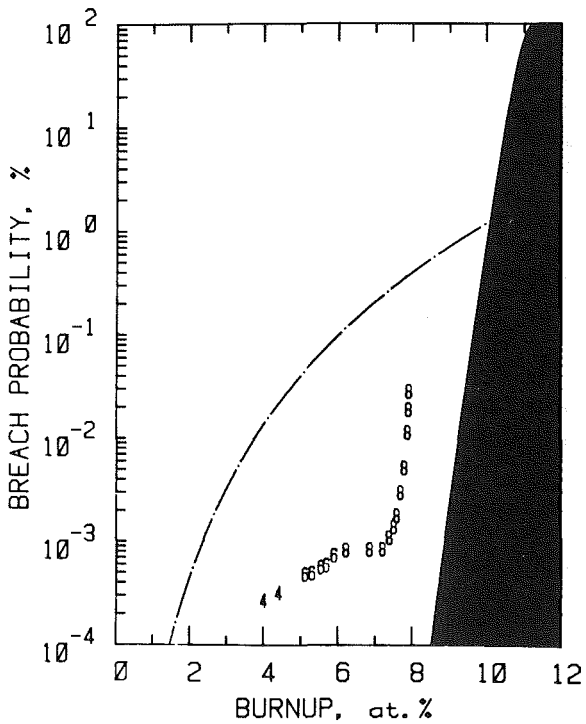

Fig. 12 Quantified reliability of Mark-II driver-fuel elements

LMFBR driver fuel on the basis of work to date, additional development is required to demonstrate commercial viability. Irradiation information to high burnup on full-size fuel

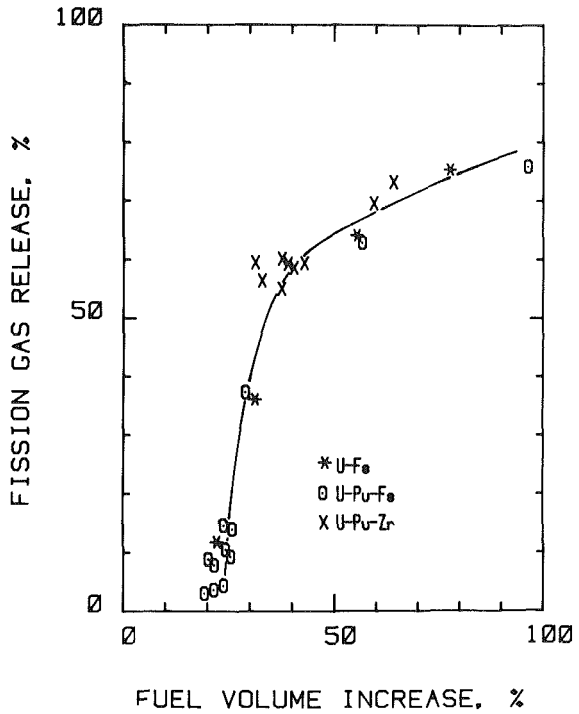

Fig. 13 Effect of fuel volume increase of fission-gas release

elements under steady-state conditions is necessary, and additionally, transient tests on these elements are desirable to understand the consequences of fuel-cladding mechanical interaction under transient-overpower and loss-of-flow situations. The superior breeding performance of metal-fueled systems [19] justifies the additional development work required to establish these fuels as an attractive alternative to ceramic fuels of current interest.

Conclusions

The metallic EBR-II driver fuel of uranium-5 wt percent fissium clad with austenitic stainless steel has demonstrated exceptional performance to high degree of confidence under real operating conditions that equal or surpass the requirements of the next generation of power systems. The consistent behavior of the driver fuel from fabrication, through irradiation, to remote reprocessing has allowed the EBR-II reactor system to operate without constraint to high plant factors.

The exceptional irradiation performance to high burnup with high reliability has been achieved by a close coupling of element design and materials selection. Improvements in performance have been reached through better understanding of a large body of irradiation performance data. The most significant step was taken after it was learned that interconnected porosity with subsequent fission-gas release occurred after about 25 percent fuel volume swelling. The design was changed by reducing the fuel smear density to 75 percent and also increasing the plenum volume. The fuel structure was then allowed to evolve dynamically as the fuel matrix deformed into open porosity, generating new open porosity. As a consequence, the fuel swelling was more easily constrained. The decreased smear density and increased plenum also provided better accommodation of fission products. The improved cladding material and increase in thickness provided increased strength, decreased swelling, decreased component interaction, and decreased fuel-cladding chemical interaction. As a result, the lifetime was significantly increased.

Quantification of lifetime by statistical analysis allowed full utilization of the element lifetime. Irradiation of intentional run-to-cladding-breach subassemblies under all expected irradiation conditions and irradition of a large number of driver-fuel elements to high burnup without breach has verified a margin of reliability between the exposure limit and the expected end of life. The lifetime could be extended by a design change of the restrainer which currently limits life.

Where temperatures greater than those generated in EBR-II are required, the U-Pu-Zr fuel alloy offers additional advantages. Performance equal to the EBR-II driver fuel has been demonstrated to moderate burnups and, furthermore, the U-PU-Zr fuel has higher solidus and eutectic temperatures and decreased fuel-cladding chemical interactions.

Metallic fuel systems, with their inherently superior breeding and irradiation performance under conditions of interest, are capable and attractive as next-generation power systems.

Acknowledgments

The authors acknowledge the contributions of numerous Argonne National Laboratory staff who over the years have furthered the understanding and the achievements of EBR-II metallic driver fuel. The continued support and participation of the U.S. Department of Energy is appreciated.

Sincere appreciation is extended to each colleague who participated in the preparations of text and graphics of this manuscript.

References

1 Olson, N. J., Walter, C. M., and Beck, W. N., "Statistical and Metallurgical Analysis of Experimental Mark-IA Driver Fuel Element Cladding Failures in the Experimental Breeder Reactor II," *Nuclear Technology*, Vol. 28, 1976, pp. 134–151.

2 Beck, W. N., et al., "The Irradiation Behavior of High-Burnup Uranium-Plutonium Alloy Prototype Fuel Elements," ANL-7388, May 1968.

3 Walter, C. M., Olson, N. J., and Hofman, G. L., "EBR-II Driver-Fuel Qualification and Performance," *Nuclear Methods*, Vol. 19, Am. Inst. of Mining, Metallurgical, and Petroleum Engineers, 1973, pp. 181–202.

4 Foote, F. G., in ANL Metallurgy Division Annual Report for 1966, ANL-7299, pp. 102–113.

5 Burris, L., et al., "The Melt Refining of Irradiated Uranium: Application to EBR-II Fast Reactor Fuel, I. Introduction," *Nuclear Science Engineering*, Vol. 6, 1959, pp. 493–495.

6 Shuck, A. B., and Ayer, J. E., "Engineering Consideration for Remote Refabrication of EBR-II Fuel Elements," *Nuclear Science Engineering*, Vol. 12, 1962, pp. 398–404.

7 Burris, L., et al., "Pyrometallurgical and Pyrochemical Fuel Processing," *Proceedings of the Third International Conference on the Peaceful Uses of Atomic Energy*, Geneva, Vol. 10, 1965, pp. 501–507.

8 Feldman, M. J., et al., "Remote Refabrication of EBR-II Fuels," *Nuclear Methods*, Vol. 15, 1969, pp. 77–96.

9 Hampson, D. C., Fryer, R. M., and Rizzie, J. W., "Melt Refining of EBR-II Fuel," *Nuclear Methods*, Vol. 15, 1969, pp. 57–76.

10 Haas, M., et al., "Fabrication of Driver-Fuel Elements for EBR-II," ANL-79-38, Sept. 1979.

11 Reactor Development Program Progress Report, ANL-RDP-7640, 1969, pp. 70–77.

12 Seidel, B. R., and Einziger, R. E., *In-Reactor Cladding Breach of EBR-II Driver-Fuel Elements*, "Radiation Effects in Breeder Structural Materials," Bleiberg, M. L., and Bennett, J. W., eds., TMS-AIME, New York, 1977, pp. 139–158.

13 Hofman, G. L., "Irradiation Behavior of the Experimental MK-II EBR-II Driver Fuel," *Nuclear Technology*, Vol. 47, 1980, pp. 7–22.

14 Maeck, W. J., "Fast Reactor Fission Yields for U-233, U-235, U-238, Pu-239," ICP-1050-1, Jan. 1975.

15 Einziger, R. E., and Seidel, B. R., "Irradiation Performance of Metallic Driver Fuel in EBR-II to High Burnup," *Nuclear Technology*, Vol. 50, 1980, pp. 25–39.

16 Reactor Development Program Progress Report, ANL-RDP-65, 1.12, 1977.

17 Walter, C. M., Golden, G. H., and Olson, N. J., "U-Pu-Zr Metal Alloy: A Potential Fuel for LMFBR's," ANL-76-28, Nov. 1975.

18 Walters, L. C., and Kittel, J. H., "Development and Performance of Metal Fuel Elements for Fast Breeder Reactor" *Nuclear Technology*, Vol. 48, 1980, pp. 273–280.

19 Lam, P. S. K., Turski, R. B., and Barthold, W. P., "Performance of U-Pu-Zr Metal Fuel in 1000 MWe LMFBRs," *Proceedings International Conference on Fast Breeder Reactor Fuel Performance*, Monterey, Calif., Mar. 5-8, 1979, pp. 935–953.

D. P. Chan
Senior Engineer.
Mem. ASME

R. J. Jackson
Staff Manager.

Westinghouse Hanford Company,
Richland, Wash.

Creep Relaxation of Fuel Pin Bending and Ovalling Stresses

Analytical methods for calculating fuel pin cladding bending and ovalling stresses due to pin bundle-duct mechanical interaction taking into account nonlinear creep are presented. Calculated results are in close agreement with finite element results by MARC-CDC program. The methods are used to investigate the effect of creep on the FTR fuel cladding bending and ovalling stresses. It is concluded that the cladding of 316 SS 20 percent CW and reference design has high creep rates in the FTR core region to keep the bending and ovalling stresses to acceptable levels.

Introduction

Stresses in fuel pins in a fast reactor are due to a variety of physical phenomena. These phenomena are fission gas release, fuel-clad mechanical interaction, clad-wire mechanical interaction, flow-induced vibration, thermal bowing and bundle/duct mechanical interaction. It is desirable but unwieldy to calculate the resultant stresses due to the combined effects of all phenomena. As a common engineering practice, stresses due to each physical phenomena are calculated separately, added together if necessary, and then evaluated against a stress criteria. For the steady state operation and with the proper design of the fuel plenum volume, smear density and fuel/clad gap, the stresses due to the first two phenomena are in general considerably lower than the stress rupture value of the cladding material. With the proper fabrication process and the judicious selection of clad, wire and duct sizes and materials, the stresses due to the third and fourth phenomena are also low. The thermal bowing of a wire-wrapped edge pin, however, can induce significant bending stresses in the cladding. The thermal bowing phenomenon is due to the temperature gradient across the pin diameter, and the differential swelling and creep during irradiation. The authors have analyzed the thermal bowing of edge pins in the FTR core by means of the finite element method. For a discussion on the subject and quantitative results, the readers are referred to reference [1]. The bundle/duct mechanical interaction (BDMI) phenomenon is mainly due to the differential swelling between a hot pin bundle and a relatively cold duct, reference [2]. In addition to reducing the spacing between pins, the BDMI phenomenon can induce bending and ovalling stresses in the pins. This paper represents the first attempt by the LMFBR industry to assess the stresses created by the BDMI. Since the BDMI interaction increases with time, the cladding bending and ovalling stresses without creep relaxation will in turn increase with time. However, in the fuel region of the pin, fast neutron flux and temperature induce creep which relaxes the stresses.

Contributed by the Nuclear Engineering Division of THE AMERICAN SOCIETY OF MECHANICAL ENGINEERS and presented at the Century 2 Nuclear Engineering Conference, San Francisco, Calif., August 19-21, 1980. Manuscript received at ASME Headquarters April 4, 1980. Paper No. 80-C2/NE-24.

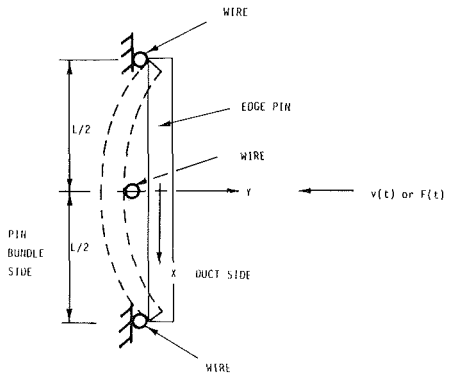

Fig. 1 Bending of a section of an edge pin

The final stress levels in the cladding will depend on the BDMI interaction and the creep relaxation rates. In the following, analytical methods for calculating bending and ovalling stresses taking into account both increasing interaction and creep relaxation are presented.

Analytical Methods

To perform cladding stress analysis, an analyst must first determine the BDMI and the amount of bending and ovalling on critical pins from the BDMI for different increments of time. Reference [3] discusses how the BDMI can be calculated. Reference [2] discusses how the amount of bending and ovalling on individual pins can be calculated from the BDMI for any time increment. Knowing the BDMI and the amount of bending and ovalling, cladding bending and ovalling stresses can be calculated as follows:

Pin Bending. Figure 1 shows the bending of a span of an edge pin by compression at the mid-span. For an edge pin wrapped with a 30 cm (12 in.) axial pitch wire, there are support points every 5 cm (2 in.) along the bundle side of the pin, and they are not in the same plane. For simplicity and a conservative estimate of the cladding bending stress, it is assumed that the compression is resisted by 2 simple supports 5 cm (2 in.) apart and in the same plane. The compression can

be either force or displacement function of time. The method calls for dividing the total time into steps. The mid-span force of displacement is assumed constant within each time step and is incremented from step to step. In the following, equations for calculating bending stress in time increments are presented for the case of mid-span force. As will be seen later, the same equations and iterative solution procedure are applicable for mid-span displacement with minor modification.

Let the transverse displacement due to the mid-span force at the beginning of a time increment be:

$$v = v_0\left[1 - 6\left(\frac{x}{L}\right)^2 + 4\left(\frac{x}{L}\right)^3\right] \tag{1}$$

The curvature of the deformed pin is:

$$\kappa = \frac{d^2v}{dx^2}$$

The strain of any fiber along the pin is:

$$\epsilon = y\frac{d^2v}{dx^2} = \frac{12yv_0}{L^2}\left[1 - 2\left(\frac{x}{L}\right)\right] \tag{2}$$

The stress and stress change during the time increment of any fiber along the pin are:

$$\sigma = E(\epsilon - \epsilon^c) \tag{3a}$$

$$\Delta\sigma = E(\Delta\epsilon - \Delta\epsilon^c) \tag{3b}$$

Since the thermal strain and the swelling strain do not affect bending under uniform temperature and flux, they are neglected from the stress-strain relationship.

Let the creep strain be linearly varying along the pin.

$$\epsilon^c = \epsilon_0^c\left[1 - 2\left(\frac{x}{L}\right)\right] \tag{4}$$

The principle of virtual work states that the work done by the internal forces in a structure equals the work done by the applied loads for any small geometrically admissible displacement variation from the true one.

$$\int_V \Delta\epsilon^*\sigma\, dV = \frac{1}{2}F\,\Delta v_0^* \tag{5}$$

where

$$\Delta\epsilon^* = \frac{12y\Delta v_0^*}{L^2}\left[1 - 2\left(\frac{x}{L}\right)\right] \tag{6}$$

and Δv_0^* is the virtual mid-span displacement. Substituting equations (3*a*, 2, 4), and (6) into (5), carrying out the integrations, and setting the coefficient of Δv_0^* to zero, the following expression for mid-span displacement at the end of a time increment is obtained:

$$v_0 = \frac{FL^3}{48EI} + \frac{L^2}{12I}\int_{\text{Area}} y\,\epsilon_0^c dA \tag{7}$$

Alternatively, the change in mid-span displacement during a time step is:

$$\Delta v_0 = \frac{L^2}{12I}\int_A y\,\Delta\epsilon_0^c dA \tag{8}$$

The integral in equation (8) can be expressed in polar coordinates as:

$$\int_A \Delta\epsilon_0^c y dA = \int_0^{\pi/2} g(\theta)d\theta \tag{9}$$

where $g(\theta) = 4\,\Delta\epsilon_0^c R_m^2\, t\cos\theta$.

Numerical integration of the right-hand-side of equation (9) can be performed using Newton-Cotes quadrature formula:

$$\int_0^{\pi/2} g(\theta)di = \frac{5\Delta}{288}[19\,g(\theta_0) + 75\,g(\theta_1) + 50\,g(\theta_2) + 50\,g(\theta_3) + 75\,g(\theta_4) + 38\,g(\theta_5) + 75\,g(\theta_6) + 50\,g(\theta_7) + 50\,g(\theta_8) + 75\,g(\theta_9) + 19\,g(\theta_{10})]$$

where $\Delta = \pi/20$

and $g(\theta_i)$ are the values of g at $\theta = 0, \pi/20, \pi/10, \ldots \pi/2$.

The displacements, strains, and stresses of the fuel pin at any time can be calculated by the following step-by-step iteration procedure:

1 Calculate the elastic displacement, strain, and stress at time zero using equations (7, 2) and (3*a*).

2 Take a time step, assume a stress change, $\Delta\sigma^i$ ($\Delta\sigma^i = 0$ for the first iteration), and calculate the creep strain change according to given material law.

3 Calculate the mid-span displacement change and the total strain change according to equations (8) and (6).

4 Calculate the stress change $\Delta\sigma^{i+1}$ according to equation (3*b*).

5 Check to see if

$$\text{TEST} = \left|\frac{\Delta\sigma^{i+1} - \Delta\sigma^i}{\Delta\sigma^{i+1}}\right| \le 0.005$$

6 If TEST is bigger than 0.005, use $\Delta\sigma^{i+1}$ and repeat items 2 through 5 of the procedure.

7 If TEST is less than or equal to 0.005, add changes of stress, strain and displacement to total stress, strain and displacement respectively, and take another time step.

In summary, the method calls for the exact satisfaction of the compatibility and stress-strain relations, and the approximate satisfaction of the equilibrium equation through the virtual work principle. Iteration is required because of nonlinearity in the stress-strain relation.

If the mid-span displacement (instead of force) is specified, there is no change in displacement or total strain during any time step. The iteration procedure is the same as for the mid-

Nomenclature

a = major axis of ellipse, Figure 2
b = minor axis of ellipse, Figure 2
E = Young's Modulus
F = applied mid-span force
I = moment of inertia
L = Length of unsupported span
r = distance from the pin midwall
R_o = pin outside radius
R_m = pin mean radius
s = distance in the hoop direction, Figure 2
t = pin thickness
v = transverse displacement of the pin axis
v_0 = transverse displacement at the mid-span
$\bar{v}_0$ = applied transverse displacement
V = volume
w = radial compression of pin
$\bar{w}$ = applied radial compression
x,y,z = co-ordinates, Figs. 1 and 2
α = angle from x-axis, Fig. 2
ϵ = strain
ϵ^c = creep strain
ϵ_0^c = creep strain at the point of compression
σ = stress
κ = curvature
Δvo = virtual transverse displacement
Δw^* = virtual radial compression
$\Delta\epsilon^*$ = virtual incremental strain
$\Delta\sigma$ = change of stress during time step
$\Delta\epsilon$ = change of total strain during time step
$\Delta\epsilon^c$ = change of creep strain during time step

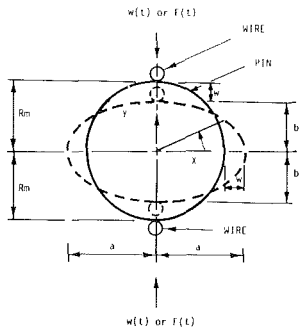

Fig. 2 Ovalling of cladding cross-section

span force case with the exception of eliminating item 3 in the procedure.

Pin Ovalling. Figure 2 shows the ovalling of the fuel pin cross-section under diametrical compression. Ovalling occurs in the pin-wire contact (pinching) planes of fuel bundles. The size of the contact area depends on the pin and wire diameters, relative stiffnesses, wire angle, etc. For a conservative estimate of the ovalling stress, the compression is assumed to be two-dimensional, diametrical, and distributed along the longitudinal direction. The actual length of the pin/wire contact line at every time increment can be determined approximately by the procedure given in the appendix. Since the equations below for calculating ovalling stress are based on a pin of unit length, the pin compression by the wire is adjusted in accordance with the actual length of the pin/wire contact line. Again the compression can be either force or displacement function of time. The method calls for dividing the total time into steps. The force or displacement is assumed constant within each time step, and is incremented from step to step. In the following, equations for calculating stress history are presented for the case of force. The same equations and iterative solution procedure are applicable for the case of displacement with minor modification.

Let the deformed shape of the fuel pin cross-section be an ellipse, and the decrease of the diameter in the compression direction equal to the increase of the diameter in the orthogonal direction. Then the major and minor axes of the ellipse are:

$$a = R_m + w$$
$$b = R_m - w$$

The parametric equations for the ellipse are:

$$x = a\cos\alpha$$
$$y = b\sin\alpha \tag{10}$$

Substituting equation (10) into the general equation for curvature

$$\kappa = \left| \frac{\frac{d^2y}{dx^2}}{\left[1+\left(\frac{dy}{dx}\right)^2\right]^{3/2}} \right|,$$

the following is obtained,

$$\kappa = \frac{ab}{(a^2\sin^2\alpha + b^2\cos^2\alpha)^{3/2}}. \tag{11}$$

The change in curvature at any point (from circle to ellipse) is

$$\Delta\kappa = \frac{ab}{(a^2\sin^2\alpha + b^2\cos^2\alpha)^{3/2}} - \frac{1}{R_m} \tag{12}$$

The differential arc length on the ellipse is

$$ds = \sqrt{a^2\sin^2 + b^2\cos^2}\ d\alpha \tag{13}$$

Assuming $w << R_m$ and retaining only the first two terms of the Binomial series, equations (12) and (13) reduce to:

$$\Delta\kappa = \frac{3w}{R_m{}^2}\cos 2\alpha$$

$$ds = R_m\left(1 - \frac{w}{R_m}\cos 2\alpha\right)d\alpha$$

The strain and strain change of any fiber in the hoop direction are

$$\epsilon = r\Delta\kappa$$
$$= \frac{3\Delta w r}{R_m{}^2}\cos 2\alpha \tag{14a}$$

$$\Delta\epsilon = \frac{3\Delta w r}{R_m{}^2}\cos 2\alpha \tag{14b}$$

The stress and stress change of any fiber in the hoop direction are

$$\sigma = E(\epsilon - \epsilon^c) \tag{15a}$$
$$\Delta\sigma = E(\Delta\epsilon - \Delta\epsilon^c) \tag{15b}$$

Membrane strains, due to thermal expansion, irradiation swelling and internal pressure are neglected in the analysis to avoid complication. However, membrane strains and stresses can be easily calculated by one-dimensional analysis. They should be superimposed onto the results by the present analysis. Let

$$\epsilon^c = \epsilon_0^c\cos 2\alpha \tag{16}$$

Applying the virtual work principle, the following expression for radial displacement at any time is obtained:

$$w = \frac{8R_m{}^3F}{3\pi Et^3} + \frac{4R_m{}^2}{t^3}\int_{\frac{-t}{2}}^{\frac{t}{2}} r\epsilon_0^c dr \tag{17}$$

For any time step, the change in radial displacement is

$$\Delta w = \frac{4R_m{}^2}{t^3}\int_{\frac{-t}{2}}^{\frac{t}{2}} r\Delta\epsilon_0^c dr \tag{18}$$

Numerical integration of the right-hand-side of equation (18) can be performed using Newton-Cotes quadrature formula. The displacement, strain, and stress of the fuel pin at any time can be calculated by the same step-by-step iteration procedure as for the pin bending analysis.

Results

The methods developed in the preceding section have been implemented in two computer codes, namely, BEND for pin bending stress calculation, and OVAL for pin ovalling stress calculation. Before the codes were used for stress calculation of fuel pins in the FTR core, their results were checked against MARC-CDC [4] results for constant compression cases. Figure 3 shows the bending stress results for an edge pin with a 3.4 cm (1.333 in.) unsupported span corresponding to a wire axial pitch of 20.3 cm (8 in.). The mid-span displacement is 0.127 mm (0.005 in.) constant with time. The dimensions of the pin are 5.84 mm (0.230 in.) in outside diameter, and 0.381 mm (0.015 in.) in thickness. The temperature and fast neutron flux are 811 K (1000°F) and 5×10^{15} n/cm^2-s respectively. The pin material is 316 SS 20 percent CW. The proposed revision 5 irradiation creep for the Nuclear Systems Materials Handbook was used in the analysis. In Fig. 3 the solid curve and the dashed curve correspond to BEND and MARC-CDC results respectively. The results are in close agreement, and

Table 1 Compression rates, 10^{-3} mm/hr (10^{-3} mils/hr)

	Bundle/Duct Interference Rate 10^{-3} mm/hr (10^{-3} mils/hr)	Pitch 36.48 cm (12 in.)	20.32 cm (8 in.)	15.24 cm (6 in.)
Bending	0.25 (10)	0.013 (6.525)	-	-
	0.51 (20)	0.029 (1.124)	0.016 (0.627)	0.009 (0.354)
	0.76 (30)	0.042 (1.649)	-	-
Ovalling	0.25 (10)	0.004 (0.138)	-	-
	0.51 (20)	0.007 (0.295)	0.014 (0.556)	0.019 (0.744)
	0.76 (30)	0.011 (0.433)	-	-

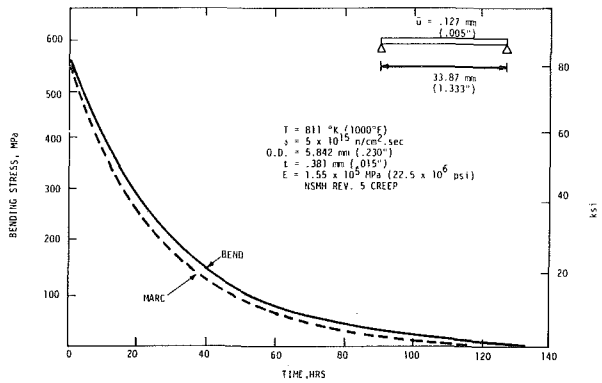

Fig. 3 Comparison of bending stress results

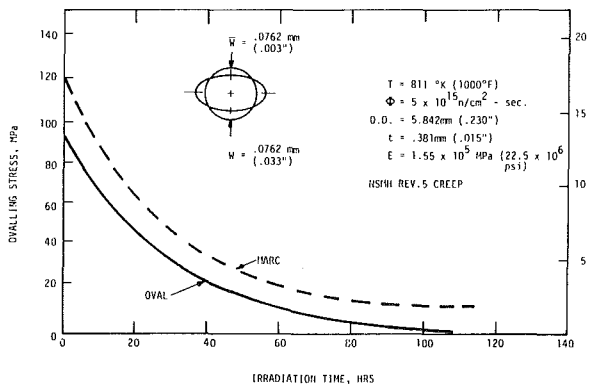

Fig. 4 Comparison of ovalling stress results

indicate that the particular creep law used provides fast relaxation of stress. Figure 4 shows the ovalling stress results for a pin of unit length. The diametrical compression is 0.076 mm (0.003 in.) constant with time. The dimensions, temperature, fast neutron flux, and material properties are the same as those for the pin bending check case. The results are in reasonable agreement with each other. In the pin bending analysis, the deformed shape assumed is a cubic function which is the exact solution. In the pin ovalling analysis, the deformed shape assumed is an ellipse which is not the true shape. That is why, the agreement between results is better for the pin bending case than for the pin ovalling case. In any event, uncertainties involved in related analytical predictions (like environmental data, material law, bundle-duct interference, etc.) do not warrant exact calculation of stresses. It is to be noted that the relative computer costs for running MARC-CDC and BEND (or OVAL) for the test cases were 50 to 1.

Having established agreement with the MARC-CDC code, the BEND and OVAL codes were used to predict the bending and ovalling stresses of fuel pin cladding in the FTR core. The parameters varied were the compression rate, wire-wrap axial pitch, and the fast neutron flux. Shown in Table 1 are the pin bending and ovalling rates corresponding to three bundle-duct interference rates. The medium interference rate of 0.51×10^{-3} mm/hr (20×10^{-3} mils/hr) is that of the reference driver fuel assembly in row 1 position of the FTR core. The low interference rate of 0.25×10^{-3} mm/hr (10×10^{-3} mils/hr) is that of the reference driver fuel assembly in an outer row position where the fast neutron flux is less and therefore the differential swelling between the bundle and the duct is less. The high interference rate of 0.76×10^{-3} mm/hr (30×10^{-3} mils/hr) is that of a reference bundle in an advanced alloy duct which has less swelling characteristics. All interferences rates are estimated mean values over 3 cycles. Pins of reference dimension, and NSMH Revision 5 irradiation creep law were assumed. It was further assumed that the bundle-duct contact occurred at the end of 1 1/2 reactor cycles (3600 hr).

Figure 5 shows the variation of pin bending stresses with time for three different wire-wrap axial pitches. The temperature, flux, and bundle-duct interference rate correspond to those of a reference assembly in row 1 position. The bending stresses increase nonlinearly with time, and reach steady state values in approximately 140 hrs. Physically at the beginning of bundle-duct interference, the bending stress created is low, and therefore the creep relaxation (which is dependent on stress) is also low. Stress continues to increase because of increasing bundle-duct interference to a point such that the creep relaxation balances increasing bundle-duct interference. The steady-state bending stress values for 15.2 cm (6 in.) and 20.3 cm (8 in.) axial pitch pins are almost the same at 2.8 MPa (0.4 ksi). The steady-state value for 30.5 cm (12 in.) pitch pin is 2.3 MPa (0.3 ksi). Even though the bending compression rates go down as the wire pitch is reduced, Table 1, the shortening of the unsupported span causes the stress to go up. For the 15.2 cm (6 in.) and the 20.3 cm (8 in.) wire pitch cases, the two effects offset each other to produce essentially the same stress curve in Fig. 5. For comparison, the stress rupture of 316 SS 20 percent CW at 811

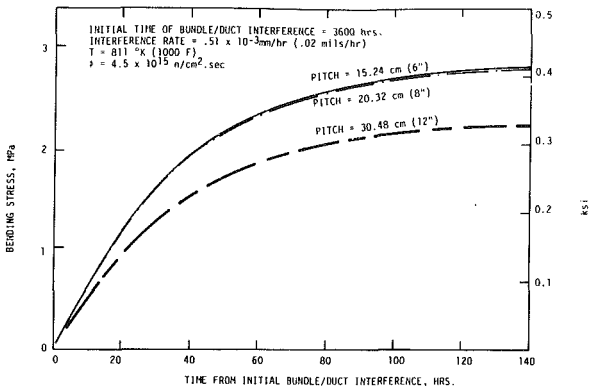

Fig. 5 Variation of bending stress with irradiation time and wire axial pitch

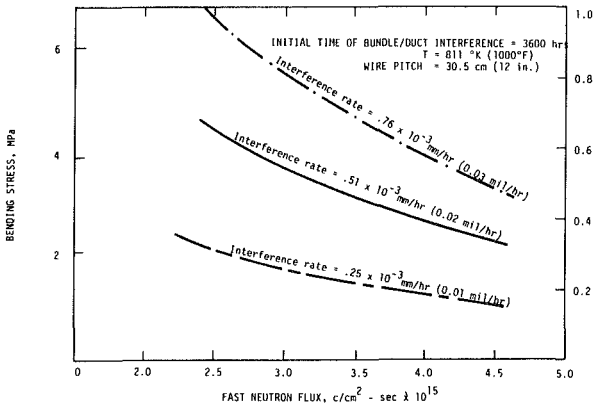

Fig. 6 Variation of steady-state bending stress with interference rate and fast neutron flux

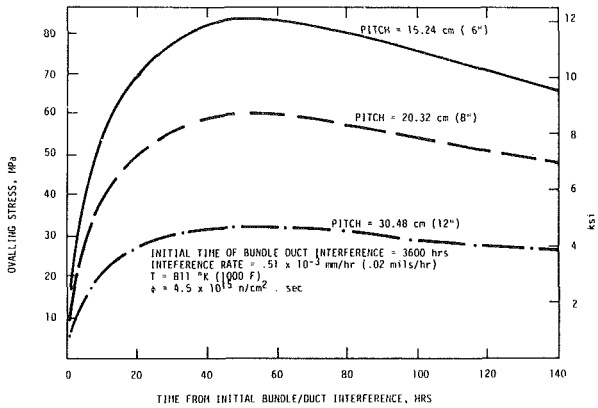

Fig. 7 Variation of ovalling stress with irradiation time and wire axial pitch

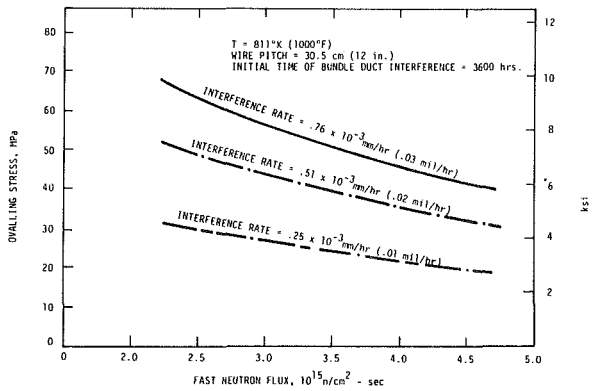

Fig. 8 Variation of maximum ovalling stress with interference rate and fast neutron flux

K (1000°F) in 3 cycles (7200 hrs) is approximately 248 MPa (36 ksi).

Figure 6 shows the variation of pin bending stress with fast neutron flux for three different bundle-duct interference rates. As expected, the stress decreases with fast neutron flux and increases with bundle-duct interference rate. Even with the highest bundle-duct interference rate and the lowest fast neutron flux for creep relaxation, the stress is still well below the stress rupture value.

Figure 7 shows the variation of pin ovalling stresses with time for three different wire axial pitches. The temperature, flux and bundle-duct interference rate correspond to those of a reference assembly in row 1 position. The ovalling stresses increase nonlinearly with time and reach maximum values in approximately 50 hr. After 50 hr, the stresses decrease with time because of increasing pin/wire contact length. The maximum values for 15.2 cm (6 in.), 20.3 cm (8 in.) and 30.5 cm (12 in.) axial pitch cases are 84 MPa (12.2 ksi), 60 MPa (8.7 ksi), and 32 MPa (4.6 ksi) respectively. The increase of stress with decreasing wire pitch is due to increasing compression rate with decreasing wire pitch, Table 1.

Figure 8 shows the variation of pin ovalling stress with fast neutron flux for three different bundle-duct interference rates. As expected, the stress decreases with fast neutron flux and increases with bundle-duct interference rate. Even with the highest bundle-duct interference rate and the lowest fast neutron flux for creep relaxation, the stress is still below the stress rupture value.

Conclusions

On the basis of the results obtained, the following conclusions are drawn:

1 Methods have been developed which can be used to assess the bending and ovalling stresses in the fuel pins taking into account the effects of nonlinear creep.

2 The driver fuel pin cladding of 316 SS 20 percent CW and reference design has high creep rate in the FTR core region to keep the bending and ovalling stresses to acceptable levels.

References

1 Chan, D. P., Jackson, R. J., "Thermal Bowing of Wire-Wrapped Fuel Pins in the Fast Reactor," Hanford Engineering Development Laboratory SA-1839, presented at the ANS Winter Annual Meeting, Nov. 1979.

2 Chan, D. P., Jackson, R. J., "Fuel Pin Bundle and Hexagonal Duct Mechanical Interaction," 78-PVP-48, Joint ASME/CSME Pressure Vessels and Piping Conference, Montreal, Canada, June 25-30, 1978.

3 Hill, R. G., Jackson, R. J., "Bundle-Duct Clearance of HEDL Mixed Oxide Subassemblies," HEDL-TME 76-29, June 1977, Westinghouse Hanford Company Richland, Wash.

4 "MARC-CDC, General Purpose Finite Element Analysis Program," *Rev. Journal*, 1977, Control Data Corporation, Minneapolis, MI.

5 Roark, R. J., *Formulas for Stress and Strain*, 4th Edition, McGraw-Hill, 1965.

6 Roark, R. J., "The Strength and Stiffness of Cylindrical Shells Under Concentrated Loading," ASME *Journal of Applied Mechanics*, Vol. 2, No. 4, 1935, p. A-147.

APPENDIX

For two solid bodies in contact, the minimum and maximum radii of curvature at the contact point being R_1 and R_1' for body 1 and R_2 and R_2' for body 2, and the plane containing curvature $1/R_1$ in body 1 making an angle ϕ with the plane containing curvature $1/R_2$ in body 2, the contact

surface is an ellipse with semi-major and minor axes as follows:

$$c=\alpha\sqrt[3]{\frac{P\delta}{K}}$$

$$d=\beta\sqrt[3]{\frac{P\delta}{K}}$$

where P = contact load

$$\delta=\frac{4}{\frac{1}{R_1}+\frac{1}{R_2}+\frac{1}{R_1'}+\frac{1}{R_2'}}$$

$$K=\frac{8}{3}\,\frac{E_1E_2}{E_2(1-\nu_1^2)+E_1(1-\nu_2^2)}$$

$$\cos\theta=\frac{\delta}{4\sqrt{\left(\frac{1}{R_1}-\frac{1}{R_1'}\right)^2+\left(\frac{1}{R_2}-\frac{1}{R_2'}\right)^2+2\left(\frac{1}{R_2}-\frac{1}{R_1'}\right)\left(\frac{1}{R_1}-\frac{1}{R_2'}\right)\cos 2\phi}}$$

E_i = Young's modulus of body i
ν_i = Poisson's ratio of body i

and α and β are constants varying with θ as given on page 321 of reference [5].

For a fuel pin wrapped with a wire at an axial pitch of H, it can be shown that

R_1 = pin outside radius
$R_1' = \infty$
R_2 = wire radius

$$R_2' = R_1 + \frac{1}{R_1}\left(\frac{H}{2\pi}\right)^2$$

$$\phi \simeq \tan^{-1}\frac{4R_1}{H}$$

Since the wire is solid, E_2, ν_2 correspond to the Young's modulus and Poisson's ratio of the wire material. Pin, however, is hollow. An equivalent E for a solid pin has to be determined such that its deformation under diametrical loading is the same as that for an actual hollow pin under the same loading. According to page 320 of reference [5], the deformation for a solid pin is

$$y=\frac{2(1-\nu^2)}{E}\,\frac{p}{\pi}\left(\frac{2}{3}+\ln\frac{2D_1}{b}+\ln\frac{2D_2}{b}\right)$$

where p = load per distance.
D_1 = diameter of solid pin
D_2 = very small

$$b=2.15\sqrt{\frac{p}{E}\,\frac{D_1D_2}{D_1+D_2}}$$

E = Young's modulus of solid pin
ν = Poisson's ratio of solid pin.

According to page 172 of reference [5], the deformation of a hollow pin is

$$y=0.149\frac{PR^3}{EI}=1.78\,\frac{pR^3}{Et^3}$$

By equating the two deformations and the Poisson's ratios of the solid and the hollow pins, an equivalent Young's modulus for the solid pin can be determined for a specific load. For a load range between 0 and 1751 N/m (10 lb/in.), the equivalent Young's modulus practically stays constant.

Knowing R_1, R_2, R_1', R_2', ϕ, E_1, E_2, ν_1 and ν_2, the semi-major axis of the pin/wire contact surface can be calculated for any load P. For conservatism, the ovalling stress calculation method presented in this paper assumes zero semi-minor axis. If the pin compression is in terms of displacement y instead of P, the conversion from P to y is done as follows:

$$y=\frac{0.149\,R^3p}{EI}$$

where $$I=\frac{7Rt^3}{12}.$$

The above equations are in accordance with reference [6] which states that the deformation of a cylinder under diametrically opposite and equal, concentrated loads is the same as that of an equivalent ring under the same loads uniformly distributed along diametrically opposite lines. The equivalent ring has the same radius and thickness of those of the cylinder. It's length is seven times its mean radius.

Pellet-Cladding Interaction of LMFBR Fuel Elements at Unsteady State

An Introduction to Computer Code ISUNE-5

B. M. Ma
Dept. of Nuclear Engineering and Engineering Research Institute, Iowa State University, Ames, Iowa
Mem. ASME

The fuel pellet-cladding interaction (PCI) of liquid-metal fast breeder reactor (LMFBR) fuel elements or fuel rods at unsteady state is analyzed and discussed based on experimental results. In the analyses, the heat generation, fuel restructuring, temperature distribution, gap conductance, irradiation swelling, irradiation creep, fuel burnup, fission gas release, fuel pellet cracking, crack healing, cladding cracking, yield failure and fracture failure of the fuel elements are taken into consideration. To improve the sintered $(U,Pu)O_2$ fuel performance and reactor core safety at high temperature and fuel burnup, it is desirable to (a) increase and maintain the ductility of cladding material, (b) provide sufficient gap thickness and plenum space for accommodating fission gas release, (c) keep ramps-power increase rate slow and gentle, and (d) reduce the intensity and frequency of transient PCI in order to avoid intense stress fatigue cracking (SFC) and stress corrosion cracking (SCC) due to fission product compounds CsI, CdI_2, Cs_2Te, etc. at the inner cladding surface of the fuel elements during PCI.

Introduction

The economics of nuclear power plant operation depends heavily on fuel pellet-cladding interaction (PCI) at unsteady state. The PCI, which greatly influences fuel performance, fuel-element safety and reactor-core operating lifetime, results from the combination of basic thermal, irradiation, chemical and mechanical effects. These combined effects can induce stress corrosion cracking (SCC) and stress fatigue cracking (SFC) and, finally, cause fuel-element failure. Experimental measurements and post-failure examinations of transient PCI have strongly supported the result of the combined effects [1,2].

The combination of the thermal, irradiation, chemical and mechanical effects on the fuel-element materials that produce transient PCI consists primarily of:

- Thermal expansion, temperature gradient, thermal cycling, fuel densification, pellet-cladding gap opening and closure (of the thermal effect).
- Irradiation growth, irradiation swelling, irradiation creep, fuel restructuring, fission product accumulation, fission gas release (of the irradiation effect).
- Fission products (Cs, I, Cd, Te, etc.) and chemical compounds (CsI, CdI_2, Cs_2Te, $CdCl_2$, $CsCl_2$, etc.) (of the chemical effect).
- Induced elastic-plastic stresses and strains, fuel cracking, stress corrosion cracking (SCC) and stress fatigue cracking (SFC) at cladding surface (of mechanical effect).

Among these, the most crucial factors are (1) fuel pellet-cladding gap opening and closure affecting the gap conductance (or heat transfer and removal), and (2) fuel cracking, fission gas release and induced stresses to initiate and accelerate SCC and/or SFC. The former can cause central fuel meltdown and the latter can result in cladding breach. Either central fuel meltdown or cladding breach can bring about the failure of fuel elements or rods, particularly during the transient PCI of liquid-metal fast breeder reactor (LMFBR).

In previous papers [3–4], the thermal, radiation and mechanical analysis for unsteady-state fuel restructuring of cylindrical oxide fuel elements in a LMFBR and Computer Codes ISUNE-1 and ISUNE-3 were presented. In this paper, the pellet-cladding interaction (PCI) of LMFBR fuel elements due to the combination of thermal, irradiation, chemical, and mechanical effects on the fuel and cladding materials at unsteady state and variable power level is analyzed and discussed. (On this basis, a Computer Code ISANE-5 may be developed in a forthcoming paper.)

The primary objectives of this paper are:

1 To analyze the cause and effect of transient PCI on gap (thermal) conductance related to heat transfer, removal and utilization.
2 To propose the basic theories and formulate the basic equations for irradiation swelling and irradiation creep; to postulate the fuel and cladding cracking theory for stress fatigue cracking (SFC), stress corrosion cracking (SCC), and crack healing during PCI.
3 To discuss the desirability of sintered $(U,Pu)0_2$ performance and reactor core safety related to the cladding material development, fuel-element design, and reactor operation of LMFBR.

Contributed by the Nuclear Engineering Division of the American Society of Mechanical Engineers and presented at the Century 2 Nuclear Engineering Conference, San Francisco, Calif., August 19–21, 1980. Manuscript received at ASME Headquarters April 4, 1980.

Heat Generation Rate, Temperature Distribution and Gap Conductance Temperature Distribution in Cladding

The proportion of heat generated in the nuclear fuel (e.g., sintered $(U,Pu)0_2$ pellets) is about 90 percent; the rest is generated in the structural (chiefly cladding) coolant, reflector, and shielding materials of a LMFBR. If Σ_f is the macroscopic fission cross section, Φ is the average fast neutron flux, and E_f is the nuclear energy liberated per fission event, the volumetric heat generation rate q_v is given by

$$q_v = \Sigma_f \phi E_f \tag{1}$$

which is equivalent to the reactor power density.

For a LMFBR with sodium coolant, the heat transfer coefficient h under the convective turbulent flow condition through a long hexagonal lattice of fuel rods (parallel to the rods) is represented by [5,6]

$$N_{\mathrm{Nu}} = \frac{hD_e}{k} = 6.66 + 3.126(s/d) + 1.184(s/d)^2 + 0.0155(\Psi N_{\mathrm{pe}})^{0.86} \tag{2}$$

where N_{Nu} is the Nusselt number, N_{pe} is the Peclet number, D_e is the equivalent diameter of the coolant channel, k is the thermal conductivity of the coolant (Na), and s/d is the ratio of lattice pitch to rod diameter. ψ is a complicated function, defined by, for instance

$$\Psi \equiv 1 - \frac{0.942(s/d)^2}{N_{\mathrm{Pr}}(N_{\mathrm{Re}}/10^3)^{1.281}} \tag{3}$$

in which N_{Pr} is the Prandtl number and N_{Re} is the Reynolds number.

When the bulk coolant (operating) temperature T_{co} is prescribed, the outer and inner cladding surface temperatures T_0 and T_i and the temperature distribution $T(r)$ in the cladding can be determined from the basic heat transfer equations

$$T_0 = T_{co} + \frac{q}{2\pi r_0 h} \tag{4}$$

$$T_i = T_0 + \frac{q}{2\pi k_c} ln(r_0/r_i) \tag{5}$$

$$T(r) = T_0 + \frac{q}{2\pi k_c} ln(r_0/r) \tag{6}$$

where q is the linear power, k_c is the thermal conductivity of the cladding material, r_o and r_i are the outer and inner radii of the cladding, and r is the variable radius or radial ordinate of the fuel element.

Heat Generation and Temperature Distribution in Fuel. Heat generation rate in fuel elements is approximately equal to that in the system of a LMFBR. Hence, it is common practice for the linear power rating q of the fuel elements to represent the linear power rating of a nuclear reactor.

Fuel restructuring (or grain growth) and redistribution occurring in the oxide (or ceramic) fuel after a sufficient period of nuclear irradiation can influence temperature distribution in the fuel. During the fuel restructuring, four distinct regions (or zones) are usually formed in the fuel: (1) the central void (hole), (2) the columnar grain region, (3) the equiaxed grain region, and (4) the unaffected (or sintered) grain region. In these regions, the central void radius r_v, the outer radius of the columnar grain region r_1, the outer radius of the equiaxed grain region r_2 and the outer radius of the unaffected grain region r_s, the corresponding temperature at the regional surfaces, are shown in Fig. 1.

In a LMFBR, the distribution of fast neutron flux Φ penetrating into the fuel of a fuel element with a long stack of fuel pellets is essentially uniform. Thus, for a given linear power rating q, the volumetric heat generation rate q_v per unit length in the unaffected grain region, equiaxed grain region, and columnar grain region are respectively expressed as

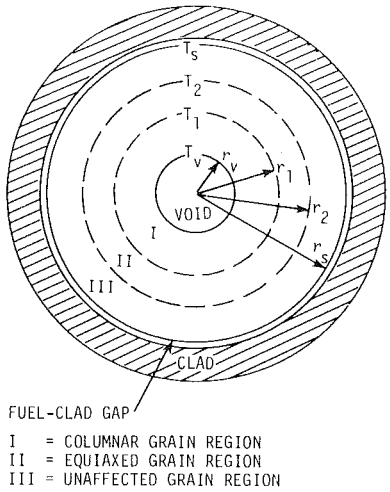

Fig. 1 Typical cross section of an irradiated oxide fuel element

$$\begin{aligned} q_{v_3} &= q/\pi r_s^2 \\ q_{v_2} &= q_{v_3}\rho_2/\rho_3 \\ q_{v_1} &= q_{v_3}\rho_1/\rho_3 \end{aligned} \tag{7}$$

where ρ_1, ρ_2 and ρ_3 are the actual densities (fractions of theoretical density) of the mixed fuel $(U,Pu)0_2$ in the three regions.

At the unsteady state of power reactor operation during startup, power up, power down, or shutdown, the linear power rating can vary as ramp functions from a base (initial or preceding) linear power rating q_0 at any time t

$$q = q_0(1+mt) \qquad \text{for power up} \tag{8}$$

$$q = q_0(1-mt) \qquad \text{for power down} \tag{9}$$

The thermal conductivity k or k_f of the mixed oxide fuel depends on the fuel temperature T and density ρ for a prescribed fuel preparation process [1]

$$k = k_f(T,\rho) = C_1 + [T(C_2 - C_3\rho)]^{-1} \tag{10}$$

where C_1, C_2 and C_3 are the constants prescribed.

To determine the temperature distribution in three respective regions of the oxide fuel rod, the heat transfer per unit volume of the unaffected grain region at any temperature $T(r,t)$ is first considered. On the basis of angular and axial symmetry and in the equilibrium state of heat generation, the heat conduction equation is

$$\frac{\partial^2 T}{\partial r^2} + \frac{1}{r}\frac{\partial T}{\partial r} = -q_v/k = -q_{v_3}/k \tag{11}$$

Introducing equation (10) into equation (11) and integrating with appropriate limits give the temperature distribution in the unaffected grain region

$$q_{v_3} r_s^2(1 - r^2/r_s^2)/4 = C_1(T - T_2) + (C_2 - C_3\rho_3)^{-1} ln(T/T_2)$$

for

$$r_2 \le r \le r_s,\ T_2 \ge T \ge T_s \tag{12}$$

Similarly, the heat conduction and temperature dis-

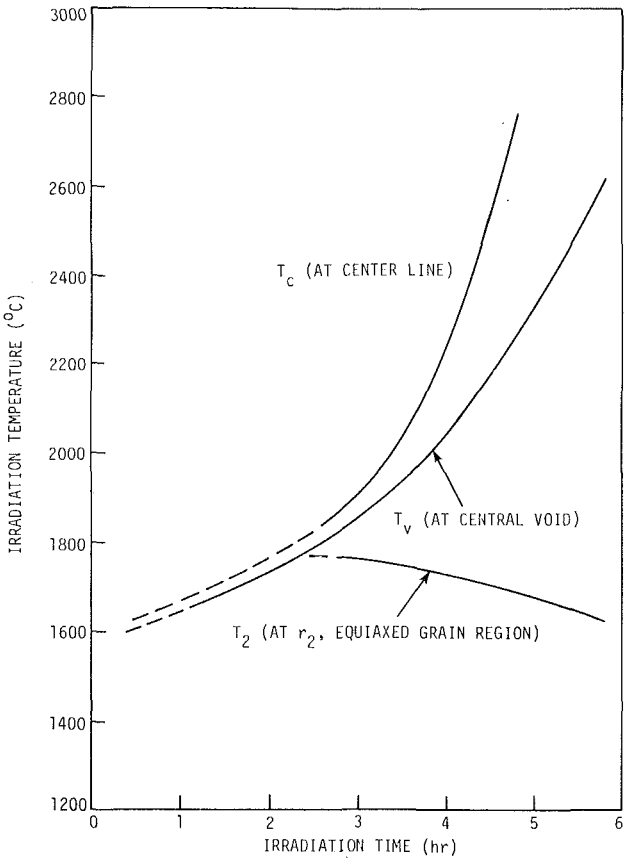

Fig. 2 Variations of fuel temperature with irradiation time during the reactor startup

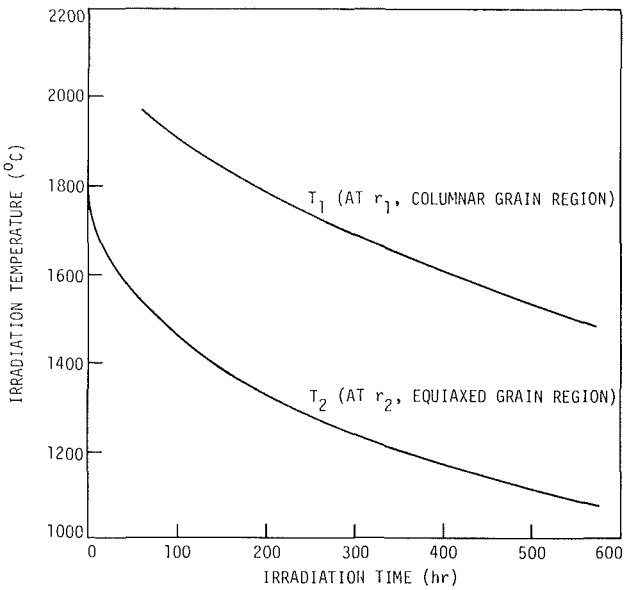

Fig. 3 Variations of fuel temperature with irradiation time at the columnar and equiaxed grain regions of the fuel zone

tributions in the equiaxed and columnar grain regions are given by

$$q_{v_2}(r_2^2/4)[(1-r^2/r_2^2)+(1-q_{v_3}/q_{v_2})ln(r/r_2)]$$

$$=C_1(r-r_2)+(C_2-C_3\rho_2)^{-1}ln\ (T/T_2)$$

for

$$r_1 \le r \le r_2,\ T_1 \ge T \ge T_2 \tag{13}$$

$$q_{v_1}(r_1^2/4)[(1-r^2/r_1^2)+(1-q_{v_2}/q_{v_1})ln(r/r_1)]$$

$$=C_1(r-r_1)+(C_2-C_3\rho_1)ln\ (T/T_1)$$

for

$$r_v \le r \le r_1,\ T_v \ge T \ge T_1 \tag{14}$$

From the balance of power output or volumetric heat generation rate before and after formation of the four regions in the fuel, a relation to determine the central void radius r_v/r_1 is

$$r_v/r_1=\left[\left(\frac{r_2}{r_1}\right)(q_{v_2}-q_{v_3})/q_{v_1}+(q_{v_1}-q_{v_2})/q_{v_1}\right]^{1/2} \tag{15}$$

For given data of material constants, the values of r_v/r_1, r_1/r_2, r_2/r_s, T_v/T_1, T_1/T_2, T_2/T_s and the temperature distribution in the three grain regions can be determined from equations (12–15), respectively.

In a sufficient time of high-temperature operation the columnar grain growth is formed by the development and movement of porosity-fabricated pores of fission gases out of this region. These pores move up with thermal gradients. The migration of these pores up to the central region results in a central void and a columnar grain region in the fuel. The fuel density ρ_3 in the columnar grain region is near the theoretical density (TD) of $(U,Pu)0_2$. During the pore migration up with the thermal gradients, the velocity v of a migrating pore of fission gas has been given in reference [3]. The migrating velocity is directly proportional to the thermal gradient $\partial T/\partial r$, inversely proportional to the pore pressure P, and independent of pore shape (sphere or ellipsoid) and size.

As the temperature distribution in fuel is parabolic or exponential [3], the average thermal gradient, $(\partial T/\partial r)_{av}$, occurs at $r_s/3$. There, the threshold temperature for columnar grain formation as well as concomitant central void formation as a function of irradiation time t is represented by

$$\frac{r_s}{3t}=[C_4\exp(-C_5/T)T^{3/2}]\left(\frac{\partial T}{\partial r}\right)_{av} \tag{16}$$

where C_4 and C_5 are constants. For given values of r_s,t and $(\partial T/\partial r)_{av}$, the threshold central temperature T_c (or T_v) can be computed from equation (16).

The equiaxed grain growth related to the initial grain size D_0 before operation and the grain size D after irradiation temperature annealing through irradiation time t is, on the basis of experimental data, given by

$$D^3-D_0^3=k_0t\exp(-Q/RT) \tag{17}$$

in which k_0 is constant, Q is the activation energy, R is the universal gas constant and T is the temperature for the process of the equiaxed grain growth. In the equiaxed grain region, a minimum grain size of 15 um at the outer radius r_2 and a fuel smeared density of 95–97 percent TD of $(U,Pu)0_2$ can be assumed.

From Computer Code ISUNE-3, the typical variations of fuel temperature with irradiation time during the reactor startup and steady-state operation are respectively shown in Figs. 2, 3, and 4. The typical variation of temperature distribution with irradiation time in the fuel element during a constant power operation is given in Fig. 5. It is seen from these curves that the temperature variations in the LMFBR fuel zone as well as in the fuel elements gradually become stabilized during (*a*) fuel restructuring (grain growth), (*b*) increase in irradiation time, and (*c*) accumulation in fission products and neutron absorbers (such as xenon-135 and samarium-149).

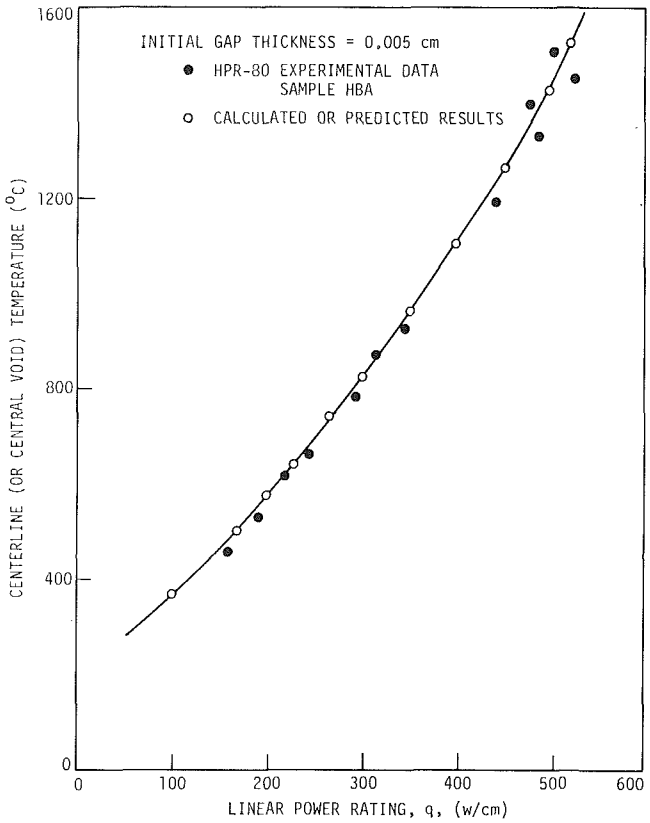

Fig. 4 Variations of calculated and measured centerline temperature with linear power rating of the oxide fuel element

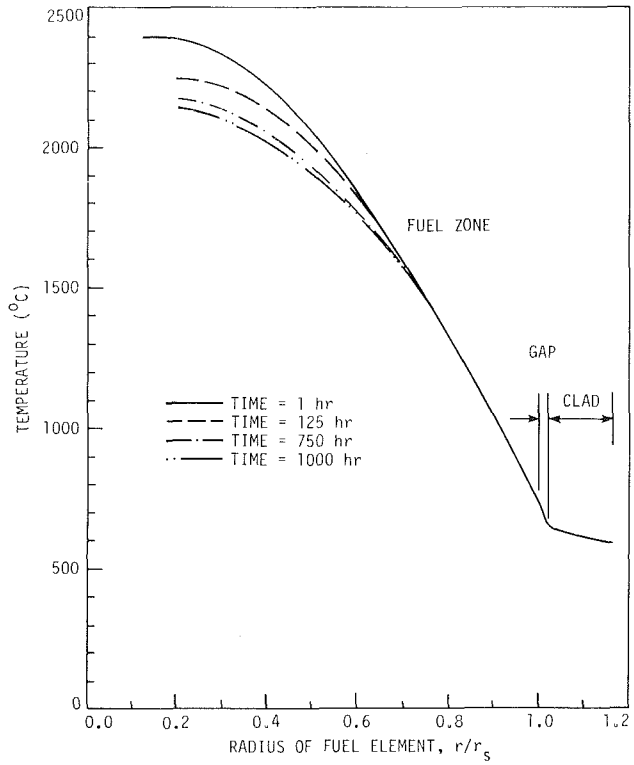

Fig. 5 Temperature distribution varies with radius and irradiation time in the oxide fuel element

Fuel Pellet-Cladding Interaction (PCI) and Gap Conductance. Heat removal from the fuel to the coolant occurs through a helium (or sodium) bonding gap between the fuel and the cladding. The main functions of the bonding gap are to (*a*) increase the heat conductance from the fuel to the clad, (*b*) reduce any interface thermal resistance, (*c*) decrease interdiffusion between the fuel and cladding materials, (*d*) facilitate fission and volatile gas flow, and (*e*) provide free space for thermal expansion, irradiation growth and irradiation swelling of the fuel and cladding materials when the gap tends to be closed.

Sources of gap closure are primarily comprised of thermal expansion, elastic-plastic deformation, irradiation creep, irradiation growth, irradiation swelling, and fuel cracking. Among them, the thermal expansion, irradiation swelling, and radial dislocation produced by fuel cracking are the predominant factors of gap closure. Gap opening and gap closure can have a great effect on the gap conductance (or heat transfer coefficient), h_{gap}. As predicted theoretically and observed experimentally, partial or complete gap closure occurs in the early hours when new fuel elements are in operation. The gap could reopen after it was closed [7]. This may be attributed to irradiation-induced fuel densification and crack healing processes.

Gap Conductance and Gap Opening. The gap conductance h_{gap} consists generally of (1) gas conductance, h_{gas}, (2) radiant heat conductance, h_r, and (3) gap surface constriction conductance, h_s. In the case of gap opening during operation of the fuel element, the gap conductance is expressed as

$$h_{gap} = h_{gas} + h_r, \quad h_s = 0 \tag{18}$$

When the gap distance or length, L_g, between the outer fuel surface and inner cladding surface is sufficiently large,

$$L_g \geq a_1(\delta_f + \delta_c) \tag{19}$$

the gas conductance can be represented by

$$h_{gas} = k_{gas}/(L_g + \xi_f + \xi_c) \tag{20}$$

where k_{gas} is the thermal conductivity of volatile, fission, and filling gases contained in the gap, a_1 is constant about 1.10-1.25, δ_f and δ_c are the arithmetic mean roughness heights of the fuel and clad surfaces, and ξ_f and ξ_c are the temperature jump distances of the fuel and cladding, respectively.

The radiant heat conductance h_r is derived from the relations of the balance of radiant heat flux, q_{rad}/A, and the Stefan-Boltzmann law [7]

$$h_r = \sigma_{sB}[e_f^{-1} + e_c^{-1} - 1]^{-1}(T_s + T_i)(T_s^2 + T_i^2) \tag{21}$$

and the gap conductance for the case of complete gap opening from equation (18) is

$$h_{gap} = \frac{k_{gas}}{L_g + \xi_f + \xi_c} + \sigma_{sB}[e_f^{-1} + e_c^{-1} - 1]^{-1} \times (T_s + T_i)(T_s^2 + T_i^2) \tag{22}$$

where σ_{sB} is the Stefan-Boltzmann constant, e_f and e_c are emissivities of the outer fuel and inner clad surfaces, and $T_f = T_s$, $T_c = T_i$ are temperatures at the outer fuel and inner clad surfaces, respectively.

Complete Gap Closure. In the case where the gap is completely closed predominantly by thermal expansion, irradiation swelling, and fuel cracking, L_g vanishes but h_s comes into play. Then the gap for complete gap closure becomes

$$h_{gap} = h_{gas} + h_r + h_s \tag{23}$$

In previous work [1], equations derived on the basis of experimental data and analytical results for the gas conductance h_{gas}, radiant heat conductance h_r, and surface constriction conductance h_s, have been obtained. Hence, the gap conductance for the case of complete gas closure can be given by

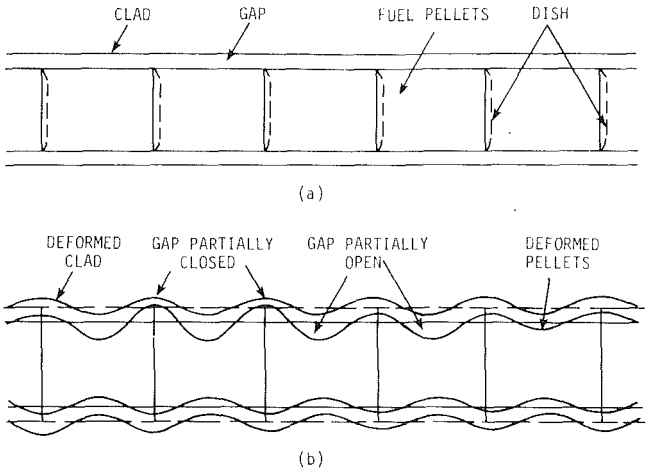

Fig. 6 Bambooing or ridging of oxide fuel element after a period of in-reactor operation (*a*) initial state, (*b*) deformed state

$$h_{\text{gap}} = \frac{k_{\text{gas}}}{a_1(\delta_f+\delta_c)+(\xi_f+\xi_c)} + \sigma_{sB}[e_f^{-1}+e_c^{-1}-1]^{-1} \times (T_s+T_i)(T_s^2+T_i^2) + \frac{k_m P_{\text{int}}}{aH} \tag{24}$$

in which $k_m = 2k_fk_c/(k_f+k_c)$, the harmonic mean of fuel and clad thermal conductivities, P_{int} is the interfacial contact pressure between fuel and clad surfaces, a is the radius of contact spot due to P_{int} in cm, H is effective hardness of the clad (e.g., for austenitic stainless steel Type 316, the average effective hardness $H \simeq 1.5\ (10^4)$ Kg/cm^2) [8], and k_f, k_c, δ_f, δ_c, etc., have been defined.

The relationships between temperature $T_s\,(=T_f)$ at the outer fuel surface and temperature $T_i\,(=T_c)$ at the inner clad surface and the gap distance L_g for a slight gap opening can also be expressed as

$$T_s = T_i + \frac{q}{2\pi k_{\text{gap}}} ln\left[\frac{r_i(1+\epsilon_{\theta_i}+\epsilon_{I_c})}{r_s(1+\epsilon_{\theta_s}+\epsilon_{th_f}+\epsilon_{I_f})}\right] \tag{25}$$

$$L_g = r_i(1+\epsilon_{\theta_i}+\epsilon_{IF_c}) - r_s(1+\epsilon_{\theta_s}+\epsilon_{th_f}+\epsilon_I) \tag{26}$$

where $\epsilon_{\theta i}$, ϵ_{th_c} and ϵ_{Ic} are tangential, thermal (expansion) and irradiation strains at the inner clad surface, ϵ_{θ_s}, ϵ_{th_f} and ϵ_I are tangential, thermal and irradiation swelling strains at the outer fuel surface, and k_{gap}, q, r_i, and r_s were defined previously. The tangential (mechanical), thermal and swelling strains may include the effect of fuel cracking during reactor operation.

If the mean temperature T_g of the gases contained in the gap is taken as

$$T_g = (T_i+T_o)/2 \tag{27}$$

the thermal conductivity of the thin gaseous gap k_{gap} can then be evaluated approximately by adding the gas thermal conductivity k_{gas} and the radiant thermal conductivity k_r

$$k_{\text{gap}} = k_{\text{gas}} + k_r = k_{\text{gas}} + 4L_g\sigma_{sB}[e_f^{-1}+e_c^{-1}-1]^{-1}T_g^3 \tag{28}$$

Partial Gap Open and Partial Gap Closed, "Bambooing" (Ridging). In the case the gap is partially open and partially closed due to bambooing (ridging or ovalling) along the longitudinal direction of the fuel element, an average gap conductance can be obtained from equations (22) and (24) derived in the cases of complete gap opening and complete gap closure, respectively.

The source for the case of partial gap opening and partial gap closure is resulted from the phenomenon of bambooing of the oxide (or ceramic) fuel elements operated in a LMFBR. Figure 6 illustrates the bambooing phenomenon: (*a*) the initial cold state of an oxide fuel element filled with many fuel pellets, (*b*) the deformed state of an oxide fuel element after a sufficient operation time of neutron irradiation. It can be seen that apart from the axial elongation reduced by some dishing device, the lateral expansion outward at the ends of each fuel pellet is in contrast with the lateral shrinkage at the middle section. This is attributed to the combined effect of fuel densification, isotropic shrinkage, thermal expansion, irradiation swelling, and induced stresses and strains in different proportions at the different portions of the fuel pellet and, consequently, cladding. As a whole, the gap at the ridge (or the node of the bamboo) is closed while the gap in the valley is open along the longitudinal direction of the fuel element or fuel rod.

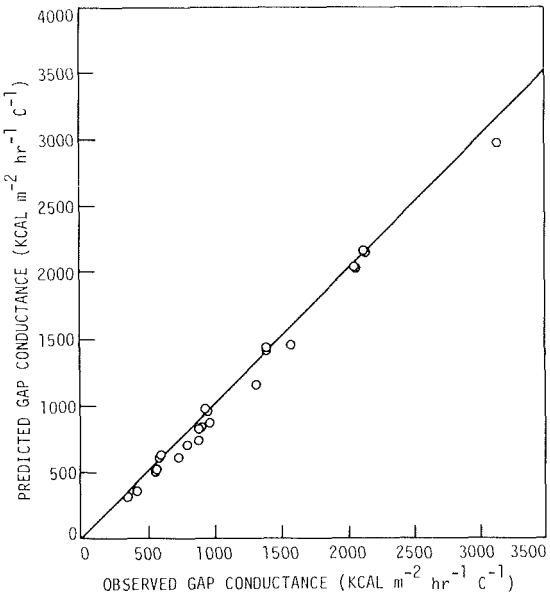

Fig. 7 Variation of predicted and observed fuel pellet-cladding gap conductance

Verification of some reported and predicted gap conductances of UO_2 and $(U,Pu)O_2$ fuel pellets with helium bonding is shown in Fig. 7. The reported and predicted gap conductances are in good agreement.

Irradiation Swelling in Fuel and Cladding Materials

Apart from thermal-cycling growth and irradiation growth, the most important irradiation (or radiation) effects on nuclear fuel and cladding (or structural) materials are irradiation swelling and irradiation creep, which limit the performance of fuel elements (or rods) and influence reactor safety during operation. Irradiation swelling that increases the fuel and clad volumes is induced by void and bubble formation and agglomeration of inert fission gases ^{85}Kr, ^{133}Xe and nuclear transmutation ^{4}He. Irradiation creep that increases the fuel and clad plastic deformation is developed and enhanced by intense neutron irradiation environment at elevated, irradiation temperature.

Irradiation Swelling in Nuclear Fuel $(U,Pu)0_2$. The irradiation swelling in the nuclear fuel is comprised of solid-solution swelling and inert fission gas swelling (major part).

The fission product solid-solution swelling volume increase, $(\Delta V/V)_{sld}$ is represented by

$$(\Delta V/V)_{sld} = C_b\dot{F}t = C_bq_v/C_1' \tag{29}$$

where C_b is the constant volumetric contribution per fission per unit volume, $\dot{F}=q_v/C_1'$ is the fission rate per unit time per unit volume of the fuel, q_v is the volumetric heat generation rate and C_1' is the conversion constant.

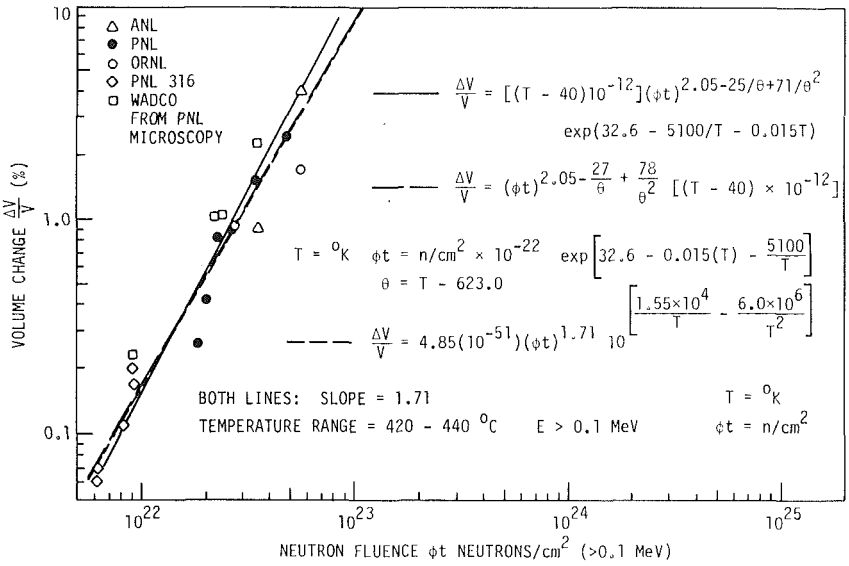

Fig. 8 Volume change varies with neutron fluence for 316 stainless steel

The total volumetric increase of inert fission gas swelling, $(\Delta V/V)_{\text{gas}}$ due to fission gas bubbles anchored in the grain boundaries, $(\Delta V/V)_{sgb}$, gas bubbles in the dislocations, $(\Delta V/V)_{sgd}$, and gas bubbles moving in the grain, $(\Delta V/V)_{sgm}$, is expressed as [3]

$$(\Delta V/V)_{\text{gas}} = (\Delta V/V)_{sgb} + (\Delta V/V)_{sgd} + (\Delta V/V)_{sgm} \tag{30}$$

in which

$$(\Delta V/V)_{sgb} + \frac{1}{L}\sum_{i=0}^{n-1}\left[N_{i,n}\left(\frac{1}{6}\pi d_i^3\right)\right] \tag{31}$$

$$(\Delta V/V)_{sgd} = \frac{1}{6}\pi(d')^3 N_0 \tag{32}$$

$$(\Delta V/V)_{sgm} = \frac{t-t_{cg}}{t_g}\left(\frac{1}{6}\pi \mathrm{d}_{\mathrm{cg}}^3\right)\mathrm{N}_0 \tag{33}$$

$L(=\pi/4D)$ is the average parallelepiped length of gas bubbles in the direction of thermal gradient, D is the average diameter of the grain in the equiaxed grain region, d_i is the bubble diameter at the dislocation, $t_g = L/v_b$ is the time required for a bubble to travel across the parallelepiped in the grains, v_b is the migrating velocity of the bubble derived from the surface diffusion theory, t_{cg} is the time required for a bubble to attain its critical size to begin moving, d_{cg} is the critical diameter of the grown bubble size, $n(>x)$ is the number of time intervals, $N_{2,n}$ is the number of bubbles per unit area at the ith collision after xth time intervals, and $N_o = (N_{o,i})^{3/2}$ is the number of bubbles with diameter d per unit volume. For $t \geq (t_{cq}+t_g)$, $(\Delta V/V)_{sgm} = 0$. For the isotropic swelling, the irradiation swelling strain $\epsilon_I = (\Delta V/V)/3$.

Irradiation Swelling in Cladding or Structural Material, Stainless Steel. There are two direct experimental methods for investigating the irradiation swelling of nuclear fuel and structural materials: (1) the transmission electron microscopy (TEM), whereby the number of voids and the total swelling volume are determined, and (2) the macroscopic dimension measurement (MDM), whereby the dimensions of specimens are measured before and after neutron irradiation. The MDM data are more easily obtained and generally more accurate than TEM data for large changes in volumes ($\Delta V/V > 0.005$).

From experimental data collected for AISI Types 304 and 316 cold-worked austenitic stainless steel, the empirical equations for change in volumes due to irradiation swelling obtained from the respective TEM and MDM methods are

$$\frac{\Delta V}{V} = [(T-40)10^{-12}](\phi t)^{2.05-25/\theta+71/\theta^2} \times \exp\,[32.6-5100/T-0.015T] \tag{34}$$

$$\frac{\Delta V}{V} = (\phi t)^{2.05-27/\theta+78/\theta^2}[(T-40)10^{-12}] \times \exp\,[32.5-5000/T-0.015T]$$

for

$$\phi t = 10^{-22} n/\mathrm{cm}^2 \text{ and } T \text{ in K} \tag{35}$$

$$\frac{\Delta V}{V} = 4.85(10^{-51})(\phi t)^{1.71} 10^{[1.55(10^4)/T - 6.0(10)^6/T^2]} \text{ for } \phi t \text{ in } n/\mathrm{cm}^2 \text{ and } T \text{ in } K \tag{36}$$

in which ϕ is the neutron flux, t is the irradiation time, ϕt is the integrated neutron flux or neutron fluence, and $\theta = T - 623$ K, the effective temperature.

For purposes of comparison of equations (34-36), the variation in volume change, $\Delta V/V$, of Types 304 and 316 cold-worked stainless steel with fast neutron fluence, ϕt, is plotted in Fig. 8. The empirical equations developed from the TEM and MDM fit quite well with the experimental data in the irradiation temperature range 420 – 440°C.

Experimental data for volume change obtained from three groups of specimens (made of austenitic stainless steel 304 and 316 and irradiated in the EBR-II at different neutron fluences, $E > 0{,}1$ Mev) show possible multi-peaks (instead of a single peak predicted by the empirical equations) of irradiation swelling as irradiation temperature increases continuously. This feature of multi-peaks of irradiation swelling in the solution-treated specimens illustrated in Fig. 9 (with twin peaks) reveals some trends: for a cladding material (austenitic stainless steel 304 or 316, of LMFBR) with increasing irradiation temperatures, the irradiation swelling initially increases, passes through a peak, drops to a very low valley, then rises to a new peak and drops again. The height of the peaks appears to increase with the neutron fluence ϕt (see Fig. 9). The peak of the swelling occurring at a certain irradiation temperature is called the irradiation swelling breakaway. A comparison of irradiation swelling varying with irradiation temperature in solution-treated and 20 percent cold-work 316 stainless steel is shown in Fig. 10.

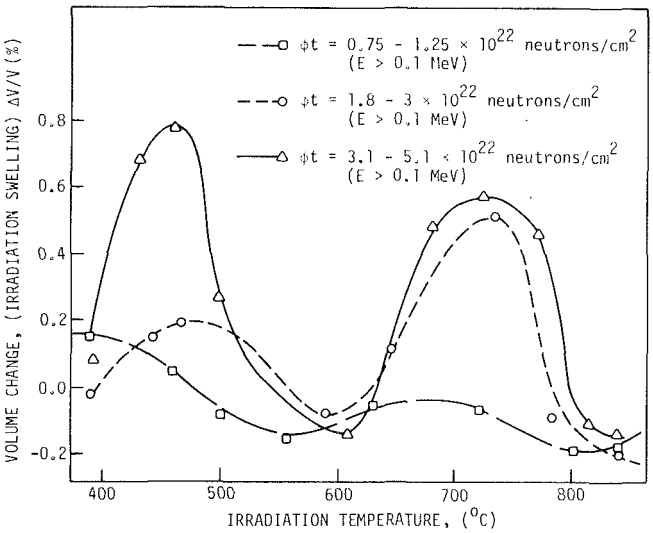

Fig. 9 Irradiation swelling varies with irradiation temperature in solution treated and 50 percent cold work 316 stainless steel

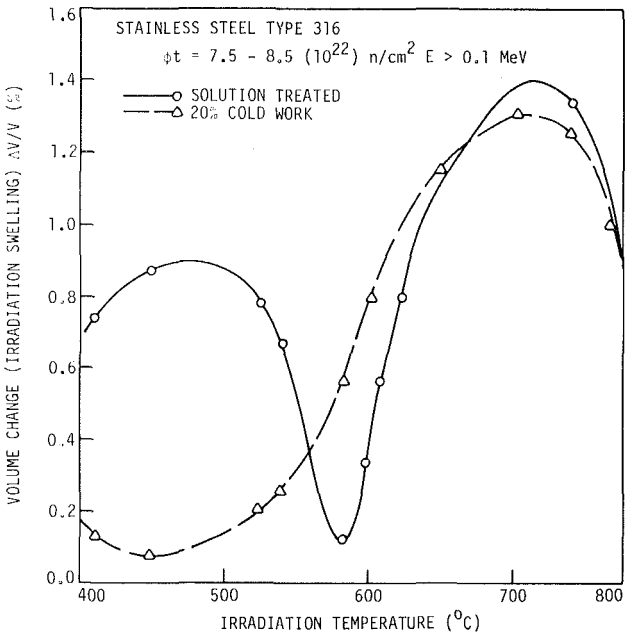

Fig. 10 Variation of irradiation swelling with irradiation temperature in solution treated and 20% cold work 316 stainless steel.

Irradiation Creep in Nuclear Fuel and Cladding Materials

Nuclear radiation can induce irradiation creep in the fuel and cladding materials of LMFBR fuel elements during reactor operation. The rate of irradiation creep, ϵ is much greater than that of ordinary thermal creep. In other words, the irradiation creep rate is highly enchanced in an intense neutron radiation environment.

Based on the analytical results and experimental data, it is postulated that the irradiation creep strain ϵ and creep rate $\dot{\epsilon}$ of $(U, Pu)0_2$ in the reactor are expressed as

$$\epsilon = (\sigma/\sigma_0)^n t \exp(-Q/RT) \tag{37}$$

$$\dot{\epsilon} = (\sigma/\sigma_0)^n \exp(-Q/RT) \tag{38}$$

where σ is the applied creep stress, σ_0 is the material creep modulus, n is the material creep number, and Q, R, and T have been defined. Both σ_0 and n depend moderately on fuel structure, density, irradiation time, neutron fluence and experimental condition. The last (exponential) term represents the effect of thermal (irradiation) diffusion in the Arrhenius form.

On the basis of experimental data obtained from specimens of stainless steel 316 irradiated in the EBR-II, the irradiation creep strain ϵ and strain rate $\dot{\epsilon}$ at stress σ, neutron flux ϕ, irradiation time t and irradiation temperature T have been postulated (9)

$$\epsilon = [A(1 - e^{-\phi t/(\phi t)_0})(\sigma/\sigma_0)^n + B\sigma\phi t] \exp(-Q/RT) \tag{39}$$

$$\dot{\epsilon} = \left[A\frac{\phi}{(\phi t)_0} e^{-\phi t/(\phi t)_0}(\sigma/\sigma_0)^n + B\sigma\phi\right] \exp(-Q/RT) \tag{40}$$

where the product $(\phi t)_0$ is reference neutron fluence, A and B are constants, and σ_0, n, Q and R are as defined above. On the right side of equation (40), the first term in the brackets represents the irradiation growth, swelling and creep rate due to neutron fluence ϕt and induced applied stress σ. The second term expresses the correlation between neutron flux intensity and applied stress. Outside of the brackets, the Arrhenius form gives the effect of thermal (irradiation) diffusion during irradiation creep in a nuclear reactor.

In the normal case, the irradiation temperature T is practically constant for cladding material tested in a research or power LMFBR. Hence, the term $\exp(-Q/RT)$ becomes constant, and equation (40) reduces to

$$\dot{\epsilon} = A_1 \frac{\phi}{(\phi t)_0}(\sigma/\sigma_0)^n e^{-\phi t/(\phi t)_0} + B_1\sigma\phi \tag{41}$$

in which $A_1 = A\exp(-Q/RT)$, $B_1 = B\exp(-Q/RT)$.

Fuel Burnup and Fission Gas Release

An important consideration in relation to cost of nuclear fuel per kilowatt-hour of electricity generated is the amount of fuel burnup and fission gas release in the fuel elements. The fuel burnup is a measure of quantity of fissile material consumed or electric power generated before the fuel elements are discharged from the reactor core for reprocessing.

There are three ways to express the magnitude of the fuel burnup: (1) number of megawatt-days of thermal energy generated per tonne of uranium (U-235), *MWD/T*, (2) number of fissile atoms fissioned per cm^3 of nuclear fuel, and (3) percentage of fissile nuclei consumed from the fuel. Both (2) and (3) are scientifically preferable in many respects and can be converted to the *MWD/T* unit used in nuclear industry [10].

It is of interest to note that 1 gram of U-235 can generate 1 *MWD/T* nuclear fission energy and 1 gram of deuterium (D_2) can generate 4 *MWD/T* nuclear fusion energy, approximately. On the other hand, the cost of deuterium is much less than that of U-235 for equal weight.

The number of fissions per cm^3 of fissile fuel is usually expressed in terms of burnup, *BU*, equal to fission rate $\dot{F}$ multiplied by time t, i.e.,

$$BU = \dot{F}t \tag{42}$$

Fission gas release is mainly a function of fuel (irradiation) temperature and burnup, as is irradiation swelling in fuel. Figure 11 shows the variations of observed irradiation swelling and fission gas release with fuel (irradiation) temperature and burnup of an oxide fuel, $U0_2$ or $(U,Pu)0_2$. For fuel temperature below 1350°C, the irradiation swelling and fission gas release depends on the fuel burnup and linear power rating. For fuel temperature above 1600-1700°C, irradiation swelling and fission gas release increase rapidly in a nonlinear manner. The chief reason is that at high temperatures, most fission gases are released through micro- and

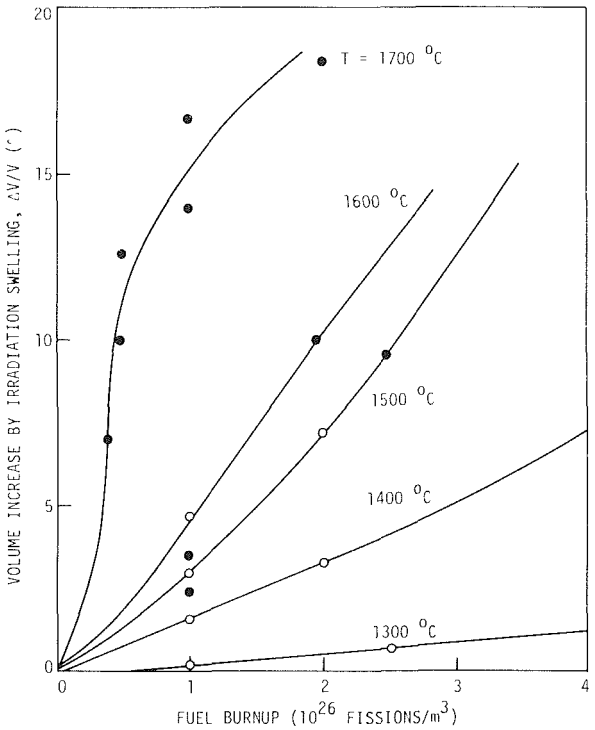

Fig. 11 Comparison of predicted and observed irradiation swelling varies with fuel burnup and irradiation temperature

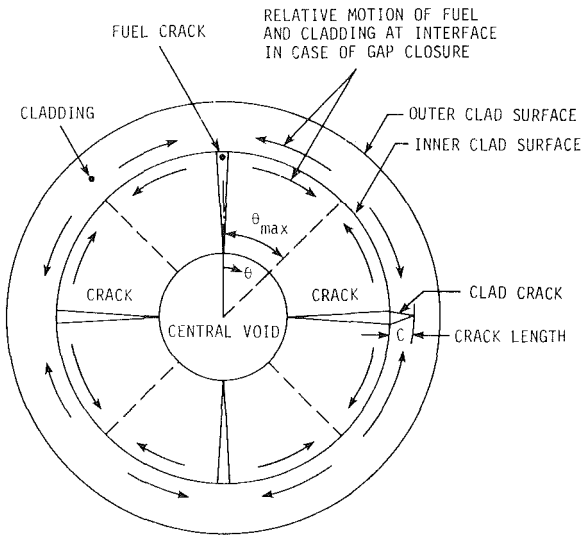

Fig. 12 Simplified thin shell model representing fuel pellet-cladding interaction and cracking

macro-cracks of an oxide fuel. The fission gases released in the radial direction of fuel cracks can influence irradiation swelling and initiate stress fatigue cracking (SFC) and stress corrosion cracking (SCC) at the inner clad surface during pellet-cladding interaction (PCI).

At high fuel temperature and burnup, fission gases released from the oxide fuel consist of two components: (*a*) that due to fuel restructuring (or grain growth), and (*b*) that due to gas bubble migration through the micro- and macro-cracks in the fuel.

For component (*a*) the total number of fission gas atoms, m_g, released to the central void can be computed from the semiempirical equation

$$m_g = m_f \pi r_2^2 \dot{F} t \tag{43}$$

where $m_f = 0.27$, based on the average experimental data of fission gas atoms produced per unit volume, and r_2, $\dot{F}$ and t have been defined.

For component (*b*), the total number of fission gas atoms, m_b, released from the grain boundaries to the central void, and then migrating through micro- and macro-cracks from bubbles located between the radius r_j and r_{j-1} of the fuel can be given by [3]

$$m_b = N_t(4\gamma - \sigma_H d_{cb}) \frac{\pi d_{cb}^2}{6k_B T} \pi (r_j^2 - r_{j-1}^2) \tag{44}$$

where N_t is the total number of bubbles migrating away from the grain boundaries per unit volume, γ is the surface tension of fuel material, σ_H is the hydrostatic pressure in fuel around the bubble, d is the critical diameter of collided bubbles during migration, k_B is the Boltzmann constant and T has been defined.

Adding equations (43) and (44) yields the total fission gas atoms, m_T, released first to the central void and then to the pellet-cladding gap and plenum of the fuel elements

$$m_T = m_g + m_b \tag{45}$$

Fuel Pellet and Cladding Cracking

Concerning multiaxial stresses of nuclear fuel elements, the initiation of crack nucleation and the extension of crack propagation are due mainly to thermal shock, temperature gradient, nonuniform thermal expansion, thermal-cycling fatigue, and/or stress corrosion effect. On the basis of solid mechanics, it was postulated for the cracking theory and mechanism that the shearing stress (micro-structural, intergranular, and macroscopic stress) nucleates cracks and the principal stress propagates and extends cracks along the plane normal to the principal stress [9]. Nuclear fuel and cladding (or structural) materials are particularly susceptible to cracking, i.e., stress fatigue cracking (SFC) and stress corrosion cracking (SCC).

Fuel Pellet Cracking and Crack Healing

A simplified thin shell model representing fuel pellet-cladding interaction and cracking during the gap closure (or near closure) is illustrated in Fig. 12. Just as the development of cracking in the oxide fuel pellet can occur in an early beginning of life (BOL) during a rapid increase in power level, the cracks (see Fig. 12) can also be closed after the cracking healing takes place because of grain growth and power decrease. The cracks can reopen when a ramp power increases again. Fuel crack healing and reopening can relieve fracture stress and release fission gases from the central void to the gap and plenum. As a result, the gap conductance could change appreciably.

In regard to the crack healing due to annealing grain growth after cracking development, the recovery in mechanical strength or rate of crack healing depends mainly on the irradiation-annealing time t and temperature T. From the principle of linear-elastic fracture mechanics, before the development of cracking the material is considered as elastic, while after cracks take place the material around the tip of the crack is considered as inelastic. Based on this principle, it is assumed that the rate of crack healing, $\partial c/\partial t$, is a function of a second-order (inelastic property) of crack length c and irradiation temperature T in the Arrhenius form

$$\frac{\partial c}{\partial t} = gc^2 \exp(-Q/RT) = g_T c^2 \tag{46}$$

where g is a constant, $g_T = g \exp(-Q/RT)$, and Q and R have been defined.

The Griffith relation for crack length c and fracture strength σ of a cylindrical fuel pellet (or clad) is expressed as

$$\sigma = (E\eta/\pi c)^{1/2} \tag{47}$$

in which E is the elastic modulus and η is the specific energy per unit area. Integrating equation (46) from $t = 0$ (for $c = c_0$) to any time t (for any crack length c) during crack healing, the ratio c/c_0 is obtained

$$\frac{c}{c_0} = [1 + c_0 g_T t]^{-1} \tag{48}$$

where c_0 is the maximum crack length just before the healing process takes place. The ratio c/c_0 diminishes as the healing time t increases. Since from equation (47), $c = E\eta/\pi\sigma_0^2$, $c_0 = E\eta/\pi\sigma_0^2$, by introducing these values into equation (48) to eliminate c and c_0, the ratio of measurable fracture stresses at any time t is

$$\frac{\sigma}{\sigma_0} = \left[1 + \frac{E\eta}{\pi\sigma_0^2} g_T t\right] \text{ for } \sigma > \sigma_0 \tag{49}$$

At the end of complete healing time t_f and the original strength σ_f (or elastic limit) being recovered, equation (49) becomes

$$\frac{\sigma_f}{\sigma_0} = \left[1 + \frac{E\eta}{\pi\sigma_f^2} g_T t\right]^{1/2} \tag{50}$$

Therefore, the healing time needed to recover the original strength just before cracking occurs is

$$t_f = (\sigma_f^2 - \sigma_0^2)\frac{\pi}{E\eta g_T} = (\sigma_f^2 - \sigma_0^2)\frac{\pi}{E\eta g} e^{Q/RT}$$

for

$$\sigma_f > \sigma_0 \tag{51}$$

It is noted that the cracking and crack healing in fuel pellets are the predominant factors to affect the pellet-cladding gap closure, gap reopening and, in turn, gap conductance for heat removal from the fuel and reactor core safety during PCI at the unsteady state.

Cladding Cracking. Post-irradiation examination of failed fuel elements indicates that crack (microstructural, intergranular or macroscopic) nuclection process at the inner clad surface could be begun with pits or hydride patches of iodine, cadnium, tellurium, etc., compounds of fission products followed by (crack) propagation, SFC and SCC mechanisms during PCI. The compounds CsI, CdI_2, Cs_2Te, etc., are very aggressive to initiate SFC and/or SCC at the inner clad surface opposite to the fuel pellet cracks (see Fig. 12).

It is postulated from post-irradiation results that SFC and/or SCC is initiated by the combination of threshold (mechanical) stress and corrosive (chemical) reactants in an environment of fission products that promote fatigue and/or corrosion cracking. The threshold stress and corrosive reactants are considered intrinsic properties of the combined loading-material-environment resulting system related to the formation of SFC and/or SCC during PCI.

The corrosion effect of sodium (liquid metal) on cladding material (austenitic stainless steel 316) depends mainly on operating temperature, time and impurity involved in the liquid-metal coolant.

Cladding Material Requirements and PCI

In addition to the nuclear, physical and thermal properties required, the cladding or structural materials require high mechanical strength and ductility in the elevated temperature and intensive irradiation environment. The maximum allowable or threshold stess (or strain) to failure for each cladding or structural material in the reactor design and operation must always be observed.

When a cladding material maintains sufficient mechanical strength and ductility under the thermal, irradiation, creep, cracking and liquid-metal corrosion condition, the LMFBR fuel elements fail to (material) yield only. It would follow the yield criterion of the distortion energy theory, no matter how the PCI operates in the fuel elements or rods. This is called the yield failure.

On the other hand, if the cladding material subject to the environment of high temperature, irradiation swelling, irradiation creep, irradiation hardening, helium embrittlement (due to (n, α) nuclear transmutation with elements such as Ni, Cr, Fe, etc., present in the cladding material), thermal shock or cycling, and fission product corrosion (especially I, Cd, Te) at high burnup undergoes SFC and/or SCC (nucleated and propagated from the inner cladding surface) is called the fracture failure.

In general, the fracture failure of LMFBR fuel elements or rods at their bamboo-like nodes (or oval ridges) due to SFC and/or SCC during PCI is more frequent and serious than the yield failure when the fuel rod or reactor core safety of LMFBR is concerned.

Primary Conclusions

From the preceding analysis for the heat generation, fuel restructuring, temperature distribution, gap opening, gap closure, gap conductance, irradiation swelling, irradiation creep, fuel burnup, fission gas release, fuel pellet cracking and healing, cladding cracking, yield failure and fracture failure of LMFBR fuel elements or rods the following primary conclusions are made:

1 The temperature distribution, thermal gradient, fuel restructuring, densification, and cracking, and change in the gap conductance vary with the radial space (radius or variable), irradiation time, and linear power rating of the LMFBR fuel elements or rods.

2 The change in the fuel pellet-cladding gap thickness (or length) during the gap opening, gap closure, and partial gap opening and partial closure during fuel cracking, crack healing, and bambooing (or ovally ridging) can have a great effect on the gap conductance, heat removal (and utilization), and safety of the fuel elements.

3 The basic crack theory and mechanism that the shearing stress (microstructural, intergranular and macroscopic) nucleates cracks and the principal stress propagates and extends cracks along the plane normal to the principal stress was postulated and verified by experimental observation and post-irradiation examination for stress fatigue cracking (SFC) and/or stress corrosion cracking (SCC) during PCI. The fission product compounds CsI, CdI_2, Cs_2Te, etc., are very aggressive to initiate SFC and/or SCC at the inner clad surface opposite to the fuel pellet cracks.

4 If the cladding material could maintain sufficient mechanical strength and ductility in the thermal, irradiation, creep, thermal shock or cycling, and corrosion environment, the fuel-element failure would be attributed to yield that obeys the yield criterion of the distortion energy theory.

5 To improve the fuel performance and fuel rod safety at high temperature and fuel burnup, these important factors desired (or required) should be taken into consideration: (a) maintaining ductility of cladding material (material development), (b) providing sufficient gap thickness and plenum space for fission gas accommodation (fuel element design), (c) keeping ramp power increase rate slow and gentle (reactor operation), and (d) reducing the intensity and frequency of transient PCI to avoid intense PCI-SFC and/or PCI-SCC at the inner cladding surface of LMFBR fuel elements or rods (reactor design and operation).

On the other hand, if the cladding material subject to the high temperature, irradiation swelling, irradiation creep, irradiation hardening, helium embrittlement, and fission

product corrosion undergoes SFC and/or SCC the fuel elements would suffer from fracture failure.

In general, the fracture failure of LMFBR fuel elements located at the bamboo-like nodes (or oval ridges) is more frequent and serious than the yield failure when the fuel element or reactor core safety is concerned.

Acknowledgment

The author wishes to express his appreciation to the Department of Nuclear Engineering, the Engineering Research Institute, and the College of Engineering of Iowa State University for their encouragement and assistance for the research and for the preparation of this work.

References

1 Ranjan, G. V., and Smith, E., *Proceedings of the 4th International Conference on Structural Mechanics in Reactor Technology*, Vol. C, Paper No. 2/C, San Francisco, Calif., 1977.

2 Roberts, J. T. A., et al., *Nuclear Technology*, Vol. 35, 1977, p. 131.

3 Cheng, C. K. and Ma, B. M., "Thermal, Radiation and Mechanical Analysis for Unsteady-State Fuel Restructuring of Cylindrical Oxide (Fuel) Elements in Fast Reactors," *Nuclear Science and Engineering*, Vol. 48, 1972, pp. 139–158.

4 Ma, B. M., "Computer Code ISUNE-3: Transient Fuel Element Performance and Safety Analysis of LMFBR," Lecture Notes, Bologna University, Bologna, Italy, 10–14, April, 1978.

5 Dwyer, O.E., *Liquid Metals Handbook, Sodium and Nak Supplement*, U.S. AEC, 1970.

6 Dwyer, O. E., Berry, H. C. and Hlavac, P. J., *Nuclear Engineering and Design*, Vol. 23, 1972, pp. 273–295.

7 Ma, B. M., "Irradiation Swelling, Creep and Thermal Stress Analysis of LWR Fuel Elements, Computer Code ISUNE-2," *Nuclear Engineering and Design*, Vol. 34, 1975, pp. 361–378.

8 Boeschaten, F. and Van der Held, E. F. M., "The Thermal Conductance of Contacts between Aluminum and Other Metals," *Physics*, Vol. 23, 1957, pp. 37–44.

9 Ma, B. M., "Irradiation Swelling, Creep, Thermal-Shock and Thermal-Cycling Fatigue Analysis of Cylindrical Controlled thermonuclear Reactor First Wall," *Nuclear Engineering and Design*, Vol. 28, 1974, pp. 1–30.

10 Huebatter, P. R., "Nuclear Fuel Burnup Conversions," *Nucleonics*, Vol. 18, 1960, p. 176.

Effects of Coolant Air Inlet Conditions on Turbulent Flow Between a Turbine Disk and its Casing

T. Uzkan[1]
Bogazici University,
Department of Engineering,
Bebek, Istanbul, Turkey

An integral method to predict the performance of the incompressible, turbulent flow between a rotating disk and a parallel stationary wall, when there is radial outflow of ventilation air, is presented. Using this method, the effects of the inlet conditions of the ventilation air on the core rotation, on the radial velocity profile development, on the radial inflow rates, on the separation streamlines between outflow and inflow regions and on the disk torque coefficient are calculated and presented. The method is general enough to calculate other effects. The important conclusions are: (a) that inlet radial velocity profile should be skewed toward the stationary wall, to reduce radial inflow, and (b) that disk friction can be decreased by increasing the rotation of the ventilation air.

1 Introduction

This investigation is a study of the flow regime between a rotating disk and a parallel wall in the presence of radial outflow as shown in Fig. 1. It is important because of its implications to the cooling of gas turbine disks.

In order to decrease the operating temperatures of gas turbine disks while maintaining high disk speeds and high inlet gas temperatures, some means of cooling the disks are necessary. Among other methods, the radial outflow cooling method is used, particularly for turbines with short blades. In this method ventilation air[2] from the compressor is introduced into the gap between the turbine disk and the housing and it is allowed to flow radially outward. Utilization of minimum ventilation air for the specified temperature limit is an important design requirement.

There are two different mechanisms to be considered for the calculation of the amount of ventilation air: (*a*) The heat is conducted from the blades toward the center of the disk and is convected to the air between the wheel and casing. (*b*) The side surfaces of the turbine disk behave like a pump and cause air to flow outward near the disk due to the wheel rotation.

If the ventilation air flow rate is less than the amount of air pumped by the disk, a radial inflow of hot gas occurs on the housing, due to continuity, and increases the average temperature of the ventilation air. This general trend was observed in the earlier, unpublished experiments of the author [1,2] and is consistent with the data of Daily, et al. [3], Dorfman [4] and Sokolov [5]. The gases beyond the outer radius are the hot gases coming out of the combustion chamber of the turbine.

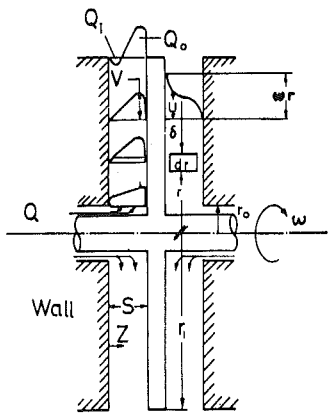

Fig. 1 Structure of flow field in the gap

There is considerable information in the literature concerning convection aspects, e.g., Sedack and Nespela [6], and Daily, et al. [7,8], but little is known about mechanism (*b*). On the other hand, if the disk pumping capacity is much larger than the rate of ventilation air necessary to convect the heat from the disk, mechanism (*b*) can be the dominant one. In any case, calculating the temperature of air without taking account of the radial inflow of hot gases toward the axis of rotation produces erroneous results as shown by Sokolov [5].

The pumping capacity of a disk is a function of several design and operating parameters. When all these parameters are specified, the minimum amount of ventilation air necessary to prevent radial inflow of hot gases is called the critical flow rate. At overcritical flow rates, the amount of ventilation air necessary to cool the disk can be determined by

[1] Present Address: Senior Research Scientist, International Harvester Company, Science and Tech. Lab., 16 W. 260 83rd. Street, Hinsdale, Ill. 60521.

[2] Cool air introduced into the gap between the turbine disk and its casing, through the gap along the turbine shaft, is usually called ventilation air.

Contributed by the Gas Turbine Division and presented at the Gas Turbine Conference, San Diego, Calif., March 12-15, 1979 of THE AMERICAN SOCIETY OF MECHANICAL ENGINEERS. Revised manuscript received at ASME Headquarters March 4, 1981. Paper No. 79-GT-35.

mechanism (a) alone (heat conduction and convection), but at undercritical flow rates mechanism, (b) can be the dominant one.

An approximate heat transfer analysis of an air cooled turbine disk with radial inflow of hot gases is given by Sokolov [5]. His analysis assumes that the volume flow rate of the ventilation air, Q, and the radial inflow rate, Q_1, are known. However, the inlet conditions of the ventilation air are expected to have considerable effect in determining the radial inflow rates of hot gases.

Within the last decade, there have been several studies of the flow field between a rotating disk and a stationary wall but none of them covers the present problem of turbulent flow regime between a rotating disk and stationary wall with radial outflow. They are either laminar flow problems solving the Navier-Stokes equations by numerical techniques, e.g., Truman, et al. [9], Holodniok, et al. [10], and Raal [11], or by approximate methods, e.g., Bein, et al. [12]. Metzger, et al. [13] presented an integral method of calculating the disk pumping capacity for turbulent flows, but they did not consider radial outflow. Senoo and Hayami [14] solved the turbulent flow problems between a rotating disk and casing but for the case of radial inflow. Gosman, et al. [15] presented a numerical solution scheme for the stream function, by using a two-equation turbulence model. However, their solution was for the problem of Bayley and Owen [16] with a cylindrical shroud at the end of the disk, and the effects of ventilation air inlet properties are not investigated. To the author's knowledge, there has been no systematic analysis of the effects of ventilation air inlet conditions on the flow regime, in general, or on the radial inflow characteristics, in particular. Therefore, an analysis having the ventilation air inlet conditions as parameters and predicting the amount of radial inflow of gases is needed.

This paper presents a physical model and a integral method of solution for the flow regime between a rotating disk and a parallel stationary wall with ventilation air introduced to the gap at radius r_0. The physical model used in the analysis is based on experimental data [1,2,3,6,7]. The effects of the inlet conditions (namely the preswirl, the inlet radius and the velocity profiles) upon the flow regime are investigated. The results are presented and compared with the data available in the literature. It should be noticed that this is the first analysis available to treat the turbulent flow in the present situation.

2. Analysis:

a. Assumptions. The flow of an incompressible, turbulent fluid between a rotating disk and a stationary wall, both perpendicular to the axis of rotation, is considered (Fig. 1). The axial spacing, s, is assumed to be small compared with the disk diameter. Between the wall and the disk the tangential component of the fluid velocity varies from zero to the disk speed. The tangential velocity boundary layers completely fill the gap. The ventilation air is introduced to the gap at r. There is radial outflow near the disk and there may be radial inflow near the wall. The flow is assumed to be turbulent throughout the gap.

Using power laws as for fully developed turbulent boundary layer flows [17], one may assume the radial velocity profile to be of the form

$$V = B_0 \cdot \left[b(r) + \frac{z}{\bar{s}} c(r) \right] \left(\frac{z}{\bar{s}} \right)^n \left(1 - \frac{z}{\bar{s}} \right)^n \tag{1}$$

This form of the radial velocity profile not only satisfies the boundary conditions on the wall and the disk, but also simplifies the analysis. B_0 is considered constant with r and z. The nondimensional parameters b and c are assumed to be taken as functions of r only. The component b can be interpreted globally as representing the radial diffuser effects caused by the increase in flow area. The component c represents the effects causing skewness in the velocity profile toward the disk with increasing r. Based on physical considerations one expects a decrease in b and an increase in c from the ventilation air inlet radius r_0 to r_1.

From the definitions of shear stress velocities for turbulent flows, the radial and tangential disk and wall friction can be written as:

$$\tau_{dr} = \rho V^{*2} \tag{2}$$

$$\tau_{wr} = \rho V_w^{*2} \tag{3}$$

$$\tau_d = \rho U_d^{*2} \tag{4}$$

$$\tau_w = \rho U_w^{*2} \tag{5}$$

In these relations, the shear stress velocities are to satisfy:

$$\frac{V}{V_d^*} = A \left[\frac{V_d^* \ (s-z)}{\nu} \right]^n \tag{6}$$

Nomenclature

A = Constant for turbulent velocity profile, $A = 8.74$

B_0 = constant for inlet radial velocity profile, equation (1)

b = dimensionless radial velocity function, corresponding to radial diffusion effects, equation (1)

C_m = disk torque coefficient, $C_m = M/(\rho\omega 2_{r_1}{}^5/2)$

C_v = dimensionless parameter, $C_v = K_v/(A^2.\mathrm{Re}^{2n}.(\bar{s})^{3n+1}.x_1^{n+3})$

c = dimensionless radial velocity function, corresponding to skewness effects, equation (1)

$e.$ = axial location where $V = 0$

E = dimensionless axial location where $V = 0$, $E = e/s$

K_v = throughflow parameter, $K_v = 2\pi r_1^2.s.\omega/Q$

K = core rotation, $K = \beta/\omega$

k = a constant equal to 1 or -1

M = torque on one side of the disk

n = exponent for turbulent velocity profile

P = pressure

P = dimensionless pressure, $\bar{P} = (P - P_1)/\omega^2 r_1^2 \rho$

Q = volume throughflow rate

Q_i = volume inflow rate

Q_o = volume outflow rate, $Q_o = Q + Q_i$

Re = disk reynolds number, $\mathrm{Re} = \omega r_1^2/\nu$

r = radial coordinate

r_1 = disk radius

$$\frac{V}{V_w^*} = A\left[\frac{V_w^* z}{\nu}\right]^n \tag{7}$$

$$\frac{r\omega - U}{u_d^*} = A\left[\frac{U_d^* \cdot (s-z)}{\nu}\right]^n \tag{8}$$

$$\frac{U}{U_w} = A\left[\frac{U_w^* \cdot z}{\nu}\right]^n \tag{9}$$

In these equations A and n represent turbulent flow constants to be determined empirically for the turbulent flow Reynolds number range under consideration as presented by Schlichting (17) for pipe flow. They correspond to $A = 8.74$ and $n = 1/7$ for the classical turbulent profiles. These values are assumed for the present calculation due to lack of velocity profile measurements.

b. Definitions. The dimensionless variables and parameters used in the following analysis are defined below:

$$X = r/r_0 \tag{10}$$

$$\bar{s} = S/r_1 \tag{11}$$

$$\bar{z} = z/s \tag{12}$$

$$E = e/s \tag{13}$$

$$K = \beta/\omega \tag{14}$$

$$\mathrm{Re} = \frac{\omega r_1^2}{\nu} \tag{15}$$

$$T = \frac{\omega r_1}{B_0} \tag{16}$$

$$\bar{P} = \frac{P - P_1}{\rho\omega 2_{r1}^2} \tag{17}$$

$$K_v = \frac{2\pi r_1^2 s\omega}{Q} \tag{18}$$

$$C_m = \frac{M}{1/2\rho\omega^2 r_1^5} \tag{19}$$

Additionally, the following volume flow averages of the velocities are used:

Radial
$$V_r = \frac{Q}{2\pi rs} \tag{20}$$

Tangential
$$\bar{U} = \frac{\int_0^s UVdz}{\int_0^s Vdz} = \beta r \tag{21}$$

Moreover, certain combinations of dimensionless numbers encountered in the analysis are found to be very useful in presenting the results in a compact way. They are:

$$\theta = \left(\frac{T}{R_e}\right)^{\frac{2n}{1+n}} \cdot \frac{1}{X_1} \cdot \frac{1}{\bar{s}^{\left(\frac{3n+1}{n+1}\right)}} \tag{22}$$

$$C_v = K_v \frac{1}{A^2 . \mathrm{Re}^{2n} \bar{s}^{(3n+1)} X_1^{n+3}} \tag{23}$$

The complete and incomplete Beta functions used in the analysis are defined as:

$$\beta_e(a,w) = \int_0^1 t^{a-1}(1-t)^{w-1} dt \tag{24}$$

$$\beta_i(a,w,h) = \int_0^h t^{a-1}(1-t)^{w-1} dt \tag{25}$$

c. Governing Equations.

i. Continuity Relation. The application of the continuity principle on a surface of radius r gives:

$$Q = \int_0^s 2\pi r V dz = \text{constant} \tag{26}$$

If equation one is used in the integrand and the result is simplified by applying equation (24), equation (26) becomes

$$Q = 2\pi r B_0 \beta e(n+1,\ n+1)\quad (b + \frac{c}{2}) = \text{constant} \tag{27}$$

Applying equation (27), once for a surface of radius r, and once for r_0, yields

$$b_0 + \frac{c_0}{2} = X(b + \frac{c}{2}) \tag{28}$$

If there is radial inflow on the stationary wall at a radial

Nomenclature (cont.)

r_0 = radius at the inlet for ventilation air
s = axial spacing between disk and wall
$\bar{s}$ = dimensionless axial spacing, $\bar{s} = s/r_1$
T = dimensionless radial velocity parameter, $T = \omega r_1/B_0$
U = tangential component of velocity
$\bar{U}$ = average tangential velocity based on volume flow rate, equation (21)
V = radial component of velocity
V_r = average radial velocity based on volume flow rate, $V_r = Q/2\pi rs$, equation (20)
X = dimensionless radius, r/r_0
z = distance from wall
$\bar{z}$ = dimensionless distance from wall, $\bar{z} = z/s$
β = angular velocity of the fluid at $\bar{z} = 0.5$
$\beta(a,\omega)$ = beta function
$\beta_i(a,\omega,h)$ = incomplete beta function
θ = dimensionless parameter, $(T/\mathrm{Re})^{\frac{2n}{n+1}} / (X_1 . \bar{s}^{\frac{(3n+1}{n+1}})$
ν = kinematic viscosity
ρ = density of fluid
ω = disk angular velocity
τ = shear stress

Subscripts

d = values on the disk
0 = values at inner radius r_0
r = radial direction
1 = values at outer radius r_1
ϕ = tangential direction
w = values on the wall

Superscripts

* = friction velocities

distance r, then there is a point in the gap where the radial velocity is zero. The axial distance e, from this point to the stationary wall, is obtained from equation (1) as

$$E=\frac{e}{s}=\frac{Z}{s}\Big|_{v=0}=-\frac{b}{c} \tag{29}$$

At any given radius r, the radial inflow on the wall can be calculated from the relation

$$Q_i=\int_0^e 2\pi r V dz \tag{30}$$

Using equations (1,25) and (27) in this relation and simplifying, one obtains:

$$\frac{Q_i}{Q}=\frac{b\beta_i(n+1,n+1,E)+c\beta_i(n+2,n+1,E)}{(b_0+\frac{c_0}{2})\beta_i(n+1,n+1)}.X \tag{31}$$

The radial outflow between point e and the rotating disk can be calculated from

$$\frac{Q_o}{Q}=1+\frac{Q_i}{Q} \tag{31.b}$$

ii. Radial Momentum Equation. The application of the momentum principle to an elemental control volume dr, at radius r, gives

$$\frac{\partial}{\partial_r}\int_0^s \rho r V^2 dz=\int_0^s \rho U^2 dz-r\frac{\partial}{\partial r}\Big|_0\int^s P dz\Big| - \Big|\tau_{dr}\mp\tau_{wr}\Big|.r \tag{32}$$

Using equation (1) in the first term of equation (32) and simplifying, one finds

$$\frac{\partial}{\partial_r}\Big|r\int_0^s V^2 dz-B_0^2 s\beta_e(2n+1;\ 2n+1)\frac{d}{dr}\Big|r(b^2+bc+\frac{n+1}{4n+3}c^2)\Big| \tag{33}$$

Using equation (2, 3, 6) and (7) in the last term of equation (32) and simplifying, one obtains

$$\tau_{dr}\mp\tau_{wr}=\rho(\frac{\nu}{s})^{\frac{2n}{n+1}}.(\frac{B_0}{A})^{\frac{2}{n+1}}\Big|(b+c)^{\frac{2}{1+n}}+k\,b^{\frac{2}{1+n}}\Big| \tag{34}$$

Here the multiplier k is introduced to indicate the direction of the radial flow on the stationary wall. If this flow is radially outward, $k=1$; if inward, $k=-1$.

To simplify the centrifugal and the pressure terms in equation (32), it is assumed that the pressure is a function of r only and is constant in the z direction. This assumption is expected to be valid for small values of s/r. Moreover, in the midsection (i.e., $\bar{z}=0.5$), it is assumed that the radial pressure gradient is mainly influenced by:

(*a*) the centrifugal force due to the fluid rotation, and

(*b*) the radial diffuser effects due to the enlargement of the flow area.

For an elemental control volume in the core, the balance of forces in the radial direction is

$$r\frac{dP}{dr}=\rho U^2-\rho\frac{d}{dr}(rV^2) \tag{35}$$

Using equations (18) and (20) in equation (35), one obtains

$$r\frac{dP}{dr}=\rho U^2-\rho\frac{r_1^4}{r^2}\frac{\omega^2}{K_v^2} \tag{36}$$

and

$$\int_0^s(\rho U^2-r\frac{dP}{dr})dz=t\rho\ \frac{r_1^4}{r^2}\frac{\omega^2 s}{K_v^2} \tag{37}$$

Substituting equations (28, 33, 34) and (37) in equation (32), nondimensionalizing by equations (10 – 25) and simplifying, one obtains the governing equation for the nondimensional radial velocity component,

$$\frac{dc}{dx}=\frac{8n+6}{x.c}-\Big[\frac{(b_0+\frac{C_0}{2})^2}{x^2}-\frac{c^2}{16n+12}-\frac{1}{\beta_e(2n+1,2n+1)}\cdot\Big|\frac{(b_0+\frac{c_0}{2})^2}{2}\beta_e^2(n+1,n+1)+\theta.\Big|\frac{X}{A\frac{2}{n+1}}\cdot\Big|(b+c)^{\frac{2}{n+1}}+k\,b^{\frac{2}{n+1}}\Big|\Big] \tag{38}$$

iii. Tangential Momentum Equation. The equation of the moment of momentum on an elemental control volume at radius r, between the disk and the stationary wall, is:

$$\rho\frac{d}{dr}\Big|r^2\int_0^s VU dz\Big|=r^2\Big|\tau_{d\rho}\mp\tau_{\omega\phi}\Big| \tag{39}$$

Assuming the validity of equations (8) and (9) to $z=s/2$, using equations (4) and (5), and nondimensionalizing by equation (23) for C_v, one obtains

$$\frac{d}{dx}[X^2K]=2^{\frac{2n}{1+n}}.C_v.X^{\frac{4+2n}{1+n}}\Big[K^{\frac{2}{1+n}}-(1-K)^{\frac{2}{1+n}}\Big] \tag{40}$$

This relation is the basic equation for the core rotation k, at $\bar{z}=0.5$.

To calculate the pressure distribution in the gap, one can nondimensionalize equation (36) by using equations (10 – 18) and can obtain

$$\frac{d\bar{P}}{dx}=X^2K^2\frac{1}{X_1^2}+\frac{X^2}{X^2.K_v^2} \tag{41}$$

iv. Disk Torque Calculation. The torque on one side of the disk is

$$M=2\pi\int_{r_0}^{r_1} r^2\tau_{d\rho}dr \tag{42}$$

Using equations (4) and (8) in equation (42) and simplifying gives the disk torque coefficient

$$C_M=4\pi\Big(\frac{2^n}{A}\Big)^{\frac{2}{1+n}}.\Big(\frac{1}{\bar{s}\,\mathrm{Re}}\Big)^{\frac{2n}{1+n}}\cdot\frac{1}{X_1^{\frac{3n+5}{1+n}}}\int_{x_0}^{x_1}(1-K)^{\frac{2}{1+n}}.X^{\frac{2n+4}{2n+4}}.dX \tag{43}$$

d. Boundary Conditions and Solution Procedure. To solve the governing equations of Section 2*c*, the rotating disk and the housing design parameters, (r_1, r_0 and s), the disk operation parameters, (ω, Q), and the inlet velocity profile parameters (K_0,b_0,c_0), are assumed known. The dimensionless parameters occuring in the equations (38, 40, 41) and (43) can then be calculated. Equation (40) is solved for K, as a function of r, starting from r_0. Using this solution in equation (38) will give $c(r)$, and then substituting this result in equation (28) will yield $b(r)$. Similarly using K in equation (41) will give P and, finally, applying these solutions in equations (29, 31) and (42) will give the values of E,Q_i/Q, and C_m.

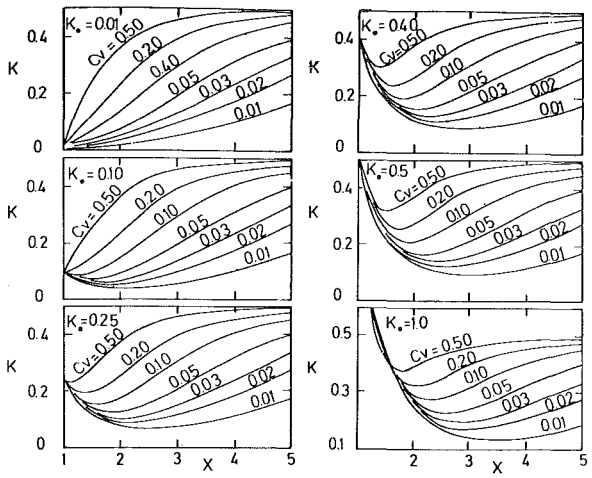

Fig. 2 Predictions of local core rotation

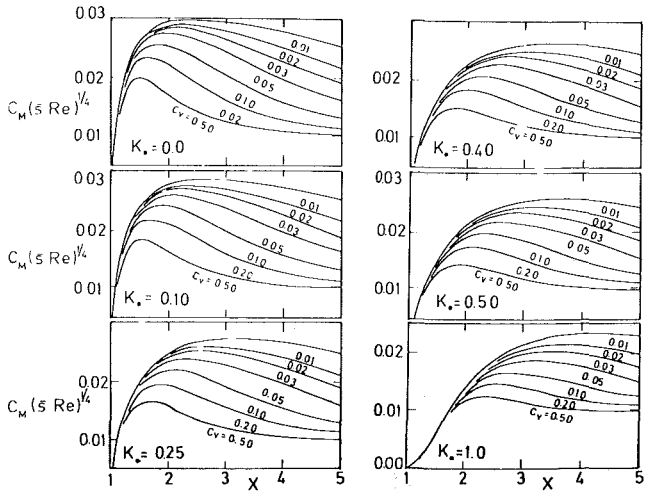

Fig. 3 Predicted local disk torque coefficient

The equations were integrated numerically from r_0 to r_1, in one hundred equal sized steps. A fourth order Runge-Kutta method was used for integration. Various step sizes and parameter ranges were tried. Numerical instabilities were not observed. For the solutions presented, the values for A and n were taken as 8.74 and 1/7, respectively, corrresponding to fully developed turbulent flow (17). Sensitivity to this choice of constants is examined later in this paper.

Numerically calculated solutions for K and C_m are presented in dimensionless coordinates in Figs. 2 and 3 for a wide range of the parameter K_0. Comparable compact representations for the solutions of the other properties are not possible, as the number of the independent parameters is more than two. Therefore, only representative solutions are presented for the others.

3 Discussion:

a. Results. The core rotation[3] K from equation (40) is presented in Fig. 2, as a function of X with C_v as the parameter, for a range of values of the inlet rotation K_0 in different graphs. It should be noted that K is independent of b and c, as equations (27, 38) and (40) are uncoupled by the simplifying assumptions made in the derivation of equation (40).

[3]The term "core rotation" is used to represent the nondimensional tangential velocity at $\bar{z}=0.5$, the midsection.

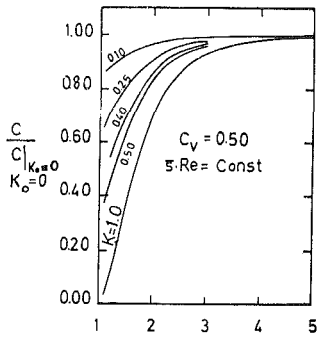

Fig. 4 Effect of inlet core rotation on disk torque coefficient

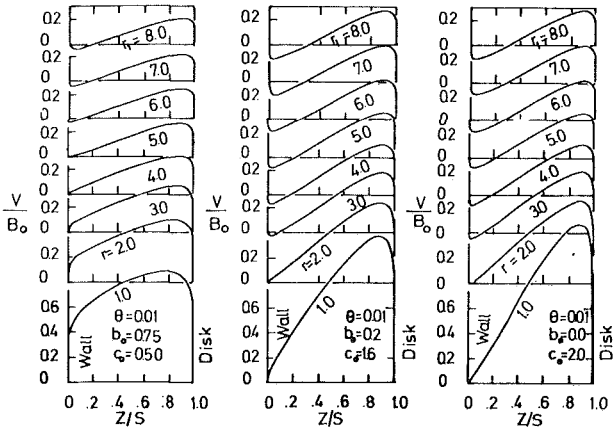

Fig. 5 Development of radial velocity profiles

The disk torque coefficient is shown in Fig. 3, as a function of X with C_v as parameter, for the same values of inlet core rotation K_0 as in Fig. 3. One should note that the ordinate also involves Re and $\bar{s}$. This form is chosen for ease of presentation. When the other parameters are held fixed, considerable decrease in the disk torque coefficient is observable with the increase of the inlet rotation K_0. This effect is clearly shown on Fig. 4 where C_M with inlet rotation, normalized with the C_M with zero inlet rotation, is presented. As expected, the decrease in normalized disk torque coefficient is more pronounced near the inlet (i.e., at smaller values of X) and for larger values of K_0.

The development of some representative radial velocity profiles is presented in Fig. 5 at various normalized radial distances for a series of different values of b_0, and c_0. These solutions are for constant θ and through flow rates. As the inlet velocity profile is skewed toward the disk by increasing c_0, the radial inflow on the wall increases and penetrates to smaller radial distance from the axis. As the profiles develop with increasing X, the location of the zero radial velocity point moves toward the disk.

The location of the separation streamline between the radial inflow and radial outflow regions in the gap is presented in Fig. 6 and 7 in terms of X versus z/s with b_0 and θ as the parameters. On these graphs, the intercepts with the ordinate show the innermost *penetration distance* of the inflow for each value of b_0 (since $b_0 + c_0/2 = 1$, each value of b_0 corresponds to a particular value of c_0).

There is radial inflow only in the domain above any particular separation streamline, and there is radial outflow in the domain below. Figure 6 indicates that as the inlet velocity profile is skewed toward the disk (as b_0 becomes smaller and therefore c_0 + becomes larger), the radial flow penetration distance moves toward the center and the inflow region enlarges. The effect of the shape of the inlet radial velocity

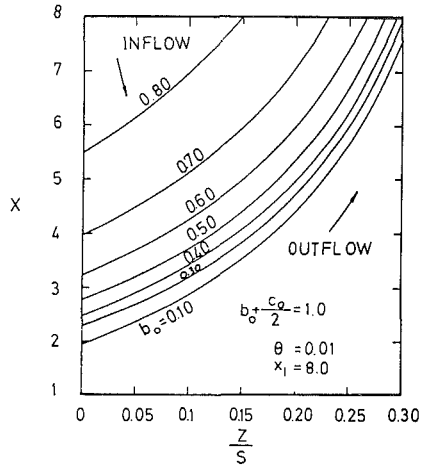

Fig. 6 Location of separation streamlines between inflow and outflow regions with shape of inlet velocity profile as parameter

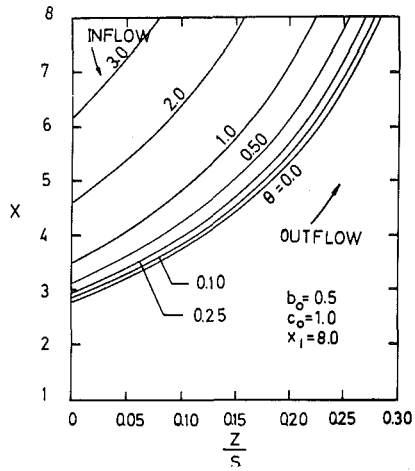

Fig. 7 Separation streamlines between inflow and outflow regions with Θ as parameter

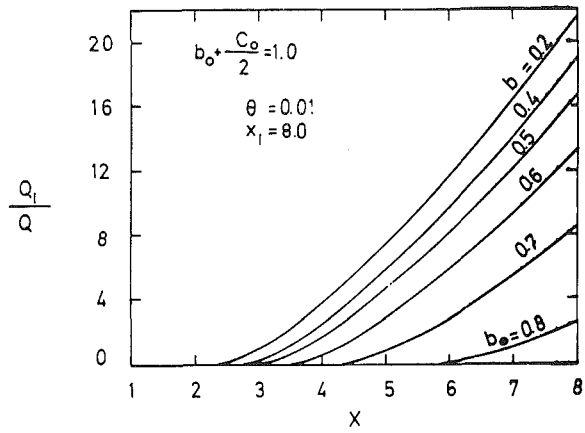

Fig. 8 Local normalized radial inflow rate with inlet profile shape as parameter

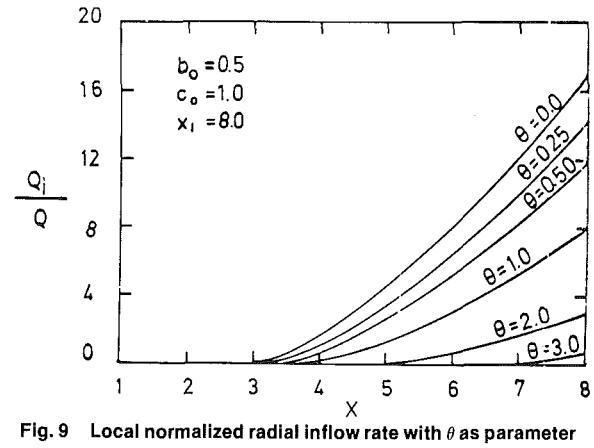

Fig. 9 Local normalized radial inflow rate with θ as parameter

profile on the radial inflow can be estimated from Fig. 6. For example, if one considers a particular disk with $X_1 = r_1/r_0 = 4.0$, then there will be no radial inflow for inlet velocity profiles having $b_0 > 0.7$ according to Fig. 6. At this value of b_0, the radial inflow is just starting at $X = 4$ and the flow becomes critical. If the inlet profile is more skewed toward the disk (having $b_0 < 0.7$), then there will be radial inflow to $X = 3.25$, 2.8, 2.5 for $b_0 = 0.6$, 0.5 and 0.4, respectively. Similar trends are observed in Fig. 7 where the parameter is the defined quantity θ.

Figures 8 and 9 show the percent radial inflow, Q_i/Q, as a function of X with b_0 and θ as parameters. Figure 8 indicates that as the inlet radial velocity profile is skewed toward the disk, the radial inflow increases considerably. Comparable curves are shown in Fig. 9 with θ as the parameter. A comparison of Figs. 8 and 9 indicates that increasing b_0 and increasing θ creates the same tendencies on radial inflow. From Fig. 9 and the definition of θ by equation (22), one concludes that increasing Re, r_1/r_0 and s and decreasing T will increase the radial inflow. These general trends are in agreement with the qualitative description of the flow behavior, in the measurements of Daily, et al. [7] and Uzkan [2].

b. Comparison with Available Data. The data found in the literature for the flow around rotating disks in housings with radial outflow are rather limited, and do not contain information about r_0 and inlet velocity profiles [3,6,7,8]. The data in references [2,3,4] and [7] and the analysis of Sokolov [5] suggest the physical model used in the present analysis, but, again, the data on the inlet velocity profiles are very limited. Therefore, a critical test of the present analysis requires further experimental work.

Although direct comparison with data is not possible, an indirect comparison of the analysis can be made. In the report by Daily, et al. [3], tangential velocity profile measurements are given at different radial distances. The core rotation K may be estimated from these profiles for comparison. The K and r values at the smallest values of r which they presented were taken as K_0 and r_0 for the inlet conditions of the analytic model. The development of K with r was calculated and compared with the measured K values at larger r. Results are presented in Table 1. The analytic predictions are in reasonable agreement with the measurements.

Daily, et al. [3] give the following empirical equation for K with throughflow:

$$K = \frac{\bar{K}}{25.48 \frac{\bar{s}}{K_v} \mathrm{Re}^{1/5} \quad X_1^{13/5} + 1} \tag{44}$$

Here $\bar{K}$ denotes the core rotation for the case with zero throughflow. In Fig.10, the core rotation calculated by the present method is compared with the prediction of equation (44) for a typical case typical of turbulent flow. In this case the present analysis overpredicts K at values of X larger than about 8.

Dorfman [4] gives a closed form solution of the tangential momentum equation for the case where $K_0 = 0$ and provides an approximate solution for nonzero K_0. A comparison of the solution presented in this paper with the solution of Dorfman

Table 1 Comparison of core rotation calculations with experiments of Daily, et al. [3]

Source and conditions	$x = r/r_1$	Test Data K	Prediction
Fig. 28	* 0.469	0.21	0.21
$\bar{s} = 0.069$	0.648	0.36	0.375
$Re = 6.9 \times 10^5$	0.828	0.41	0.44
$Q = 3.35$ cfm			
Fig. 29	* 0.469	0.04	0.04
$\bar{s} = 0.069$	0.648	0.08	0.10
$Re = 2.95 \times 10^5$	0.828	0.20	0.18
$Q = 12.9$ cfm			
Fig. 30	* 0.469	0.04	0.04
$\bar{s} = 0.069$	0.648	0.20	0.17
$Re = 6.9 \times 10^5$	0.828	0.32	0.282
$Q = 12.9$ cfm			
Fig. 31	* 0.469	0.04	0.04
$\bar{s} = 0.069$	0.628	0.06	0.061
$Re = 2.95 \times 10^5$	0.828	0.07	0.105
$Q = 26$ cfm			

* Taken as initial condition.

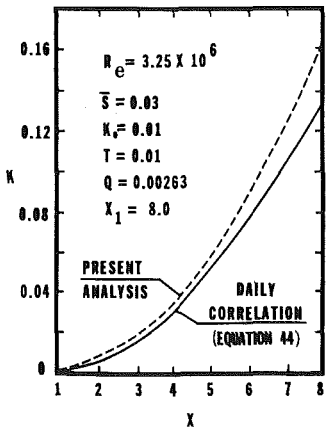

Fig. 10 Present prediction of core rotation compared with empirical correlation of daily, et al. [3]

is given in Fig.11. The difference between the approximate result and the present solution is less than 5 percent.

c. Evaluation of Assumptions. For turbulent flows, the assumption of power law representations of the velocity profile is a well known method. However, the extrapolation of values of A and n to entirely different flow geometry is questionable. For this reason, the theory is developed in general terms of A and n, to give the user a chance to apply the most reasonable values for his particular application. The solutions are presented for the widely used values of $A = 8.74$ and $n = 1/7$ [17]. In Table 2, the solutions for C_m, K, Q_i/Q, and the radial penetration distance are given for the values 1/7, 1/8, 1/9 and 8.74, 9.71, 10.6 for n and A, respectively. As the exponent n decreases from 1/7 to 1/9 (with corresponding values of A) the solutions for C_m decrease, for Q_i/Q increase, and for the penetration distance, decrease. The effect on K is almost negligible. All other trends presented on Figs. 2 – 9 remain the same. Further experiments are necessary to determine the most appropriate values of A and n to be used in the above analysis.

The shape assumed for the inlet radial velocity profile imposes its own characteristics on the solution obtained. By the integration of the velocity profiles in the governing equations, it is expected that the errors in the local results would average out and the technique will therefore give a good approximate solution for the integral results. It seems appropriate to expect reasonable solutions for C_m, K, and

Table 2 Comparison of solutions for different power law constants, A and n

	n	1/7	1/8	1/9
	A	8.74	9.71	10.6
$X = 5$, $C_v = 0.01$, $K_0 = 0.5$				
Disk Torque Coefficient, C_m		0.02431	0.0194	0.0161
Core Rotation	K	0.175	0.177	0.179
$X = 8$, $b_0 = 1$, $C_0 = 1$, $\theta = 1$				
Inflow	Q_i/Q	0.0052	0.0119	0.0147
Radial Penetration X		6.47	5.87	5.70

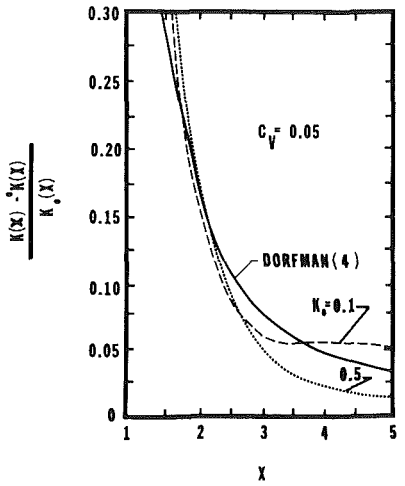

Fig. 11 Comparison with the approximate solution of dorfman [4] (0_K indicates the solution for $K_0 = 0.0$)

Q_i/Q, but larger errors in the separation streamlines, in the point of zero radial velocity, or even in the radial penetration distance.

4. Conclusion:

An integral analytical method to predict the effects of the different design parameters on the flow between a rotating disk and a parallel wall is presented. The effects of varying the ventilation air inlet conditions on the important flow properties, such as the core rotation, the radial velocity profiles, the radial inflow rates, the separation streamlines between inflow and outflow regions and the disk torque coefficient, are described.

Detailed consideration of the figures indicates that:

1 When the inlet rotation of the ventilation air K_0 is increased, the region under the influence of the inlet conditions enlarges to a larger radius. K decreases to a minimum and then increases again with increasing r. The decreasing K region can be identified as the "Inlet rotation dominated region" whereas the increasing K region can be identified as the "disk pumping effect dominating region". The region influenced by K_0 is larger for small values of the parameter C_v.

2 When K_0 is increased, the disk torque coefficient will decrease somewhat. This effect is attributed to the decrease of the tangential momentum which is transferred from the disk to the incoming ventilation air.

3 When the inlet radial velocity profile is skewed toward the disk, the radial inflow increases, the inflow penetrates closer to the axis of rotation and the point with zero radial velocity moves toward the disk.

Related to the cooling of gas turbine disks, there are two important consequences of the analysis:

1 In order to prevent the radial inflow of hot gases on the wall more effectively, the inlet radial velocity of the ventilation air should be directed toward the stationary wall.

2 The disk friction can be decreased by increasing the rotation of the fluid at the inlet.

References

1 Uzkan, T., "The Effects of the Stationary Wall Geometry on the Flow Regime Between a Rotating Disk and a Stationary Wall. Part I, No Throughflow," *General Electric Co. Research and Development Center,* Report No. 66-1-345, 1966.

2 Uzkan, T., "The Effects of the Stationary Wall Shape on the Flow Behavior Between a Rotating Disk and a Parallel Wall. Part II, With Radial Throughflow," *General Electric Co. Research and Development Center,* Report No. 66-C-389, 1966.

3 Daily, J. W., Ernst, W. D., and Asbedian, V. V., "Enclosed Rotating Disks with Superposed Throughflow, Mean Steady and Periodic Unsteady Characteristics of Induced Flow," MIT Hydrodynamics Lab. Report No. 64, 1964. Available from Microproduction Lab, MIT.

4 Dorfman, L. A., "Influence of Radial Flow Between Disks and Casing on Their Resistance and Heat Transfer," *Izvestiya Akademii Nauk SSSR. OTN. Mechanica i Machino,* No. 4, 1961, p. 26. Also available as FDT-TT-62-1038/1.

5 Sokolv, V. S., "Determining the Temperature of the Coöling Air around the Side Surface of a Rotor Disc with Radial Cooling," *Teploenergetika,* Vol. 21, No. 5, 1974, p. 66.

6 Sedack, V. S., and Nespela, A. N., "The Effects of a Discharge of Fluid Through a Gap on the Resistant Moment of a Rotating Disk," *Teploenergetika,* Vol. 5, No. 12, Dec. 1958, p. 62.

7 Daily, J. W., and Arndt, E. A., "Enclosed Rotating Disks with Superposed Throughflow. A Survey of Basic Effects," MIT Hydrodynamics Lab. Report No. 53, 1962. Available from Microproduction Lab MIT.

8 Daily, J. W., and Nece, R. E., "Chamber Dimension Effects on Induced Flow and Frictional Resistance of Enclosed Rotating Disks," *Transactions ASME Journal of Basic Engineering* Vol. 82, Mar. 1960, p. 217.

9 Truman, C. R., Rice W., and Jankowski, D. F., "Laminar Throughflow of Varying-Quality Steam Between Co-Rotating Disks," *Transactions ASME Journal of Fluids Engineering* Vol. 100, 1978, p. 194.

10 Holodniok, M., Kubicek M., and Hlavacek V., "Computation of the Flow Between Two Rotating Co-axial Disks," *Journal of Fluid Mechanics* Vol. 81. Part 4, 1977, p. 689.

11 Raal, J. D., "Radial Source Flow Between Parallel Disks," *Journal of Fluid Mechanics* Vol. 85, Part 3, 1978, p. 401.

12 Bein M., Shavit A., and Solan A., "Nonaxisymmetric Flow in the Narrow Gap Between a Rotating and a Stationary Disk," *Transaction ASME Journal of Fluids Engineering,* Vol. 98, 1976, p. 217.

13 Metzger, D. E., Mathis W. J. and Grochowsky L. D., "Jet Cooling at the Rim of a Rotating Disk," ASME Paper No. 78-GT-25, 1978.

14 Senoo Y., and Hayami, H., "An Analysis of the Flow in a Casing Induced by a Rotating Disk Using a Four-Layer Flow Model," *Transaction ASME, Journal of Fluids Engineering,* Vol. 98, 1976, p. 192.

15 Gosman A. D., Lockwood F. C., and Loughhead J. N., "Prediction of Recirculating, Swirling Turbulent Flow in a Rotating Disc System," *Journal Mechanics Engineering Science* Vol. 18, No. 3. 1976, 1976, p. 141.

16 Bayley, F. J., and Owen, J. M., "The Fluid Dynamics of Shrouded Disc System with Radial Outflow of Coolant," *Transaction ASME Journal of Engineering for Power,* Vol. 92, 1970, p. 335.

17 Schlichting, H., *Boundary Layer Theory,* McGraw-Hill, New York, Sixth Edition, 1968, p. 565.

Stalling Pressure Rise Capability of Axial Flow Compressor Stages

C. C. Koch
Aircraft Engine Group,
General Electric Co.,
Evendale, Ohio 45215
Mem. ASME

A procedure for estimating the maximum pressure rise potential of axial flow compressor stages is presented. A simplified stage average pitchline approach is employed so that the procedure can be used during a preliminary design effort before detailed radial distributions of blading geometry and fluid parameters are established. Semi-empirical correlations of low speed experimental data are presented that relate the stalling static-pressure-rise coefficient of a compressor stage to cascade passage geometry, tip clearance, bladerow axial spacing and Reynolds number. Blading aspect ratio is accounted for through its effect on normalized clearances, Reynolds number and wall boundary layer blockage. An unexpectedly strong effect of airfoil stagger and of the resulting flow coefficient of the stage's vector triangle is observed in the experimental data. This is shown to be caused by the differing ability of different types of stage vector triangles to re-energize incoming low-momentum fluid. Use of a suitable "effective" dynamic head in the pressure rise coefficient gives a good correlation of this effect. Stalling pressure rise data from a wide range of both low speed and high speed compressor stages are shown to be in good agreement with these correlations.

Introduction

Rotating stall and surge phenomena in axial flow compressors rank among the most serious problem areas in turbomachinery aerodynamics. Gas turbine engines, for example, may encounter severe performance and durability problems if the compressor is not able to avoid stalls or surges over its entire range of operation. Great difficulty and expense may be involved in correcting compressor stall margin problems, because detailed refinement and development may not be sufficient to correct the problem if the basic design has not been chosen to permit the required stall margin to be achieved. Clearly there is a need for a reliable method to assess a new compressor's stall margin capability during the early preliminary design phase: the aerodynamic designer must be assured that critical design features such as blade speed, number of stages, aspect ratio, solidity, through-flow Mach number and blade tip clearance are consistent with the stall margin requirements.

Early efforts to define a quantitative measure of aerodynamic loading and to determine the loading at stall, notably those of Lieblein [1 and 2], that defined the well-known Diffusion Factor and Diffusion Ratio, concentrated on the airfoil suction surface diffusion process. Useful correlations of profile loss versus airfoil diffusion were obtained, but experience indicated that there was a wide variation in the stall limiting diffusion that could be achieved. It was generally recognized that these variations were related to end-wall effects such as clearances and to blading aspect ratio, and the influence of these factors on the stall margin and efficiency of multistage compressors was described in a paper by L. H. Smith, Jr. in 1970 [3]. It was demonstrated that variations in the thickness of the end-wall boundary layers produced the variations in airflow, pressure rise and efficiency usually associated with aspect ratio. A major element of this paper was a correlation of experimentally determined wall boundary layer thickness data versus blade end-wall staggered spacing, tip clearance and most importantly, percent stall pressure rise. The correlation showed that stall was likely to occur when the wall boundary layers grew to a limiting value that depended on tip clearance. It was concluded that the problem of predicting multistage compressor stall "becomes one of predicting end-wall boundary layer growth as a function of geometry near the blade ends, Reynolds number, Mach number and pressure coefficient". Although analytical studies have been conducted to predict end-wall boundary layer growth from first principals, this has proven to be a major challenge, particularly for the case of multistage compressors where substantial blade tip clearance and secondary flow effects are present.

An engineering approach to the problem of predicting the maximum pressure rise capability of axial flow compressor stages is presented in this paper. While this stall prediction method relies on semi-empirical correlations of experimental data, it does account in a rational manner for the major factors influencing wall boundary layer growth and achievable pressure rise. It will be shown that the compressor data are consistent with well-established two-dimensional diffuser performance trends, when the compressor performance and geometry are represented by parameters analogous to those used for diffusers. The model has proven to be most applicable to multistage compressors, where the blading tends to have sufficient circulation capacity to

Contributed by the Gas Turbine Division and presented at the International Gas Turbine Conference and Products Show, Houston, Texas, March 9-12, 1981, of THE AMERICAN SOCIETY OF MECHANICAL ENGINEERS. Manuscript received at ASME Headquarters, December 4, 1980. Paper No. 81-GT-3.

produce limiting end-wall loading levels without exceeding the diffusion and incidence limits of airfoils in cascades. The procedure does not address the overall system stability aspects of compressor surge, such as are described in reference [4]. It does, however, give the peak pressure rise capability of an individual stage operating in the multistage environment, and when used in conjunction with a stage stacking off-design performance prediction method, it can indicate when the limiting conditions that de-stabilize the system and lead to surge will occur within a multistage compressor. An important advantage of the method is that, being a pitchline procedure, it can be used as a convenient preliminary design tool.

General Approach

The stall margin model was originally developed by correlating data from a series of General Electric low-speed multistage compressor test configurations in which blade geometry and clearances had been systematically varied. These tests, plus some additional low speed experimental configurations, also provide data on the effect of Reynolds number variations and on the effects of extreme values of stagger angle, flow coefficient and reaction. Finally, data at stall from high speed multistage compressor tests were compared to the predictions of the model to demonstrate its applicability to modern gas turbine compressors.

In general terms, the approach used to establish a correlation of stalling pressure rise data was to argue that since an axial flow compressor stage functions by diffusing the working fluid, its limiting pressure rise ought to be a function of cascade geometrical parameters that are analogous to those used to correlate two-dimensional diffuser data. Two-dimensional diffuser performance is often presented as shown in Fig. 1, taken from reference [5], in which contours of constant static-pressure-rise coefficient are plotted versus area ratio and length-to-inlet-width ratio. Different maps of this sort are obtained for different amounts of inlet boundary layer blockage. For a given diffuser length-to-inlet-width ratio, there is an area ratio for which the static-pressure-rise coefficient is at a maximum; further increases in area ratio only increase the amount of separated flow and actually decrease the pressure rise. In a compressor cascade the area ratio experienced by the fluid is not fixed by the blade geometry alone; instead, it increases when the cascade is throttled to higher incidence angles and lower flow rates. Eventually the cascade stalls, and a maximum static-pressure rise is obtained. In either a diffuser or a compressor cascade, both the maximum static-pressure rise and the corresponding limiting area ratio should be functions of an appropriately formulated ratio of the diffusion length to some characteristic dimension of the flow's cross-sectional area. For a compressor cascade it is the exit flow area that remains roughly constant over the range of operation, while the flow area at the inlet varies. Thus it seemed sensible to use a correlating parameter for compressors that consisted of the ratio of diffusion length to a cascade exit dimension rather than using an inlet dimension as is done for diffusers. The selected quantity was the arc, or meanline, length of the cambered airfoil divided by the cascade trailing edge staggered spacing, L/g_2. For each experimental configuration, the rotor and

Nomenclature

A = area
C = airfoil chord length
C_p = two-dimensional diffuser static-pressure-rise coefficient
C_h = enthalpy-equivalent static-pressure-rise coefficient, based on pitchline free-stream dynamic head

$$C_h = \frac{Jc_p t_1 \left[(p_2/p_1)^{\frac{\gamma-1}{\gamma}} - 1 \right]_{\text{stage}} - (U_2^2 - U_1^2)_{\text{rotor}}/2g_o}{(V'^2_{1\,\text{Rotor}} + V^2_{1\,\text{Stator}})/2g_o}$$

$C_h)_{\text{adj}}$ = C_h adjusted to Re = 130,000, ϵ/g = 5.50 percent, $\Delta Z/S$ = 38 percent
$C_h)_{\text{ef}}$ = $C_h)_{\text{adj}}$ based on effective pitchline dynamic head
c_p = specific heat at constant pressure
$\mathcal{F}_{\text{ef}}$ = ratio of effective pitchline dynamic head to free-stream pitchline dynamic head

$$\mathcal{F}_{\text{ef}} = (1 + 2.5\, V^2_{\text{min}} + 0.5\, U_1^2)/4.0\, V_1^2$$

g_o = gravitational const, 32.174 lbm-ft/lb$_f$-sec^2
g = gap, or staggered spacing between adjacent blades
h = annulus height
J = energy equivalent of heat, 778 ft-lb$_f$/BTU
L = meanline length of circular-arc airfoil

$$L = C \frac{2\pi}{360} \frac{\phi}{2} \Big/ \sin \frac{\phi}{2}$$

N = two-dimensional diffuser length
P = total pressure
p = static pressure
Re = Reynolds number, based on pitchline chord and bladerow inlet velocity
S = tangential spacing between adjacent blades
t = static temperature
U = blade speed
V = flow velocity in absolute frame of reference
V' = flow velocity in relative frame of reference
V_{min} = minimum possible bladerow inlet velocity in the presence of upstream wakes or wall boundary layers

$V_{\text{min}} = V \sin(\alpha+\beta)$ if $(\alpha+\beta) \leq 90$ deg
$V_{\text{min}} = V$ if $(\alpha+\beta) > 90°$
$V_{\text{min}} = U$ for rotors if $\alpha_1 < 0$ deg
$V_{\text{min}} = U$ for stators if $\beta_1 < 0$ deg

V_Z = flow velocity in axial direction
ΔZ = pitchline axial spacing between bladerows
α = flow angle in absolute frame of reference, deg
β = flow angle in relative frame of reference, deg
γ = ratio of specific heats
ϵ = blade end radial clearance
λ = effective area, or blockage, coefficient
ρ = density
Φ_{tip} = flow coefficient based on tip speed, V_z/U_{tip}
ϕ = camber angle, deg
ψ_{tip} = total-pressure-rise coefficient based on tip speed, $\Delta P/(\rho\, U^2_{\text{tip}}/2g_o)$

Subscripts

1 = inlet to compressor bladerow or stage, or diffuser inlet
2 = exit from compressor bladerow or stage, or diffuser exit

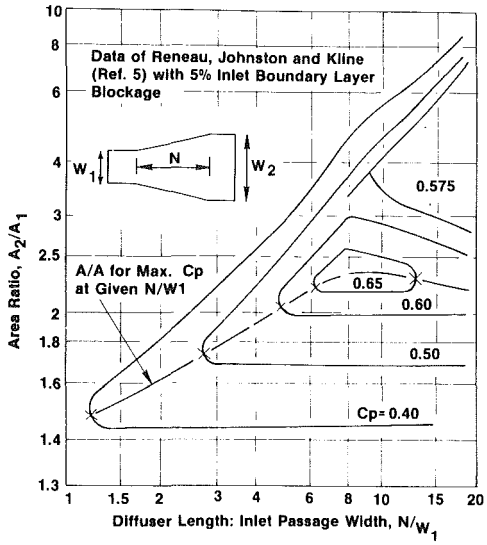

Fig. 1 Two-dimensional diffuser performance map

stator values were combined into a weighted average stage value in which the bladerow inlet dynamic head was used as the weighting factor. This geometric parameter depends primarily upon solidity, with weaker dependence upon camber and stagger angles. Note that it does not explicitly depend upon the aspect ratio of the stage. The sketch in Fig. 13 illustrates how L and g_2 are defined.

The term chosen as the primary dependent variable relating to stall pressure rise was overall stage enthalpy-equivalent static-pressure-rise coefficient, C_h. This was based upon stage overall static-pressure rise converted to the equivalent isentropic enthalpy rise, less any enthalpy change attributed to changes in pitchline radius across the rotor. This latter adjustment was made because such enthalpy changes are essentially "free," since they do not require any diffusion of the relative velocity. The sum of rotor and stator relative dynamic heads was used as the denominator in the static-pressure-rise coefficient.

The stall margin correlations were based upon simplified stage average pitchline quantities. A computer program was written to analyze the test data by calculating the appropriate pitchline vector diagram quantities and correlation terms. Compressor geometry, inlet fluid properties, speed, airflow, stage exit static pressures, stator exit swirl angles, overall total-pressure ratio and overall adiabatic efficiency were input to the program. The calculated pitchline vector diagrams satisfied the continuity and turbomachinery energy input equations on a one-dimensional basis. The annulus blockage effect of end-wall boundary layers was accounted for using the displacement thickness correlation described in references [3 and 6]. At the stalling value of aerodynamic loading, this model predicts that the blockage is a function only of the ratio of average bladerow tip clearance to staggered spacing and the ratio of average bladerow staggered spacing to blade height, according to the following equation:

$$\lambda = 1 - (0.34 + 2\,\overline{\epsilon/g}) \times \overline{(g/h)} \qquad (1)$$

A minimum value of the blockage coefficient of 0.83 was used, since this is approximately the value at which parabolic axial velocity boundary layers on the hub and casing walls would intersect; this was thought to be about as nonuniform as the through-flow velocity was likely to become.

The justification for using a stage-average pitchline model to describe a process believed to be caused by end-wall effects comes primarily from expedience. This simplified approach avoids the need to rely on experimental data measured deep in the end-wall regions or the need to calculate the data to be correlated using a full radial equilibrium/axisymmetric flow procedure coupled with sophisticated secondary flow, tip clearance leakage and end-wall loss models. Although a sophisticated streamline-by-streamline, bladerow-by-bladerow model can be employed, the calculations needed to apply such a procedure are often beyond the scope of a preliminary design effort. This paper will present data to show that further sophistication usually is not required. Data from stages covering a wide range of radius ratio will be presented to show the adequacy of the pitchline approach. Test data from stages having extreme values of reaction ratio, and from other stages where rotor and stator aspect ratios are quite different, will be presented to show the adequacy of the stage averaging approach.

Correlation of Low-Speed Data

Experimental Compressor. The majority of the experimental data used to establish the stall pressure rise correlation were from the General Electric Company's Low Speed Research Compressor. During the 1960's nearly 50 different configurations were tested in which stage geometry was systematically varied; the major focus of the extensive series of tests was to isolate the effect of design variables on achievable stall margin. A photo of the Low Speed Research Compressor is shown in Figure 2. This is a 1.524-m- (60-in) tip-dia compressor having up to four stages of identical blading in a cylindrical annulus. Tip speed is about 61 m/s (200 ft/sec), so the flow is essentially incompressible. Repeating stage conditions, in which stage inlet and exit vector diagrams are nearly identical, are generally established by the third stage, so the multistage environment is properly simulated. The axis of rotation of the test compressor is vertical, and the rig is driven from below by a steam turbine. Air enters the test compressor through the inlet filters and bellmouth at the top, is compressed by the test blading in the section having transparent plastic casings, and is discharged to the atmosphere after passing through a discharge throttle valve (located below the floor shown in the photo).

The test configurations built for the parametric evaluation of stall margin capability all had hub: tip radius ratios of 0.7. For all these parametric tests, aspect ratios, solidities and clearances of the rotor and stator blades were always nearly equal to each other. About half of the configurations tested used a single baseline airfoil design that is described in some detail in reference [3]. This design was built in three different aspect ratios: 2.0, 2.8 and 5.0. Solidity variations for this baseline design were accomplished by changing the number of airfoils in each bladerow; pitchline solidities ranged from 0.6 to 1.5. Tip clearance variations were accomplished by cutting the rotor blades and stator vanes to various lengths; clearance: blade height varied from 0.7 percent to 3.4 percent. The blades were constructed so that stagger angles were easily adjustable; average pitchline stagger angles ranged from 22 deg to 51 deg, with a value of about 36 deg being the design condition. A special set of stators was also built to produce the baseline vector diagrams; these had radially nonuniform chord length in order to maintain radially constant axial gaps between bladerows. Average aspect ratio of these Tight Gap stators was 2.3. These special stators are also described in detail in reference [3]. Another set of airfoils, having slightly higher values of stagger and camber, was built with an aspect ratio of 1.0. These were tested over a range of solidities from 1.0 to 3.0. Two other sets of airfoils were built with a 2.8 aspect ratio; one set had about 8 deg higher camber than the baseline design (which had an average pitchline value of approximately 31 deg), and one set had about 5 deg lower camber. These also were tested over a range of stagger angles, solidities and clearances. As a final configuration, the low camber rotor blades set at high stagger angles were combined with the high camber stators set at low stagger angles to form

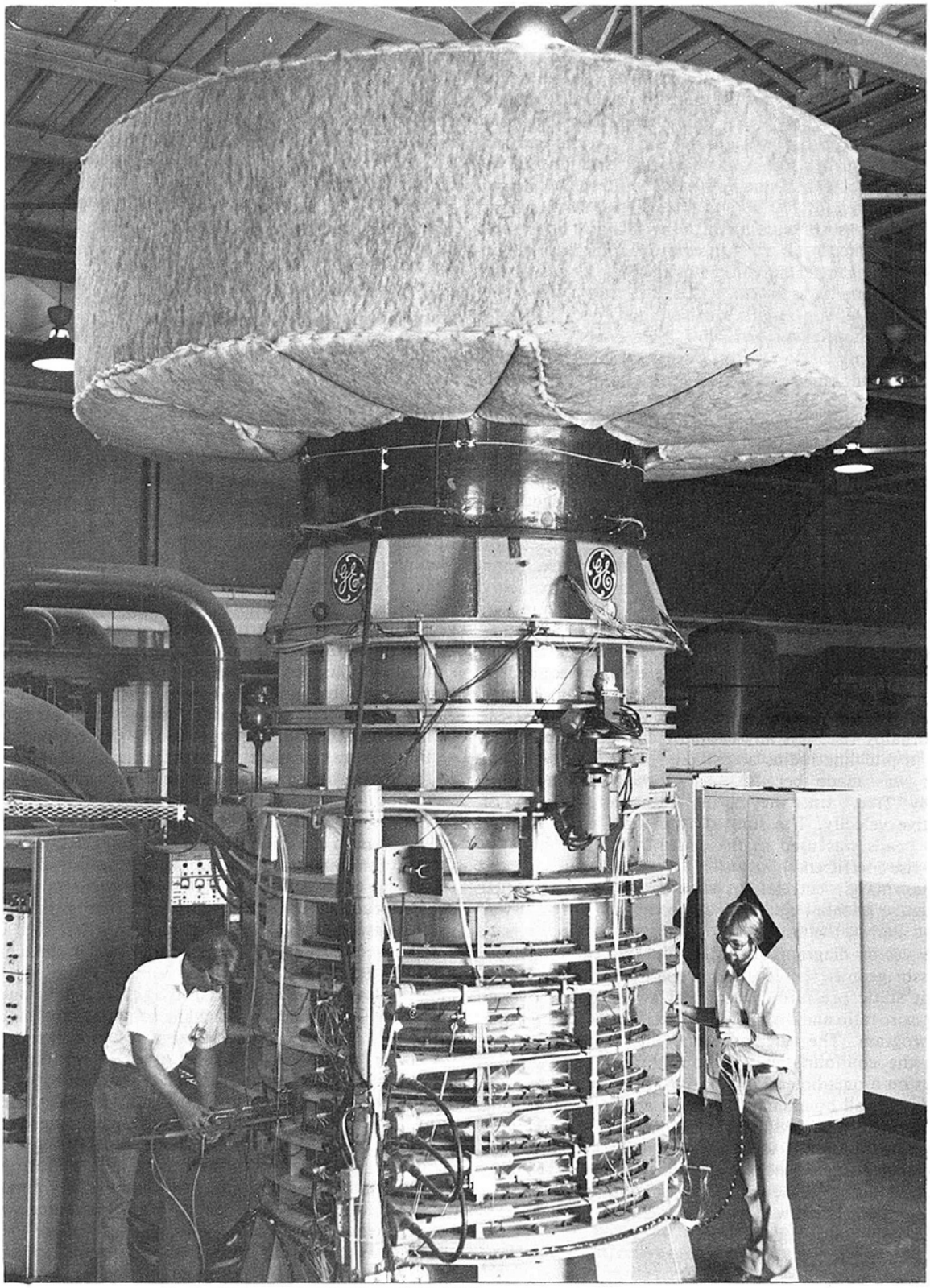

Fig. 2 Photograph of the General Electric low-speed research compressor

a stage in which the reaction was about 0.65 compared to a value of about 0.50 for all the other stages. The high reaction blading was also tested over a range of stagger angles and clearances. Data from several other tests that were not part of the parametric series are also presented in this paper.

Tests were conducted so that Reynolds number was maintained constant for all configurations of a given aspect ratio. Airflow was measured by the calibrated bellmouth; overall total-pressure rise was determined by extensive radial and circumferential surveys at the inlet of the first rotor and the exit of the last stator; work input was measured by a torque meter with appropriate adjustments for windage and bearing friction; individual stage static-pressure rise was determined from casing static-pressure measurements. Stall was always either full-span or part-span rotating stall and was easily detected by audio and visual observations. Unstalled

data could be taken within 1 or 2 percent in stall margin of the stall point, so extrapolation of the data to the exact stalling condition was a simple procedure. The data were almost always repeatable when comparable test conditions were maintained. The basic airfoil designs (when tested at their design solidity, stagger and clearance) achieved a flow and pressure rise very close to their design values. The test results thus were not compromised by badly mismatched or overloaded blading, and the data are believed to represent the performance achievable by well-designed, well-matched stages.

Effects of Airfoil Solidity, Reynolds Number and Clearances. Experimental values of stalling static-pressure-rise coefficient were first computed from the data for 13 low-speed compressor configurations. A single value was computed per configuration, representing the arithmetic average of the three or four individual stage values. Average values were used because in these tests all stages were geometrically identical and the stage-to-stage variation in pressure rise was very small. These 13 test configurations were selected out of nearly 50 designs because they covered the full range of aspect ratio, from 1 to 5, and the full range of pitchline solidity, from 0.6 to 3.0, that were included in the available data. All 13 designs had a pitchline stagger angle of 36–39 deg and a pitchline camber angle of 31–36 deg. The stages with aspect ratios of 2.0, 2.8 and 5.0 had the baseline airfoil design. Reaction ratio at stall was approximately 0.5 for all test configurations. Tip clearance was 1.4 percent of blade height for all cases. Reynolds number, based on pitchline values of chord and bladerow inlet relative velocity, was 130,000 for the designs with aspect ratios of 5.0 and 2.8, 180,000 for the design with an aspect ratio of 2.0 and 350,000 for the design with an aspect ratio of 1.0.

Results of this analysis of experimental data for the 13 configurations are shown in Fig. 3. Also shown, for comparison with the compressor data, are the diffuser data of Kline and Reneau from Fig. 1, and the predicted peak pressure rise of two-dimensional diffusers given by the correlation of Sovran and Klomp [7] for assumed inlet boundary layer thicknesses of 1 percent and 9 percent (a thickness of about 9 percent gives the minimum recovery in this correlation). It is seen that the compressor data display the trend of increasing pressure rise with increasing length that is displayed by the diffuser results, although the slopes of the compressor curves are not as steep, and most of the compressor data are at a somewhat lower level.

There is a noticeable variation among the compressor data in Fig. 3 that appears to be a function of aspect ratio: the lower aspect ratio designs achieved significantly higher values of static-pressure recovery than did the higher aspect ratio designs. However, as demonstrated in reference [3], this aspect ratio effect is primarily the result of differences in Reynolds number and clearance. The fact that the lower aspect ratio designs had higher Reynolds numbers has already been mentioned, and the fact that all cases had the same tip clearance: blade height ratio gave the lower aspect ratio designs an advantage in terms of clearance: staggered spacing. In addition, for each aspect ratio there is a significant variation in the ratio of clearance: staggered spacing as L/g_2 varies with solidity. The remainder of this section will present data to allow the effects of variations in normalized clearances and of Reynolds number to be evaluated.

Data from several General Electric low speed test configurations run at differing speeds, and Reynolds number data from other sources [8 and 9], were used to determine the effect of Reynolds number upon stalling pressure rise coefficient. These data are shown in Fig. 4. The curve shown in this figure was taken as representative of the trend of the data versus Reynolds number, and allowed all the stalling static-

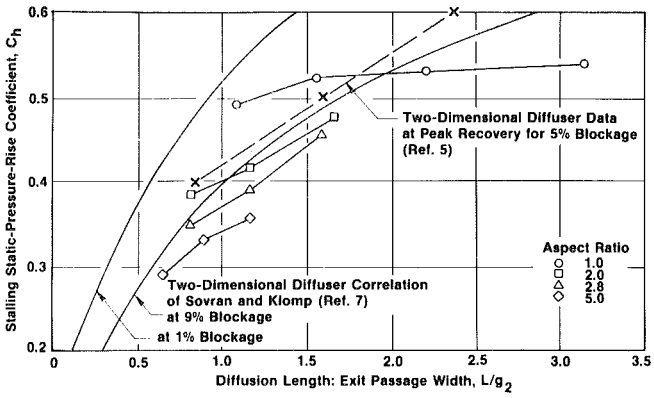

Fig. 3 Effect of cascade geometry on stalling pressure rise coefficient

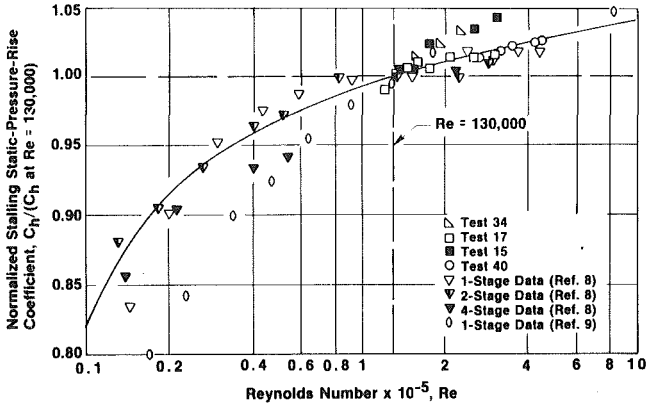

Fig. 4 Effect of Reynolds number on stalling presure rise coefficient

pressure-rise coefficient data to be adjusted to the value expected at a Reynolds number of 130,000, the average value of the aspect ratio 2.8 and 5.0 configurations.

All 13 compressor test configurations selected to display the influence of the geometrical parameter L/g_2 on peak pressure rise had rotor and stator tip clearances of 1.4 percent of blade height. However, as a result of the aspect ratio and solidity variations encompassed by this collection of data, the clearance: pitchline staggered spacing ratio varied from 2.6 to 9.4 percent. This variation in normalized clearance was believed to be a major source of the data scatter in Fig. 3. Additional experimental data showing the effect of clearance variations at constant aspect ratio, solidity and stagger were therefore employed to determine a tip clearance adjustment. Stalling static-pressure-rise coefficients for cases having a pitchline solidity of 1.08, camber of 31 deg and stagger of 36 deg are plotted versus clearance: pitchline staggered spacing in Fig. 5. Data are shown for aspect ratios of 2.0, 2.8 and 5.0; these cases all have a value of L/g_2 of approximately 1.17. All data points were adjusted to a Reynolds number of 130,000 using the curve given in Fig. 4. The curve shown in Fig. 5 represents the trend of the clearance data, and was used to adjust the data to a representative clearance: staggered spacing of 5.5 percent.

It was expected, based on the work described in reference [3], that there also would be an effect on achievable pressure rise due to variations in the ratio of axial clearance: pitchline tangential blade spacing. Data from two additional four-stage test configurations labeled TG1 and TG2 were available to define this effect. These Tight Gap stages used the baseline aspect ratio 2.0 rotors, but special nonconstant-chord stators were built that maintained a radially constant axial gap between bladerows. The TG stators were designed for the same vector diagrams as the baseline stators; they had nearly the same pitchline stagger and camber, although the radial distributions were somewhat different. The TG blading was run at two different axial clearances simply by providing

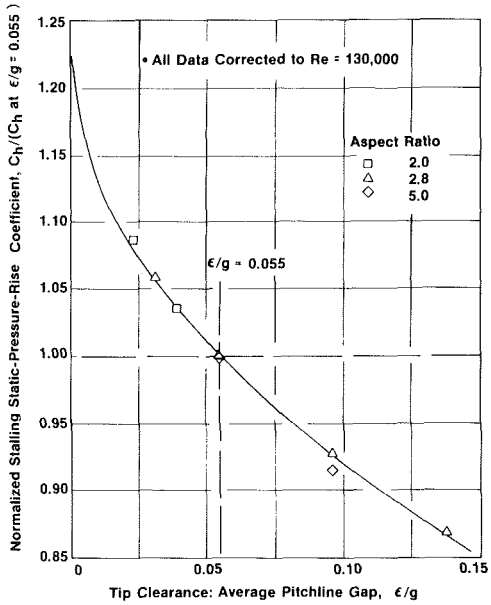

Fig. 5 Effect of tip clearance on stalling pressure rise coefficient

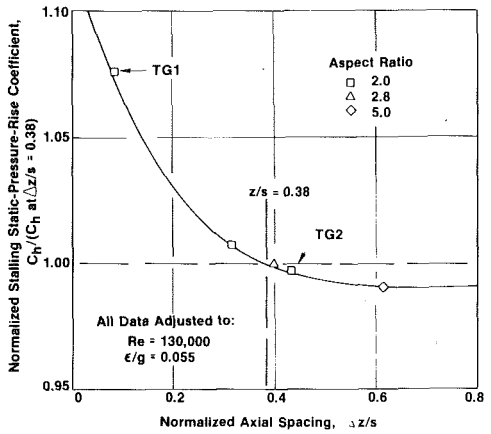

Fig. 6 Effect of axial spacing on stalling pressure rise coefficient

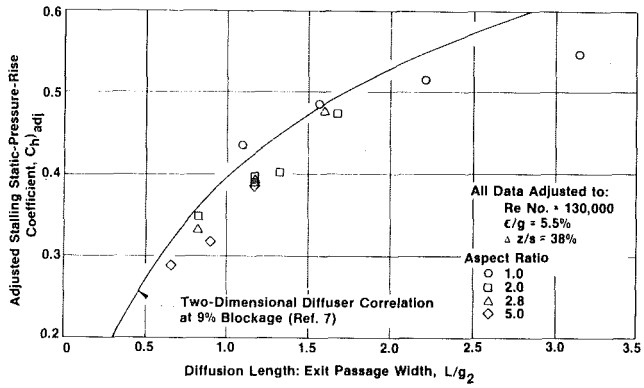

Fig. 7 Correlation of stalling pressure rise data for baseline stages

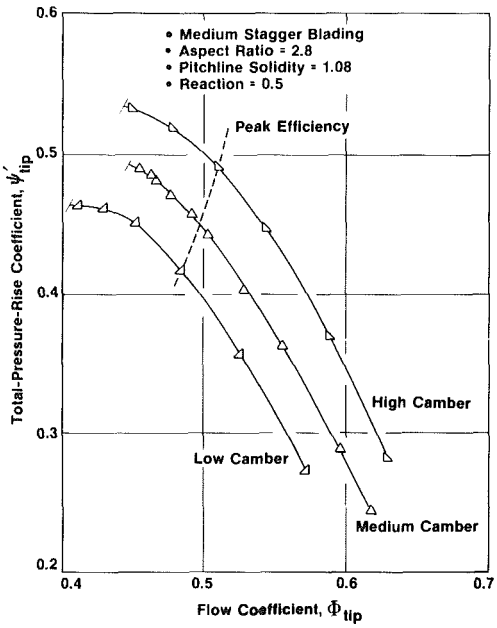

Fig. 8 Effect of camber on stage performance

suitable spacers in the test hardware. Figure 6 plots static-pressure-rise coefficients, adjusted to 130,000 Reynolds number and 5.5 percent tip clearance: staggered spacing, versus normalized axial spacing. The trend of the data for the baseline configurations was reasonably consistent with the trend of the data from the TG stages, and the recovery data do come into better agreement when represented by the curve shown in Fig. 6. This curve was used to adjust stalling static-pressure-rise coefficient data to a representative level of axial clearance: tangential spacing ratio equal to 0.38.

The adjustments to standard levels of Reynolds number, tip clearance and axial spacing were made to the data previously shown in Fig. 3, and the results are shown in Fig. 7. It is seen that much of the data scatter has been removed, and that the adjusted static-pressure-rise coefficient data follow rather closely the trend of the two-dimensional diffuser correlation [7] using an inlet blockage of 9 percent.

Effect of Airfoil Camber. Thus far, correlations that account for cascade L/g_2 ratio, Reynolds number, tip clearance and axial spacing effects have been defined for one particular class of designs having a reaction ratio of about 0.5, a pitchline camber of 32-36 deg and a pitchline stagger of 36-39 deg. Additional data were available from General Electric Low Speed Research Compressor tests to evaluate the adequacy of the model for other levels of camber. Four-stage configurations at three levels of camber were tested at several different stagger settings each, while maintaining constant values of aspect ratio, solidity, clearance: blade height and reaction. An appreciation of the practical significance of these differences in airfoil camber is gained by examination of Fig. 8, in which stage total-pressure rise versus flow characteristics for low, medium and high camber designs are compared. These three designs had all of their stage average geometry parameters identical except for camber, although some variations in radial distributions of twist and camber did exist. All three designs had essentially the same peak efficiency, approximately 89.8 percent, and this occurred at nearly the same flow coefficient for each case. As expected, at peak efficiency the high camber stage did in fact produce about 20 percent higher total-pressure rise than the low camber stage. The high camber stage, however, had somewhat less stall margin above peak efficiency and stalled at a higher flow rate and a lower incidence than the low camber stage. The stall correlation, however, is formulated in terms of stage static-pressure-rise coefficient rather than the total-pressure-rise coefficient used in Fig. 8. The stalling static-pressure-rise coefficients from the camber variation tests, adjusted as described above to reference levels of Reynolds number and normalized clearances, are plotted versus stage average pitchline camber angle in Fig. 9. The rather surprising result is that at a fixed stagger angle virtually the same value of stalling static-pressure-rise coefficient was reached for any level of airfoil camber in the range tested.

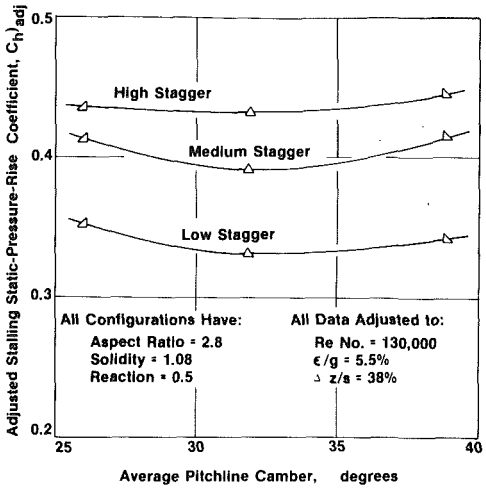

Fig. 9 Effect of camber on stalling pressure rise coefficient

The reason that these results are at first surprising is that they violate the sort of common sense reasoning that is based on isolated airfoil aerodynamics, since for isolated airfoils it certainly is true that more camber does increase the peak lift coefficient. Isolated airfoil results also indicate that incidence angle or blade surface diffusion limits are responsible for stall. Examination of the above compressor test data, however, indicated that the stalling incidence angle of the high camber stage was quite close to the minimum loss value given by cascade design rules, and the stalling incidence of the low camber stage was only about 6 deg higher than the minimum loss value. Thus for both stages, it seems unlikely that stall was initiated as a result of the flow reaching a limiting incidence condition. Instead, it is believed that the stall limiting condition occurred when the flow broke down in the end-wall regions. This type of stall loading limit is predictable from the diffuser-type considerations used in this model, and is evidently not strongly influenced by camber.

One could argue, in terms of the diffuser analogy presented in the previous section, that an increase in airfoil camber would increase the area ratio and would thus increase the static-pressure rise capability of a compressor stage. It is true that an increase in camber would increase the geometrical area ratio of the passage between adjacent blades. One can define this passage area ratio as

$$(A_2/A_1)_{\text{passage}} = g_2\, h_2/g_1\, h_1 \tag{2}$$

noting that the pitchline staggered spacings g_1 and g_2 are based on leading edge and trailing edge meanline angles. The stage average value of this passage area ratio, for the test configurations in which camber and stagger were varied, are plotted in Fig. 10 versus the diffusion length: passage exit width parameter L/g_2. It can be seen that increasing either camber or stagger will increase the passage area ratio substantially.

The dashed line that also appears in Fig. 10 indicates the diffuser area ratio that yields peak recovery at a given length. For a two-dimensional diffuser, this curve establishes a limit on useful area ratio; increases in area ratio above this dashed curve are not able to increase recovery. A similar limit on useful area ratio evidently exists for compressor stages. What is believed to happen is that a compressor stage can only be throttled to flows that are low enough and to inlet air angles that are high enough to produce, simultaneously, the limiting flow area ratio and the corresponding maximum static-pressure-rise coefficient. The stalling incidence angle can be reduced by increasing the camber, but beyond a certain point the effect on peak recovery is likely to be small. If this reasoning is correct, then the significant area ratio for compressors should involve the stream area normal to the

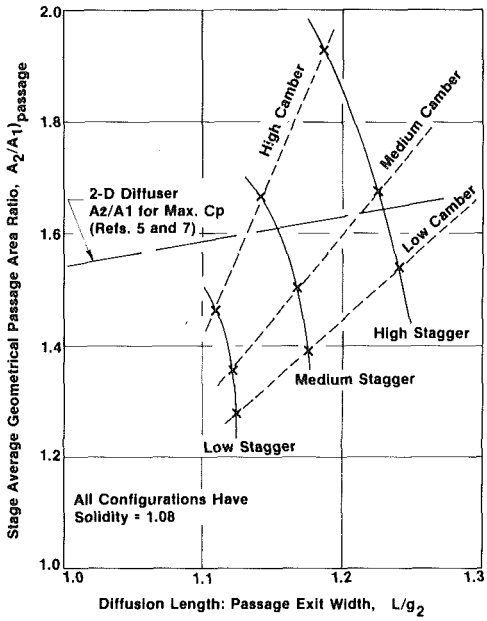

Fig. 10 Variation of cascade passage area ratio with camber and stagger

flow direction just ahead of the blade rather than the geometrical passage inlet area:

$$(A_2/A_1)_{\text{flow}} = g_2\, h_2/S_1 * \cos\beta_1 * h_1 \tag{3}$$

where S_1 is the tangential spacing between blades and β_1 is the inlet flow angle. Stage average values of this flow area ratio are plotted versus L/g_2 in Fig. 11. It is now apparent from these data that the stalling flow area ratio (and thus also the stalling recovery) is nearly a constant for a given L/g_2, despite the substantial variations in the geometrical passage area ratio and the stalling incidence that are produced by camber variations.

This discussion of airfoil camber effects leads to an important restriction that must be met in order for this stall correlation to be applicable: the blading must have sufficient leading edge camber that the resulting incidence angle and suction surface diffusion at the end-wall loading limit do not exceed what is achievable by a two-dimensional cascade free of end-wall boundary layer effects. Obviously, for designs in which quite low camber is used, the cascade might encounter a limiting incidence or limiting suction surface diffusion condition before the limiting end-wall loading could be produced. Other stall prediction methods, such as those based on airfoil surface diffusion limits, would then have to be applied.

Effect of Vector Diagram Type. The available General Electric parametric test data that show the effect of stagger angle on stalling static-pressure-rise coefficient are plotted in Figure 12. These data are compared to the trend for two-dimensional diffusers that is predicted by the Sovran and Klomp correlation (for the variation in L/g_2 produced, at constant solidity, by this variation in stagger angle). It can be seen that the tendency of the compressors to produce higher pressure rise at higher stagger angles, while expected, is much more pronounced than can be predicted by the diffuser correlation. An examination of the test data did not reveal any clear reason for the low pressure rise capability of the low stagger blading. These configurations ran fairly close to optimum incidence, and there was little sign of significant radial imbalances in loading. It thus appeared that this stagger angle effect involved some mechanism qualitatively different from a simple change in the value of g_2 in the diffuser length parameter L/g_2.

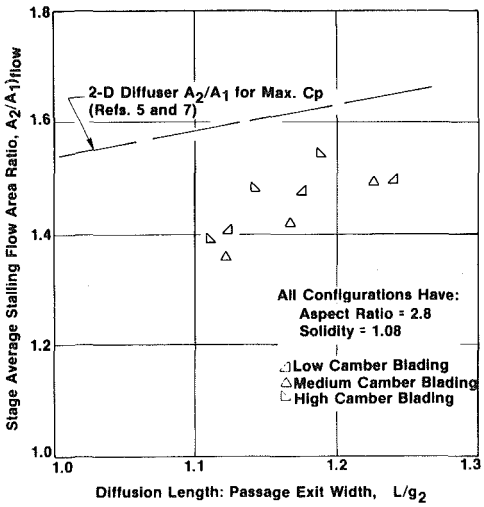

Fig. 11 *Variation of cascade flow area ratio at stall with camber and stagger*

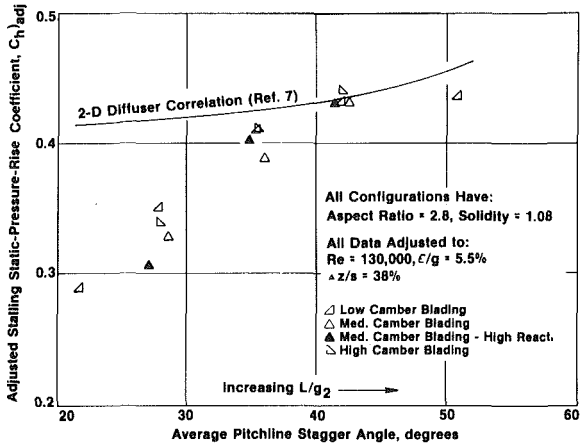

Fig. 12 Effect of stagger angle on stalling pressure rise coefficient

An explanation for the unexpectedly large stagger angle effect was found by considering the ability or inability of a compressor stage to re-energize low momentum boundary layer fluid leaving an upstream bladerow as this fluid impinges upon the following blade or vane in the other frame of reference. This boundary layer energizing/skewing characteristic is unique to rotating machinery, and thus was not present in the data upon which the diffuser correlation was based. The sketch shown in Fig. 13 is a schematic of a typical compressor stage showing rotor and stator orientations; the rotor exit free stream vector triangle is shown by the solid lines. If there was low-momentum wake or wall boundary layer fluid leaving the rotor at the free stream relative flow angle β, the effect upon the flow in the absolute frame of reference approaching the following stator would be to reduce the absolute velocity below the undisturbed free stream value V, and to increase the absolute flow angle above the undistorted free stream value α. If the upstream relative momentum defect was large enough, the stator inlet absolute velocity would reach a minimum value V_{min} at an air angle labeled α_{Vmin} (as shown by the dashed lines in Fig. 13). It can be seen that V_{min} occurs when $(\alpha_{Vmin} + \beta) = 90$ deg. Even more severe upstream disturbances would cause the stator inlet velocity to increase again and approach blade speed U, and the flow angle to approach 90 deg. In low stagger, high flow coefficient stages, where the free stream value of $(\alpha + \beta)$ is much less than 90 deg, the value of V_{min} is much lower than the free stream velocity V. The available dynamic head tends to be severely weakened by incoming low momentum flow.

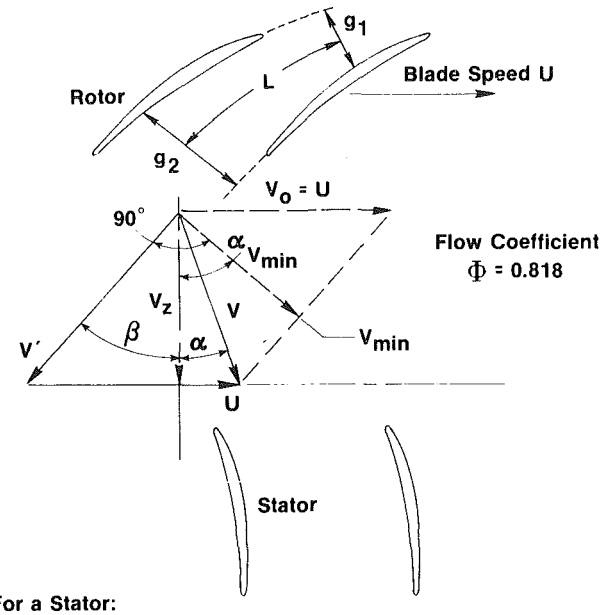

For a Stator:

$$\mathcal{F}_{ef} = \frac{V^2_{ef}}{V^2} = \left(V^2 + 2.5\ V^2_{min} + 0.5\ V_o^2\right)\Big/4.0V^2$$

$$\frac{V^2_{min}}{V^2} = \sin^2\left(\alpha+\beta\right), \text{if } \left(\alpha+\beta\right) \leq 90^\circ \text{ and } \beta \geq 0^\circ$$

$$\frac{V^2_{min}}{V^2} = 1.0\ , \quad \text{if } \left(\alpha+\beta\right) > 90^\circ$$

$$\frac{V^2_{min}}{V^2} = \frac{V_o^2}{V^2}\ , \text{if } \beta < 0^\circ$$

Fig. 13 Schematic diagram giving definition of the effective dynamic pressure factor, $\mathcal{F}_{ef}$

This type of low stagger stage thus might be more prone to stall for any given wall boundary layer thickness, L/g_2 value or clearance. Conversely, for high stagger, low flow coefficient stages, where the free stream value of $(\alpha + \beta)$ equals or exceeds 90 deg, incoming low momentum boundary layer fluid is transformed into high momentum fluid relative to the downstream bladerow. Such higher stagger stages thus might be less likely to stall. The significance of vector triangles in which $(\alpha + \beta)$ equals 90 deg was first pointed out by members of the Cascade Aerodynamics Branch of the NACA Langley Aeronautical Laboratory, and first published in G. C. Ashby's discussion of a 1958 paper by L. H. Smith, Jr. [10]. This concept appears to explain the strong stagger angle effect shown by the data in Fig. 12.

A parameter giving a quantitative measure of this flow coefficient/stagger angle effect, termed the effective dynamic pressure factor $\mathcal{F}_{ef}$, was defined as the effective dynamic head divided by the pitchline free stream dynamic head. As indicated by the equations in Fig. 13, the effective dynamic head was represented by a weighted average of the free stream dynamic head, the minimum possible dynamic head, and the dynamic head at zero axial velocity. By trial and error, the best fit of the data was found to occur if the minimum dynamic head was weighted 2.5 times as heavily as the free stream head, and the head at zero axial velocity was weighted one half as heavily as the free stream head. The minimum dynamic head was set equal to the free stream value for vector triangles where $(\alpha + \beta)$ was greater than 90 deg, because in such a case the minimum possible dynamic head could only occur at axial velocities higher than the free stream value. Also, for vector triangles in which the upstream bladerow turned the flow past the axial direction, the minimum dynamic head was not allowed to become less than the zero through-flow value, because in this case the mathematical

minimum dynamic head could only occur at negative axial velocities.

The stage average effective dynamic pressure factor, $\mathcal{F}_{ef}$, was computed for numerous General Electric low speed compressor test configurations, and was found to be in the range from 0.78 to 1.11. Experimental data from other sources [11–13] were also evaluated, because these designs had very high flow coefficients and thus very low values of $\mathcal{F}_{ef}$ (as low as 0.39). For each test configuration the stalling static-pressure-rise coefficient, adjusted for Reynolds number and clearances, was divided by the value predicted from the two-dimensional diffuser correlation of Sovran and Klomp using an inlet blockage of 9 percent, and this pressure rise ratio was plotted versus average $\mathcal{F}_{ef}$ in Fig. 14. The effective dynamic pressure factor is seen to produce a linear variation of stalling pressure rise ratio, and the data points from the best configurations lie near a line that has a slope of about unity. This strongly suggests that stalling static-pressure rise for well-designed stages, even those employing markedly different types of vector triangles, is indeed directly proportional to the empirically-determined effective dynamic head defined above.

Final Correlation. As a final adjustment to the static-pressure-rise correlation, the bladerow inlet pitchline free stream dynamic head was replaced by the effective dynamic head in the pressure coefficient. The final form of the correlation for stalling static-pressure-rise coefficient, $(C_h)_{ef}$, versus the diffusion length: exit passage width parameter, L/g_2, is shown in Fig. 15. Data from all the General Electric low speed test configurations are shown in this figure, as are data from the stages described in references [11–13], those having very low values of $\mathcal{F}_{ef}$. The significant finding is that the trend of the compressor data in Figure 15 is the same as that of two-dimensional diffusers having fairly thick inlet boundary layers; the L/g_2 parameter does indeed account for the effect of cascade geometry on stall pressure rise capability, once the important effects of clearances, Reynolds number and type of vector diagram have been properly accounted for.

For stages having a value of L/g_2 less than about 2.2 (and this covers most cases of current interest in gas turbine compressors) the highest data points are represented very well by the Sovran and Klomp two-dimensional diffuser correlation using an inlet boundary layer thickness of 9 percent, and nearly all of the data points are within 10 percent of the correlation curve. It is conspicuous that the highest of the compressor data points in Fig. 15 still have rather low recovery levels, about equal to those predicted for diffusers having thick inlet boundary layers. Multistage compressors do, of course, have fairly thick wall boundary layers near stall (average predicted blockage factor for the compressors in Fig. 15 was 0.877), so perhaps the relatively low recovery is not surprising. It should be remembered, too, that many of the compressor data points have had substantial adjustments applied for clearance and Reynolds number effects. In fact, if zero tip clearance and zero axial spacing had been selected as the reference levels instead of the more typical compressor clearances actually used, the adjusted compressor data would have agreed quite well with the higher predicted performance of diffusers having an inlet boundary layer blockage of only 1 percent.

There is only one data point shown in Fig. 15 having a value of L/g_2 greater than 2.2; this configuration had an aspect ratio of 1.0 and a pitchline solidity of 3.0. This data point lies 13 percent below the diffuser curve, which is among the poorest agreement of any of the configurations. This stage did have unaccountably high losses, and perhaps could have given better stall pressure rise and efficiency if it had been developed further. However, the high surface area: flow area ratio and the high potential for large blade thickness blockage effects that exist at high values of L/g_2 (due to use of high solidity and/or high stagger blading) may place limits on achievable recovery. Some circumstantial evidence that this

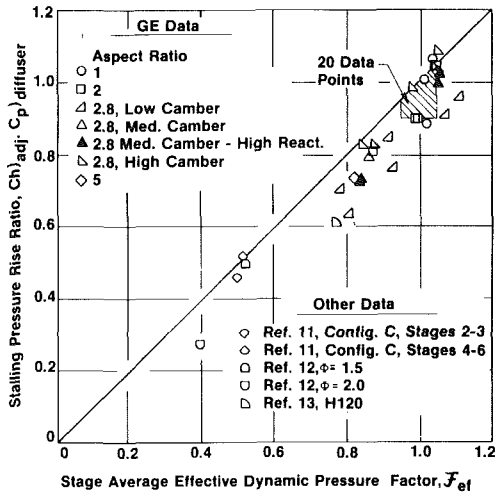

Fig. 14 Effect of dynamic pressure factor on stalling pressure rise

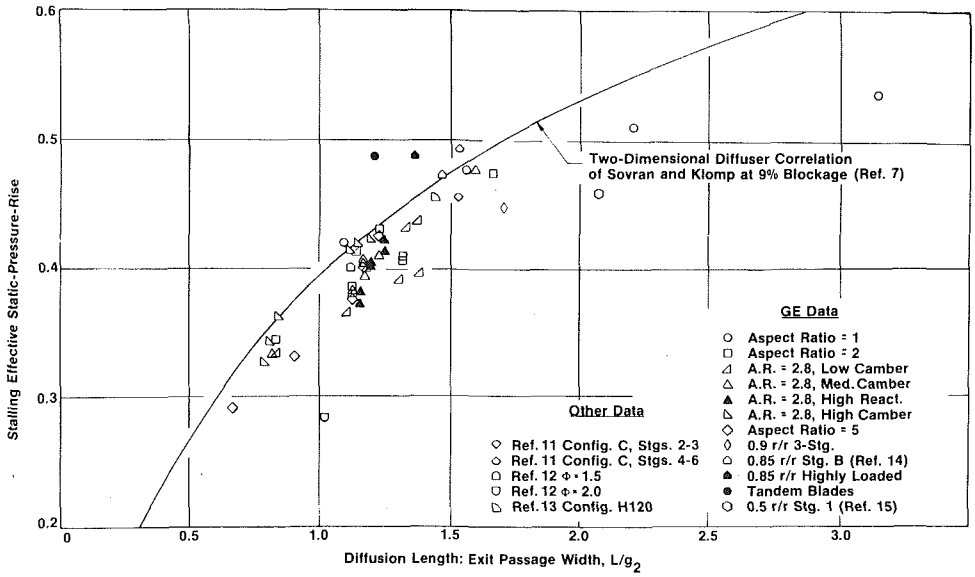

Fig. 15 Correlation of stalling effective static-pressure-rise coefficients for low-speed stages

limit can occur was seen in Figure 1, where the diffuser data of Kline and Reneau for 5 percent inlet boundary layer blockage reach a peak pressure recovery of 0.65 and then show decreased peak recovery for longer diffusers. This is typical of diffusers having thick inlet boundary layers. Although the evidence is very limited, there is reason to be concerned that the diffuser correlation may be somewhat optimistic for compressor stages having L/g_2 larger than about 2.2, at least for those operating in the multistage environment.

The configuration having the highest stalling pressure recovery of all the cases shown in Fig. 15 was a 3-stage, 0.7 radius ratio design using tandem bladerows for both rotors and stators. Average aspects ratio and solidity (based on the sum of forward and aft airfoil chords) were 1.2 and 1.1, respectively. It had a reaction ratio of 0.55, utilized rather conventional vector diagrams and had an average $\mathcal{F}_{ef}$ factor of 0.996. Its high stalling value of effective static-pressure rise for its level of L/g_2 (13 percent above the diffuser correlation) did not result from having large adjustments applied to the actual test data or from having any unusual geometry other than the tandem bladerow feature. The tandem bladerow concept is often thought of as a means of providing blade surface boundary layer control, and it also appears to have beneficial effects on the end-wall region boundary layer processes that control stall.

The majority of the configurations used to establish the correlation of Fig. 15 had a hub: tip radius ratio of 0.7, and the question naturally arises whether this pitchline model of a predominantly end-wall effect is valid only for this one radius ratio. A number of stages were analyzed, however, that had hub: tip radius ratios considerably different from 0.7, and most of the recovery data from these cases also agreed well with the correlation, supporting the use of the simple pitchline model. Three General Electric configurations are shown in Fig. 15 that had radius ratios of 0.85 to 0.90. One of these, Stage B of reference [14], had a pressure rise coefficient almost exactly equal to the diffuser correlation's predicted value, a second had a value about 10 percent below the correlation, and the third had a recovery about 7 percent above the correlation. The data from Stages 4–6 of the NACA compressor [11] had a pressure rise about 3 percent above the correlation; the average radius ratio of these stages was 0.843. One low-speed configuration, described in reference [15], was analyzed that modeled the aerodynamics of a multistage fan and had a radius ratio of 0.5. The stages were not identical in this case, and only the first stage was highly loaded at stall. Unfortunately, this design had a radial imbalance in loading and stalled first at the hub. As a result, the first stage's peak pressure rise coefficient was 15 percent below that predicted by the diffuser correlation. This design also had a rather high L/g_2 value of 2.07, so its relatively poor performance perhaps shouldn't be attributed entirely to its low radius ratio and unbalanced loading. Admittedly, it is more difficult to achieve a balance of aerodynamic loading between hub and tip at low radius ratios, and the pitchline approach cannot be expected to work too well for unbalanced stages. It is possible to design a well-balanced low radius ratio stage, however, and in the next section the recovery of a high-speed, low radius ratio design will be shown to agree reasonably well with the correlation.

The validity of using a stage average approach instead of a bladerow-by-bladerow model is addressed by the data presented in Fig. 16, in which the ratio of demonstrated stalling recovery to that given by the diffuser correlation is plotted versus reaction ratio for all the available test configurations. The data points in Fig. 16 cover a range of reaction ratio from 0.39 to 1.09, and good agreement with the correlation can be found for any reaction in this range. This is

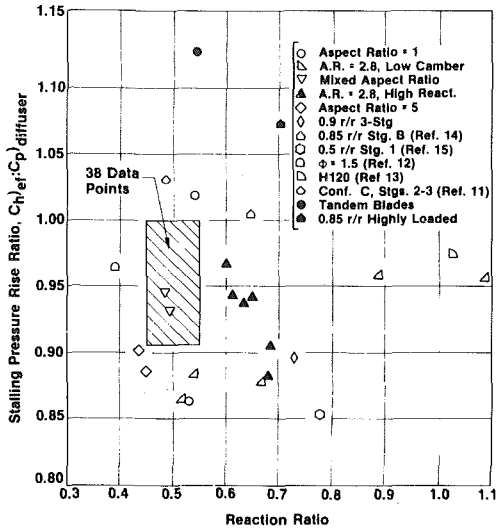

Fig. 16 Effect of reaction ratio on stalling pressure rise

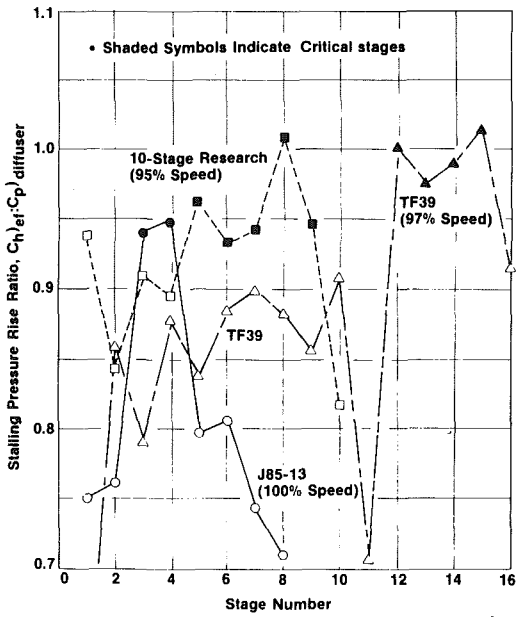

Fig. 17 Stagewise distributions of static-pressure rise at stall for high-speed compressors

particularly surprising for those cases having reaction ratios over 1.00. The rotor in the highest reaction case shown, for example, is estimated to have a stalling static-pressure-rise coefficient 40 percent higher than the correlation value, yet the stage average value is 96 percent of the correlation. It is not known if the rotor could still produce its pressure rise as an isolated bladerow, or if the net acceleration of the flow in the upstream and downstream stators exerts a necessary stabilizing influence on the rotor in the multistage environment. In any event, it is clear that a better correlation can be obtained for these extreme cases using a stage average model than would have been possible using a blade-by-blade approach. Two other cases are shown in Fig. 16 that also verify the stage average approach. These are named the mixed aspect ratio tests, and have reaction ratios of about 0.49. These two configurations were made up of the baseline blading set at its design stagger; one stage used the aspect ratio 2.0 rotors with the aspect ratio 5.0 stators, and the other used the aspect ratio 5.0 rotors with the aspect ratio 2.0 stators. In both cases the stage average chord length was the same as with the aspect ratio 2.8 blading, but there were sizable differences

in Reynolds number and normalized clearance between individual bladerows. As seen in Fig. 16, however, the performance was virtually the same for either case and consistent with stages using aspect ratio 2.8 rotors and stators.

Comparison with High-Speed Compressor Data

The stalling static-pressure-rise coefficient correlation of Fig. 15 was compared to data from three General Electric high speed multistage compressors operating at their stall limit at or near design corrected speed. In Fig. 17, stall pressure rise coefficients for each stage of each machine are ratioed by that stage's predicted value from the diffuser correlation, and this ratio is plotted versus stage number. Because of stage matching effects, not all stages are loaded up to the level of the correlation; overall average values of the ratio of actual to predicted pressure rise range from 0.808 for the J85-13 to 0.921 for the highly loaded 10-stage research compressor. The J85-13 compressor has a low average pressure rise ratio because its rear stages are rather lightly loaded relative to the correlation. The average pressure rise ratio of stages 3 and 4 is 0.946, however, and there is independent evidence [4] suggesting that these are the stall limiting stages in this design. In the TF39 core compressor, stages 12 through 15 are highly loaded at the 97 percent speed stall point (average pressure rise ratio for these stages is 0.996), while the front and middle stages are matched so as to operate well below the correlation's predicted limit. The 10-stage research compressor (whose stall pressure ratio is nearly as high as the 16-stage TF39) is matched so as to have many of its stages quite highly loaded at its high-speed (95 percent of design) stall point. The average pressure rise ratio of stages 5 through 9 is 0.960. The most significant finding is that in each high speed compressor, there is a group of stages whose pressure rise at stall is consistent with that of the low speed compressors and with that predicted from the diffuser correlation. These groups of stages are likely to be those responsible for stalling the overall compressor. The data shown in Fig. 17 indicate that the model should be used in conjunction with an off-design performance prediction procedure so that stage matching effects on overall pressure rise at stall can be accounted for properly.

The applicability of the stall prediction model is further indicated in Fig. 18 where the average stalling static-pressure-rise coefficients for stall limiting groups of high speed stages have been plotted versus average values of L/g_2. Data from references [11 and 12], described in the previous section, are repeated here because these designs actually had average pitchline Mach numbers typical of high speed compressors. Agreement of the high-speed data with the two-dimensional diffuser performance correlation of reference [7] is as good as for the low speed data points from Fig. 15, which are indicated by the cross-hatched regions and the solid symbols.

Data from several other high speed compressors are also shown in Fig. 18 in order to broaden the range of geometries and Mach numbers considered. Configurations 3S1 and 3S2 from reference [16] were high radius ratio, three-stage designs that modeled the rear stages of an advanced technology core compressor. The two were virtually identical with respect to flowpath, speed, reaction and solidity and had nearly the same value of L/g_2; they differed primarily in average aspect ratio and camber. The 0.8 aspect ratio Configuration 3S1 had more flow range and a higher stalling total-pressure ratio, but the 1.2 aspect ratio Configuration 3S2 had the same static-pressure recovery at stall once the data were adjusted to the same normalized tip clearance and Reynolds number. The level of stalling recovery achieved by these stages was reasonably close to that given by the diffuser correlation.

Data from two high-speed, low radius ratio fans are also presented in Fig. 18. The average stalling recovery of the two-

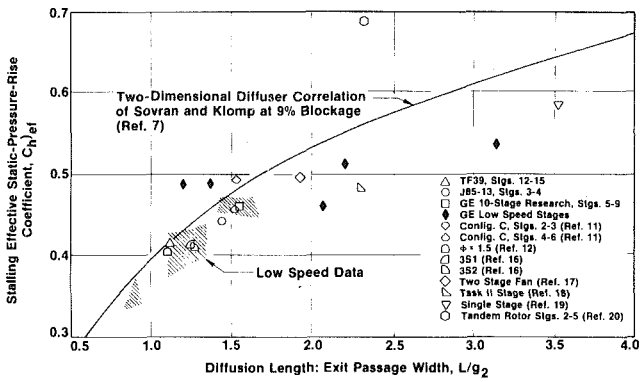

Fig. 18 Correlation of stalling effective static-pressure-rise coefficients for high-speed stages

stage fan described in reference [17] was within 6 percent of the value given by the diffuser correlation. The tip Mach number of the first stage was about 1.5, and the first stage's radius ratio was 0.4. The recovery of the single stage Task II fan described in reference [18] was within approximately 14 percent of the correlation curve. This stage also had a rotor tip Mach number of about 1.5 and had an inlet radius ratio of 0.5. Although primarily of interest because of their high L/g_2 values, these fan designs also indicate the applicability of the correlation to very high speed cases where strong shocks are present in the rotors. The data from these fans, particularly that from the two-stage fan of reference [17], also demonstrate the applicability of the correlation to low radius ratio stages.

The data from the single stage compressor described in reference [19] is of interest for several reasons. First, it has one of the highest values of L/g_2 of any design known to the author ($L/g_2 = 3.53$), and has a stalling pressure rise that is in reasonable agreement with the diffuser correlation. This design had a high tip speed and used very high blading solidities and low aspect ratios to achieve a high pressure ratio. The stage is also of interest because its vector diagrams employed considerable counter swirl leaving the inlet guide vane. The resulting $\mathcal{F}_{ef}$ factor adjustment to the rotor's inlet free stream dynamic head was thus substantial: the stage average value of $\mathcal{F}_{ef}$ was 0.72. Without this adjustment, the stalling static-pressure-rise coefficient would have been well below the level of the diffuser correlation and well below the trend of the data from other stages having high L/g_2 values.

The final data point shown in Fig. 18 is from a novel compressor described in reference [20]. This 5-stage design had tandem rotor blading in the three middle stages, a reaction ratio of about 100 percent and considerable stator exit counter swirl. The three middle stages also had high solidity blading (based on the sum of forward and aft airfoil chords in the case of the tandem rotors), giving them the rather high average L/g_2 value of 2.33. The stalling stage-average effective static-pressure-rise coefficient for the tandem rotor middle stages exceeded the value predicted by the diffuser correlation by a surprising 23 percent. This high recovery value certainly resulted in part from the large adjustment made to the free stream dynamic head to account for use of high flow coefficient, counter swirl vector diagrams (the stage average value of $\mathcal{F}_{ef}$ was 0.73). Since the $\mathcal{F}_{ef}$ factor adjustment was substantiated by the above-mentioned single stage configuration that had similar counter swirl vector diagrams [19], it may well be that the ability of this three-stage group to significantly exceed the predicted recovery is due primarily to the tandem rotor design feature. This was clearly the case for the low speed tandem bladerow configuration described earlier, so it may be advisable to consider

tandem bladerow designs as a separate class of machines that in effect incorporate a means of boundary layer control.

In summary, the data presented in Fig. 18 cover a range of average L/g_2 values from 0.65 to 3.5, inlet radius ratios from 0.40 to 0.92, inlet rotor tip relative Mach numbers from 0.1 to 1.6, reaction ratios from 0.4 to 1.1, and average aspect ratios from 0.35 to 5.0. Reasonably good agreement with the diffuser correlation can be found for configurations having design characteristics anywhere in the ranges noted above. The data points on the upper side of the scatter in Fig. 18 are of particular interest, since they correspond to stages having the highest pressure rise coefficients relative to their inherent potential (as determined by their cascade geometry, clearances and type of vector diagram). These data points thus serve to define an upper limit for well-designed axial flow compressor stages. There are, of course, many reasons why the less successful stages may have failed to equal the pressure rise predicted by the diffuser correlation: insufficient camber, excessively high incidence angles, radial imbalances in aerodynamic loading, unbalanced loading between rotor and stator or any number of airfoil quality or mechanical design compromises. Skillful design is needed to avoid these problems and to produce a stage capable of equalling the diffuser correlation. At this time, however, the experience of the author is that very few stages, no matter how skillfully designed, will be capable of exceeding the correlation by more than a few percent.

Conclusions

Data from numerous low speed multistage compressors have been used to obtain a correlation of stalling static-pressure-rise coefficient versus a pitchline cascade geometry parameter L/g_2 that is analogous to N/W_2 for a two-dimensional diffuser. The test data also allowed the effects of Reynolds number, blade tip clearance, bladerow axial spacing and the type of vector diagrams used to be identified. Blading aspect ratio was implicitly accounted for through its effect on Reynolds number, normalized clearances and wall boundary layer blockage. When these effects were accounted for, the highest of the compressor stalling pressure rise data were consistent with an accepted correlation of two-dimensional diffuser performance. It was shown that the relatively simple stage-average pitchline approach used was valid over a wide range of stage design parameters, including reaction ratio and hub:tip radius ratio. Stalling pressure rise data at or near design speed for a number of high speed compressors were shown to be consistent with the low speed correlation, once stage matching effects were accounted for. When used with an off-design performance prediction proceedure, the model can provide a useful estimate of a high speed multistage compressor's stalling pressure ratio potential. Because of its simplicity, it is particularly well suited for preliminary design studies.

Acknowledgments

The author wishes to thank the Aircraft Engine Group of the General Electric Company for its permission to publish this paper. Particular thanks are due L. H. Smith, Jr., and the many individuals who have worked under his direction, for the experimental data from the Low Speed Research Compressor upon which much of this work is based.

References

1 Lieblein, S., Schwenk, F.D., and Broderick, R.L., "Diffusion Factor for Estimating Losses and Limiting Blade Loadings in Axial-Flow-Compressor Blade Elements," NACA RM E53D01, June 8, 1953.

2 Lieblein, S., "Loss and Stall Analysis of Compressor Cascades," ASME *Journal of Basic Engineering*, Sept. 1959, pp. 387–400.

3 Smith, L.H., Jr., "Casing Boundary Layers in Multistage Axial-Flow Compressors," *Flow Research on Blading*, ed., L.S. Dzung, Elsevier Publishing, Amsterdam, Netherlands, 1970.

4 Tesch, W.A., Moszee, R.H., and Steenken, W.G., "Linearized Blade Row Compression Component Model, Stability and Frequency Response Analyses of a J85-13 Compressor," NASA CR-135162, Sept. 1976.

5 Reneau, L.R., Johnston, J.P., and Kline, S.J., "Performance and Design of Straight, Two-Dimensional Diffusers," ASME Paper No. 66-FE-10.

6 Koch, C.C., and Smith, L.H., Jr., "Loss Sources and Magnitudes in Axial-Flow Compressors," ASME JOURNAL OF ENGINEERING FOR POWER, Vol. 98, No. 3, July 1976.

7 Sovran, G., and Klomp, E.D., "Experimentally Determined Optimum Geometries for Rectilinear Diffusers with Rectangular, Conical or Annular Cross Section," *Fluid Mechanics of Internal Flow*, Elsevier Publishing, Amsterdam, Netherlands, 1967.

8 Greengard, R.L., "Effects of Reynolds Number on the Performance of an Axial Flow Compressor with One, Two, and Four Stages," Propulsion Research Corporation Report No. R-116, Sept. 1954, unpublished.

9 Carter, A.D.S., Moss, C.E., Green, G.R., and Annear, G.G., "The Effect of Reynolds Number on the Performance of a Single Stage Compressor," NGTE Report No. R.204, May 1957.

10 Smith, L.H., Jr., "Recovery Ratio — A Measure of the Loss Recovery Potential of Compressor Stages," *Trans. ASME*, Vol. 80, No. 3, Apr. 1958.

11 Westphal, W.R., and Maynard, J.W., Jr., "Design and Tests of a Six-Stage Axial-Flow Compressor Having a Tip Speed of 550 Feet per Second and a Flat Operating Characteristic at Constant Speed," NACA TN-4253, 1958.

12 Vlasak, M., "The Effect of Major Design Parameters on the Efficiency of an Axial Compressor," Monographs and Memoranda No. 4, The National Research Institute of Heat Engineering, Prague, 1964.

13 Turner, R.C., and Burrows, R.A., "Some Tests on High-Reaction Compressor Blading," Ministry of Aviation (U.K.) Aeronautical Research Council, R. & M. No. 3380, 1964.

14 Wisler, D.C., "Core Compressor Exit Stage Study, Volume 1 — Blading Design," NASA CR-135391, Dec. 1977.

15 Wisler, D.C., and Hilvers, D.E., "Stator Hub Treatment Study," NACA CR-134729, Dec. 1974.

16 Behlke, R.F., et al., "Core Compressor Exit Stage Study, Volume II — Final Report," NASA CR-159812, Oct. 1979.

17 Messenger, H.E., and Keenan, M.J., "Two-Stage Fan, II Data And Performance With Redesigned Second Stage Rotor, Uniform and Distorted Inlet Flows," NASA CR-134710, Oct. 1974.

18 Bilwakesh, K.R., "Task II Stage Data And Performance Report For Undistorted Inlet Flow Testing," NASA CR-72787, Jan. 1971.

19 Muller, C.H., and Cox, L.R., "Single-Stage Axial Compressor Component Development For Small Gas Turbines, Volume III, Supersonic Compressor Stage Development," USAAVLABS Technical Report 68-90C, June 1969.

20 Bammert, K., and Beelte, H., "Investigations of an Axial Flow Compressor with Tandem Cascades," ASME Paper No. 80-GT-39, presented at the Gas Turbine Conference and Products Show, New Orleans, La., Mar. 1980.

Transonic Flow Computations in Cascades Using Finite Element Method

H. U. Akay
Research Associate

A. Ecer
Professor, Mechanical Engineering

Purdue University,
at Indianapolis,
Indianapolis, Ind. 46205

Analysis of transonic flow through a cascade of airfoils is investigated using the finite element method. Development of a computational grid suitable for complex flow structures and different types of boundary conditions is presented. An efficient pseudo-time integration scheme is developed for the solution of equations. Modeling of the shock and the convergence characteristics of the developed scheme are discussed. Numerical results include a 45 deg staggered cascade of NACA 0012 airfoils with inlet flow Mach number of 0.8 and angles of attack 1, 0, and −1 deg.

Introduction

Application of the finite element method for the analysis of inviscid transonic flow problems has been considered by several during the last five years [1-4]. Also recently, the method has been extended to the solution of transonic flows in cascade configurations [5].

One of the main advantages of the finite element method has been the practicability of setting an irregular computational grid to fit a particular flow problem and to modify it with ease, if necessary. This property proves to be quite important for the solution of transonic flows in cascade configurations, not only to describe the complex cascade geometry but also to choose the most suitable computational grid for a particular flow. Some of the problems associated with the analysis of transonic flows through cascades of airfoils have been considered by the authors in [5]. The importance of designing a computational grid suitable for both the subsonic leading edge and the supersonic pockets to obtain accurate and efficient solutions have been investigated. Numerical results have been presented for basic cascade geometries. It was demonstrated that the finite element method is a practical and efficient tool in treating these problems.

In the present paper, the same approach is extended to the analysis of a more complex set of problems. Namely, highly staggered cascades are considered. The adaptability of the finite element method to the solution of more complicated flow structures is illustrated. In particular, the treatment of periodic boundary conditions and the trailing edge Kutta conditions are discussed. The choice of a simple yet efficient finite element grid is demonstrated. A combined shock-fitting and shock-capturing scheme is employed. Moreover, in the present paper, the previously developed pseudo-time integration technique is modified so that a constant coefficient matrix is obtained which leads to a considerable improvement in the efficiency. The convergence rate of this new scheme is shown to be competitive with that of the variable coefficient shceme. The numerical results presented herein provide an insight into the generality and efficiency of the developed computational procedure.

Governing Equations

We consider the solution of the full potential equation for steady, inviscid and irrotational flows expressed in the conservative form

$$(\rho\phi_{,x})_{,x} + (\rho\phi_{,y})_{,y} = 0 \text{ in } \Omega \tag{1}$$

where ϕ is the velocity potential, Ω is the solution domain, and ρ is the mass density of the fluid. The general boundary conditions of equation (1) are

$$\phi = \phi_0 \text{ on } S_1 \tag{2}$$

and

$$\rho\phi_{,n} = f \text{ on } S_2 \tag{3}$$

where ϕ_0 and f are some specified quantities on the boundary $S = S_1 + S_2$, and n is the outward normal on S_2.

By combining the isentropic equation of state with the Bernoulli equation, one obtains the relation

$$\rho = \text{const}(K^2 - q^2)^{\frac{1}{\gamma-1}} \tag{4}$$

for the mass density, where γ is the ratio of specific heats, and

$$K^2 = \frac{2a^2}{\gamma-1} + q^2, \tag{5}$$

$$q^2 = \phi_{,x}{}^2 + \phi_{,y}{}^2. \tag{6}$$

K is the maximum attainable speed which is constant throughout the flow, a is the local speed of sound, and q is the local flow speed.

For the cascade geometries shown in Fig. 1, if the inlet speed of sound a_{in} is normalized, then equation (5) becomes

Contributed by the Gas Turbine Division and presented at the International Gas Turbine Conference and Products Show, Houston, Texas, March 9-12, 1981, of THE AMERICAN SOCIETY OF MECHANICAL ENGINEERS. Manuscript received at ASME Headquarters, December 1, 1980. Paper No. 81-GT-4.

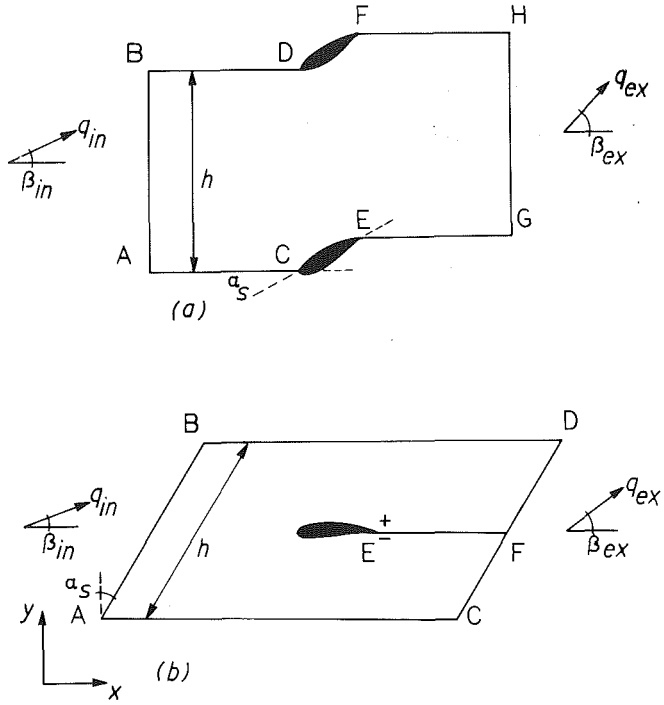

Fig. 1 Possible solution domains for cascade flows

$$K^2 = \frac{2}{\gamma - 1} + \mathrm{M}_{in}{}^2 \tag{7}$$

where $\mathrm{M}_{in} = q_{in}/a_{in}$ is the inlet Mach number.

Cascade Geometry

Either of the solution domains shown in Fig. 1 can be used to model two-dimensional cascades. In each case, a set of periodic boundaries together with the blade surfaces, the inlet and exit boundaries, the stagger angle α_s and the pitch h define the cascade geometry. Since the domain in Fig. 1(*b*) is multiply connected, a splitting boundary such as the slit line *E-F* shown in the figure is required in order to allow the velocity potential to be discontinuous across *E-F*. This assures ϕ to be single valued.

The use of the configuration shown in Fig. 1(*b*) is found to be more advantageous for highly staggered cascades, firstly because it lends itself easily to the generation of less distorted grids especially at the rounded leading and trailing edges. Secondly, since the periodic boundaries are furthest from the blade surfaces, the effects of approximations introduced in satisfying the periodicity conditions in this case are minimal.

The boundary conditions for configuration of Fig. 1(*a*) have previously been discussed in [5]. Therefore only the case *b* will be discussed here. Assuming that the farfield inlet and exit flow conditions are uniform and M_{in}, β_{in}, β_{ex} are known, referring to Fig. 1(*b*) the boundary conditions become

$$\text{i)}\quad f = f_{in} = -\rho_{in} q_{in} \cos\beta_{in} \text{ on } A-B \tag{8}$$

$$\text{ii)}\quad f = f_{ex} = -f_{in} \text{ on } G-H \tag{9}$$

$$\text{iii)}\quad f = 0 \text{ on the airfoil surface} \tag{10}$$

$$\text{iv)}\quad \phi^+ - \phi^- = \lambda \text{ on } E-F \tag{11}$$

where λ is the circulation which may be determined from the farfield conditions as

$$\lambda = q_{in}(h_x \cos\beta_{in} + h_y \sin\beta_{in}) - q_{ex}(h_x \cos\beta_{ex} + h_y \sin\beta_{ex}) \tag{12}$$

where

$$h_x = h\sin\alpha_s, h_y = h\cos\alpha_s, \tag{13}$$

and q_{ex} is computed iteratively from the continuity equation

$$f_{in} + f_{ex} = 0 \tag{14}$$

$$\text{v)}\quad \phi(x+h_x, y+h_y) = \phi_1(x,y) + q_{in}(h_x \cos\beta_{in} + h_y \sin\beta_{in}) \text{ on } B-D \tag{15}$$

where $\phi_1(x,y)$ is the unknown distribution of ϕ on $A-C$.

$$\text{vi)}\quad \phi = 0 \text{ on } A. \tag{16}$$

In the above, the condition (ii) is due to conservation of mass, (v) is due to perodicity, and (vi) is needed to avoid the arbitrariness of the potential function ϕ.

In some cases the exit flow angle β_{ex} is not known a priori, therefore the circulation λ is also an unknown. To determine λ in this case, the Kutta condition

$$q^2|_{E^+} = q^2|_{E^-} \tag{17}$$

must be satisfied at the sharp trailing edge of the airfoil. A convenient way of satisfying equation (17) and determining λ in an iterative fashion will be discussed later.

Finite Element Formulation

For a finite element formulation of equations (1)-(3) we use the Bateman's variational functional

$$\pi = \int_\Omega p d\Omega + \int_{S_2} f\phi dS \tag{18}$$

where for isentropic and perfect gases

Nomenclature

a = local speed of sound
a_{in} = inlet speed of sound
C = chord length of airfoil
e = subscript used to denote an element
f = mass flux
$\mathbf{f}$ = vector of mass fluxes at the boundaries
h = pitch
K = maximum attainable flow speed
$\mathbf{K}^0$ = constant coefficient matrix (function of ρ_{in})
$\mathbf{K}^n$ = variable coefficient matrix (function of ρ_e^n)
M = Mach number
M_{in} = inlet Mach number
n = pseudo-time step
$\mathbf{N}$ = vector of element shape functions
p = pressure
q = local flow speed
q_{ex} = exit flow speed
q_{in} = inlet flow speed
s = flow direction
y,y = Cartesian coordinates
α_e = artificial viscosity coefficient
α_s = stagger angle
β_{ex} = exit flow angle
β_{in} = inlet flow angle
δ = variational operator
$\Delta\boldsymbol{\phi}_e$ = vector of errors in nodal point velocity potentials
Δq_e = error in element flow speed
Δs_e = element size in flow direction
Δt = pseudo-time increment
Δx_e = element size in x-direction
γ = ratio of specific heats
λ = circulation
μ_e = artificial viscosity multiplier
ϕ = potential function
$\boldsymbol{\phi}$ = vector of nodal point velocity potentials
π = Bateman's variational functional

$$p = \frac{\gamma - 1}{2\gamma} \text{const}\, \rho^{\gamma} \tag{19}$$

is the pressure. To introduce the finite element approximations, we express equation (18) for an element e and sum the contributions of all elements in the domain. The stationary values of the resulting expression yield the following variational statement.

$$\delta\pi = \sum_e \left[-\int_{\Omega_e} \rho_e (\phi_{,x}\delta\phi_{,x} + \phi_{,y}\delta\phi_{,y})\, d\Omega + \int_{S_{2_e}} f_e \delta\phi ds \right] = 0. \tag{20}$$

We then choose C_0 shape functions $N_i^e(x,y)$ so that within each element the interpolation

$$\phi^e(x,y) = N_i^e(x,y)\,\phi_i^e = \mathbf{N}^T \boldsymbol{\phi}^e \quad (i = 1, \ldots, m) \tag{21}$$

holds, where ϕ_i^e are the nodal values of velocity potentials and m is the number of element nodal points. Substituting equation (21) into (20) we obtain the following system of equations

$$\mathbf{K}\,\boldsymbol{\phi} = \mathbf{f} \tag{22}$$

where

$$\mathbf{K} = \sum_e \int_{\Omega_e} \rho_e (\mathbf{N}_{,x}\mathbf{N}_{,x}^T + \mathbf{N}_{,y}\mathbf{N}_{,y}^T)\, d\Omega \tag{23}$$

$$\mathbf{f} = \sum_e \int_{S_{2_e}} \mathbf{f}_e \mathbf{N} dS \tag{24}$$

$$\boldsymbol{\phi} = \sum_e \boldsymbol{\phi}^e \tag{25}$$

Pseudo-Unsteady Formulation

For the solution of the above nonlinear equations a pseudo-unsteady formulation has been proposed in [5] as follows:

$$\Delta t \mathbf{C}\,\dot{\boldsymbol{\phi}} + \mathbf{K}\,\boldsymbol{\phi} = \mathbf{f} \tag{26}$$

where Δt is a pseudo-time increment, and

$$\mathbf{C} = \frac{\mathbf{K}}{\omega} \tag{27}$$

is the damping matrix of the above time-dependent problem. Here ω is a relaxation parameter controlling the stability of the numerical integrations. Using backward - differencing in time, the following step-by-step numerical integration scheme for equation (26) is obtained

$$\mathbf{K}^{n+1}\tilde{\boldsymbol{\phi}}^{n+1} = \mathbf{f}^{n+1} \tag{28}$$

with

$$\boldsymbol{\phi}^{n+1} = \omega\tilde{\boldsymbol{\phi}}^{n+1} + (1-\omega)\boldsymbol{\phi}^n \tag{29}$$

where n is the pseudo-time step.

Equation (28) is nonlinear, and a "good" estimate of the coefficient matrix is necessary at each time step to assure the stability of the numerical integrations. It has been shown in [5] that an appropriate procedure for evaluating $\mathbf{K}^{n+1}$ and consequently $\mathbf{C}^{n+1}$ at a time step n is to use

$$\rho_e^{n+1} \approx \rho_e^n \tag{30}$$

when the local flow is subsonic, and

$$\rho_e^{n+1} \approx \rho_e^n - \alpha_e \Delta s_e \rho_{e,s}^n \tag{31}$$

when it is supersonic. In the above equation s is the streamline direction, Δs_e is the element size in the direction of s, and α_e is known as the coefficient of artificial viscosity.

The extrapolation scheme of equation (30) takes into account the elliptic nature of the equations in the subsonic region whereas equation (31) takes into account the hyperbolic nature of the equations in the supersonic region. For sufficiently streamlined elements and uniform grids, equation (31) can further be computed as follows

$$\rho_e^{n+1} \approx \alpha_e \rho_{eu}^n + (1-\alpha_e)\rho_e^n \tag{32}$$

where ρ_{eu} is the mass density of the nearest element at the upstream side of e. This corresponds to the well-known "upwinding" technique used in finite differences [6]. For uniform convergence of pseudo-time integrations to a steady state, it has further been verified that the artificial viscosity coefficient must be [5]:

$$\alpha_e \geqslant \mu_e \left(1 - \frac{1}{M_e^2}\right) \tag{33}$$

where μ_e is an artificial viscosity multiplier governed by

$$\mu_e = \frac{\Delta q_e^n}{\Delta q_e^n - \Delta q_{eu}^n} > 0. \tag{34}$$

In equation (34) Δq_e^n and Δq_{eu}^n respectively denote the errors in the local speed of elements e and eu measured as deviations from the true steady solution.

As can be seen in equation (33), the amount of artificial viscosity required for uniform convergence of the pseudo-time integration scheme depends on the local Mach number as well as the computational grid and the distribution of the errors in the initial solution. For larger values of the artificial viscosity, the scheme is uniformly convergent in a wider range of initial conditions and the rate of convergence is faster, which will be discussed later in more detail. To take advantage of this behavior, the numerical solution of the inviscid transonic flow problem is obtained by introducing a high artificial viscosity parameter initially for a solution with a faster convergence rate. Once a convergent solution is obtained, the artificial viscosity is reduced and the integration scheme is repeated. The main objective of this procedure is to obtain an improved set of initial conditions for lower values of the artificial viscosity with guaranteed convergence.

The Numerical Integration Technique

The numerical integration scheme based on a direct solution of the system defined in equation (28) has been employed with success for the solution of transonic flow problems in [5]. However, since the left-hand side of equation (28) is nonlinear, a full decomposition of the coefficient matrix $\mathbf{K}$ is needed at each step which makes the scheme computationally somewhat inefficient. For efficiency considerations in the present case, we propose to modify the time integrations in equation (28) as follows:

$$\mathbf{K}^0\tilde{\boldsymbol{\phi}}^{n+1} = \mathbf{f}^{n+1} + (\mathbf{K}^0 - \mathbf{K}^{n+1})\boldsymbol{\phi}^n \tag{35}$$

with

$$\boldsymbol{\phi}^{n+1} = \omega\tilde{\boldsymbol{\phi}}^{n+1} + (1-\omega)\boldsymbol{\phi}^n \tag{36}$$

where

$$\mathbf{K}^0 = \mathbf{K}(\rho_\infty) \text{ and } \rho_\infty = \rho_{\text{in}} \tag{37}$$

are constant for all time steps. Hence the decomposition of $\mathbf{K}^0$ is needed only for the first time step and subsequent solutions can be obtained with relatively inexpensive forward and backward substitutions. We shall refer to the scheme in equation (28) as the variable coefficient scheme (VCS) and the one defined by equation (35) as the constant coefficient scheme (CCS).

Convergence Properties of CCS

Following the procedure outlined in [5] we consider a one-dimensional version of equation (35). For a single element e and $\gamma = 2$, equation (35) takes the form

$$\{K^2 - q_\infty^2\}\mathbf{N}_{,x}\mathbf{N}_{,x}^T\tilde{\boldsymbol{\phi}}_e^{n+1} = \{q_\infty^2 + (q_e^n)^2 - \alpha_e \Delta x_e[(q_e^n)^2]_{,x}\}\mathbf{N}_{,x}\mathbf{N}_{,x}^T\boldsymbol{\phi}_e^n = 0. \quad (38)$$

If the estimate to the nth solution is close to the steady state solution $\boldsymbol{\phi}_e$ in element e, i.e., if

$$\boldsymbol{\phi}_e^{n+1} = \boldsymbol{\phi}_e + \Delta\boldsymbol{\phi}_e^{n+1} \text{ with } \|\boldsymbol{\phi}_e\| >> \|\Delta\boldsymbol{\phi}_e^{n+1}\| \quad (39)$$

and

$$q_e^n = q_e + \Delta q_e^n \text{ with } |q_e| >> |\Delta q_n^e|, \quad (40)$$

then equation (38) becomes

$$[K^2 - q_\infty^2]\mathbf{N}_{,x}\mathbf{N}_{,x}^T\Delta\,\tilde{\boldsymbol{\phi}}^{n+1} = [-2q_\infty^2 + q_e^2 - \alpha_e\Delta x_e(q_e^2)_{,x}]\mathbf{N}_{,x}\mathbf{N}_{,x}^T\Delta\boldsymbol{\phi}^n + [2q_e\Delta q_e^n - 2q_\infty\Delta q_\infty^n - 2\alpha_e\Delta x_e q_e\Delta q_e^n]\mathbf{N}_{,x}\mathbf{N}_{,x}^T\boldsymbol{\phi}_e. \quad (41)$$

Recognizing that

$$\mathbf{N}_{,x}^T\Delta\tilde{\boldsymbol{\phi}}^{n+1} = \Delta\tilde{q}_e^{n+1} \text{ and } \mathbf{N}_{,x}^T\boldsymbol{\phi}_e = q_e, \text{ etc.}, \quad (42)$$

equation (41) is simplified as follows

$$[\mathbf{K}^2 - q_\infty^2]\mathbf{N}_{,x}\Delta\tilde{q}_e^{n+1} = [-q_\infty^2 + 3q_e^2 - 2\alpha_e\Delta x_e(q_e^2)_{,x}]\mathbf{N}_{,x}\Delta q_e^n - 2\alpha_e\Delta x_e q_e^2\mathbf{N}_{,x}\Delta q_{e,x}^n. \quad (43)$$

Using equation (36) and the identities:

$$2a_e^2 = K^2 - q_e^2; \quad 2q_\infty^2 = K^2 - q_\infty^2 \quad (44)$$

we obtain

$$\frac{\Delta t}{\omega}a_\infty^2\frac{\Delta q_e^{n+1} - \Delta q_e^n}{\Delta t}\mathbf{N}_{,x} = [q_e^2 - a_e^2 - \alpha_e\Delta x_e(q_e^2)_{,x}]\Delta q_e^n\mathbf{N}_{,x} - \alpha_e\Delta x_e q_e^2\Delta q_{e,x}^n\mathbf{N}_{,x}. \quad (45)$$

The above difference relationship implies that the error $\Delta q_e^n(x,t)$ satisfies the following differential equation

$$\Delta q_{e,t}^n + c\Delta q_{e,x}^n = b\Delta q_e^n \quad (46)$$

where for small amounts of artificial viscosities

$$c = \alpha_e\Delta x_e\mathrm{M}_e^2\frac{a_e^2}{a_\infty{}^2}\frac{\omega}{\Delta t} \quad (47)$$

$$b = \frac{a_e^2}{a_\infty{}^2}(\mathrm{M}_e^2 - 1)\frac{\omega}{\Delta t} \quad (48)$$

with

$$\mathrm{M}_e = q_e/a_e. \quad (49)$$

It can be seen from the solution of equation (46) that the errors decay exponentially in the case of subsonic flows even when no artificial viscosity is used, i.e., when $c = 0$. In the case of supersonic flows the errors are magnified since $b > 0$, but are at the same time propogated downstream with a wave speed c which is proportional to the artificial viscosity. Artificial viscosity determines the rate at which errors are convected at the supersonic pocket till they reach the shock and also the rate the errors are magnified for supersonic flows. At high values of artificial viscosity, the rate of convergence is greater due to higher convection speeds of the errors. On the other hand, the magnification of the errors require smaller ω values for providing stable results.

Comparison of the above stability analysis with the results obtained for VCS shows that in this case the coefficients b and c are both magnified with a factor of $a_e^2/a_\infty{}^2$. However, calculation of a bound for the artificial viscosity, α_e, again produces the same relationship as shown in equation (33). Thus, it was concluded that both CCS and VCS schemes exhibit similar stability characteristics, although CCS is computationally more efficient.

A von Neumann stability analysis of equation (46) yields the following bound for the relaxation parameter

$$\omega < \frac{1}{\alpha_e\mathrm{M}_e{}^2} < \frac{1}{\mu_e(\mathrm{M}_e^2 - 1)} \quad (50)$$

which is the result obtained also for VCS. The above relationship indicates that with higher artificial viscosities a smaller value of ω is needed to provide uniform convergence. For faster convergence, ω can be increased when lower values of α_e are used.

Treatment of Shocks

In the present formulation, the potential function ϕ is continuous across the element interfaces whereas the derived quantities ρ, q, and a are discontinuous. Supersonic elements are treated by adding artificial viscosity as discussed previously. While the flow is changing from supersonic to subsonic, the continuity of the mass flux in the form

$$\tilde{\rho}^+\phi_{,n}^+ = \rho^-\phi_{,n}^- \quad (51)$$

is satisfied as a natural consequence of the variational formulation, where + and − denote the upstream and downstream sides of the interface, and $\tilde{\rho}$ is the modified density defined by equation (31). Hence, provided that the interfaces are sufficiently aligned with the shock lines, the shocks are allowed to appear between elements, and the continuity of the actual mass flux

$$\rho^+\phi_{,n}^+ = \rho^-\phi_{,n}^- \quad (52)$$

is satisfied in the limit as the artificial viscosity multiplier μ_e approaches to zero. For finite values of μ_e, equation (52) can be imposed as an additional constraint to the variational form as discussed in [5]. However, the effect of violating equation (52) is found to be insignificant for small values of μ_e.

Since, across the shock, the influence from downstream to upstream is still present, the above is basically a shock-capturing scheme. The scheme requires grid refinement at the shock in order to localize the smearing effects due to downstream influence. Moreover, high frequency oscillations appearing in the shock vicinity require relatively more artificial viscosity in this region to damp out such oscillations. The resulting solution at the shock is extremely sensitive to the way these difficulties are handled; consequently, no unique solution is readily available. To remedy this situation, we propose to use a shock-fitting technique for checking the uniqueness of the obtained results.

In the shock-fitting procedure, the shock is also assumed to occur at the element interfaces. However, after a shock is detected as a change from supersonic to subsonic flow between two adjoining elements, these elements are uncoupled, and appropriate boundary conditions are imposed on both sides of the shock as discussed in [5]. Although this technique is computationally straight-forward to implement, as in all other shock fitting techniques, it relies strongly on the prior determination of the shock position. For this reason a combined version of shock capturing and shock fitting techniques is used.

Since, as it may be observed from equation (34) that for higher artificial viscosities the scheme is uniformly convergent in a wider range of initial conditions, shock-capturing solutions are first obtained by selecting a large artificial viscosity multiplier μ_e, e.g. $\mu_e = 6$ in all supersonic elements. Following this, a series of shock capturing solutions are obtained by gradually decreasing μ_e until convergence difficulties are detected. Using the previously converged shock-capturing solution as an initial guess, an attempt to shock fitting is subsequently made to check the shock position. If the initial shock position is correct and the artificial viscosity content is optimum, the influence from downstream to upstream at the shock is minimal in the shock capturing. Hence, both techniques yield essentially the same solution beyond which no further decrease in the artificial viscosity is possible. If the initial position of shock is incorrect, shock moves to a different position after fitting, generally towards the

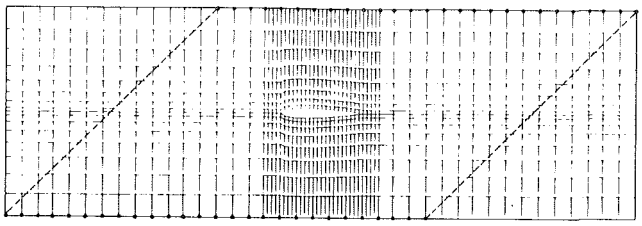

Fig. 2 Proposed computational grid

downstream direction. In that case the shock capturing is again tried by lowering the artificial viscosity, and the above process is repeated until a unique solution is obtained.

Computational Grid and the Computer Program

Transonic cascades with small stagger angles have already been analyzed using the variable coefficient scheme in [5]. Results obtained with various degrees of mesh refinement have been presented and a good agreement with other available solutions in the literature observed. It has been demonstrated that the combined shock-capturing and shock-fitting schemes yield accurate results even with fairly coarse meshes.

The problems investigated in [5] are also solved with the present constant coefficient scheme for comparison and no significant difference in the convergence and accuracy characteristics of the two schemes are observed. Hence, we shall only present additional results here for highly staggered cascades obtained using the constant coefficient scheme. Shown in Fig. 2 is a typical finite element grid we propose to employ in modeling highly staggered cascades. Four-noded isoparametric elements with bilinear shape functions are used throughout the grid.

On the grid shown in Fig. 2, the broken lines denote the farfield inlet and exit boundaries of the solution domain shown in Fig. 1(*b*). The extensions at the inlet and exit boundaries are used to maintain a rectangular outer domain instead of a parallelogram for efficiency and ease in the grid generation. Uniform farfield flow conditions are imposed in these extended regions. The use of rectangle-like elements in the grid has the advantage of providing grid lines which are aligned better with the direction of the flow as well as the direction of the shock lines. Moreover, with this grid severe element distortions can readily be avoided at the rounded leading and trailing edges.

Along the periodic boundaries every node need not have a matching node on the opposite periodic side. The matching periodic nodes are identified with solid circles in Fig. 2 for which the periodicity constraint given by equation (15) is imposed. Equation (15) is satisfied by assigning the same equation number to each pair of the periodically located nodes and modifying the right-hand side of the element equations on the boundary line $B-D$ in Fig. 1(*b*), with the potential difference q_{in} ($h_x \cos\beta_{\text{in}} + h_y \sin\beta_{\text{in}}$). The nodal values of the intermediate periodic nodes are computed by interpolations from the values of the nearest pair of nodes. The final periodicity is then attained iteratively. This scheme allows a flexibility in placing the periodic nodes, hence leads to the generation of more efficient grids with refinements only in the regions of interest.

A symmetric frontal solver [7] is employed in solving the system of equations. In this solution procedure, only those equations that are currently required for the elimination of a specific nodal point variable need be assembled and saved in the high-speed storage. As opposed to banded solvers the effectiveness of the scheme does not depend on the nodal point numbering sequence. Hence the periodic boundary conditions can be imposed conveniently by assigning the same equation numbers to each pair of periodically located nodes. This may be accomplished without renumbering the grid points, and also with no loss of computational efficiency.

If the exit flow conditions are not known a priori, Kutta condition at the trailing edge is iteratively satisfied as follows [8]: The circulation around the airfoil is determined from a previous iteration, using the computed velocity potential values of the two uncoupled nodes at the sharp trailing edge, as follows:

$$\lambda = (\phi^+ - \phi^-)|_E \tag{53}$$

where + and − denote the two sides of the slit which extends from the trailing edge to the exit boundary. This value of circulation is then imposed all along the slit as a constant discontinuity in velocity potential for the new iteration. The procedure is repeated until an overall convergence is reached and the Kutta condition

$$q^2|^+ = q^2|^-$$

at the trailing edge is satisfied.

Discussion of Results and Conclusions

A cascade of NACA 0012 airfoils with a 45 deg stagger angle and $h/c = 3.6$ is analyzed for the following inlet flow conditions:

Case I: $M_{\text{in}} = 0.8$, $\beta_{\text{in}} = 1$ deg
Case II: $M_{\text{in}} = 0.8$, $\beta_{\text{in}} = 0$ deg
Case III: $M_{\text{in}} = 0.8$, $\beta_{\text{in}} = -1$ deg

The chordwise distribution of the pressure coefficients obtained for each case using the finite element grid shown in Fig. 2 are respectively given in Figs. 3(*a*)-3(*c*). There are only 20 elements over each surface of the airfoil, the plotted results are those computed at the centroid of each element. With the combined shock-capturing and shock-fitting scheme convergent unique solutions were reached at $\mu_e = 1.25$, 1.5, and 4.2 respectively for cases I, II, and III. For these cases the maximum computed local Mach numbers were respectively $M_e = 1.25$, 1.16, and 1.07 over the upper surface, and $M_e = 1.11$, 1.26, and 1.39 over the lower surface of the airfoil.

The need for more artificial viscosity in Case III is attributed to the size of the supersonic pocket, as has been implied by the von Neumann convergence analysis presented in [5]. Greater the size of the supersonic pocket is, the higher the amount of artificial viscosity required for uniform convergence. This general trend is evident in all three cases analyzed herein.

The development of sharp shock fronts with almost no smearing and the satisfaction of the trailing edge Kutta conditions are apparent in all cases. Also as can be seen from Figs. 3(*a*)-3(*c*) that, with the above set of artificial viscosity multipliers, μ_e, more smearing is produced along the upper surface of the airfoil regardless of the local Mach number. This may be attributed to the slight misalignment of the mesh with the local flow direction.

Iso-Mach line plots of the above three cases are presented in Figs. 4(*a*)-4(*c*). On these figures sonic lines are denoted by solid contour lines. The size of the supersonic pocket and the extension of the shock beyond the mid-channel of the cascade in Case III are of interest. In this case for higher values of artificial viscosity, convergent solutions were obtained initially with the shock placed close to the mid-chord of the airfoil. As the artificial viscosity was reduced, the shock moved downstream and the size of the supersonic pocket was increased. Each time the artificial viscosity was reduced, shock fitting was applied to the convergent shock capturing solution. This was repeated until the shock moved downstream far enough to satisfy the shock-jump conditions, in

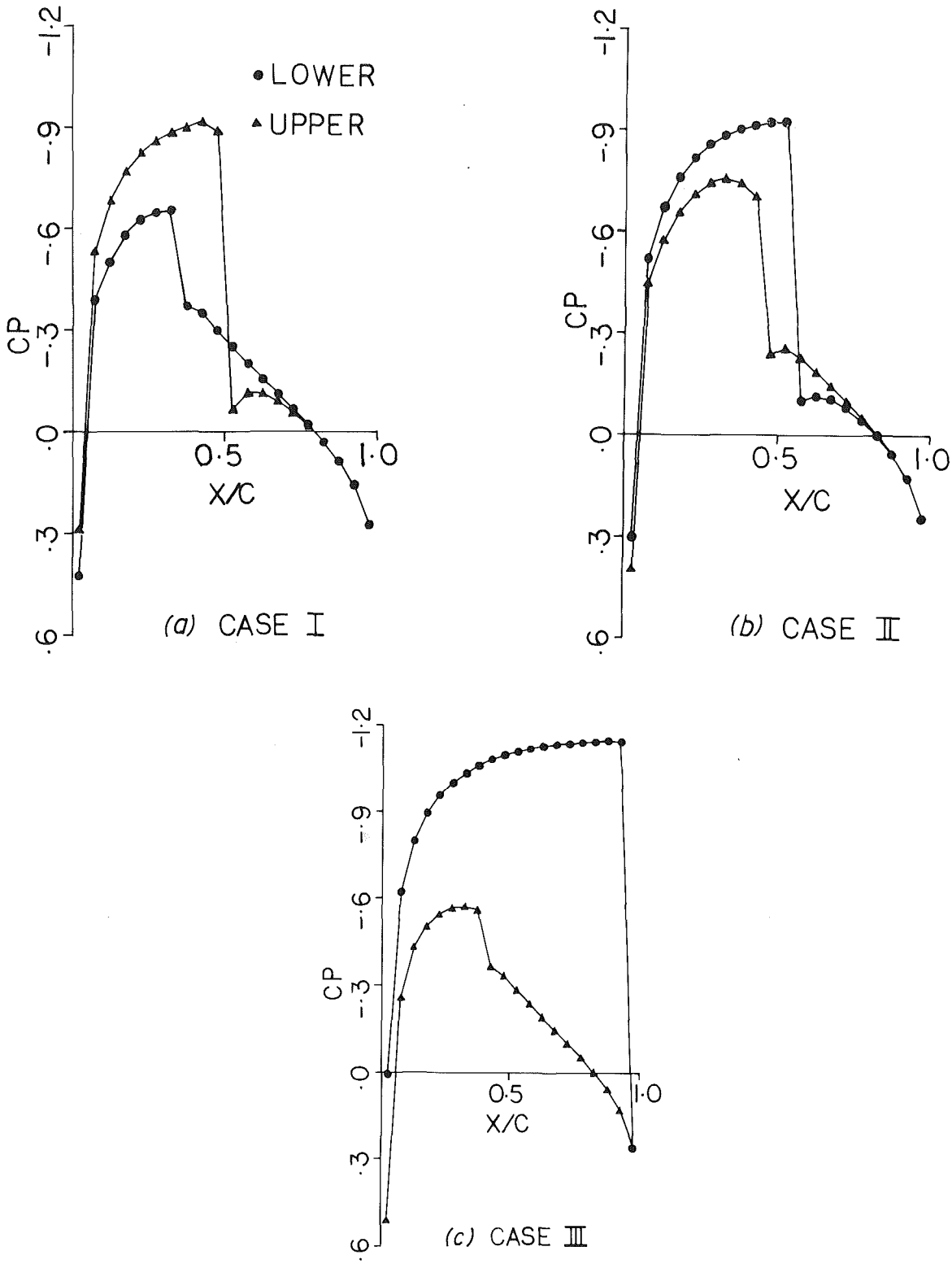

Fig. 3 Computed pressure coefficients on the airfoil

which case both the shock-fitting and the shock-capturing yielded the same solution.

Finally, the chordwise pressure distributions obtained for an additional test case are presented in Fig. 5, in which the inlet flow conditions of Case II were used. However, instead of determining the exit flow angle from the trailing edge Kutta condition, a value of $\beta_{e_x} = 0$ deg was applied along the exit stations in this case. Also shown in Fig. 5 for comparison, are the results of a finite difference - artificial compressibility scheme employed by Farrell and Adamczyk [9]. As it is seen, the results obtained by both methods are within the modeling accuracy. The effect of Kutta condition, which is evident from the comparison of Figs. 3(*b*) and 5, is of interest.

The above set of results demonstrates that the finite element method can be employed quite effectively for the analysis of rather complex transonic flow problems in cascades. Simple

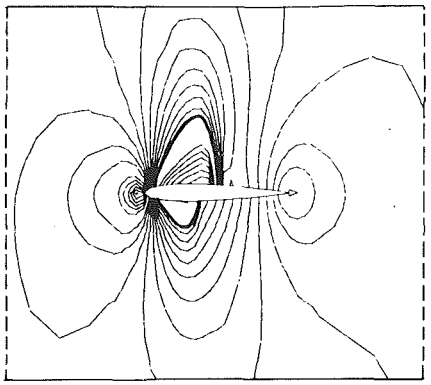

(a) CASE I

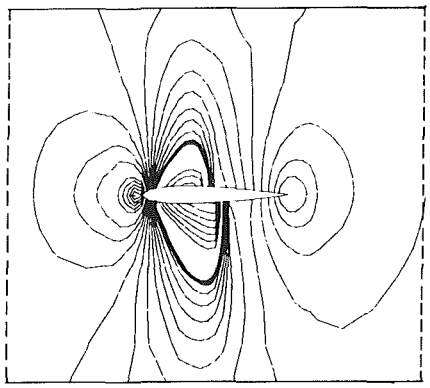

(b) CASE II

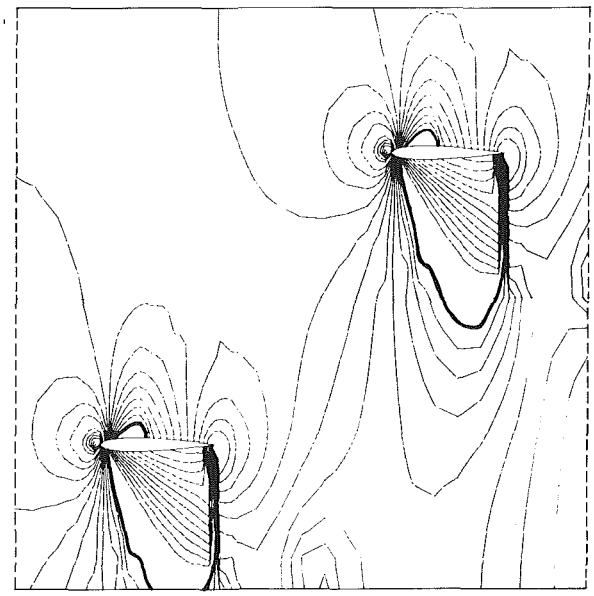

(c) CASE III

Fig. 4 Iso-Mach lines

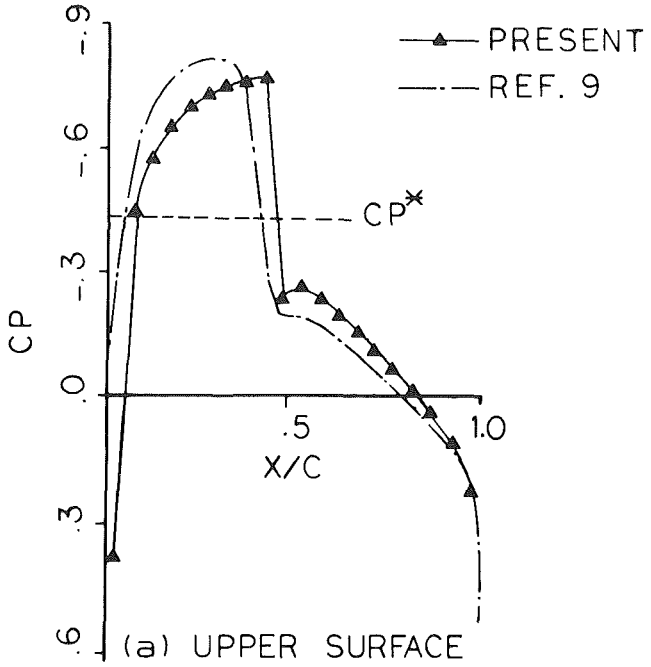

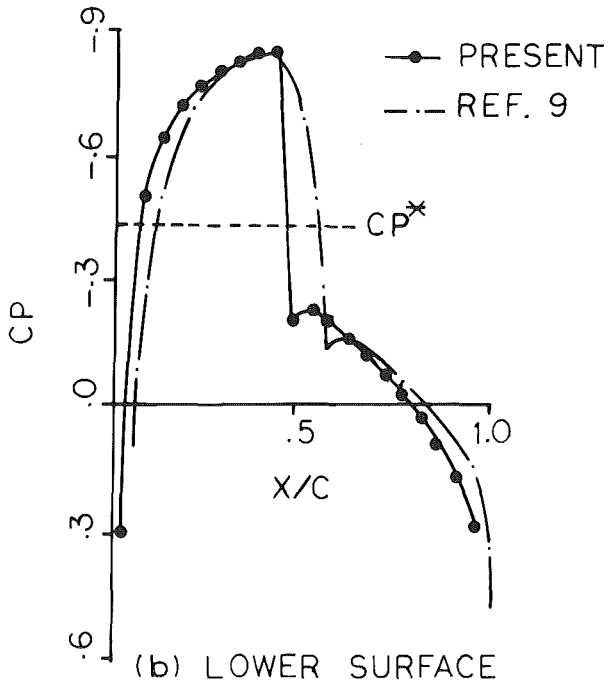

Fig. 5 Pressure distribution for Case II with β_{ex} = 0 deg

grids can be generated quite efficiently that will provide accurate results as well as fast convergence. The boundary conditions at the inlet, at the exit and over the airfoil, as well as the Kutta condition and the periodicity can be treated in a general manner without an excessive computational effort. A typical final solution with the present scheme is obtained for the presented test cases within the range of 400-600 pseudo-time steps. The introduction of the numerical integration technique CCS described in this paper makes the method competitive with the other existing solution schemes.

Acknowledgments

This research was supported by the NASA Grant NSG-3294. The authors express their appreciation to the project monitor Dr. R. Chima of NASA Lewis Research Center for his encouragements and suggestions during the course of this investigation. The computer service provided by the IUPUI Computer Center is acknowledged.

References

1 Chan, S.T.K., and Brashear, M.R., "Finite Element Analysis of Unsteady Transonic Flow," AIAA paper 75-875, 8th Fluid and Plasma Dynamics Conference, Hartford, Conn., 1975.

2 Ecer, A., and Akay, H.U., "Application of Finite Element Method for the Solution of Transonic Flow," *Proc. 2nd Int. Symp. on Finite Element Methods in Flow Problems*, S. Margherita, Italy, 1976, pp. 191–201.

3 Glowinski, R., Periaux, J., and Pironneau, O., "Transonic Flow Simulation by the Finite Element Method via Optimal Control," *Proc. 2nd Int. Symp. on Finite Element Methods in Flow Problems*, S. Margherita, Italy, 1976, pp. 249–259.

4 Eberle, A., "Eine Methode Finiter Elemente zur Berechnung der Transsonischen Potentialstromung um Profile," Messerschmitt-Bolkow-Blohm-UFE, 1352, (0), 1977.

5 Ecer, A., and Akay, H.U., "Investigation of Transonic Flow in a Cascade Using an Adaptive Mesh," AIAA 13th Fluid and Plasma Dynamics Conference, Paper No. AIAA-80-1430, Snowmass, Colo., July 14-16, 1980.

6 Hafez, M., South, J., and Murman, E., "Artificial Compressibility Methods for Numerical Solutions of Transonic Full Potential Equation," *AIAA Journal*, Vol. 17, No. 8, Aug. 1979, pp. 838–844.

7 Irons, B.M., "A Frontal Solution Program for Finite Element Analysis," *Int. Journal Numerical Meth. Engng.*, Vol. 2, No. 1, 1970, pp. 5–32.

8 Eberle, A., Private Communications, June 1980.

9 Farrell, C., and Adamczyk, J.J., "Solution of the Transonic Quasi-3D Flow Through a Cascade Using Artificial Compressibility," ASME 26th International Gas Turbine Conference, Houston, Texas, March 8-12, 1981.

Finite Element Methods for Transonic Blade-to-Blade Calculation in Turbomachines

H. Deconinck

Research Assistant IWONL.

Ch. Hirsch

Professor.

Vrije Universiteit Brussel,
Dept. of Fluid Mechanics,
Pleinlaan 2,
1050 Brussels, Belgium

The transonic cascade flow is calculated with an efficient and flexible Galerkin Finite Element method applied to the full potential equation in Artificial Compressibility form. Some of the typical advantages of finite element techniques are demonstrated such as the use of higher order discretization with biquadratic elements besides the classical bilinear second order accurate element, automatic treatment of the body fitted mesh due to the locally defined isoparametric mapping, easy and exact introduction of arbitrary Neumann boundary conditions along curvilinear boundaries. On the other hand, the conceptual simplicity and efficiency of the finite difference methods based on the same equation and developed for external flows are fully maintained by the use of line relaxation or approximate factorization for the iterative solution algorithm, eventually combined with a multigrid approach. The important problem of obtaining a well-constructed mesh is solved satisfactorily by automatic grid generation based on the solution of two elliptic partial differential equations. Calculations are presented and compared with experimental data for both compressor and turbine cascade flows containing shocks.

Introduction

One of the main steps in the aerodynamic design of turbomachines is the determination of the profile shape of the blades starting from the desired in and outlet conditions. Besides the experimental approach, different numerical approaches are possible depending on the flow model assumed: The analysis and design can be fully three-dimensional or the different blade sections can be investigated separately based on a two-dimensional flow in an approximately axisymmetric stream surface, the blade-to-blade surface.

Only few three-dimensional transonic methods for internal flow calculations have been published in the past. Dulikravich [1] solves the full potential equation with finite volume discretization, artificial viscosity, and line relaxation along the principles used by Jameson in external transonic aerodynamics. Applications are limited to irrotational homoentropic flows, in practice free-vortex designs. Thomkins [2] uses MacCormack's time-marching finite difference scheme to integrate the unsteady Euler equations until the steady state solution is obtained. In this case, the practical use is limited by the slow convergence inherent to unsteady time integrating Euler methods which in three dimensions results in extremely long computation times.

Therefore most applications make use of the two-dimensional blade-to-blade approximation, eventually corrected for radius and streamtube thickness variations, with methods based on a potential function or on the Euler equations. The time-dependent Euler equations are hyperbolic in subsonic as well as in supersonic regions and classic initial value methods are applicable which explains their frequent use in transonic methods. The Euler equations can be treated in integral form with finite volume methods, McDonald [3], Denton [4], Couston [5] as well as in differential form with finite differences, Gopalakrishnan and Bozzola [6], and Veuillot [7]. However the time step in the explicit time integration is limited by severe stability bounds, the Courant-Friedrichs-Lewi conditions depending on the space and time discretization scheme as well as on the mesh size. In general this causes slow convergence and several hundreds of time steps are needed. Even if the CFL conditions are satisfied stability problems may occur caused by a lack of dissipation allowing amplification of nonlinear oscillations generated by shockwaves in the solution. Therefore all methods need an additional damping mechanism such as spatial smoothing [3], explicit artificial viscosity terms [7] or more elaborated methods [4, 5]. Some work has been done to increase the convergence speed of Euler methods by embedding the steady mixed elliptic hyperbolic equations in a higher order system as proposed by Johnson [8]. Essers [9] uses additional time-dependent equations whose unsteady terms are completely artificial and constructed in order to obtain strong internal damping of the perturbation oscillations and hence better convergence. However these methods are somewhat difficult to optimize.

Contributed by the Gas Turbine Division and presented at the International Gas Turbine Conference and Product Show, Houston, Texas, March 9-12, 1981, of THE AMERICAN SOCIETY OF MECHANICAL ENGINEERS. Manuscript received at ASME Headquarters, December 1, 1980. Paper No. 81-GT-5.

The need for more efficient methods in routine applications made it necessary to consider the potential flow model even in two dimensions by adding to the Euler equations the assumption of irrotationality. For moderately supersonic flows ($M \lesssim 1.5$) the isentropic shocks in the potential solution are valid approximations to the physical shocks governed by the Rankine-Hugoniot relations and the errors introduced in this way are acceptable within the frame of a two-dimensional approximation to an essentially three-dimensional flow.

In the past, finite difference methods for the potential equation, based on Murman and Cole's type-dependent discretization with central differences in subsonic and upwind differences in supersonic points, together with line relaxation have been developed for cascade flows by Dodge [10] and Ives and Liutermoza [11].

Considering finite element (F.E.) approaches one observes a rapid and widespread development of subsonic blade-to-blade calculations based on a Galerkin approximation and direct solution of the system of equations, e.g. the Newton iterative scheme of Prince [12] and the constant stiffness scheme of Hirsch and Warzee [13]. However the global stiffness matrix is no longer positive definite if the equation operator ceases to be elliptic. Moreover, without entropy condition the generalized solution of the mixed equation is nonunique. Three distinct problems delayed the development of transonic F.E. methods. The first and basic problem is to find an adequate integral formulation of the transonic flow problem in order to be able to implement a F.E. approximation. Due to the basic "elliptic" nature of the Galerkin, weighted residual approach, which leads to schemes which do not allow a distinction or a separation between upsteam and downstream points, the methods used for the subsonic calculations cannot be used in the transonic or supersonic regions. The second is the problem of finding a convergent solution algorithm which in finite difference (F.D.) methods was available in a natural way by the use of relaxation methods. The third problem is the exclusion of expansion shocks which was done in an implicit way in F.D. methods by upwind differencing in supersonic points and later by addition of explicit Artificial Viscosity (A.V.) terms to the equation. Different directions were explored to overcome these difficulties and a detailed survey is given by Hafez, Wellford and Murman [14]: Hyperbolic approaches were developed such as explicit time marching methods with Galerkin F.E. in space and Lax-Wendroff scheme in time or implicit time schemes resulting in a system of ordinary differential equations with respect to time. These methods again suffer from slow convergence properties. Mixed-type methods are based on a finite element analogue for type dependent differencing, e.g. by using asymmetric shape functions in supersonic points to eliminate the influence of downstream points. Application of this approach with an arbitrary mesh nonaligned with the flow is not easy. A third class of elliptic methods contains mixed variational principes, optimal control methods and least squares methods. Mixed variational principles were constructed by Hafez, et al. in a way such that the second variation of the functional is always positive definite even for supersonic flows and the resulting equations may be solved with direct methods as in the elliptic case. Additional A.V. terms are needed, otherwise these procedures are not convergent. The optimal control method devised by Glowinski and Pironneau [15] has been applied to transonic flow problem in a way which is formally identical Shockfree flows were computed without introduction of an entropy condition. In general the F.E. methods described above need more computation time than relaxation methods due to the higher mathematical complexity of the formulation.

Due to the introduction of the concept of artificial compressibility [26], it has become possible to formulate the transonic flow problem in a way which is formally identical to the subsonic formulations. Therefore, the need for elaborate integral formulation disappears and a standard Galerkin method can be applied in the whole flow region, independently of the subsonic and supersonic nature of the flow. The coupling of conceptual simple relaxation methods applied to the potential flow equation formulated in a special convenient artificial density form, with the advantages of a Galerkin F.E. treatment was first used by Eberle [18] in an external aerodynamics application. In this paper, an F.E. approach, with artificial compressibility, together with a multigrid extension and with the use of higher order biquadratic elements besides the classic bilinear ones, is presented. Also an Approximate Fractorization (ADI) approach with finite elements next to the relaxation method is discussed. ADI methods are considered the most efficient of today's external transonic calculation methods. The F.E. methods presented in this paper contain the following aspects and advantages: automatic and built-in transformation of the physical body fitted coordinate system to a uniform computational grid; easy and exact introduction of arbitrary mixed-type boundary conditions on curved boundaries without losing accuracy; and the flexibility of changing the order of accuracy in the discretization by changing the type of

Nomenclature

b = blockage in radial direction
c = chord
C = iteration operator (in differential or integral form)
K = stiffness operator
n = direction normal to the boundary
N_{ij} = shape function corresponding to meshpoint (i,j)
R = residual (in differential or integral form)
r = gas constant
s = pitch; direction along streamline
t = artificial time
T = temperature; with subscript t: stagnation temperature
$\bar{u}$ = wheel speed
$\bar{w}$ = (w_x, w_y) velocity
x,y = Cartesian coordinates
γ = ratio of specific heats
Γ = circulation
μ = switching function
ξ,η = coordinates in the transformed computational plane
ρ = density; with subscript t: stagnation density
$\tilde{\rho}$ = artificial density
ϕ = potential function
ω = relaxation factor
∇ = gradient operator

Subscripts

1 = quantities on inlet boundary
2 = quantities on outlet boundary

Abbreviations

A.C. = Artificial Compressibility
A.V. = Artificial Viscosity
ADI or AF = Alternating Direction Implicit or Approximate Factorization
F.D. = Finite Difference
F.E. = Finite Element
SLOR = Successive Line Overrelaxation

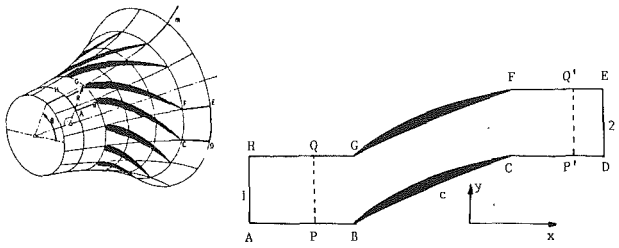

Fig. 1 Blade-to-blade surface

the element. These features are introduced without losing the important realizations of previously presented methods such as multigrid techniques and shock-capturing capacity by means of artificial compressibility.

Results for both compressor and turbine cascade flows containing shocks are presented and compared with experimental data. Leading edge regions with stagnation points are very well simulated without modification of the nose geometry, and excellent shock capturing properties are observed.

Comparison of bilinear and biquadratic elements shows an improved accuracy for the latter without supplementary cost.

Potential Equation and Boundary Conditions

Inviscid irrotational flow is governed by the potential equation, written in a fixed coordinate system

$$\partial_x(\rho b\phi_x)+\partial_y(\rho b\phi_y)=\bar{u}\,\bar{\nabla}\,(\rho b) \tag{1}$$

where ϕ_x and ϕ_y are the Cartesian velocity components, ρ the density, and b a blockage factor taking in account the variation of streamtube thickness in radial direction. The right-hand side contains the effect of rotation with $\bar{u}$, the wheel speed.

Since no entropy can be created in irrotational flow the density is obtained from the isentropic relation

$$\rho=\rho_t\left[1-\frac{\gamma-1}{2\gamma rT_t}(\phi_x^2+\phi_2^y)\right]^{1/(\gamma-1)} \tag{2}$$

where T_t and ρ_t are stagnation temperature and density, constants for nonrotating cascade flow. Equation (1) is second order quasilinear of the elliptic type in subsonic, parabolic in sonic, and hyperbolic type in supersonic points of the flow.

The computational domain consists in one passage of a blade row (Fig. 1) where x and y are coordinates respectively along the meridional and tangential directions. For elliptic quasilinear equations the boundary conditions (B.C.) are well known and given by Dirichlet ($\beta = 0$), Neumann ($\alpha = 0$) or mixed boundary conditions:

$$\alpha\phi+\beta\rho b\frac{\partial\phi}{\partial n}=q \tag{3}$$

In conformity with the physics one obtains for the inlet and outlet boundaries (which are taken far enough upstream and downstream to allow uniform flow conditions)

$$\rho b\frac{\partial\phi}{\partial n}=\rho_1 b_1 w_{x1} \qquad \text{at inlet}$$

$$\rho b\frac{\partial\phi}{\partial n}=\rho_2 b_2 w_{x2} \qquad \text{at outlet} \tag{4}$$

Along the blade walls zero normal velocity is imposed for nonrotating cascades

$$\frac{\partial\phi}{\partial n}=0 \qquad \text{and} \tag{5a}$$

$$\frac{\partial\phi}{\partial n}=\bar{u}\bar{1}_n \tag{5b}$$

in the case of rotating cascade.

A particularity in cascade flows is the presence of periodic boundaries upstream (AB,HG) and downstream the blades (CD,FE).

In corresponding periodic points all physical quantities are equal. This results in a constant difference in potential between two corresponding points such as P and Q in Fig. 1:

$$\phi_Q=\phi_P+s_1 w_{y1} \qquad \text{upstream}$$

$$\phi_Q=\phi_P+s_2 w_{y2} \qquad \text{downstream} \tag{6}$$

where s is the pitch.

From equations (4) and (6) together with the mass conservation

$$\rho_1(w_{x1},w_{y1})b_1 w_{x1}=\rho_2(w_{x2},w_{y2})b_2 w_{x2} \tag{7}$$

it is clear that only three independent quantities can be specified for both upstream and downstream boundaries including periodicity. Hence inlet Mach number and angle together with the outlet Mach number or alternatively the outlet angle completely determine the flow for a given geometrical configuration and blockage.

If the circulation

$$\Gamma=s_2 w_{y2}-s_1 w_{y1} \tag{8}$$

is determined in the calculation by applying a Kutta-Joukowski condition at the trailing edge, only two independent quantities are left and the mass flow is part of the solution leading to a unique incidence if changing occurs.

Artificial Viscosity

As soon as supersonic regions occur in the flow, a continuous solution of equation (1) is no longer assured. ϕ is called a generalized or weak solution of equation (1) allowing for discontinuities in its derivatives ϕ_x and ϕ_y if it satisfies the following integral form of equation (1):

$$-\int_S \rho b\,\nabla\phi\,\nabla W dS+\oint_s \rho b\frac{\partial\phi}{\partial n}W ds=\int\bar{U}\,\bar{\nabla}\,(\rho b)\,W dS \tag{9}$$

for any continuous test function W and domain S bounded by s.

Mathematical analysis and numerical experience made clear that in general many generalized solutions of equations (9) or (1) exist for the same boundary conditions and a criterion called entropy condition is needed to select the physically significant solution. A well-known and analyzed example of this nonuniqueness of weak solutions is the flow through a symmetric convergent-divergent nozzle. At least three different solutions are known: the first was obtained by the authors with the optimal control method without any entropy condition and is perfectly symmetric with an expansion shock in the convergent part of the nozzle and a compression shock in the divergent part. The second and only physical acceptable solution presents a single compression shock in the divergent part of the nozzle and can be obtained, for example, with upwind differencing and successive line relaxation sweeps from upstream to downstream. A third solution containing only an expansion shock in the convergent part of the nozzle is found by using downwind differences and relaxation sweeps from downstream to upstream. Physical considerations may illustrate this behavior. Since the potential equation is fully isentropic it describes a perfectly reversible siutation allowing expansion shocks as well as compression shocks as is seen in the first symmetric solution. In the second solution mentioned

above the symmetry is broken by the upwind differencing and sweep direction in a way which is equivalent to an entropy law enforcing entropy only to increase through a shock. The third solution describes a situation allowing only decreasing entropy.

Lax [19] proves for first order hyperbolic systems of conservation laws of the type

$$u_t + \mathrm{A}u_x = 0 \tag{10a}$$

that weak solutions containing only physical shocks, i.e., satisfying a correct entropy condition, are obtained as the limit for vanishing viscosity $\nu > 0$ of:

$$u_t + \mathrm{A}u_x = \nu u_{xx} \tag{10b}$$

From this it results that introduction of dissipation by means of A.V. is sufficient for the selection of the correct weak solution of equation (9) or (1). Indeed, Jameson [21] has shown that upwind differencing in supersonic points used in the first successfull transonic calculations of Murman and Cole [20] can be considered as the central discretization of the same equation however with some additional terms similar to the right hand side of equation (10), namely with highest order derivatives

$$u_{xx} = \phi_{xxx} \quad \text{and} \quad v_{yy} = \phi_{yyy}$$

He used this observation for the construction of similar A.V. terms written in divergence form in order to conserve mass across a shock and which are added explicitly to the equation taking the following form:

$$\partial_x(\rho b \phi_x + P) + \partial_y(\rho b \phi_y + Q) = 0 \tag{11}$$

where $\partial_x P + \partial_y Q$ are the A.V. terms given by

$$P = -\mu \phi_x b \rho_x \Delta x$$
$$Q = -\mu \phi_y b \rho_y \Delta y \tag{12}$$

The amount of A.V. is controlled by the switching function μ which is zero in subsonic points:

$$\mu = \max\left(0, 1 - \frac{1}{\mathrm{M}^2}\right) \tag{13}$$

Δx and Δy are the mesh spacings and have to be included in order to obtain a consistent approximation of the original equation for vanishing mesh width. In this approach the equation is discretized in a central way in the whole flow domain except for the A.V. terms.

The artificial compressibility (A.C.) form [17] amenable for F.E. application is obtained by requiring a slight modification of definition (12)

$$\frac{P}{\phi_x} = \frac{Q}{\phi_y} = -\mu b \rho_s \Delta s \tag{14}$$

where s is the streamwise direction. This form is very convenient since substitution of equation (14) in equation (11) together with the definition of the artificial density

$$\tilde{\rho} = \rho - \mu \rho_s \Delta s \tag{15}$$

results in a transonic equation with A.V. terms which is formally indentical to the unmodified form only valid for subsonic flows

$$\partial_x(\tilde{\rho} b \phi_x) + \partial_y(\tilde{\rho} b \phi_y) = 0 \tag{16}$$

A classic fully elliptic Galerkin F.E. discretization can be applied since the upwind differenced A.V. terms are included in the nonlinear coefficient $\tilde{\rho}\ b$ which in the solution procedure is updated after each iteration by means of the new approximate solution. A derivative of ρ along a streamline with only upstream influences can be obtained in a general coordinate independent way by using only the upstream element for this calculation.

Galerkin Approximation and Solution Algorithms

A weighted residual approach [23] is based on the integral form (9) where the uniqueness of the solution is granted by the use of artificial density

$$R(\phi) = \int_S \tilde{\rho} b (\phi_x W_x + \phi_y W_y)\, dS - \oint_s \tilde{\rho} b \frac{\partial \phi}{\partial n} W ds = 0 \tag{17}$$

The functional $R(\phi)$ is called residual. A finite element method is obtained in a classic way by approximating the potential function within an element as a linear combination of its mesh point values based on the locally defined shape functions $N_{ij}(x,y)$ assigned to each meshpoint (i, j)

$$\phi(x,y) = \sum_{k,1} \phi_{k1} N_{k1}(x,y)$$

$$\nabla \phi(x,y) = \sum_{k,1} \phi_{k1} / N_{k1}(x,y) \tag{18}$$

With the Galerkin technique the discrete residual in each point is defined by choosing a single weight function W for each meshpoint equal to its shape function N_{ij} and by taking the arbitrary domain S equal to the entire flow field with boundary s

$$R_{ij} = \sum_{k,1} \phi_{k1} K_{ij}^{k1} - f_{ij} \tag{19}$$

where K is the classic stiffness matrix defined as

$$K_{ij}^{k1}(\phi) = \int_S \tilde{\rho} b \nabla N_{k1} \nabla N_{ij} dS \tag{20}$$

and f the contribution of the boundaries

$$f_{ij} = \int_s \tilde{\rho} b \frac{\partial \phi}{\partial n} N_{ij} ds \tag{21}$$

Due to the local definition of the shape functions only the surrounding elements contribute to the surface integrations in equation (20) and the boundary integral is zero except if (i, j) is a point of a Neumann boundary.

For the bilinear four-point quadrilateral element this results in a summation over nine points as in the classic curvilinear F.D. scheme, while with the third order accurate biquadratic Lagrange element [23] from nine surrounding points for a centernode to 25 for a cornernode contribute to the residual (Fig. 2).

As distinct from a discrete residual in differential form the present residual contains the boundary conditions since this is included in the integral formulation. The integrations in equation (20) are carried out in a standard way with Gauss quadrature after transformation to a unit square in the ξ-η plane with the help of the locally defined isoparametric transformation

$$x = \sum_{i,j} x_{ij} N_{ij}(\xi, \eta)$$

$$y = \sum_{i,j} y_{ij} N_{ij}(\xi, \eta) \tag{22}$$

This transformation is contained in the Standard FE Galerkin method and explains the flexibility of the FE approach for arbitrary meshes. Moreover, the type of discretization in FE methods, namely the area average of the residual calculation allows the approach to maintain the order of accuracy of the orthogonal mesh also in the arbitrary mesh calculation within certain limits of distortion of the mesh.

A general solution procedure for the nonlinear system of

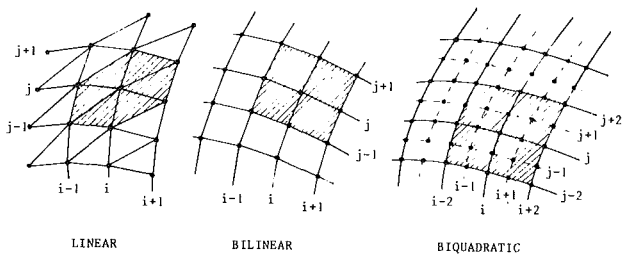

Fig. 2 Grid structure with isoparametric elements: linear triangles, bilinear, and biquadratic Lagrange elements

equations obtained after discretization is given by

$$C^n \delta\phi = -\tau R^n \tag{23a}$$

followed by

$$\phi^{n+1} = \phi^n + \delta\phi \tag{23b}$$

where n is the iteration number, R^n the residual based on the previous approximate solution ϕ^n and C^n a general iteration operator. Depending on the choice of C different iteration algorithms are obtained such as direct, implicit, or explicit methods.

The classic direct subsonic algorithm discussed in [24] where C^n is given by

$$C^n = \int_S \tilde{\rho}^n \nabla N_{ij} \nabla N_{kl}\, dS \tag{24}$$

has been found to diverge for M > 1 in spite of the use of artificial density [17] as is explained by Hafez and South [22] for a one-dimensional analogue. Analysis of equation (23) as a time-dependent equation [21, 22] where ϕ_t is discretized by

$$\phi_t \approx \frac{\delta\phi}{\tau}$$

indicates that upwind discretized ϕ_{xt} and ϕ_{yt} terms in the left hand side may improve the convergence in supersonic regions although they are not strictly necessary in most cases. Such terms are introduced in an implicit way in the successive line over-relaxation (SLOR) scheme if the proper sweep direction is applied. Explicit addition together with under-relaxation makes the scheme (24) convergent, however with a very low convergence speed.

In principle the iteration algorithms developed for solving the artificial density finite difference equations can be applied to the system of equations discretized with Galerkin FE. These algorithms were presented in external aerodynamics applications by Holst and Ballhaus (ADI schemes AF1 and AF2) [25], Hafez, South, and Murman (SLOR, ADI, three level explicit schemes) [17] and South, Keller, and Hafez (vectorizable schemes) [26].

At present only two of these schemes were investigated in detail for F.E. application, namely SLOR and AF1 for which a finite element frame had to be developed. Both are discussed in the subsequent sections and the discrete forms are compared on a uniform mesh with the F.D. equivalents for the Laplace equation.

Successive Line Overrelaxation (SLOR)

Successive line over-relaxation is the standard device for transonic F.D. calculations due to the natural presence of an upwind discretized $\phi_{\bar{x}t}$ term in the iteration operator if the proper sweep direction is applied. For example, on an orthogonal mesh with sweeps in the x direction one obtains the following differential form for C [21]:

$$C = \alpha\partial_{\bar{x}} + \beta\partial_y \tilde{\rho}\partial_y + \gamma \tag{25}$$

which is explicit in the x direction and implicit in the y direction leading to tridiagonal systems for each $x = c^t$ line if second order central differences are applied.

A similar upwind bias is seen in the F.E. form with bilinear quadrilaterals or linear triangles with K given by expression (20) evaluated at iteration number n:

$$\sum_{l=j-1}^{j+1} \delta\phi_{il} K_{ij}^{il} = -\omega\left[R_{ij}^n + \sum_{l=j-1}^{j+1} \delta\phi_{i-1,l} K_{ij}^{i-1,l}\right] \tag{26}$$

This F.E. scheme is equally valid for an arbitrary mesh with curvilinear ξ and η coordinates. The discrete F.E. residual is a seven-point operator with triangles (in the configuration of Fig. 2) and a nine-point operator with bilinear quadrangles giving also tridiagonal systems along each coordinate line $\xi = \xi_i$ except for lines where periodicity is prescribed in the extreme points (see for example PQ in Fig. 1). For these lines the coupling of the extreme points results in cyclic tridiagonal systems. The solution can be obtained efficiently as a linear combination of two solutions of tridiagonal systems with the same matrix but different right-hand sides.

In order to illustrate the relationship between the FE and FD schemes some comparisons are given for the Laplace equation with Dirichlet boundary conditions on an orthogonal mesh with

$$\Delta\xi = \Delta\eta = 1$$

The FD form and FE form with triangles lead to exactly the same system of equations:

$$(-1 \quad 4 \quad -1) \begin{pmatrix} \delta\phi_{i,j+1} \\ \delta\phi_{ij} \\ \delta\phi_{i,j-1} \end{pmatrix}$$

$$= -\omega \left[R_{ij} + (0 \quad -1 \quad 0) \begin{pmatrix} \delta\phi_{i-1,j+1} \\ \delta\phi_{i-1,j} \\ \delta\phi_{i-1,j-1} \end{pmatrix} \right] \tag{27}$$

where the residual R_{ij} is the classic five-point difference star:

$$R_{ij} = \begin{array}{ccc} & -1 & \\ -1 & 4 & -1 \\ & -1 & \end{array}$$

With bilinear elements a very similar scheme is obtained however with nonzero contribution of points $(i \pm 1, j \pm 1)$ in the residual and in the right-hand side of equation (27):

$$(-1 \quad 8 \quad -1) \begin{pmatrix} \delta\phi_{i,j+1} \\ \delta\phi_{i,j} \\ \delta\phi_{i,j-1} \end{pmatrix}$$

$$= -\omega \left[R_{ij} + (-1 \quad -1 \quad -1) \begin{pmatrix} \delta\phi_{i-1,j+1} \\ \delta\phi_{i-1,j} \\ \delta\phi_{i-1,j-1} \end{pmatrix} \right] \tag{28}$$

and

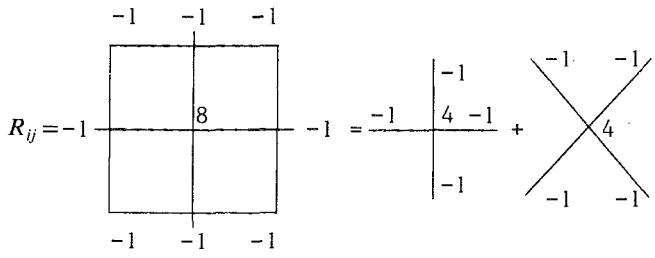

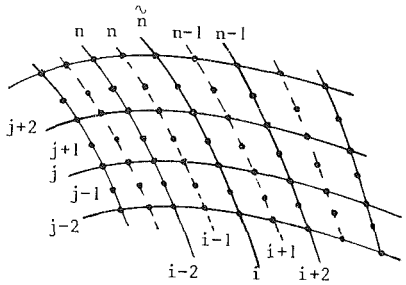

Fig. 3 Illustration of SLOR scheme with biquadratic Lagrange elements

In the presence of a right-hand side (Poisson equation) the F.E. residual contains a surface average of the right-hand side term over the surrounding elements while the F.D. residual simply contains the local value in (i,j).

A third order accurate F.E. scheme is obtained if quadratic elements are used, for example, the nine points biquadratic Lagrange element. The shape functions extend over a maximum of five points in one dimension (namely for corner nodes) leading to the following general pentadiagonal systems for each

$$\xi_i = c^t$$

line:

$$\sum_{l=j-2}^{j+2} \delta\phi_{il} K_{ij}^{il} = -\omega\Big[R_{ij} + \sum_{l=j-2}^{j+2} K_{ij}^{i-1,l}\,\delta\phi_{i-1,l} + \sum_{l=j-2}^{j+2} K_{ij}^{i-2,l}\,\delta\phi_{i-2,l}\Big] \tag{29}$$

The upwind bias extends over two meshpoints for $i = c^t$ coordinate lines which coincide with element boundaries (Fig. 3, full lines) while for the coordinate lines consisting of midside and central nodes (dotted lines) the upwind influences $K_{ij}^{i-2,l}$ are zero, and one has only a single meshpoint bias. The half of the equations are tridiagonal $(K_{ij}^{ij\pm 2} = 0)$ resulting in a considerable reduction of the cost for inversion of the pentadiagonal system.

Numerical experiments on two simple test cases [27] indicate that the calculation time with quadratic elements is of the same order of magnitude as with bilinear elements which is comprehensible considering that the number of elements is four times lower. Cyclic pentadiagonal systems obtained on coordinate lines with periodic extreme points require the solution of three pentadiagonal systems.

The previous schemes can be modified in order to control the amount of implicitness by using Hopscotch techniques or black-white point ordering [26]. A complete iteration cycle consists of a sweep of black points followed by a sweep of the white points using the solution of the previous sweep in points of the other color. In this way the pentadiagonal systems can be reduced to tridiagonal and various explicit and vectorizable schemes can be obtained. Numerical results obtained with bilinear and biquadratic elements are discussed in the final section.

Approximate Factorization (ADI)

Since the early application of ADI methods with F.D. to the transonic small perturbation equation by Ballhaus, Jameson, and Albert [31] in 1977, the method has known a wide development with extensions to full potential equation and arbitrary meshes in two-and three-dimensional external flows. On the other hand, no practical F.E. applications are known to us although some theoretical formulations on rectangular meshes can be found in the F.E. mathematical literature [28, 29]. Recently, the authors have developed Galerkin ADI methods on curvilinear grids with bilinear [30, 24] and biquadratic elements [27]. A brief outline of these methods in the context of internal flow applications is given in this section. The starting point is a factorizable form of the iteration operator C which allows for a splitting of the solution procedure in two steps, each with a one-dimensional iteration operator requiring only simple matrix operations. For fast convergence the one-dimensional operators are chosen so that their product is a close approximation to the residual operator K. Different ways for the construction of a factored F.E. scheme are possible. One could start from a weak formulation of potential equation (16) followed by the splitting procedure as was suggested by Douglas and Dupont [28]. More flexibility is obtained if the split equations are defined in differential form before the Galerkin F.E. technique is applied.

AF1 Scheme. On an orthogonal mesh the classical AF1-ADI scheme results from the choice

$$C^n = C_x C_y = (1 - \sigma\partial_x p\partial_x)(1 - \sigma\partial_y q\partial_y) \tag{30}$$

where for the potential equation

$$p = q = \tilde{\rho}$$

Equation (23*a*) is now split in two steps, with g an intermediate approximation:

$$(1 - \sigma\partial_x p\partial_x) g = -\sigma\tau R^n \tag{31}$$

$$(1 - \sigma\partial_y q\partial_y)\,\delta\phi = g \tag{32}$$

Simplified discrete systems with equations containing only unknown g or $\delta\phi$ along one coordinate line ($y = c^t$ for g and $x = c^t$ for $\delta\phi$) can be obtained with a F.E. discretization:

1 if the standard shape functions used in the discretization of ϕ and as weight function for equation (31) are factorizable namely

$$N_{ij}(x,y) = N_i(x) N_j(y)$$

and

2 if an appropriate choice is made for the form functions used in the discretization of g and as weight functions in the second equation (32).

From condition 1 which is satisfied for the three types of elements considered in this paper it is clear that the residual in (31) is computed in the standard Galerkin F.E. way described before.

The discrete equations are then given by:

$$(M_x + \sigma K_x) g = -\sigma\tau R^n \tag{33}$$

$$(M_y + \sigma K_y)\,\delta\phi = g \tag{34}$$

where M_x and M_y are one-dimensional mass matrices

$$(M_x)_{ik} = \int N_i(x) N_k(x)\,dx \tag{35}$$

$$(M_y)_{kj} = \int N_k(y) N_j(y)\,dy \tag{36}$$

and K_x and K_y one-dimensional stiffness matrices:

$$(K_x)_{ik} = \int \partial_x N_i(x)\,\partial_x N_k(x)\,dx \tag{37}$$

$$(K_y)_{kj} = \int \partial_y N_k(y)\,\partial_y N_j(y)\,dy \tag{38}$$

On an arbitrary mesh the one-dimensional operators must act along the curvilinear $\xi = c^t$, respectively $\eta = c^t$ coordinate lines. The transformed potential equation in conservative form is given by

$$\partial_\xi\left[\frac{\tilde{\rho}}{J}(A_1\partial_\xi + A_2\partial_\eta)\phi\right] + \partial_\eta\left[\frac{\tilde{\rho}}{J}(A_2\partial_\xi + A_3\partial_\eta)\phi\right] = 0 \tag{39}$$

with the metric tensor

$$\begin{pmatrix} A_1 & A_2 \\ A_2 & A_3 \end{pmatrix} = \begin{pmatrix} \xi_x^2 + \xi_y^2 & \xi_x\eta_x + \xi_y\eta_y \\ \xi_x\eta_x + \xi_y\eta_y & \eta_x^2 + \eta_y^2 \end{pmatrix} \tag{40}$$

and J the Jacobian determinant

$$J = \xi_x\eta_y - \xi_y\eta_x \tag{41}$$

Due to the presence of mixed ξ-η derivatives, the operator in equation (39) is not factorizable in ξ and η, but an approximation can still be obtained by neglecting the mixed terms for the construction of the factorizable iteration operator [25]

$$C = C_\xi C_\eta$$

$$C_\xi = 1 - \sigma\partial_\xi \frac{\tilde{\rho}}{J} A_1 \partial_\xi \tag{42}$$

$$C_\eta = 1 - \sigma\partial_\eta \frac{\tilde{\rho}}{J} A_3 \partial_\eta \tag{43}$$

giving the following splitted equations on an arbitrary mesh:

$$\left(1 - \sigma\partial_\xi \frac{\tilde{\rho}}{J} A_1 \partial_\xi\right) g = -\sigma\tau R^n \tag{44}$$

$$\left(1 - \sigma\partial_\eta \frac{\tilde{\rho}}{J} A_3 \partial_\eta\right) \delta\phi = g \tag{45}$$

These equations are formally identical to equations (31) and (32) after replacing x by ξ and y by η and for

$$p = \frac{\tilde{\rho}A_1}{J} \qquad q = \frac{\tilde{\rho}A_3}{J} \tag{46}$$

Hence the discretized forms (33) to (38) are equally valid in the computational ξ-η plane in the case of an arbitrary mesh. An even simpler AF1 scheme where $\tilde{\rho}$ is dropped in the left-hand side of equations (44) and (45) works satisfactorily as was also experienced with F.D. [17].

It turns out that the one-dimensional stiffness operators (37) and (38) when calculated with linear elements (triangles or quadrilaterals) give rise to exactly the same expression as obtained from classical second-order central conservative F.D. while the diagonal F.D. mass matrix can be found back by lumping the F.E. mass matrix. Thus the following tridiagonal discrete equations are obtained, f.i. along a $\eta = \eta_j$ line with $\Delta\xi = 1$, for internal points:

$$\text{F.E.}\left\{\left(\frac{1}{6}\ \frac{4}{6}\ \frac{1}{6}\right) + \sigma(-p_{i-1/2}p_{i-1/2} + p_{i+1/2} - p_{i+1/2})\right\}$$

$$\text{F.D.}\left\{\left(0\ \frac{6}{6}\ 0\right)\right. \begin{pmatrix} g_{i-1,j} \\ g_{i,j} \\ g_{i+1,j} \end{pmatrix} = -\sigma\tau R_{ij} \tag{47}$$

where with linear elements the classical F.D. approximation of $p_{i\pm1/2}$ is recovered, namely

$$p_{i+1/2} = \int_i^{i+1} p\,d\xi = \frac{1}{2}(p_{ij} + p_{i+1,j}) \tag{48}$$

The function p is evaluated in different ways with F.E. and F.D. methods. This is also true for the residual R which in the F.E. computation is given by expression (19) including the contributions of Neumann boundary conditions in a systematic natural way.

Suitable boundary conditions for the intermediate solution g and for $\delta\phi$ appear in a natural way, namely

$$g = 0,\ \delta\phi = 0 \qquad \text{on Dirichlet boundaries}$$

$$\frac{\partial g}{\partial \xi} = 0,\ \frac{\partial \delta\phi}{\partial \eta} = 0 \qquad \text{on Neumann boundaries} \tag{49}$$

which are compatible with the steady state $\delta\phi = g = 0$ over the whole flow field.

In particular the zero Neumann B.C. leads to the following equation instead of (47) for a point (i,j) on a Neumann boundary:

$$\left\{\left(\frac{2}{6}\ \frac{1}{6}\right) + \sigma(p_{i+1/2} - p_{i+1/2})\right\} \begin{pmatrix} g_{ij} \\ g_{i+1,j} \end{pmatrix} = -\sigma\tau R_{ij} \tag{50}$$

Biquadratric Lagrange shape functions are also factorizable and lead to pentadiagonal systems composed of alternating tridiagonal and pentadiagonal equations, for example, along lines $\eta = \eta_j$ for the Laplace equation ($p = q = 1$):

$i = \text{odd}\ \{(-4\ \ 8\ \ 32\ \ 8\ \ -4)$

$i = \text{even}\ \{0\ \ 8\ \ 64\ \ 8\ \ 0)$

$$+\sigma \begin{matrix} (10\ \ -80\ \ 140\ \ -80\ \ 10)\} \\ (0\ \ -80\ \ 160\ \ -80\ \ 0)\} \end{matrix} \begin{pmatrix} g_{i-2,j} \\ g_{i-1,j} \\ g_{i,j} \\ g_{i+1,j} \\ g_{i+2,j} \end{pmatrix}$$

$$= 60\,\sigma\tau R_{ij} \tag{51}$$

where the residual is computed in the standard way discussed before.

In all these cases formal identical systems are solved along $\xi = \xi_i$ lines. Coupling of periodic boundaries along these lines results again in cyclic tridiagonal or pentadiagonal systems. The parameters σ and τ are determined in a standard way [25].

AF2 Scheme. These schemes have been developed in F.D. applications [25] in order to introduce ϕ_{xt} and ϕ_{yt}, terms which improve convergence when large supersonic flow regions are present. An AF2 scheme replacing the ϕ_t term in the AF1 by a $\phi_{\bar{\xi}t}$ term is obtained by the choice

$$(1 - \sigma\vec{\partial}_\xi p)(\overleftarrow{\partial}_\xi - \sigma\partial_\eta q\partial_\eta)\delta\phi = -\sigma\tau R \tag{52}$$

giving the split form

$$(1 - \sigma\vec{\partial}_\xi p)g = -\sigma\tau R \quad \text{along } \eta = c^t \text{ lines}$$

$$(\overrightarrow{\partial} - \sigma\partial_\eta q\partial_\eta)\delta\phi = g \quad \text{along } \xi = c^t \text{ lines} \tag{53}$$

Special care is needed in the F.E. treatment to conserve the forward and backward derivatives, which is obtained by applying F.E. discretization to the central forms

$$\vec{\delta}_\xi = \partial_\xi + \frac{\Delta\xi}{2}\partial^2_{\xi\xi}$$

$$\overleftarrow{\delta}_\xi = \partial_\xi - \frac{\Delta\xi}{2}\partial^2_{\xi\xi} \tag{54}$$

and the following discrete F.E. equations are obtained with linear elements, along $\eta = \eta_j$ lines:

$$\left\{\left(\frac{1}{6}\ \frac{4}{6}\ \frac{1}{6}\right) + \sigma(0\ \ p_{i-1/2}\ \ -p_{i+21/2})\right\} \begin{pmatrix} g_{i-1,j} \\ g_{i,j} \\ g_{i+1,j} \end{pmatrix}$$

$$= -\sigma\tau R_{ij} \tag{55}$$

and along $\xi = \xi_i$ lines

$$\left\{\left(\frac{1}{6}\ \frac{4}{6}\ \frac{1}{6}\right) + \sigma(-q_{i-1/2}\ \ q_{i-1/2}+q_{i+1/2}\ \ -q_{i+1/2})\right\}$$

$$\begin{pmatrix} \delta\phi_{i,j-1} \\ \delta\phi_{i,j} \\ \delta\phi_{i,j+1} \end{pmatrix} = g_{ij} + \left(\frac{1}{6}\ \frac{4}{6}\ \frac{1}{6}\right) \begin{pmatrix} \delta\phi_{i-1,j-1} \\ \delta\phi_{i-1,j} \\ \delta\phi_{i-1,j+1} \end{pmatrix} \tag{56}$$

Various numerical results obtained with schemes described in this section are presented in the final section.

Mesh Generation, Refinement and Multigrid Method

Mesh Generation. As distinct from subsonic blade-to-blade calculation, a carefuly constructed mesh is essential in transonic computations in order to obtain a sufficient resolution for shock capturing and in regions where strong velocity gradients occur such as the leading edge zone of thick turbine blades. Therefore a regular mesh is desired whereby the mesh spacing can be controlled in an easy way in critical regions. Such an automatic grid generation procedure has been developed which allows a user specified distance in the η-direction between the blade boundary (which is an $\eta = \eta_{\min}$ or $\eta = \eta_{\max}$ coordinate line) and the next $\eta = c^t$ line. This method is an adaptation for cascade geometries of the technique developed by Sorenson and Steger [33] for external flow geometries.

In a first step, according to the Thompson-Thames-Mastin approach in its simplest form, a system of Laplace equations for ξ and η in the physical domain is transformed and solved in the rectangular computational domain covered with a uniform grid with

$$\Delta\xi = \Delta\eta = 1$$

(Fig. 4):

$$\alpha x_{\xi\xi} - 2\beta x_{\xi\eta} + \gamma x_{\eta\eta} = 0$$
$$\alpha y_{\xi\xi} - 2\beta y_{\xi\eta} + \gamma y_{\eta\eta} = 0 \tag{57}$$

where:

$$\alpha = x_\eta^2 + y_\eta^2,\ \beta = x_\xi x_\eta + y_\xi y_\eta,\ \gamma = x_\xi^2 + y_\xi^2 \tag{58}$$

Once the values of x_{ij} and y_{ij} on the boundaries are given (Dirichlet conditions) the interior Cartesian coordinates are obtained by SLOR and classic F.D. discretization. Indeed, the advantages of F.E. methods appear only on curvilinear meshes with mixed boundary conditions. In this way a smooth and regular mesh is obtained, however with poor qualities in the leading and trailing edge region and with a quasi-uniform uncontrollable spacing in the η-direction. Therefore in a second step the coordinate lines $\eta = c^t$ are dropped and the meshpoints are redistributed along the $\xi = c^t$ lines in order to obtain an exponentially decreasing spacing from the center of the blade passage to the blade walls. The minimal spacing near the boundaries $\eta = \eta_{\min}$ and $\eta = \eta_{\max}$ is constant and given as a parameter. The spacing in the ξ-direction is sufficiently controlled by the meshpoint distribution on the blade walls and on the periodic boundaries where an exponential clustering towards the leading and trailing edge is applied. In Figs. 5 and 6 examples of the grid obtained for a compressor and turbine cascade are shown. The coordinate generation is executed by a separate program module which also performs some tests on the quality of the curvilinear grid.

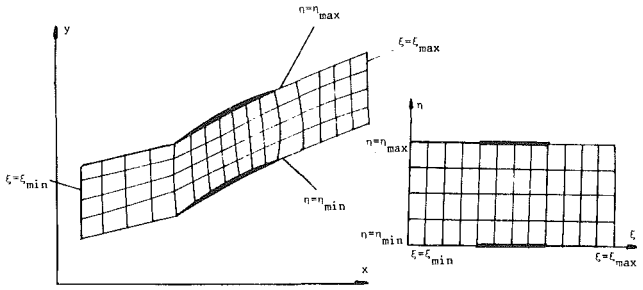

Fig. 4 Boundary fitted coordinate generation

Grid Refinement and Multigrid. In all our transonic computations a grid-refining procedure is included: calculations are initiated on a coarse mesh and an initial approximation on a fine mesh is obtained by interpolation of the converged course mesh solution. Besides the practical advantages this technique accelerates the convergence in particular for the SLOR algorithm as was reported by Eberle [18]. Indeed the SLOR method is very effective for the elimination of high frequency errors in the approximate solution which depend on the mesh width. Hence the low frequency errors which prohibit fast convergence on a fine grid are eliminated efficiently on a coarse grid where they correspond to high freqency errors.

In general four consecutive grids are used with 10×4; 19×7; 37×13 and 73×25 meshpoints. Work is continuing on calculations with a full multigrid method [34] which consists of two elements. The first element is a smoothing process, namely the elimination of high frequency errors which can be achieved very efficiently by SLOR or ADI. This effect is also used in the grid-refining technique discussed before.

The second essential element is a "correction by approximation" procedure. In this process the correction for the fine grid which is a low frequency quantity after smoothing is computed on a coarse grid and then interpolated back to the fine grid. The computation of the correction on a coarse grid is again performed with a smoothing procedure such as SLOR or ADI but requires much fewer operations and converges faster since the low frequency correction on the fine mesh has become a higher frequency quantity on the coarse mesh.

Consider the nonlinear equation to be solved on a grid with spacing h:

$$R_h(\phi_h) = K_h(\phi_h) - f_h = 0 \tag{59}$$

or written in correction form with an approximate solution ϕ_h^μ:

$$\hat{K}_h(\delta\phi_h) = K_h(\phi_h^\mu + \delta\phi_h) - K_h(\phi_h^\mu) = -R_h(\phi_h^\mu) \tag{60}$$

with

$$\phi_h = \phi_h^\mu + \delta\phi_h \tag{61}$$

For sufficiently smooth $\delta\phi_h$ and residual $R(\phi_h^\mu)$ obtained with SLOR or ADI an approximation of $\delta\phi_h$ is sought on the mesh with spacing $2h$ and interpolated back to the fine mesh giving the following updating formula for ϕ_h^μ:

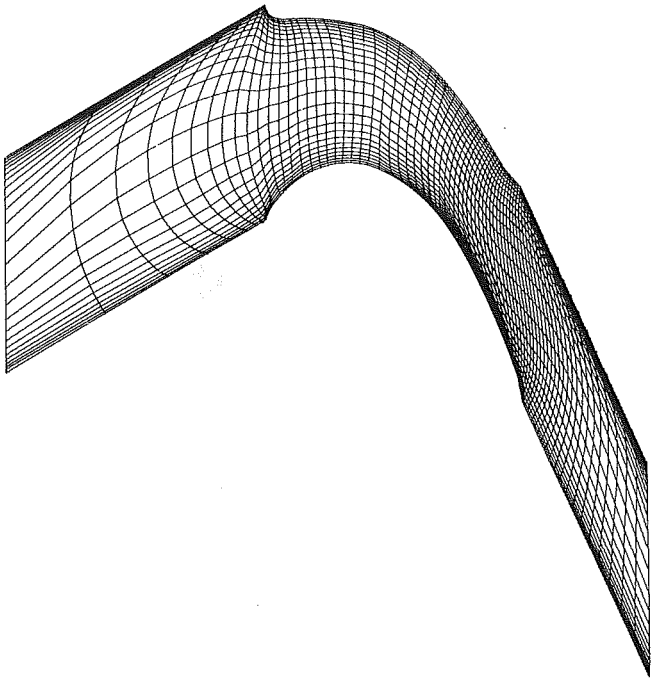

Fig. 5 F.E. mesh for VKI-LS59 gas turbine cascade

$$\phi_h^{\mu+1} = \phi_h^{\mu} + I_{2h}^{h} \delta\phi_{2h} \tag{62}$$

where I_{2h}^{h} is the interpolation operator from the coarse mesh to the fine, called prolongation. Hence the following equation for $\delta\phi_{2h}$ is solved:

$$\hat{K}_{2h}(\delta\phi_{2h}) = -I_h^{2h} R_h(\phi_h^{\mu}) \tag{63}$$

The restriction operator I_h^{2h} transfers the fine mesh values to the coarse mesh and $\delta\phi_{2h}$ is defined with respect to ϕ_h^{μ}:

$$\phi_{2h} = I_h^{2h} \phi_h^{\mu} + \delta\phi_{2h} \tag{64}$$

Subsitution in equation (63) leads to the following equation to be solved on the coarse mesh:

$$K_{2h}(\phi_{2h}) = f_{2h} \tag{65}$$

where the right-hand side is a known function given by

$$f_{2h} = I_h^{2h} f_h + K_{2h}(I_h^{2h} \phi_h^{\mu}) - I_h^{2h} K_h(\phi_h^{\mu}) \tag{66}$$

and the updating formula (62) for ϕ_h^{μ} becomes

$$\phi_h^{\mu+1} = \phi_h^{\mu} + I_{2h}^{h}(\phi_{2h} - I_h^{2h} \phi_h^{\mu}) \tag{67}$$

The procedure is recursive and is equally applied to the coarse grid equations (65). In the results presented in the subsequent section the prolongation operator is bilinear interpolation, while the restriction consists in keeping the fine mesh values for the coarse grid in coincident points (injection).

No other F.E. application of the multigrid method on transonic flow problems are known to the authors while different F.D. applications have been reported, for instance by Jameson [35].

Numerical Results

Results are described for different types of geometry which are implemented in the same program in a systematic way by including the appropriate boundary contributions in the residual: single airfoil, channel, and cascade geometries.

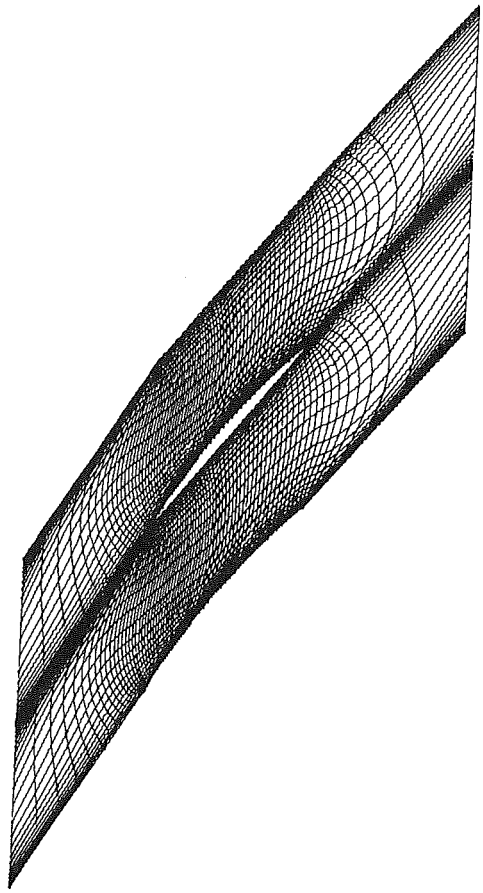

Fig. 6 F.E. mesh for DCA-9.5 deg camber compressor cascade

Reliable test cases with shocks are known for single airfoils and channels geometries which make them more suitable for testing the algorithms.

The cascade geometries consist of the VKI-LS59 gas turbine cascade and the DCA 9.5 deg camber compressor cascade described in [36] and [37]. The finest mesh used in the calculations is shown in Figs. 5 and 6 and contains 1825 meshpoints. The distance between the blade boundary and the nearest coordinate line $\eta = c^{t}$ is 1 percent of the pitch.

For turbine cascade with an inlet Mach number $M_1 = 0.281$, inlet angle $\beta_1 = 30$ deg, outlet Mach number $M_2 = 0.975$ and blockage $b_2 = 1$ the Mach distribution along the blade computed with bilinear SLOR and grid refining is shown in Fig. 8. The full line is the computed solution and the experiments [36] are denoted by 0 and X. Fifty SLOR interations were performed on each mesh with a residual drop of three orders on the finest mesh. When compared to the calculation of the same case presented in [24] a strong improvement is observed which is due to the modification of the trailing edge in the present calculation in order to include the wake. This modification also reduces the unphysical expansion on the pressure side trailing edge. The isomach plot is shown on Fig. 9. Figure 10 shows the Mach distribution along the blade for the compressor cascade with $M_1 = 1.05$, $\beta_1 = 58$ deg, $M_2 = 0.761$ and $b_2 = 0.86$ equally computed with bilinear SLOR. The deviations between computation and experiments [37] are explained by the presence of large boundary layers inherent to compressor flows. Nevertheless the basic properties are well reflected in the computational results. The isomach plot corresponding to this case is given in Fig. 11*a* where an oblique shock can be seen from the suction side extending before the nose of the blade while a subsonic

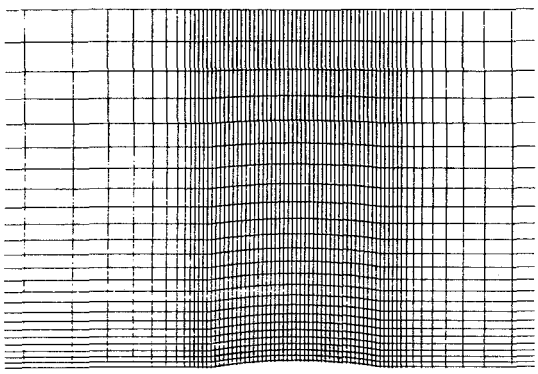

Fig. 7 F.E. mesh for channel flow

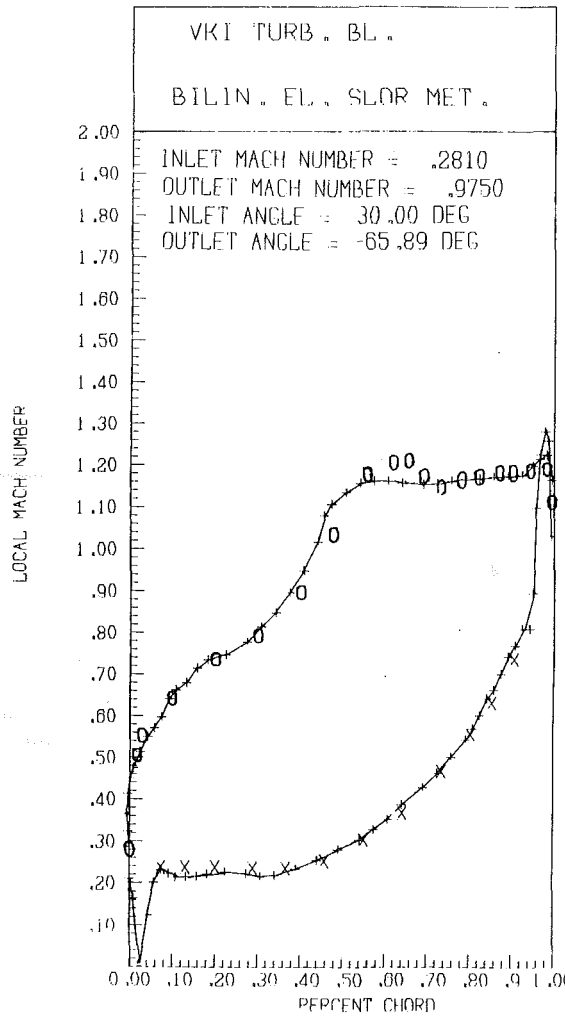

Fig. 8 Mach distribution along the blade walls for the VKI-LS59 gas turbine blade computed with the bilinear SLOR scheme

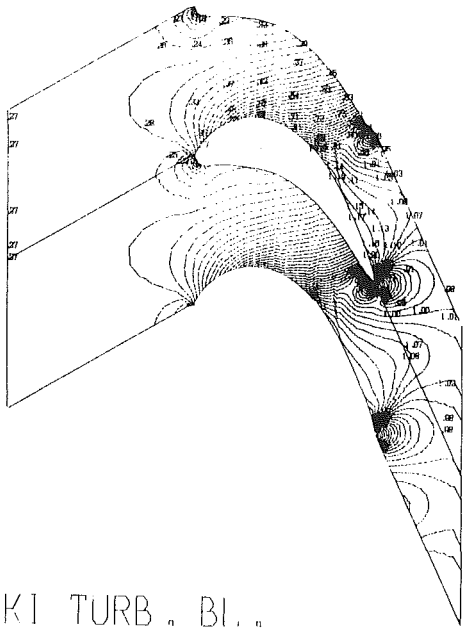

Fig. 9 Isomach lines for VKI-LS59 gas turbine blade computed with the bilinear SLOR scheme

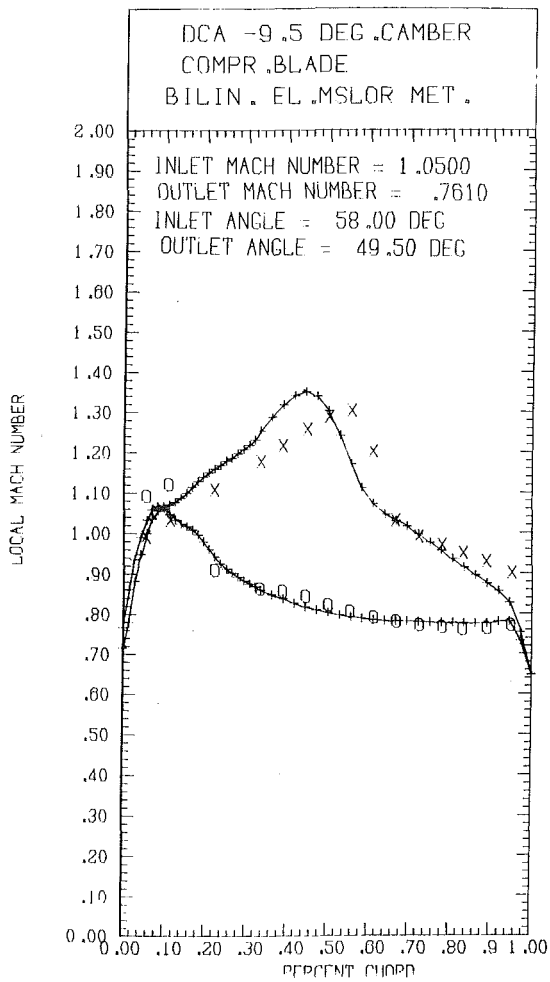

Fig. 10 Mach distribution along the blade walls for the DCA-9.5 deg camber compressor blade computed with the bilinear SLOR scheme

pocket exists in front of the leading edge. A small change of the inlet angle from 58 to 55 deg moves the shock downstream where it becomes a normal shock with much stronger intensity (Fig. 11*b*).

Computations with ADI - AF1 and bilinear as well as biquadratic elements are shown for a channel flow with an inlet Mach number of 0.85. The geometry (Fig. 7) is obtained from the Gamm Workshop on Transonic Calculations [38]. Almost indentical results are obtained along the bump (Fig. 12) which are in good agreement with the solutions presented

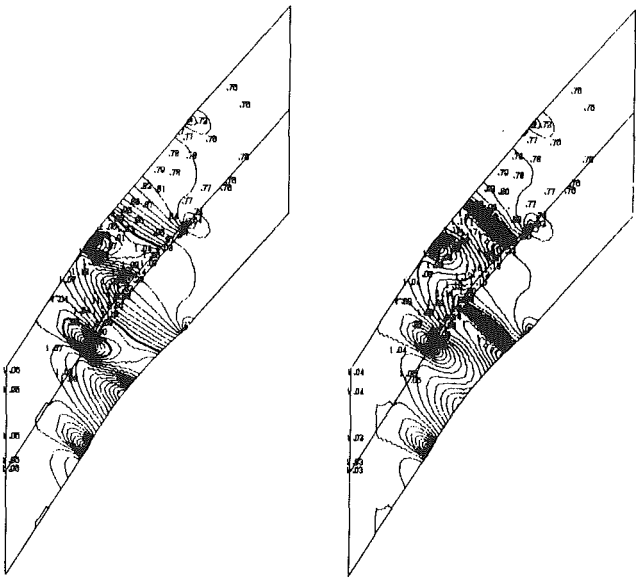

Fig. 11 Isomach lines for the DCA-9.5 deg camber compressor blade at different inlet angles, computed with the bilinear SLOR scheme

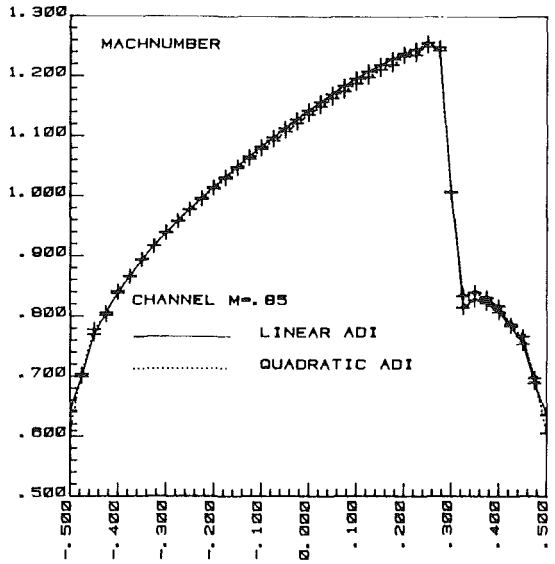

Fig. 12 Mach distribution along bump and opposite wall for the channel flow

in the workshop and obtained with various F.D., F.E. and finite volume methods, also with Euler equations. The higher accuracy of the quadratic element is only perceptible for the stagnation velocity at the leading and trailing edge of the bump which is better simulated than with the bilinear elements. A sequence of five σ values was used in these calculations which are distributed in order to cover the whole error spectrum of the mesh, while $\tau = 2\sigma$. The isomach plot is shown in Fig. 14. The shock is spread over only three meshpoints and a small re-expansion is found after the shock (Fig. 12).

The multigrid algorithm presented in the previous section was tested on a nonlifting NACA 0012 flow with a freestream

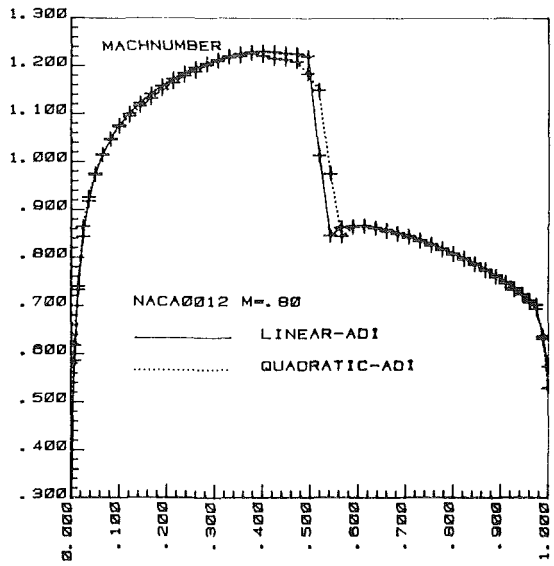

Fig. 13 Mach distribution along the NACA 0012 air foil calculated with multigrid and biquadratic ADI as smoothing element, compared with bilinear ADI and grid refining

Mach number of 0.80 and with biquadratic ADI as smoothing component. The solution in Fig. 13 is compared to our standard solution with bilinear ADI and grid refining. A sequence of three grids was used in the multigrid with five ADI sweeps per smoothing operation. This solution required a calculation time equivalent to 30 ADI sweeps on the finest mesh after four multigrid cycles. The leading edge stagnation Mach number is M = 0.05 while with bilinear solutions a value M = 0.22 is obtained.

In Fig. 15 the isomach plot for the same geometry but with a free-stream Mach number of 0.90 computed with linear SLOR is shown. A strong shock from Mach number 1.4 to 0.7 is found, spread over three mesh points, Fig. 16.

Conclusions

The conceptual simple Galerkin approach used in subsonic F.E. applications has been extended to solve the transonic potential equation for different geometries, with main emphasis on turbomachinery cascades.

This allows the full use of the F.E. capabilities concerning the treatment of mixed boundary conditions and body-fitted meshes. Iterative techniques for the solution of the nonlinear system of equations resulting from the discretization were developed such as the straight forward line over-relaxation and a F.E. formulation of approximate factorization (ADI). The influence of the discretization accuracy was investigated by the use of bilinear and biquadratic elements resulting in an improved accuracy in the leading edge region for the latter without supplementary cost. The convergence is accelerated, first by the application of a grid refining technique, and secondly, by the implementation of a multigrid method allowing the corrections for a fine grid to be calculated on a coarse grid where the convergence rate is better and the calculation time devided by four.

Results are presented for compressor and turbine cascade flows containing shocks and for a channel and single airfoiled geometry showing sharp shocks without smearing or overshoot.

The application of a straightforward F.E. method in combination with an efficient multigrid approach, body-fitted coordinate generation and different choices of elements and solution procedures results in a flexible tool for transonic blade-to-blade calculations in the physical domain.

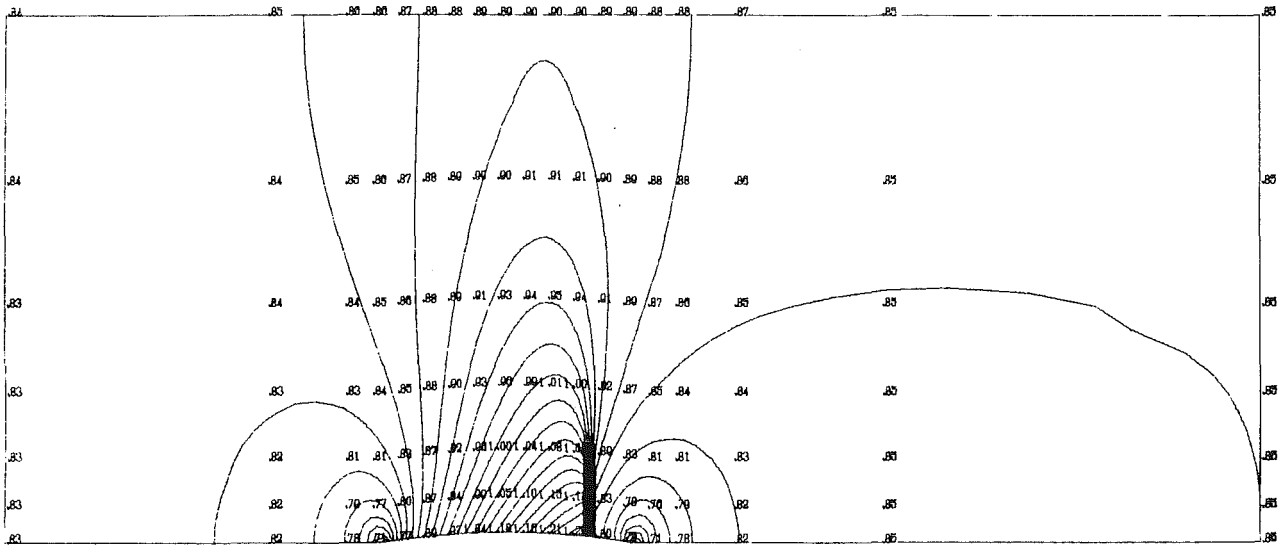

Fig. 14 Isomach lines for channel flow calculated with the bilinear ADI scheme

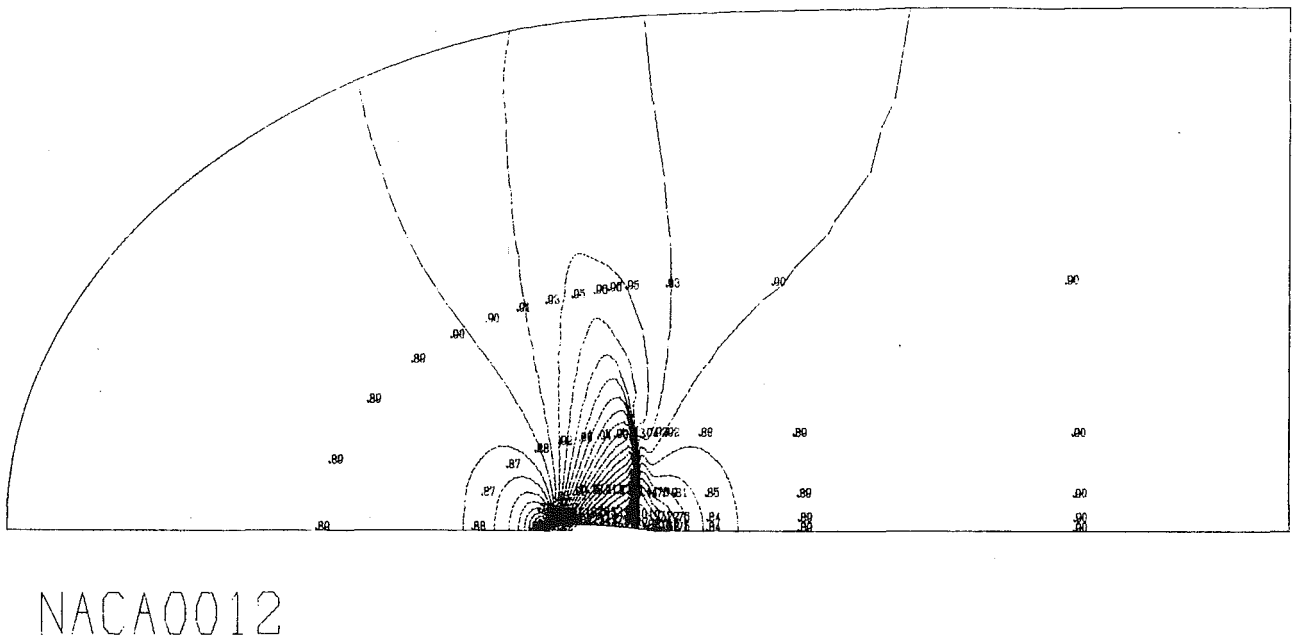

Fig. 15 Isomach lines for NACA 0012 with a free-stream Mach number of 0.90 calculated with the bilinear SLOR scheme

References

1 Dulikravich, D.S., "Numerical Calculation of Transonic Axial Turbomachinery Flows," *Proc. 7th Int. Conference on Numerical Method in Fluid Dynamics,* June 23-27, 1980, Stanford, Calif.

2 Thompkins, T., and David, A.O., "Three-Dimensional Flow Calculation for a Transonic Compressor Rotor," AGARD-195, 1976.

3 McDonald, P.W., "The Computation of Transonic Flow through Two-Dimensional Gas Turbine Cascades," ASME Paper 71-GT-89, 1971.

4 Denton, J.D., and Singh, U.K., "Time Marching Methods for Turbomachinery Flow Calculation," LS 1979-7, Von Karman Institute for Fluid Mechanics.

5 Couston, M., "Time Marching-finite Area Method," VKI-LS84, Von Karman Institute for Fluid Mechanics, 1976.

6 Gopalakrishnan, S., and Bozzola, K., "A Numerical Technique for the Calculation of Transonic Flows in Turbomachinery Cascades," ASME Paper 71-GT-42.

7 Veuillot, J.P., "Calcul Numérique de l'écoulement transsonique d'un Fluide parfait dans une grille d'aubes," *La Recherche Aérospatiale,* No. 1975, pp. 327-338.

8 Johnson, G.M., "An Alternative Approach to the Numerical Simulation of Steady Inviscid Flow," Proc. 7th International Conference on Numerical Method in Fluid Dynamics, June 23-27, 1980, Stanford, Calif.

9 Essers, J.A., "Time-Dependent Methods for Mixed and Hybrid Steady Flows," VKI-LS, 1978-4, Von Karman Institute for Fluid Dynamics.

10 Dodge, P., "Transonic Flows in Axial Turbomachinery - Transonic Relaxation," VKI-LS 84, and Von Karmon Institute for Fluid Dynamics, 1976.

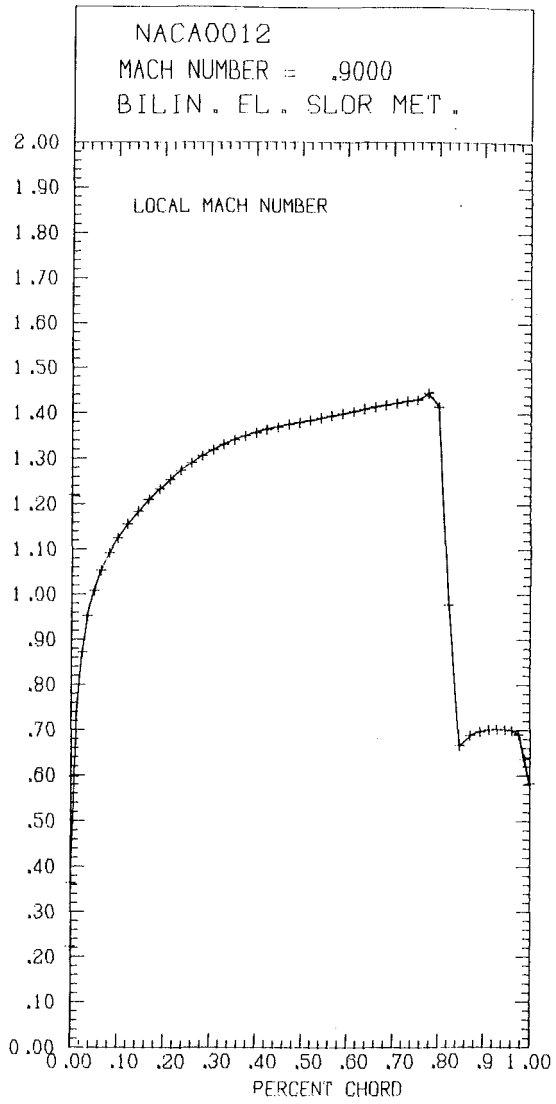

Fig. 16 Mach distribution for NACA 0012 with a free-stream Mach number of 0.90 calculated with the bilinear SLOR scheme

11 Ives, D.C., and Liutermoza, J.F., "Second-Order Accurate Calculation of Transonic Flow over Turbomachinery Cascades," AIAA Paper 78-1149, 1978.

12 Prince, T.C., "Prediction of Steady Inviscid Compressible Flow on a Blade-to-Blade Surface by Finite Element Method," AIAA Paper 78-244, 1978.

13 Hirsch, Ch., and Warzee, G., "Finite Element Computation of Subsonic Cascade Flows," *Proc. of 6th Canadian Congress on Applied Mechanics,* Vancouver, 1977.

14 Hafez, M.M., Wellford, L.C., and Murman, E.M., "Finite Elements and Finite Differences for Transonic Flow Calculations," *Finite Elements in Fluids,* Vol. 3, John Wiley, 1978.

15 Glowinsky, R., Periaux, J., and Pironneau, O., "Transonic Flow Simulation by the Finite Element Method Via Optimal Control," *Second Int. Symp. on Finite Elements in Fluid Flow,* Rapallo, 1976.

16 Deconinck, H., and Hirsch, Ch., "A Finite Element Method Solving the Full Potential Equation with Boundary Layer Interaction in Transonic Cascade Flow," AIAA Paper 79-0132, 1979.

17 Hafez, M.M., Murman, E.M., and South, J.C., "Artificial Compressibility Methods for Numerical Solution of Transonic Full Potential Equation," AIAA Paper 78-1148, 1978.

18 Eberle, A., "Eine Methode Einiter Elemente zur Berechnung der Transsonischen Potential-Strömung um Profile," MBB Bericht UEE 1352(0), 1977.

19 Lax, P.D., "Weak Solutions of Nonlinear Hyperbolic Equations and their Numerical Computation," Comm. Pure & Appl. Math. VII, 1954.

20 Murman, E.M., and Cole, J.D., "Calculation of Plane Steady Transonic Flows," *AIAA Journal,* Vol. 9, 1971, pp. 114–121.

21 Jameson, A., "Numerical Computation of Transonic Flows with Shock Waves," *Symposium Transsonicum II,* Springer-Verlag, 1975.

22 Hafez, M.M., and South, J.C., "Vectorization of Relaxation Methods for Solving Transonic Full Potential Equation," Flow Research, 1979.

23 Zienkiewicz, O.C., *The Finite Element Method in Engineering Science,* McGraw-Hill, London, 1977.

24 Deconinck, H., and Hirsch, Ch., "Subsonic and Transonic Computation of Cascade Flows," *Proc. IV Int. Symp. on Computing Methods in Applied Sciences and Engineering,* IRIA Paris, Dec. 1979.

25 Holst, T.L., and Ballhaus, W.F., "Conservative Implicit Schemes for the Full Potential Equation Applied to Transonic Flows," NASA TM 78469, 1978.

26 South, J.C., Keller, J.D., and Hafez, M.M., "Vector Processor Algorithms for Transonic Flow Calculations," *AIAA Journal,* Vol. 18, No. 7, 1980, pp. 786–792.

27 Deconinck, H., and Hirsch, Ch., "Transonic Flow Calculations with Higher Order Finite Elements," *Proc. of 7th Int. Conf. Numerical Method Fluid Dynamics,* June 23-27, 1980, Stanford, Calif.

28 Douglas, J., and Dupont, T., "Alternating Direction Galerkin Methods on Rectangles," *Proc. Symp. on Numerical Solution of Partial Differential Equations II,* Synspade II, 1975, pp. 133–214.

29 Dendy, J., and Fairweather, G., "Alternating Direction Galerkin Methods for Parabolic and Hyperbolic Problems on Rectangular Polygones," SIAM, *Journal of Num. Analysis.,* Vol. 12, 1975.

30 Deconinck, H., and Hirsch, Ch., "Finite Element Methods for Transonic Flow Calculations," *Proc. III GAMM Conf. on Numerical Methods in Fluid Mechanics,* DFVLR, Köln, 1979.

31 Ballhaus, W.F., Jameson, A., and Albert, J., "Implicit Approximate Factorization Schemes for Steady Transonic Flow Problems," *AIAA Journal,* Vol. 16, No. 6, June 1978.

32 Ecer, A., and Akay, H.U., "Investigation of Transonic Flow in a Cascade Using an Adaptive Mesh," AIAA paper presented 13th Fluid and Plasma Dynamics Conf., Colorado, 1980.

33 Sorenson, R.L., and Steger, J.L., "Simplified Clustering of Nonorthogonal Grids Generated by Elliptic Partial Differential Equations," NASA TM 73252, Aug. 1977.

34 Brandt, A., "Multilevel Adaptive Solutions to Boundary-Value Problems," *Math. Comp.* 31, 1977, pp. 333–390.

35 Jameson, A., "Acceleration of Transonic Potential Flow Calculations on Arbitrary Meshes by the Multiple Grid Method," AIAA Paper 79-1458, 1979.

36 Sieverding, C., "Base Pressure Measurements in Transonic Turbine Cascades," Von Karman Institute for Fluid Dynamics, LS84, 1976.

37 Breugelmans, F.A.E., in Von Karman Institute for Fluid Dynamics, LS59, 1973.

38 "Numerical Methods for the Computation of Inviscid Transonic Flow with Shocks," Proc. of the GAMM Workshop, Stockholm, Sweden, Sept. 18-19, 1979.

Development of a Large-Scale Wind Tunnel for the Simulation of Turbomachinery Airfoil Boundary Layers

M. F. Blair
Mem. ASME

D. A. Bailey
Assoc. Mem. ASME

R. H. Schlinker

Research Engineers,
Gas Dynamics Section,
United Technologies Research Center,
East Hartford, Conn.

The procedures employed for the design of a closed-circuit, boundary layer wind tunnel are described. The tunnel was designed for the generation of large-scale, two-dimensional boundary layers on a heated flat surface with Reynolds numbers, pressure gradients, and free-stream turbulence levels typical of turbomachinery airfoils. The results of a series of detailed tests to evaluate the tunnel performance are also described. Testing was conducted for zero pressure gradient flow with natural boundary layer transition. Heat transfer data and boundary layer profiles are presented for a flow with 0.25 percent free-stream turbulence. The flow in the tunnel test-section was shown to be highly uniform and two-dimensional. Test boundary layer profile and convective heat transfer data were self-consistent and in excellent agreement with classic correlations. Test-section free-stream total pressure, multi-component turbulence intensity, longitudinal integral scale, and spectral distributions are presented for grid-generated turbulence levels ranging from 1 to 7 percent. The test-section free-stream turbulence was shown to be both homogeneous and nearly isotropic. Anticipated applications of the facility include studies of the heat transfer and aerodynamics for conditions typical of those existing on gas turbine airfoils.

Introduction

Turbomachinery boundary layers can, depending upon specific blading design, be laminar, transition, fully turbulent, and even relaminarizing along the airfoil surface. These boundary layers develop beneath highly turbulent free-streams with large streamwise pressure gradients, and in the case of turbine airfoils, are exposed to significant wall heat transfer. These effects combine to produce flows which are exceptionally difficult to model analytically.

This paper describes the design and performance evaluation of a large-scale wind tunnel which was developed to produce test flows which will provide guidance for such modeling efforts. The tunnel can generate large-scale, two-dimensional incompressible boundary layers with Reynolds numbers, pressure gradients, and free-stream turbulence levels typical of turbomachinery airfoils. The large scale of the test boundary layers facilitates the measurement of accurate profile data including details of the fluctuating quantities necessary for the development of turbulence models. In addition, extremely accurate boundary layer convective heat transfer measurements can be obtained through the use of an electrically heated uniform heat flux plate.

Contributed by the Gas Turbine Division and presented at the International Gas Turbine Conference and Products Show, Houston, Texas, March 9-12, 1981, of THE AMERICAN SOCIETY OF MECHANICAL ENGINEERS. Manuscript received at ASME Headquarters, December 1, 1980. Paper No. 81-GT-6.

Generation of two-dimensional boundary layers requires extremely uniform swirl-free flow. The importance of these requirements for low turbulence wind tunnels has been demonstrated in numerous wind tunnel/boundary layer development programs (e.g., refs. [1 – 3]). Many of the recommendations developed in these earlier studies have been incorporated in the design of the present facility. An additional design requirement for the present tunnel was that the test-section turbulence be adjustable from very high levels to a level that could be considered negligibly small for turbomachinery flows. The turbulence generating grids for this tunnel were designed to provide homogeneous, nearly isotropic turbulence without producing significant free-stream total pressure or boundary layer nonuniformites. The design of the present facility has incorporated many features of other operational low turbulence, two-dimensional tunnels as well as the results of numerous studies of grid-generated turbulence. The tunnel combines the abilities to vary test-section turbulence and pressure gradient with the capacity to accurately measure local boundary layer heat transfer rates in highly two-dimensional flow.

The following design objectives were selected in order to simulate a range of conditions representative of most turbomachinery flows: (1) maximum $Re_\theta \approx 7000$ for $\partial P/\partial x = 0$, (2) maximum free-stream velocity 30 m/s at 320 m^3/s, (3)

minimum free-stream velocity 3 m/s, (4) maximum streamwise acceleration rate (constant for 1.2 m) $K = \nu/U^2\ \partial U/\partial x = \pm 1 \times 10^{-6}$, (5) free-stream turbulence intensity range 1/4 percent – 7 percent, (6) two-dimensional flow with $\partial P/\partial x = 0$ for 2.4 m.

The details of the procedures employed in the design of the tunnel components are presented in the following sections together with the results of a comprehensive series of tests examining the resulting flow. It is anticipated that these procedures and test data will prove useful to other experimentalists requiring similar test facilities.

Tunnel Design

An overall schematic of the boundary layer wind tunnel is shown in Fig. 1. The tunnel is of recirculating design and consists of a blower, a settling chamber/plenum, a contraction nozzle, the boundary layer test section, a downstream diffuser, and a return duct. The various tunnel components are discussed in the following sections.

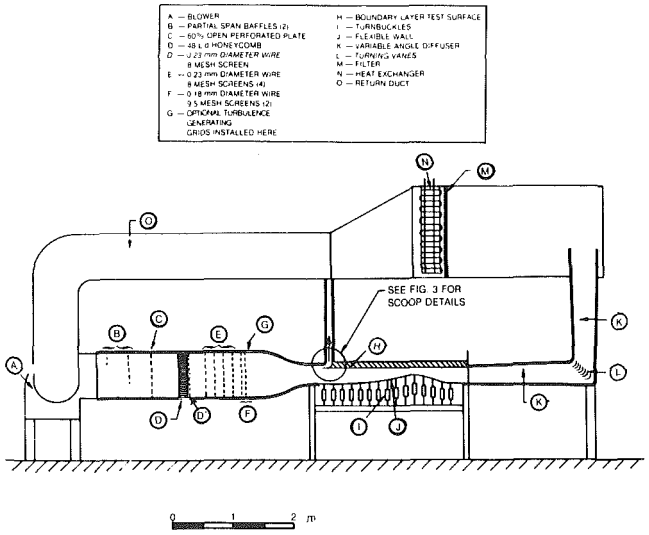

Fig. 1 United Technologies Research Center boundary layer wind tunnel

Blower. The tunnel is driven by a Clarage, model 54 NH, Class III centrifugal fan with a flow rate of 370 m^3/s at 2500 N/m^2 at 2300 rpm (maximum speed). Flow rate and output pressure of the fan are controlled by an inlet vortex valve and the impeller rotation speed. Severe flow unsteadiness can result when a centrifugal fan of this type is operated with a nearly closed vortex valve. Ability to reduce impeller speed permits operation of the blower with the inlet vortex valve opened 50 percent or more.

Settling Chamber/Plenum. The plenum downstream of the tunnel blower contains a series of flow/turbulence control devices selected to improve the uniformity and reduce the turbulence level of the flow. These control devices are labeled in Fig. 1 and described in Table 1. In addition to the use of conventional fine mesh damping screens and a honeycomb straightener to control swirl, three other flow control devices were employed in the plenum: (1) two partial-span perforated plate baffles (Item B – Fig. 1), (2) a full-span perforated plate (Item C – Fig. 1), and (3) a fine mesh damping screen (Item D' – Fig. 1) located at the exit plane of the honeycomb. The partial-span baffles (B) consist of 2 "tailored" pieces of perforated plate located approximately half a duct height downstream of the blower exit. The purpose of these baffles is to force the highly nonuniform flow from the blower to spread across the entire plenum. Downstream of the baffles a 60 percent open perforated plate (C) spanned the entire plenum flow area. Based upon the measurements of ref. [5], this device was expected to produce the greatest improvement in flow uniformity for a given total pressure loss while requiring a minimum length for flow redistribution. The full-span perforated plate was located half a duct height downstream of the baffles and upstream from the honeycomb to permit large-scale redistribution of the highly nonuniform plenum flow. An 8-mesh, 0.23 mm-dia wire damping screen (D') was installed 3 mm (one honeycomb cell diameter) downstream of the honeycomb flow straightener. As reported in ref. [5] there is an important benefit derived from locating a fine scale flow control device, such as a damping screen, near the exit plane of a honeycomb section. A honeycomb-screen combination produces a much lower exit turbulence level than a honeycomb alone since the large-scale jets exiting from the honeycomb cells are broken up into smaller scale eddies.

Nomenclature

b = turbulence grid bar width
C_L = tunnel centerline
c_p = specific heat at constant pressure
h = heat transfer coefficient
k = thermal conductivity
K = acceleration parameter, $\frac{\nu}{U^2}\frac{\partial U}{\partial x}$
K_ℓ = loss coefficient
L = overall contraction length
Pr = molecular Prandtl number, $\frac{\mu c_p}{k}$
P_t = total pressure
q = dynamic pressure (area average)
Re_x = length Reynolds number, $\frac{Ux}{\nu}$
Re_θ = momentum thickness Reynolds number, $\frac{U\theta}{\nu}$
St = Stanton number $\frac{h}{\rho U c_p}$
U = velocity
u' = streamwise fluctuating velocity
v' = normal fluctuating velocity
w' = transverse fluctuating velocity
x = distance from plate leading edge
X = distance from contraction entrance
X_G = distance from turbulence grids
X_Λ = distance from origin of turbulence growth
Λ_f = longitudinal integral scale of turbulence
ν = kinematic viscosity

Subscripts

e = free-stream value
w = wall value

Superscripts

$(\ )^+$ = dimensionless distance, velocity, and temperature
$(\ )'$ = fluctuating quantity
$(\bar{\ })$ = average quantity

TABLE I

FIGURE 1 LABEL	FLOW CONTROL DEVICE	DETAILED DESCRIPTION	LOSS COEFFICIENT $K = \frac{\Delta P_t}{q}$	CALCULATED TURBULENCE u'/U DOWNSTREAM	CALCULATED NONUNIFORMITY ΔU/U DOWNSTREAM	REFERENCES for CALCULATIONS	STREAMWISE SPACING
BLOWER EXIT							
B	PARTIAL-SPAN PERFORATED PLATES (2)	TAILORED BLOCKAGE TO SPREAD FLOW FROM BLOWER	≈2				30 cm FROM BLOWER EXIT TO FIRST PLATE — 20 cm BETWEEN PLATES
C	FULL-SPAN PERFORATED PLATE	60% OPEN	1.5	10%	100% (ASSUMED)	1	36 cm (1/2 DUCT HEIGHT)
D	ALUMINUM HEXCELL HONEYCOMB	d = 1/8 in., L/d = 48	2.5	COMBINED EFFECT 2%	COMBINED EFFECT 15%	1	36 cm (1/2 DUCT HEIGHT)
D	SCREEN AT HONEYCOMB EXIT	8 MESH, d = 0.23 mm	0.7			1,2,3	3 mm (ONE CELL DIAMETER)
E	DAMPING SCREENS (4)	8 MESH, d = 0.23 mm	0.7	0.7%	1%	2,3	25 cm
F	DAMPING SCREENS (2)	9.5 MESH, d = 0.18 mm	0.7	0.3%	0.25%	2,3	15 cm (120 MESH LENGTHS) BETWEEN SCREENS — TOTAL LENGTH 60 cm
G	TURBULENCE GENERATING GRIDS (OPTIONAL)	SEE FIGURE 2		10% MAX 1.5% MIN		4	12.6 cm (120 MESH LENGTHS) BETWEEN SCREENS OR TO GRIDS
CONTRACTION ENTRANCE							GRIDS 2 cm UPSTREAM OF CONTRACTION ENTRANCE

Using the loss coefficient and turbulence reduction data of ref. [5], calculations indicate that with the full-span perforated plate and the honeycomb-screen combination the turbulence level should be 2 percent and the mean velocity nonuniformity 15 percent when the flow reaches the first of the six fine-mesh damping screens. Standard calculation procedures ([6] and [7]) were employed to predict the aerodynamic performance of the damping screens. The predicted turbulence level and flow nonuniformity downstream of the final screen were 0.3 percent and 0.25 percent, respectively. Measured values approximately equal to these predictions were obtained during evaluation testing. For test cases requiring a minimum turbulence level the flow from the final damping screen passed directly into the contraction and test section. For higher test section turbulence levels various generating grids are installed at the exit plane of the plenum, downstream of the fine mesh damping screens.

Turbulence Generating Grids. Various turbulence levels within the tunnel test section are generated by inserting grids at the entrance to the contraction. This particular design feature differs from the arrangement employed in most tunnels in which the generating grids are located in the test section itself. The contraction entrance location was selected for the present tunnel as having significant advantages for the studies of two-dimensional boundary layer development. As described below, the benefits of this arrangement are that the generated turbulence will be more homogeneous and have a lower decay rate along the test section. Since grid-generated turbulence decays approximately as $u'/U \alpha (x/b)^{-5/7}$ [8], the change in turbulence level with distance along the test section will be reduced by increasing the distance from the grid to the test section entrance. In addition, the results of ref. [8] indicate that approximately 10 grid mesh lengths are required to establish a uniform turbulent flow. These advantages of locating the grid a distance upstream of the test section require, of course, a coarser grid to achieve a given test section turbulence intensity. Another effect considered was the influence of the contraction on the components of the grid-generated turbulence. It was recognized that rearrangement of the relative magnitudes of the turbulence components would occur due to the contraction. However, since the contraction ratio was small (2.8) it was concluded that any effects of induced anisotropy would be small in comparison to the advantages gained in homogeneity and reduced decay rate. To determine the validity of the assumption all three components of the test-section turbulence were documented during the evaluation testing of the tunnel.

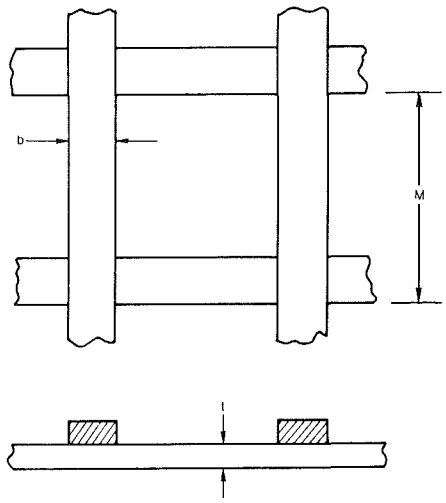

GRID NUMBER	b (cm)	M (cm)	t (cm)	M/b	% OPEN AREA
1	0.48	2.24	0.48	4.67	62
2	1.27	6.51	0.96	5.13	65
3	3.81	17.79	1.27	4.67	62
4	5.08	22.86	1.27	4.50	61

Fig. 2 Turbulence generating grid configurations

The turbulence-generating grids, designed using the correlations of ref. [8], consist of rectangular bar arrays with approximately 60 percent open area. The grids were designed to produce test section turbulence levels ranging from approximately 1 to 7 percent. Details of the grid configurations are given in Fig. 2. For grid numbers 1 and 2 (small bars) a locating jig was employed to secure the grid bars at precise intervals while the bars were welded at their intersections. This step assured that the grid configurations were both permanent and uniform over their entire area. For grid numbers 3 and 4, the bars were rigid making this step unnecessary.

Contraction. Downstream from the plenum the flow accelerates through a 2.8 to 1 contraction before entering the tunnel test section. The contraction is two-dimensional with no convergence in the transverse direction and consists of matched cubic arc wall contours. Potential flow [9] and two-dimensional boundary layer [10] analyses were employed to locate the contraction inflection point so as to avoid local boundary layer separation. Wall pressure distributions for a

series of assumed inflection locations were calculated using the potential flow solution while the boundary layer calculation deck served to determine if a separation-free flow would result for each velocity distribution. It was determined that if the boundary layer is turbulent and the inflection point falls between $0.4 < X/L < 0.7$ the flow will be separation-free. In order to avoid any possible corner flow separation near the test section it was decided to minimize the downstream adverse pressure gradient and locate the inflection at $X/L = 0.4$. The important shape parameters of the tunnel contraction are as follows: inlet height/inlet width = 0.823, contraction ratio = 2.8:1, overall length/inlet height = 1.32, inflection point/overall length = 0.4. The contraction was fabricated of plexiglass and all corners were filled to approximately 2 cm inside radius to minimize corner vortex formation. Ink flow visualization was employed to evaluate the resulting contraction flow. No evidence of flow separation was observed during these tests.

Test Section. The test section of the wind tunnel consists of the flat plate upper test surface, a lower flexible, adjustable stainless-steel wall and transparent vertical sidewalls. Although not presently incorporated in the tunnel instrumentation system, the test section is arranged so that it will be practical to employ various optical instrumentation techniques. Schlieren, shadowgraph, and laser Doppler anemometry could all be utilized when appropriate. The test section is 86 cm wide, 244 cm long, and 20 cm high at the entrance. The vertical sidewalls were constructed of plexiglass to facilitate positioning of boundary layer probes and for purposes of conducting flow visualization studies. At the entrance to the test section a bleed scoop forms the leading edge of the boundary layer test surface. The purpose of this bleed scoop is to remove the boundary layer and corner flows near the upper wall of the contraction. With this arrangement the test section flow consists of the uniform "core" flow from the contraction. A sketch showing details of the scoop assembly is presented in Fig. 3. The scoop assembly consists of a two-stage leading edge adjustable bleed and is attached smoothly to the test surface. The upstream and by far the larger of the two scoops removes the flow nearest the upper wall of the contraction exit duct. This large scoop is intended to trap both the two-dimensional boundary layer which develops along the contraction nozzle wall and the vortices which develop in the contraction corners. The flow rate along the scoop opening is adjusted by locally restricting portions of the perforated plate located at the scoop exit (see Fig. 3). The local scoop flow rate can be adjusted to produce uniform pressure (in the transverse direction) at the static taps along the entire scoop. Sample data for resulting scoop pressure distributions are presented in ref. [13]. The downstream and much smaller of the two scoops is mounted directly on the front edge of the flat heated plate model. The test section boundary layer begins growing a the leading edge of this smaller scoop. The purpose of this small-scale second scoop is to provide as short an unheated starting length upstream of the heated test surface as practical by bleeding off any boundary layer which develops along the large scoop lip. As with the larger upstream scoop the flow rate along the small scoop is adjusted by locally restricting portions of the perforated plate located at the small scoop exit (see Fig. 3). The leading edge of the small downstream scoop is a 4 × 1 ellipse in order to prevent a local separation bubble and premature transition of the test surface boundary layer. As shown in both Figs. 1 and 3 the flow diverted by the leading edge scoop assembly is returned to the main tunnel loop through a small duct. Tests to evaluate the test section flow indicated that no sidewall bleeds are required to produce highly two-dimensional test wall boundary layers.

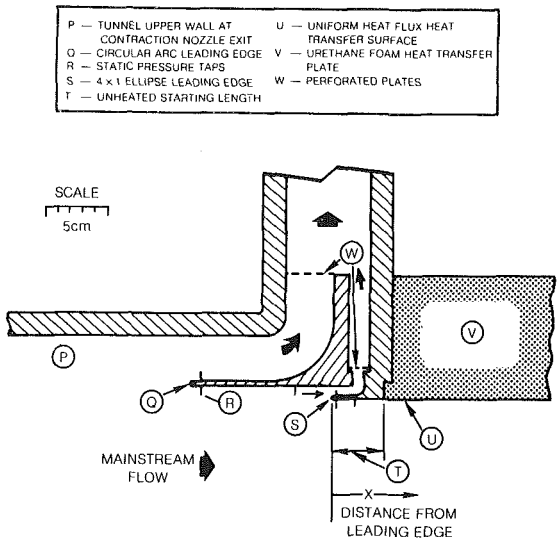

Fig. 3 Test wall leading edge bleed scoop

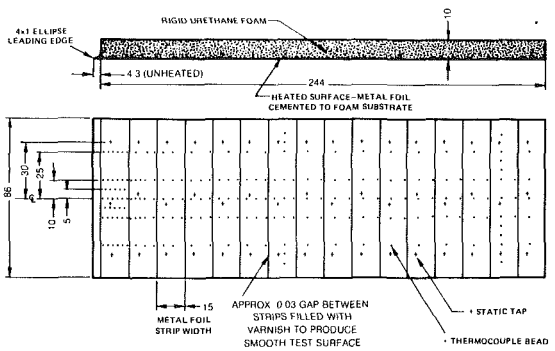

Fig. 4 Instrumentation diagram for the heated flat plate

Heated Flat Plate Model. Boundary layer development begins in the test section at the leading edge of the small bleed and continues along the flat test plate. The test surface consists of a uniform heat flux electrically heated plate instrumented for the measurement of local convective coefficients. The flat plate model is constructed from a block of rigid urethane foam 86 cm wide by 244 cm long by 10 cm thick mounted in a plexiglass frame with 15.3 cm wide strips of 316 stainless steel foil cemented to the test surface. A sketch of the flat plate model and its instrumentation is presented in Fig. 4. Rigid foam was employed for the substrate of the flat plate model because of its extremely low thermal conductivity (125 J/m-s-K). Because of this low foam conductivity less than 1/2 percent of the heat generated on the surface of the plate is conducted away from the test surface. Electric current passing through the metal foil strips cemented to the test surface produces the surface heating. The metal foil strips are wired in series and are powered by a single low ripple, regulated dc power supply. The foil test surface is instrumented with an array of 203 Cr-Al 0.13 mm wire diameter bead welded thermocouples. Each thermocouple was welded to the back surface of the foil through a hole in the rigid foam plate. Forty-eight surface static pressure taps were also installed in the model. The thermocouples and static tap locations are shown in Fig. 4.

The d-c current passing through the surface strips is measured using two precision shunt resistors and a digital voltmeter. The temperatures of the test surface thermocouples

are measured relative to a single test section freestream reference junction using a digital voltmeter.

In order to ensure a known, constant test surface emissivity and hence a known radiation loss, the completed foil test surface was coated with 3M C-101 high emissivity flat black paint ($\epsilon = 0.99$). Test results indicate that this surface is aerodynamically smooth, producing no premature boundary layer transition.

The local convective coefficients are determined by ignoring the negligible conductive losses, substracting power lost through thermal radiation and dividing by the temperature difference from the wall (T_w) to the freestream (T_e).

As an example to illustrate the magnitude of the radiation losses from the test surface, for $U_e = 30$ m/s, for turbulent boundary layer flow with $T_w - T_e = 14°C$, the radiation loss is approximately 4 percent of the total surface power.

Diffusers and Corner. As shown in Fig. 1, downstream of the test section the flow passes through an adjustable angle horizontal diffuser, a 90 deg corner and an adjustable angle vertical diffuser before entering a large return duct. To minimize flow unsteadiness in the test section and maximize system pressure recovery the diffusers were designed for attached flow and the corner for minimum loss. Using the performance curve of ref. [11], design diffuser angles of 7 deg (diffuser length/inlet height = 6) and 5 deg (diffuser length/inlet height = 3.5) were selected for the horizontal and vertical diffusers respectively. The 90 deg corner, following the recommendations of reference [12], is constructed with 85 deg circular arc corner vanes and a gap/chord ratio of 0.25.

Temperature Control and Air Filter. For studies of heat transfer and film cooling the accuracy of measurements of surface coefficients, film cooling effectiveness, and mean and fluctuating boundary layer temperature profiles is improved if the tunnel mainstream temperature does not vary with time. Hot wire/hot film anemometry errors induced through air temperature drift are also eliminated by having a constant temperature flow. For these reasons the present tunnel was designed to recirculate with a water-cooled heat exchanger (Item *N*, Fig. 1) spanning the tunnel ductwork. Under normal operating conditions the tunnel operating temperature remains constant within about ± 1 deg over an 8-hour period.

To minimize contamination of the plenum damping screens and hot wire/hot film sensors a replaceable filter consisting of 5 cm thick spun Kodel Polyester (Airgard PSF-20) was incorporated into the tunnel. The filter is located in the tunnel ductwork (Item *M*, Fig. 1) and is retained by a frame and screen holder. No intentional vents to atmosphere are incorporated in the tunnel. Leaks of tunnel air through instrumentation slots, etc. are made up through a filtered port located at the blower inlet.

Probe Traversing and Data Recording System. Experimental data are recorded using a data acquisition system specifically designed for this facility. This data acquisition system is capable of recording time averaged analog signals from various pressure, thermocouple and hot wire/hot film probes, and test section transducers. In addition, the system controls the movement of various boundary layer probes through the use of an L.C. Smith ball/screw traverse drive linked to an InterData Model 6/16 computer. Signals from the probes and transducers are recorded using InterData magnetic disks. The data system consists of two units: (1) a console containing the InterData computer and disk recording unit and a Perkin-Elmer Model 1110 scope/keyboard control terminal, and (2) a remote cabinet unit, linked by cables to the console unit, which contains the sensor transducers and traverse controls. A telescope sighted through the tunnel sidewall is used to accurately position probes relative to the test wall. The boundary layer traverse mechanism is suspended on a linear ball bearing track beneath the test section. The traverse can be located anywhere in the center 75 percent of the test section width from the nozzle exit to the test section trailing edge. The traverse mechanism can both translate and rotate the various probes employed.

Flow Evaluation Testing

Evaluation testing for this facility was conducted with the flexible test section bottom wall adjusted to produce zero pressure gradient flow along the flat upper test plate. Test section total pressure surveys and surveys of the multicomponent turbulence intensity, longitudinal integral scale, and spectral distributions were obtained for five turbulence configurations: (1) minimum turbulence (no generating grid) and (2 through 5) with grids 1 through 4 installed. Heat transfer and boundary layer velocity and temperature profile data were obtained for the minimum turbulence configuration only.

Total Pressure Uniformity. Surveys of the total pressure distribution in the tunnel test section core flow were obtained for all five tunnel turbulence configurations using a traversing impact probe. These distributions were measured at both the tunnel contraction exit plane (30 cm upstream of the test wall leading edge) and near the test section exit plane (224 cm downstream of the test wall leading edge). Total pressure measurements were obtained over each survey plane at 2.5 cm intervals (vertical and horizontal). At the tunnel contraction exit this resulted in a 300 point matrix of measurements for each turbulence configuration. At the test-section exit plane the extent of tunnel core flow is reduced by boundary layer growth along the test section walls. The thickness of the boundary layers at the exit plane is a function of the freestream turbulence level and depending upon which grid was installed, the measurement matrix resulted in a 75 to 125 point array. These survey data are available in ref. [13]. Examination of these data revealed that there were no large scale "cells" of high or low total pressure for any of the turbulence configurations. In addition, these survey data indicate that the total pressure nonuniformities are randomly distributed and do not correspond to the bar spacing of the various grids.

The ranges of total pressure measured within the tunnel test section core flow for the five turbulence configurations are presented as $\pm \Delta P_t/q$ in Fig. 5. The data presented in Fig. 5 represent a conservative measure of test-section total pressure nonuniformity in that all the boundary profile data measured for this program were obtained within the center 30 cm of the tunnel span. If pressures measured within the center 30 cm of the tunnel span only were included in Fig. 5 the indicated nonuniformities would be reduced by a factor of approximately 1/3. For all five configurations, core flow mixing results in decreasing total pressure nonuniformity with increasing distance from the grids. In addition, for all configurations and measurement planes, except grid No. 2 - downstream, core flow nonuniformities increase directly with increased grid coarseness.

The conclusion reached from Fig. 5 is that, on the scale of the tunnel test-section, the flow through the various grid configurations is extremely uniform (particularly for the finer grids). The turbulence grids appear to have been fabricated accurately (even bar spacing) and to produce uniform flow resistance over their surfaces.

Test Section Turbulence Distributions. Measurements of the turbulence quantities doenstream of the various generating grids were obtained with single and *X* hot film probes and their associated anemometry. These data include

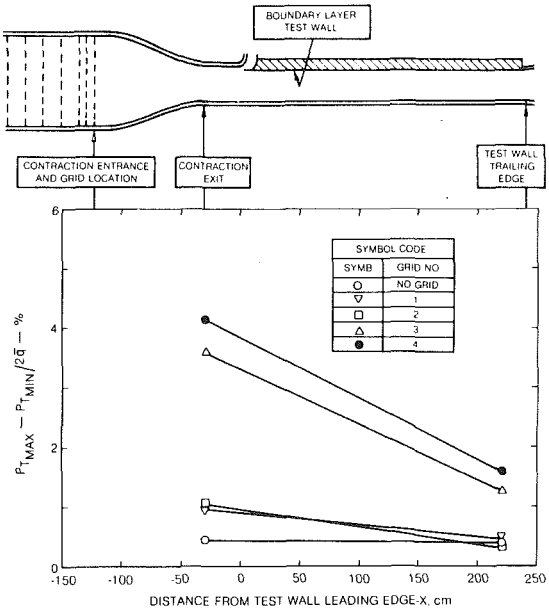

Fig. 5 Test section total pressure nonuniformity

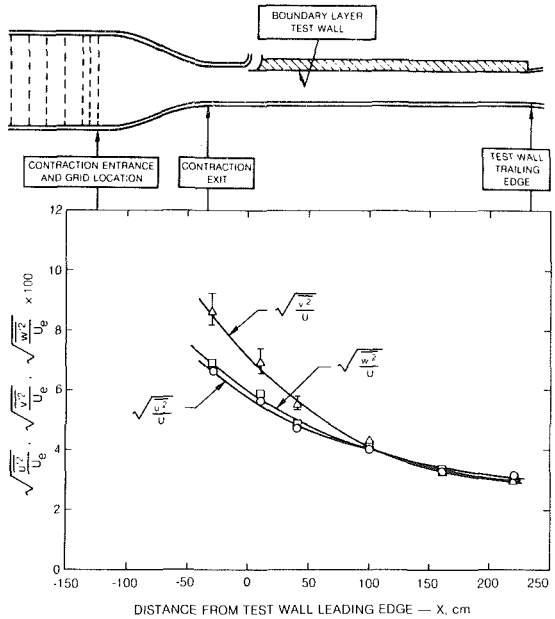

Fig. 6 Distribution of the components of the turbulence in the test section with grid number 3 installed

measurements of multi-component (u', v', and w') distributions of turbulence intensity and measurements of the streamwise component (u') distributions of the integral scale and power spectral density. Descriptions of the anemometer and signal processing equipment used to obtained these data as well as descriptions of the techniques employed to reduce and interpret the measured quantities can be found in ref. [13].

Free-Stream Turbulence Intensity Distribution. The u' (streamwise) and v' (vertical) components of the turbulence were measured with an X film oriented in a plane parallel to the streamwise direction and perpendicular to the horizontal test wall. For measurements of the u' and w' components, the X film array was oriented in a plane parallel to the streamwise direction and parallel to the horizontal test wall. Turbulence distributions were obtained for all five tunnel turbulence configurations. Surveys of the turbulence distributions were obtained over six planes located at the following streamwise distances from the test plate leading edge: $X = -30$ (the plane of the contraction exit), 10, 40, 100, 163, and 224 cm. For each survey plane data were obtained at 5 cm vertical intervals for the following three transverse locations: $Z = C_L$ and $\pm$ 15 cm. At the contraction exit ($X = -30$ cm) where the sidewall boundary layers were still very thin, these spacings resulted in a 12-point matrix of measurements for each turbulence configuration. At survey planes further downstream the extent of the free-stream flow was reduced by boundary layer growth along the test section walls and the number of measurement locations was restricted accordingly. For most of the streamwise location/turbulence grid combinations, turbulence measurements were obtained at six locations.

A sample multi-component (u', v', and w') turbulence intensity distribution for the various grids is presented in Fig. 6. A composite plot showing the total turbulence intensity distributions for all five turbulence configurations is presented in Fig. 7. The u' turbulence levels are the average of the u' values determined with the X-probe oriented in the vertical and horizontal directions while for all three components of turbulence the levels plotted are the average of all values measured at the data plane. For cases when all the turbulence levels over the data plane did not fall within the

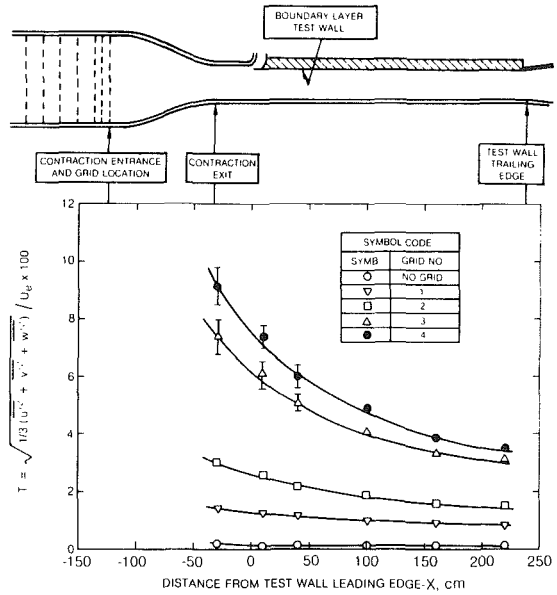

Fig. 7 Distributions of total turbulence intensity in the test section

plotting symbol, uncertainty bars indicate the range of the measured results.

For all grid configurations the relationship between the magnitudes of the three turbulence components in the test section was $v' > w' > u'$ with the difference between the various components decreasing with increasing distance from the grids. The anisotropy of the turbulence in the tunnel test-section results from combined effects of flow through coarse grids and the influence of the tunnel contraction on the grid turbulence. As shown by Comte-Bellot and Corrsin [14], for flows without a contraction, lattice-type turbulence generating grids produce turbulence with $v' = w'$ and $u' \approx 5/4$ of the other components. For the present test facility (see Fig. 1) the contraction is located just downstream of the turbulence generating grids. Prandtl [15] has provided a well-known semiquantitative model for predicting the influence of a contraction on the various components of turbulence.

Prandtl's theory has been verified as being at least qualitatively correct for small contraction ratios by a large number of experiments (e.g., Uberoi, [16]). Applying Prandtl's arguments to the present contraction shape, it would be expected that in passing through the nozzle, u' would decrease (≈ 1/contraction ratio) and v' and w' would increase (less than the decrease in u'). Because the contraction is two-dimensional (no contraction in the w' direction), the increase of the w' component should be less than the increase of the v' component. As shown in Fig. 6, the measured turbulence intensity levels for the various components are arranged as expected ($v' > w' > u'$). The streamwise component (u') which should have had a slightly greater intensity than the other components at the grid location was significantly reduced as the flow passed through the contraction. The vertical and transverse (v' and w') components should have been approximately equal at the grid location and as the flow passes through the contraction, the v' component was increased and the w' component was slightly increased.

For all locations with grid Nos. 1 and 2 and for the far downstream locations for grid Nos. 3 and 4 the turbulence data over the various survey planes were extremely uniform with all data falling within the plotting symbols. The largest nonuniformities in measured turbulence resulted for $X \gtrsim 50$ cm for grid No. 3 and for $X \gtrsim 100$ cm for grid No. 4. These regions are within 10 grid mesh spacings (M) from the respective grid locations. This result is in agreement with reference [8] which indicates that a distance of approximately 5 to 10 mesh lengths downstream of a grid is required to establish uniform flow. The specific reason for locating the turbulence grids at the contraction entrance instead of at the test section entrance was to minimize turbulence nonuniformities in the test section. If the turbulence grid station had been located at the test section entrance, most of the test section would have fallen within the 5 to 10 mesh length flow establishment region and the test section turbulence would have been less uniform.

Total turbulence distributions for the various grid configurations were calculated from the multi-component turbulence data and are presented in Fig. 7. The nonuniformity of the turbulence very near grid Nos. 3 and 4 is evident. Figure 7 shows that the downstream decay rate of the turbulence decreased progressively with increasing distance from the grids. A quantitative comparison can be made between the present results and those of Baines and Peterson [8] in which the decay of turbulence downstream of bar lattices was documented. Although the grid configurations of Baines and Peterson were very similar to those employed for the present study, there was one important difference in the experimental arrangement. Baines and Peterson employed a constant velocity section downstream of the turbulence grids while the present study includes the additional complexity of the tunnel contraction.

Two different methods (see Fig. 8) have been used to relate the present results to those of ref. [8]. In Fig. 8(a) the present turbulence intensity measurements are plotted as a function of dimensionless distance from the grid location (X_G/bar width). In this form the present data are seen to have a lower intensity than the data of Baines and Peterson when compared at similar locations. The turbulence decay rate, however, is identical. In this format the reduction of the turbulence level for similar distances from the grids is interpreted to be the overall effect of the contraction on the total turbulence intensity. In Fig. 8(b) the section turbulence data are compared to the results of Baines and Peterson on the basis of "equivalent" turbulence decay time. The time required for the flow to pass from the grid location to the test section entrance was calculated from the known nozzle velocity distribution. If the flow is considered to have been at the test

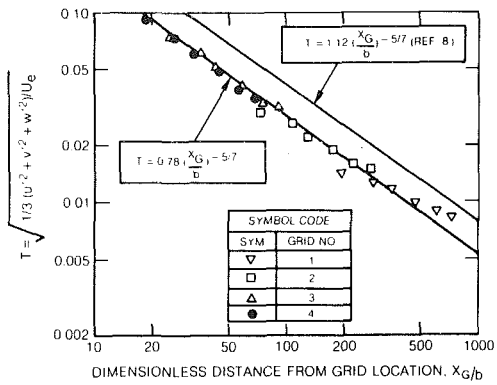

Fig. 8(a) Test section turbulence distribution as a function of distance from the grids

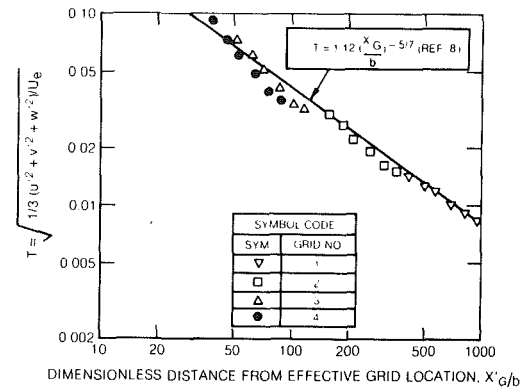

Fig. 8(b) Test section turbulence distribution as a function of distance from the "effective" grid location

Fig. 8 Distribution of total turbulence intensity in the test section compared with the results of Baines and Peterson

section velocity at all stations, this total flow time corresponds to a new longer "effective" distance from the grid to the measurement stations. For the present nozzle configuration this calculated effective distance is $X'_G = X_G + 100$ cm. Figure 8(b) shows that by plotting the present results as a function of distance from this effective grid location both the absolute turbulence intensity levels and the turbulence decay rate agree with the results of ref. [8]. The two different interpretations of the turbulence distributions presented in Figs. 8(a) and 8(b) are both physically reasonable. These comparisons between the data of the present study and those of Baines and Patterson indicate that there was excellent agreement between the results of the two studies.

In summary, the conclusions reached from the free-stream turbulence intensity distribution measurments are:

1 The relationship between the three components of the free-stream turbulence measured in the test section for all four turbulence grids was $v' > w' > u'$. This anisotropy resulted from the turbulence generating grids and the specific shape of the main tunnel contraction nozzle and can be predicted using the theory of ref. [15].

2 The turbulence intensity measurements were very uniform over all transverse survey planes for grid Nos. 1 and 2 and for the downstream survey planes for grid Nos. 3 and 4. At the near-grid survey planes (less than 10 grid mesh lengths) for grid Nos. 3 and 4 minor nonuniformities were detected.

3 The turbulence intensity levels and decay rates measured for the various grids and survey locations are in excellent agreement with the results reported in ref. [8].

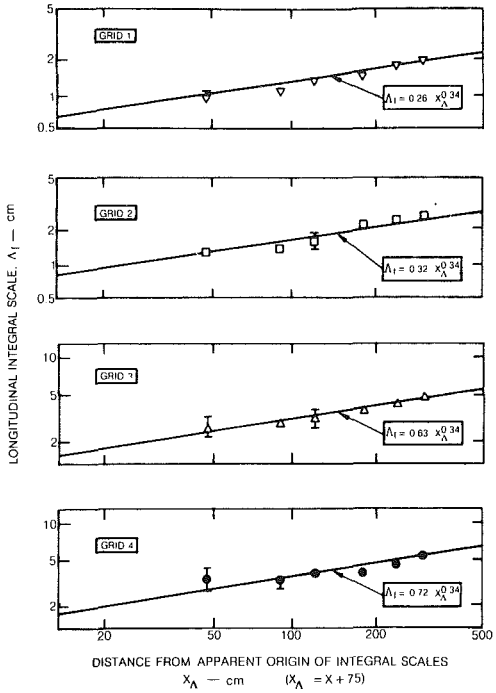

Fig. 9 Growth of the longitudinal integral scale along the test section

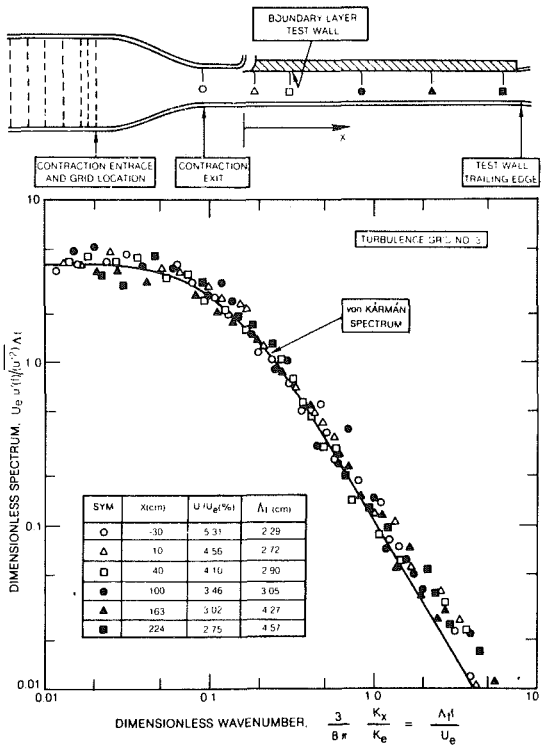

Fig. 10 Free-stream power spectral density distributions measured at various streamwise locations in the test section with grid number 3 installed

For the tunnel configuration with no grid installed the turbulence level in the tunnel test was 1/4 percent. For applications related to internal flows and turbomachinery 1/4 percent turbulence is extremely low. Turbulent boundary layer heat transfer and profile data obtained for this "no-grid" configuration can be considered as having negligible effects from the free-stream turbulence. Figure 7 indicates, as would be expected far downstream of a fine screen such as this, that the turbulence decays only slightly over the entire length of the test section.

Free-Stream Turbulence Length Scale Distribution. Measurements of the longitudinal integral scale of the free-stream turbulence downstream of the various turbulence grids were obtained using single sensor hot film probes, an anemometer system and a Saicor correlator. Integral scale measurements were obtained for the four-grid configurations over the same survey plane locations as described in the previous section (Turbulence Intensity Distributions). Integral length scale growth can be approximately represented by a power law of the form $\Lambda_f = A_i\ (X_\Lambda)^m$ [14], where X_Λ is the distance from the apparent origin of the growth and A_i is a constant related to the scale of the turbulence source. A best-fit power law was determined for the present data by constructing logarithmic plots with a series of assumed apparent origins and selecting the one which produced the longest straight line fits. A single apparent origin (75 cm upstream of the test plate leading edge) common to all four turbulence grids was selected. The integral scale measurments plotted as a function of distance from their apparent origin are presented in Fig. 9. For this figure the symbols plotted represent the average of the integral scale measurements obtained at each survey plane. The vertical bars indicate the range of the individual measured values. The power law exponent ($m = 0.34$) determined from these logarithmic plots is in excellent agreement with the values determined by Comte-Bellot and Corrsin [14].

Free-Stream Power Spectal Density Distributions. Spectral distribution data were obtained along the tunnel centerline at tunnel mid-height for the following streamwise locations: X

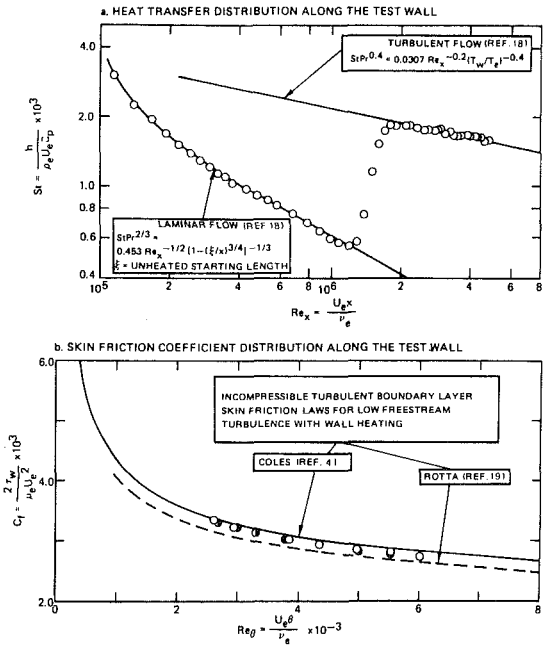

Fig. 11 Heat transfer and skin friction coefficients distributions for T = 0.25 percent; ◯ tunnel C_L; ◐ 15 cm east of C_L; ◐ 15 cm west of C_L

$= -30$, 10, 40, 100, 163 and 224 cm. These data were obtained using a single sensor hot-film probe, an anemometer and a narrow band spectrum analyzer. Figure 10 presents sample spectral distribution data for grid No. 3. For all four grids the measured data were in excellent agreement with the von Karman one-dimensional spectrum for isotropic turbulence [17]. This result indicates that the test section turbulence has the classic characteristics of grid generated

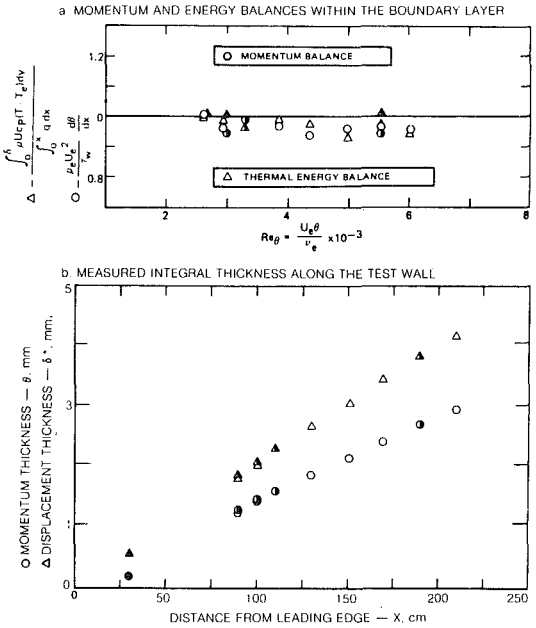

Fig. 12 Boundary layer properties measured for T = 0.25%; ◯ tunnel C_L; ◑ 15 cm east of C_L; ◐ 15 cm west of C_L

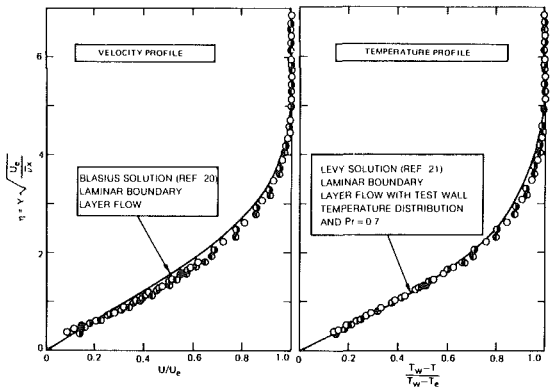

Fig. 13 Velocity and temperature profiles measured upstream of boundary layer transition for T = 0.25% and (Re_x = 0.03 × 10^6) at three transverse locations; ◯ tunnel C_L; ◑ 15 east of C_L; ◐ 15 cm west of C_L

FLOW CONDITIONS AND BOUNDARY LAYER PROPERTIES			
U_e = 30.3 m/sec	C_f = 0.00302	Re_θ = 3880	Π = 0.56
δ = 1.80 cm	S_t = 0.00179	H = 1.38	G = 7.01

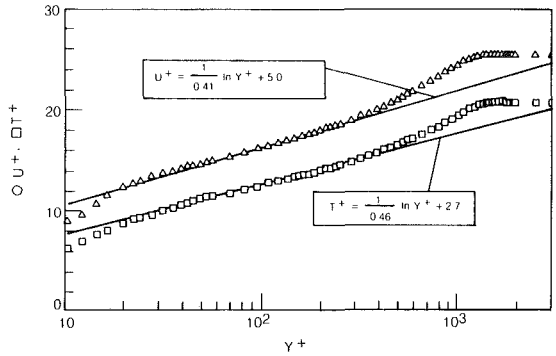

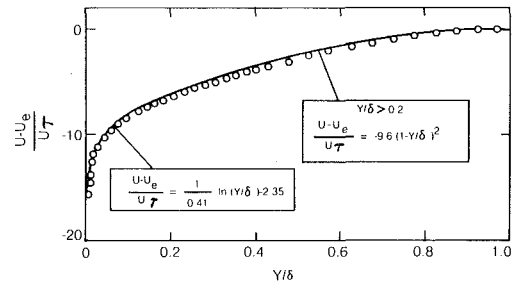

Fig. 14 Sample turbulent boundary layer profile data

turbulence. Note that there were no significant spikes of higher or lower contributions to the overall turbulence level from discrete or narrow frequency bands.

Boundary Layer Profile and Heat Transfer Data. Convective heat transfer, boundary layer mean velocity and temperature profile, and wall static pressure distribution data were obtained for a constant free-stream velocity of 30.3 m/s and the minimum free-stream turbulence intensity. Static pressure measurements on the flat plate test surface and along the leading edge bleed scoops indicate that both the transverse and streamwise pressure gradients were negligible.

The Stanton number distribution for this case is presented in Fig. 11(a). Upstream of boundary layer transition ($Re_x < 1.2 \times 10^6$, $x < 58$ cm) the measured heat transfer agrees very well with the analytical solution of ref. [18]

$$St\, Pr^{2/3} = 0.453\, Re_x^{-1/2} [1 - (\xi/x)^{3/4}]^{-1/3} \quad (1)$$

for zero pressure gradient, laminar boundary layer flow with a uniform convective heat flux wall, and unheated starting length ξ. For this test plate ξ = 4.3 cm.

Downstream of $Re_x \approx 1.2 \times 10^6$ the boundary layer passed through transition. From $Re_x \approx 1.8 \times 10^6$ to the downstream end of the plate the measured heat transfer data agreed within ± 2 percent with the fully turbulent correlation of ref. [18].

In Fig. 11(b) skin friction coefficient levels inferred from the mean velocity profile data are compared to the well-known incompressible turbulent boundary layer skin friction law formulations of Coles [4] and Rotta [19]. These correlations, which apply for isothermal incompressible turbulent boundary layer flow have been corrected for density variations due to wall heating using Coles' "law of corresponding stations" [4]. As can be seen from Fig. 11(b), the measured skin friction coefficients are bracketed by the two correlations.

Fig. 12(a) presents accuracy and consistency checks calculated for the measured profile data. The momentum balance of Fig. 12(a) consists of a ratio of the experimentally measured terms of the two-dimensional von Karman momentum integral equation. Coles [4] in a comprehensive turbulent boundary layer survey article, selected 10 studies as having produced the best available two-dimensional profile results. A direct comparison can be made between the momentum balance results of Fig. 12(a) and the results from these best available profiles presented by Coles in Fig. 12 of Appendix A in ref. [4]. For the comparable Reynolds number range the present results deviate from an exact momentum balance approximately one-half as much as these best selected data. This favorable comparison indicates a high degree of flow two-dimensionality for the present tunnel.

The thermal energy balance data of Fig. 12(a) is a ratio of the total convective heat generated per unit tunnel width upstream of any profile location to the measured thermal energy contained in the boundary layer at the location. Figure 12(a) reveals that this thermal energy balance is also within approximately 5 percent of unity for all the measured profiles. The conclusion reached from Fig. 12(a) is that the profile data form an accurate, consistent set and that the flow is highly two-dimensional.

The measured momentum and displacement thicknesses for

the various boundary layer profiles are presented in Fig. 12(*b*). As can be seen from an examination of this figure, there is negligible variation between profiles measured at various transverse but fixed streamwise locations on the test surface. Mean velocity and temperature profiles measured at three transverse locations in the laminar flow upstream of boundary layer transition are presented in Fig. 13. The profiles of Fig. 13 were obtained on the tunnel centerline and at stations 15 cm on either side of the tunnel centerline at x = 30 cm, $Re_x = 0.63 \times 10^6$. The measured velocity and temperature profile data agree extremely well with the laminar boundary layer profile solutions of Blasius (velocity, [20]) and Levy (temperature, [21]) and show negligible transverse variations. Mean velocity and temperature profiles measured in the turbulent boundary layer flow at $Re_x = 2.693 \times 10^6$, x = 133 cm are presented in Fig. 14. The profiles are presented in both the universal coordinates of the velocity and temperature for turbulent boundary layers and in the Clauser Defect coordinates. The profile data are in excellent agreement with these standard turbulent velocity and temperature profile "laws".

The conclusion reached for Figs. 11 through 14 is that the data obtained for this low free-stream turbulence, natural transition case are in excellent agreement with classic two-dimensional correlations.

Summary of Results

This new facility has been demonstrated to be a valuable potential tool for the study of the aerodynamics and heat transfer of turbomachinery boundary layers. The results of the flow evaluation testing indicate that the tunnel design techniques employed were satisfactory and accurate. Specific conclusions reached from the tunnel evaluation testing are: (1) The minimum test section turbulence level achieved with this facility is sufficiently low that it can be considered negligible for many studies applicable to turbomachinery flows and turbulent boundary layer phenomena. (2) Homogeneous and nearly isotropic test section free-stream turbulence ranging in intensity from approximately 1 to 7 percent can be generated using coarse lattice grids. (3) The flow in the tunnel test section is highly uniform and two-dimensional. Test boundary layer profile and convective heat transfer data are self-consistent and in excellent agreement with classic correlations.

Acknowledgments

The authors wish to acknowledge the contributions of the following people towards the successful completion of this project: Dr. Hassan Nagib of the Illinois Institute of Technology and Drs. Robert Paterson and Robert Dring of UTRC for many helpful discussions and suggestions, Mr. John Nelson who conducted the mechanical design of the facility, Mr. Raymond Whitmore who designed the data system, and Mr. Charles Coffin who obtained most of the data.

Funding of the design and construction of this facility was provided by United Technologies Corporation. Portions of the flow evaluation data were obtained as part of a study of turbulent boundary layer flow sponsored by the U.S. Air Force Office of Scientific Research, Contract No. F49620-78-C-0064. The contract monitors for this Air Force project were Col. Robert C. Smith (Ret.), Dr. D. George Samaras, and Dr. James D. Wilson.

References

1 Winkelmann, A. E., and Melnik, W. L., "An Experimental Investigation of a Two and a Three-Dimensional Low Speed Turbulent Boundary Layer," ONR Report NR061-212, Dec. 1976.

2 Bradshaw, P., "The Effect of Wind-Tunnel Screens on Nominally Two-Dimensional Boundary Layers," *Journal Fluid Mechanics,* Vol. 22, Part 4, 1965, pp. 679–687.

3 deBray, B. G., "Some Investigations into the Spanwise Non-uniformity of Nominally Two-Dimensional Incompressible Boundary Layers Downstream of Gauze Screens," *A.R.C. R&M,* 1969.

4 Coles, D. E., "The Turbulent Boundary Layer in a Compressible Fluid," *Rand Report,* R-403-PR, 1962.

5 Loehrke, R. I., and Nagib, H. M., "Experiments on Management of Free-Stream Turbulence," AGARD Report No. 598, AD-749 891, Sept. 1972.

6 Wieghardt, K. E. G., "On the Resistance of Screens," *Aeronautical Quarterly,* Vol. IV, Feb. 1953.

7 Schubauer, G. B., Spangenberg, W. G., and Klebanoff, P. S., *Aerodynamic Characteristics of Damping Screens,* NACA TN 2001, 1949.

8 Baines, W. D., and Peterson, E. G., "An Investigation of Flow Through Screens," *Trans. ASME,* Vol. 73, 1951, pp. 467–480.

9 Caspar, J. R., Hobbs, D. E., and Davis, R. L., "Calculation of Two-Dimensional Potential Cascade Flow Using Finite Area Methods," *AIAA Journal,* Vol. 18, No. 1, Jan. 1980.

10 McDonald, H., and Fish, R. W., Practical Calculations of Transitional Boundary Layers," *Int. Journal Heat and Mass Transfer,* Vol. 16, No. 9, 1973.

11 Reneau, L. R., Johnston, J. P., and Kline, S. J., "Performance and Design of Straight, Two-Dimensional Diffusers," *ASME Journal of Basic Engineering,* March 1967.

12 Bradshaw, P., and Pankhurst, R. C., "The Design of Low-Speed Wind Tunnels," *Progress in Aeronautical Sciences,* Vol. 5, MacMillian Company, 1964.

13 Blair, M. E., and Werle, M. J., "The Influence of Free-Stream Turbulence on the Zero Pressure Gradient Fully Turbulent Boundary Layer," *UTRC Report* R80-914388-12, Sept. 1980.

14 Compte-Bellot, G., and Corrsin, S., "The Use of a Contraction to Improve Isotropy of Grid Generated Turbulence," *Journal of Fluid Mechanics,* Vol. 25, 1966, pp. 657–682.

15 Prandtl, L., *Attaining a Steady Air Stream in Wind Tunnels,* NACA TM 726, 1933.

16 Uberoi, M. S., "Effect of Wind-Tunnel Contraction on Free-Stream Turbulence," *J. of Aeronautical Science,* Aug. 1956.

17 Hinze, J. O., *Turbulence,* McGraw-Hill, New York, 1959.

18 Kays, W. M., *Convective Heat and Mass Transfer,* McGraw-Hill, New York, 1966, pp. 222 and 244.

19 Rotta, J. C., *Turbulent Boundary Layers in Incompressible Flow, Progress in Aeronautical Sciences,* Vol. 2, Pergamon, London, 1962.

20 Schlichting, H., Boundary Layer Theory, 6th Edition, McGraw-Hill, New York, 1968, pp. 125–133 and 544–556.

21 Levy, S., "Heat Transfer to Constant-Property Laminar Boundary-Layer Flows with Power-Function Free-Stream Velocity and Wall-Temperature Variation," *Journal of Aeronautical Sciences,* Vol. 19, 1952, pp. 341.

A Study on Centrifugal Impeller and Diffuser Flow

H. Krain

Research Engineer,
DFVLR,
Institut für Antriebstechnik,
Cologne, West Germany

The flow field development within a centrifugal compressor stage was analyzed using an advanced laser velocimetry [4]. A splitter blade impeller coupled with a vaned and vaneless diffuser has been found to have similar internal flow patterns for both the vaneless and vaned diffuser design. Different velocity profiles have been analyzed for adjacent channels behind the splitter blade leading edge. A considerable wake flow was observed near the impeller exit. Detailed optical measurements within the vaned diffuser entrance region gave evidence of a periodically fluctuating, highly distorted diffuser inlet flow. Unsteady flow angle deviations of 13 degrees have been discovered within the diffuser throat. Maximum flow angle differences up to 27 degrees occurred from hub to shroud.

Introduction

Centrifugal compressor stage optimization requires a proper impeller/diffuser matching that influences considerably surge and efficiency of centrifugal compressor stages. For compressors equipped with radial discharge impellers the impeller and diffuser efficiency are of equivalent importance to the overall stage efficiency. If backswept impellers are employed the impeller efficiency will have a dominating influence on stage efficiency. Actually both efficiencies are interdependent due to the impeller/diffuser interaction. The diffuser recovery to be expected is largely affected by the highly distorted, unsteady impeller discharge flow. On the other hand, the diffuser blades are believed to act on the internal three-dimensional impeller flow [1].

Previous laser measurements at the DFVLR displayed the separation onset and jet/wake development within radial discharge and backswept impellers [11]. During these investigations that were primarily concerned with the internal impeller flow the compressor was equipped with a vaneless diffuser of constant area. This diffuser type was changed to meet the requirements of high pressure ratio centrifugal compressor operation. These compressors are usually equipped with vaned diffusers having generally higher pressure recovery capability. A flat straight channel diffuser has been designed and employed. The internal flow field of a splitter blade impeller coupled with the new two-dimensional vaned diffuser and a vaneless diffuser of equal and constant meridional width has been analyzed for rotor tip speeds of 300 m/s. Since the application of vaned diffusers usually leads to a distortion of the static pressure field in the impeller exit/diffuser entrance region (Fig. 1), diffuser effects on the internal impeller flow were expected, e.g., on the impeller velocity profiles.

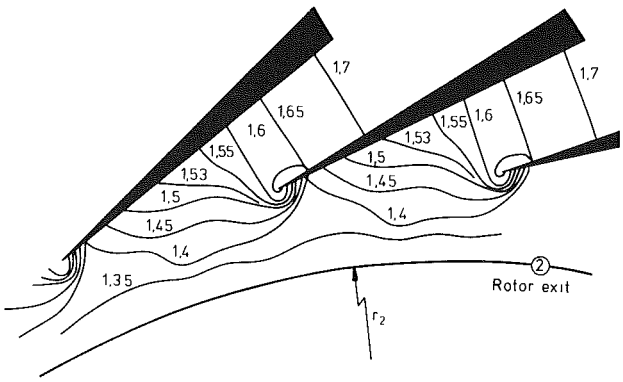

Fig. 1 Measured lines of constant static pressure in the impeller exit/diffuser entrance region.

Precise vaned diffuser recovery prediction is a still unsolved problem in centrifugal compressor design. This is mainly due to today's limited knowledge about the flow development aft of the impeller discharge and within the vaned diffuser entrance region. Extensive experimental data of flat and conical channel diffuser performance have been published by Runstadler, et al. [2]. These results are today very often used for diffuser design. A precise throat blockage prediction, however, is necessary for a reasonable application of these data. Only little success in blockage prediction has been achieved yet by applying boundary layer calculations from the impeller tip to the channel diffuser throat. Therefore the designer of centrifugal compressor diffusers has frequently to refer to compiled empirical data. A substantial improvement of this rather unsatisfactory situation is only to

Contributed by the Gas Turbine Division and presented at the International Gas Turbine Conference, Houston, Texas, March 8-12, 1981, of THE AMERICAN SOCIETY OF MECHANICAL ENGINEERS. Manuscript received at ASME Headquarters, December 4, 1980. Paper No. 81-GT-9.

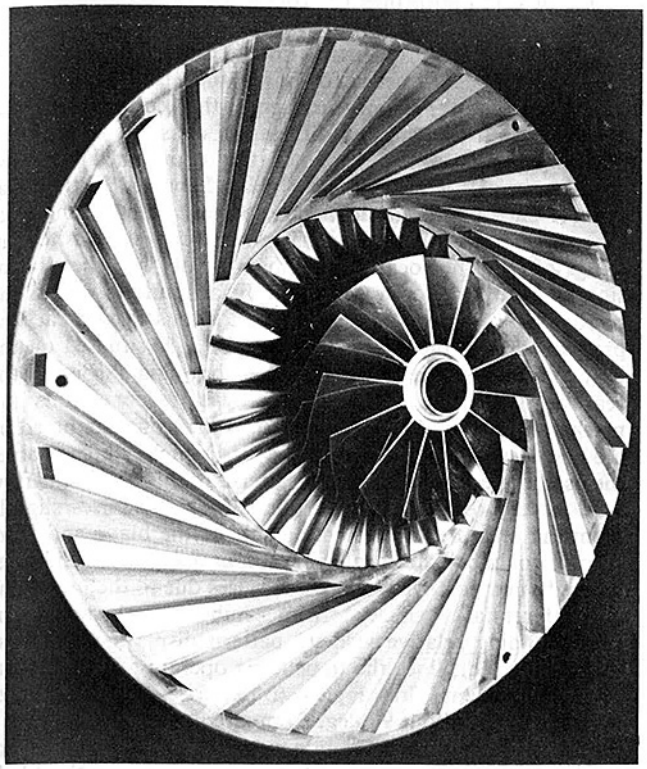

Fig. 2 Test impeller ($\beta_{2b} = 90$ deg, $z_R = 28$) and flat straight channel diffuser ($z_d = 27$)

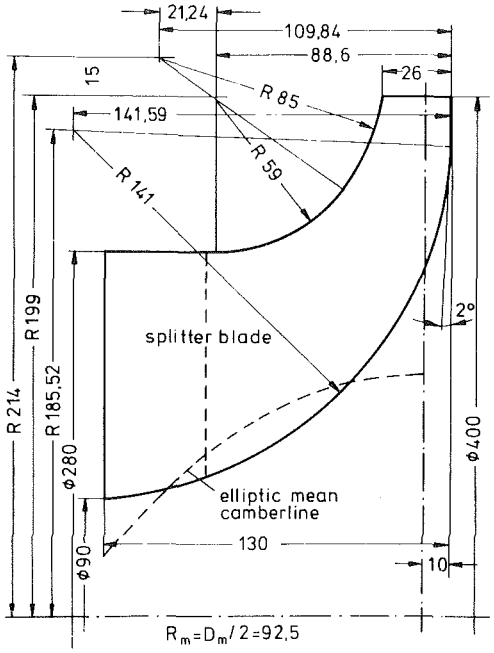

Fig. 3 Meridional geometry and blade camberline shape of the radial discharge impeller

be expected by clarifying the actual flow processes in this region. The experimental results of flow studies in a vaned diffuser entrance region, presented in this paper, are believed to accomplish the understanding of the flow within this sensitive flow area.

Test Rig and Instrumentation

A detailed description of the DFVLR centrifugal compressor test rig is given in [14]. The rig was equipped with the radial discharge impeller and the flat straight channel diffuser shown in Fig. 2.

The impeller's meridional geometry and its blade shape are displayed in Fig. 3. The rotor has 28 blades in total with 14 splitter blades.

Table 1 presents the vaned diffuser's geometry.

Table 1 Diffuser design parameters

diffuser parameter	description
$r_3/r_2 = 1.1$	radius ratio diffuser leading edge/impeller exit
$r_4/r_2 = 1.905$	radius ratio diffuser discharge/impeller exit
AS = 1.6	throat aspect ratio
$l/h_{3th} = 11.46$	length/width ratio of the channel diffuser
$2\epsilon = 7.54°$	channel divergence angle
$\alpha_{v3} = 17.32°$	diffuser vane stagger angle
$z_d = 27$	blade number

The diffuser design procedure was based on Runstadler's flat diffuser performance maps [2] and is displayed in [3].

The experimental investigations have been mainly concerned with optical impeller and diffuser entrance flow analysis. Laser measurements within the absolute and relative frame have been carried out successfully by means of the advanced automated Laser-Two-Focus (L2F) velocimeter developed by Schodl at the DFVLR, Cologne [4]. Compared to the previous, rather time consuming system [5], a con-

Nomenclature

AS = diffuser throat aspect ratio
c = absolute velocity
HU = hub
l = channel diffuser length
M = Mach number
$\dot{m}$ = mass flow rate
n = shaft speed
PS = pressure side
SH = shroud
s = impeller shroud length
SS = suction side
u = circumferential velocity or direction
w = relative velocity
x = meridional impeller shroud coordinate
y/t = dimensionless blade pitch
z = blade number
z/b = dimensionless meridional channel depth
α = absolute flow angle (reference to the positive circumferential direction)
α_{v3} = diffuser vane stagger angle (reference to the positive circumferential direction)
β = relative flow angle (reference to the negative circumferential direction)
2ϵ = diffuser channel divergence angle
Π = pressure ratio
Ψ_{ht} = work input factor $\Psi_{ht} = c_u \cdot u/(u_2^2/2)$

Subscripts

1 = inducer inlet
2 = impeller exit
3 = diffuser leading edge
4 = diffuser discharge
c = absolute
d = diffuser
i = impeller
R = rotor
rel = relative
st = stage
t = total
th = throat

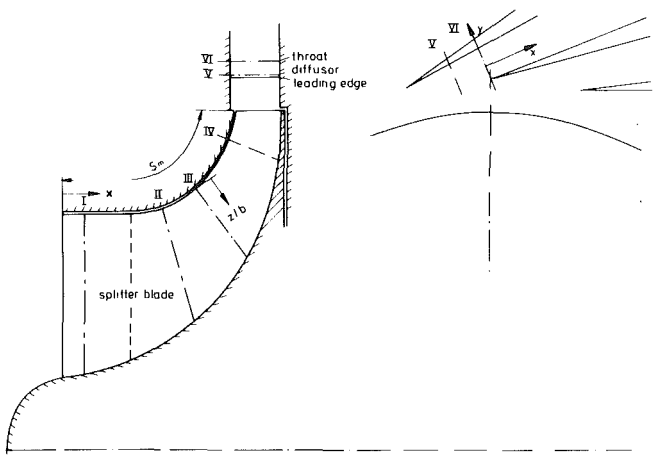

Fig. 4 Locations of the optical measurement planes within the impeller and the diffuser entrance region

siderable time reduction by a factor of 10 was achieved. The computer-controlled two-dimensional measurement system gives information about the magnitude and direction of the mean absolute flow vector and its turbulent components. The corresponding relative flow vector is easily calculated by means of the known circumferential velocity. Generally, the error of mean velocity measurements is below ± 1 percent. Only in the wake region and for measurements close to the hub and shroud an increased uncertainty must be taken into account (± 3 percent). The uncertainty of flow angle measurements generally is less than ± 1 deg; within regions of separated flow the estimated error may raise up to ± 3 deg. Furthermore the advanced laser velocimetry offers the possibility to perform separate flow field measurements within adjacent blade channels of a centrifugal compressor impeller permitting a detailed experimental flow field study also within a splitter blade impeller. Non intrusive optical measurements within the rotor and diffuser display the flow field development from inducer inlet to diffuser entrance. Thus, useful information about the real flow process within a centrifugal compressor stage, operating under realistic conditions is available, e.g. to support advanced flow field theories [6,7,8,9,10,12].

During compressor operation total temperature as well as total pressure measurements have been performed. A computer-controlled operating ensured a continuous shaft speed and mass flow correction throughout the test period. Mass flow was measured by means of a venturi nozzle located within the inlet pipe.

Discussion of the Experimental Results

Figure 4 illustrates the arrangement of the optical measurement planes from inducer inlet to diffuser entrance. The positions within the rotor are submitted in Table 2. The measurement planes are throughout perpendicular to the shroud.

Table 2 Positions of laser measurement planes within the rotor region

Measurement plane	Location x/sm
I	0.08
II	0.43
III	0.59
IV	0.87

Measurement planes V and VI are located within the vaned diffuser entrance region, with plane V situated within the "zone of rapid adjustment," 20mm ahead of plane VI that coincides with the diffuser throat.

Figures 5 to 8 represent the flow field development within the splitter blade impeller for n = 14000 min^{-1}, $\dot{m}$ = 5.8 kg/s. During these measurements the compressor was equipped with the vaneless diffuser of constant width mentioned before. Figure 5 shows the comprehensive flow characteristics for measurement plane I located in the axial inducer part, 28mm ahead of the splitter blade leading edge (Fig. 4). The meridional velocity, referred to the rotor tip speed c_m/u_2, the local work input factor Ψ_{ht}, the dimensionless relative velocity w/u_2 and the absolute as well as the relative flow angles (α,β) are plotted versus flow area. The pressure side of the blade, designated PS, is situated on the left, the suction side SS on the right, hub and shroud in the rear and in front, respectively. Measurement points are marked by circles. Obviously up to 14 points are gathered by the new laser technique across one blade pitch, which enables the user to reconstruct the flow pattern. In this region the flow field is very regular. The meridional velocity raises slightly from the pressure to the suction side of the blade and from shroud to hub. The local work input factor Ψ_{ht} indicates throughout a positive loading and raises due to the increasing circumferential velocity from hub to shroud. The corresponding relative velocity pattern displays the reverse shape expected. Since the impeller is operating without inlet swirl, the absolute flow angle α to be expected at the inducer leading edge is about 90 deg. Compared to this value, Fig. 5 reveals a weak flow deflection near the shroud and an increased turning close to the hub. This is due to the blade geometry (elliptical camberline, radially directed blades), which imposes an enhanced flow turning near the hub. Correspondingly the relative flow angle β raises from shroud to hub, whereas it is nearly constant across the blade pitch, indicating a blade congruous flow in this region. Altogether the flow field exhibits the characteristics of an inviscid fluid, which agrees largely with experimental and theoretical results obtained previously at the DFVLR [9,11].

Similarly Fig. 6 illustrates the meridional flow pattern for plane II located aft of the splitter blade leading edge. The two channels shown are divided by the splitter blade.

Compared to plane I the flow exhibits an increased velocity gradient in the shroud region (z/b = 0.1), which is slightly steeper within both channels. Due to the lengthened flow path a more pronounced boundary layer thickness is recognized at the suction side of the right channel, accompanied by a declining meridional velocity near shroud (z/b = 0.1).

Significantly deviating flow patterns within adjacent channels are observed in plane III (Fig. 7). The velocity profile displays an increased blade loading within the left, whereas a declined gradient is observed within the right channel.

A noticeable boundary layer accumulation occurs at the suction side of the right flow channel, accompanied by an increased meridional velocity along the pressure side, which indicates a premature tendency for separation.

The following Fig. 8 shows the flow situation in plane IV near impeller exit. In this position the velocity profile exhibits a distinct jet/wake pattern. The wake accumulates near the shroud. Particularly in the shroud/suction side region the wake is observed to be farther developed within the right than in the left flow duct. Compared to previous measurements within radial discharge and backswept impellers [11], the wake now covers a larger fraction of the flow area and its point of minimum velocity has shifted towards the middle of the flow channel. The stronger wake development seems to be due to the increased blade number (28 instead of 20) resulting in an increased blade friction surface of about 14 percent.

Figure 9 shows an additional result taken in plane IV and demonstrating the effect of a vaned diffuser on the internal

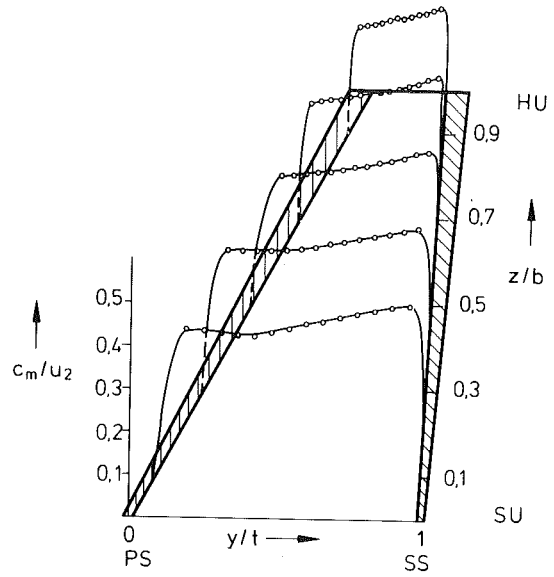

5(*a*) Meridional velocity

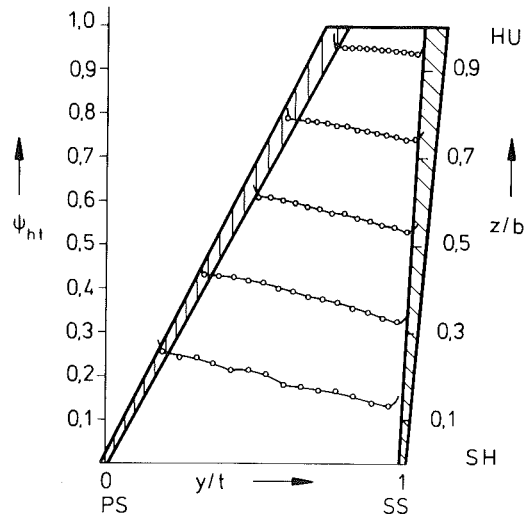

5(*b*) Work input factor

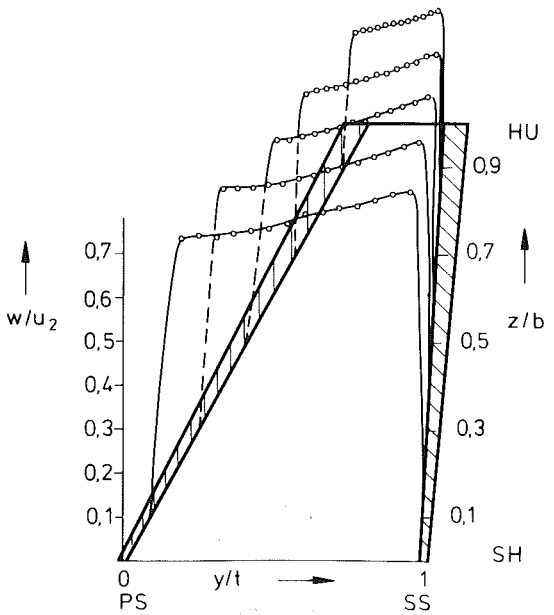

5(*c*) Relative velocity

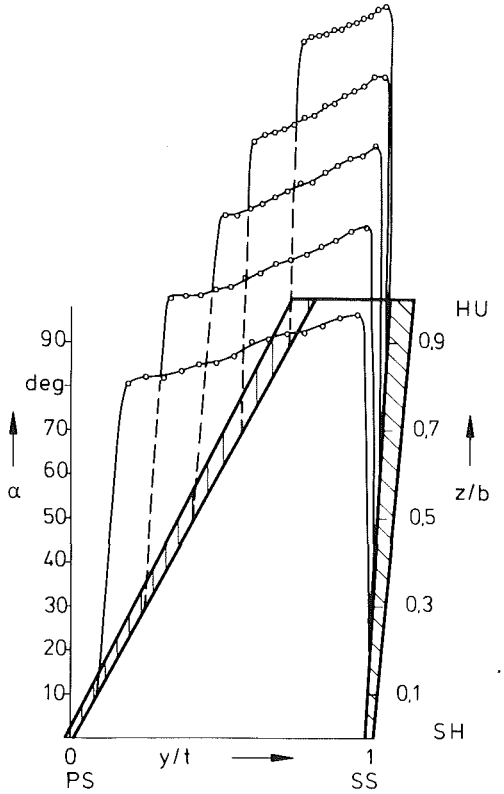

5(*d*) Absolute flow angle

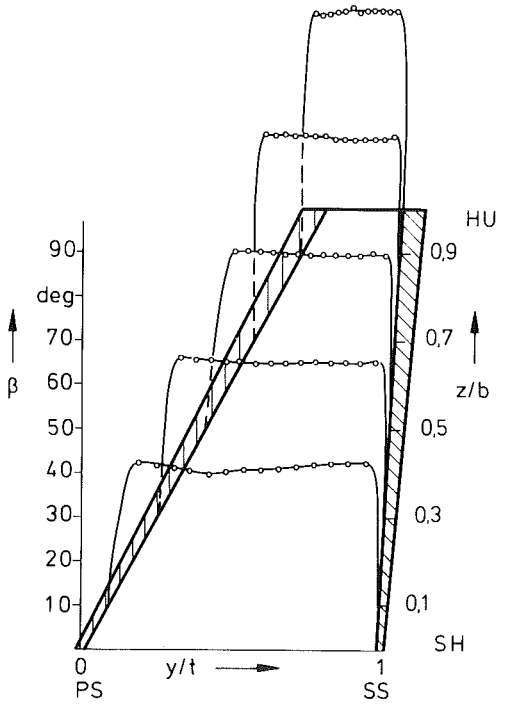

5(*e*) Relative flow angle

Fig. 5 Flow characteristics at measurement plane I: Meridional velocity c_m/u_2, work input factor Ψ_{ht}, relative velocity w/u_2, absolute flow angle α, relative flow angle β, n = 14000 min^{-1}, $\dot{m}$ = 5.8 kg/s

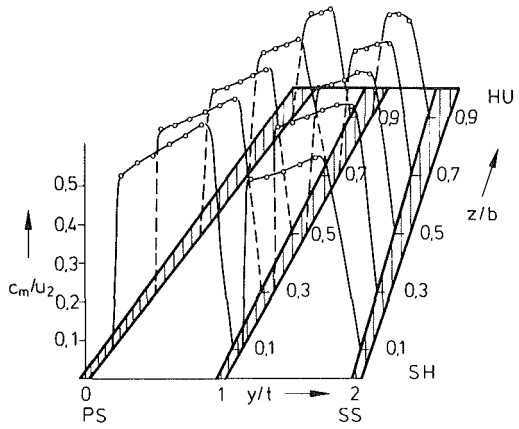

Fig. 6 Distribution of the meridional velocity within neighboring channels at measurement plane II, n = 14000 min^{-1}, $\dot{m}$ = 5.8 kg/s

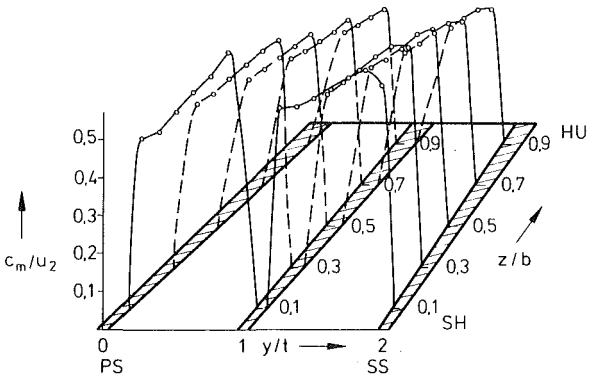

Fig. 7 Distribution of the meridional velocity at measurement plane III, n = 14000 min^{-1}, $\dot{m}$ = 5.8 kg/s.

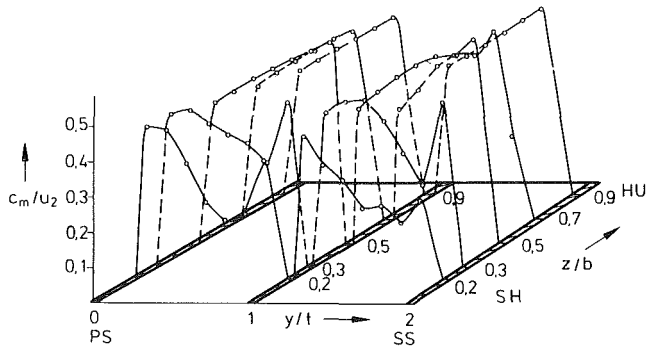

Fig. 8 Distribution of the meridional velocity at measurement plane IV, n = 14000 min^{-1}, $\dot{m}$ = 5.8 kg/s, vaneless diffuser

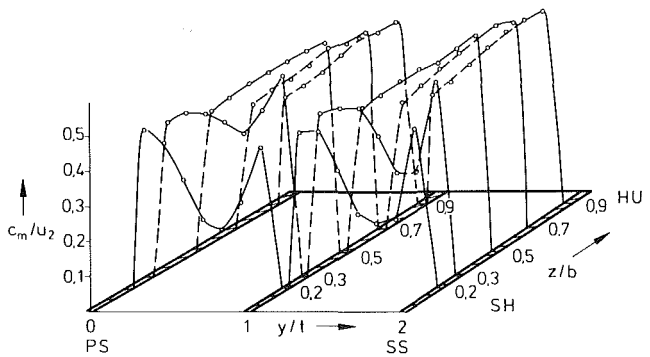

Fig. 9 Distribution of the meridional velocity at measurement plane IV, n = 14000 min^{-1}, $\dot{m}$ = 5,8 kg/s, vaned diffuser

impeller flow. The compressor is now equipped with the wedge vaned diffuser shown in Fig. 2. Compared to Fig. 8 a slightly different velocity profile is observed in the shroud region, whereas the velocity patterns are very similar to each other in the hub region. The diffuser blade reaction on the internal impeller flow is already negligible near impeller exit for the operating point investigated (II_t = 2, Mc_2 = 0.7).

This may change if supersonic diffuser leading edge Mach numbers occur and shocks extend into the impeller discharge region. Furthermore the result obtained certainly depends on the special diffuser parameters involved (Table 1). For instance a decreased diffuser leading edge/impeller exit radius ratio r_3/r_2 may result in a more pronounced deviation of the internal impeller flow patterns.

The diffuser is exposed to the highly distorted flow shown in Fig. 9 that points to the heavily unsteady flow character within the absolute frame. Measurements within this region are extremely difficult because the flow is very sensitive and any merging probes may change the flow pattern significantly. Therefore the nonintrusive laser velocimetry seems to be the most appropriate measurement technique to analyze this three-dimensional unsteady flow field.

Dean and Senoo [13] claimed that the distorted flow pattern discharged from the impeller should be mixed out at very low radius ratios in the radial plane, sometime as low as 1.02. It is assumed that this is due to the shear and work exchange between the jet and wake in the absolute frame resulting already in axisymmetric flow at relatively low radius ratios. It has been pointed out by Dean [1] that this is not true for the meridional plane distortion, which is presumed to mix rather slowly.

The following figures reveal the optically measured, unsteady flow character within the diffuser entrance region. Four of 16 analyzed rotor positions have been selected to illustrate the complex flow phenomena within this area (positions 1,5,9,13). Figure 10 represents the unsteady flow behavior within the "zone of rapid adjustment," plane V. The absolute flow vector, referred to the rotor tip speed c/u_2, is plotted versus flow channel for 30 distinct points. Rotor position 1 shows a flow pattern slightly twisted from hub to shroud. The flow is mainly directed towards the suction side of the blade which agrees with the results of conventional flow angle measurements performed ahead of the diffuser leading edge [3]. However, a considerable flow angle variation is observed from hub to shroud. The succeeding rotor positions (positions 5,9,13) illustrate the unsteady flow character within this plane. In conjunction with the proceeding rotor the velocity vector turns towards the "pressure side" in the shroud region, whereas near hub the vector keeps bent towards the suction side of the diffuser blade. A highly twisted flow pattern occurs for rotor position 9, where the flow has a pronounced tendency towards the blade pressure side within the shroud region (z/b = 0.1), whereas in the rear part of the channel the flow tends predominantly toward the blade suction side.

A detailed illustration of the unsteady flow motion is given in Fig. 11. The angle $\Delta\alpha^*$ between the velocity vector and the normal of measurement plane V is plotted versus flow channel. Thus, $\Delta\alpha^*$ represents the velocity component parallel to the measurement plane. The proceeding rotor initiates a continuous variation of $\Delta\alpha^*$ within the whole flow channel. Maximum flow angle fluctuations of about 17 deg are observed in the shroud region (z/b = 0.1), which is obviously due to the wake pattern discharged by the rotor. A smaller variation is observed within the remaining part of the flow channel (z/b > 0.1). Nevertheless local flow angle

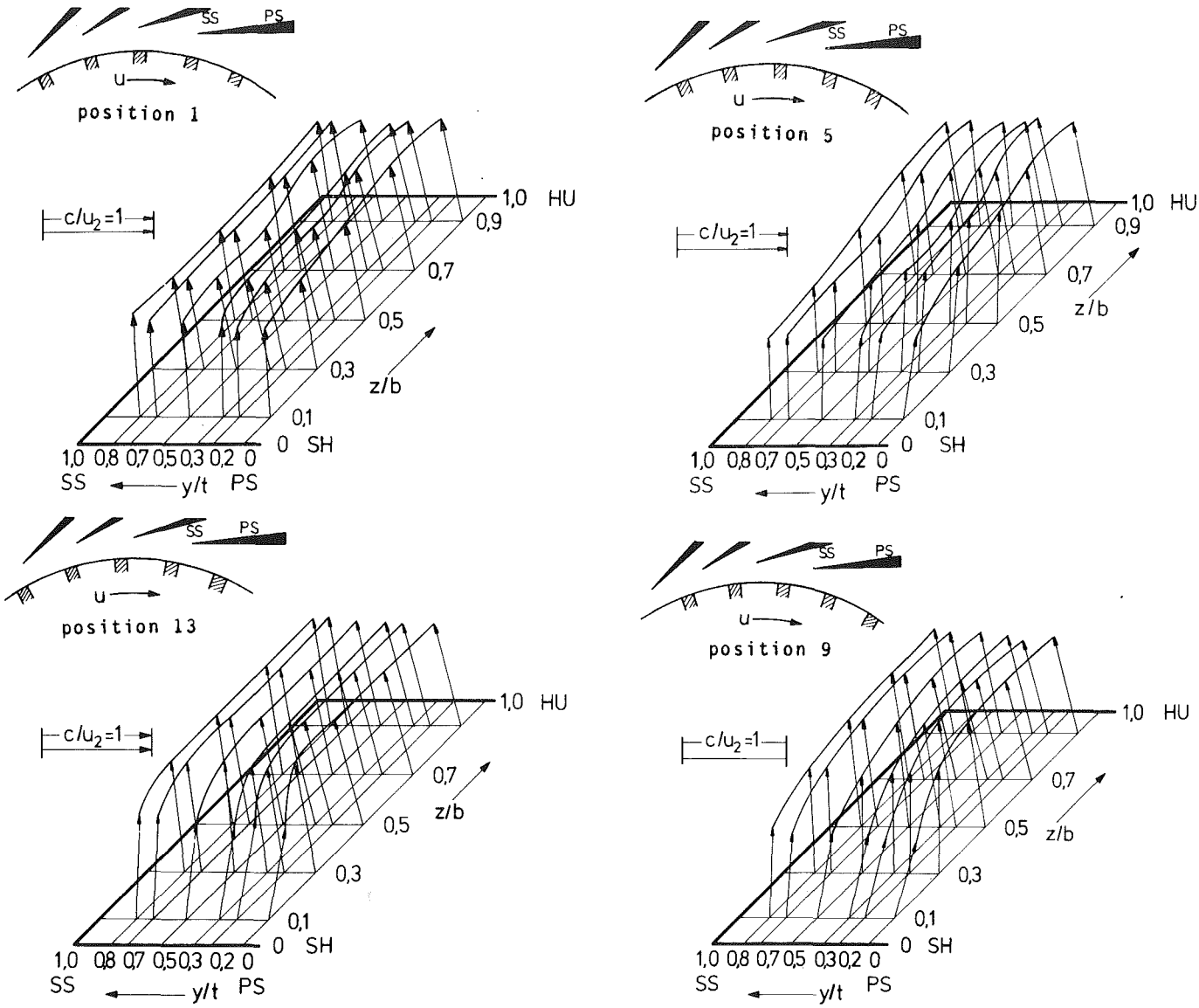

Fig. 10 Unsteady flow vector field at measurement plane *V*, n = 14000 min^{-1}, $\dot{m}$ = 5.8 kg/s

differences up to 7 degrees occur even in the rear part ($z/b \geq 0.7$). For the fixed rotor position 9 a maximum flow angle difference from hub to shroud of 22 deg is present at the channel mean center line ($y/t = 0.5$).

Besides the flow angle the magnitude of the flow vector fluctuates too, as illustrated in Fig. 12. The magnitude of the absolute flow vector, referred to the rotor tip speed c/u_2, is plotted against rotor positions for three meridional locations on the channel mean center line ($z/b = 0.1,0.5,0.9$; $y/t = 0.5$). Maximum velocities, accompanied by fluctuations of about 20 percent are observed in the middle of the flow channel ($y/t = 0.5$, $z/b = 0.5$), whereas decreasing velocities and fluctuations are recognized near the shroud ($z/b = 0.1$) and hub ($z/b = 0.9$). Lowest velocities with a still 17 percent fluctuation during one period are observed near the shroud. The flow approaches already steady state conditions in the hub region.

A flow field similar to that in plane V, but shifted in time, is discovered within the diffuser throat (plane VI). The unsteady flow character at this position is illustrated in Figs. 13 to 15. The flow field is plotted for the same rotor positions as previously discussed (positions 1,5,9,13). Figure 13 shows the variation of the absolute flow vector. As in plane V, a continuous change in flow direction is recognized in the shroud region, whereas the flow has a component towards the suction side of the blade in the rear part of the channel. A comparison between Figs. 10 and 13 reveals a timelag of about 8 rotor positions, which is equivalent to 50 percent rotor blade pitch. For example the flow observed for rotor position 1 in plane V corresponds to the flow measured at rotor position 9 in plane VI. A similar time shift is observed for the additional three rotor positions presented.

The following Fig. 14 represents the flow angle variation $\Delta\alpha^*$ within the throat area. Corresponding with the upstream flow conditions in plane V, maximum flow angle fluctuations are observed in the shroud region (13 deg). Although the flow does not change its direction within the residual part of the channel ($z/b > 0.1$), the local flow angles differ up to 10 degrees at the channel center line ($y/t = 0.5$) and along the blade pressure side ($y/t = 0.1$). Due to the prediffuser's guidance a decreased variation is recognized near the suction side of the blade. For the fixed rotor position 1 a maximum

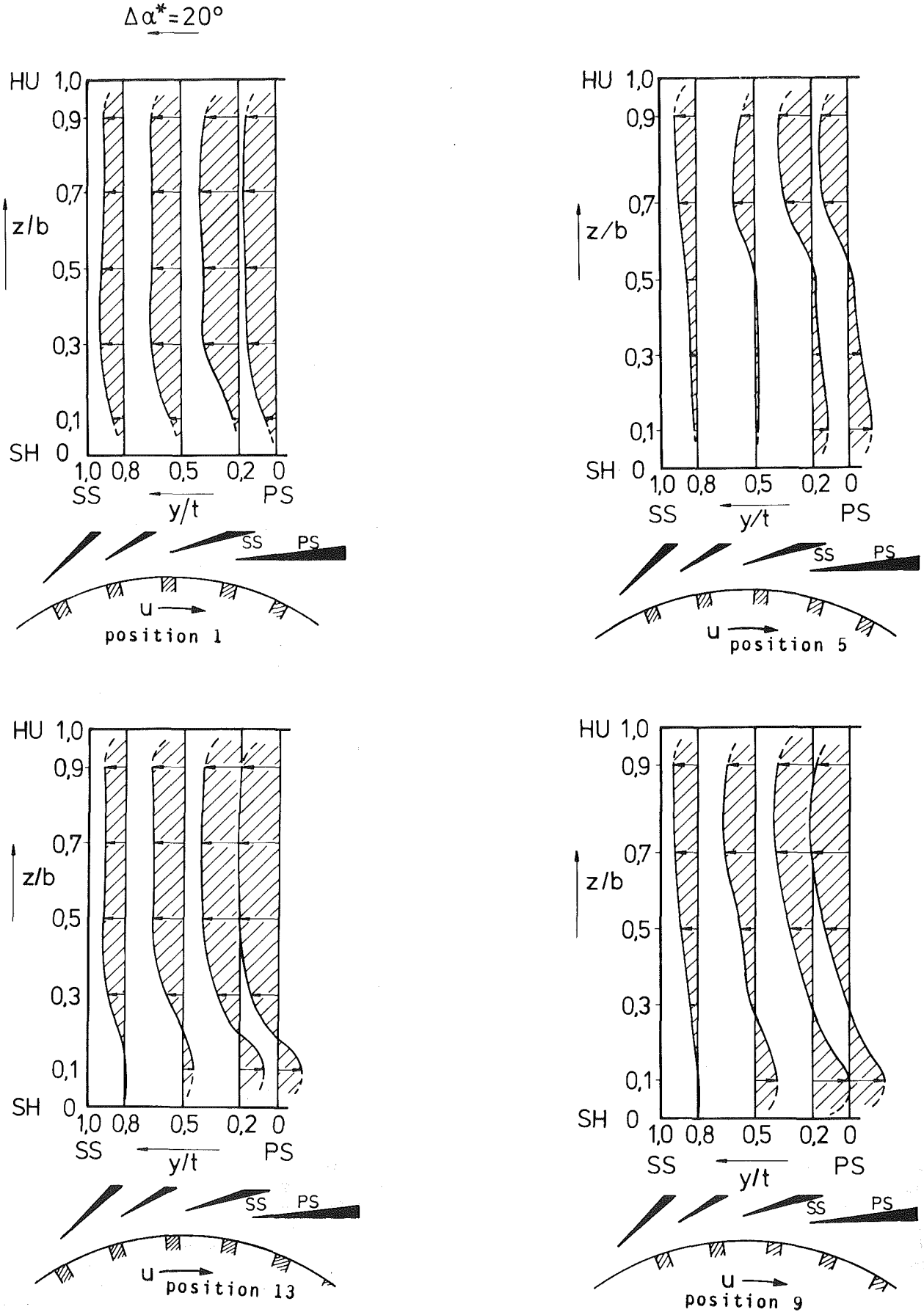

Fig. 11 Unsteady flow direction at measurement plane V, n = 14000 min^{-1}, $\dot{m}$ = 5.8 kg/s

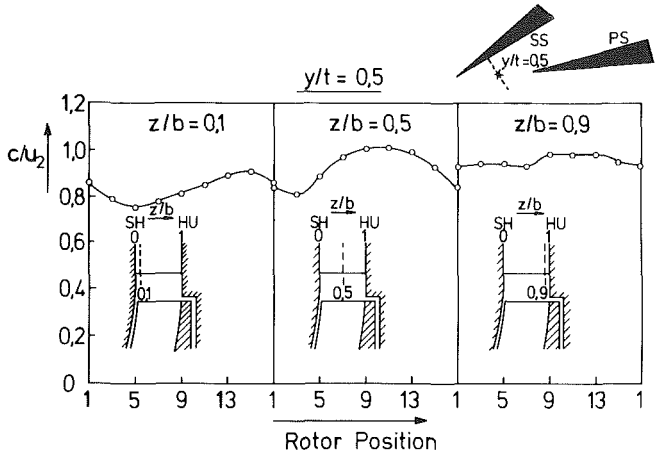

Fig. 12 Fluctuations of the flow vector's magnitude at the channel mean center line (y/t = 0.5), measurement plane V, n = 14000 min^{-1}, $\dot{m}$ = 5.8 kg/s

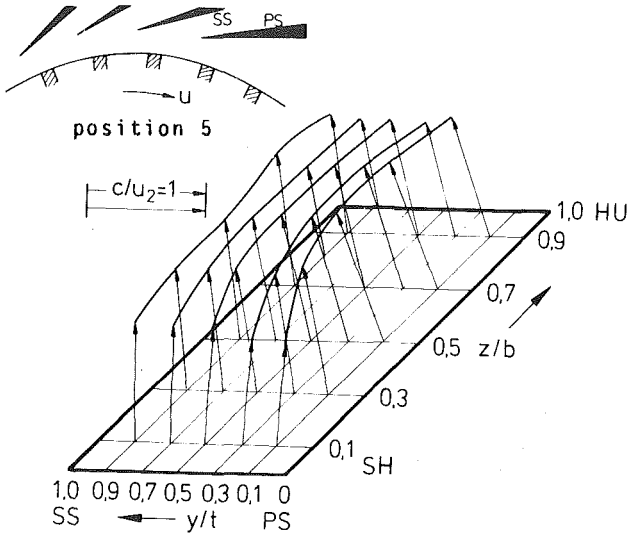

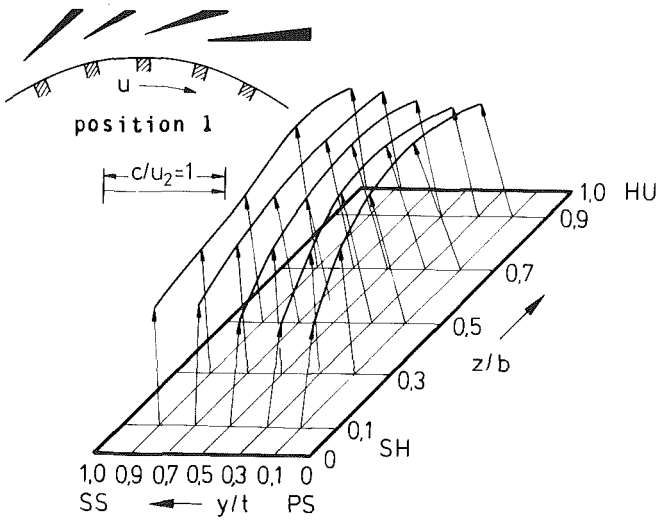

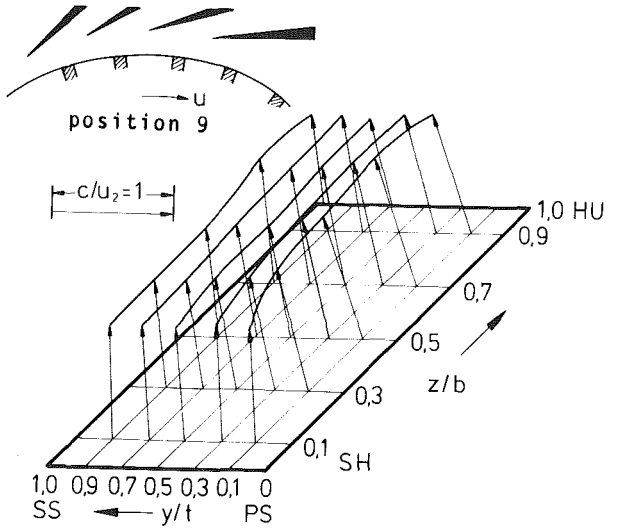

Fig. 13 Unsteady flow vector field within the diffuser throat, measurement plane VI, n = 14000 min^{-1}, $\dot{m}$ = 5.8 kg/s

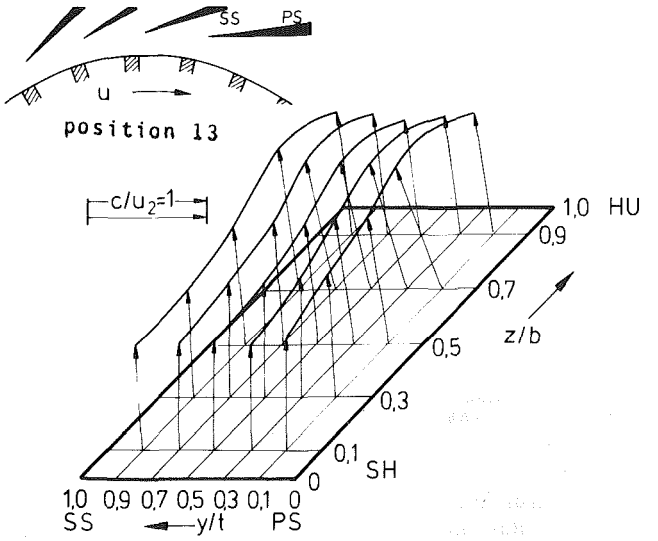

flow angle variation of 27 deg is present from hub to shroud near the blade pressure side (y/t = 0.1), which is due to the diffuser leading edge displacement effect.

It should be noted that according to the results presented there doesn't exist any station ahead of the diffuser throat where the flow is fully mixed out. Consequently diffuser design procedures, based on steady state and/or mixed out conditions, seem to be questionable. Perhaps it is the heavily unsteady flow behavior in the prediffuser and channel diffuser entrance region, which causes very often incorrect diffuser recovery prediction. It has been pointed out previously that the application of Runstadler's channel diffuser performance maps [2] requires a precise throat blockage prediction. However, today's boundary layer calculation methods are predominately based on a steady-state approach and therefore don't take care of unsteady crossflows like those shown in Figs. 11 and 14. The extraordinary flow behavior discovered will cause such an analysis to fail. Furthermore, a significant velocity profile

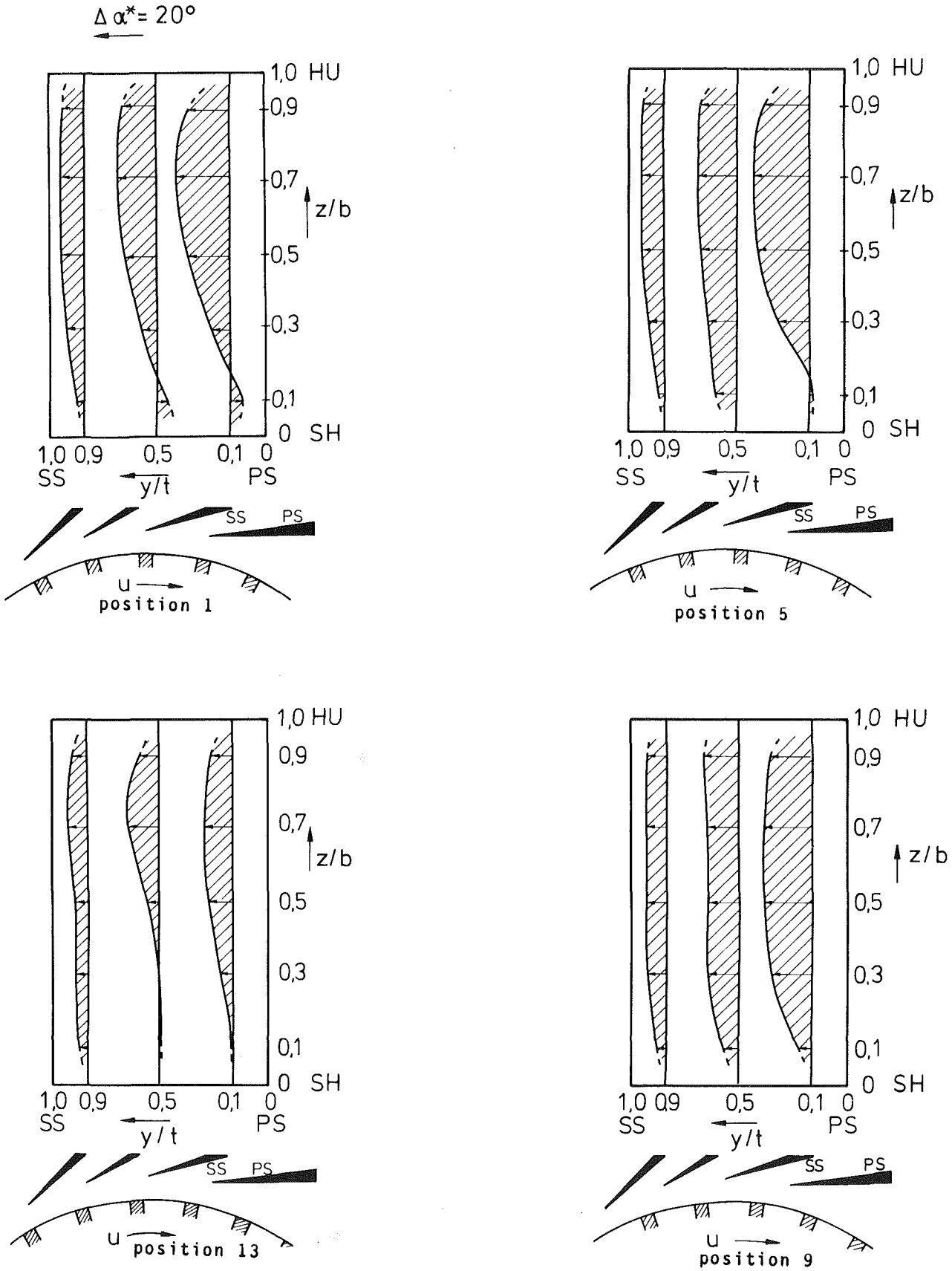

Fig. 14 Unsteady variation of the flow direction within the diffuser throat, measurement plane VI, n = 14000 min^{-1}, m = 5.8 kg/s

distortion from hub to shroud and a pulsating flow, even within the channel diffuser throat, is observed, which additionally complicates precise channel diffuser recovery prediction, because these effects are very often neglected in empiricial diffuser data available.

Fig. 15 illustrates the unsteady and periodically fluctuating

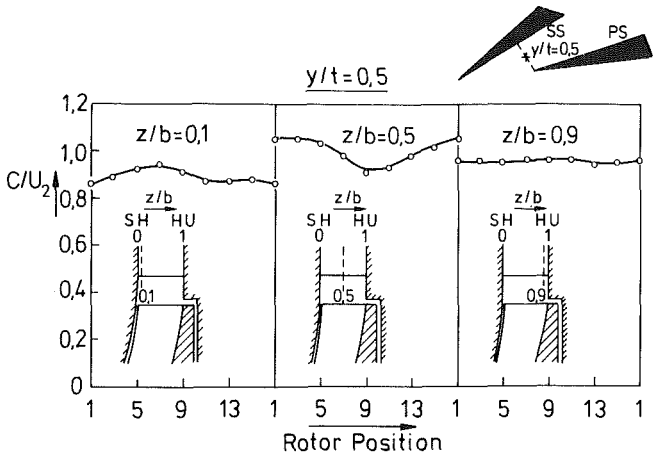

Fig. 15 Fluctuations of the flow vector's magnitude at the channel mean centerline (y/t = 0.5), measurement plane VI, n = 14000 min^{-1}, $\dot{m}$ = 5.8 kg/s.

magnitude of the flow at the channel mean centerline (y/t = 0.5). As in Fig. 12, three equally spaced meridional positions have been selected (z/b = 0.1,0.5,0.9). Compared with the flow conditions in plane V, the time lag of 8 rotor positions is again clearly identified. However, the fluctuation intensity has decreased from plane V to plane VI. A decline of 6 and 4.5 percent occurs at the middle of the flow channel (y/t = 0.5, z/b= 0.5) and close to the shroud (y/t = 0.5, z/b = 0.1) respectively. The rather small fluctuation observed near the hub at plane V has faded out at plane VI.

Conclusions

The internal flow field development within a centrifugal compressor stage has been investigated by means of an advanced automated Laser-Two-Focus velocimeter. The compressor has a radially ending splitter blade impeller coupled with a vaneless and vaned diffuser, respectively.

Comparative measurements within the impeller discharge region for both the vaneless and vaned diffuser design reveal only weak influences of the vaned diffuser on the rotor flow field. It is presumed that this is due to the low subsonic diffuser leading edge Mach number and to the special vaned diffuser design with a rather high diffuser leading edge/impeller exit radius ratio (r_3/r_2 = 1.1).

Separately performed measurements within adjacent channels of a splitter blade impeller reveal different flow patterns aft of the splitter blade leading edge. The lengthened flow path along the suction side of the main blade causes an increased boundary layer development, accompanied by a premature tendency to separation.

A highly distorted, unsteady flow character has been analysed within the vaned diffuser entrance region. Unsteady local flow angle variations up to 17 deg occur within the "zone of rapid adjustment." Within the diffuser throat, a variation of 13 deg in flow angle is analyzed indicating that the impeller discharge flow keeps highly unsteady up to the channel diffuser throat. With respect to the flow vector's magnitude maximum periodical fluctuations of 14 percent are discovered within the throat.

References

1 Dean, R.C.,Jr. "The Fluid Dynamic Design of Advanced Centrifugal Compressors," Creare, TN-185, July 1974, p. 76.

2 Runstadler, P.W.,Jr., Dolan, F.X., Dean, R.C., Jr. *Diffuser Data Book,* Creare, TN-186, 1975, p. 88.

3 Krain,H., Experimental and Theoretical Investigations on the Internal Flow in a Centrifugal Compressor Diffuser, AGARD-Conference "Centrifugal Compressor, Flow Phenomena and Performance" in AGARD-CP 282, 1980, pp. 1/1 - 1/17.

4 Schodl,R., A Laser-Two-Focus (L2F) Velocimeter for Automatic Flow Vector Measurements in the Rotating Components of Turbomachines, ASME-Paper 1980, in "Measurement Methods in Rotating Components of Turbomachinery," pp.139–147.

5 Schodl,R., "Laser-Dual-Beam Method for Flow Measurements in Turbomachines," ASME-Paper, 74-GT-157, p. 7.

6 Howard,J.H.G., and Osborne,C., A Centrifugal Compressor. Flow Analysis Employing a Jet-Wake Passage Flow Model." ASME JOURNAL OF FLUIDS ENGINEERING, 1977, pp. 141–147.

7 Moore, J., Moore, J.G., "Calculations of Three-Dimensional, Viscous Flow and Wake Development in a Centrifugal Impeller," ASME-Paper 1980, in "Performance Prediction of Centrifugal Pumps and Compressors," pp. 61–67.

8 Hirsch, Ch., Warzee, G., "A Finite Element Method for Through-Flow Calculations in Turbomachines," ASME-Paper, 76-FE-12.

9 Krain, H., and Eckardt, D., "The Flow Field in a High-Speed Centrifugal Impeller. A Comparison of Experimental and Theoretical Results," *Proc. First International Conference on Centrifugal Compressor Technology,* Feb. 1978, B1-25, Madras.

10 Bosman, C., and El-Shaarawi, M.A.I., Quasi-Three-Dimensional Numerical Solultion of Flow in Turbomachines, ASME *Journal of Fluids Engineering,* Vol. 99, 1977, pp. 132–140.

11 Eckardt, D., "Flow Field Analysis of Radial amd Backswept Centrifugal Compressor Impellers, Part. 1: Flow Measurements Using a Laser Velocimeter," ASME-Paper 1980, in "'Performance Prediction of Centrifugal Pumps and Compressors," pp. 77–86.

12 Schuster, P. and Schmidt-Eisenlohr, U., "Flow Field Analysis of Radial and Backswept Centrifugal Compressor Impellers, Part 2: Comparison of Potential Flow Calculations amd Measurements," ASME-Paper 1980, in "Performance Prediction of Centrifugal Pumps and Compressors," pp. 87–95.

13 Dean, R.C., Jr., and Senoo, Y., "Rotating Wakes in Vaneless Diffusers," ASME *Journal of Basic Engineering,* Sept. 1960, pp. 563–570.

14 Eckardt, D., "Instantaneous Measurements in the Jet-Wake Discharge Flow of a Centrifugal Compressor Impeller," ASME JOURNAL OF ENGINEERING FOR POWER, Vol. 97, No. 3, July 1975, pp. 337–346.

A Blockage Model for Centrifugal Compressor Impellers

R. C. Pampreen
Chrysler Corporation,
Power Plant Research,
Detroit, Mich. 48231
Mem. ASME

This paper presents and discusses the results of an analysis in which the blockage distributions of four impellers were deduced from shroud static pressure measurements. The purpose of the analysis was to provide a means of estimating blockage for the jet-wake flow model for use in impeller design calculations. A parameter was investigated for correlating the blockage values against the combined effect of diffusion, curvature, and Coriolis acceleration. It was found that gross blockage accumulation correlates against this parameter with an uncertainty in blockage of ± six percentage points. Up to the point of the axial-radial bend of the flowpath, the analysis shows that blockage is controlled equally by diffusion, flowpath curvature, and the combined effect of blade curvature and Coriolis acceleration. In the radial portion of the impeller, further increase in blockage is controlled by Richardson number.

Introduction

The design of centrifugal compressor impellers usually begins with a one-dimensional vector diagram analysis. The purpose of the calculations is to optimize performance parameters at design point or to obtain a balance in performance between design and off-design conditions. This is primarily a one-dimensional analysis with loss, stall, and flow deviation models to establish estimates of efficiency and surgefree range. The calculations determine overall flowpath dimensions and inlet and exit blade angles. Examples of preliminary design methods are shown in [1-3].

The next step consists of two-dimensional calculations within the blade-row to obtain the final blade shape and flowpath configuration. These calculations frequently use the equations of motion formulated in terms of streamline curvature with the assumptions of compressible, axisymmetric flow. Examples of the equations are shown in [4] for isentropic flow and in [5, 6] for flow with losses. Blade surface velocities are computed from the assumption of zero absolute rotational motion between blades.

The designer performs these calculations with estimates for loss, blockage, and deviation angle. The flow direction is assumed to follow the blade direction within the blade-row. At the leading and trailing edges, incidence is assumed to decay, and deviation is assumed to start somewhere within the passage, based on experience or design judgment. The assumptions of loss and blockage also depend on the designer's past experience or judgment. Examples are shown in [2, 3, 7, 8]. However, for many years, the jet-wake flow model has been advocated in many published works.

Moore, et al. [9] present a summary of experimental and analytical work in support of this model. It is pointed out in [9] that this model dates back to 1902 in the blade-to-blade flow visualization tests of Smith [10]. Also mentioned in [9] is the analytical support of the model from the work of Carrard [11, 12] (also discussed by Stodola [13]) and the elaborate flow visualization tests of Fischer and Thoma [14]. Quantitative experimental support for the model and for 3-D effects are shown by the flow distribution measurements of Hamrick et al. [15] and of Eckardt [16]. Additional measurements are reported by Fowler [17] and Johnson and Moore [18] at impeller tip speeds of 5 to 7 m/s and 24 m/s, respectively. Additional flow visualization results are reported by Senoo et al. [19], Lennemann and Howard [20] and Mizuki, et al. [21, 22, 23].

The velocity distributions and flow patterns from impeller tests show a variety of results that are informative but may only have significance for a particular design or test point. Tip speeds in the references vary from 5 to 400 m/s, and the flow field in the blade channel changes between stall and maximum flow. Nevertheless, the test results show the effects of streamline curvature, Coriolis force and secondary flow on the flow kinematics. These effects, plus the pressure gradient of the diffusing flow in the blade passage, make a combined impact on the stability of the impeller boundary layer. Consequently, it would be difficult to generate a flow model which, on the basis of such tests, quantitatively estimates the relative influence of the individual effects.

There has, however, been basic research into the influence of the individual effects on the stability of boundary layer and fully developed channel flows. The effect of curvature on stability is summarized in a comprehensive review by Bradshaw [24]. The effect of Coriolis force on stability is

Contributed by the Gas Turbine Division and presented at the International Gas Turbine Conference, Houston, Texas, March 8-12, 1981, of THE AMERICAN SOCIETY OF MECHANICAL ENGINEERS. Manuscript received at ASME Headquarters, December 4, 1980. Paper No. 81-GT-11.

shown in the rotating duct tests of Moore [25] and Koyama, et al. [26], and in the water channel tests of Halleen and Johnston [27] and Lezius and Johnston [28]. The combined effect of pressure gradient (diffusion) and Coriolis force is shown in the work of Rothe and Johnston [29]. The combined effect of pressure gradient, Coriolis force and secondary flow is shown in the rotating duct test of Moore [30]. The combined effect of Coriolis force and secondary flow is shown in the rotating duct tests of [31, 32, 25].

Ultimately, the impeller designer or flow analyst would like a 3-D boundary layer calculation procedure to combine with a 3-D, or at least a 2-D, axisymmetric potential flow calculation. Some progress has been made toward this goal in boundary layer flow. From the rotating duct and channel tests, mathematical correlations have been deduced for the effect of rotation on skin friction coefficient and the velocity distribution [25, 26, 27, 30] and the mixing length [33]. The combined effect of curvature and rotation has been correlated by Johnston and Eide [34]. The effect of rotation on diffuser static pressure recovery has been measured by Rothe and Johnston [29] for a length/width ratio of 6 and for area ratios from 1 to 3. However, as the authors point out, more investigations are needed to obtain a comprehensive comparison against stationary diffuser data with other values of length/width ratio and over a wider range of area ratio. In the area of complete flow model calculations, Moore [35] presents a 3-D calculation for the effect of rotation on secondary flows in low aspect ratio rotating ducts; the results agree well with the experimental results in [30].

To start progress toward an improved impeller design approach and in lieu of a fully developed boundary layer calculational procedure, the designer could use a blockage model in combination with isentropic potential flow. For such a model, the designer would need to know how rotor exit blockage varies with blade and flowpath curvatures and with rotation number. This would permit the designer to estimate the static pressure recovery of the blade channel. In addition, the meridional distribution of blockage must be known in order to accurately estimate the velocity distribution through the rotor and the blade loading.

As a step toward establishing such a model, the experimental blockage distributions of four rotors are presented in this paper. These distributions are based on shroud static pressure measurements made at a variety of tip speeds and mass flows for each rotor. An attempt is made to correlate blockage against a parameter which reflects the components of centripetal and Coriolis accelerations, along with the effect of flow deceleration within the blading. The derivation of such an acceleration parameter from the equations of motion is outlined below. Then the acceleration parameter is reviewed for possible correlation against blockage data. The blockage values used are the blockages at the point of minimum velocity within the blade channel and the blockage at rotor exit.

Blockage Correlation Approach

Experimental results in the references previously cited have shown that boundary layer stability in curved channels depends on the ratio of the boundary layer thickness to the radius of curvature of the wall. Curvature stabilizes the boundary layer on the convex surface and destabilizes it on the concave surface. Likewise, the stability of boundary layers in rotating channels depends on the rotation number, with boundary layer thickness as the reference dimension. System rotation stabilizes the boundary layer on the trailing surface and destabilizes it on the leading surface. Johnston and Eide [34] combine these effects to obtain an expression for mixing length which accounts for rotation and curvature.

The view taken in the channel experiments is to investigate the stability of the boundary layer as it is affected by curvature and rotation and as it, in turn, affects such things as pressure recovery and free-stream velocity distribution. In lieu of established procedures for computing boundary layer characteristics in impellers, the designer would find it useful to know the distribution of blockage in terms of the forces imposed on the boundary layer by freestream conditions. This is similar to diffuser recovery characteristics. The boundary layer in the diffuser is affected by the pressure gradient imposed by the geometry of the diffuser and the inlet blockage, and the boundary layer development, in turn, affects the static pressure recovery. Without knowing the internal boundary layer characteristics, the static pressure recovery can be related to the forces imposed on the boundary layer through diffuser area ratio and length/width ratio.

Similarly for impellers, it would be useful to relate experimentally determined values of blockage to the ideal flow conditions with zero loss, blockage and deviation angle. Such a relationship could provide the designer with an estimate of actual blockage to expect from the forces intended to be imposed on the flow under ideal conditions. The designer could then plan a blade angle distribution or flowpath width based on diffusion values closer to reality.

To obtain this relationship, it is necessary to use a

Nomenclature

a = blade spacing at maximum curvature, m
B = aerodynamic blockage, dimensionless
b = flowpath width at maximum curvature, m
g = gravitational constant, m/s/s
p = static pressure, kPa
R = radius, m
R_a = blade radius of curvature, m
R_b = meridional radius of curvature, m
S = flow direction, m
U = linear speed, m/sec
V = absolute velocity, m/s
W = relative velocity, m/s
β = relative flow direction, degrees
δ = meridional streamline direction, degrees
ρ = density, kg/m^3
ω = angular velocity, rads/sec

Subscripts

1 = impeller inlet
2 = impeller exit
max = maximum
min = minimum
r = radial direction
θ = tangential direction
z = axial direction

Figure Notation

st. pr. tap loc. = static press. tap location, vnls diff. = vaneless diffuser, vnd. diff. = vaned diffuser, calc. sta. = calculation station, $B(W_{min})$ = blockage at minimum velocity; positions of items on Figs. 4, 5, 6, and 7 on 50 percent massflow streamsheet: closed symbols = actual min. suct.-surf. vel., ideal min. vel. = ideal minimum velocity, splt. l. e. = splitter leading edge, t = center of throat, mbc = maximum blade curvature, mfc = maximum flowpath curvature

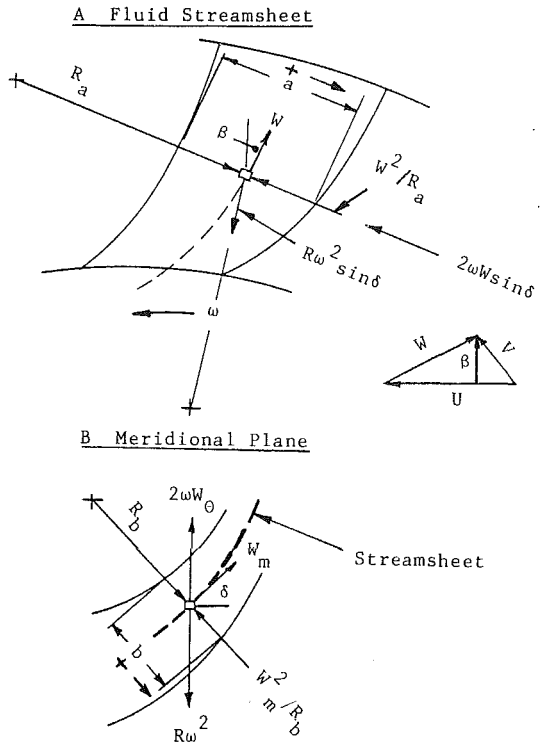

Fig. 1 Acceleration imposed on fluid particle as viewed on meridional plane and streamsheet

parameter that combines the parameters which relate to the physical effects of rotation and curvature (as shown by the channel experiments) with the effect of diffusion (as illustrated by the diffusion factor [36]). Such a parameter can be derived from the free-stream equations of motion in relative coordinates. To bring curvature into the equations, the acceleration components can be formulated as illustrated in Fig. 1 (similar to Balje [37]).

Summing forces in the direction of the blade radius of curvature,

$$R\omega^2(\sin\delta)\sin\beta - 2\omega W_r\cos\beta - 2\omega W_\Theta(\sin\delta)\sin\beta - W^2R_a = -(1/\rho)\partial p/\partial a$$

Since $W_r = W_m \sin\delta = W\cos\beta\sin\delta$, then, upon rearranging,

$$(1/\rho)\partial p/\partial a + R\omega^2\sin\delta\sin\beta = W^2/R_a + 2\omega W\sin\delta \quad (1)$$

Perpendicular to the blade radius of curvature,

$$2\omega W_\Theta\cos\beta\sin\delta - 2\omega W_m\sin\beta\sin\delta - R\omega^2\sin\delta\cos\beta + W\,dW/dS = -(1/\rho)\partial p/\partial S$$

Rearranging and putting in terms of resultant relative velocity,

$$(1/\rho)\partial p/\partial S - R\omega^2\sin\delta\cos\beta = -W\,dW/dS \quad (2)$$

Summing forces in the meridional plane and in the direction of the radius of curvature,

$$-W_m{}^2/R_b + R\omega^2\cos\delta - 2\omega W_\Theta\cos\beta = -(1/\rho)\partial p/\partial b$$

Rearranging and putting in terms of resultant relative velocity,

$$(1/\rho)\partial p/\partial b + R\omega^2\cos\delta = (W^2/R_b)\cos^2\beta + 2\omega W\sin\beta\cos\delta \quad (3)$$

It is next assumed that, for compressible flow, the speed of sound can be used as the characteristic velocity.

Introducing the channel widths, a and b, equations (1) - (3) become in dimensionless form,

$$(a/c^2)[(1/\rho)\partial p/\partial a + R\omega^2\sin\delta\sin\beta] = M^2[(a/R_a) + (2\omega a/W)\sin\delta] = P_B \quad (4)$$

$$(b/c^2)[(1/\rho)\partial p/\partial b + R\omega^2\cos\delta] = M^2[(b/R_b)\cos^2\beta + (2\omega b/W)\sin\beta\cos\delta] = P_F \quad (5)$$

Using the flowpath length, S, as reference dimension, equation (2) becomes

$$(S/c^2)[(1/\rho)\partial p/\partial S - R\omega^2\sin\delta\cos\beta] = -(M^2\ dW/W)\,dS/S \quad (6)$$

For diffusion without rotation and curvature, we are left with equation (6), and parameters such as loss coefficient or momentum thickness can be correlated against a diffusion parameter such as

$$\Delta V/V = 1 - V_{\min}/V_{\max}$$

This is the essence of diffusion factor for axial compressors [36]. If the flowpath is purely axial ($\delta = 0$ and $R_b \to \infty$), equations (4) and (5) simplify to terms containing the ratio of blade spacing to blade radius of curvature and to a Coriolis component that is perpendicular to the hub boundary layer but parallel to the blade boundary layers. If diffusion is accomplished primarily by blade curvature, then $\Delta V/V$ is related to a/R_a, and it is sufficient to correlate loss with diffusion.

For the centrifugal compressor, of course, blade curvature is large, and the flowpath has meridional curvature. Consequently, it will be necessary to keep all acceleration terms. A possible parameter to use for a blockage correlation would be one which is the vector sum of all three accelerations, namely,

$$AP = \sqrt{P_D^2 + P_B^2 + P_F^2} \quad (7)$$

where

$$P_D = M^2(\Delta W/W) = M^2(W_{\max} - W_{\min})/W_{\max} \quad (8)$$

It was thought that the value of the acceleration parameter, AP, could be based on fluid mechanic and geometric conditions at the points of maximum blade and flowpath curvatures and on the maximum diffusion achieved in the blading. Thus, the first term was evaluated on the suction surface of the 50 percent massflow streamline. The maximum and minimum velocities are taken from the velocity distribution based on ideal conditions. The values required in the second term are taken from ideal conditions at the blade minimum radius of curvature on the 50 percent streamline. The values in the third term are taken from ideal conditions at the flowpath minimum radius of curvature on the 50 percent streamline.

It was hypothesized that blockage might correlate against such a formulation of the acceleration parameter that contains the principal geometric and fluid mechanic features. If the points of minimum velocity and of the blade and flowpath curvatures coincided, the vector sum would be precisely true. Otherwise, the sum of the squares only approximates a vector sum, but it might be adequate for correlation purposes. The distance between the points of maximum blade and flowpath curvatures varied from 10 to 20 percent of the meridional distance of the impellers used in the study. The point of minimum velocity almost always occurred at or within 10 percent of the meridional distance of the maximum flowpath curvature.

Blockage Calculation Method

Blockage was computed from the shroud static pressure distributions obtained from compressor rig testing. The calculations were performed with a streamline curvature type of solution to the fluid mechanic equations of motion. The

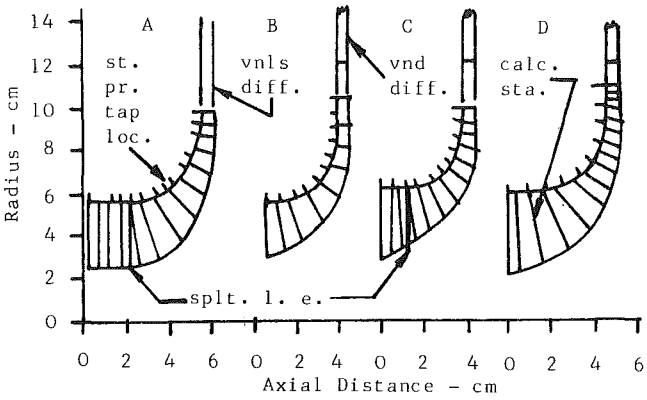

Fig. 2 Impeller geometry and design data

Impeller	A	B	C	D
Design speed, rpm × 10^{-3}	50	46	50	50
Design flow, kg/sec	1.2	0.9	1.3	1.3
No. of full blades	15	18	16	24
No. of splitters	15	0	16	0
Exit blade angle, deg.	0	30	0	30

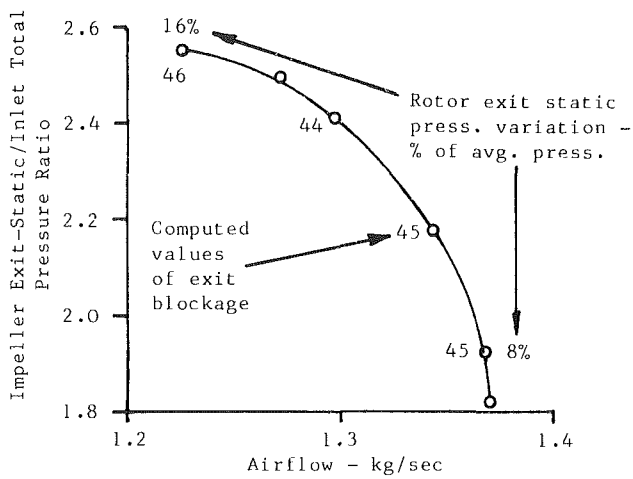

Fig. 3 Design-speed characteristics for Impeller C

equations are formulated to be solved along quasi-orthogonal calculation stations. Axial symmetry is assumed between blades, and the fluid is assumed to be compressible. The flow was assumed to follow the blade direction, except at the rotor exit. Temperature and static pressure measurements were used to establish the exit vector diagram. Flow deviation angle was computed without any assumption for windage loss. Zero relative total pressure loss was in the calculations, consistent with the jet-wake model. The blade surface velocities were computed from the assumption of zero absolute rotational motion and a linear velocity distribution, in a manner identical to that of Stanitz [38].

Seven streamlines were used in carrying out the computations. The blockage distribution obtained on the shroud streamline was applied to the other streamlines at the same equivalent distance along the streamline from inlet to exit. For instance, the blockage used at 50 percent meridional distance along the shroud was also used at the 50 percent meridional distance for the other streamlines. It is not intended to imply that this simplified model precisely reflects the real blockage distribution among the streamlines. The intent is to obtain a variation of gross blockage accumulation as a first approximation of an update in the approach taken in impeller design and analysis.

Calculations proceeded by first matching conditions at the rotor tip. The level of deviation angle was adjusted until the mass-averaged temperature matched the measured data within ± 0.5C. The tip static pressure was taken from the tap which was in line with the rest of the shroud taps. All values of shroud static/inlet-total pressure ratio were matched within ± 0.003. After the rotor tip conditions were met, all other shroud pressures were matched. Fifteen major iterations were sufficient to obtain solutions which were within ± 1.2 m/s between the fourteenth and fifteenth major iterations. Results generally were within 1/3 m/s.

Data Uncertainty

The flowpaths of the impellers which were examined and the location of the static pressure taps are shown in Fig. 2. Tip static pressure was measured by four taps, approximately 90 deg apart. The other locations along the shroud had only one tap. Figure 2 shows that Compressor A was tested with a vaneless diffuser, and Compressors B, C, and D were tested with vaned diffusers. The vaneless diffuser gaps in the latter compressors varied from 11 percent to 22 percent of the rotor tip radius. These gaps were felt to be sufficiently large to isolate the influence of the vanes on the rotor tip static pressure measurements. Past test experience had shown that tip static pressures in vaneless tests could be reproduced in vaned tests with gaps of 10 percent and with diffuser inlet Mach number of about 0.8.

The circumferential variation of rotor tip static pressure depended on the rotor tip speed and on the position of massflow between surge and choke. Up to 310 m/s, the pressure varied by 1 - 2 percent of the average value at flows near surge to 3 - 4 percent at flows near choke. At 490 m/s, the pressure varied from 2 percent of the average value for flows near surge to 8 percent at flows near choke. At 520 m/s, the pressure variation was 8 - 17 percent of the average value, and at 570 m/s, it was 27 percent. The data at these latter two tip speeds was primarily taken from flows on the choke characteristic of the impeller. This is illustrated in Fig. 3, which shows the compressor characterisitc at design speed for Rotor C. Indicated on the figure are the points used in the analysis, the tip static pressure variation at the extreme points, and the tip blockage values deduced from the calculations.

The uncertainty in static pressure measurement varies from 0.1 percent to 0.9 percent of the value measured. The temperature uncertainty is ± 0.5C. Massflow measurement uncertainty is within ±0.5 percent, and rotational speed uncertainty is within 0.3 percent of the measured values. At 20:1 odds, all values measured are believed to be within the uncertainties stated. This is an estimate based on uncertainties of data recording and instrument errors. What is not known, of course, is the uncertainty of the value of the time-averaged static pressure measurement for the time-varying flow field at the point of measurement.

Presentation and Discussion of Results

Calculations were performed at 50, 80, and 95 percent of design speed for Impeller A; at 50, 60, 70, 80, 90, and 100 percent of design speed for Impeller B; at 60, 70, 80, and 100 percent speeds for Impeller C; and at 80 and 100 percent speeds for Impeller D. From one to four massflow points were analysed at the various rotational speeds, depending on the amount and credibility of the individual data points. Note in Fig. 2 that data points were taken from two splitter-bladed radial impellers and two non-splittered backswept impellers.

Blockage results are presented in Figs. 4 through 7, for each impeller at different rotational speeds as a percent of design speed. Indicated on the figures are positions of the passage throat, the maximum blade curvature (mbc), and the

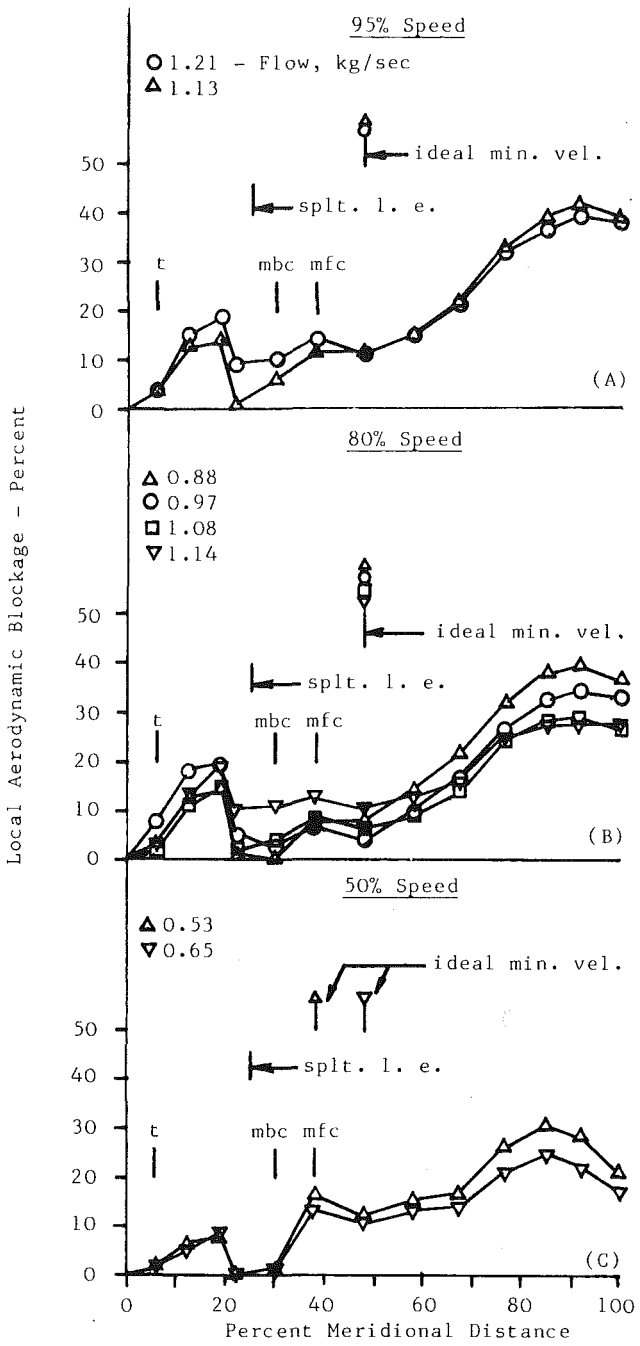

Fig. 4 Blockage distribution for Impeller A

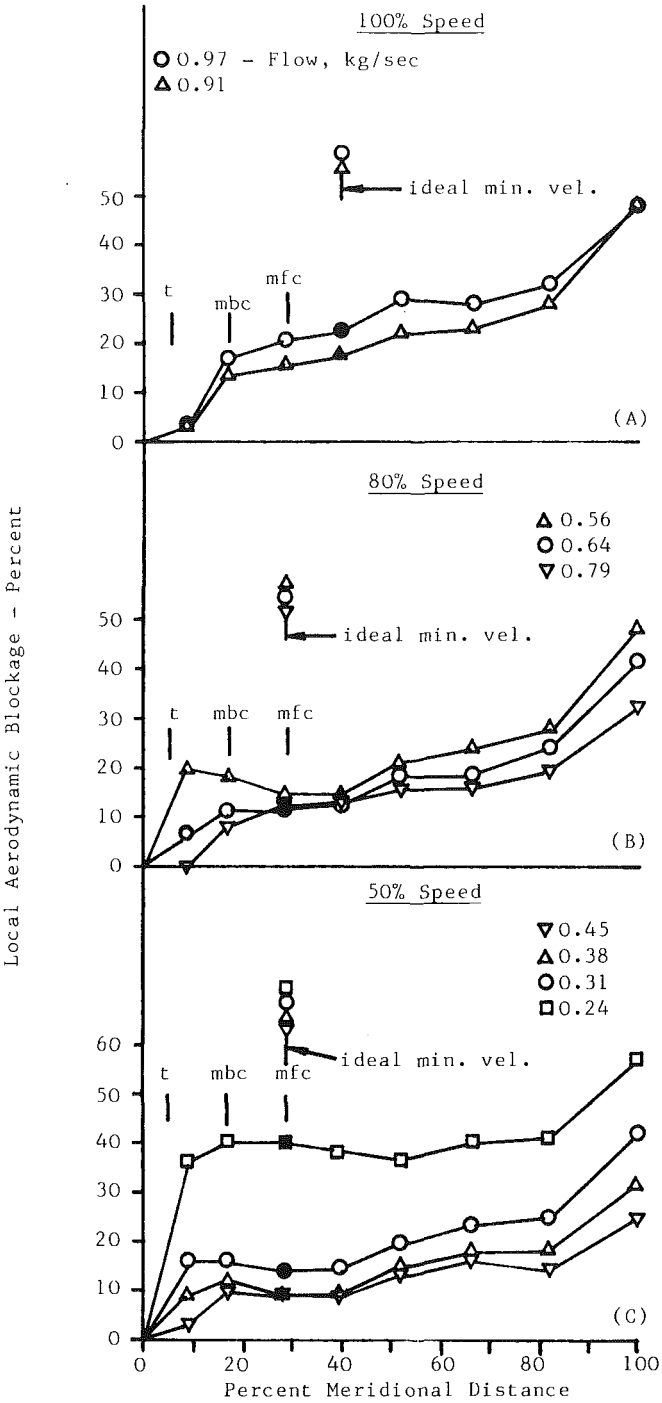

Fig. 5 Blockage distribution for Impeller B

maximum flowpath curvature (mfc). A detailed examination of the figures yields the following comments.

For Impeller A, the blockage ahead of the mbc and mfc points is strongly influenced by the splitter blades. Minimum velocity occurs at or slightly beyond mfc, at the two high speeds, and at the mbc point at the lowest speed. The blockage increases nonlinearly in the radial portion of the impeller, and the increase generally starts at the point of minimum velocity.

For Impeller B, blockage increases linearly to the mbc point at high flows. At low flows, there is a sharp increase near the throat. At all but the lowest flow at the lowest speed, there is little or no change in blockage until the point of minimum velocity, which occurs at the mfc point or slightly beyond. The blockage then increases approximately linearly to 82 percent meridional distance, with a sharp rise to the exit. For Impeller C, blockage rises linearly to the mbc point at the highest speed and flows. This changes to a sharp rise between the throat and mbc point, at lower speeds and flows. There is a slight drop from the mbc point to the mfc point. There is a nonlinear rise in blockage from the point of mfc. The splitter does not seem to influence blockage growth.

For Impeller D, there is a nearly linear increase in blockage to the point of mbc. There is then a small decrease in blockage to the mfc point, where the minimum velocity also occurs, except for the flow at design speed. The blockage rise in the radial portion is approximately linear from the point of minimum velocity.

Three generalizations are made from these summaries.

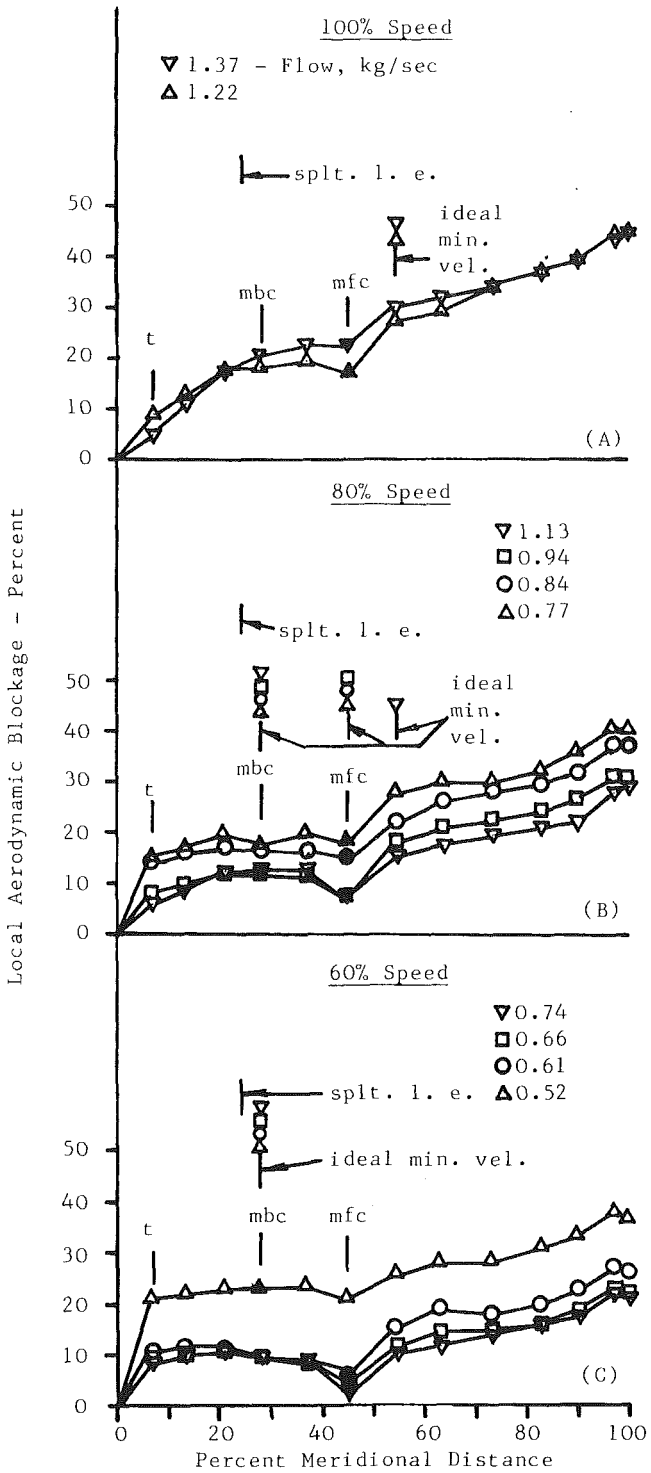

Fig. 6 Blockage distribution for Impeller C

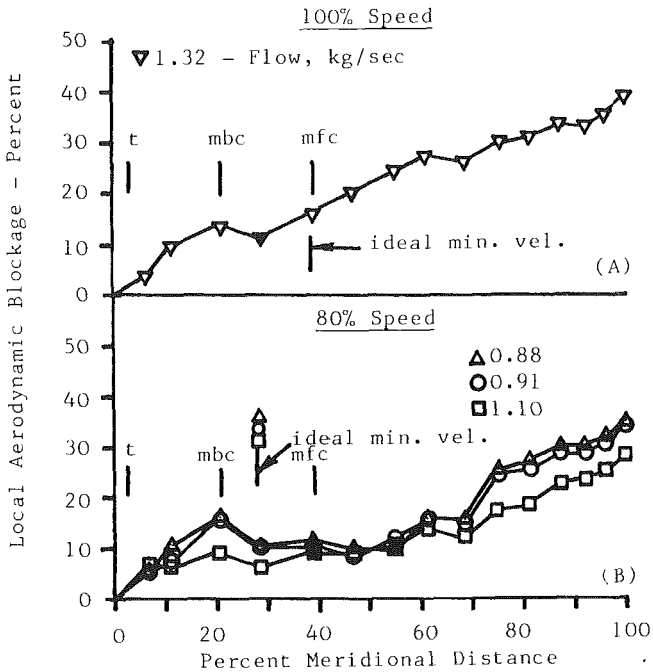

Fig. 7 Blockage distribution for Impeller D

First, except for Impeller A, blockage rises nearly linearly to the point of mbc at high flows (Figs. 5, 6, and 7) but to a position near the throat at low flows (Figs. 5 and 6). Secondly, from the point of mbc to the point of minimum velocity, there is a small increase (Fig. 5(A)), no increase at all (Figs. 4(A), 4(B), 5(B), 5(C), 6(A) and 6(B)) or a small decrease (Figs. 4(A), 4(B), 5(B), 5(C), 6(B) and 6(C)). Thirdly, the blockage increase in the radial portion generally starts at the point of minimum velocity when it occurs at a position different from the point of mfc (Figs. 4(A), 4(B), 4(C), 5(B) and (7)). Only in Fig. 6(C) does blockage increase from the point of mfc instead of the point of minimum velocity. It is not clear which is the reference point in Fig. 6(A). At all other flows, minimum velocity occurs at the point of mfc.

From these generalizations, one could say acceleration parameter should be correlated against the blockage computed at the point of minimum velocity on the 50 percent mass flow streamsheet and against the exit blockage. The results are shown in Fig. 8. At any given value of acceleration parameter, the range of blockage at minimum velocity is about 11 percentage points, but the range of exit blockage is poorly correlated about a spread of 16 percentage points. It could be expected that the correlation of exit blockage might be poor since the principal influence in the radial portion is Coriolis acceleration. It was, therefore, thought that it would be better to correlate the increase in blockage from the point of minimum velocity to the rotor exit against Richardson number, R_i, defined as

$$R_i = \omega B / W_{\min} \tag{9}$$

which is consistent with the definition used in [27-29]. It is appropriate to change the viewpoint from freestream forces to a boundary layer parameter, since the blockage has now been established at the "inlet" to the radial portion of the impeller.

The results are presented in Fig. 9. The increase in blockage through the radial portion of the impeller correlates against Richardson number within a range of 11 percentage points of blockage. This is as good as the correlation for the blockage at minimum velocity in Figure 8.

As an additional check on the results, a study was made of the relative importance of the constituents of the acceleration parameter (equation (7)) as defined by equations (4), (5), and (8). Each of these constituents was also reviewed for the significance of the inclusion of the square of Mach number as a factor. The purpose of this check was to investigate whether one of the constituent parameters by itself could provide as good a correlation as shown in Fig. 8(A) or whether no correlation is as good as the one which combines all the constituents.

Figure 10 shows plots of the blockage at the points of minimum velocity versus the diffusion parameter, P_D, with and without Mach number squared as a factor. Figure 10A

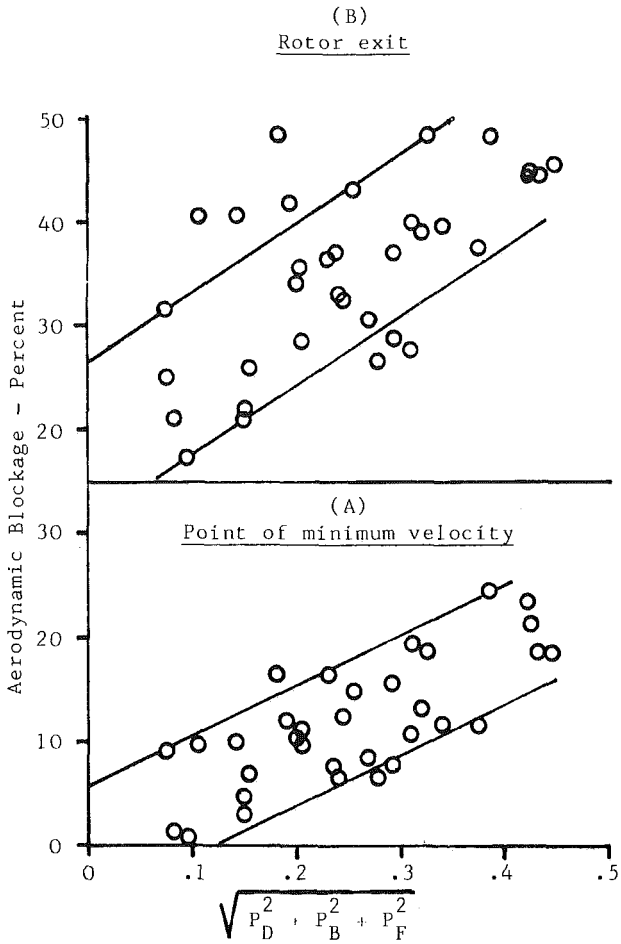

Fig. 8 Influence of Acceleration Parameter on aerodynamic blockage at minimum velocity and at rotor exit

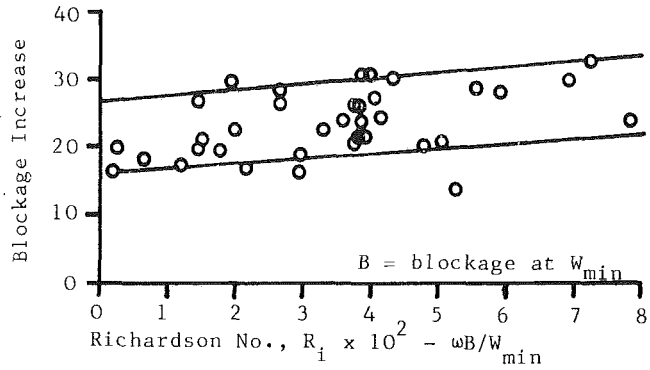

Fig. 9 Influence of Richardson number on the increase of blockage beyond point of minimum velocity

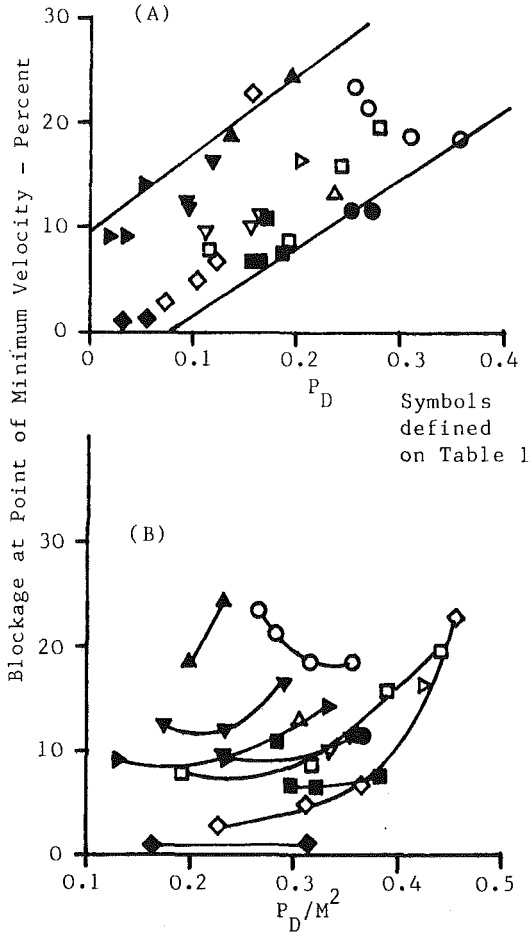

Fig. 10 Variation of blockage at point of minimum velocity with diffusion parameter, with and without Mach number included

shows a general trend in the group of points for blockage to increase linearly with P_D. This is supported by all but one of the individual data sets for which there are three points or more. The data spread, as defined by the straight lines, is 16 percentage points in blockage at any given value of P_D. Without Mach number squared as a factor, Fig. 10(B), the points cannot be collected between meaningful data bands. However, for a given impeller configuration and rotational speed, blockage generally increases as diffusion increases.

Figure 11 shows plots of blockage versus the blade acceleration parameter, P_B, with and without Mach number squared as a factor. Figure 11A shows a general trend in the group of points for blockage to increase linearly with P_B, but this trend is not generally shown by the individual data sets. The data spread, as defined by the straight lines, is 15 percentage points in blockage at a given value of P_B. This is four points wider than the band in Fig. 8(A). Without Mach number squared as a factor, Fig. 11(B), no correlation exists at all.

Figure 12 shows plots of blockage versus the flowpath acceleration parameter, P_F, with and without Mach number squared as a factor. No trend exists for data correlation. However, Figure 12(A) does suggest a trend at 80 percent speed for all impellers. The minimum velocity blockage is a double-valued function, similar to loss buckets, with a minimum between values of P_F of 0.15 and 0.20.

The conclusion from this review is that the blockage at minimum velocity is best correlated against the total acceleration parameter, AP, as expressed by equation (7). The figures also show the relative importance of the individual parameters, P_D, P_B, and P_F. At low values of the total acceleration parameter, the constituent parameters are of about equal importance. At high values, the diffusion parameter is about 20 percent larger than the flowpath parameter, P_F, which is in turn about 15 percent larger than the blade parameter, P_B. Scrutiny of the calculations showed that the Coriolis and curvature terms in P_B were generally about equal. In P_F, the Coriolis term was near-zero to only about 25 percent of the curvature term. Consequently, the blockage in the vicinity of the maximum flowpath curvature is about equally determined by diffusion, flowpath curvature and the combined effect of blade curvature and Coriolis acceleration, whereas the blockage increase in the radial portion is primarily determined by Coriolis acceleration.

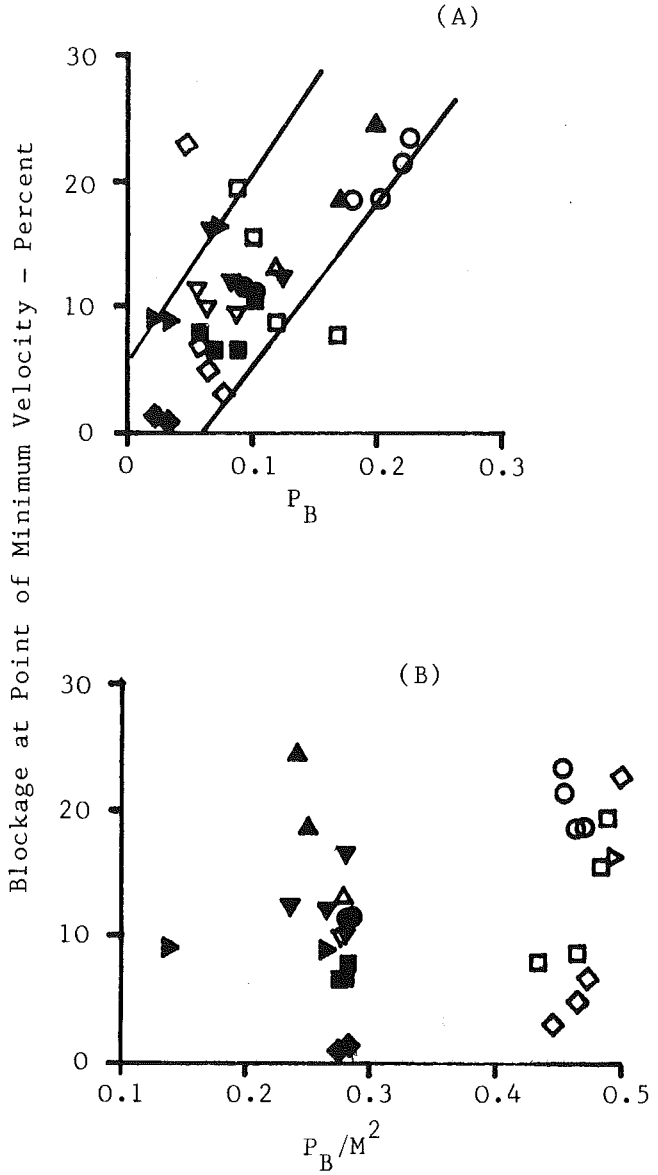

Fig. 11 Variation of blockage at point of minimum velocity with blade acceleration parameter, with and without Mach number included

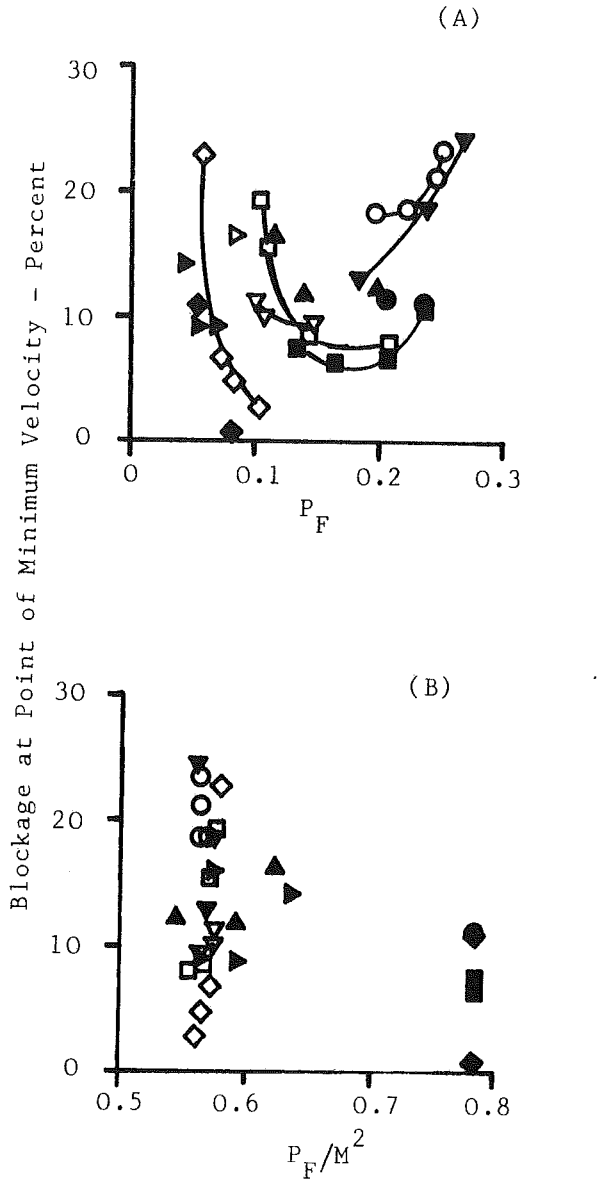

Fig. 12 Variation of blockage at point of minimum velocity with flowpath acceleration parameter, with and without Mach number included

Table 1 Symbols for Figs. 10, 11 and 12

Impeller	A	B	C	D
Symbol, % Speed	● 95	▲ 100	○ 100	△ 100
	■ 80	▼ 80	□ 80	▽ 80
	◆ 50	► 50	▷ 70	
			◇ 60	

Application of Results

The spread of the data bands in Figs. 8(A) and 9 is rather wide for accurate engineering use. The average values taken from these figures have an uncertainty of ± 6 percentage points. A large contribution to the data spread could be due to the assumption of the blockage distribution in the analytical determination of the blockage values. As mentioned previously, it was assumed that the blockage value on any given streamline was the same as the value on the shroud streamline at the same percentage distance along the streamline from inlet to exit.

Actual data [16, 17, 21, 22, 23] show large blockage buildup occurring on the suction surface near the shroud. At the rotor exit, blockage is concentrated near the suction surface for test conditions where the Coriolis effect predominates and spreads to the center of the passage on the shroud line for conditions where the shroud curvature effect predominates. Moore illustrates this in [35]. The low-speed results of Fowler [17] show strong indication of shroudline blockage buildup and this is probably due to flowpath curvature. Eckardt's data [16] shows the combined effect of blade and flowpath curvatures deteriorating the velocity distribution on the suction surface near the shroud at the point of maximum flowpath curvature. This was followed by the combined effect of Coriolis acceleration and flowpath curvature on the rotor exit distribution all along the suction surface and partway along the shroudline.

Despite the simplicity of the blockage distribution, it should be recalled that the intent was to obtain a variation of gross blockage accumulation as a first approximation for an improved flow model for the design of impellers. The use of shroud static pressure data is an inexpensive method for obtaining such information in contrast to the cost of interblade measurements by lasers and low-speed probing.

Despite the data spread, the analysis shows certain trends that can be deduced for minimizing blockage values. Mach number levels should be low. Design points on the choke characteristic should be avoided. Large values of blockage occur because of the high passage Mach number levels at choke. Refer to the values shown on Fig. 3, for instance. Blade and flowpath curvatures should be minimized, and blade solidity should be high (small "a"). These are not new considerations in impeller design, but Figs. 8(A) and 9 can help to give a first order assessment of blockage at expected values of the acceleration parameter.

Dean [39] has suggested that all diffusion should be accomplished in the inducer before the flow enters the Coriolis field of the radial portion. Figs. 8(A) and 9 suggest that this approach can lead to high values of blockage at minimum velocity, followed by a high value of blockage increase in the radial portion due to a high Richardson number caused by the value of blockage at the minimum velocity point. The analysis shows that the diffusion should probably be moderate or small to minimize the amount of blockage in both the inducer and the radial portion. The analysis also emphasizes the use of backswept blading to control diffusion and blade curvature. To minimize blade curvature further, the wrap angle (angular distance from inlet to exit) should be large. The results also support the use of mixed flow impellers to minimize the flowpath curvature.

Some blockage considerations may not be practical in a design. The use of a low value of rotational speed could lead to an unfavorable specific speed. An acceptable value of specific speed could force the inducer to operate at transonic tip speeds at high values of single-stage pressure ratio [40]. Consequently, large values of blockage could be inherent in an impeller because of design conditions. For instance, the exit blockage of the impeller in [40] varied from 52 to 57 percent (Fig. 60 in [40]). The inducer tip relative Mach number of the impellers analyzed in this paper were between 0.9 and 1.0 at design speed.

Conclusions

The analysis discussed in this paper provides an approximate model for gross blockage accumulation in centrifugal compressor impellers. It is not a precise model, for the uncertainty of a blockage estimate is ± 6 percentage points. It does, however, provide general trends to be considered in impeller design calculations. Up to the point of the axial-radial bend of the flowpath, the analysis shows that blockage is controlled equally by diffusion, flowpath curvature, and the combined effect of blade curvature and Coriolis acceleration. In the radial portion of the impeller, further increase in blockage is controlled by Richardson number. It is difficult to do much about flowpath curvature. Diffusion can be partially controlled by backsweeping and partially be designing for low inlet Mach number at a flow sufficiently far removed from choke. Blade curvature can be partially minimized by appropriately large wrap angles.

References

1 Sparkes, D. W., and Smith, D. J. L., "The Selection of the Leading Design Features of Centrifugal Compressor Impellers," NGTE, Note No. NT 930, July 1974.

2 Came, P. M., "The Development, Application and Experimental Evaluation of a Design Procedure for Centrifugal Compressors," *Institution of Mechanical Engineers Proceedings,* Mar. 1978, pp. 49–67.

3 Osborne, C., Runstadler, P. W., Jr., and Stacy, W. D., "Aerodynamic and Mechanical Design of an 8:1 Pressure Ratio Centrifugal Compressor," NASA CR-134782, Creare, Inc., Apr. 1975.

4 Hamrick, Joseph T., Ginsburg, A., and Osborn, Walter, M., "Method of Analysis for Compressible Flow Through Mixed-Flow Centrifugal Impellers of Arbitrary Design," NACA Report 1082, Apr. 1950.

5 Katsanis, Theodore and McNally, William D., "Fortran Program for Calculating Velocities and Streamlines on the Hub-Shroud Mid-Channel Flow Surface of an Axial- or Mixed-Flow Turbomachine," NASA TN-7343, 1973.

6 Smith, L. H., Jr., "The Radial-Equilibrium Equation for Turbomachinery," ASME *Journal of Engineering for Power,* Vol. 88, Jan. 1966, pp. 1–12.

7 Bryce, C. A., Paine, C. J., McCutcheon, A. R. S., Tu, R. K. and Perrone, G. L., "Advanced Two-Stage Compressor Program, Design of Inlet Stage," NASA CR-120943, AiResearch Manufacturing Co. of Arizona, Aug. 1973.

8 Bryce, C. A., Erwin, J. R., Perrone, G. L., Nelson, E. L., Tu, R. K. and Bosco, A., "Small, High Pressure Ratio Compressor, Aerodynamic and Mechanical Design," NASA CR-120941, AiResearch Manufacturing Co. of Arizona, June 1973.

9 Moore, J., Moore, J. G. and Johnson, M. W., "On Three-Dimensional Flow in Centrifugal Impellers," Aeronautical Research Council, C. P. No. 1384, Feb. 1977.

10 Smith, J. A., "Notes on Some Experimental Researches on Internal Flow in Centrifugal Pumps and Allied Machines," *Engineering*, Vol. LXXIV, Dec. 5, 1902, p. 763.

11 Carrard, A., "Sur le Calcul des Roues Centrifuges," La Technque Moderne, T. XV No. 3, pp. 65–71 and No. 4, pp. 100–104, Feb. 1923.

12 Carrard, A., "On Calculations for Centrifugal Wheels," Translation by J. Moore, University of Cambridge, Department of Engineering, Report No. CUED/A Turbo/TR 73, 1975.

13 Stodola, A., "Steam and Gas Turbines," Vol. II, pp. 1268–1270, Peter Smith, NY, 1945.

14 Fischer, K. and Thoma, D., "Investigation of the Flow Conditions in a Centrifugal Pump," ASME Transactions HYD-54-8, 1932.

15 Hamrick, J. T., Mizisin, J. and Michel, D. J., "Study of Three-Dimensional Flow Distribution Based on Measurements in a 48-inch Radial-Inlet Centrifugal Impeller," NACA TN 3101, 1954.

16 Eckardt, D., "Detailed Flow Investigations within a High-Speed Centrifugal Impeller," ASME JOURNAL OF FLUIDS ENGINEERING, Vol. 98, 1976, pp. 390–402.

17 Fowler, Howard S., "Some Measurements of the Flow Pattern in a Centrifugal Compressor Impeller," ASME Paper 65-WA/GTP-7, 1965.

18 Johnson, M. W., and Moore, J., "The Development of Wake Flow in a Centrifugal Impeller," ASME Paper 79-GT-152, Mar. 1979.

19 Senoo, Y., Yamaguchi, M. and Nishi, M., "A Photographic Study of the Three-Dimensional Flow in a Radial Compressor," ASME Paper 68-GT-2.

20 Lenneman, E. and Howard, J. H. G., "Unsteady Flow Phenomena in Rotating Centrifugal Impeller Passages," ASME Paper 69-GT-35.

21 Mizuki, S., Hattori, T., Ariga, I. and Watanabe, I., "Reversed Flow Phenomena within Centrifugal Compressor Channels at Lower Flow Rate," ASME Paper 76-GT-86, 1976.

22 Mizuki, S., et al., "A Study on the Flow Pattern within the Centrifugal and Mixed-Flow Impellers," ASME Paper 71-GT-41.

23 Mizuki, S., et al., "A Study on the Flow Mechanism within Centrifugal Impeller Channels," ASME Paper 75-GT-14.

24 Bradshaw, P., "Effects of Streamline Curvature on Turbulent Flow," AGARDograph 169, 1973.

25 Moore, John, "Effects of Coriolis on Turbulent Flow in Rotating Rectangular Channels," MIT Gas Turbine Laboratory Report No. 89, Jan. 1967.

26 Koyama, H., Masuda, S., Ariga, I. and Watanabe, I., "Stabilizing and Destabilizing Effects of Coriolis Force on Two-Dimensional Laminar and Turbulent Boundary Layers," ASME Paper No. 78-GT-1, Apr. 1978.

27 Halleen, R. M. and Johnston, J. P., "The Influence of Rotation on Flow in a Long Rectangular Channel - An Experimental Study," Report MD-18, Thermosciences Division, Dept. Mechanical Engineering, Stanford University, May 1967.

28 Lezius, D. K., and Johnston, J. P., "The Structure and Stability of Turbulent Wall Layers in Rotating Channel Flow," Report MD-29, Thermosciences Division, Dept. Mechanical Engineering, Stanford University, 1971.

29 Rothe, P. H., and Johnston, J. P., "The Effects of System Rotation on Separation, Reattachment and Performance in Two-Dimensional Diffusers," Report PD-17, Thermosciences Division, Dept. Mechanical Engineering, Stanford University, May 1975.

30 Moore, John, "The Development of Turbulent Boundary Layers in Centrifugal Machines," MIT Gas Turbine Laboratory Report No. 99, June 1969.

31 Hill, Philip G. and Moon, I-Man, "Effects of Coriolis on the Turbulent Boundry Layer in Rotating Fluid Machines," MIT Gas Turbine Laboratory Report No. 69, June 1962.

32 Moon, I-Man, "Effect of Coriolis Force on the Turbulent Boundary

Layer in Rotating Fluid Machines," MIT Gas Turbine Laboratory Report No. 74, June 1964.

33 Johnston, James P., Halleen, Robert M. and Lezius, Deitrich K., "Effects of Spanwise Rotation on the Structure of Two-Dimensional Fully Developed Turbulent Channel Flow," *Journal of Fluid Mechanics,* Vol. 56, Part 3, 1972, pp. 533–557.

34 Johnston, J. P., and Eide, S. A., "Turbulent Boundary Layers on Centrifugal Compressor Blades: Prediction of the Effects of Surface Curvature and Rotation," ASME JOURNAL OF FLUIDS ENGINEERING, pp. 374–381, Sept. 1976.

35 Moore, J., Moore, J. G., and Johnson, M. W., "On Three-Dimensional Flow in Centrifugal Impellers," Aero. Res. Council C. P. No. 1384, Feb. 1977.

36 Lieblein, Seymour, Schwenk, Francis C. and Broderick, Robert L., "Diffusion Factor for Estimating Losses and Limiting Blade Loadings in Axial-Flow-Compressor Blade Elements," NACA RM E53D01, June 1953.

37 Balje, O. E., "A Flow Model for Centrifugal Compressor Rotors," ASME *Journal of Engineering for Power*, Vol. 100, No. 1, Jan., 1978, pp. 148–158.

38 Stanitz, J. D., and Prian, V. D., "A Rapid Approximate Method for Determining Velocity Distribution on Impeller Blades of Centrifugal Compressors," NACA TN 2421, 1951.

39 Dean, R. C., Jr., "The Fluid Dynamic Design of Advanced Centrifugal Compressors," Creare, Inc., Technical Note TN-153, 1972.

40 Dolan, Francis X., and Runstadler, P. W., Jr., "Design, Development and Test of a Laser Velocimeter for a Small 8:1 Pressure Ratio Centrifugal Compressor," NASA CR-134781, Mar. 1979.

The CIVIC—A Concept in Vortex Induced Combustion, Part II

J. R. Shekleton
Development Engineer,
TURBOMACH,
A Division of Solar Turbines International,
An Operating Group of International Harvester,
San Diego, Calif. 92123

Turbomach, A Division of Solar Turbines International, An Operating Group of International Harvester, manufactures the small 10kW Gemini gas turbine. The very small size of the combustor precluded the use of conventional gas turbine combustor design techniques. A novel solution was arrived at based primarily on an amalgam of design practices used in furnaces and reciprocating engines. Use was made of the centrifugal force effects of swirl flow (Rayleigh Instability Criteria) both as a method of fuel evaporation and as a method of control of the rate of flame propagation. Substantial advantage can be obtained by this design technique provided that a fine and accurately located fuel spray is achieved. Various applications of this method of combustor design are outlined with emphasis on aerodynamics and fuel atomization and volatility rather than reaction rate criteria as the dominant influences.

Introduction

The weather is strongly influenced by small temperature differences between adjacent air masses under earth's gravitational influence. Thermals and inversion layers are two examples. In the former case, mixing between the two air masses is speeded up and, in the latter case, mixing is slowed down. It is the buoyancy force, resulting from the small density difference between the air masses, that causes these mixing phenomena.

In all practical combustors, control of mixing is dominant in attainment of good combustion. The buoyancy controlled mixing, as seen in nature, has found use in the design of many diesel engine combustors. By swirl of all the combustion air, high centrifugal forces are generated and may exceed 100,000g. Such high forces, in conjunction with large density differences resulting from temperature gradients of several thousand degrees within the combustor, are used to modify mixing rates to great effect.

The CIVIC concept (Concept in Vortex Induced Combustion) is used in Turbomach's 10kW Gemini gas turbine combustor. The CIVIC concept uses buoyancy-controlled mixing to considerable advantage. In a breakaway from traditional gas turbine combustor design practice, the concept is strongly influenced by furnace design and by design techniques involving buoyancy mixing of the highspeed diesels of Ricardo [1] and M.A.N. [2]. This paper describes the origins of the CIVIC concept and illustrates common bonds existing in combustor design for reciprocating engines, furnaces and gas turbines. Emphasis is placed on the fundamental importance of accurately located and well atomized fuel, which enables the excellent combustion characteristics of natural gas to be attained with liquid fuels.

Aerodynamics of Vortex Flow

Consider a row of constant height and constant radius air swirl blades as shown in Fig. 1. Air approaches and leaves the swirl blades with a constant axial velocity, V_{ax}, and, because of acceleration through the blade row, is given a tangential or swirl component of velocity $V_{\tan}$. Consider a small cube of air as part of the larger mass of swirling air. In order that this small cube of air is not centrifuged outward, the centrifugal force must be balanced by a pressure force [3]. Hence, equating the centrifugal to the pressure force, we have

$$\frac{\rho \bullet \delta A \bullet dr}{r} \bullet V_{\tan}^2 = (p+dp)\,\delta A - p \bullet \delta A \bullet \qquad (1)$$

where p = static pressure at radius of rotation r, dr = height of the air cube, δA = base area of the air cube, $V_{\tan}$ = rotational or tangential velocity, $p + dp$ = static pressure at radius $r + dr$, ρ = air density which is assumed constant.

Hence we have

$$\frac{dp}{dr} = \frac{\rho \bullet V_{\tan}^2}{r} \qquad (2)$$

Equation (2) describes the necessary radial air pressure gradient, in terms of the tangential velocity and radius, for radial equilibrium. Radial equilibrium is a proper design requirement for vortex flow. Improper design of the means of vortex generation, resulting in lack of radial equilibrium, causes excessive turbulence and high pressure loss.

A pressure gradient has been established for radial equilibrium with a uniform density of air. If combustion occurs locally within this vortex flow, the density is lowered and then radial equilibrium is disturbed. Heat addition, circumferentially uniform at the outer periphery of the vortex

Contributed by the Gas Turbine Division and presented at the International Gas Turbine Conference, Houston, Texas, March 8-12, 1981, of THE AMERICAN SOCIETY OF MECHANICAL ENGINEERS. Manuscript received at ASME Headquarters, December 4, 1980. Paper No. 81-GT-12.

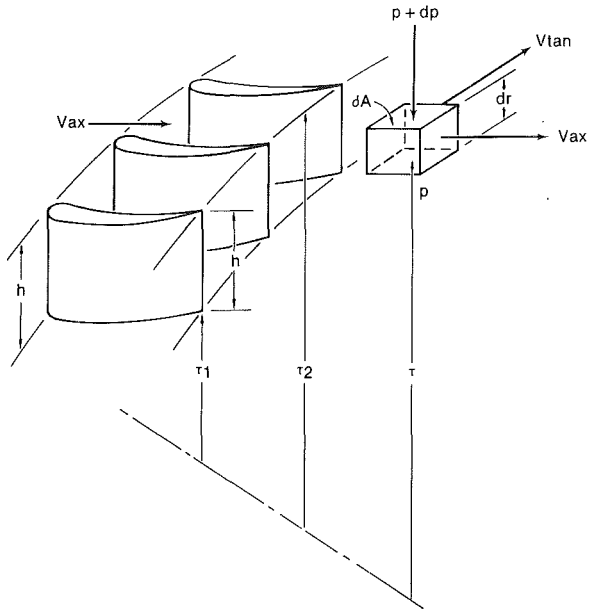

Fig. 1 Vortex flow through a row of swirl vanes with radial equilibrium

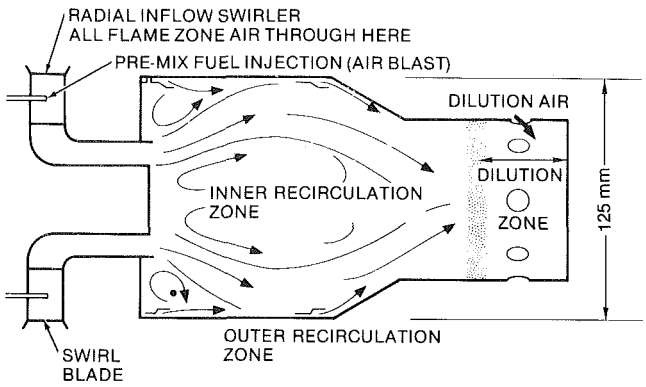

Fig. 2 CIVIC vortex can combustor with premixed fuel

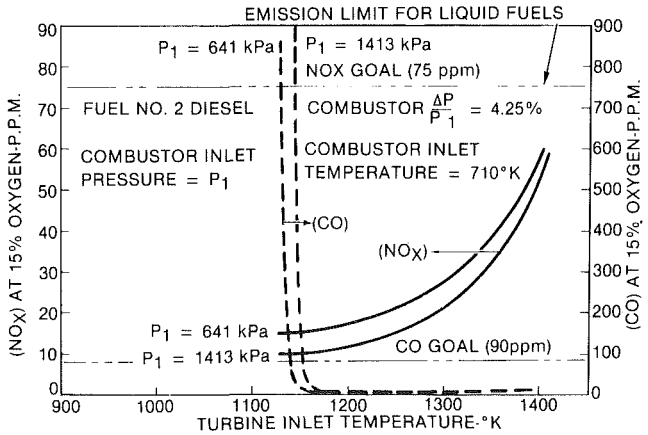

Fig. 3 CIVIC vortex combustor emissions using premix no. 2 diesel fuel

flow, causes a radial inward movement of the hot gas, similar to what occurs with a thermal. Conversely, heat addition, circumferentially uniform at the inner periphery of the vortex flow, results in enhanced equilibrium, or reduced mixing and laminarisation as in the case of the inversion layer. It is the particular use of these phenomena of heat addition to vortex flow in modifying the radial equilibrium, that distinguishes the CIVIC concept from typical vortex combustion in furnaces and gas turbines. In the CIVIC, use is made of both these modes of mixing. To distinguish them, the enhanced mixing is called unstratified and the slow mixing is called stratified flame propagation.

If the vortex flow of Fig. 1 has been obtained efficiently with no pressure loss, the total pressure, P, at all parts of the swirling air mass is constant. Thus, from Bernoulli, assuming incompressible flow, at any radius r we have,

$$\frac{p}{\rho} + \frac{V_{\tan}^2}{2} + \frac{V_{ax}^2}{2} = \frac{P}{\rho} = \text{a constant} \tag{3}$$

Consequently with axial velocity, V_{ax}, and the blade height h a constant, differentiation gives

$$\frac{1}{\rho}\frac{dp}{dr} + V_{\tan} \bullet \frac{d\,V_{\tan}}{dr} = 0 \tag{4}$$

Assuming that radial equilibrium is obtained, substituting from equation (2) gives

$$\frac{V_{\tan}^2}{r} + V_{\tan} \bullet \frac{d\,V_{\tan}}{dr} = 0 \tag{5}$$

and therefore, integrating,

$$V_{\tan} \bullet r = \text{a constant} \tag{6}$$

This relationship between tangential velocity and radius, with radial equilibrium and constant axial velocity, is called free vortex flow, and occurs in nature in tornados and whirlpools. Such a flow is commonly used as a design criteria in machinery using vortex flow, such as in gas turbine compressors and turbines, in diesel engines, and in furnaces [4, 5, 6]. Other vortex flows that fulfill the requirement of radial equilibrium, such as forced vortex flow [3], are used. Free vortex flow is easy to achieve, and is the common method of vortex generation used in the CIVIC concept and many other combustors. The influence of other methods of vortex flow on the combustion phenomena is of considerable interest and awaits future exploration.

Reaction Criteria in Vortex Combustors

Gas Turbine Combustor. In adopting the CIVIC combustion concept for Solar gas turbines, considerable evaluation and development were done. These results are reported elsewhere [7, 8, 9, 10, 11]. A conceptual design for preliminary tests is shown in Fig. 2. The combustor differs from conventional gas turbine combustors in several respects. All the air for complete combustion is passed through a radial inflow free vortex swirler assembly. On entering the combustion zone, the air expands in free vortex motion and moves downstream without impediment from the usual primary air jets. Due to this sudden expansion, inner and outer zones of forced vortex recirculation are established and serve as ignition sources to the air-fuel mixture.

The premix diesel fuel injection used consists of 16 small, simple tubes, located in the radial inflow passageway, and using air blast atomization. In trying to ensure complete fuel evaporation, a long premix passageway was used. Injection of liquid fuel into a radial inflow vortex results in unusually effective fuel evaporation. The centrifugal force of the radially inward vortex motion serves to centrifuge the fuel droplets radially outwards and prevents fuel droplets of any appreciable size exiting into the combustor [10]. Tests over a range of air pressures (Fig. 3) showed that NO_x, combustion efficiency, and flame stability are independent of pressure. On the assumption that evaporation and pre-mix of the fuel is achieved prior to combustion, this suggests that the reaction

time required during the process of combustion is small compared to the mixing time, even at the point of flame out.

Reciprocating Engine Combustor. The mechanism of flame propagation in the spark ignition engine and in the above CIVIC combustor can be visualized as follows.

Heat and active species are transferred, through turbulence, from the burned to the unburned gas. A certain length of time is required for mixing of the hot and cold gases and another length of time is required for the subsequent reaction. The combustion can be characterized as "mixing controlled" if the time required for mixing is large compared to the time required for reaction. Conversely, the combustion is "reaction controlled" if the time required for reaction is dominant. Practical combustors are mixing controlled and only laboratory models, using high pressure loss to insure a very high mixing rate are "reaction controlled" [12]. This is well illustrated in the gasoline engine because the crank angle for flame travel, in degrees of crank angle, increases by only a small amount as engine speed increases, so that the flame speed increases in near proportion to the engine speed [13]. This is true of even a very small highspeed engine of cylinder (combustor) size of 44 mm [14]. The fastest flame propagation occurs near stoichiometric air-fuel ratios and slows down with either excessive fuel or air. Therefore, the gasoline engine is "mixing controlled" as in the CIVIC gas turbine combustor described above. The dominant effect of change in air-fuel ratio is to lower the flame temperature, which slows down the turbulent mixing rather than, as might be expected, slowing down the reaction.

Similar characteristics are reported for the high speed diesel, including those using swirl flow [1, 15]. In the diesel, it would be anticipated that the fixed time required for autoignition which, as with reaction time, is controlled by pressure, temperature, and air-fuel ratio this might cause a large increase in flame propagation crank angle as engine speed increases.

This does not occur because of other influences. Heat losses are reduced with increased speed, as is fuel droplet size consequent to increased fuel injection velocity. A nearly constant crank angle of flame propagation is maintained over a wide speed range [1]. Therefore, in the reciprocating engine, as in the CIVIC combustor, mixing controls the flame propagation with secondary, but important influences of fuel evaporation and heat loss [16, 1].

Buoyancy Criteria in Vortex Combustion

Mixing takes up most of the volume in the combustion process. It is desirable to speed up mixing without excessive pressure loss. This is particularly true of the diesel engine where the fast constant volume combustion of the Otto cycle is preferred. This cycle provides higher thermal efficiency compared to the slow constant pressure combustion of the Diesel cycle. Several diesel engines use buoyant mixing to achieve this goal of fast, near constant volume combustion.

MAN Diesel Engine. The combustor for this engine is shown in Figure 4. The design of the combustor, with particular emphasis on the buoyant mixing employed, is well described in the references [2, 15]. Despite the use of a free vortex air inlet, the airflow in the combustor, at the moment of combustion, is almost certainly of the forced vortex type [17]. The flame propagation is "mixing controlled" [15].

In the MAN combustor, nearly all the fuel is injected onto the wall of the combustor with a small pilot flame in close proximity to the wall. The flame, occurring at the interface between the air and evaporated fuel, is considerably less dense than the adjacent fuel and air. Consequently, the radial equilibrium of vortex flow no longer exists. "The flame, the

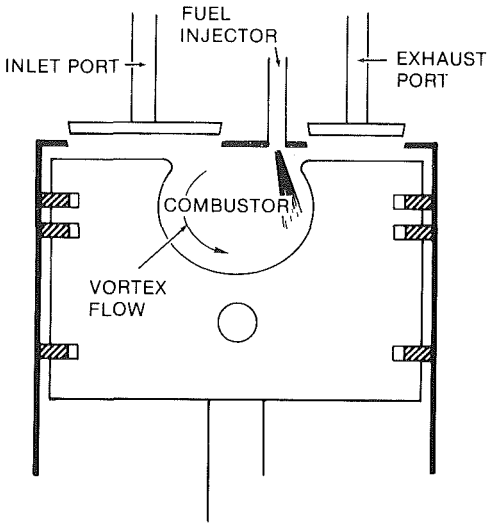

Fig. 4 MAN diesel using vortex combustion

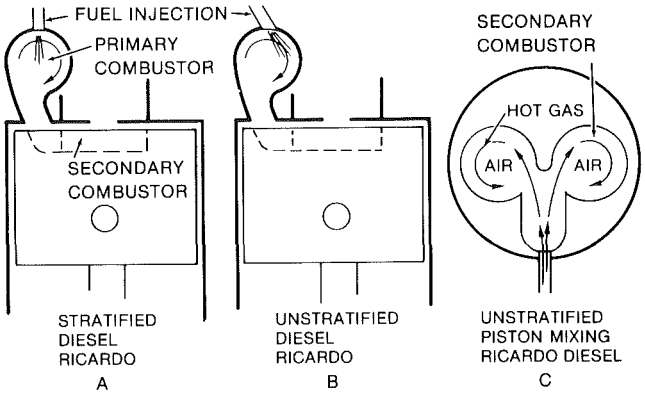

Fig. 5 Ricardo comet diesel vortex combustion

burning region, spirals slowly inward and around the bowl (of the combustor) with the rate of combustion controlled by the rate of vaporization (of fuel) and the centrifugal convection" [18]. Lewis has described tests, in a rotating tube [19], conceptually simulating constant volume combustion in a centrifugal force field. His results show that the speed of flame propagation is directly proportionate to the square root of the centrifugal force. It is a "mixing controlled" phenomenon. Mestre [20] has described use of this form of buoyant mixing to speed up the flame propagation in a conceptual gas turbine combustor.

Ricardo Comet Diesel. The Comet diesel engine combustor is schematically shown in Fig. 5 and the design method, referencing the buoyant mixing, is reported in [21, 22]. Unlike MAN, the Comet does not use a vortex inlet airport, but uses a tangential offset port, between the primary combustor and the cylinder. This generates a high air swirl into the primary combustor on the air compression stroke. About half the available air is therefore rotating in the primary combustor, and the other air is contained in a secondary combustor within two circular depressions that are cut into the top of the piston. In normal operation, the fuel is injected in the direction of swirl as in Fig. 5(*B*). Some fuel is deposited on the wall, while some remains as a fine spray adjacent to the wall. Ignition occurs and spreads a diffusion flame in the primary combustor "with an incurling spiral towards the center of the chamber while the heavier air is forced outward by the cen-

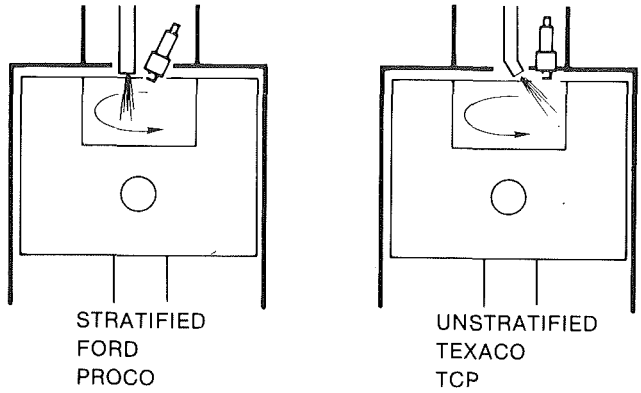

Fig. 6 Vortex spark ignition engine combustion

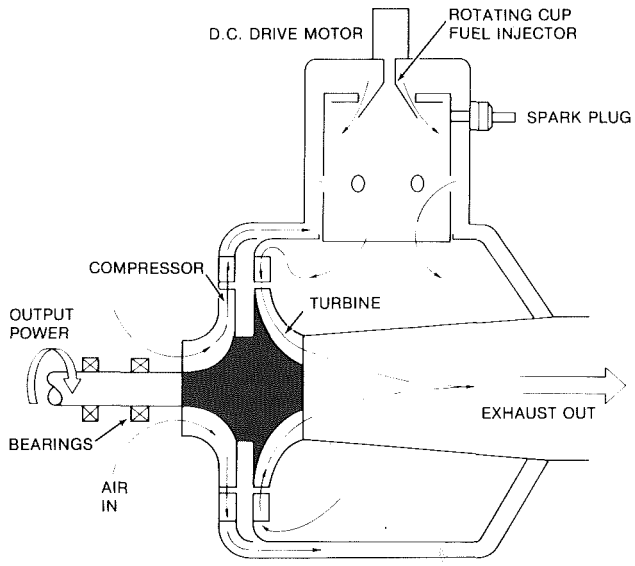

Fig. 7 Turbomach Gemini 10 kW gas turbine

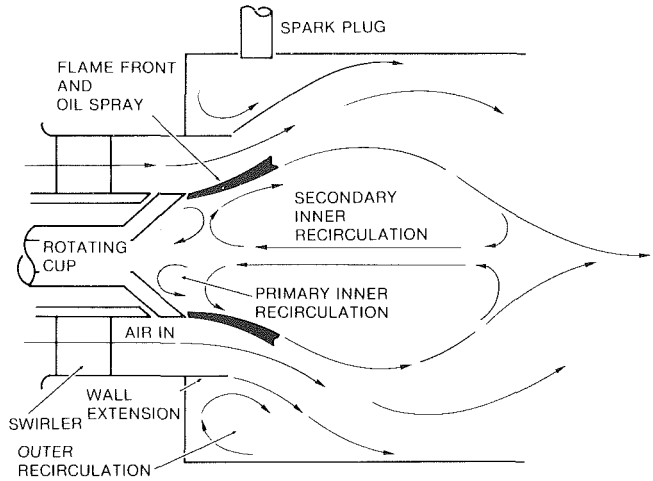

Fig. 8 Schematic, Gemini, CIVIC vortex combustor

trifugal field" [22]. Flame spreads from the primary combustor into the air contained within the two circular depressions in the piston top, as in Figure 5(*C*). "A very high secondary swirl is thereby created in each recess mixing any combustible element with the air" [22]. "The stream (of gases) meets the air in the depressions tangentially and mixes with it, since the rotary movement applied to the air particles, causes them to be forced outward owing to their higher specific gravity and to the action of centrifugal force" [21]. Thus, the Ricardo Comet uses buoyant forces to speed up the combustion process. This also occurs in the MAN engine, except that the vortex motion occurs in two distinctly separate vortex combustors. The Ricardo Comet combustion process is mixing controlled [1] and commonly used in automobiles. Heater plugs are frequently used to overcome the slow fuel evaporation of cold start. Very high compression ratios, on the order of 22, are also used to facilitate fuel evaporation and ignition. This results in a loss of thermal efficiency because, at compression ratios much higher than 12, the increasing friction loss more than offsets gains in indicated thermal efficiency [23].

A version of the Comet combustor uses a unique twin spray Pintaux injector [1]. During cold start, the spray is injected toward the center of the primary combustor as in Fig. 5(*A*), and this allows starts without a heater plug, as the air, under centrifugal force effects, is hotter in this region. It is speculated that the radial equilibrium of vortex flow is enhanced by such fuel placement and, with the hot gases at the center of the vortex flow, mixing is considerably slowed down. Obert [22] reports a considerable loss in thermal efficiency consequent to fuel injection toward the center of the combustor, together with a loss in power and increase in smoke. This strongly suggests a reduction in mixing because of buoyancy effects. To obviate this deficiency, the Pintaux injector is designed such that, in normal operation, at higher fuel flows the fuel spray is directed toward the outer periphery of the combustor as in Figure 5B, and as previously described, to achieve by means of enhanced mixing through buoyancy effects, improved efficiency with increased power and less smoke.

Beer [24] describes the effects of fuel location toward the center of a vortex flow in a simulated furnace flame and reports a considerable decrease in mixing. Similar effects of centrifugal force fields are reported elsewhere [25, 26].

The two methods of stratified and unstratified fuel injection of the Ricardo Pintaux injector are used in the Texaco TCP [27, 28], and the Ford Proco [28, 29] spark ignition engines. In the Texaco engine, unstratified fuel injection enhances mixing and in the Ford, stratified fuel injection slows down mixing (Fig. 6).

Turbomach Gemini Combustor. The CIVIC concept is used in the Gemini 10 kW gas turbine. A detailed description of the combustor development is presented in reference [11]. The Gemini turbine is shown in Fig. 7 and the combustor is schematically shown in Fig. 8. The combustor design is similar to the premix fuel injection combustor previously described (Fig. 2) except that stratified charge fuel injection, to provide stratified (reduced mixing) flame propagation, is used. This method of fuel placement, toward the center of the vortex flow, is designed to facilitate starting as in the case of the similarly designed Ricardo Pintaux fuel injector. The extremely small size of the combustor results in significant difficulties in obtaining good fuel atomization when using conventional gas turbine fuel injectors, and was resolved by use of a rotating cup fuel injector. The good fuel atomization of the cup provides excellent lightoff capabilities even in extreme arctic conditions with very viscous fuels, and is superior in this respect to much larger combustors, because of this improved fuel atomization.

The centrifugal force effects of vortex flow are used in the CIVIC. This not only controls the speed (or rate of mixing) of the flame, but also is used as an unusually effective method of achieving fast fuel evaporation prior to combustion. The

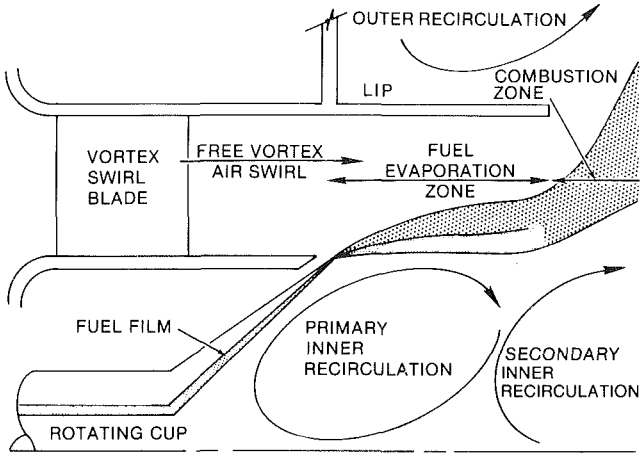

Fig. 9 Schematic half section of the CIVIC fuel evaporation zone

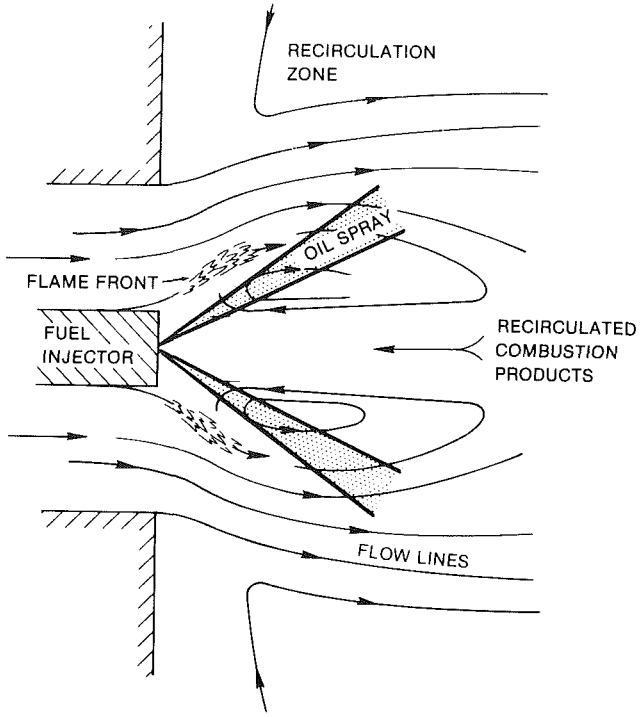

Fig. 10 Stabilization of pressure jet oilflame by internal recirculation zone in swirling annular jet (after Beer)

Gemini exemplifies this method as the rotating cup, in a simple fashion, provides the necessary accurate placement of a circumferentially uniform and fine fuel spray exactly at the inner periphery of the vortex airflow and immediately adjacent to, but not into, the primary hot gas inner recirculation. An enlarged schematic half section of the CIVIC fuel evaporation zone is shown in Fig. 9. In a typical swirl stabilized furnace flame [30], or gas turbine flame, the fuel is injected as a wide spray as shown in Fig. 10 [30]. Though, in many respects such a combustor aerodynamically resembles the CIVIC, small but important distinctions exist. In the furnace flame a significant amount of fuel enters the inner zone of recirculated combustion products, and this has been found, in tests of the CIVIC, to be the cause of high flame luminosity and exhaust smoke. In the furnace flame, some of the fuel is shown entering and mixing with the swirl air. This is a design aim in a typical gas turbine air blast fuel injector [31]. This mixing with the swirl air has been found, in the CIVIC, to drastically slow fuel evaporation. It causes flame inefficiency, instability, and increased length. In the furnace flame, some of the fuel is shown as being swept backwards to create a "laminarized" pilot flame, as shown in Figure 10, at the juncture between the inner periphery of the swirl air and the recirculation zone [30]. In the CIVIC, all the fuel is injected precisely at this juncture between the inner periphery of the swirl air and the recirculation zone, and fuel entry either into the air of recirculation zone is kept as small as possible. This provides, with liquid fuels, a clear blue flame indistinguishable from natural gas with excellent stability and a wide range of efficient combustion.

Another important distinction between the furnace flame and the CIVIC is the use, in the CIVIC, of a lip, extending downstream of the swirl blades, to delay expansion of the swirling air into the combustor, as shown in Figs. 8 and 9. By this means, the centrifugal force during the period of fuel evaporation, is maintained high to provide reduced mixing. This causes a minimum of combustion. With a combustor entry dynamic head of 1.75 percent and a swirl angle of 45 deg, the tangential and axial air velocities at the inner periphery of the swirling air (corresponding exactly to the exit diameter of the cup) are both 50 meters per second. With a rotating cup diameter of 2 cm, the resulting centrifugal force is 25,500 g. Relying on probing of the flame [10], but mostly on flame observation, the mechanism of fuel evaporation appears to be as follows. Rotation of the cup, at 13,000 rpm, in opposition to the air swirl, enhances fuel atomization and, most importantly, the centrifugal force effects of the swirl air acting on the fuel droplets are momentarily impeded. The high axial air velocity deflects the fine fuel droplets into an axial direction, to lie exactly at the juncture of the inner periphery of the swirling air and hot gas recirculation as shown in Fig. 9. Ignition from the hot gas recirculation causes a flame at the juncture between the layer of fuel droplets and the swirl air. The hot flame, moving inward because radial equilibrium is disturbed, serves as an unusually effective means of fuel evaporation. The hot gasified fuel, having now accelerated up to air velocity, is subject to a high centrifugal force. It is prevented from mixing with the swirl air because of the unmixedness created by the enhanced radial equilibrium. This mechanism not only provides a means of fast fuel evaporation giving all the characteristics of natural gas combustion, but also provides exceptional flame stability because a stoichiometric interface between fuel and air is maintained over a wide range of overall air-fuel ratios. On the other hand, rotation of the cup in the same direction as the air swirl results in a very significantly different flame. The increased fuel droplet size, in conjunction with an immediate swirl of the fuel, results in fuel droplet centrifuge outward before ignition and consequent evaporation and laminerisation can be achieved. Flame length is greatly increased and flame stability much reduced as a consequence of excessive mixing of the fuel and air. Such a flame commonly would occur in a furnace using a rotating cup, since for simplicity and low cost, the cup and air swirl ordinarily corotate.

Given flame stratification, with counter rotation of the cup, combustion is no longer possible because the hot gasified fuel cannot mix with the air due to the suppression of turbulent mixing. Maintenance of a constant diameter fuel evaporation zone (Figure 9), 30 cm. long did not permit combustion to be completed. Consequently, it is necessary to provide a sudden enlargement, into the combustor proper, so as to reduce the centrifugal force. This permits turbulent mixing and resultant combustion.

This presents an idealized picture as, in such a small combustor, some of the fuel escapes the fuel stratification and evaporation zone. A second outer recirculatory hot gas zone is provided, as in Figure 8, to ensure a source of heat for

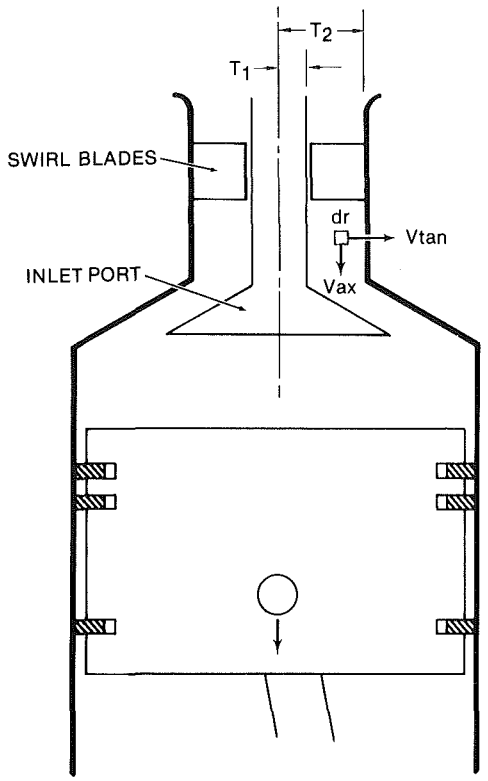

Fig. 11 Vortex air inlet port for a diesel engine combustor

ignition and consequent evaporation and rapid combustion, in the unstratified charge mode, of this escaping fuel. Some flame stability is lost as a consequence of this fuel escape.

Considering two different size CIVIC combustors, in geometric scale and at the same pressure loss, it can be shown that, to maintain flame performance, the fuel droplet must be scaled down in the following proportion [11]:

$$\frac{d}{D} = \sqrt{\frac{r}{R}} \tag{7}$$

where r and R = swirl annulus radius, d and D = fuel droplet size, for the small and large combustors respectively. Given adequate fuel atomization so that fuel evaporation is completed prior to droplet centrifuge, the characteristics of a natural gas flame can be achieved and simple geometric scaling of the combustor can be applied [10].

It is not ordinarily possible to reduce the scale of the fuel droplet sufficiently when using a small combustor. Consequently, because of increased difficulties in fuel evaporation, a small combustor suffers more problems of excessive flame length, instability and inefficiency than a large combustor does. Also, more difficulties are attendant to burning the less volatile heavy fuels.

Mixing Criteria in Vortex Combustors

Mixing in the combustor involves two processes, a mixing process for fuel evaporation and a mixing process for combustion. In a premixed combustor, with fuel evaporated and mixed with air prior to entry into the combustor, the fuel evaportation is external to the combustor and takes up much volume on account of the low air temperatures. Typically, as in a gasoline engine, a volume comparable or greater than the volume for combustion is required. In a stratified fuel injection process (diffusion flame), the volume required for fuel evaporation is small compared to the volume required for combustion, and is intrinsically linked to the combustor. In either flame, premixed or stratified, the volume required for reaction is small. We here define mixing in regards to combustion and as the mass rate of air consumption per unit pressure and area. A first priority in combustor design is to establish the volume required for combustion. Allowance must be made for imperfections in fuel evaporation in the stratification zone. In the smaller scale combustor, lack of complete stratification, and the consequent premix of some of the fuel, will require an increase in volume beyond that otherwise dictated by the requirements of combustion. In normal practice, imperfections in fuel evaporation are allowed for by use of volatile, well atomized fuel in the small combustor. The heavy, nonvolatile fuel is reserved for the larger combustors.

Consider again the free vortex motion of the small element of rotating air shown in Fig, 1, having also axial motion through the inlet air port of a reciprocating engine as shown in Fig. 11.

The instantaneous mass flow rate, m, is given by

$$\int_R^{R_2} 2\pi\, r\, dr\, \rho\, V_{ax} = m \tag{8}$$

where R_2 and R_1 are the outer and inner radii of the air inlet port.

As, in free vortex flow, V_{ax} is constant

$$m = A_v\, \rho\, V_{ax} \tag{9}$$

where Av = the inlet air port flow area
Substituting for density

$$\frac{m\sqrt{T}}{Av \bullet P} = \frac{V_{ax}}{R\sqrt{T}} \tag{10}$$

where T = air temperature and R = air gas constant.

Assuming that the pressure loss, ΔP, of the air entering the combustor, via the air inlet port, is proportional to the square of the entry air velocity and neglecting compressibility effects

$$\frac{m\sqrt{T}}{Av \bullet P} = \frac{V_{ax}}{R \bullet \sqrt{T}} = C\sqrt{\frac{\Delta P}{P}} \tag{11}$$

where C is a constant.

The air velocity varies continuously during each operating stroke as does the flow area of the inlet air port and it is customary to base the mean air flow, M, on average values of flow area and air velocity as arrived at by airflow tests, ie.,

$$\frac{M\sqrt{T}}{A\,P} = \frac{V}{R\sqrt{T}} = C\sqrt{\frac{\Delta P}{P}} \tag{12}$$

where A = mean inlet port flow area and V = mean inlet port entry velocity. This equation is equally valid for the sizing of an air inlet port of a combustor for a reciprocating engine, furnace and gas turbine, with or without swirl.

A limit is placed on the allowable pressure loss in any combustor. In a gas turbine this might be on the order of four percent of the total pressure, and less in a furnace. In a reciprocating engine, the pressure loss is expressed as a function of maximum allowable piston speed which is typically on the order of 800 meters/minute [32]. The use of overhead cam operated inlet air ports enables a somewhat larger port to be used as compared to the typical pushrod operated ports. This reduces the pressure loss and permits a higher piston speed, providing a higher airflow for greater power.

Given a fixed amount of air to be consumed or, by the same token, fuel to be burned we have some flexibility in establishing the size of the combustor from equation (12). In a

steam generator furnace, a relatively large inlet air port, together with a comparable sizing up of the combustor, might be used. This provides a lower pressure loss for economy and more time for fuel evaporation, therefore allowing use of heavy nonvolatile fuels. More area for radiation to the water tubes is also provided. In an industrial gas turbine, where space is more at a premium, a smaller inlet air port would be used with an associated higher pressure loss but with less wall area permitting easier cooling. Heavy fuels cannot be so effectively burned in such a combustor when compared to a furnace, because there is less time for evaporation.

The maximum flexibility in sizing the combustor is, however, obtained by using a multiplicity of air inlet ports, with each inlet port having an associated combustor and fuel injector assembly. With a fixed amount of fuel to be consumed and, with a fixed combustor pressure loss, we might consume all the fuel in one or "n" combustors and equation (12) can be written as

$$\frac{M\sqrt{T}}{A_p} = \frac{M_1\sqrt{T}}{A_1 p} = C\sqrt{\frac{\Delta p}{p}} \tag{13}$$

where $n\,M_1 = M$

As the basic dimension, D, of the combustor or the inlet air port is directly proportionate to the square root of the inlet port flow area A, we can write

$$\frac{M}{D^2} = \frac{M}{nD_1^2} \tag{14}$$

where D = basic dimension of the single large combustor and D_1 = basic dimension of one of the n small combustors

From equation (14)

$$\frac{D}{D_1} = \sqrt{n} \tag{15}$$

and so,

$$\left(\frac{D}{D_1}\right)^3 = \left(\sqrt{n}\right)^3, \text{ or } \frac{D^3}{nD_1^3} = \sqrt{n}$$

Therefore

$$\frac{D}{D_1} = \sqrt{n} = \frac{D^3}{nD_1^3} \tag{16}$$

which is to say that for a fixed pressure loss and a fixed airflow

$$\frac{\text{The length of the single large combustor}}{\text{The length of } n \text{ small combustors}} = \sqrt{n} \tag{17}$$

$$\frac{\text{The volume of the single large combustor}}{\text{The volume of } n \text{ small combustors}} = \sqrt{n} \tag{18}$$

$$\frac{\text{The surface area of the single large combustor}}{\text{The surface area of } n \text{ small combustors}} = \text{constant} \tag{19}$$

$$\frac{\text{Volume/Surface of the single large combustor}}{\text{Volume/Surface of a single small combustor}} = \sqrt{n} \tag{20}$$

These four equations, derived purely from mixing criteria, dominantly establish the choice of the type of combustor and its performance for reciprocating engines, furnaces and gas turbine combustors. There is no regard for fuel evaporation or chemical reaction criteria. These two problems must be resolved strictly within the context of the sizing criteria established by equation (13). Thus an evaporation problem is resolved by increasing the dimension of the combustor, or by improving atomization and fuel volatility. A chemical reaction problem such as gasoline engine detonation is minimized by keeping the size of the combustor small and using a multiplicity of cylinders to achieve the power required. Conversely with the chemical reaction delay problem of the diesel, increased combustor size helps. In addition, the burning of heavy fuels is facilitated with the penalty of much higher weight and volume per unit power. The increased volume/surface reduces heat loss and hence aids fuel evaporation. As a result, compression can be kept low for higher thermal efficiency. Where space and weight are at a premium, as in an automobile, an eight-cylinder reciprocating engine, of equal displacement to a four-cylinder engine, will produce 41 percent more power, and will, at the same time, reduce detonation. Doubling the number of fuel injectors as in an aero gas turbine will reduce the length and combustor volume by 30 percent. In both these applications, aero and automobile, volatile fuels are required to minimize the deleterious effects of reduced time for fuel evaporation when small-sized combustors are required.

CIVIC Low Emission Combustor Concept

Increasing emphasis on reduced emissions has resulted in considerable research and development. Two principal methods of achieving low emissions have been conceptually demonstrated for gas turbine combustors: staged combustion, using a fuel rich zone followed by a fuel lean zone as in the Ricardo Comet diesel, and single-staged fuel-lean combustion as in the gasoline engine. Staged combustion is favored for fuels of the future containing fuel bound nitrogen, since nitrogen can be inhibited from forming NO_x [33]. Single-stage combustion has attained more nearly the realms of practicality, and is suited to the current conventional fuels (7). There are considerable complexities and problems involved in the two approaches. These include the need for pre-mix of fuel and air, with attendant problems of flashback and instability, and the need for two sets of fuel injectors so that light-off and operational range, together with a premix capability, can be achieved. Ricardo has shown how, by use of the Pintaux fuel injector, two entirely different modes of combustion can be achieved in the Comet diesel engine using only one fuel injector and without apparent complexity. This consists of a stratified fuel injection mode for light-off using buoyancy inhibited mixing, and an unstratified fuel injection mode for normal operation using buoyancy enhanced mixing. Borrowing from this idea of Ricardo, Solar has pursued development, in conceptual evaluation, of a similar dual mode fuel injector designed to be used in the CIVIC combustor. The combustor design is based on the Turbomach Gemini combustor, except that a non-rotary fuel injector is used.

Combustor Design. The CIVIC combustor is shown in Fig. 12. It is based on previous designs shown in Fig. 2 and 8. A radial inward vortex swirl generator is used to form a free vortex flow, which establishes forced vortex flow hot gas recirculations, for purposes of ignition, on the outer and inner extremities of the free vortex flow. No film cooling of the combustor walls, as in typical practice, is used. The air to the combustor is brought, by reverse flow, over the walls to convectively cool them. Particularly effective cooling can be achieved by the use of trip strips [34]. This cooling technique has a considerable advantage in that the air temperature immediately adjacent to the fuel injection zone is raised by several hundred degrees above the air compressor delivery temperature. The significant problem of fuel evaporation, when using nonvolatile diesel oil in small combustors, is considerably reduced just as was the case, using the same technique, in the Gemini combustor. The amount of air used for combustion depends on the application of the concept. In a single-stage, lean premix combustor, air considerably in excess of stoichiometric requirements is used. Figure 12 shows

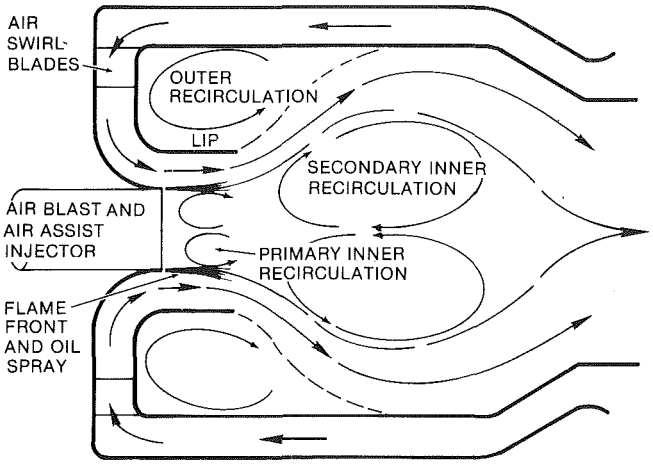

Fig. 12 CIVIC vortex low emission combustor concept

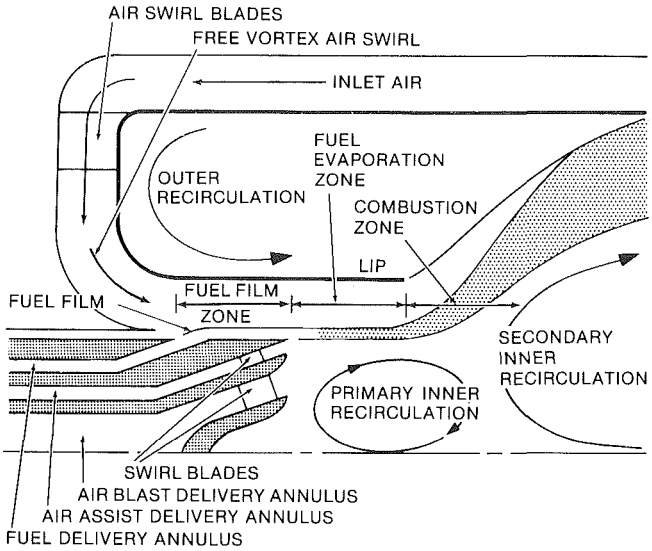

Fig. 13 CIVIC stratified charge fuel injection

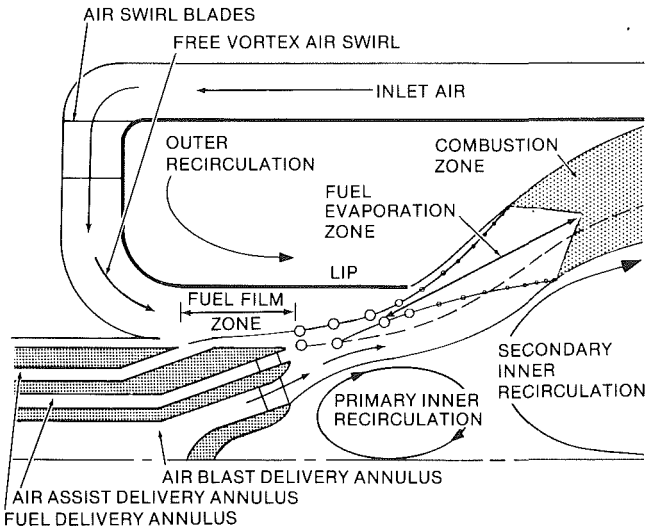

Fig. 14 CIVIC premix fuel injection

the first stage of a two stage, premix combustor, in which about 70 percent of the stoichiometric air is used. This level of excess fuel suffices to suppress NO_x formation while permitting blue flame combustion.

The air blast, air-assisted fuel injector is located to exactly place a circumferentially uniform sheet of fuel at the inner periphery of the free vortex air swirl. This duplicates the critical fuel placement of the rotating cup fuel injector shown in Fig. 9.

A mean swirl angle of 45 deg is used. Airflow development of the vortex swirler indicated that much of an increase in swirl beyond this would cause airflow separation at the fuel injector. Flow separation results in premature ignition and burnout of the combustor (7). The entry dynamic head of the air swirl into the combustor was 4.5 percent of the total pressure. With an injector diameter of 3.0 cm this results in a centrifugal force, at the inner periphery of the free vortex swirl and immediately adjacent to the fuel spray, of 83,500g. The density ratio, between the hot evaporated fuel and the immediately adjacent cooler air, on the order of 2, is enhanced by a factor of 83,500g compared to a factor of 1g, with an inversion layer, having a density ratio of about 1.04 in the earth's atmosphere. Unmixedness is much enhanced as a result.

Fuel Injector Design. Figures 13 and 14 show the stratified charge and premixed modes of fuel injection. Detailed descriptions of the two modes of flame propagation are references [10, 11].

Stratified Charge Fuel Injection. As shown in Fig. 13, fuel is delivered, through an annulus, onto a filming surface forming the inner periphery of the free vortex air delivery. The swirling air thins out the fuel film which somewhat surprisingly remains attached to the wall. Air-assist atomizing air of a relatively small amount, swirling in opposite rotation to the main air swirl, serves to atomize the fuel well at the end of the fuel injector, and to momentarily inhibit outward centrifuging of fuel. During light-off this air assist is boosted, by an air pump, to provide improved atomization in the critical light-off phase where the low air pressure and temperature slow evaporation. In normal operation, the air assist operates at combustor pressure loss levels. Ignition and consequent fuel evaporation and laminarization are as previously described for the rotating cup combustor.

Premixed Fuel Injection. As shown in Fig. 14, the air-assist air is shut off and air blast air is supplied in a relatively large amount. This air blast air at combustor delivery pressure, swirls in the same direction as the main air supply, through an appropriate valve, to the fuel injector. It serves both as a means of atomization of the fuel film, and as a means of preventing immediate ignition. Ignition is prevented because, free from the counter swirl turbulence of the air assist mode, the primary ignition recirculation is momentarily isolated. Therefore, under the high centrifugal force, the fuel droplets centrifuge outward. They evaporate in the main air swirl, just as in the case of corotation of the rotating cup and air swirl. Ignition occurs downstream from both the outer and the secondary inner recirculation zones. In the former case, flame propagation is unstratified and, in the latter case, it is stratified. Premixing inside the combustion zone results in imperfections in mixing. Although avoiding the combustor burnout problems of premature ignition, which may occur when premixing ahead of the combustor (Fig. 2), it takes up considerable combustion volume. The use of two ignition zones, and particularly the fast mixing outer ignition of unstratified charge, serves to keep the volume required low and compatible with the stratified charge fuel injection volume requirements.

Therefore, by operating an air valve, the fuel injector can be made to operate in two entirely different modes. The first

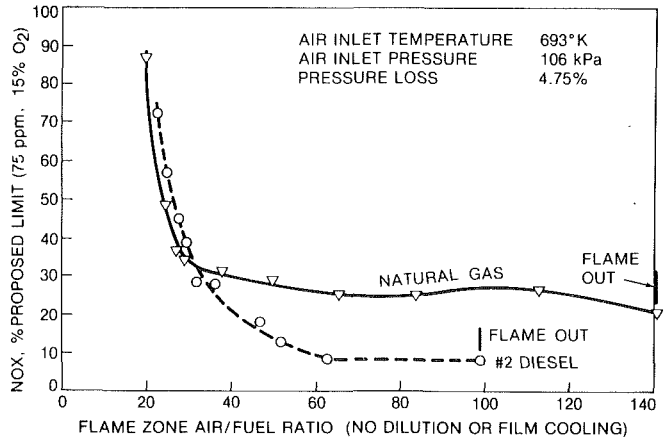

Fig. 15 CIVIC flame performance, stratified charge fuel injection, natural gas and no. 2 diesel oil

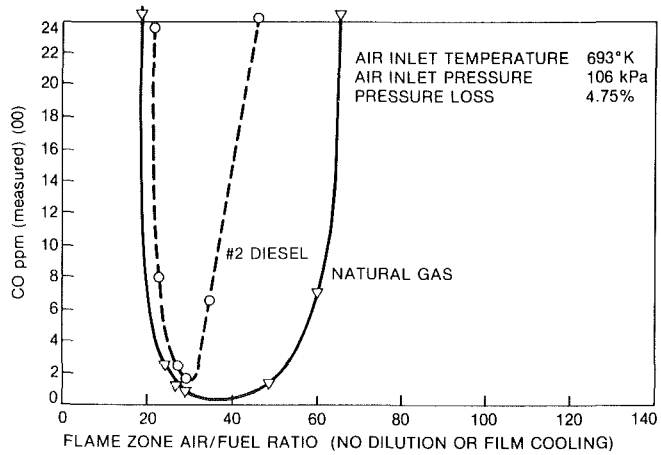

Fig. 16 CIVIC flame performance, stratified charge fuel injection, natural gas and no. 2 diesel oil

is a stratified mode for wide operational range with high NO_x, and the second is a premixed mode for low NO_x with low operational range.

Test Results. All tests were at atmospheric pressure using No. 2 diesel and natural gas, with a combustor inlet air temperature of 700 K, and a combustor pressure loss of 4.75 percent. Blue flame combustion was obtained with both liquid and gas fuels. Figure 15 shows the NO_x characteristics against flame zone air-fuel ratio for No. 2 diesel and natural gas in the stratified charge mode. The natural gas was supplied through the air blast swirl annulus. The flame stability was excellent in either case but the significantly better flame stability with gas can be attributed to the better stratification obtained with gas. This is also reflected in the higher NO_x obtained with gas. The improved stratification with gas is also reflected in the wider range of operation with low CO as shown in Fig. 16. Obviously improvements in the atomization of the diesel fuel will permit an improvement of the flame efficiency and stability. These tests illustrate the fundamental importance of fuel atomization, fuel volatility, and fuel placement in achieving a wide range of stable, efficient operation. Figure 17 shows the NO_x characteristics against flame zone air-fuel ratio for No. 2 diesel when operating in the premixed mode. The considerable reduction in flame stability, together with the reduced NO_x, is to be anticipated with a premixed flame. This test again shows the crucial importance of fuel spray location in relation to flame stability. The deliberate movement of the fuel spray, a fraction of a centimeter from the ignition source, has resulted in a large loss in flame stability. Therefore in small vortex combustors, fuel atomization, fuel spray location, and fuel volatility are of prime importance, together with the proper design for fuel-air mixing. Reaction rate criteria, in their influence on combustor performance, are by comparison inconsequential.

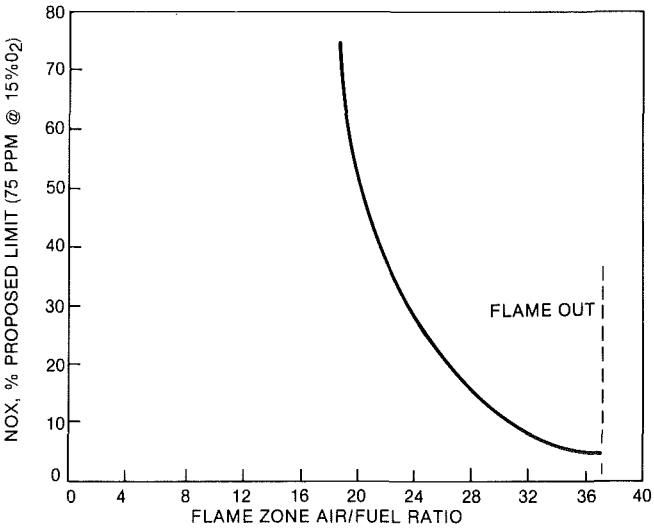

Fig. 17 CIVIC flame performance premixed fuel injection no. 2 diesel oil

Summary

Vortex combustion without the customary jet-stirred combustion of typical gas turbine practice, shows potential advantage. The need for proper aerodynamic design to most effectively use buoyancy for fuel evaporation and subsequent mixing is crucial. Fine and accurately located fuel droplets dominate the design of the typical small vortex combustor.

References

1 Ricardo, H.R., and Hempson, T.G.G. *The High-Speed Internal-Combustion Engine*, Blackie, Glasgow, 1968, pp. 32–43.

2 Schweitzer, P.H., and Grunder, L.J. "Hybrid Engines," *SAE Transactions*, 1963, pp. 541–562.

3 Shepherd, D.G., *Introduction to the Gas Turbine*, Constable and Co., London, 1960, pp. 137–140.

4 Obert, F.E., *Internal Combustion Engines and Air Pollution*, Intext, New York, 1973, pp. 583–585.

5 Beer, J.M., and Chigier, N.A. *Combustion Aerodyamics*, Halstead, New York, pp. 107–117.

6 Ricardo, H.R., and Hempson, J.G.G. *The High-Speed Internal-Combustion Engine*, Blackie, Glasgow, 1968, pp. 22–28.

7 Sood, V.M., and Shekleton, J.R. "Ongoing Development of a Low Emission Industrial Gas Turbine Combustion Chamber," ASME Paper No. 79-GT-203.

8 Roberts, P.B., et al., "Advanced Lox NO_x Combustors for Supersonic High-Altitude Aircraft Gas Turbines," ASME Paper No. 76-GT-12.

9 Duffy, T.E., et al., "Low Emissions Combustor/Vapor Generator for Automotive Rankine Cycle Engines," 7th Intersociety Energy Conversion Engineering Conference, San Diego, Calif., 1972, Paper No. 729129.

10 Sood, V.M., and Shekleton, J.R., "Ongoing Development of a Low Emission Axisymetric Annular Vortex Combustor for an Industrial Gas Turbine," ASME Paper No. 80-GT-58.

11 Shekleton, J.R., "The CIVIC: A Concept in Vortex Induced Combustion for the Solar Gemini 10kW Gas Turbine," ASME Paper No. 80-GT-54.

12 Herbert, M.F., "A Theoretical Analysis of Reaction Rate Controlled Systems," *Combustion Researches and Reviews*, Mullins and Fabri, ed., Butterworths, London, 1957.

13 Hodgetts, D., ed., *Advances in Automobile Engineering (Part IV)*, Combustion Processes in the Spark Ignition Engine, Pergamon Press, Oxford, 1966, p. 114.

14 Kumagai, S., and Kudo, Y. "Flame Studies by Means of Ionization Gap in a High-Speed Spark-Ignition Engine," *Ninth Syposium (International) on Combustion*, Academic Press, New York, 1963.

15 Lyn, W.T., "Study of Burning Rate and Nature of Combustion in Diesel Engines," *Ninth Symposium (International) on Combustion*, Academic Press, New York, 1963.

16 Stewert, R.M., "Engine Combustion At Large Bore-To-Stroke Ratios," SAE Paper No. 780968.

17 Catania, A.E., "Airflow Investigation in the Open Combustion Chamber of a High-Speed, Four-Stroke Diesel Engine," ASME Paper No. 80-FE-5.

18 Obert, F.E., *Internal Combustion Engines and Air Pollution*, Intext, New York, 1973, p. 593.

19 Lewis, G.D., "Centrifugal Force Effects on Combustion," *Proceedings of the Fourteenth Symposium on Combustion*, Combustion Institute, Pittsburgh, Pa, 1973.

20 Mestre, A., and Benoit, A., "Combustion in a Swirling Flow," *Proceedings of the Fourteenth Symposium on Combustion*, Combustion Institute, Pittsburgh, Pa, 1973.

21 Hoffman, H., et al., "Combustion in Diesel Engines with Divided Combustion Chambers," *Proceeding of the Joint Conference on Combustion*, ASME Boston, 1955, p. 285.

22 Obert, F.E., *Internal Combustion Engines and Air Pollution*, Intext, New York, 1973, p. 596.

23 Maleev, V.L., "Engine Efficiencies," *Internal Combustion Engines: Theory and Design*, McGraw-Hill, New York, 1945.

24 Beer, J.M., and Chigier, N.A., *Combustion Aerodynamics*, Halstead, New York, pp. 136–144.

25 Lee, Y., "Flames Trajectory and Its Experimental Determination in Vortex Combustion," Dept., Mech. Eng. Penn State U., May 1963.

26 Karim, G.A., and Tsang, P., "Flame Propagation Through Atmospheres Involving Concentration Gradients Formed By Mass Transfer Phenomena," *Fluid Mechanics of Combustion*, Dussourd, J.L., et al., ed., ASME, New York, 1974.

27 Mitchel, E., et al., "Design and Evaluation of a Stratified Charge Multi-Fuel Military Engine," SAE Paper No. 680042.

28 Givens, L., ed., "Stratified Charge Mixing Strategies Compared," *Automotive Engineering*, Aug. 1978, SAE, Warrendale, Pa.

29 Simko, A. et al., "Exhaust Emission Control by the Ford Programmed Combustion Process-PROCO," SAE Paper No. 720052.

30 Beer., J.M., and Chigier, N.A. *Combustion Aerodynamics*, Halstead, New York, pp. 188–193.

31 Rizkalla, A.A., and Lefebure, A.H., "Influence of Liquid Properties on Airblast Atomizer Spray Characteristics," ASME Paper No. 73-GT-1.

32 Ricardo, H.R., and Hempson, J.G.G., *The High-Speed Internal Combustion Engine*, Blackie, Glasgow, 1968, pp. 196–201.

33 Schultz, F.D., and Wolfbrandt, G., "Flame Tube Parametric Studies for Control of Fuel Bound Nitrogen Using Rich-Lean Two-Stage Combustion," NASA TM-81472 DOE/NASA/2593-80/15. Western States Section, Combustion Institute, Irvine, CA, Apr., 1980.

34 Evans, D.M., and Nobel, M.L., "Gas Turbine Combustor Cooling by Augmented Backside Convection," ASME Paper No. 78-GT-33.

E. Macchi
Professor.
Mem. ASME

A. Perdichizzi
Research Engineer.

Istituto di Macchine,
Politecnico di Milano,
20133 Milano, Italy

Efficiency Prediction for Axial-Flow Turbines Operating with Nonconventional Fluids

The need for a simple and reliable method for predicting the efficiency of a turbine stage without carrying out a detailed aerodynamic design is enhanced. The results of an optimization study carried on a large number of turbine stages are presented. The turbine stage efficiency is found to be a function of three main parameters: the expansion ratio, defined as the specific volume variation across the turbine in an isentropic process; the dimensional parameter $\sqrt{\dot{V}_{out}}/\Delta h_{is}^{1/4}$, *which accounts for actual turbine dimensions, and the specific speed. The presented method is believed to be useful mainly for nonconventional turbine stages, the efficiency of which cannot be anticipated on previous machines experience.*

Introduction

In the optimization procedure of the thermodynamic cycle and of the working fluid of a power plant, operating either with a Rankine or Joule cycle, it is of primary importance to assume realistic predictions of the various components' performance, in particular of the turbine efficiency. While the efficiency of conventional turbines can be anticipated on the basis of previous experience on similar models, for unusual turbines, like for instance the ones operating in Organic Rankine Cycles, one has to rely on more general prediction methods. Not considering oversimplified methods, which obviously cannot account for the peculiarities of the machine, all the loss correlations existing in the literature [1–5] require the knowledge of a number of flow features (the velocity triangles) and blade characteristics (chord, height, thickness, etc.). Hence, a rather detailed design is to be carried out to predict the turbine efficiency, a requirement which is clearly impractical in thermodynamic analyses which must consider a great number of possible cycles, and therefore turbines.

It is the purpose of this paper to present a method which allows for a very simple efficiency prediction of a turbine stage. It is applicable for a wide range of working fluids, expansion ratios, turbine dimensions, etc. The obtained results are a consequence of several assumptions, which are presented and discussed in the paper. Besides the efficiency, other results are given which show the influence of the various parameters on the most important aerodynamic and geometric data of a turbine stage. The most significant difference of the present results, with respect to other previously published methods [6], is that the compressibility effects are explicitly accounted for.

Contributed by the Gas Turbine Division and presented at the International Gas Turbine Conference and Products Show, Houston, Texas, March 9–12, 1981, of THE AMERICAN SOCIETY OF MECHANICAL ENGINEERS. Manuscript received at ASME Headquarters, December 1, 1980. Paper No. 81-GT-15.

Method of Solution

The design of a turbine stage can be looked at as an optimization problem. As in all optimization problems, three main points should be made clear: (1) definition of the function to be optimized; (2) independent variables; and (3) constraints which limit the range of the search. As far as the first point is concerned, the turbine efficiency was chosen as the function to be optimized; the optimization results depend on the assumptions made about the utilization of the leaving kinetic energy. As shown in the example of Fig. 1, if the stage total-to-static efficiency is optimized ($\Phi_E = 0$), lower flow coefficients will be obtained than for stages optimized for total-to-total efficiency ($\Phi_E = 1$); the two solutions exhibit different velocity triangles and turbine dimensions. Unless otherwise specified, the results in the paper refer to cases where the assumption $\Phi_E = 0.5$ was made.

The stage efficiency is calculated, with a one dimensional approach, by the computer program described in [7], which requires the calculation of: *a*) loss coefficients, *b*) restriction factors, *c*) leakage losses, *d*) blade profiles, and *e*) exit flow angles. The main assumptions made for these calculations will be described in the following:

Loss Coefficients. On the authors' experience, the Craig and Cox [1] correlation is the most complete, coherent and realistic method available in the literature to calculate the loss coefficients of a turbine stage. For this reason, it was assumed as a basis for the loss coefficient calculation. It requires the knowledge of all the geometric parameters represented in Fig. 2. For converging-diverging nozzles, it was assumed that the loss coefficients can be computed with the same procedure used for converging blades. This simple hypothesis seems to be not too far from reality, for operation at design point [4]. Only full admission stages were considered in the analysis. The loss coefficients account for profile, secondary, and annulus losses. They are computed at the minimum loss incidence. For simplicity, it is assumed that the relative flow angle and the blade angle at rotor inlet are equal. Disk

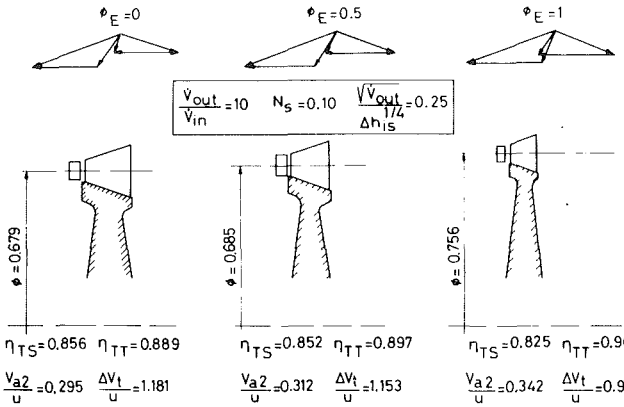

Fig. 1 Example of the influence of the assumed value for the utilization factor of leaving loss Φ_E on the results obtained in the optimization

windage losses were not included, since they depend on the various turbine arrangements.

Restriction Factors. They are used in the continuity equation, which is solved in blade opening sections, or in the critical throats for converging-diverging nozzles. According to Vavra [8], they are computed from the profile loss coefficients, for an assumed boundary layer wake form/energy factor ratio equal to 0.9.

Leakage Losses. They are assumed to be null across the stator blade, owing to the possibility of using an almost hermetic sealing on the turbine shaft, while for the rotor the correlation suggested in [1] for unshrouded blades is applied; hence, the actual formulation for calculating the efficiency is:

$$\eta = \frac{u\ \Delta V_t}{\Delta h_{is} - \Phi_E \dfrac{V_2^2}{2}} - \Delta\eta_{CL}$$

Blade Profiles. The correlation doesn't require the knowledge of the blade profile, but only of some parameters, which are either optimized, or computed from approximate geometric relations (backbone length), or assumed as fixed variables in the program, according to the specifications given in Table 1. For converging-diverging blades, reference is made to Deich [4] method, which suggests an empirical relationship between the design Mach number and the blade degree of divergence (o/o_{min}). The rotor blades are assumed to be converging, with a rectilinear profile on the suction side surface from throat to trailing edge.

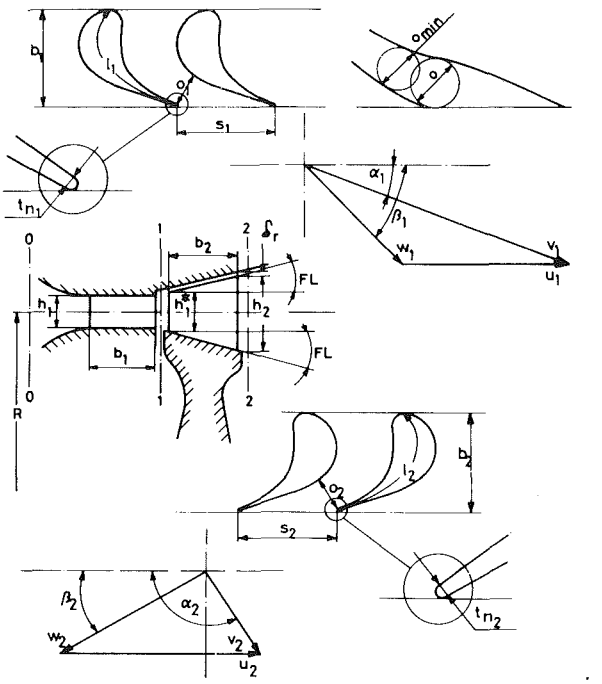

Fig. 2 Nomenclature for the velocity triangles and the geometric data of the turbine stage

Nomenclature

b = axial chord, m
FL = flaring angle (see Fig. 2), deg
D = mean diameter, m
h_1 = stator blade height, m
h_1^* = rotor blade height at the inlet section, m
h_2 = rotor blade height at the outlet section, m
k_{is} = head coefficient = $2\,\Delta h_{is}/u^2$
k_s = blade surface roughness, m
l = blade backbone length, m
M_V = Mach number of the absolute velocity
M_W = Mach number of the relative velocity
n = speed of revolution, rps
N_S = specific speed = $n\sqrt{\dot{V}_{out}}/\Delta h_{is}^{3/4}$
o = blade throat opening, m
o_{min} = blade critical throat, m
P = static pressure, Pa
P_T = total pressure, Pa
R = turbine mean radius, m
r^* = isentropic degree of reaction
Re = Reynolds number, relative to blade opening
s = blade spacing, m
t_n = trailing edge thickness, m
u = peripheral speed, m/s
W = relative velocity, m/s
V = absolute velocity, m/s
$\dot{V}_{in}$ = volumetric flow rate, at turbine inlet total conditions, m^3/s
$\dot{V}_{out}$ = volumetric flow rate at turbine exit static pressure, calculated for isentropic process throughout the turbine, m^3/s
z = number of blades
α = absolute flow angle, deg
β = relative flow angle, deg
γ = heat capacity ratio
δ_r = radial clearance, m
Δh_{is} = total-to-static enthalpy drop, J/kg
$\Delta\beta$ = relative flow deviation in the rotor blade, deg
$\Delta\eta_{CL}$ = efficiency loss due to leakage across the rotor blades
Φ_E = utilization factor of leaving loss
η_{TS} = total-to-static efficiency
η_{TT} = total-to-total efficiency

Subscripts

0,1,2 = station
a = axial component
max = maximum value
min = minimum value
opt = optimized value
t = tangential component

Table 1 Optimizing variables, fixed input variables, variable input data and constraints used in the present analysis

1 Optimizing variables
$r^*\ k_{is}\ (o_{min})_1\ (o/s)_1\ b_1\ o_2\ (o/s)_2\ b_2$

2 Fixed input variables
$\alpha_o = 0$
$Re = 5.10^5$
$k_s = 2.10^{-3}$ mm
$R_1/R_2 = 1$
$h_1^*/h_1 = 1.10$
δ_r = max (0.2 mm or $R/1000$)
t_{n1} = max (0.2 mm or $o_1/10$)
t_{n2} = max (0.2 mm or $o_2/10$)

3 Variable input data
Fluid thermodynamic properties (molecular mass, specific heat ratio)
Inlet conditions (total pressure and temperature)
Outlet conditions (static pressure)
Mass flow rate
Speed of revolution

4 Constraints
$0 < M_{W1} < 0.8$
$0 < M_{W2} < 1.4$
$-20° < FL < +20°$
$0.001 < (h/D)_1, (h/D)_2 < 0.25$
$0 < (b/D)_1, (b/D)_2 < 0.25$
$13° < (o/s)_1, (o/s)_2 < 60°$
$2\,o_1 < b_1 < 100$ mm
$2\,o_2 < b_2 < 100$ mm
1.5 mm $< o_{min1}, o_1 < 100$ mm
1.5 mm $< o_2 < 100$ mm
$-0.1 < r^* < 0.9$
$10 < z_1 < 100$
$10 < z_2 < 100$

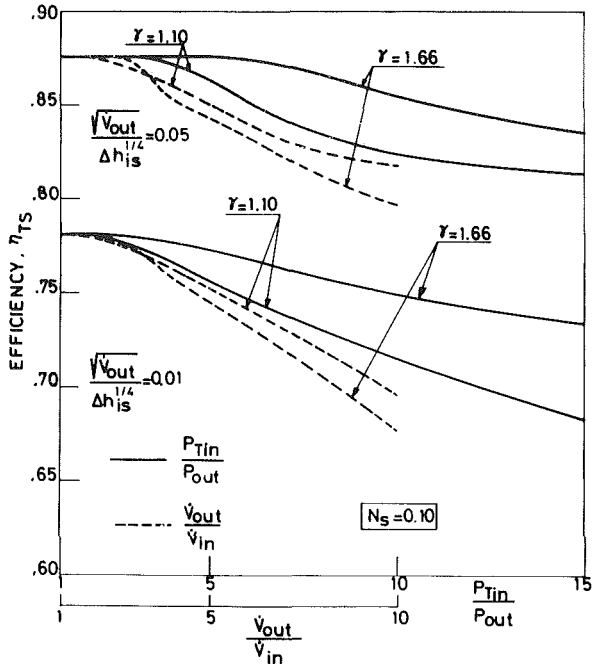

Fig. 3 Influence of the pressure ratio and of the volume flow rate variation on the efficiency of a turbine stage, for two values of γ and two values of turbine dimensions

Exit Flow Angles. The Ainley-Mathieson [9] correlation is applied for subsonic conditions. For supersonic flows, the flow angle is computed according to the Vavra [8] equation for the so-called after-expansion process, both for converging and converging-diverging blades.

The selected independent optimizing variables, the variable and fixed input data, and the assumed constraints are summarized in Table 1. It can be seen that eight optimizing variables are sufficient to identify a turbine stage. The physical significance of the various constraints is in most cases self explanatory: some limits are due to practical limitations in blade machining, others are necessary to restrict the search of solutions in the validity range of the assumed correlations. The adopted procedure is a numerical optimization technique, fully automatized by an available computer program [10], which makes use of an iterative method, with tentative changes of the variables up to the attainment of the optimum value. The required number of iterations (each iteration performs a complete turbine stage calculation) varied within 3000 ÷ 6000. Average CPU time on the Univac 1100 for the solution of one case was about 15 s.

Discussion of Results

In the attempt to derive results of general validity from the analysis, it is useful to resort to the use of similarity parameters, and in particular to the specific speed N_S. The so-called specific diameter is not introduced, because it is not an independent variable, but a result of the optimization; in other words, only cases with optimum specific diameters are considered. According to the similarity rules, results obtained for a particular turbine will hold for all other turbines having the same specific speed, provided that:

a) Reynolds number effects are neglected.

b) The thermodynamic behavior is the same, i.e., either incompressible flows, or fluids with the same pressure ratio and the same heat capacity ratio are considered.

c) The geometric similarity is preserved (including tip clearance, surface roughness, etc.).

As far as Reynolds number effects are concerned, they were not included in the analysis. In applying the loss correlation, it is assumed that the Reynolds number effects vanish for Re larger than a limiting value, which depends on the blade relative surface roughness. All the presented results refer to turbines having Reynolds numbers in that range. Of course, for lower Re one could correct the results with some appropriate rule, like the one suggested in [6].

The thermodynamic properties of the working fluid affect the turbine design and performance in two main ways: (1) loss coefficients are a function of Mach numbers; (2) the fluid volume variation during the expansion influences the geometry of the turbine. Therefore, two optimized turbines having the same specific speed and, say, the same pressure ratio will not have either the same geometry or the same efficiency, if they have working fluids with different heat capacity ratios. In fact, the same pressure ratio will cause different Mach numbers and different volume variation for the two fluids.

Let's consider the two turbines of Fig. 3, which were optimized for two very different fluids, one with a complex molecule ($\gamma = 1.10$) and the other monoatomic ($\gamma = 1.66$): for low pressure ratios, the compressibility effects are negligeable; for large pressure ratios, important efficiency differences appear for the two fluids; the efficiency decrease is larger for the complex molecule fluid, which experiences larger volume variations. If the turbines working with different fluids are compared for equal $\dot V_{out}/\dot V_{in}$ ratios, the efficiency difference becomes much lower, and it is mostly due to the different Mach numbers. The situation is confirmed by the results of Fig. 4, which shows that γ has a small influence on the turbine efficiency for equal $\dot V_{out}/\dot V_{in}$. For the above reasoning, we will use the $\dot V_{out}/\dot V_{in}$ parameter for accounting of compressibility effects. All the calculations presented in the followings were performed for a low value of

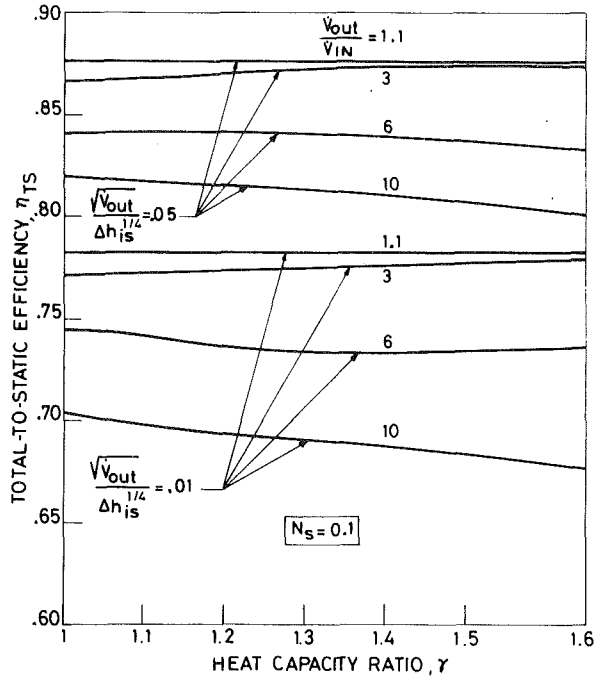

Fig. 4 Influence of the heat capacity ratio γ of the working fluid on the efficiency of a turbine stage, for two turbine dimensions; the comparison is made for constant volume flow rate ratios $\dot{V}_{out}/\dot{V}_{in}$

γ(1.10), which is representative of most organic fluids; this assumption will yield conservative efficiency values if the results are applied to fluids having simpler molecules.

As far as the geometric similarity is concerned, it can be seen from Table 1 that several dimensional constraints have been introduced in the analysis. Therefore, small turbines will behave differently from large turbines, because they have larger relative thickness, clearance, etc. According to the similarity rules, the parameter which accounts for the "size" of the considered turbine is the ratio $\sqrt{\dot{V}_{out}}/\Delta h_{is}^{1/4}$. That is to say that similar turbines having the same $\sqrt{\dot{V}_{out}}/\Delta h_{is}^{1/4}$ have the same actual dimensions.

From the above discussion, it seems appropriate to state that the results obtained by optimizing a particular turbine can be transferred to other turbines having the same specific speed, provided that they have the same $\dot{V}_{out}/\dot{V}_{in}$ (similar compressiblity effects) and $\sqrt{\dot{V}_{out}}/\Delta h_{is}^{1/4}$ ratios (geometric similarity) and that Reynolds number effects are not considered.

Results for Optimum Specific Speed. Also the specific speed N_S can of course be optimized: in this case, the results of Fig. 5 and 6 are obtained. As seen in Fig. 5, a strong influence on the efficiency achievable by a turbine stage is exerted both by the compressibility effects and by the turbine actual dimensions. The two effects are combined, i.e. for small turbines with large volume variations, large efficiency penalties take place. It can be seen that optimum specific speeds increase for smaller turbine dimensions, owing to the increased importance of radial clearance effects. An idea of the actual turbine dimensions is given by the curves of Fig. 7, where the stator blade h_1 variation is represented. For large expansion ratios, smaller stator blade heights occur, due to lower volume flow rate at stator exit.

The compressibility effects cause important variations in the velocity triangles. The optimum degree of reaction (Fig. 8), which is about 50 percent as expected for incompressible cases ($\dot{V}_{out}/\dot{V}_{in} \simeq 1$), decreases for larger expansion ratios; consequently, larger values of the head coefficients are required. These modifications of the velocity triangles allow a reduction of the volume flow variation across the rotor blades

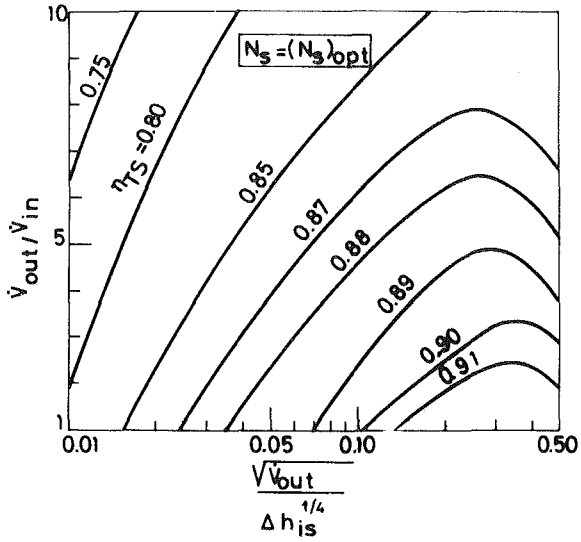

Fig. 5 Efficiency prediction for a turbine stage at optimum specific speed

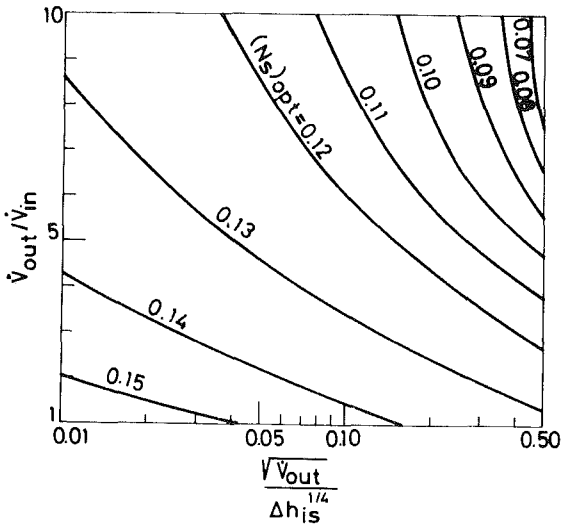

Fig. 6 Optimum values of specific speed for a turbine stage

and of the rotor outlet Mach numbers, with beneficial effects on the efficiency. It is of interest to notice that the number of blades coming out from the optimization yields rotor blade solidities not very different from the ones suggested by Zweifel [11] loading criteria (Fig. 9). This is somewhat surprising, since the present results are obtained by the contemporary optimization of all losses, while the Zweifel blade loading criterion was based only on profile losses. With large volume variations, lower values of Zweifel coefficients take place, i.e. larger axial chords are required, to achieve the necessary blade height variation across the rotor blades without exceedingly high flaring angles. The flow deflections in the rotor blades (Fig. 9) increase for large expansion ratios, owing to the larger head coefficients.

The regions in which some of the imposed constraints occur are evidenced in Fig. 10. For large turbine dimensions, the assumed maximum value of blade number is reached (Fig. 10(a)), while the minimum number for stator blades is obtained for very small turbines. In a large portion of the diagram, also absolute limits on the trailing edge thickness of both stator and rotor blades are reached (Fig. 10(b)). The limits for Mach numbers (Fig. 10(c)) influence the solution

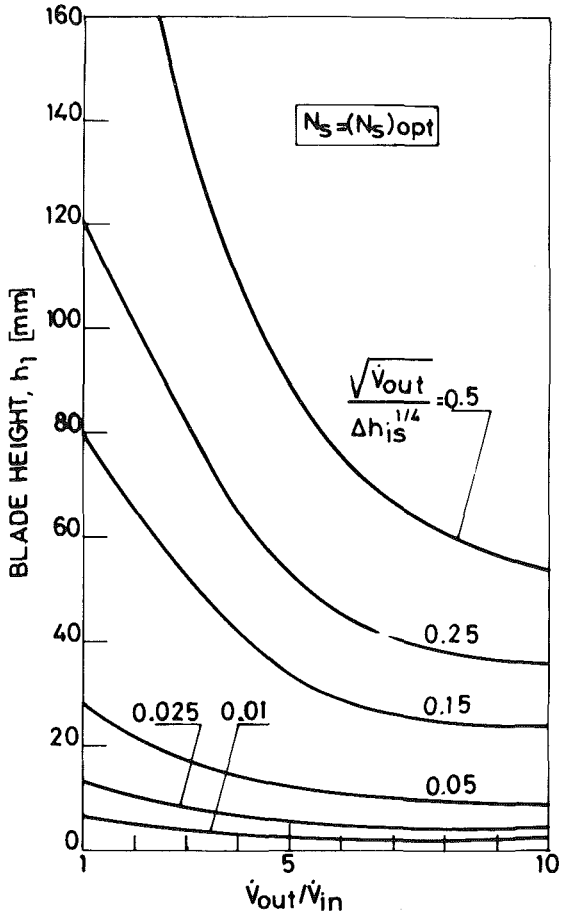

Fig. 7 Variation of the stator blade height of a turbine stage operating at optimum specific speed

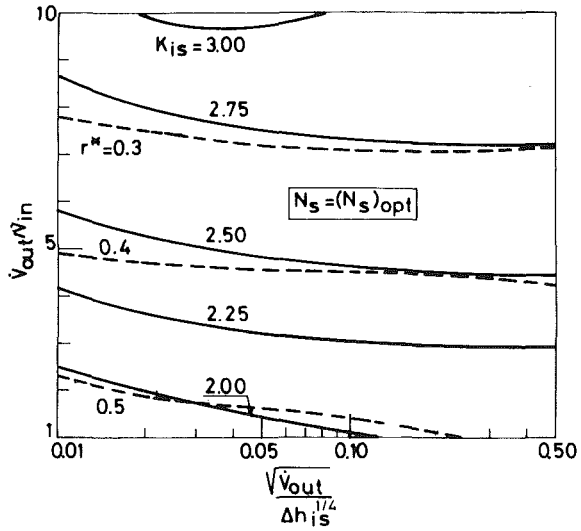

Fig. 8 Variation of the isentropic degree of reaction r^* and of the head coefficient k_{is} for various turbine stages at optimum specific speed

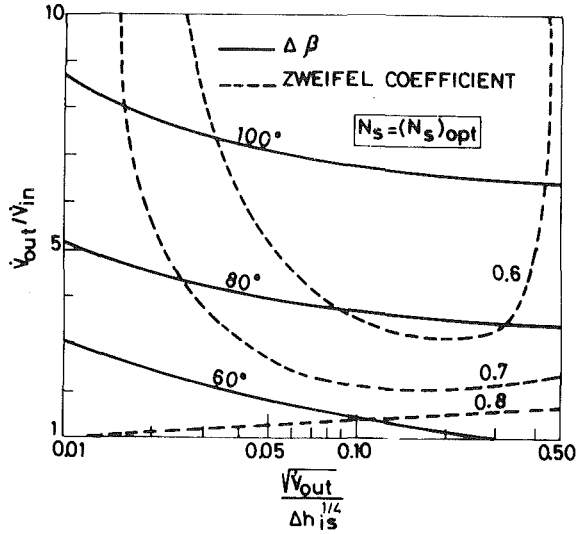

Fig. 9 Variation of the Zweifel coefficient [11] and of the rotor flow deflection angle for various turbine stages at optimum specific speed

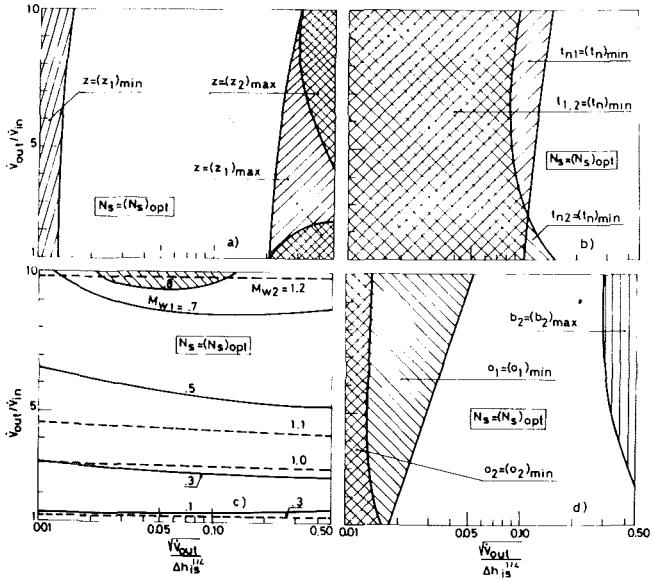

Fig. 10 Regions of influence of some constraints assumed in the turbine stage optimization, at optimum specific speed: *a)* blade number; *b)* trailing edge thickness; *c)* relative Mach number; *d)* blade opening and axial chord

only for very large expansion ratios, where the limit value for the relative rotor inlet Mach number is reached. The turbine stages become transonic in the rotor blade for expansion ratios of about 3, but the outlet Mach numbers don't exceed 1.2 even for large expansion ratios. The limits for the minimum blade opening (Fig. 10(*d*)) are reached for small turbines, while the limit for the maximum rotor blade axial chord occurs for large turbines with large expansion ratios.

Results for Various Specific Speeds. Often the turbine stages cannot be designed for their optimum specific speed. For instance, in multi-stage turbines, the speed of revolution must be a compromise among the requirements of the various stages, which operate at different specific speeds. The efficiency dependence on specific speed is shown in Fig. 11, where results obtained for various turbine dimensions and expansion ratios are given. In the figure, the present results are compared with the Baljè [6] data, which were obtained with a similar approach, but using a different loss correlation [5]. It can be seen that, for nearly incompressible flows ($\dot V_{out}/\dot V_{in}$ = 1.1), the Baljè curve is very close to the one relative to "large" turbines in the most significant portion of the considered specific speed range. This result demonstrates that the efficiency-specific speed relationship has a similar behavior, irrespective of the assumed loss correlation. The Baljè loss correlation is somewhat more optimistic than the Craig and Cox one (it should be pointed out that in the Baljè

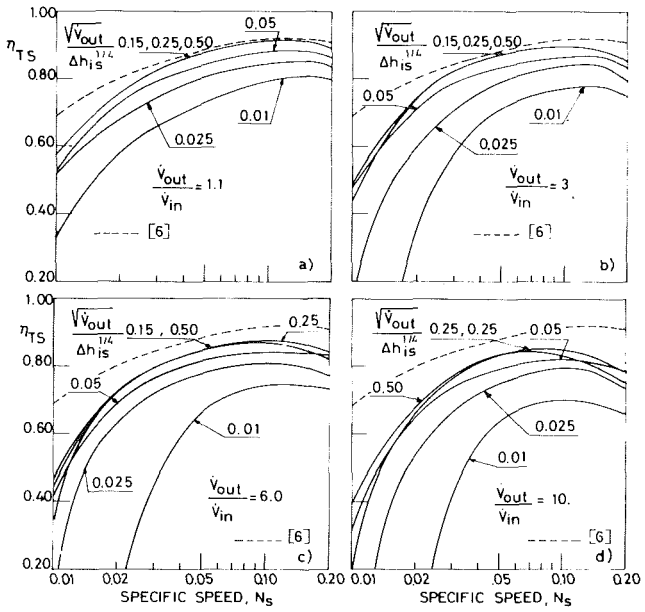

Fig. 11 Efficiency prediction for turbine stages at various expansion ratios, characteristic dimensions ($\sqrt{\dot{V}_{out}}/\Delta h_{is}^{1/4}$) and specific speed

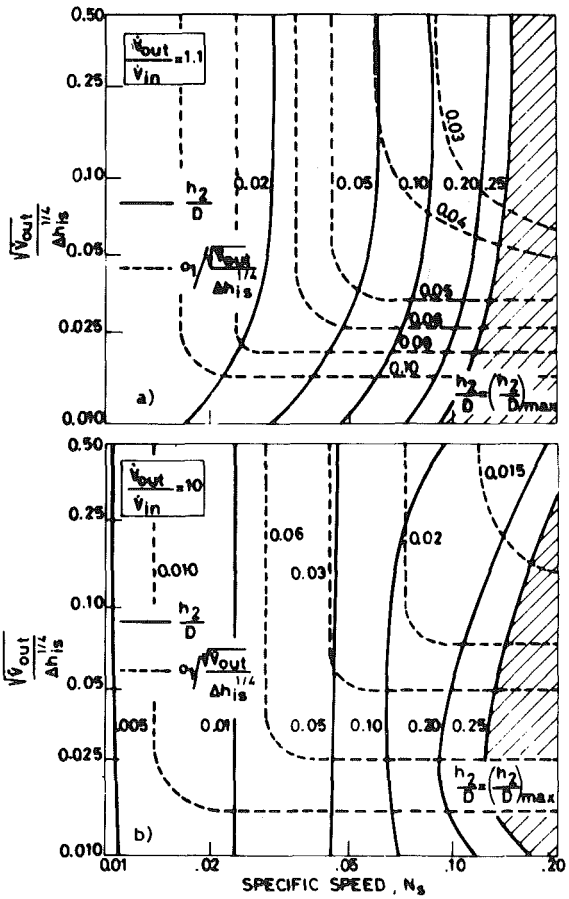

Fig. 12 Variation of the rotor blade height/mean diameter ratio and of the $o_1/(\sqrt{\dot{V}_{out}}/\Delta h_{is}^{1/4})$ parameter for nearly incompressible turbine stages (a) and for large expansion ratios stages (b)

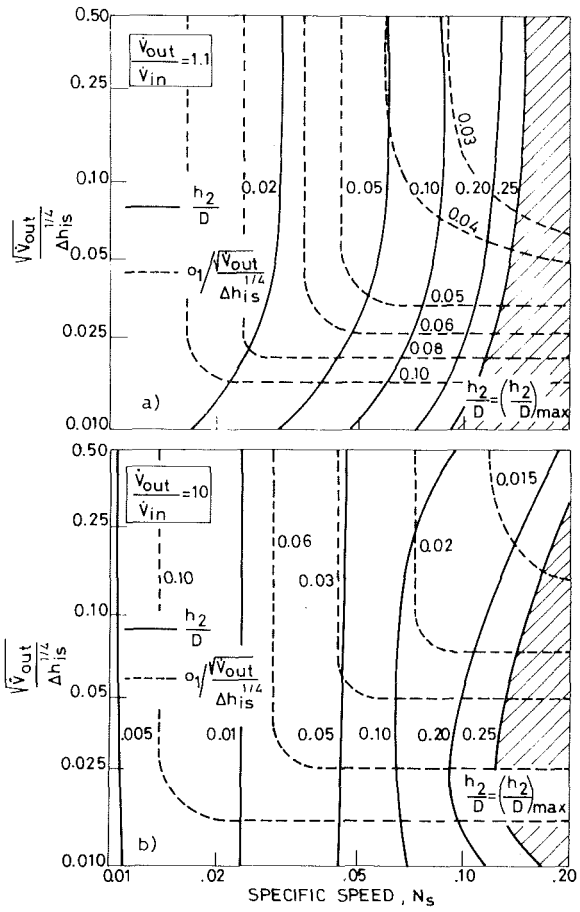

Fig. 13 Variation of the isentropic degree of reaction r^* and of the relative rotor outlet angle for small (a) and large expansion ratios (b)

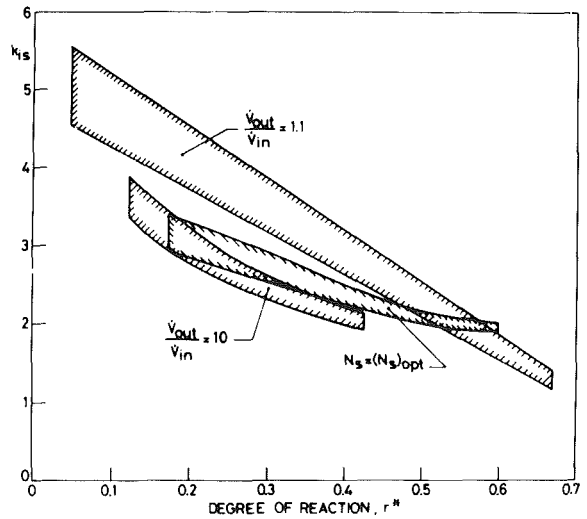

Fig. 14 Relationship between head coefficient and isentropic degree of reaction for optimized turbine stages

results also the disk friction losses, not included in the present analysis, are accounted for). The higher efficiency found by Baljè at low specific speed could be anticipated, on the ground of the more favorable constraints assumed in his analysis.

For small turbine dimensions, and/or for large expansion ratios, the efficiency curves reach considerably lower values. Again, the two effects are combined, and for the contemporary occurence of large volume variations and small dimensions, drastic efficiency decreases are obtained. Furthermore, the efficiency dependence on the specific speed is quite marked, and the adoption of optimum or near optimum

specific speed becomes mandatory. The variation of the degree of reaction is shown in Fig. 12, for a nearly incompressible case (a) and for large expansion ratios (b). It can be seen that in case (a) the degree of reaction decreases both for low specific speeds and for low turbine dimensions. Since small blade heights occur in both circumstances, a reduced value of the degree of reaction allows a diameter decrease, with beneficial influence on the secondary losses. For the incompressible case, both exit flow angles from stator and rotor blade rows, α_1 and β_2, were found to be optimized at their lowest value, about 15 deg for low Mach numbers. For the compressible case (Fig. 12(b)), as anticipated in a previous discussion, lower degrees of reaction are found. The most relevant difference from the incompressible case is the large volume variation across the rotor blade, which yields an increase of the rotor exit angle, in order to decrease the blade height change in the rotor blade. The blade height/mean diameter ratio increases, as obvious, with specific speed, both for compressible and incompressible cases (Fig. 13(a) and (b)). It can be seen that the stator blade opening o_1 (and therefore the blade number z_1) can be optimized only in a small region, since it reaches its lower limit for large specific speeds (horizontal lines in Fig. 13) and the blade number limit for small specific speed (vertical lines).

Conclusions

It has been shown that the efficiency achievable by a turbine stage can be predicted by the curves of Fig. 5 and/or Fig. 11, as a function of three parameters, namely (a) the $V_{out}/\dot{V}_{in}$ ratio, which accounts for the compressibility effects, (b) the $\sqrt{\dot{V}_{out}}/\Delta h_{is}^{1/4}$ parameter, which accounts for the actual turbine dimensions, and (c) the specific speed N_S, which can either be optimized, with values given in Fig. 6, or selected as an independent variable. The effects of compressibility become very important for turbine stages having large pressure ratios, and yield significant alterations of the optimized velocity triangles. This circumstance is evident in Fig. 14, where the dependence of the stage head coefficient k_{is} versus the theoretical degree of reaction r^* is represented. The regions indicated in Fig. 14 include all the turbine cases run in this analysis (about 350 cases) it can be seen that different k_{is} must be chosen for incompressible and compressible cases. For large expansion ratios, lower k_{is}, and therefore larger peripheral speeds, are required to decrease the Mach numbers in the rotor blades. These examples demonstrate that it is not warranted to transfer the design rules derived for turbine stages operating at low expansion ratios to turbine stages where the compressibility effects are of importance.

It should be pointed out that the obtained results were derived by adopting a particular design philosophy, that is to say looking for the maximum efficiency, not taking care either of turbine dimensions or peripheral speeds. This mode of design is appropriate for working fluids with large molecular mass and low speed of sound, but can be questionable for light molecules for which the adoption of larger flow and/or head coefficients can be more practical.

References

1 Craig, H.R.M., and Cox, H.J.A., "Performance Estimation of Axial Flow Turbines," *Proceedings of the Institution of Mechanical Engineers,* Vol. 185 32/71, pp. 407–423.

2 Dunham, J., and Came, P.M.., "Improvements to the Ainley-Mathieson Method of Turbine Performance Prediction," ASME JOURNAL OF ENGINEERING FOR POWER, Series A 92, pp. 252–256.

3 Traupel, W., *Thermische Turbomaschinen,* 2nd Edition, Vol. 1, Springer Verlag, Berlin, 1966, pp. 363–375.

4 Deich, M.E., Filippov, G.A., and Lazarev, L.Y., *Atlas of Axial Turbine Blade Characteristics,* Maschinostroenie Publishing House, Moscow, 1965.

5 Baljé, O.E., and Binsley, R.L., "Axial Turbine Performance Evaluation. Part A — Loss-Geometry Relationships," ASME JOURNAL OF ENGINEERING FOR POWER, Series A 90, pp. 341–348.

6 Baljé, O.E., and Binsley, R.L., "Axial Turbine Performance Evaluation: Part B — Optimization With and Without Constraints," ASME JOURNAL OF ENGINEERING FOR POWER, Series A 90, pp. 349–360.

7 Macchi, E., "Design Criteria for Turbines Operating with Fluids Having a Low Speed of Sound," in *Closed Cycle Gas Turbines,* Lecture Series 100, Von Karman Institute for Fluid-dynamics, Brussels, 1977.

8 Vavra, M.H., "Axial Flow Turbines," Lecture Series 15, Von Karman Institute for Fluid-dynamics, Brussels, 1969.

9 Ainley, D.C., and Mathieson, G.C.R., "A Method of Performance Estimation for Axial-Flow Turbines," British Aeronautical Research Council, R&M 2974, 1951.

10 Buzzi-Ferraris, M., "Subroutine OPTNOV," CILEA Technical Note, Milan, 1976.

11 Zweifel, O., "The Spacing of Turbo-Machine Blading, Especially with Large Angular Deflections," *Brown Boveri Review,* Vol. 32, Dec. 1945, pp. 436–444.

James S. Wilbeck[1]
Senior Engineer.

James L. Rand
Staff Engineer.
Mem. ASME

Division of Engineering Sciences
Southwest Research Institute,
San Antonio, Texas 78284

The Development of a Substitute Bird Model

A comprehensive program was conducted to develop a model synthetic bird for use in engine blade impact testing. A hydrodynamic theory of the impact event was used to aid in determining the bird properties which had to be duplicated in the model. Of the two candidate models studied extensively, it was determined that a projectile fabricated from commercial gelatin impregnated with phenolic mircoballoons most nearly duplicated the impact loading history of real birds.

Introduction

One of the major hazards to flight safety today is the in-flight impact of birds. Aircraft windshields and engine blading are especially vulnerable to damage. Because of the importance of this problem, both NASA and the Air Force are conducting extensive programs aimed at improving the impact tolerance of these components by developing better materials and better structural designs.

Extensive impact testing is required to evaluate these new concepts. Each of the major engine manufacturers has a test facility in which dead birds are impacted against single and multiple blades for design studies and ingested into entire engines during qualification testing. The use of real birds in the testing process lends realism to the test results, but greatly complicates the testing procedure while raising several questions as to the validity of the results.

One of the major drawbacks to the use of real birds in testing is the lack of repeatability. The actual impact loads vary from test to test due to the inability to control projectile orientation; lack of homogeneity, isotropy, or symmetry; and variations in bird structure. Secondly, it is very difficult to conduct scaled tests since small birds, such as starlings, are not exact replicas of much larger birds, and it would be difficult to find a small scale model of a starling. Testing with real birds also has obvious sanitary and aesthetic disadvantages.

For these reasons, a program was conducted at the Air Force Materials Laboratory (AFML) to develop a synthetic bird model for use in impact testing. Requirements for such a model were that the loads generated during impact of the model with a deformable structure be similar to those generated during the impact of a real bird, the loads should be highly reproducible, and the model should be easily manufactured, readily available, and relatively inexpensive.

In order to develop a synthetic bird model which would properly replicate the impact loads, initial efforts were concentrated on developing a fundamental understanding of the impact process. Based on this understanding, a general hydrodynamic theory was developed to predict the impact loads. The selection of a substitute bird model was based on those parameters identified in the hydrodynamic theory as necessary to simulate the loadings observed from the impact of actual birds. The development of a hydrodynamic model of bird impact has been reported previously [1, 2]. The purpose of this paper is to document the selection and validation of a substitute bird model. A brief overview of the hydrodynamic model will be given to help the reader to better understand the selection process.

Blade Response

The response of any structural element, when subjected to dynamic loading, is significantly different than its response to a static force. It is assumed that the impact of a bird against a rotating engine blade will create forces for a finite duration of time which is less than the natural period of the blade in any given mode. Since the blade is a deformable medium, stress waves are generated which tend to mitigate the applied forces and spread the effects over a larger area and for a longer period of time. Under this assumption, engine blading is susceptible to failure in two distinctly different modes when impacted by a bird. Localized failure of the blade may occur when the stresses generated are sufficiently high to cause compressive (or shear) failure at the point of contact. In addition, release waves may cause back surface spall or tensile delamination. The second mode is gross structural deformation which may be sufficient to cause failure at some point other than the point of contact.

Typical examples of local failure are delamination of the leading edge (in composite blades), local cracking or cratering, back surface spall, and internal crack nucleation. Material failures of this nature are governed by two dominating considerations: the strength of the material under the existing conditions of stress, strain and strain rate, and the mechanics of the loading which may produce adverse wave interactions.

In order to duplicate local failures of this nature, use of the actual blade to be evaluated will serve to replicate the material and geometric properties if it is rotated to produce the actual stress state. In order to duplicate the mechanics of loading

[1] Formerly of the Metals and Ceramics Divisions, Air Force Materials Laboratory, Wright-Patterson Air Force Base, Ohio 45433.

Contributed by the Gas Turbine Division and presented at the International Gas Turbine Conference and Products Show, Houston, Texas, March 9-12, 1981, of THE AMERICAN SOCIETY OF MECHANICAL ENGINEERS. Manuscript received at ASME Headquarters, November 26, 1980. Paper No. 81-GT-23.

with a substitute bird, it is necessary to produce not only the identical pressures generated during impact, but also the time history of that pressure. This feature of the impact process is important because finite amplitude waves generated by contact with the blade will subsequently be reflected from discontinuities in the blade and may interact with other waves to cause intense stresses within the blade.

This type of failure will generally be caused during the initial phase of the impact process when very large pressures are generated for a very short period of time. The initial Hugoniot pressure created by the impact of a bird must not only be duplicated, but the rapid release of this pressure at the correct time must also be duplicated.

Gross structural failure occurs when the momentum imparted to the blade is sufficient to cause blade deflections of sufficient magnitude to cause bending or tensile failures. Root failure, tip break off, and blade interference are typical examples of this type of response. Studies by various groups, such as Tsai, et al. [3], have shown that the long time stresses and deformations in a blade are proportional to the impulse imparted to the blade during impact.

The response of structures to impulsive loading is at least phenomenologically understandable. Since the blade has mass, conservation of momentum requires that a change in velocity of that mass must occur locally. The integral effect of that local change is the total impulse applied to the blade. In the absence of any further external forces, the blade will move to equilibrate the local changes in velocity. This may create large tensile stresses near the root due to bending or large shear stresses near the tip.

It is apparent that a substitute bird model should be capable of reproducing not only the total impulse of the actual bird impact process, but also the pressure history across the impact surface. This would be accomplished if pressures generated by the substitute bird have the same magnitude of initial pressure, time of release of the initial pressure, and the integral of the pressure over the total time of contact. When these conditions are duplicated, both local and gross structural failure modes will be apparent if they exist.

Bird Impact Tests

Initial efforts in the AFML program were aimed at developing a fundamental understanding of the bird impact process. An extensive program was conducted in which chickens were impacted against rigid targets. Chickens were used to represent birds because of their widespread use in qualification testing of aircraft parts, including engines. Rigid steel targets were used to eliminate the effects of target displacement on the amplitude and duration of the impact pressures. Tests were conducted at AFML and at Arnold Engineering Development Center (AEDC).

A compressed air gun located at AFML was used to launch birds ranging in mass from 60 to 600 g. A much larger compressed air gun, located at AEDC, was used to launch birds ranging in mass from 1 to 4 kg. The launch velocities obtained from both guns varied from 50 to 300 m/s. The targets were flat, rigid plates with pressure transducers embedded flush with the surface. The birds were launched such that they would impact end on, rear end first. This orientation resulted in a projectile which could be approximated by a cylinder with hemispherical ends and a length-to-diameter ratio of two. The target orientations were both normal and oblique to the trajectory of the bird. The test procedures are documented more fully in [2] and [4].

Typical pressure traces recorded by the plate transducer located at the center of impact are given in Fig. 1. Several distinguishing characteristics can be seen. The pressure is dominated by an initial peak pressure followed by a lower, approximately constant pressure. The pressure profile measured by transducers away from the center of impact displayed similar characteristics, but with a decrease in the amplitude of pressure with radial distance from the center of impact. Another outstanding feature of the pressure profile was the observation that the duration of impact, as evidenced by the duration of the pressure trace, was equal to the time that it takes for a bird to travel through its length. This can be expressed analytically as

$$T = \frac{L}{U_0} \tag{1}$$

where T is the duration of impact, L is the length of the bird, and U_0 is the initial impact velocity. An extensive report of the pressure measurements is given in [5].

Several comments about the pressure measurements should be added at this point. The lack of axial symmetry and homogeneity of the bird caused large variations in the measured pressure profiles as seen in Fig. 1. These variations preclude exact replication or representation of a bird impact. It should also be noted the duration of the peak pressure appears to have been so short that it is doubtful if the pressure transducers could accurately measure the peak amplitude. This would explain the differences seen in Fig. 1(*a*) and 1(*b*).

Formulation of Theory

Since the pressures measured during the impact tests were so much greater than the reported strength of the bird's flesh and bone [6], it was felt that the impact process could be modeled analytically by a hydrodynamic theory. A theory was developed in [1] in which the bird was approximated by a cylinder of fluid. This theory was based on previous studies of water drop and water jet impacts ([7] through [11]).

At the initial instant of impact of a fluid cylinder impinging normally against a rigid target, a shock wave is formed at the target-projectile interface. As this shock wave propagates into the projectile, the pressure at the surface is given by the relationship

$$P_H = \rho_0 U_s U_0 \tag{2}$$

where P_H is the Hugoniot (shock) pressure, ρ_0 is the initial density of the fluid, U_s is the shock velocity, and U_0 is the initial impact velocity. For impact on a rigid target, the shock velocity (which increases with impact velocity) is always greater than the impact velocity. For most fluids, the shock velocity is, in fact, much greater than the impact velocity, so that

$$P_H >> \rho_0 U_0^2 \tag{3}$$

The importance of this relationship will be seen later.

The duration of the shock pressure at the target face depends on the shock release process. At the first instant of

Nomenclature

k = compressibility
L = projectile length, m
P = impact pressure, MPa
T = time, s
U = velocity, m/s
ρ = density, kg/m^3

Subscripts

H = Hugoniot (shock) value
0 = initial conditions
s = shock value
ss = steady-state stagnation value

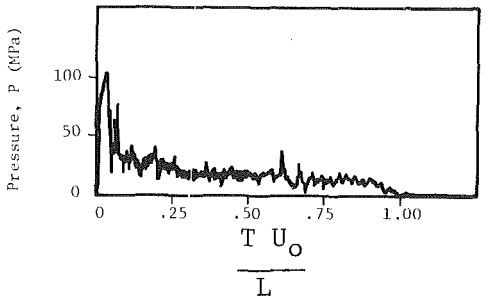

(a) Impact velocity, U_0 = 225 m/s

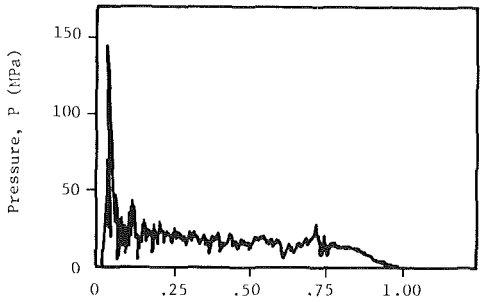

(a) Impact velocity, U_0 = 197 m/s

Fig. 1 Typical pressure data, center transducer, for the normal impact of a bird [1]

impact, the high shock pressure exists all along the impact surface. At the boundaries of the impact surface, the material is bounded on one side by a high pressure and on the other side by a free surface. This results in an outward acceleration of the material, thereby developing a pressure release wave which propagates inward towards the center of impact. This release wave causes a dramatic decrease in the pressure at the target face. As a result, the duration of the high shock pressure is greatest at the center of impact and is on the order of only tens of microseconds.

After the release process is completed, the impact process attains an approximate steady state condition. During this steady state, the pressure on the target surface at the center of impact is the stagnation pressure, P_{ss}, is given by Bernoulli's relationship

$$\int_{P_0}^{(P_{ss}+P_0)} \frac{dP}{\rho} = \frac{U_0^2}{2} \tag{4}$$

P_0 and U_0 are the pressure and velocity of the uniform flow field some distance away from the impact surface and are approximated by the atmospheric pressure and initial impact velocity. Equation (4) can be solved to give

$$P_{ss} = k\ \rho_0\ U_0^2 \tag{5}$$

For an incompressible fluid, k = ½. However, for most materials, the density tends to increase with applied pressure, so that k will have values which may approach 1.0. Comparison of equations (3) and (5) shows that, for most materials, the shock pressure is much greater than the steady state pressure measured at the center of impact (as was the case in Fig. 1). Away from the center of impact, the steady flow pressure decreases with radius.

For the impact of a fluid jet against a rigid target, the duration of impact can be approximated by equation (1). Inherent in this relationship is the assumption that the fluid does not decelerate during impact. This is normally the case when the impact pressures greatly exceed the strength of the projectile material (as in bird impact) and the target is effectively rigid (the displacements are small).

In order to use equations (2) and (4) to predict the impact

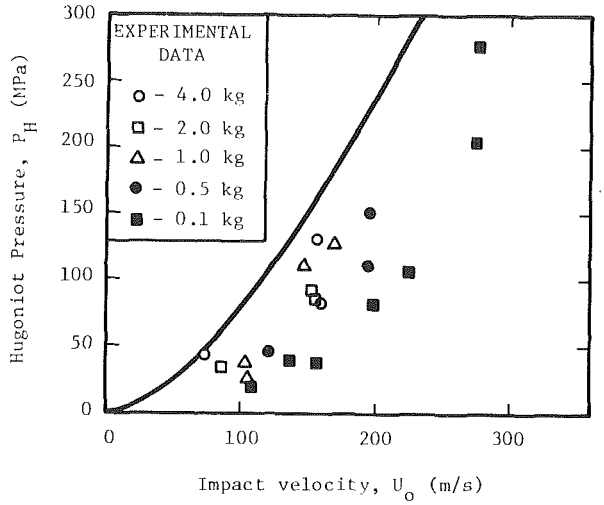

Fig. 2 Shock pressures measured at the center of impact [1]

pressures, an approximate equation of state was developed to represent the bird. Although chickens are neither homogeneous, isotropic, nor axisymmetric, it was felt that they could be reasonably approximated by a cylinder of material which was both homogeneous and isotropic. Such a simplification was required to properly apply one-dimensional impact theory.

In line with the simplified model of a bird, the initial decision was to represent the equation of state of a bird with that of water. This was a logical first choice since water makes up a very large portion of body mass, it has low strength, and its equation of state is well characterized. Since it was not possible to launch a projectile made up entirely of liquid water, projectiles were fabricated from ice and gelatin. Subsequent impact tests found that these projectiles gave shock pressures much greater than those obtained during bird impact. The pressures were so great, in fact, that several pressure gages were destroyed. From these results, it was inferred that pure water was not a good model of a bird.

Further insights were gained in laboratory measurements of bird density. An average density of 0.90-0.95 g/cm^3 was found for chickens of various sizes. These measurements of average density were in contrast to those of Tudor [6] who found the density of various parts of the chicken body to be approximately 1.06 g/cm^3. From this it was inferred that bird flesh has a density of approximately 1.06 g/cm^3, but that a whole chicken, with its voids and cavities, has an average density of only 0.90-0.95 g/cm^3.

The existence of voids in the bird serves not only to lower the average density but also to markedly decrease the speed of propagation of waves. The resulting lower shock velocity would account for the much lower shock pressures measured for bird impact than for the impact of ice or gelatin.

The equation of state for the bird had to be modified to account for the existence of the voids. This was done by treating the bird as a cylinder of water with entrapped air. Mixture theory [2] was used to develop a constitutive relationship for a homogeneous solution of water and 10-15 percent air (i.e., water with 10-15 percent porosity). By increasing the density of the water in the model to 1.06 g/cm^3, the resulting mixture had a density of 0.90-0.95 g/cm^3, which corresponds to that measured for chickens.

An extensive program was conducted to validate the appropriateness of the derived equation of state [1, 2]. Figures 2 and 3 display the values of the peak shock pressure and the average steady-flow stagnation pressure measured at the center of the target during normal bird impact. The predicted shock pressures in Fig. 2 agree well with the values measured

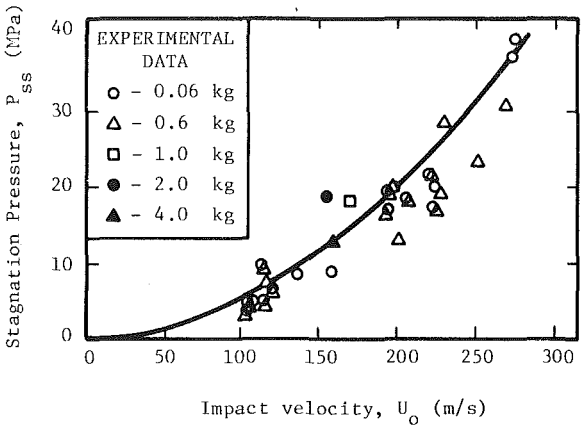

Fig. 3 Steady flow pressures measured at the center of impact [1]

for the large birds. However, the results for smaller birds show significant departures from prediction. This discrepancy, which appears to decrease with increasing bird size was not considered to be a fault of the theory or the analytical bird model chosen. As mentioned earlier, this was probably caused by the very short duration of the shock phase and the limited response time of the pressure transducers used.

The experimental data displayed in Fig. 3 were obtained by measuring the initial amplitude of the steady pressure region seen in the pressure traces of Fig. 1. Good correlation was obtained between theory and experimental data. It should be noted that large data scatter was observed. The existence of this variability in measured pressures was one of the major reasons behind the desire to develop a model substitute bird for testing.

Model Development

In the development of a model (synthetic bird), a variety of requirements was formulated. In order to accurately reproduce impact damage using a model, it was required that the loads generated during impact with a deformable structure be similar to those generated during the impact of a real bird. As an aid to design and testing, it was desired that the loads be highly reproducible. For practicality, the model should be easily manufactured, readily available, and relatively inexpensive.

Two separate approaches were taken in developing suitable models. One approach was to develop a near replica model in which the synthetic bird was made of a material having an equation of state similar to that of bird flesh, with the same average density and porosity used earlier to model real birds. Since the material properties of a replica model would be similar to those of a real bird, the impact loads should be similar. A second approach was to develop a nonreplica model. In this development process, emphasis was placed on developing a model which duplicated the impact loads, not the material properties.

Replica Model. As mentioned earlier, a chicken can be adequately modeled by a mixture of 85-90 volume percent water and 10-15 percent air, where the water has a slightly higher density of 1.06 g/cm^3. However, no scheme could be developed for fabricating a synthetic bird from such a mixture. Subsequently, an effort was made to locate another substitute with properties similar to those of flesh. A large number of materials were considered. Synthetic rubbers of various types showed promise but had too great a density. Finally, commercial gelatin was selected as the best choice.

Initially considered because of its historical use as a flesh

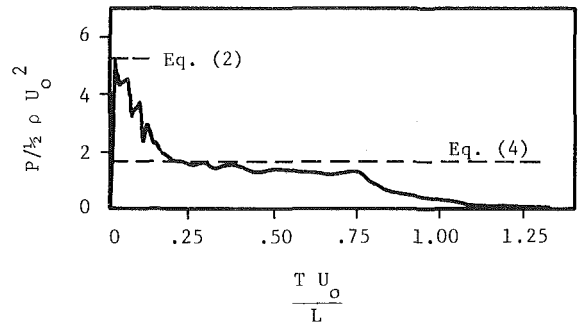

Fig 4 Normal impact of a gelatin projectile with 40 percent porosity, U_0 = 158 m/s [2]

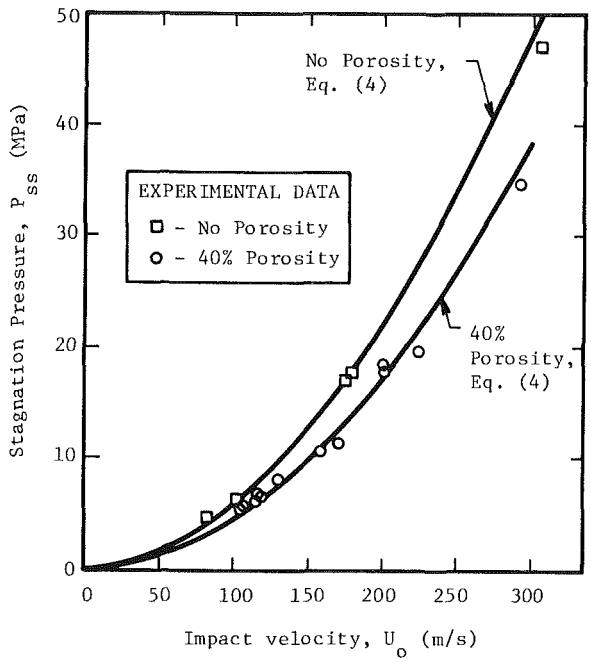

Fig. 5 Stagnation pressure measured during the normal impact of gelatin projectiles [2]

simulant, gelatin was found to possess the desired properties of a replica model. With its high water content, it was believed to possess an equation of state similar to that of bird flesh. It has a density of 1.05-1.06 g/cm^3 and its strength is great enough to hold its shape but small relative to impact pressures. The proper amount of porosity (entrapped air) can also be added by the use of phenolic microballoons, which are stirred into the gelatin and water mixture prior to the gelling process.

During initial experimental investigations, projectiles were made from gelatin with no porosity (ρ = 1.06 g/cm^3) and large porosity (40 percent porosity, ρ = 0.64 g/cm^3). It was felt that this large variation would be a good check of the hydrodynamic theory. Figure 4 shows a typical pressure trace for the impact of a projectile with 40 percent porosity. The coordinates were nondimensionalized to aid in comparison with theory. Predicted values of the Hugoniot shock pressure (equation (2)) and the steady-state stagnation pressure (equation (4)) are also shown.

Results from this series of tests are given in Figs. 5 and 6. The steady-state stagnation pressures are compared with the predictions of equation (4) in Fig. 5 and the shock pressures are compared with the predictions of equation (2) in Fig. 6. The correlation is seen to be very good in both cases. No

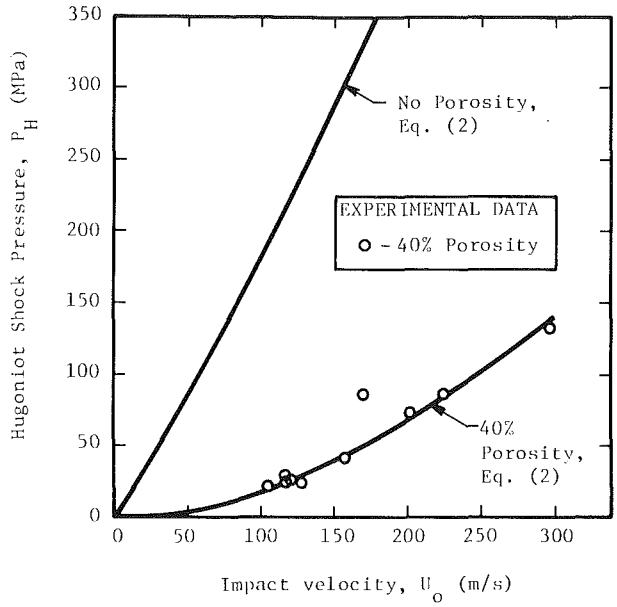

Fig. 6 Hugoniot pressures measured during the normal impact of gelatin projectiles [2]

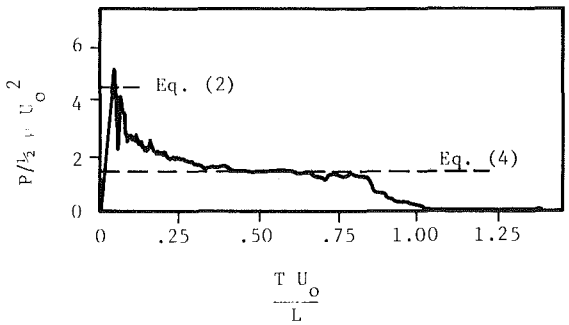

Fig. 7 Normal impact of an RTV-560 projectile with 50 percent porosity, U_0 = 160 m/s

shock data were given for nonporous gelatin since the amplitudes of the pressures were too great to measure.

From an analysis of these data, it was concluded that gelatin with 15 volume percent microballoons would make a good replica model of a bird.

Nonreplica Model. An extensive survey was made of various materials which might effectively duplicate the loading history of birds during impact. Greatest consideration was given to a variety of synthetic rubber compounds because of their ease of fabrication, low cost, availability, and good shelf life.

One of the rubber compounds studied extensively was RTV 560, a room temperature vulcanized rubber manufactured by General Electric. Although its density of 1.33 g/cm^3 was low relative to most of the other rubber compounds, it was still considerably higher than that of a bird. Initial impact tests confirmed that impact pressures were much higher than those experienced in bird tests.

One of the desirable features of the RTV compounds was that the density could be decreased in a controllable manner with the addition of blowing agent during mixing and prior to curing. The result of the addition of the blowing agent was a homogeneous, porous material with lower density and lower wave speed.

An initial test program was conducted using a projectile having 50 pecent porosity and a density (ρ = 0.66 g/cm^3)

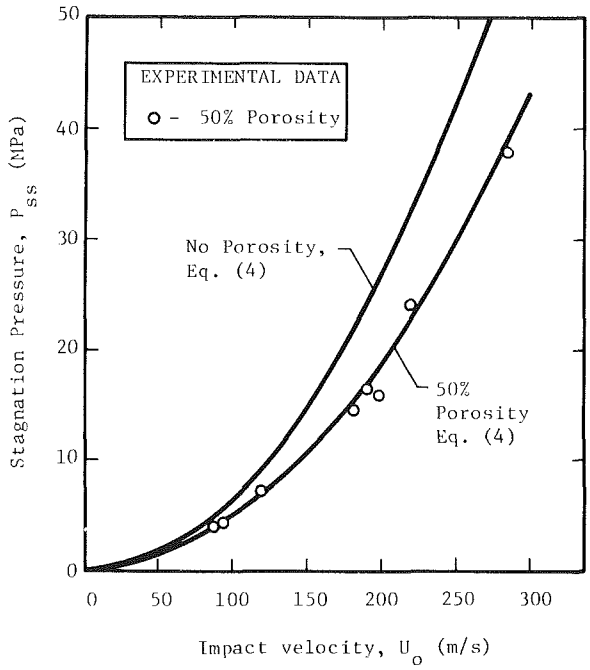

Fig. 8 Stagnation pressure measured for the normal impact of RTV-560 projectiles [2]

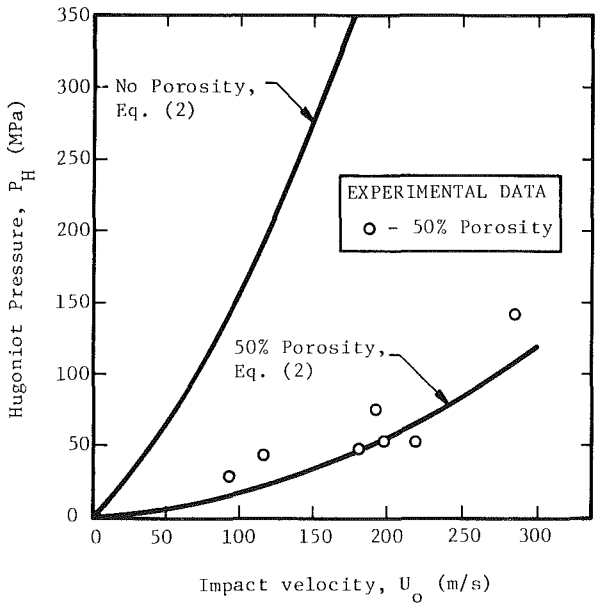

Fig. 9 Hugoniot shock pressure measured during the normal impact of RTV-560 projectiles [2]

comparable to that of the porous gelatin studied. A typical pressure trace is given in Fig. 7. Results from these tests are displayed in Figs. 8 and 9. Again, the correlation with theory is good.

From inspection of these data, it was concluded that a projectile fabricated from RTV-560 with 50 percent porosity would give impact pressures similar to those resulting during bird impact.

Model Selection. In the final selection process of a substitute bird model, two materials were given strong consideration. These were gelatin with 15 percent porosity and RTV-560 with 50 percent porosity. Both materials were readily available, relatively inexpensive, and could be easily

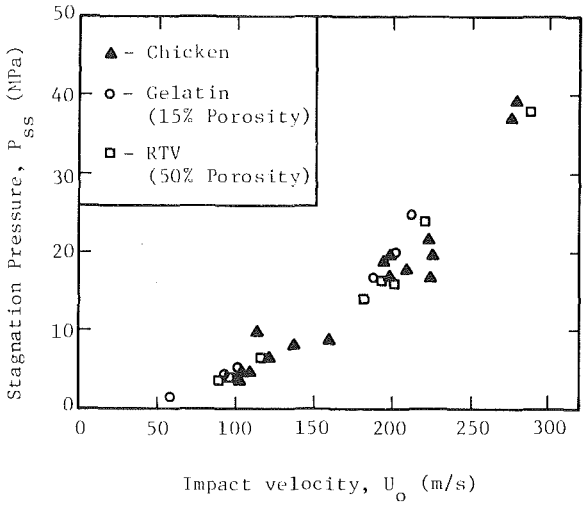

Fig. 10 Comparison of experimental stagnation pressure data for several candidate materials

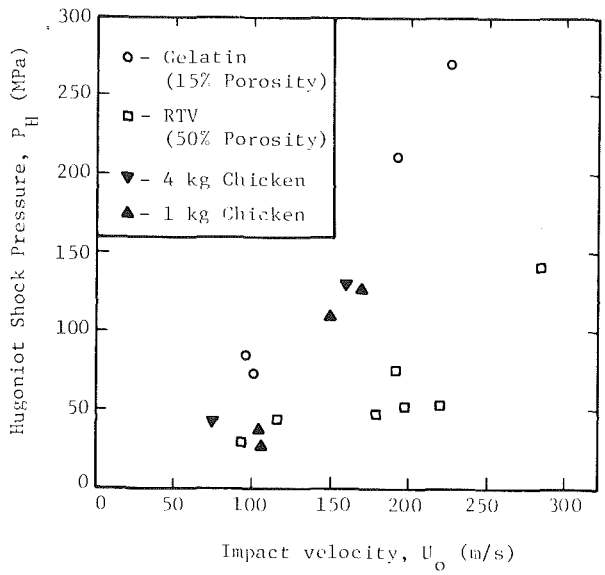

Fig. 11 Comparison of experimental shock pressure data for several candidate materials

fabricated into projectiles. The RTV-560 had the advantage of long shelf life, whereas the gelatin projectile had a shelf life of only a few hours unless refrigerated.

The microballoon gelatin bird was chosen because it more nearly replicated the impact loads of real birds. Direct comparisons of the experimentally obtained steady-state stagnation pressures and Hugoniot shock pressures are given in Figs. 10 and 11, respectively. In Fig. 10, there appears to be no significant difference between the measured stagnation pressures of birds and the two candidate materials. The major difference between the two candidate materials is seen in Fig. 11, where the high porosity of the RTV-560 has resulted in shock pressures far below those of the gelatin and the birds. Because of the importance of the initial shock pressures in the local damage problem, RTV-560 with 50 percent porosity was felt to be an unacceptable bird substitute. Efforts to increase the shock pressure by decreasing the porosity resulted in an unacceptable increase in stagnation pressure.

Summary and Conclusions

A synthetic bird model has been developed which accurately reproduces the impact loads caused by real birds. The model material is a mixture of commercial gelatin and phenolic microballoons. This material is inexpensive, readily available, and the projectile can be easily and quickly fabricated. A gelatin projectile also has sufficient strength to withstand inertial loads during launch.

In this program, a mixture of 85 percent gelatin (by volume) and 15 percent microballoons was used to model chickens, which are most commonly used in engine qualification testing. Comparison of the impact loads between model and prototype was very good. The data from both types of projectiles also compared favorably with a hydrodynamic theory developed earlier. It was also apparent that the impact-generated pressure profiles were much more reproducible for the impact of the model material than for that of birds.

In the reported test program, the model projectiles were fabricated in the form of a right circular cylinder with a length-to-diameter ratio of 2. As the program progressed, it became apparent that a bird would be more accurately modeled by a cylinder with the same length-to-diameter ratio but with hemispherical ends.

Such a geometry, though correct physically, requires extreme care during testing in control of impact orientation. Projectile yaw during impact would result in a variation in the impact loading history, thereby negating the repeatability of impact loading which is so desirable. This problem would be most prevalent in engine ingestion testing, in which projectile rotation prior to impact is almost unavoidable. For this type of testing, it is recommended that the projectile be fabricated in a spherical geometry.

Acknowledgments

This work was conducted at the Air Force Materials Laboratory under Project 7351 and Task 735106. The program manager was Dr. Alan K. Hopkins. The experimental data were obtained by the University of Dayton Research Institute on Contract F33615-73-C-5027, under the direction of Dr. John P. Barber.

References

1 Wilbeck, J. S., and Barber, J. P., "Bird Impact Loading," *The Shock and Vibration Bulletin*, Vol. 48, Part 2, Sept. 1978, pp. 115-122.

2 Wilbeck, J. S., "Impact Behavior of Low Strength Projectiles," Air Force Materials Laboratory, Technical Report No. 77-134, July 1978.

3 Tsai, S. W., Sun, C. T., Hopkins, A. K., Hahn, H. T., and Lee, T. W., "Behavior of Cantilevered Beams under Impact by a Soft Projectile," Air Force Materials Laboratory, Technical Report No. 74-94, Nov. 1974.

4 Barber, J. P., Wilbeck, J. S., and Taylor, H. R., "Bird Impact Forces and Pressure on Rigid and Compliant Targets," Air Force Flight Dynamics Laboratory, Technical Report 77-60.

5 Barber, J. P., Taylor, H. R., and Wilbeck, J. S., "Characterization of Bird Impacts on a Rigid Plate: Part 1," Air Force Flight Dynamics Laboratory, Technical Report 75-5, Jan. 1975.

6 Tudor, A. J., "Bird Ingestion Research at Rolls-Royce," *Symposium on the Mechanical Reliability of Turbo-Machinery Blading*, Derby and District College of Technology, Apr. 1968.

7 Bowden, F. P., and Brunton, J. H., "The Deformation of Solids by Liquid Impact at Supersonic Speeds," *Proceedings of the Royal Society of London*, Series A, Vol. 263, Oct. 1961, pp. 433-450.

8 Bowden, F. P., and Field, J. E., "The Brittle Fracture of Solids by Liquid Impact, by Solid Impact, and by Shock," *Proceedings of the Royal Society of London*, Series A, Vol. 263, 1964, pp. 331-352.

9 Heymann, F. J., "On the Shock Wave Velocity and Impact Pressure in High-Speed Liquid-Soil Impact," ASME *Journal of Basic Engineering*, Series D, Vol. 90, July 1968, p. 400.

10 Heymann, F. J., "High-Speed Impact Between a Liquid Drop and a Solid Surface," *Journal of Applied Physics*, Vol. 40, No. 13, Dec. 1969, pp. 5113-5122.

11 Glenn, L. A., "On the Dynamics of Hypervelocity Liquid Jet Impact on a Flat Rigid Surface," *Journal of Applied Mathematics and Physics*, Vol. 25, 1974, pp. 383-398.

C. C. Chamis

R. F. Lark

J. H. Sinclair

National Aeronautics and Space Administration, Lewis Research Center, Cleveland, Ohio 44135

Superhybrid Composite Blade Impact Studies

An investigation was conducted to determine the feasibility of superhybrid composite blades for meeting the mechanical design and impact resistance requirements of large fan blades for aircraft turbine engine applications. Two design concepts were evaluated: (1) leading edge spar (TiCom) and (2) center spar (TiCore), both with superhybrid composite shells. The investigation was both analytical and experimental. The results obtained show promise that superhybrid composites can be used to make light-weight, high-quality, large fan blades with good structural integrity. The blades tested successfully demonstrated their ability to meet steady-state operating conditions, overspeed, and small bird impact requirements.

Introduction

The superhybrid composite (SHC) concept provides one means for efficiently utilizing advanced materials in certain aerospace applications. The concept combines the best characteristics of a fiber/resin matrix composite, fiber/metal matrix composite and high strength metallic foils in a single adhesively-bonded laminate. A SHC is typically made by using titanium foil as outer plies over boron/aluminum plies and an inner core of graphite fiber/epoxy plies. All these materials are adhesively bonded using a thermosetting adhesive and a controlled bonding process. The result is a composite (laminate) with: (1) light weight comparable to glass fiber composites, (2) impact resistance approaching that of titanium on an impact-resistance-to-density ratio, (3) moisture and erosion resistance comparable to titanium, (4) longitudinal strength comparable to advanced fiber/resin composites, (5) transverse flexural strength comparable to titanium yield strength, and (6) bending and torsional stiffness comparable to boron/aluminum composite.

The fabrication feasibility and preliminary characterization of SHC using laboratory-type specimens are discussed in references [1] and [2]. Evaluation of the SHC mechanical properties and resistance to thermal fatigue are described in reference [3]. The impact resistance of SHC using double wedge (blade-simulation) specimens was extensively evaluated in a contractual investigation under NASA Lewis Research Center sponsorship [4]. Based on the promising results obtained in the aforementioned programs, an investigation was conducted by the Aircraft Engine Group of the General Electric Company under contract to NASA Lewis Research Center to evaluate the feasibility of using SHCs in large fan blades used in aircraft engines for commercial jets [5]. The objective of this report is to summarize the results obtained by the General Electric Co. investigation with emphasis on mechanical design and impact resistance aspects.

Baseline Blade Design

A CF6-type blade was selected as the configuration to demonstrate the feasibility of the superhybrid material concept in this program. This blade configuration met all the requirements necessary to demonstrate the superhybrid concept for use in large fan blades and to assess any benefits associated with weight, containment, and FOD resistance. Other benefits associated with the CF6 fan blade selection were: (1) It is representative of blades used in other large, high-bypass engines similar to the General Electric CF6. (2) It is a high-tip-speed (1500 ft/s (457.2 m/s)) configuration currently in commercial service. (3) The CF6 type aerodynamic design is being used in other composite blade programs, including the Air Force F103 engine graphite-hybrid fan blade and a CF6 boron/aluminum fan blade. (4) Titanium CF6 blades were readily available for use in machining titanium spars for this program. (5) Existing test rig hardware was available that would accept the CF6 superhybrid blade.

The titanium blade is shown in Fig. 1. There are 38 blades in the CF-6 fan rotor assembly. The blade has a 30-in. (0.762 m) length, a 9.8-in. (0.249 m) tip chord, and a 6.5-in. (0.165 m) root chord. The overall blade weight is 11.0 pounds (5.00 kg); this represents the baseline blade weight used for comparison with SHC blades made in this program. The aeromechanical characteristics of the titanium blade are summarized in Table 1. The air-foil geometry used for the superhybrid blade was the same as the CF6 titanium fan blade with the midspan shroud (Fig. 1) removed.

Two basic blade design configurations were selected for evaluation. Both designs utilized metallic spars with full-length as-designed CF6 dovetails. The first design is a standard spar/shell design (designated TiCore). The spar is completely internal to the shell, Fig. 2. The second configuration evaluated has the metal spar shaped in a way to provide spar material at the leading-edge concave side where it can have a direct benefit in dissipating the local impact forces

Contributed by the Gas Turbine Division and presented at the International Gas Turbine Conference and Products Show, Houston, Texas, March 9–12, 1981, of THE AMERICAN SOCIETY OF MECHANICAL ENGINEERS. Manuscript received at ASME Headquarters, November 26, 1980. Paper No. 81-GT-24.

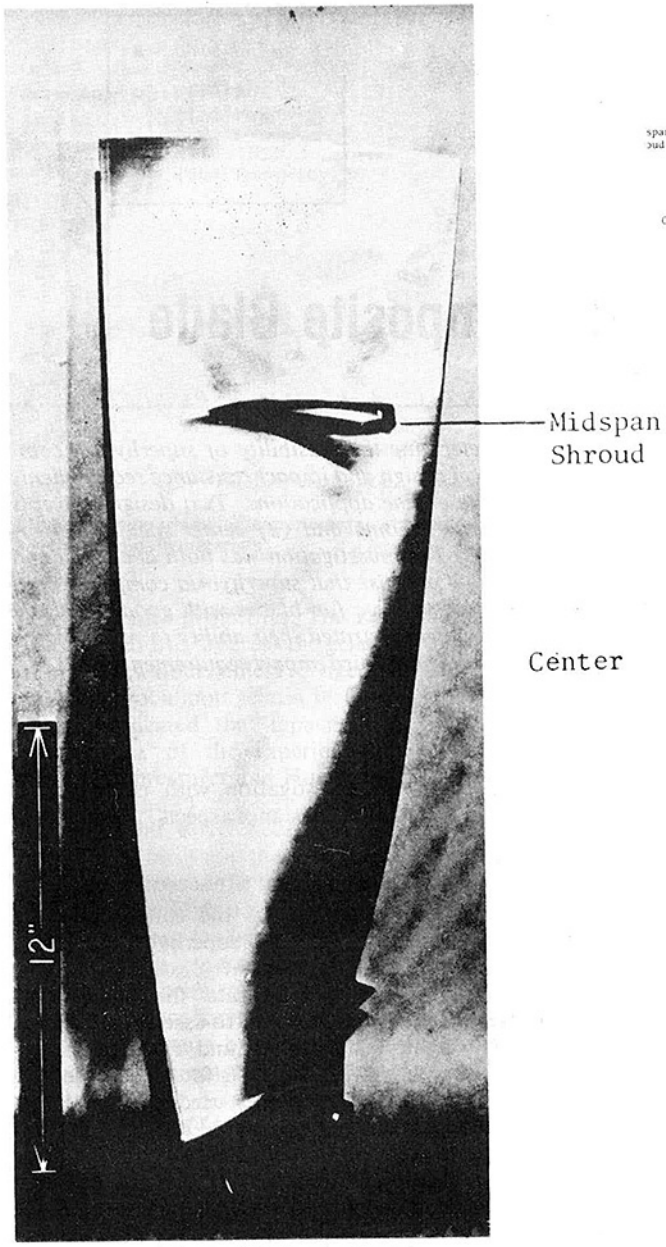

Fig. 1 CF6 titanium blade

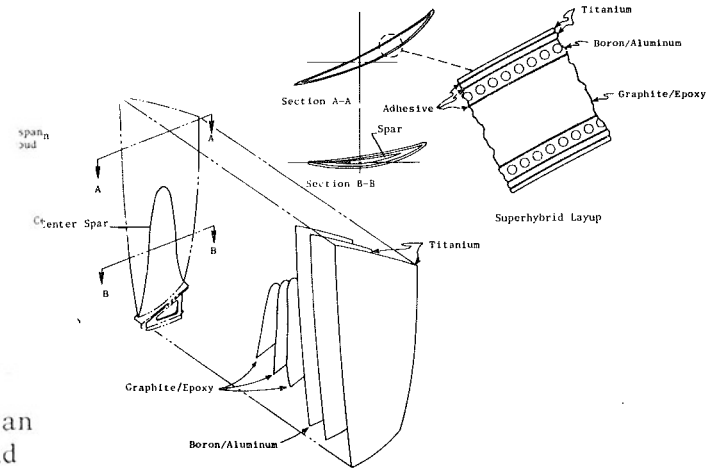

Fig. 2 Candidate TiCore blade design showing internal spar with superhybrid shell

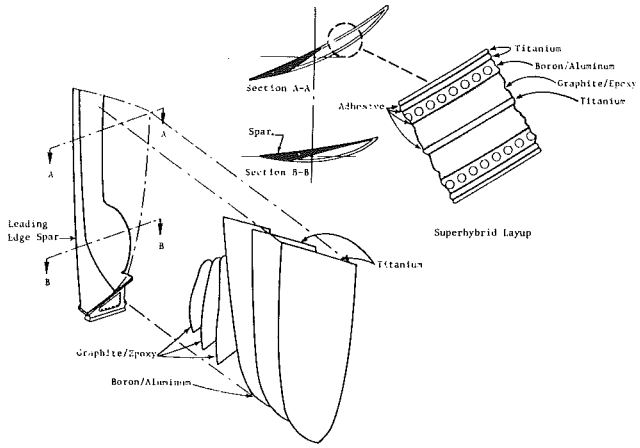

Fig. 3 Candidate TiCom blade design showing leading edge spar with superhybrid shell

from a variety of foreign objectives including birds. A schematic of the configuration for this blade (TiCom) is shown in Fig. 3.

The design conditions selected for the superhybrid blades are those used for the mechanical design of the CF6 titanium blade (Table 1). No consideration was given, however, to blade low-cycle-fatigue (LCF) behavior. The specific design conditions are: (1) Steady state operation at 4080 rpm (100 percent speed), (2) Maximum overspeed condition: 120 percent speed (operate for 5 min), (3) Allowable stresses at 100 percent speed must be less than 70 percent of material strengths.

Two different spar sizes were evaluated for each blade type (TiCom, TiCore) in the preliminary design phase. The two spar sizes evaluated represent what are considered to be the extremes of the range of practical spar sizes. The small spar is limited by leading-edge FOD protection considerations in the outer airfoil. The large spar is limited by weight consideration payoffs over a CF6 titanium blade. The results of the evaluation of the preliminary design phase are summarized in Table 2.

Several observations may be made concerning the results shown in Table 2. (1) The weight benefits of the spar/shell designs compared to an all-titanium blade can be substantial, especially if small spars can be employed about 3.1 pounds (1.41 kg) less than the shrouded blade. For a 38 blade stage this amounts to about 120 pounds weight saved per stage or about 30 percent. (2) Frequency characteristics of all the superhybrid spar/shell blades, although similar to the all-titanium cantilevered blade, are greatly reduced relative to a midspan-shroud-supported blade. Of particular interest is the low first torsional frequency of 150 Hz versus a midspan-supported titanium blade value of 426 Hz. For a SHC blade of this size to be aeromechanically (flutter) acceptable, a first torsional frequency near the 426 Hz level of the shrouded titanium blade is required. To meet this torsional frequency requirement, the SHC blade design could be changed to increase the chord and thickness of the blade. The increased chord results in a reduced number of blades but increased weight for a fan stage. The net weight benefit will be about 60 pounds or about 15 percent per stage. (3) The steady-state centrifugal stress and spar-to-shell shear stress were evaluated for each design. The maximum stress values are shown in the last three columns of Table 2. All the calculated stresses are well within the design allowables shown in Table 3. Under impact conditions, however, much higher stresses than those calculated will be present; consequently, considerable margin on steady-state stress is desirable at the evaluation of the preliminary design phase. Based on the results of the

Table 1 CF6 Titanium blade aeromechanical parameters

Number of Blades	38
Maximum Steady-State, rpm	4080
Tip Speed, ft/sec (m/sec)	1512 (460.8)
Tip Radius, in. (m)	42.48 (1.079)
Tip Chord, in. (m)	9.8 (0.249)
Root Chord, in. (m)	6.43 (0.163)
Tip Solidity	1.39
Root Solidity	2.2
Tip Tm/C	0.025
Root Tm/C	0.089
Tip Thickness, in. (m)	0.245 (6.22 x 10^{-3})
Root Thickness, in. (m)	0.57 (0.145 x 10^{-3})
Airfoil Weight, lbm (kg)	8.1 (3.674)
Blade Weight, lbm (kg)	10.8 (4.899)
Root Center Force, lb (newtons)	103,000 (458,166)
Root Center Stress, ksi (n/m^2)	37,000 (2.551 x 10^8)
Root Area, in.^{2} (m^2)	2.8 (1.806 x 10^{-3})
Airfoil Peak Stress, ksi (n/m^2)	67,000 (4.619 x 10^8)
Location of Airfoil Peak Stress	Midchord Root
Maximum Shear Stress Root, ksi (n/m^2)	N.A.
1T Frequency, cps (hz)	460 (460)
Material	Ti 6-4

evaluation of the preliminary designs, the configurations with the small spars were selected for detail analysis evaluation.

Finite Element Analysis

The 3-D finite-element model used to carry out the detailed analysis consists of 306 brick elements and 504 nodes. The finite-element model was established to represent both the TiCore and TiCom blades in a single model. Using three elements through the thickness made it possible to represent the titanium/boron/aluminum skins, the graphite/epoxy core, and the titanium spar individually and in combination in the analysis. Figure 4 shows the finite-element model as projected on the Y-Z coordinate plane. The analysis included inertial stiffening effects corresponding to the 100 percent design speed of 4080 rpm, but did not include air loads. Such aerodynamic loading generally produces a negligible effect on blade stresses. The material properties used to generate the data for the finite-element model are summarized in Table 4. The superhybrid material used in a combination of titanium (8 percent), boron/aluminum (21 percent) and graphite/epoxy (71 percent) by volume.

Typical results from the finite element analysis are presented in Figs. 5, 6, and 7 as stress contour plots. Peak stresses for both blades are summarized in Table 5. The results show that blade stresses are well within the superhybrid material strengths for the TiCore and TiCom blades (Table 4). The controlling stresses for the TiCore blade were generally in the superhybrid material; those for the TiCom blade in the titanium spar material. The stresses in the TiCom blade were considerably higher than those in the TiCore blade. The higher stresses in the leading edge region of the TiCom blade are believed to be the result of modeling problems associated with the thin solid-titanium leading edge and are believed to be unrealistic levels. Since the stresses were within the material allowable limits, no attempt was made to refine the model.

In addition to steady-state stresses, finite-element analysis was also used to determine the frequencies and mode shapes of the blades in the cantilever fixed-end condition. Table 6 summarizes the first three frequencies for the TiCore and TiCom superhybrid blades at design speed and compares them with those of the titanium midspan shrouded blade. The results indicate that the blade frequencies for both superhybrid blades are equivalent but considerably below the shrouded metal blade. A design change would thus be required, including a change in number of blades per stage, to provide an aeromechanically acceptable design as mentioned previously.

Blade Fabrication

Based on the results of the finite element analysis, TiCore and TiCom blades with small spars were fabricated for testing. Briefly, the blades were fabricated by hot pressing. The spars were machined to the desired dimensions from CF6 titanium blades. The titanium plies and the boron aluminum plies were preformed to the specified shapes. The graphite-fiber composite plies and the adhesive plies were cut to the specified shape. The spar and the various plies were stacked in a mold and hot-pressed under specified pressures and temperatures compatible with the resin and the adhesive systems.

The fabrication quality of the blades was determined by using destructive and nondestructive evaluation (NDE) tests. The destructive tests were also used to verify selected in situ strength properties as compared with those used in the finite

Table 2 Preliminary blade design summary

Design	Blade Type /Spar Size	Δ Weight, lb (kg)	Estimated Bench Frequencies, Hz 1st Flex.	1st Tors.	Layup Angles B/Al	AS	Shear Stress, ksi (n/m^2)	Centrifugal Stress Max Compression ksi (n/m^2)	Max Tension, ksi (n/m^2)
1	Small TiCom	-3.3(-1.498)	35	150	±15°	±0°, ±35°	0.6 (4.136 x 10^6)	27 (1.86 x 10^8)	30 (2.07 x 10^8)
2	Large TiCom	-2.8(-1.271)	35	150	±15°	±0°, ±35°	0.7 (4.826 x 10^6)	29 (2.0 x 10^8)	33 (2.27 x 10^8)
3	Small TiCore	-3.1*(-1.407)	35	150	±15°	±0°, ±35°	0.5 (3.447 x 10^6)	29 (2.0 x 10^8)	25 (1.72 x 10^8)
4	Large TiCore	-2.3*(-1.044)	35	150	±15°	±0°, ±35°	0.6 (4.136 x 10^6)	36 (2.48 x 10^8)	32 (2.21 x 10^8)
	All-Titanium Cantilevered	-1.1(-0.500)	22	152					
	All-Titanium Shrouded	0	202	426					

*Includes 0.5-lb (0.226 kg) Leading-Edge Protection.

Table 3 Material allowables at 4080 rpm

	Tensile, ksi (n/m^2) 0°	90°	Bending, ksi (n/m^2) 0°	90°	Shear, ksi (n/m^2)
Titanium	90	---	90	---	50 (3.45 x 10^8)
Superhybrid	92	16 (1.10 x 10^8)	120	51 (3.51 x 10^8)	---
Spar/Shell Bond	---	---	---	---	2 (1.35 x 10^7)

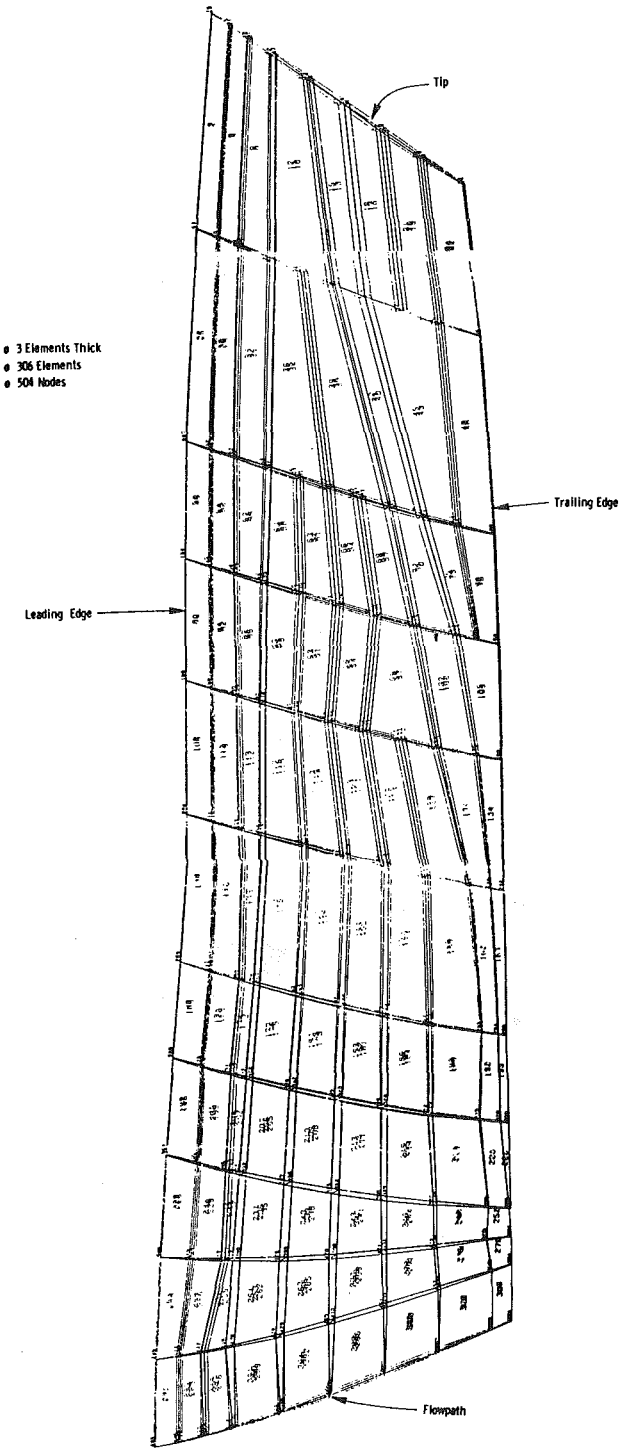

Fig. 4 TAMP model

element analysis. A correlation of NDE test results with the destructive test data was established. This correlation was used to assess the quality of the blades intended for testing in order to verify the design concept. Three blades for each TiCore and TiCom design were fabricated for verification testing.

Blade Testing

Bench Frequencies. Each of the six superhybrid test blades underwent bench frequency testing in the clamped-end cantilever condition. Table 7 presents the results of this testing for the first five frequencies. These data show little scatter in frequencies of the superhybrid blades and modest improvements in stiffness over unshrouded titanium blades.

Spin Testing. The initial spin or whirligig testing consisted of conducting a 100-cycle spin test on a TiCore and a TiCom blade at 110 percent speed (4488 rpm). Cyclic testing of both blades was completed successfully. No damage was found by using several through-transmission nondestructive test (NDT) hand scans of each blade at various cycle intervals throughout the testing. Blade temperatures during cyclic testing were held below 225° F (107.2° C) at the tip and below 200° F (93.3°C) at the root. Temperature measurements were made by a combination of temperature sensitive point dots mounted to the blade and an air thermocouple in the shroud at the blade tip.

After cyclic testing, the blades were tested for impact in a whirligig test facility. Three TiCore and one TiCom blades were tested. A typical photograph of the test setup including disk, blade, and bird injector is shown in Fig. 8.

Test results for all impact tests are summarized in Table 8. This summary shows that after starling impact the TiCore blade suffered minor damage, limited to disbond between the nickel plate and the wire mesh. The TiCom blade suffered considerably more damage under starling impact: its spar separated from the shell, causing delamination over 50 percent of the air foil. Based on the results of this TiCom blade test, it was concluded that impact testing TiCom blades with larger bird slices would result in complete blade failure. Thus no further impact testing of TiCom blades was conducted.

As shown in Table 8, three additional tests were conducted on the TiCore blades. A starling impact on TiCore blade 3 resulted in nickel-plate separation similar to the TiCore blade 1 test. In an attempt to determine whether any structural damage was done to either of the two TiCore blades 2 or 3, the nickel-plate/wire mesh leading-edge protection was removed for further NDT evaluation. With the exception of a slight buckle in the titanium surface ply of TiCore blade 2, there was no damage to the blade after removing the leading-edge protection. With improvements in the nickel-plate adhesion or the substitution of a suitable alternative leading-edge protection system, it is believed that the no-damage starling impact requirement can be achieved with a TiCore blade design.

Table 4 Superhybrid material properties used in finite element analysis

	Titanium 6-4	B/Al ±15°	Graphite/ epoxy 0 ± 35°	Superhybrid Configuration
Through-Thickness Tensile Modulus, E_{11} - 10^6 psi (10^{10} n/m^2)	16.0 (11.03)	10.6 (7.31)	1.5 (1.03)	4.6 (3.17)
Chordal Tensile Modulus, E_{22} - 10^6 psi (10^{10} n/m^2)	16.0 (11.03)	19.0 (13.10)	1.65 (1.14)	6.4 (4.41)
Radial Tensile Modulus, E_{33} - 10^6 psi (10^{10} n/m^2)	16.0 (11.03)	26.0 (17.92)	10.6 (7.31)	14.3 (9.86)
Chordal Shear Modulus, G_{12} - 10^6 psi (10^{10} n/m^2)	6.2 (4.27)	6.0 (4.13)	0.7 (0.483)	2.3 (1.59)
Cross-Fiber Shear Modulus, G_{23} - 10^6 psi (10^{10} n/m^2)	6.2 (4.27)	10.1 (6.96)	2.35 (1.62)	4.3 (2.96)
Radial Shear Modulus, G_{13} - 10^6 psi (10^{10} n/m^2)	6.2 (4.27)	6.0 (4.13)	0.7 (0.483)	2.3 (1.59)
Chordal Plane Poisson's Ratio (μ_{12})	0.3	0.3	0.3	0.3
Cross-Fiber Plane Poisson's Ratio (μ_{23})	0.3	0.34	0.67	0.54
Radial Plane Poisson's Ratio (μ_{13})	0.3	0.24	0.3	0.29
Density, lb/in.^{3} (kg/m^3)	0.161 (4456)	0.10 (2768)	0.06 (1661)	0.076 (2104)

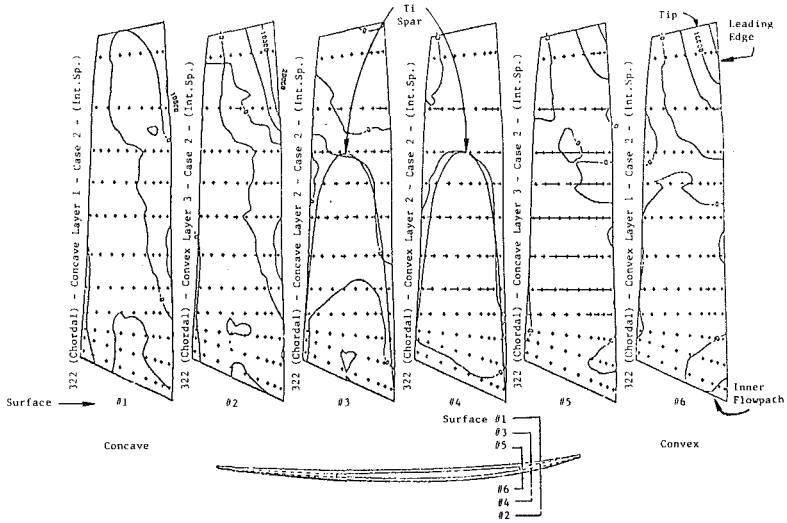

Fig. 5 Internal spar blade (TiCore), chordal stress (psi), 4080 rpm

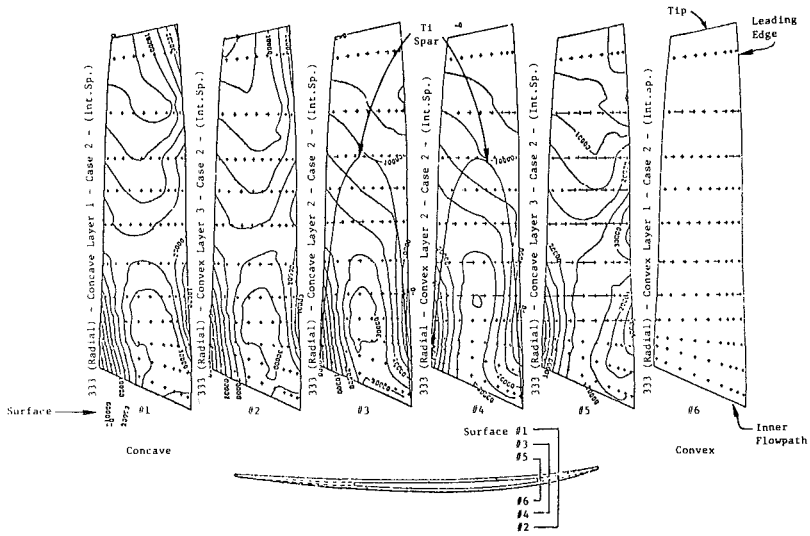

Fig. 6 Internal spar blade (TiCore) radial stress (psi), 4080 rpm

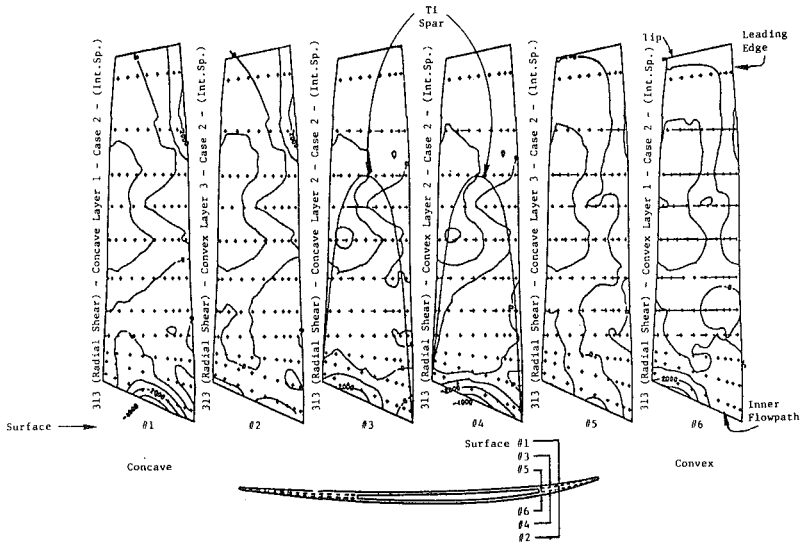

Fig. 7 Internal spar blade (TiCore) radial shear stress (psi), 4080 rpm

Table 5 Summary of peak stresses for superhybrid composite blades (4080 rpm)

(4080 rpm)

	TiCore Blades			TiCom Blades			
						Design Allowables	
	Stress	Location	Design Allowables	Stress	Location	Superhybrid Material	Titanium Material
Flatwise Tensile Stress σ_{11} - ksi (10^6 n/m^2)	1.0 (6.894)	LE 40% Span	3.0 (20.68)	10.0 (68.95)	Root Midchord Region	3.0 (20.68)	90** (620.53)
Chordal Tensile Stress σ_{22} - ksi (10^6 n/m^2)	5.0 (34.47)	LE 40% Span	22.0 (151.68)	40.0 (275.79)	LE 50% Span	22.0 (151.68)	90** (620.53)
Radial Tensile Stress σ_{33} - ksi (10^6 n/m^2)	35.0 (241.32)	Root LE Region	70.0 (482.63)	65.0 (448.16)	LE Root Region	70.0 (482.63)	90** (620.53)
Chordal Shear Stress σ_{12} - ksi (10^6 n/m^2)	0.5 (3.45)	LE 40% Span	5.0 (34.47)	8.0 (55.16)	LE 40% Span	5.0 (34.47)	50** (344.74)
Cross-Fiber Shear Stress σ_{23} - ksi (10^6 n/m^2)	5.0 (34.47)	Midchord 20% Span	17.0 (117.21)	13.0 (89.63)	LE 40% Span	17.0 (117.21)	50** (344.74)
Radial Shear Stress σ_{13} - ksi (10^6 n/m^2)	4.0 (27.58)	Midchord Root Region	8.0 (55.16)	4.0 (27.58)	Midchord Root Region	8.0 (55.16)	50** (344.74)

** Controlling allowable.

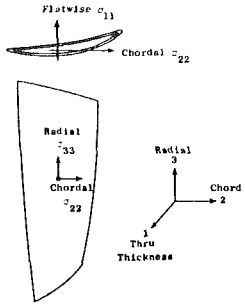

Table 6 Blade frequencies at 4080 rpm

	Frequency, Hz		
	Titanium Midspan Supported	Superhybrid Cantilevered	
		TiCore	TiCom
1st Frequency (Hz)	260	115	113
2nd Frequency (Hz)	500	165	163
3rd Frequency (Hz)	450	250	248

Table 7 Bench frequencies of superhybrid composite blades and CF6 titanium blades for comparison

Blade Type	Cycles/second (Hz)				
	1F*	2F	1T**	3F	4F
TiCore					
1	30	92	186	230	442
2	30	94	184	232	452
3	30	94	184	232	446
TiCom					
1	26	88	180	218	434
2	28	90	189	220	436
3	28	88	182	214	428
CF6 Titanium Blade					
Unshrouded (cantilevered)	22	76	152	-	-
Shrouded	176	382	458	-	-

*Flexural vibration Mode

**Torsional vibration mode

The nickel plate/wire mesh was stripped from TiCore blade 1. The blade was retested under starling impact to determine the degree of protection provided by the leading-edge protection system. The results of this test showed that without leading-edge protection local fracture occurred in the surface plies (Fig. 9). This blade suffered local fracture of the convex titanium/boron/aluminum layers with a 40 gram weight loss and 15-percent airfoil delamination.

The impact of a 9-ounce (0.255 kg) slice on blade 2, which is nearly equivalent to the ingestion of a 1-1/2 pound (0.680 kg) bird at aircraft takeoff conditions, resulted in considerable local damage and delamination, with an attendant blade weight loss of approximately 8 percent (Fig. 10). Such damage

Table 8 Superhybrid test results

Blade Type	Slice Size	Equivalent Bird Size	Remarks
TiCore			
1	2.84 oz (0.080 kg)	3.0 oz (0.085 kg)	Nickel-plate Separation
2	9.0 oz (0.255 kg)	1.5 lb (0.680 kg)	Local Fracture
3	2.86 oz (0.081 kg)	3.0 oz (0.085 kg)	Nickel-plate Separation
4 (No Leading Edge Protection)	3.0 oz (0.085 kg)	3.0 oz (0.085 kg)	Local Fracture
TiCom			
1	2.90 oz (0.082 kg)	3.0 oz (0.085 kg)	Severe Delamination

Nominal Impact Test Conditions

Impacts at 75% Span; 3.0 oz, starling; 1.5 lb, pigeon

3850 rpm

23° Incidence Angle

Simulates 300 T/Sec (91.44 m/sec) Takeoff Velocity

is acceptable if the engine can maintain 75-percent power for 5 minutes without incurring subsequent damage which would result in engine shutdown. Also advantage can be taken of the flexibility inherent in the SHC concept to improve the impact resistance locally. This can be done, for example by varying the titanium plies.

Conclusions

The results of this investigation demonstrated that the superhybrid composite concept can be utilized to produce lightweight, large fan blades. The manufacturing process developed during this program demonstrated that several prototype blades could be manufactured with good uniformity and dimensional control and that the process is capable of being scaled up for preproduction quantities of blades. Whirligig testing validated that both the TiCore and TiCom blade designs are adequate for steady-state and cyclic operating conditions. The TiCore blade proved to be the superior design from a bird-impact resistance standpoint. TiCore blades need some additional improvements in the bonding of the nickel-plate leading-edge protection system in order to avoid local separation during starling impacts.

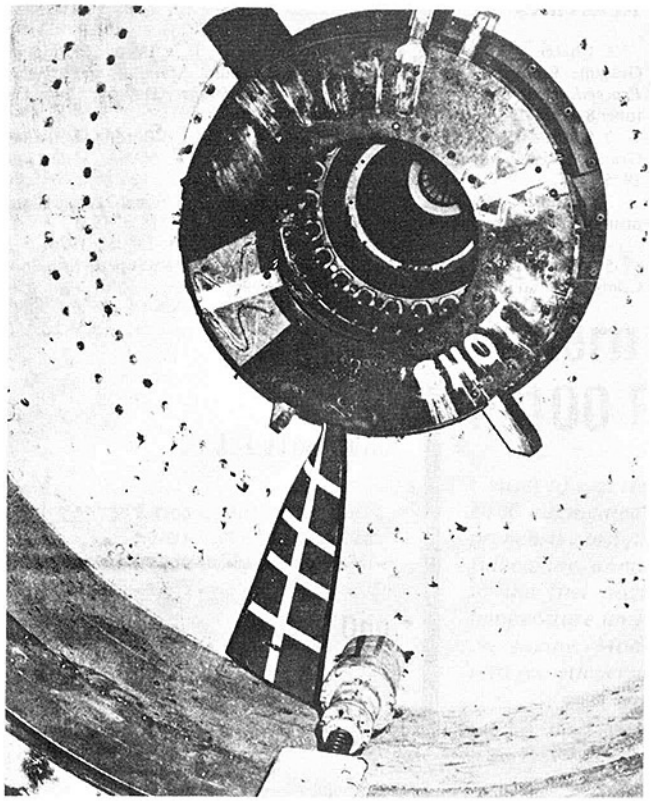

Fig. 8 Superhybrid blade whirligig impact test setup

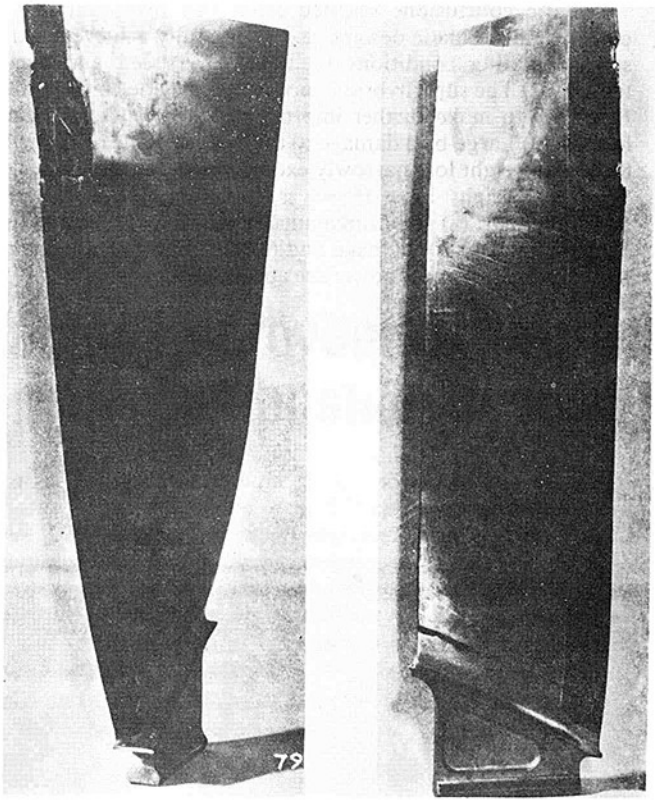

Fig. 9 TiCore superhybrid blade 4 without leading edge protection shown after impact testing of 3.0-ounce starling

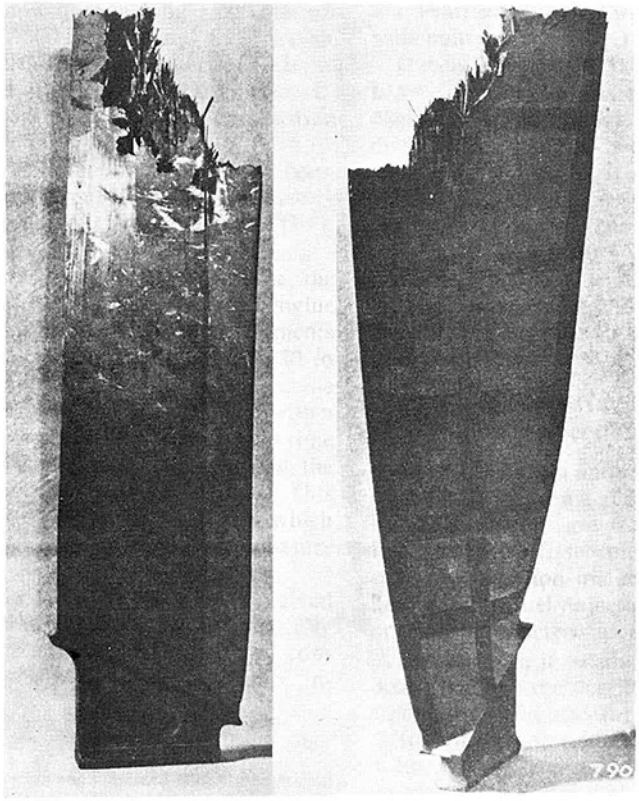

Fig. 10 TiCore superhybrid blade 2 shown after whirligig impact testing of 1.5-pound bird

Specific conclusions reached from this investigation include: (1) Both blade designs can successfully achieve steady-state operating conditions including overspeed and cyclic testing. (2) The superhybrid concept can provide considerable flexibility to make further improvements in FOD resistance locally. (3) Large-bird damage to the TiCore blade resulting in 8 percent weight loss narrowly exceeded the desirable limit of 5-percent weight loss. However, this may be acceptable providing that: (a) rotor unbalance capability, (b) the amount degree of secondary damage and (c) the ability of the engine to maintain 75 percent power are adequate.

References

1 Chamis, C. C., Lark, R. F., and Sullivan, T. L., "Boron/Aluminum-Graphite/Resin Advanced Fiber Composite Hybrids," Materials on the *Move Proceedings of the Sixth National Technical Conference,* Dayton, Ohio, October 8–10, 1979, pp. 368–385.

2 Chamis, C. C., Lark, R. F., and Sullivan, T. L., "Boron/Aluminum-Graphite/Resin Advanced Fiber Composite Hybrids," NASA TND-7879, 1975.

3 Chamis, C. C., Lark, R. F., and Sullivan, T. L., "Super-Hybrid Composites—An Emerging Structural Material," NASA TMX-71836, 1975.

4 Novak, R. C., "Multi-Fiber Composites," NASA CR-135062, 1976.

5 Salemme, C. T., and Murphy, G. C., "Material Spar/Superhybrid Shell Composite Fan Flades," NASA CR-159594, 1979.

G. B. Cox, Jr.

A. R. Tiller

J. J. LeTourneau

Pratt & Whitney Aircraft Group-UTC,
Government Products Division,
West Palm Beach, Fla. 33402

J. S. Ogg
YZ100
Wright-Patterson AFB,
Ohio 45433

Pattern Factor Improvement in the F-100 Primary Combustion System

Causes of exit temperature nonuniformity in the primary combustion system of the F100 augmented turbofan engine have been identified and investigated in a comprehensive test program. This test program involved a combination of instrumented full engine, annular combustor rig, and subscale component rig tests. Modifications to the fuel nozzle, which provide significant improvements in combustor exit temperature uniformity, are now being incorporated into the production version of the engine. Modifications to the combustor configuration are being incorporated into growth versions of the engine.

Introduction

Following the initial development, military qualification, and service introduction of the combustion system, Fig. 1, in the F100-PW-100 afterburning turbofan engine, further improvements have been made in the combustor. These improvements are being incorporated as the F100 engine matures in service. Currently, high-time F100 engines are approaching 1500 hr total operating time (TOT); the fleet total for the F100 engine is now approaching 1,000,000 hr; and, as of 1 June 1980, about 1500 F100 engines are in service with the F-15 and F-16 aircraft. This field experience has, in combination with testing at Pratt & Whitney Aircraft, Government Products Division, guided the combustion system improvements described in this paper.

The area for improvement is reduction of the F100 combustor's exit temperature nonuniformity. This nonuniformity is typically characterized by the term "pattern factor" (PF), where $PF = (T_{MAX,EXIT} - T_{AVERAGE,\ EXIT})/(T_{AVERAGE,EXIT} - T_{AVERAGE,\ INLET})$. At the qualification of the F100 engine, the pattern factor was judged to be 0.35, based on limited engine measurements. However, neither these engine measurements nor low-pressure rig tests, which gave PF levels of 0.20 to 0.25, were able to quantify the effect of variables that became evident with years of production and service experience with a large number of engines. Turbine distress seen in high-time engines in the 1976 and later time period indicated that the pattern factor was greater than the acceptable 0.35 level. This was confirmed by an engine test in December, 1976, which used 184 first-stage vane hot-gas thermocouples to measure PF.

The subsequent pattern factor improvement effort involved sufficient F100 engine testing to establish statistically significant pattern factor level and variability and, in conjunction with combustor rig testing, isolated variables influencing pattern factor. The full-annular combustor rig used during the early F100 development program was used for over 50 separate tests measuring all aspects of combustor behavior; extensive engine pattern factor tests ultimately involving nine different core and full engine configurations, and over 40 separate tests, were made; and, subscale rigs at the fuel nozzle vendor, the United Technologies Research Center (UTRC) and Pratt & Whitney Aircraft/Commercial Products Division were built and tested.

During the pattern factor improvement program, an improved fuel nozzle was qualified for production in the F100 engine. This fuel nozzle features more uniform fuel spray distribution than the previous fuel nozzle, and as a result, average pattern factor is reduced to the 0.35 level. In addition, the variability of pattern factor, as measured by the standard deviation of the pattern factor measurements of individual combustor and engine combinations, was reduced by 43 percent. Other aerodynamic improvements to the combustion system were identified, and this technology is being applied to growth versions of the F100 which are now in the early stages of development.

A Combustion Section Description

The F100 has an annular combustor, with a burning length of 27.2 cm (10.7 in.) and a maximum height of 10.2 cm (4.0 in.). The combustion section itself, from compressor stator inlet to turbine first vane inlet, is 45.7 cm (18 in.) long. The combustor section includes the diffuser case, splitter, combustor, and fuel injection system. Table 1 lists pertinent operating characteristics of the F100 combustion system.

The diffuser, immediately downstream of the compressor, is of axial, symmetrical design, with an area ratio of 1.5 and an equivalent conical angle (ECA) of about 7 deg. Within the diffuser flowpath are eight airfoil-shaped radial struts, with blunt, hollow trailing edges. The struts provide services for the shaft bearings and also bleed flow for engine and aircraft requirements. The bleed flow is taken directly from the strut trailing edge plane.

Contributed by the Gas Turbine Division and presented at the International Gas Turbine Conference and Products Show, Houston, Texas, March 8-12, 1981, of THE AMERICAN SOCIETY OF MECHANICAL ENGINEERS. Manuscript received by the Gas Turbine Division, December 5, 1980. Paper No. 81-GT-25.

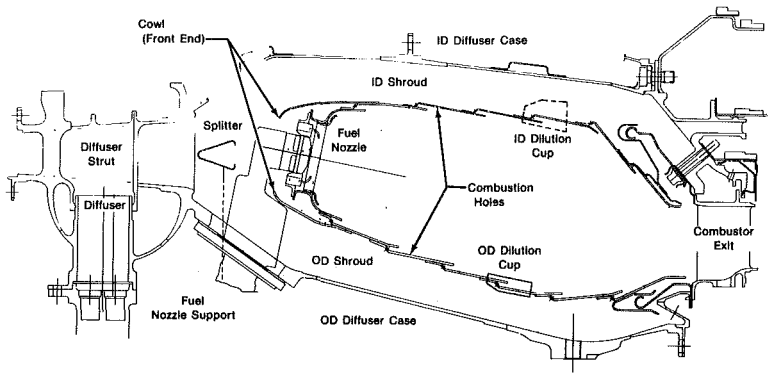

Fig. 1 F100(3) combustion system

Table 1 Combustor performance

Heat release rate	6.65×10^8 Joules/m^3/MPa/s (6.5×10^6 Btu/ft^3/atm/hr)
Combustor temperature rise	856°C (1540°F)
Temperature pattern factor (with improved fuel nozzle)	0.35 average, 0.033 standard deviation
Liner pressure drop	2.5%
Overall pressure drop	3.8%
Front end loading	24% of combustion air
Combustor discharge temperature	1410°C (2570°F)

At the exit plane of the diffuser, near the midpoint of the flow, is a circumferential, V-shaped splitter. The splitter serves to direct airflow into the shroud passages, prevents diffuser separation even with severe distortion of the diffuser inlet flow, and provides a sheltered region to ensure uniform flow into the combustor dome region. The combustor is of welded sheet-metal construction. The combustor is supported at the front end by eight hanger brackets through which pass mount pins, which also support the splitter. The combustor hanger brackets and mount pins are in line with the diffuser struts and thus do not introduce further aerodynamic disturbances into the shroud flow.

The combustion system uses 16 pure airblast fuel nozzles to introduce fuel into the combustor. Each fuel nozzle incorporates a pressurizing valve to keep the fuel system pressure requirement within manageable proportions over the more than 80:1 flow turndown ratio. Fuel atomization and mixing are done by the pressure drop of the air across the dome of the combustor. Each fuel nozzle rides within a "floating" swirler. The swirler provides additional air for combustion and flame stabilization. The swirlers "float" to allow for differential radial and circumferential growth between combustor and fuel nozzles. Additional air is metered through the dome for cooling purposes. Around 15 percent of the airflow entering the combustor section enters the combustor through the dome. The remainder flows through the inner and outer shroud passages. Most of this airflow eventually enters the combustor for liner cooling, combustion, and dilution. The remainder bypasses the combustor entirely and is used for turbine cooling.

B Test Program

The annular rig testing provided basic data needed to define combustor design revisions. More detailed measurements of the combustion system flowpaths were made than were possible in the engine. The approach taken in this phase of the testing was to measure the response of the combustion system to specific changes in inlet conditions and configuration changes, while continuing to measure flowpath behavior. In this, the rig was used as an aerodynamic tool as much as a combustion tool.

The subscale rig tests isolated, visualized, and measured specific areas of combustion system behavior. Because the engine test results showed that the areas to investigate were (1) the air flow fields in and around the outside of the combustor front end, and (2) the distribution of fuel spray within the combustor front end, these rig tests concentrated upon those specific areas. Each of these test programs was immediately successful in identifying and verifying required changes.

The engine testing characterized combustor performance in the engine environment over a wide range of power levels. Five different types of measurements were made at one point or another during the engine test program, Fig. 2. Instrumented first-stage vanes carrying a total of 184 Pt-6 percent Rh/Pt-30 percent Rh thermocouples measured combustor exit temperature distribution. A splitter carrying a total of 144 total and static pressure taps measured radial and circumferential flow distortion at the exit of the diffuser. Combustors carrying a total of 18 static pressure taps measured the pressure distribution in and around the combustor. Sixty-four combustor liner thermocouples measured metal temperatures. An emissions probe measured smoke, NO_x, ThC, and CO concentrations.

1. Engine Testing

(*a.*) *Description.* The objectives of the engine test program were threefold:

1. Characterize the performance of the Bill-of-Material (B/M) combustor, diffuser flow-path, and fuel nozzles.
2. Identify and verify combustion system modifications to improve combustor exit temperature.
3. Provide substantiation for proposed production hardware changes.

The initial tests made in 1976 indicated that the undesirably high pattern factor had at least two causes: fuel nozzles and front end distortion. Isothermal plots of the combustor exit temperature flow field, Fig. 3, showed localized "hot spots" on and between fuel nozzle center lines. These hot spots showed much the same character even with a radical change to the dilution zone contour and hole pattern. These hot spots were thus originating within the front end of the combustor, at the fuel nozzles themselves. Subsequent testing showed this deduction was correct. The hot spots were in turn imbedded in

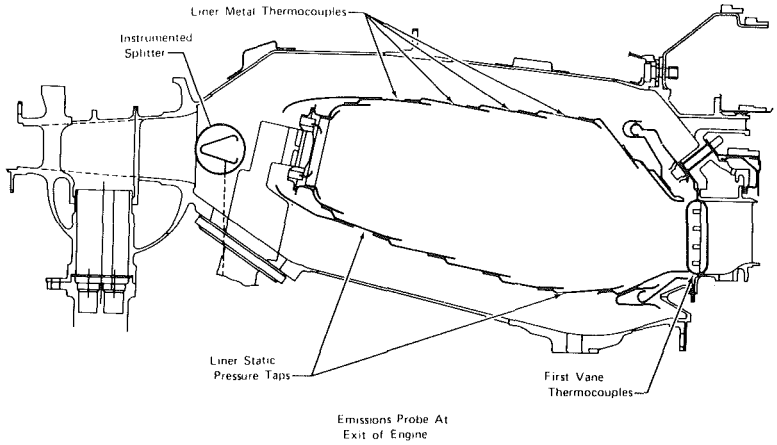

Fig. 2 F100(3) engine test combustion system instrumentation

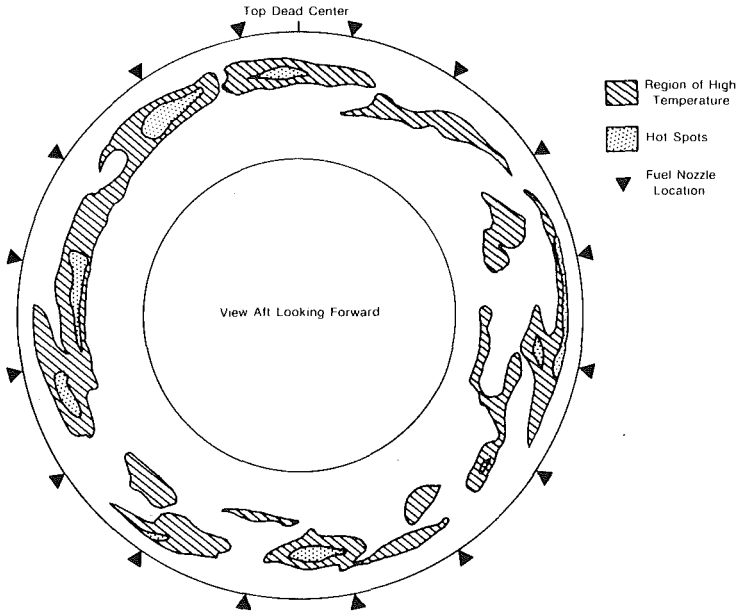

Fig. 3 F100(3) combustor exit temperature isotherm

broader regions of distortion of the exit temperature pattern, which were the result of combustor response to diffuser exit flow distortion. Subsequent testing proceeded along the lines initially determined by these early results and conclusions, with the extensive series of engine tests described herein.

Early in the subsequent test program, however, results showed a response of combustor exit temperature distribution to an unexpected interaction between combustor front-end dimensions and the compressor discharge flow field. Additional combustors and engines were added to the test program. Eventually, six different engines and engine configuration changes, and nine combustors or combustor configuration changes, were involved in the test program. A total of about 45 separate test configurations were run, involving about 1700 individual engine operating points where data were taken.

For most of the tests, high localized combustor exit temperatures prevented running the engine at full power (average combustor discharge temperature of 1410°C or 2570°F), since the first-stage vane thermocouples were limited to 1650°C (3000°F) to insure adequate sensor life. Analytical techniques were developed to project data measured at part-power operating points to full power. These methods were verified by comparing predicted peak temperatures to those measured during the limited number of tests at or near full power.

(*b.*) *Statistical Method of Analysis.* The severity of a combustor's exit temperature maldistribution is customarily described by pattern factor. A quantity such as pattern factor, since it depends upon and describes in essence a single point in the entire exit temperature distribution, is inadequate for assessing the potential impact of a given temperature distribution upon turbine durability, and therefore, gives an incomplete comparison between two combustors. Furthermore, neither normal, log-normal, nor Weibull distributions fit all measured combustor exit temperature data, although Weibull methods fit better than most. Nonetheless, statistical treatments of pattern factor data are in common usage [1].

The objectives, then, of the statistical methods developed under this program were:

1. To develop a method of analysis which reflects, more descriptively than pattern factor, the impact of the combustor exit temperature distribution upon turbine life.
2. To use temperature data measured at part-power points to predict temperature distribution at full power.
3. To reduce reliance upon calculated engine performance parameters (such as combustor exit average temperature) by using directly measured quantities such as

local combustor exit temperatures, engine fuel flowrate, and combustor pressure.

The statistical methods which were developed first use a linear model [2, 3] to describe the behavior of each thermocouple as a function of engine power setting as well as its radial and circumferential location:

$$Y_{ijk} = \mu + R_i + C_j + M_{ij}\,(WF/PB\theta_{T2}{}^{0.68})_K + \epsilon_{ijk} \qquad (1)$$

where:

Y_{ijk} = temperature at radial location i, circumferential location j, at power setting k
μ = overall mean temperature
R_i = effect of radial location i
C_j = effect of circumferential location j
M_{ij} = change in recorded temperature at radial location i, circumferential location j, for a one-unit change in $WF/PB\theta_{T2}{}^{0.68}$
ϵ_{ijk} = random error in temperature recording, distribution normally with mean zero, variance σ^2
WF = measured fuel flow rate
PB = measured combustor static pressure
θ_{T2} = ratio of ambient temperature to standard-day temperature

The ratio of measured fuel flow rate to measured combustor static pressure is, for any particular engine, a parameter which is proportional to the combustor fuel/air ratio. Its use does not, however, require the computation of combustor airflow with the uncertainties inherent in that process.

The correction term to standard-day conditions, raised to the 0.68 power, is required to account for the effect of temperature upon the air specific heat. It is in standard P&WA usage for engine performance and control calculations. The term $WF/PB\,\theta_{T2}{}^{0.68}$ is used by P&WA as an engine control parameter which represents fuel/air ratio and hence turbine inlet temperature, at standard-day conditions.

Special acknowledgement is made to Grant L. Reinman, of the Engineering Statistics Group, for the formation of this analysis method.

Using the model, we can predict the value of each thermocouple at full power. The extrapolation was verified by comparison with data taken in one run to ~99 percent full power, Fig. 4. Histograms of temperature are then generated for the thermocouples at each separate radial position along the first-stage vanes. These histograms define the turbine inlet radial temperature profile. The individual histograms are then superimposed to provide an overall histogram of the entire temperature field.

The final two items of information derived from the histograms are (1) the fraction of the turbine inlet temperature field whose temperature exceeds a threshold value, and (2) the fraction of circumferential locations where the temperature exceeds the threshold value, Fig. 5. This description of the combustor exit temperature field more closely matches the turbine distress indicators which modern engine maintenance procedures employ. The most important of these are Maximum Operating Hours (MOH) before turbine refurbishment is needed, and airfoil scrappage rate vs time. The number and severity of circumferential "hot spots" is thus directly relatable to both MOH and the number of airfoils to be scrapped at turbine refurbishment. A reduction in severity of hot spots is reflected in higher MOH, while a reduction in the number of hot spots will be reflected in a reduction in airfoil scrappage rate at turbine refurbishment.

(*c.*) *Results From Engine Test.* Results from the engine test program included:

1. A redesign to the B/M pure airblast fuel nozzle invariably produced a reduction in average pattern factor whenever a set of these nozzles was used in place of B/M nozzles, Fig. 6. In addition to reducing the average pattern factor, the improved fuel nozzle also reduced the variability in pattern factor. With the B/M nozzles, pattern factor variability as measured by the standard deviation of the measurements, was 13 percent of the mean value. The improved nozzles reduce this variability to 10 percent of the mean value. The net result is a 0.15 reduction in the pattern factor of the 2σ worst engine, using the improved fuel nozzles.
2. The improved fuel nozzles also produced a consistent shift in turbine inlet radial temperature profile, Fig. 7.
3. Both radial and circumferential diffuser exit flow variations were measured from engine to engine, Fig. 8.
4. One particular combustor showed a systematic sensitivity of pattern factor to the diffuser exit radial flow variations, Fig. 9.
5. Static pressure distributions around the combustor liner also changed in response to diffuser exit flow variations.
6. Modifications to combustor front-end dimensions could, with certain types of diffuser exit flow variation, change combustor pattern factor, while pressure distribution was unchanged.

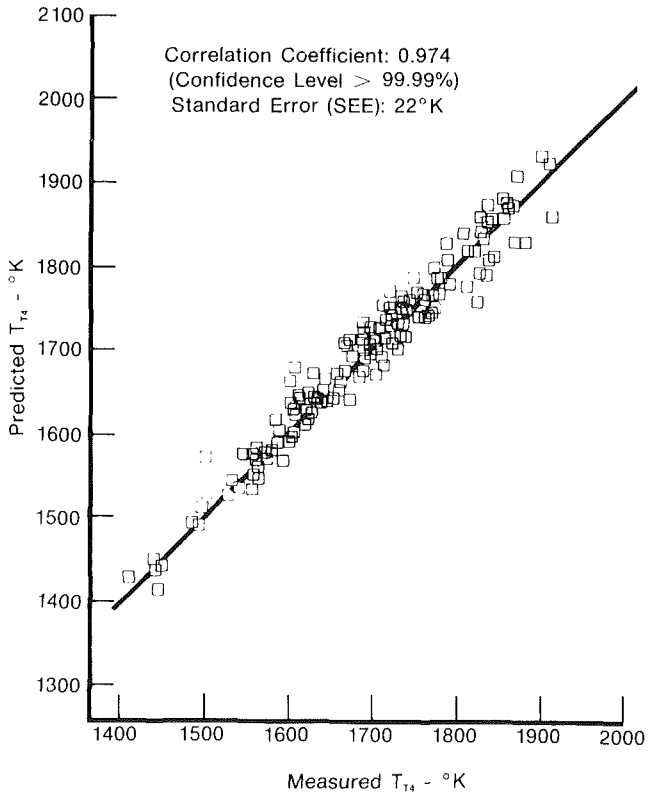

Fig. 4 Comparison of measured versus predicted temperatures at near-full-power condition

These engine test results showed that significant improvements in combustion system performance were attainable with fuel nozzle design revisions. The results also showed room for further improvements in reduction of pattern factor responsiveness to geometric or inlet profile changes. Two salient features were immediately apparent. First, the response of combustor pattern factor to inlet flow distribution and changes in hardware dimensions was consistent. Second, the response showed that conditions existed under which levels of pattern factor less than 0.30 were attained.

A particularly important conclusion drawn from the engine

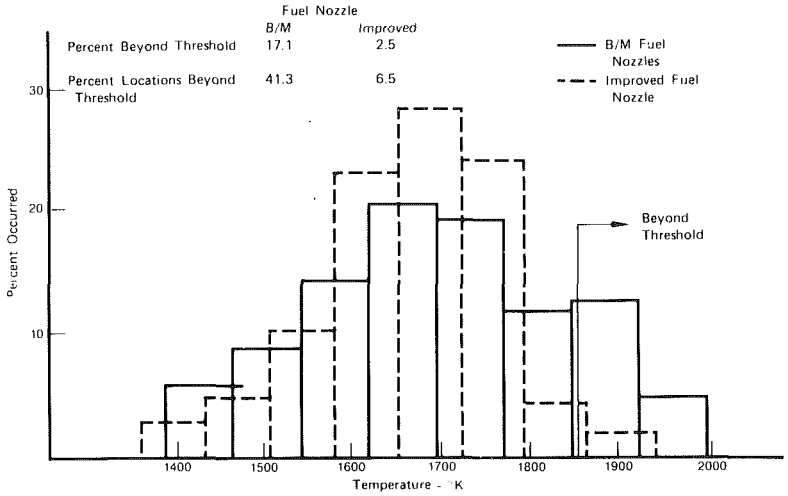

Fig. 5 Combustor exit temperature histogram shows differences between configurations

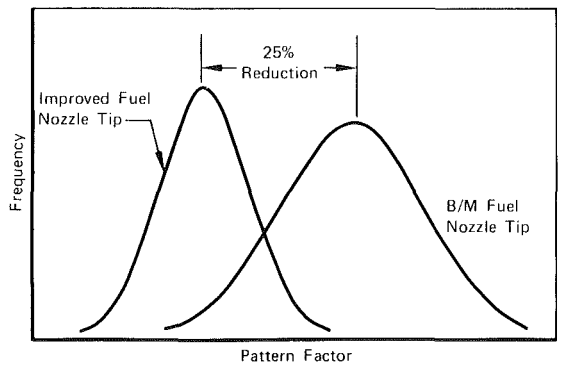

Fig. 6 New nozzles provide substantially lower pattern factor

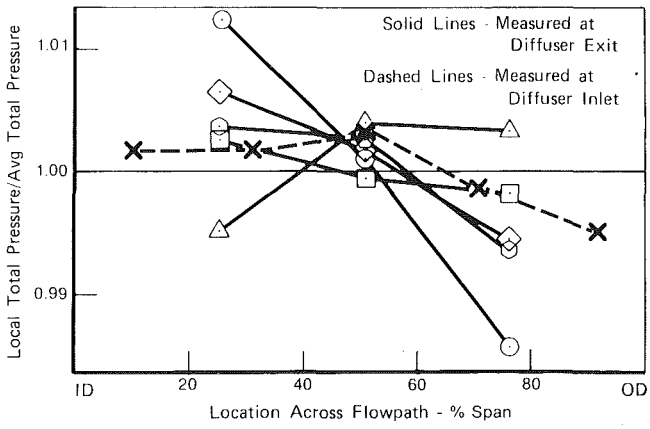

Fig. 8 Combustor inlet total pressure profiles vary from engine to engine

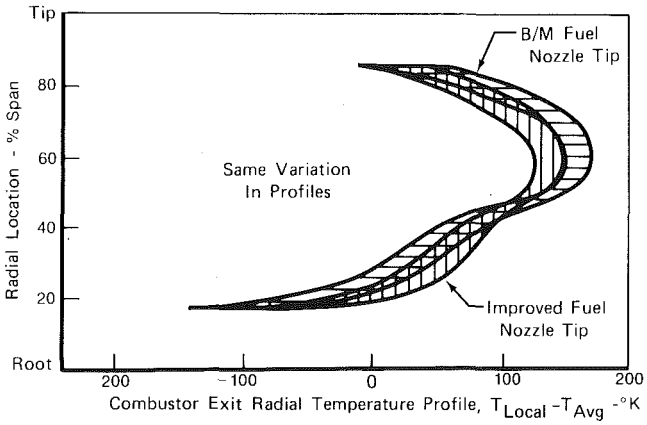

Fig. 7 Combustor radial temperature profiles show shift in profile with improved fuel nozzle

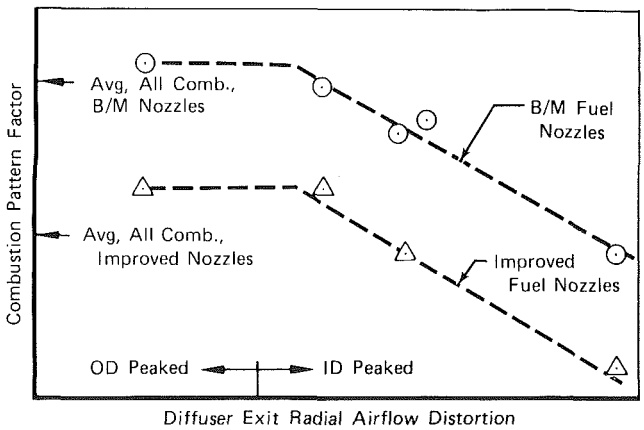

Fig. 9 Combustor response to diffuser exit flow variations pattern factor is low with ID-peaked profile

test program is that considerable variations in behavior exist from engine to engine. The true measure of the performance of a combustion system thus can only be gained from engine tests. These engine tests also must involve a number of different engines and combustors, with sufficient measurements of variations in both geometry and operating environment to ensure that a sufficiently wide range of variables is included. Comparison of the range of pattern factors measured in the engine to that measured in rig testing shows that rig data do not always give an accurate measurement of engine pattern factor, Fig. 10.

Analysis of the results of the engine tests isolated the processes within the combustor to be investigated and understood before the needed improvements could be made. Combustor pattern factor was not dependent upon the distribution of pressure loss around the combustor. Pattern

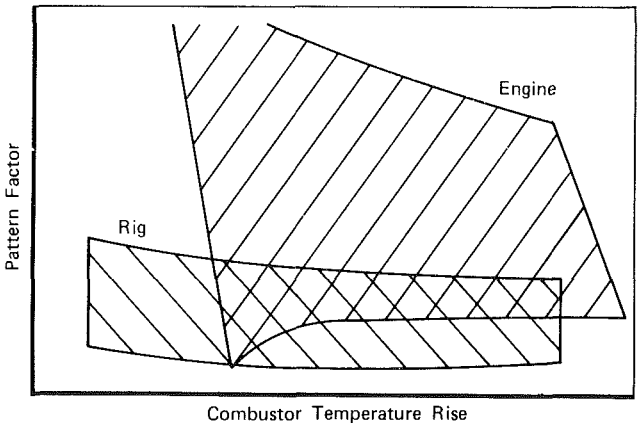

Fig. 10 Rig, engine pattern factor comparisons

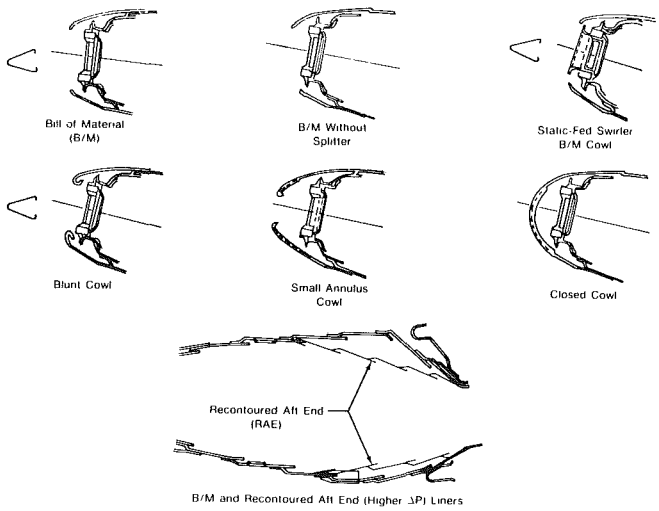

Fig. 11 Combustor front end and liner modifications

factor was dependent upon supposedly minor dimensional changes in the front-end region as well as inlet total pressure profile. Therefore, the behavior of the combustor was in all probability being controlled by subtle differences and changes in the flow field approaching the combustor dome and in the effect these subtle differences have upon the fuel/air injection and mixing process in the extreme front end of the combustor. Rig testing was done to further understand these processes.

2 Full Annular Combustor Rig Testing

(*a.*) *Description.* The full annular combustor rig is used to test F100 engine combustors at low pressure. It consists of an inlet section with bellmouth and an actual F100 diffuser case. Behind the diffuser case is an exhaust duct. Diffuser inlet Mach number can be matched to that of the engine. Reynolds number based on diffuser inlet gap height is 1×10^5, an order of magnitude lower than the engine, and turbulence levels may differ. Testing has shown that pressure recovery to the shrouds is slightly lower and pressure loss to the exit of the combustor is higher than the engine. The combustor swirler is also affected by the Reynolds number difference. See the Fuel Nozzle Spray Rig section. There is provision for simulating various levels of turbine vane and blade cooling air bleeds. It is also possible to modify inlet velocity profile by use of distortion plates. While inlet pressure and airflow are considerably lower than the engine conditions, inlet temperature is the same to provide the same combustor section Mach numbers and temperature rise. Because of the lower combustor airflow, the range of fuel flows is also lower than in the engine.

Extensive pressure instrumentation in the diffuser and shrouds allows calculation of mass flow splits and pressure recoveries. Static pressure measurements are also made along the two diffuser case walls and inside the combustor for further recovery and liner pressure loss calculations. A rotating drum at the exit of the combustor, with two instrumented rakes, obtains gas total temperature and pressure distribution. The data are read onto a magnetic tape for later access.

Testing showed that the rig pattern factor data are lower than engine data, although they respond to hardware changes similarly to engine data. Therefore, they are useful for making comparisons between burner configurations, but are only a partial simulation of engine performance.

In order to reduce the sensitivity of pattern factor to diffuser inlet profile and small dimensional changes of the cowl, a rig test program was formulated to determine the combustor exit temperature and diffuser flowpath response to inlet distortion and combustor modifications. The inlet velocity

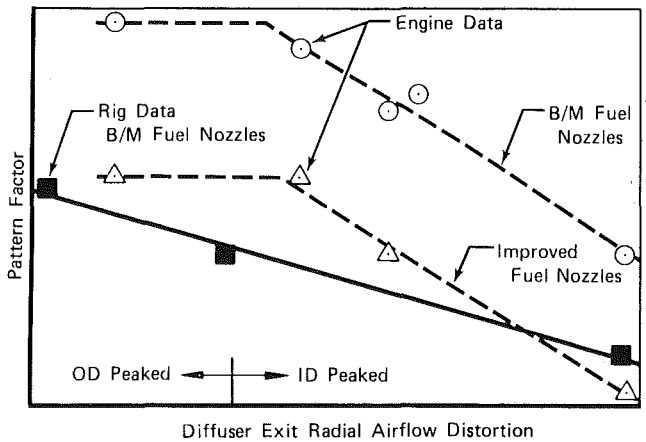

Fig. 12 Rig testing shows same trend with diffuser exit flow profile as engine testing

profiles ranged from strongly ID peaked to strongly OD peaked. Flow was circumferentially uniform. In addition to the B/M combustor, configurations tested were of three types: (1) modifications to the cowl and/or removal of splitter [6], (2) combustors with recontoured and higher pressure loss liners, and (3) different fuel nozzle and/or swirler, Fig. 11.

(*b.*) *Screening Test Results*

1. The first determination was that rig pattern factor for the B/M combustor responded to variation in inlet profile in the same manner as in the engine, figure 12. Second, when shroud passage flow is increased, the outer shroud static pressure recovery increases, which may produce instability throughout the flowfield [5], Fig. 13. This test was the baseline by which other modifications were assessed: pattern factor level and variation should be lower than B/M, and shroud static pressure recovery should be high, but should decrease with passage flow. A comparison of the configurations is shown in Table 2.
2. As a group, the front end modifications reduced pattern factor sensitivity, but level remained high. Blunting the cowl leading edges improved shroud pressure recovery and stability. Removal of the splitter from the B/M configuration causes poor shroud recovery and stability.
3. The Recontoured Aft End (RAE) combustor, which has a higher pressure loss liner, as well as more, smaller dilution holes, achieved a low pattern factor. Stability

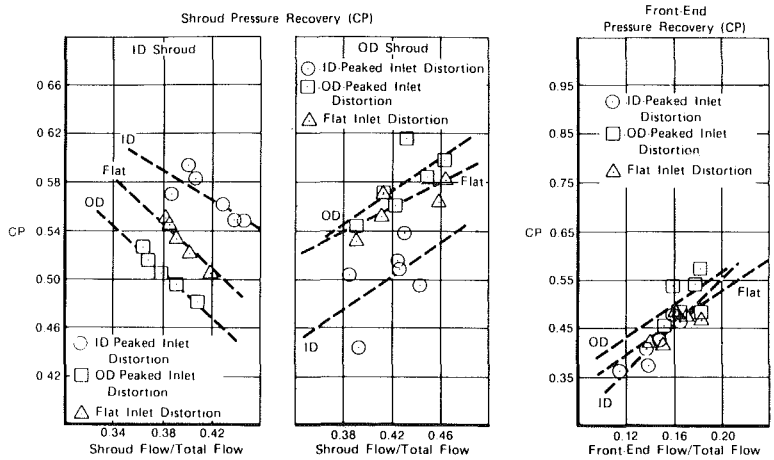

Fig. 13 Pressure recovery characteristics for B/M

Table 2 Screening test comparison

Configuration	PF Response		Shroud recovery
	Sensitivity	Level	stability
B/M Baseline	High	High	Low
B/M Combustor + No Splitter	–	High	Very Low
B/M Combustor + Static-Fed Swirler	Moderate	Moderate	–
RAE Combustor	Moderate	**Low**	Moderate
B/M Combustor + Blunt Cowl	**Low**	High	**High**
B/M Combustor + Small Annulus Cowl[1]	Low	High	Low
B/M Combustor + Closed Cowl[1]	Moderate	High	Low
B/M Rebaseline + New Splitter	Low	Moderate	Low
B/M Combustor + Improved F/N	**Low**	**Low**	–
Revised RAE	Moderate	Very High	–
B/M Combustor + Hollow-Cone SW, B/M F/N	Low	Moderate	–
B/M Combustor + Hollow-Cone SW, Improved F/N	**Moderate**	**Low**	–
New B/M Combustor + New Splitter	High	High	–

[1]No splitter

improved too. However, a revised version of this combustor, with airflow shifted from the OD liner and front end to the ID liner, gave the worst pattern factor. Since the major change was dilution hole pattern, it suggests that changes to dilution jet penetration had deteriorated pattern factor.

4. A rebaseline test of the B/M combustor, having a different B/M splitter (which was later discovered to have a local flattening of the circumference) achieved a lower PF and less sensitivity than the baseline test. It appears that, like the engine, a small dimensional change was significant to pattern factor. Later, another B/M combustor, with a machined splitter, demonstrated the same high level and variability of PF as the baseline.
5. Compared to the rebaseline, the improved fuel nozzle and Hollow Cone swirler, which were tested in the spray rig, demonstrated improved pattern factor. As in previous engine and rig tests, the improved fuel nozzles reduced PF in B/M combustor. The Hollow Cone swirler did not improve pattern factor when combined with the B/M fuel nozzle. However, when used in combination with the improved fuel nozzle, PF was lower, although more sensitive to inlet profile.

No single configuration displayed all of the improvements that were sought. In Table 2, shown in boldface type, are improvements made by modifications that could be incorporated in combination to attain all objectives. The types of modifications that merited further consideration were the RAE combustor, improved fuel nozzles and Hollow Cone swirlers for their lower pattern factor, and the Blunt Cowl for good stability and low pattern factor sensitivity to inlet distortion.

(*c.*) *Results.* Aside from the screening function performed by the annular rig, the data were examined for other aerothermal responses to inlet distortion. The most noticeable were:

1. Static pressure recovery increased in the ID shroud for ID-peaked inlet velocity profiles, and increased in the OD shroud for OD-peaked profile.
2. Combustor exit average radial temperature profile became slightly cooler on the ID side and hotter on the OD side for OD-peaked inlet distortion. The magnitude of the temperature profile peak changed little with inlet distortion and, like pattern factor, was lower in the rig than in the engine.

The considerable amount of data taken provided a means of checking the subscale rigs to insure good simulation, and was useful in correlating subscale rig observations with the annular rig.

3 Fuel Nozzle Spray Rig Tests

Fuel spray characterization studies were conducted at UTRC in a single-nozzle segment rig of an F100 combustor. The goal is to quantify fuel spray distribution changes with various diffuser inlet profiles, combustor front end configurations, and nozzle/swirler combinations. F100 jet fuel

Table 3 Fuel spray rig test conditions

	Rig	Engine		
		Lightoff	Part Power	SLTO
T_T Air Inlet, °C (°F)	494 (921)	49 (120)	494 (921)	553 (1027)
P_T Air Inlet, MPag (psig)	0.07 (10.3)	0.02 (2.3)	1.75 (254.4)	2.42 (351.6)
$W_{AIR\ INLET}$*, Kg/sec (lb/sec)	0.27 (0.60)	0.17 (0.37)	3.0 (6.5)	3.9 (8.5)
W_{FUEL}*, g/sec (lb/hr)	5.3 (42.3)	2.7 (21.6)	57.4 (455)	80.8 (641)

*Flows are for a 1/16 sector combustor.

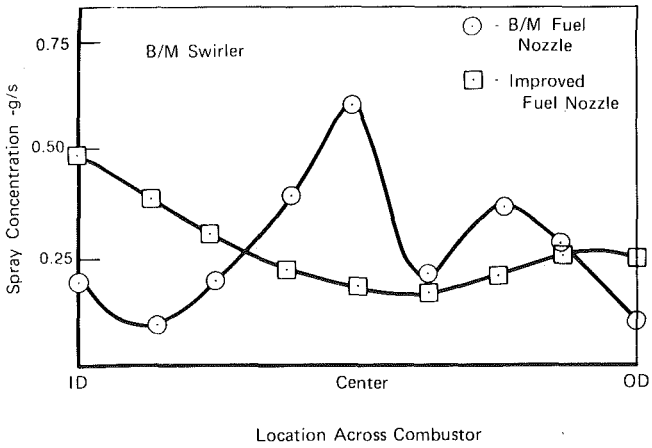

Fig. 14 Spray distribution measured in single-nozzle rig shows differences in spray, at engine conditions

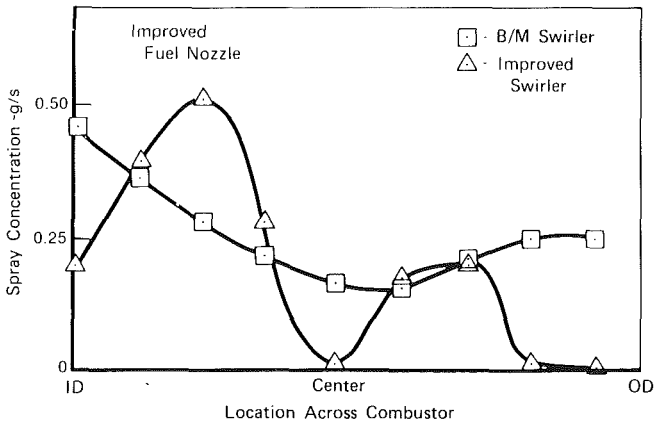

Fig. 16 Redesigned swirler produces desired hollow spray cone at engine conditions

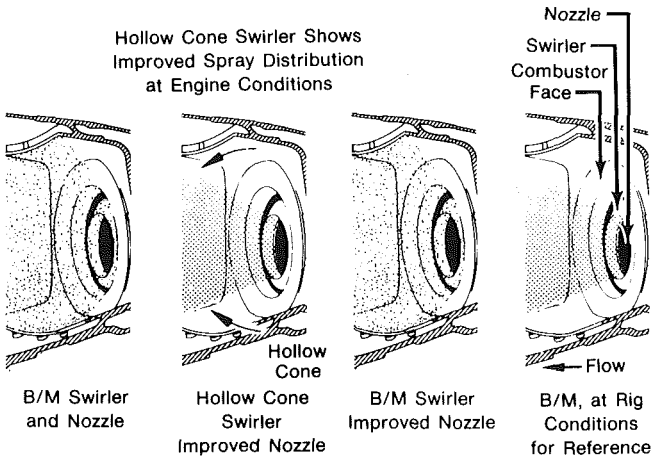

Fig. 15 Spray comparison at engine conditions

(JP-4) is not used because of the possibility of auto-ignition at engine conditions. Water has similar atomization characteristics to JP-4 and is used for this study. The spray is observed and photographed under strobe and floodlight illumination through a window in the test section. The liquid/air distribution is determined with a patternator probe which can be placed from 1 to 5 inches from the fuel nozzle. Pressure measurements allow the determination of pressure recoveries, liner losses, and mass flows. Liner temperature instrumentation aids in detecting spray impingement. Testing is conducted at full annular rig conditions as well as engine conditions from lightoff to full power, Table 3. The effect of pressure and temperature level is thereby observed as test conditions are changed.

The spray rig is a useful tool for quantifying spray behavior for various nozzle/swirler combinations and combustor inlet profiles. The Bill-of-Material (B/M) pure-airblast nozzle was shown to produce a sharp centerline liquid/air peak. An improved pure-airblast nozzle with increased central air swirl and peripheral airflow created a flatter liquid/air distribution, figure 14. This nozzle demonstrated significantly lower pattern factors in the F100 engine, a fact which is explained by its more uniform spray distribution. There is more fuel near the ID compared to B/M, resulting in the observed radial temperature profile shift at engine conditions.

The spray rig also showed an unexpected variation in spray distribution with pressure level and Reynolds number. At the low-pressure condition typical of the annular rig pressure level, the B/M swirler produces a hollow spray cone, as desired. The Reynolds number at this condition, based on the swirler diameter, is 690. However, at conditions typical of lightoff, Reynolds number 1330, and at the high-pressure condition typical of engine operation, Reynolds number 6720, the swirler airflow attaches to the dome of the combustor. The liquid spray likewise attaches to the combustor dome, impinging on both the combustor liner, verified by liner temperature data, and quartz windows, pictured in Fig. 15. A redesign of the swirler, referred to as the Hollow Cone swirler, substantially narrows the spray cone and eliminates spray impingement, Fig. 15 and 16. This redesign is based on the analysis of Beér and Chigier [4]. The difference in spray distribution between low- and high-pressure operating conditions is felt to be a major reason why rig pattern factors are generally lower than in the engine. The Hollow Cone swirler is not expected to improve PF much, when used with B/M fuel nozzles, because of its strong center-peaked spray distribution. Pattern factors should improve with redesigned fuel nozzles at engine conditions.

This single-nozzle rig has verified the expected spray distribution changes with different nozzle designs. It revealed a previously unsuspected change in spray behavior with pressure level and Reynolds number. However, measurement of the effect of combustor inlet profile upon spray distribution was not conclusively measured with the patternator probe located in its initial position, close to the dome. Relocation of the probe further downstream will,

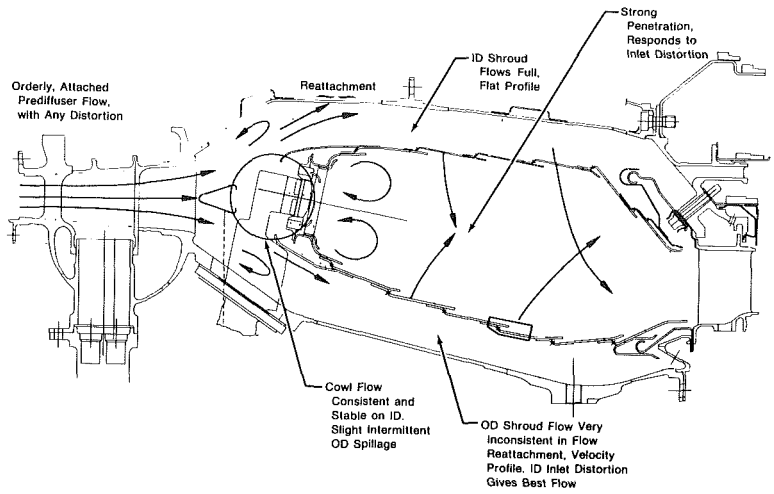

Fig. 17 Water tunnel results point to OD shroud for sensitivity

according to visual observation during the testing, measure the expected effects.

4 Water Tunnel Testing

(*a.*) *Description.* Water tunnel flow visualization and pressure measurements were made in a ¼ sector, full-scale transparent plastic model of an F100 combustor. The objective is to observe combustor flow field response to diffuser inlet profile and combustor geometry changes. Geometric similarity is maintained to a high degree. Reynolds numbers are lower than the full annular combustor rig, roughly 4×10^4. Comparison of data from the two rigs was made to check on the validity of the simulation. Inside the combustor, density differences are not simulated, resulting in about 20 percent more combustion and dilution jet penetration in the water tunnel. The model includes the diffuser and a straight inlet section forward of it, which is used to change inlet flow profile. Flow visualization is obtained by laser illumination of fine aluminum particles which are placed in the water. The flow field is recorded by sketches, still photographs, and motion pictures.

(*b.*) *Results*

1. The principal results for the B/M combustor model are depicted in Fig. 17. Flow within the diffuser is stable and invariant with inlet profile distortion. The ID shroud flow reattaches in a short distance and flows full with a flat velocity profile. Pressure recovery responds to inlet distortion, being higher for an ID-peaked profile. Stationary vortices are formed behind the spliter, which change in size asymmetrically with inlet distortion. Flow into the cowl is smooth with the exception of minor intermittent spillage from the OD lip between fuel nozzles with ID-peaked inlet distortion. Flow into the OD shroud is more disorganized. Attachment to the OD diffuser case is delayed and the point of attachment fluctuates. Shroud velocity profile, as measured at the first louver, peaks near the combustor. When inlet distortion is OD peaked, the attachment point moves aft, shroud velocity profile is more peaked, and pressure recovery increases. Inside the combustor, there is a weak recirculation at the front end between fuel nozzles. Combustion and dilution hole penetration is strong, promoting good mixing. However, penetration responds to inlet distortion; the ID jets penetrate less while OD jets penetrate further with a peaked inlet profile. This results in an ID shift of the flow distribution leaving the combustor for OD-peaked inlet distortion. Jet penetration also varies circumferentially.

Comparison of these results with annular rig data for the baseline B/M combustor showed very good agreement. Inlet velocity profiles and shroud velocity profiles matched. Shroud pressure rise coefficients were lower, but responded in the same way with inlet distortion. The observed flow shift inside the combustor corresponds qualitatively with the measured shift in combustor exit average radial temperature profile.

Pattern factor variation can be related to the observed changes in combustion and dilution jet penetration, setting aside the possibility of variation in fuel spray distribution. Dilution jets are columns of air which eventually break up and flow downstream. If a fuel-rich region impinges on the columnar portion, it will go around it like a solid body, while stripping off some of the air. On the other hand, if the fuel-rich region moves into the portion which is breaking up, it will mix better. A third possibility is that it passes beyond the reach of the jet or between two adjacent jets, being unaffected. Rig and engine data for the B/M combustor show a predominance of hot spots circumferentially located on and between fuel nozzles and radially toward the OD, at combustor exit. The OD dilution jets are directly in line with these hot spots. The OD combustion jets have some effect even though they are not circumferentially aligned with hot spots because the flow spreads circumferentially. Pattern factor data indicates that OD jet penetration is better for an ID-peaked inlet velocity profile. This suggests that for OD-peaked inlet distortion, OD jets are penetrating too far on the average and possibly there is too much circumferential variation.

There are two aspects of OD shroud flow likely to impact OD jet penetration: pressure recovery and velocity profile. With OD-peaked inlet distortion, OD shroud pressure recovery increases, which in turn increases OD liner pressure drop, resulting in higher jet velocity and further penetration. Increased velocity along the OD combustor liner, with OD-peaked inlet distortion, produces a reduction in discharge coefficients, an effect which is overwhelmed by pressure recovery in the B/M combustor. There is also a greater circumferential variation in discharge coefficients, due to the presence of neighboring low velocity regions such as strut and fuel nozzle support wakes (as well as compressor exit flow variations in an engine), causing variable penetration.

The baseline B/M had both a large increase in shroud pressure recovery and OD shroud distortion with OD-peaked inlet velocity, resulting in a large PF increase in the annular rig. All front end modifications, which produced a reduction

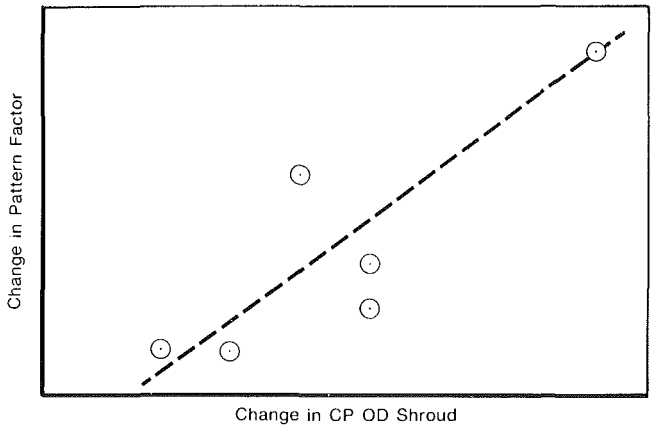

Fig. 18 Pattern factor response to OD shroud pressure recovery

in variability of pattern factor also had less variability in shroud pressure recovery, Fig. 18. The Rebaseline combustor did not seem to differ enough in pressure recovery level, relative to the baseline, to account for the PF difference with OD-peaked inlet velocity. Perhaps the lower OD shroud distortion explains it. It is clear that OD shroud flow has to be made less variant with inlet distortion to control pattern factor.

2. In order to improve the flow characteristics of the B/M combustor, the blunt cowl modification was tested for comparison. The front end is more sheltered from the high velocity flow coming off the splitter, particularly the ID side. The vortices behind the splitter were much weaker. There was no spillage from the OD cowl. The OD shroud attachment point was still delayed, but it did not fluctuate, as the B/M did when air spilled from the OD cowl. Velocity profile in the OD shroud was highly peaked like the B/M combustor.

Annular rig data shows that this flow pattern corresponds to less pressure variation in the front end and OD shroud. Static pressures, measured at the exit of the diffuser, indicate that flow on either side of the splitter varies less with inlet profile. When flow is increased to the OD shroud, additional flow is drawn from the OD side of the splitter, instead of exclusively being taken from the cowl as the B/M does. The front-end pressure recovery varies less with inlet profile and flow as a result of being more sheltered.

The OD shroud is less stable than the ID shroud because (1) it has a much larger area to fill, (2) flow must do more turning to attach to the diffuser case wall, and (3) it readily interacts with the front end. As flow increases, the shroud flows fuller. Distortion is reduced and the attachment point moves forward, which tends to increase pressure recovery. Since flow can be obtained from the front end, flow is not accelerating past the splitter and there is little depression of the static pressure on the OD side. The result is that pressure rises with flow. The blunt cowl greatly reduces interaction with the front end because the ID and OD side of the splitter have a more balanced contribution to front end flow and are less variant. It is sufficient to cause OD shroud pressure to decrease with flow slightly, i.e., produce stability. It does not, however, reduce the high level of distortion in the OD shroud.

3. A modification to the splitter, which increased the angle of the OD side by 14 deg, was tested with the B/M cowl to see the impact on OD shroud attachment. It shifted the attachment point substantially, to near the swirler axial location for ID-peaked inlet distortion and near the splitter for OD-peaked inlet distortion. It was near the second louver with the B/M combustor. However, there was massive OD cowl spillage and one large vortex behind the splitter, fed from the ID, for all conditions. This demonstrated that attachment and, by inference, shroud distortion can be controlled by modifying the splitter, which should assist in reducing level and variability of pattern factor. Further tests are needed to optimize the OD shroud distortion and pressure recovery for pattern factor without compromising the front end flow field.

5. Summary

Throughout this program, extremely close technical contact was maintained with both the U.S. Air Force's F100 System Project Office (SPO) and Aero Propulsion Laboratory at Wright-Patterson Air Force Base. This insured that the program benefited to the fullest from lessons learned in similar programs in the past.

The net results of this pattern factor improvement program were:

1. Identification and production incorporation of an improved fuel nozzle tip. The new nozzle reduces both average pattern factor and pattern factor variability. Average pattern factor is reduced by 25 percent to the 0.35 level. Pattern factor variability is reduced by about the same amount. These improvements were attained without compromising other aspects of combustor performance.
2. Development of improved statistical methods for analyzing engine pattern factor data without forcing the data to fit arbitrary distributions such as normal, log-normal, or Weibull.
3. Identification of aerodynamic improvements to the combustor and diffuser flowpaths.
4. Identification of and solution for a pressure-sensitive fuel spray distribution change in the extreme front end of the combustor.

The success with which F100 combustor improvements were identified and substantiated is due in no small part to the effort, throughout the course of the program, devoted to understanding the behavior of the combustor. The subscale rigs, full annular rig, and engine test programs were all planned to define, as fully as possible, the processes taking place within the combustion system. Each type of testing was checked and verified by the other tests. Each type of testing made its contribution toward understanding the performance of the F100 combustor. As a result, the entire program was remarkably free of "wasted" tests, side trips up blind alleys, and wasted time and money. Each type of testing is vitally necessary, especially engine testing. The engine is the true environment within which the combustor operates, and rig testing alone can never give a complete picture of combustor performance. At the same time, rig tests give the best opportunity to isolate and investigate specific aspects of combustor performance, and are also necessary to a successful program. As a result, significant improvements have been made to the F100 combustor within a comparatively short time and with funding levels far less than other similar engine programs.

References

1 Wassell, A. B, "Pattern Factor Analysis," *Gas Turbine Combustor Design Problems,* A. H. Lefebvre, ed., Hemisphere Publishing Corporation, 1980, pp. 113-131.

2 Draper, N. R., and H. Smith, *Applied Regression Analysis,* Copyright 1966 Wiley.

3 Neter, J., and Wasserman, W., *Applied Linear Statistical Models,* Copyright 1974 by Richard D. Irwin, Inc.

4 Beér, J. M., and Chigier, N. A., *Combustion Aerodynamics,* Halsted Press Division, Wiley, New York, 1972, pp. 100-146.

5 Ehrich, F. F., "Aerodynamic Stability of Branched Diffusers," ASME Paper No. 70-GT-27, 1970.

6 Lohmann, R. P., Gabriel, R. M, and Klein, M. L., "Diffuser/Combustor Interaction Studies in Annular Dump Diffuser/Burner Systems — Part II Effect of Dump Geometry, Inlet Distortion, Fuel Injectors and Diffuser Case Struts," Pratt & Witney Aircraft Commercial Products Division, TDM2488, 1978.

The Influence of Premixed Combustion Flame Stabilizer Geometry on Flame Stability and Emissions

N. A. Al Dabbagh

G. E. Andrews

Department of Fuel and Energy,
University of Leeds,
Leeds, LS2 9JT, England

Premixed combustion systems for gas turbines offer the possibility of low-pollution, high-combustion efficiency and good temperature distribution. They form a basis by which other well-mixed combustion systems may be assessed. The ultimate objective of this work is the development of nonpremixed rapid mixing combustion systems. Different geometries of baffle flame stabilizers are tested to study the influence of recirculation zone size and number of recirculation zones on flame stability, combustion efficiency and NO_x. The results show that the flame stabilizer geometry has a major influence on combustion efficiency and flame stability but a lesser influence on NO_x. Optimum equivalence ratios are identified for good combustion efficiency and low NO_x at simulated low and high-power engine conditions.

Introduction

For high-turbine entry temperatures and for low-calorific value fuels well mixed combustion systems are required. Burning well-mixed weak mixtures in the primary zone considerably reduces the heat flux to the combustion chamber walls and hence allows the proportion of combustion air used for wall cooling to be reduced. This allows more air to be used for combustion and this is beneficial for the design of high temperature gas turbines, especially those employing low calorific value fuels. Well-mixed combustion systems have the additional benefit of improving the combustor exit temperature distribution, which is again beneficial for future high-temperature gas turbines. Studies of premixed combustion systems form a basis on which the design of future high temperature gas turbine combustion systems may be based.

The original impetus for research into premixed combustion systems for gas turbines was the problem of NO_x emissions [1,2]. The work of Anderson [3,4] showed that low NO_x emissions and good combustion efficiency could be achieved with premixed combustion at gas turbine high power operating conditions. Subsequent practical developments [5,6] of premixed or prevaporised combustion systems have concentrated on the use of V gutter types of flame stabilizers with an upstream mixing and prevaporisation passage.

Various problems have been encountered with these premixed combustor designs.

1 The achievement of a uniform fully vaporized fuel and air mixture [7].

2 The reduction in combustion chamber length or residence time, leading to difficulties in achieving a good combustion efficiency [6].

3 Flashback into the mixing passage, particularly at high inlet temperature and transient operating conditions [8].

4 The mechanical durability of the flame stabilizers.

5 The requirement of a pilot combustion system to operate at low power conditions where the inlet temperature and fuel to air ratios are much lower than at the high-power conditions.

This latter problem has resulted in the development of "pilot" combustion systems for good combustion efficiency at low power conditions which has led to the generation of more NO_x at these conditions. If the gas turbine spends long periods at low power this can result in a substantial proportion of the total engine cycle NO_x emissions being generated at the lower power conditions if a well mixed low NO_x combustor is used at the high power conditions [5].

No information could be found relating to the performance of premixed systems at low-power conditions. It is not self evident that premixed systems at low inlet temperature should exhibit a poor combustion efficiency. The present work aims to identify the premixed primary zone air to fuel ratio required for good combustion efficiency and low NO_x at both low and high-power conditions. Achieving these optimum conditions in a practical engine will of course involve suitable dilution air injection and either fuel or air staging to attain the desired overall air to fuel ratio.

The disadvantages of premixed systems listed above are recognised and it is the ultimate objective of this work to develop nonpremixed combustion systems which incorporate

Contributed by the Gas Turbine Division and presented at the International Gas Turbine Conference and Products Show, Houston, Texas, March 9–12, 1981, of THE AMERICAN SOCIETY OF MECHANICAL ENGINEERS. Manuscript received at ASME Headquarters, December 5, 1980. Paper No. 81-GT-26.

rapid fuel and air mixing across the flame stabilizer area. The study of premixed systems is a logical starting point as optimum flame stabilizer geometries and primary zone air to fuel ratios can be determined. The data will also form a base to which various rapid mixing combustion systems can be compared. The NASA swirl module combustion system [9] is a good example of the type of mixing systems envisaged, although better flame stabilizers and fuel injection will be used.

Premixed Flame Stabilizer Design Considerations

The basic aerodynamic parameters which form the starting point of any combustion chamber design are mean or reference air velocity, combustion chamber pressure loss and combustion chamber residence time. These three parameters are interdependent, the residence time is a direct function of the available length and the mean velocity and the pressure loss is a function of mean velocity and inlet temperature. Equation (1) defines the relationship between the pressure loss ($\Delta P/P$) and the combustor inlet temperature (T) and mean velocity (u).

$$\frac{\Delta P}{P} = \frac{1}{2}\frac{u^2}{C_D{}^2}\frac{1}{RT}\left(\frac{A_1}{A_2}\right)^2 = \frac{\gamma}{2}\left(\frac{\mathrm{M}}{C_D}\frac{A_1}{A_2}\right)^2 \quad (1)$$

where C_D is the discharge coefficient defined by equation (2).

$$C_D = \dot{m} A_2^{-1} (2\rho\Delta P)^{-0.5} \quad (2)$$

Equation (1) shows that a series of tests at different temperatures but at a constant mean velocity must involve a variation in pressure loss. Thus residence time and pressure loss cannot be varied independently. It is usual in gas turbine work to test combustion chambers at a constant Mach number which ensures that the pressure loss is constant irrespective of the inlet temperature. Unfortunately, in most of the reported tests on premixed combustion systems this has not been done and tests at constant velocity and different inlet temperatures have been carried out [4,10,11]. In general scant attention has been paid to pressure loss in previous studies of premixed combustion and often the pressure loss is not given.

Flame stabilizer pressure loss governs the turbulent energy that is injected into the flow, which fixes the maximum rate of flame propagation [12] and consequently pressure loss is likely to have a direct influence on flame stability. Turbulence also influences the thickness of a premixed turbulent reaction zone [12] and thus an influence of pressure loss on combustion efficiency and NO_x emissions is possible. Very little quantitative information is available relating to the influence of pressure loss on combustor performance for either conventional or premixed combustion systems. Roffe and Venkataramani [13] have investigated the performance of various premixed combustion flame stabilizers at two values of blockage. However, the pressure losses of the stabilizers were different due to variations in the discharge coefficients for stabilizers with the same blockage. Presure loss varies between different combustion systems over the range 1–8 percent and it is known that some combustion systems will not operate satisfactorily at low-pressure loss. Many of the combustion systems in the NASA Clean Combustor Programme involve a relatively high pressure loss of approximately 5 percent [5,6]. It is the object of the work reported here to compare different flame stabilizer geometries

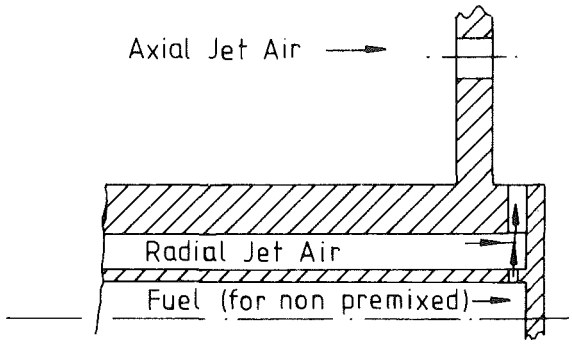

Fig. 1 Jet mix flame stabilizer

at the same pressure loss and a pressure loss of 2 percent has been chosen as this is the minimum pressure loss generally used. Some preliminary data are also given on the influence of pressure loss on flame stability and combustion efficiency.

Most conventional combustion systems, many investigations of premixed combustion [11,14,15] and most low-emission combustor designs [5,6] use flame stabilizers with large-scale recirculation zones. However, several investigations have been carried out successfully with combustion systems with a large number of small recirculation zones [9,13,16,17]. However, no systematic study of the influence of recirculation zone size on combustor performance has been carried out and this is the principal aim of this work.

As the ultimate aim of this work is the introduction of fuel at the stabilizer plane, a stabilizer has been developed involving interacting radial and axial jet mixing. By introducing fuel into the radial jet, as shown in Fig. 1, it is possible to achieve very rapid fuel and air mixing. This system was originated by Andrews and tests at elevated pressures and temperatures demonstrated low NO_x characteristics with kerosine fuel [15]. The work reported here involves a comparison of one type of this jet mixing stabilizer with the simpler grid plate designs to determine the influence of the complex jet mixing aerodynamics on the premixed combustion performance. Simple grid plates may also be adapted to introduce fuel into each hole in the plate. Flame stabilizers of this type have been shown to have very good flame stability characteristics [18] and future work in this program will establish their performance at gas turbine conditions.

Detailed Stabilizer Design

The influence of recirculation zone size was studied by utilising a flat baffle flame stabiliser and varying the number of holes for the same overall pressure loss. A 76-mm-dia cylindrical combustion chamber was used with a 76-mm-dia upstream pipe. This configuration should exhibit the pressure loss characteristics of conventional orifice plates [18,19] and the original designs were carried out on this basis. A reference Mach number of 0.0467 was chosen for the designs as this is typical of modern gas turbines and actually corresponds to that of the RB 211-524 engine. Equation (1) shows that if the grid plate discharge coefficient is known then the total flow area can be determined for the desired pressure loss of 2 percent. Standard orifice plate data [19,20] were used to determine C_D; these data are conventionally reported as

Nomenclature

A_1 = flame stabilizer and combustion chamber cross-sectional area
A_2 = stabilizer open flow area
C_D = discharge coefficient
M = upstream Mach number
$\dot{m}$ = massflow rate
R = gas constant for air
ρ = upstream gas density
γ = ratio of specific heats for air

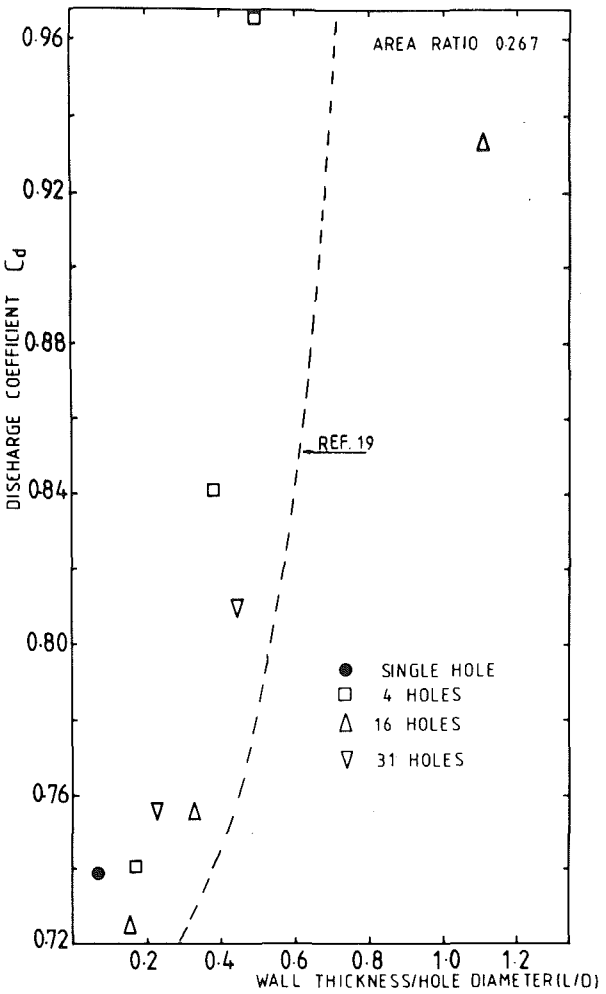

Fig. 2 Influence of grid plate geometry on the discharge coefficient

upstream dynamic head loss ($\Delta P/\frac{1}{2}\rho u^2$) which is related to $\Delta P/P$ and C_D by equations (3) and (4).

$$\frac{\Delta P}{\frac{1}{2}\rho u^2} = \frac{2}{\gamma M^2}\frac{\Delta P}{P} \tag{3}$$

$$\frac{\Delta p}{\frac{1}{2}\rho u^2} = \frac{1}{C_D{}^2}\left(\frac{A_1}{A_2}\right)^2 \tag{4}$$

Tests were carried out to determine C_D for grid plates with 1, 4, 16 and 32 holes and also a simple central baffle with three narrow supporting strips, for the same total hole area. These were carried out by metering the air flow using a venturi and monitoring the static pressure loss, from a static pressure ring 150 mm upstream of the grid plate, to atmosphere. The downstream pipe was the combustor of length 330 mm and the friction losses were negligible. The venturi pressure differences and the static pressure loss were measured using an electronic micromanometer with a resolution of better than 1 percent.

The result of these tests will be reported in detail elsewhere, but they clearly showed that conventional orifice plate data could not be applied to all grid plates. The original designs were manufactured from 3.2-mm-thick stainless steel plate and the single and four-hole designs corresponded fairly closely to the standard orifice plate data. However, the 16-hole and 32-hole plates gave drastically different values for C_D, whereas these plates with a metal thickness of 1.6 mm came much closer to the standard data. Extensive tests have shown C_D to be a complex function of A_2/A_1, hole length to diameter ratio and number of holes as shown in Fig. 2. The tests on thick plates were carried out on grid plate designs which permit fuel to be introduced into each hole, which requires a thick grid plate. Combustion tests on these devices are not reported here. Most previous work on grid plates has involved thick plates as they were water cooled [4,10,13].

No data have been published on the pressure loss characteristics of the jet mixing type of flame stabilizer. The discharge coefficient was first estimated and then the desired pressure loss was achieved by enlarging the axial holes. The geometrical details of the five baffle flame stabilizers and their discharge coefficients and pressure loss values at the reference Mach number (0.0467) are summarised in Table 1. Although the variation in pressure loss, for stabilizers A-E, is significant it is not large and is much less than that involved in testing at constant reference velocity. For the temperature range covered in this work a flame stabilizer designed for a pressure loss of 2 percent at 400 K would have a pressure loss of 3.25 percent at 650 K, as shown by equation (1). Consequently it is considered that the small pressure loss variations between the flame stabilizers A-E will not be a major cause of any combustion performance differences.

Combustion Test Equipment and Conditions

A 76-mm-dia cylindrical combustion chamber was used with a free discharge to atmosphere and then to the exhaust stack after entrainment of ambient air. The layout of the test rig is shown schematically in Fig. 3. The combustor liner was an uncooled 6.3 mm thick stainless steel tube 330 mm long and was instrumented with mineral insulated Type K thermocouples and static pressure tappings. A 76-mm-dia approach flow and fuel/air mixing pipe was mounted 1.5 m upstream. This injector consisted of 20 holes on centers of equal area across two perpendicular diameters of the pipe. Industrial propane (93 percent propane) was used as the fuel. Propane flow pressure losses of between 0.3 and 1 bar occurred across the injector, depending on the fuel flow, and this ensures a good propane distribution. An automated fuel shut down sequence with nitrogen purge was incorporated in the system to deal with any possible flame flashback or preignition. No problems of this type were encountered in the test program.

Table 1 Flame stabilizers

Stabilizer code	Type	A_2 m^2	Blockage %	Plate thickness mm	C_D	$\frac{\Delta P_{\%}}{P}$
A	1 hole	0.00157	65.6	3.2	0.804	2.01
B	4 hole	0.00158	65.6	3.2	0.818	1.94
C	16 hole	0.00158	65.5	1.6	0.781	2.14
D	Baffle	0.00158	65.4	3.2	0.727	2.41
E	Jet mix (Radial jet area 20 percent of total)	0.00169	63.0	3.2	0.777	1.88

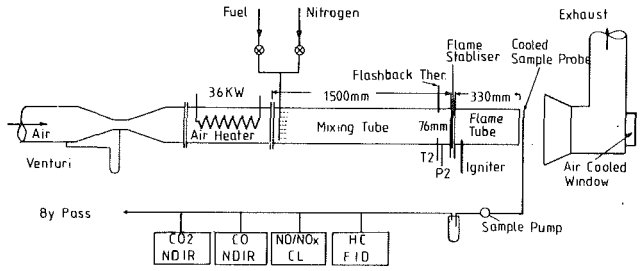

Fig. 3 Schematic of the experimental rig

The air was electrically preheated and two main test temperatures of 400 K and 650 K were used. The former was typical of low power engine operation, where combustor inlet temperatures can be as high as 480 K for modern high pressure ratio engines such as the CF6 or RB211. The 400 K value is more typical of older or smaller aero gas turbines and of current industrial gas turbines at low power. The 650 K inlet temperature was chosen as this is typical of industrial gas turbine high power operation and of aero gas turbine cruise conditions. At cruise conditions many low-pollution combustor designs have exhibited poor combustion efficiencies. Although pollutant regulations do not exist for aircraft cruise conditions the achievement of a very high combustion efficiency is essential for good fuel consumption. For industrial engines low NO_x requirements are in existence and high combustion efficiency is again essential for maximum system efficiency. Some problems were encountered in achieving a 650 K inlet in certain tests as this temperature involves the operation of the electrical heaters close to their maximum ratings.

The inlet temperatures used were measured 100 mm upstream of the flame stabilizer and correspond to engine inlet temperatures somewhat higher than the measured values as significant electrical energy is used in heating the propane to 400 K and 650 K as well as the air. Thus the corresponding engine condition will be a function of propane flow rate.

Gas samples were taken at the combustor exit plane via a water cooled stainless steel sample probe. This was of a similar form to the propane injector with 20 holes on centres of equal area in an *X* configuration. The gas sample was transported to the gas analysis equipment along a 7.6-m-long heated Teflon sample line. Considerable difficulties were encountered in analysing the NO_x and hydrocarbons with heated lines on a "wet" basis using the gas analysis system detailed in the EPA regulations [21]. An adequate (30 l/min) flow down the sample line could not be achieved with a sample pump downstream of the analysers as this reduced the sample flow to the analysers. An inline heated sample pump upstream of the instruments was required and this was not available for these tests, although one will be installed for future tests. Most of the results presented here were achieved by the use of an unheated oil free sample pump mounted upstream of the instruments but downstream of a water condenser and chemical drier. No significant difference in NO_x measurements could be detected with this system and that using heated lines and no water removal. The gas sampling instruments used are detailed in Table 2. The two NO_x meters exhibited good linearity and reasonable agreement in NO_x levels for the same calibration and sample gases.

Test Procedure

Flame ignition was achieved by the use of a 16-J high-energy ignitor mounted flush with the combustor wall 25 mm downstream of the stabilizer. No problems with ignition were encountered, although the 16-hole plate (stabilizer C) sometimes did not light on the first spark. All the five stabilizers exhibited stable flames burning well inside the combustor. A 100-mm-dia air cooled window was mounted on the combustor center line on a bend in the exhaust and the flame could be viewed directly from the control room.

Weak extinction data were obtained by establishing a stable flame close to weak extinction and then slowly reducing the fuel flow while maintaining the air flow constant. Weak extinction was observed through the exhaust window from the control room. The air flow was maintained accurately, well within 1% of the desired venturi pressure difference, by a remotely operated pneumatically controlled butterfly valve on the air blower inlet. The fuel flow was metered using rotameters with corrections for fuel temperature and pressure. The air to fuel ratio could be set and measured to an accuracy of 2 percent.

All the flame stabilisers exhibited a sudden instantaneous weak extinction which was very repeatable. None of the flame stabilisers exhibited any significant instability or fluctuations prior to the weak extinction. Some acoustically generated screeching instability was observed on certain conditions during rig light up or when changing conditions, but this disappeared once the reference Mach number had been reset. The 16-hole grid plate (C) was an exception in that the screech noise occurred for equivalence ratios richer than 0.7 at an inlet temperature of 600 K.

Once the weak extinction had been established the rig was relit and the gas analysis and wall temperature and static pressure measurements taken over a range of air to fuel ratios up to an equivalence ratio of 0.8. Some points were then obtained as the equivalence ratio was reduced. Tests at equivalence ratios above 0.8 were limited by possible damage to the flame stabilizers, particularly at high-inlet temperatures. The baffle stabilizer Type D was accidently operated at an equivalence ratio of 0.88 with an inlet temperature of 650 K and partial melting occurred which prevented further data being obtained. However all other flame stabilizers suffered no noticeable damage.

Weak Extinction Results

Influence of Recirculation Zone Size. Detailed studies of

Table 2 Gas analysis instrumentation

Component	Method	Manufacturer	Model
CO_2	NDIR	ADC	4 range digital
CO	NDIR	ADC	100 ppm – 10 percent digital
CO	NDIR	Horiba	MEXA 300
UHC	FID	Analysis Automation	523 Series 11
UHC	NDIR	Horiba	MEXA 300
NO_x	Chemilum.	TECO	12A
NO_x	Chemilum.	Grubb Parsons	Chemitox
O_2	Paramag.	Taylor Inst.	570A

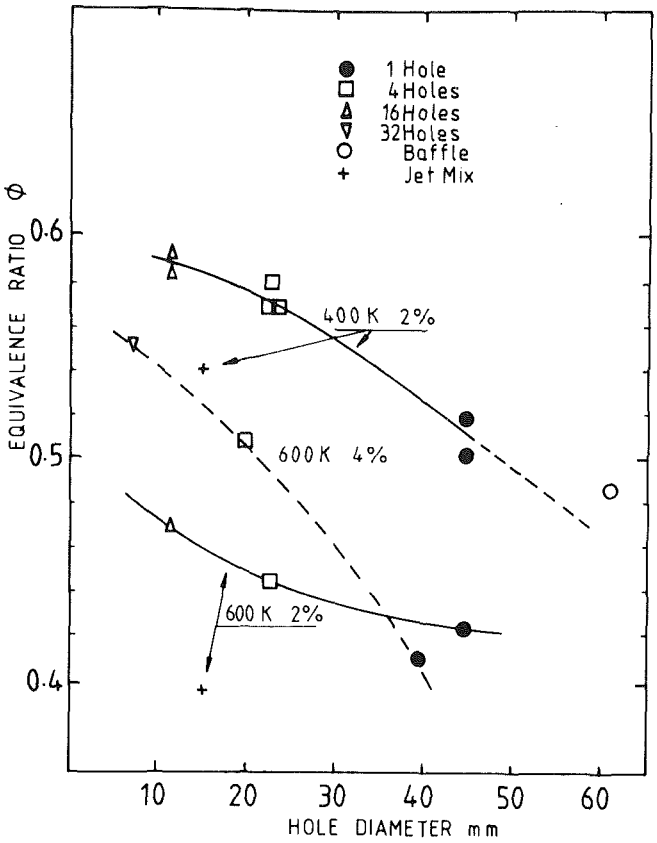

Fig. 4 Variation of weak extinction with stabiliser hole size

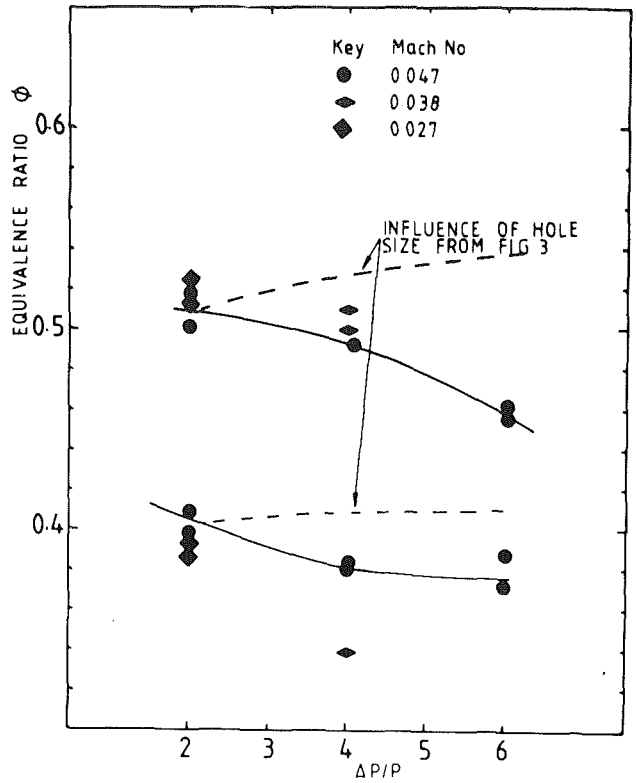

Fig. 5 Effect of stabilizer pressure loss on single-hole weak extinction

recirculation zones of disks have shown that the recirculation zone size is a function of disk diameter and blockage [21,22]. For the blockage of 65% used in this work the recirculation zone size will be very close to the disk diameter [22]. No studies of recirculation zone sizes of grid plates could be found but it is reasonable to assume that these will be a function of the hole diameter. The hole diameter is a more convenient parameter on which to base the recirculation zone size as the alternative is the web distance between holes which is a variable around the hole circumference. The varying of the number of holes in a grid plate forms a simple means of investigating the influence of recirculation zone size. The single-hole plate (A) and the baffle plate (E) give a useful comparison of the influence of recirculation direction. The central hole will give an annular recirculation zone rotating outwards and the baffle will give a central recirculation zone rotating inwards.

The weak extinction equivalence ratio (fuel flow/stoichiometric fuel flow) for stabilizers A, B and C are shown in Fig. 4 as a function of hole size for the two temperatures 400 and 600 K. The 600 K data have been interpolated from tests at different temperatures over the range 560–650 K. A significant influence of hole size on weak extinction is clearly demonstrated.

Influence of Pressure Loss. Data have been obtained at a pressure loss of 4% and an inlet temperature of 600 K on the influence of hole size and this is shown in Fig. 4. The influence of hole size is much stronger at the higher pressure loss. Figure 4 also shows that for the four and thirty two hole grid plates the weak extinction is significantly worse for the 4% pressure loss than the 2 percent. However, Fig. 5 shows the reverse is true for the single hole plates and this is in the opposite direction to the trends expected purely on the basis of the change in hole size.

Influence of Reference Mach Number. The single hole flame stabilizers all exhibited very poor combustion efficiencies. Some tests were carried out to determine the influence of residence time on combustion efficiency. The flow Mach number was changed for the 6 percent single-hole plate so that pressure losses of 4 percent (M = 0.0381) and 2 percent (M = 0.0270) could be achieved. Figure 5 shows that for the single hole plates the influence of the change in Mach number was very similar to that of pressure loss. Thus the influence of pressure loss on weak extinction appears to be more important than that of mean flow velocity.

Baffle and Jet Mix Stabilizers. The weak extinction data for these are compared with the grid plate results in Table 3.

Table 3 Weak extinction results, $\frac{\Delta P}{P}$ – 2 percent

Inlet temperature	400 K	600 K
A - 1 hole	0.51	0.43
B - 4 hole	0.57	0.45
C - 16 hole	0.59	0.47
D - Baffle	0.49	–
E - Jet mix	0.54	0.40

The data for Type D and E stabilizers is also plotted in Fig. 4 with the baffle diameter (61 mm) taken as equivalent to the hole size for Type D and the axial hole size (15 mm) for Type E. Both these flame stabilizers exhibit better weak extinction performances than any of the grid plates. The larger recirculation zone of the baffle appears to be responsible for the better weak extinction. Extrapolation of the grid plate data to the baffle size gives fair agreement with the observed weak extinction as shown in Fig. 4.

The Jet mix flame stabilizer (E) has much better weak extinction characteristics than the four and 16-hole grid plates

Table 4 Previous weak extinction data

Ref.	Combustor Dia	Hole size	No holes	Blockage	Pressure	Temp.	Weak extinction
	mm	mm		%	Bar	K	
3	102	6.0	61	75	5.5	590	0.5
13	79	7.1	37	70	10	800	0.35
13	79	5.6	37	80	10	800	0.35
13	79	63.5 Cone	1	70	10	800	0.28
13	79	70.0 Cone	1	80	10	800	0.38
13	79	21.3 Gutter	Annular	70	10	800	0.42
13	79	24.9 Gutter	Annular	80	10	800	0.35
26	76×38	6.7	18	80	1	750	<0.42
27	89	1.6	165	95	2	700	0.3

with which its design is closely comparable. The reason for this is probably connected with the influence of the radial jet on the rate of spread of the axial jet. Water flow visualization studies have been carried out into the jet mixing process using fine air bubbles as a flow tracer in a large scale single radial and axial jet mixing system. For the equivalent proportion of radial jet flow on the Type E stabilizer the rate of spread of the axial jet was found to increase markedly when the radial jet was flowing. A jet spreading angle of approximately 90 deg was observed compared with 10 deg for the axial jet with no radial jet present. This means that the combined jet entrainment rate is much greater than for a simple axial jet and that a more uniform radial velocity profile will exist. Both of these factors will aid flame stability, but the major factor is likely to be the rapid reduction in jet velocity.

Studies of the rate of mixing of the radial jet with the axial jet have been carried out using the water visualization test rig with a salt solution added to the radial jet. Mixing, monitored using the conductivity technique, was found to be very rapid and 90 percent complete within five axial hole diameters. Andrews [25] has tested a jet mix stabilizer under non-premixed conditions with kerosine as the fuel. Under conditions similar to those of the present tests the weak extinction (φ = .57) is close to that with premixed propane as shown in Fig. 4. This indicates that the jet mixing process does provide rapid fuel and air mixing with a resultant performance which approaches that of a premixed system.

Comparison with Existing Data. The variations in weak extinction shown in Figs. 4 and 5 have also been observed by Ballal and Lefebvre for conical baffles, with premixed propane-air flames [24]. The tests were mainly carried out at very low blockage and apply more to reheat systems than to gas turbine main combustors. However, the influence of baffle diameter, blockage, inlet temperature and mainstream velocity are all qualitatively the same as in the present work. For gas turbine main combustor conditions the available data are scant and are summarized in Table 4. Reference [13] provides weak extinction data for a variety of stabilizer designs at test conditions of 800 K and 10 atm pressure, with two blockage values for each design. The weak extinction was found to be approximately the same at 0.35 to 0.4 equivalence ratio irrespective of flame stabilizer geometry and blockage. This is in direct contrast with the present results where a significant influence of geometry and blockage has been identified.

All the data in Table 4 were obtained at a higher grid plate blockage than the present series of tests, this means that they were carried out at significantly higher pressure drops. All the results in Table 4 fall below those of the present study as shown in Fig. 4. Many of the results were obtained at high test pressure and the difference between the results is probably partially due to the influence of inlet pressure. This increases turbulent Reynolds numbers for the same plate pressure loss and this will permit a greater increase in flame speed, and hence improve the weak extinction [12]. The other results can be explained as mainly due to the much higher pressure losses combined with higher inlet temperatures.

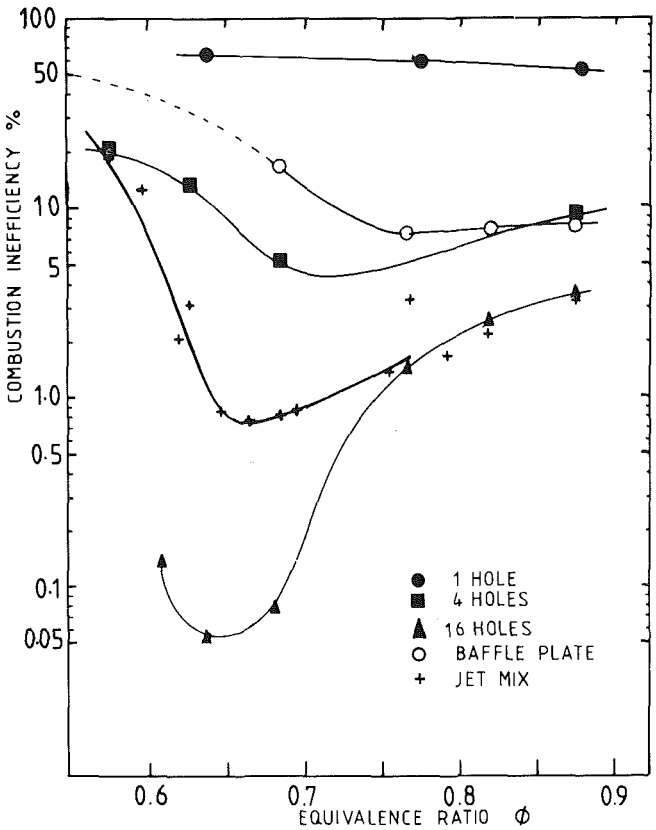

Fig. 6 Combustion inefficiency at 400 K inlet temperature

Combustion Efficiency Results

Simulated Low Power Operation - 400 K Inlet Temperature. The results are presented in Fig. 6 for all five 2 percent pressure loss stabilizers in terms of inefficiency for an inlet temperature of 400 K. Major differences in the combustion efficiency characteristics of all five flame stabilizers are demonstrated. For large recirculation zone systems the baffle flame stabilizer has a much superior combustion efficiency to the single central hole stabilizer. However, even the best combustion efficiency of 92 percent for the baffle flame stabilizer is completely inadequate. The baffle system has a

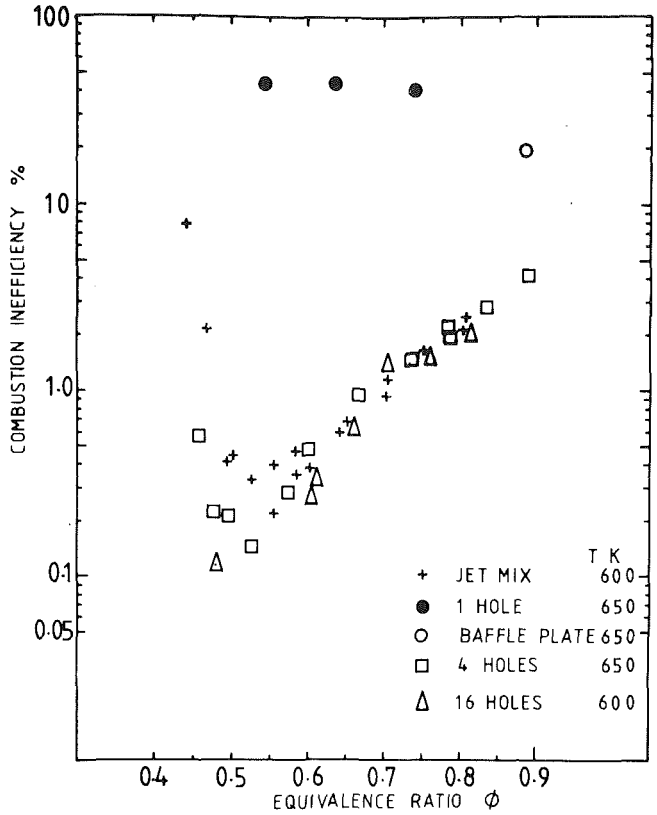

Fig. 7 Combustion inefficiency at 600-650K inlet temperature M.No. = 0.047

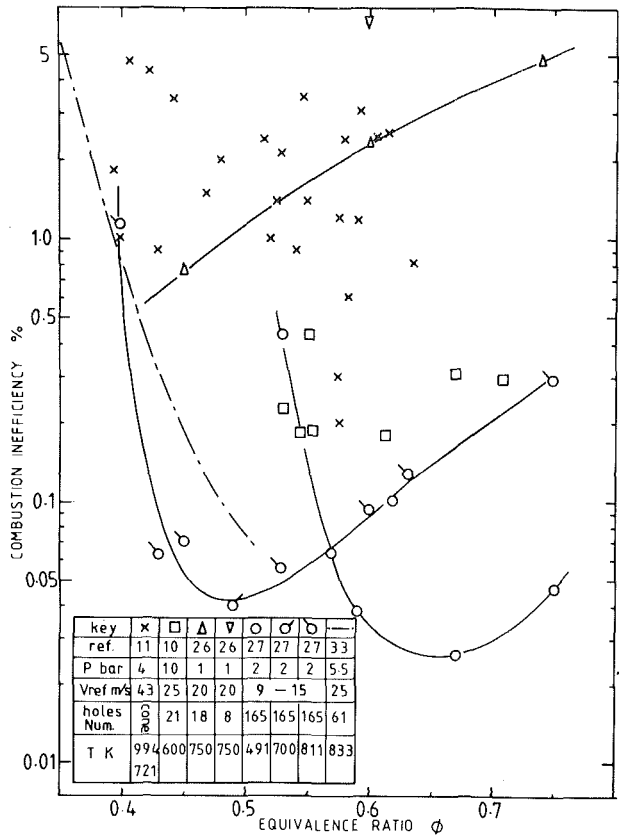

Fig. 8 Combustion inefficiency data of other workers

CO-burn-out problem for equivalence ratios richer than 0.75 and an unburnt fuel problem at weaker equivalence ratios. The single hole stabilizer has a major unburnt fuel problem with 90 percent of the combustion inefficiency arising from this source.

Modern gas turbine combustion systems need to offer combustion efficiencies much better than 99 percent at all conditions if the requirements of low-pollution and high-fuel efficiency are to be met. Although the present tests were carried out at atomospheric pressure, it is extremely unlikely that the pressure of 2–4 bar existing at engine low-power conditions will drastically improve the poor combustion efficiencies of the baffle and single hole flame stabilizers.

These test results indicate that for premixed systems large recirculation zones are not conducive to good combustion efficiency. Unfortunately many fundamental investigations of premixed combustion systems related to gas turbine applications have been carried out on large-scale recirculation systems [11,14,15]. The data of Sawyer [15] for a step stabilized flame was obtained at a maximum upstream flow Mach no. of 0.008 and a maximum stabilizer pressure loss of 0.2 percent, these conditions are well removed from those of practical gas turbines. However, the tests were carried out at inlet temperatures corresponding to low-power gas turbine operation and on this basis may be compared with the present results. The step stabilizer is similar to the baffle or single-hole stabilizers in that a large recirculation zone is involved. The test results are in qualitative agreement with the present work and demonstrate very poor combustion efficiencies which deteriorate as the flow velocity is increased.

Figure 6 shows that the combustion efficiency is significantly improved with the four-hole grid plate. The inefficiency is principally due to unburnt hydrocarbons below an equivalence ratio of 0.65 and CO becomes of increasing importance at richer mixtures. The maximum efficiency of 95 percent is still significantly below the goal of > 99 percent.

Both the Jet Mix and 16 hole grid plate exhibit much superior efficiency characteristics to all the other flame stabilizers. Both stabilizers have demonstrated combustion efficiencies greater than 99 percent at equivalence ratios of approximately 0.65. For the 16-hole plate the inefficiency is mainly due to CO and would be expected to be reduced at the higher pressures of practical gas turbines. The accuracy of the CO and hydrocarbon measurements for the 16-hole results is poor as the Mexa gas analyzer was used, which is not very sensitive at very low concentrations. The jetmix stabilizer inefficiency is mainly due to CO for equivalence ratios greater than 0.65. For weaker mixtures unburnt hydrocarbons are of increasing importance. This optimum equivalence ratio of 0.65 is also evident in the high-blockage grid plate tests of Spadaccini [27] as shown in Fig. 8.

The form of the combustion efficiency curves can partially be explained from a viewpoint of CO kinetics [28,29], with the assumption that similar arguments are likely to apply to the hydrocarbon burn out. At maximum efficiencies the inefficiency has been found to be mainly due to CO. Sheppard (28) has shown that for a perfectly mixed combustion system the CO emissions are strongly influenced by the residence time distribution. Minimum CO emissions are predicted at progressively weaker mixtures as the residence time distribution is decreased. This trend is apparent in Fig. 6. Sheppard advocates at low power conditions that for minimum CO emissions well mixed combustion at an equivalence ratio of 0.7 is required. In a later publication [29] this optimum condition is modified to an equivalence ratio of 0.65 with optimum gas temperature in the range 1600–1800° K. This prediction is in very close agreement with the best efficiency stabilizer (Type C) shown in Fig. 6.

Simulated High Power Operation - 600-650 K Inlet Temperature. The combustion efficiency data is presented in terms of inefficiency in Fig. 7 and compared with that of

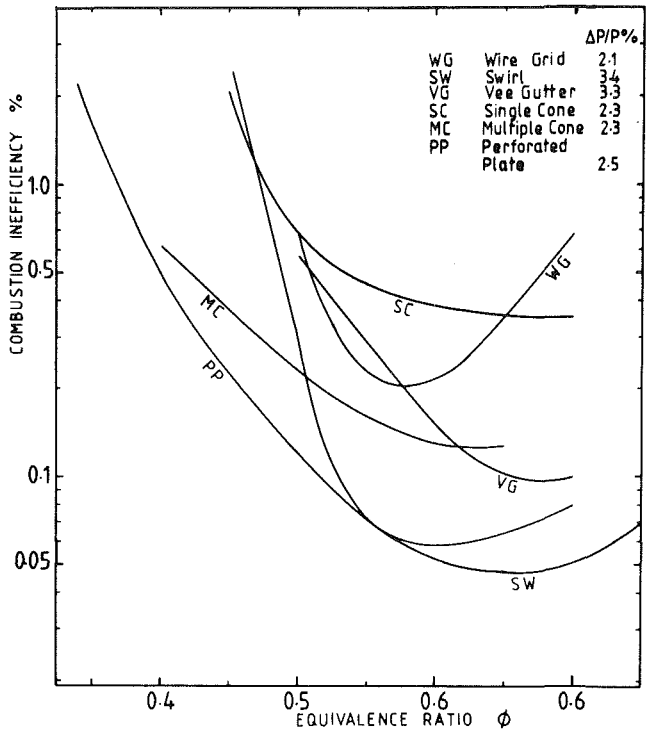

Fig. 9 Influence of geometry on combustion efficiency from reference [18] – $T = 800K$ $P = 10$ ATM $V = 25$m/s

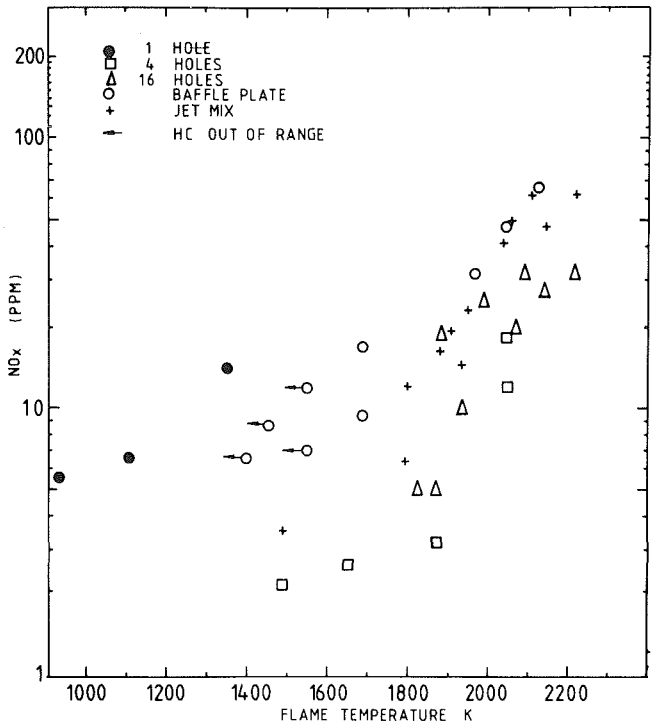

Fig. 10 NOx emissions at 400 K inlet temperature

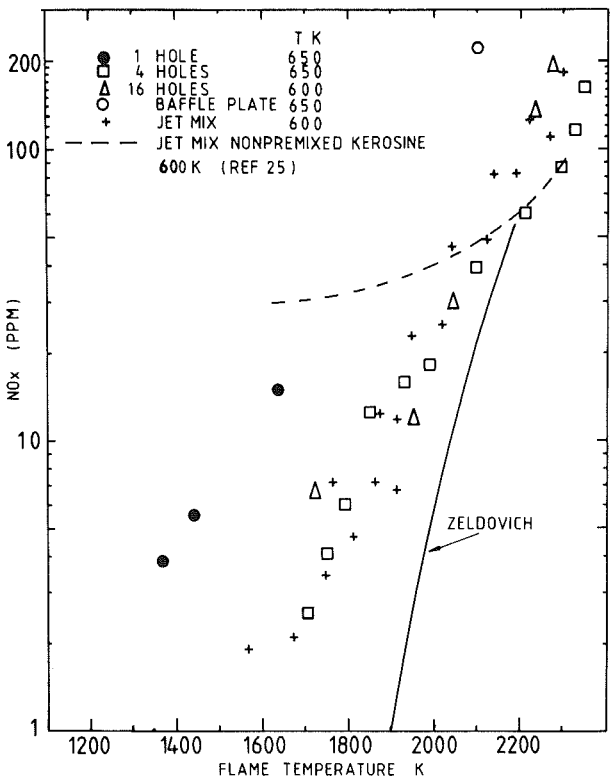

Fig. 11 NO_x emissions at 600 650 K inlet temperature M.No. = 0.047

other premixed systems in Figs. 8 and 9. The data of other workers were mainly obtained at high pressure conditions, where higher efficiencies would be expected due to higher CO burn out rates (28). The data in Fig. 7 show similar trends to those at lower inlet temperatures with improved combustion efficiencies at all equivalence ratios as expected. The optimum equivalence ratio for maximum combustion efficiency has moved to weaker mixtures with an optimum at $\varphi = 0.52$. This trend to lower optimum equivalence ratios for well mixed combustion systems at high power conditions has also been predicted by Sheppard [28] and observed by Spadacinni [27] as shown in Fig. 8.

Figures 8 and 9 show that many other premixed combustion systems have inferior combustion efficiences to those of the present tests, particularly when their higher operating pressures are taken into account. In general the phenomena observed in the present work, of a maximum combustion efficiency, and hence low CO and hydrocarbon emissions over a particular, relatively narrow band, of equivalence ratios close to 0.5-0.6, are also evident in the results of many other workers. However, this feature of the results does not appear to have been previously identified. The data of Roffe and Venkataramani [13] in Fig. 9 appear to indicate a signficant influence of flame stabilizer geometry on combustion inefficiency even at their ideal operating conditions for high efficiency, of 800 K and 10 bar.

The data of Roffe [11] using a V gutter-type of flame stabilizer show very poor combustion efficiencies. This system may be considered to involve large recirculation zones and large residence time variations, which this work has shown to be detrimental to combustion efficiency. The very high combustion efficiencies of Spadaccini [27] are likely to be due to the very high pressure loss used and the large number of small holes which are conducive to minimising residence time fluctuations. Jamieson [30] has also presented data that indicate that the combustion efficiency increases with pressure loss. Future work in this programme will involve a study of the influence of pressure loss. Preliminary work using single-hole stabilizers indicates that the combustion efficiency is decreased. This may not apply to stabilizers where the combustion inefficiency is mainly due to CO.

NO_x Emissions

The NO_x data at low and high inlet temperatures are

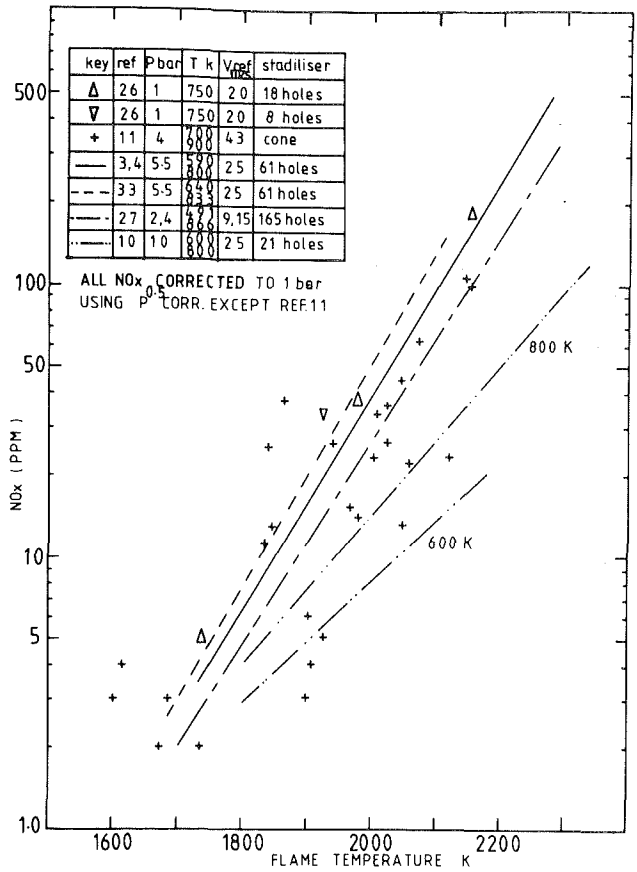

Fig. 12 NO emission measurements of other workers

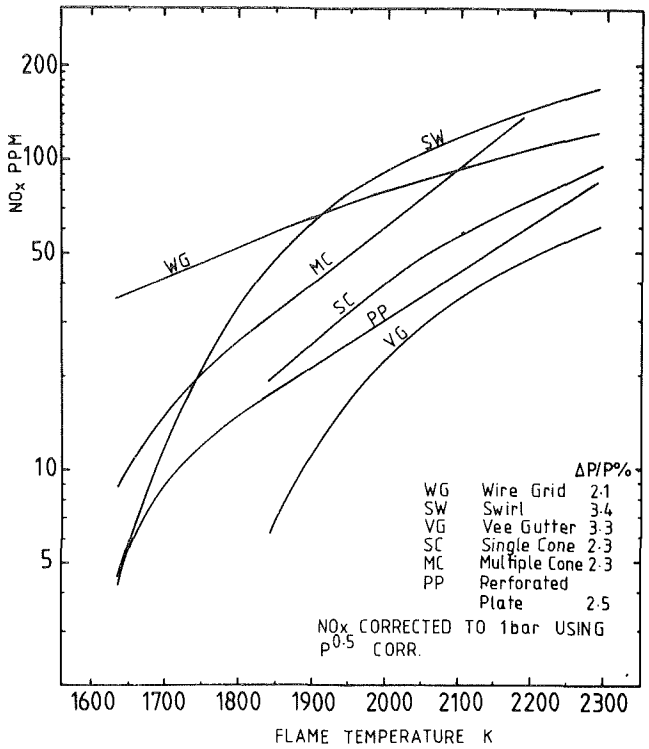

Fig. 13 Influence of geometry on NO_x emissions from reference [18] – $T = 800K$, $P = 10$ atm. $V = 25$ m/s

presented in Figs. 10 and 11, respectively, and compared with those of other workers in Figs. 12 and 13. The test data are plotted as a function of flame temperature as Zeldovich NO_x formation kinetics show that this is the major factor governing NO_x. Comparison of Figs. 10 and 11 show similar NO_x levels for the same flame temperature. The flame temperature was calculated by multiplying the adiabatic temperature rise by the combustion efficiency and then adding the inlet temperature.

Figures 10 and 11 show some differences in NO_x characteristics between the different flame stabilizers. The most important result is that the large recirculation zone systems have inferior NO_x characteristics. This would be expected from Zeldovich NO_x kinetics as the NO_x is a direct function of residence time. Large recirculation zones would give large residence times compared with systems with a large number of small holes.

However, although Zeldovich NO_x kinetics can explain the general trend of the results they cannot quantitatively predict the result as shown in Fig. 11. The Zeldovich NO_x predictions are based on the basic Zeldovich kinetics with equilibrium O atom concentration [31]. An instantaneous heat release was assumed and NO_x predicted with a residence time corresponding to the combustor length divided by the burnt gas mean velocity. At low flame temperatures the measured NO_x emissions, which are in broad agreement with those of other workers shown in Figs. 12 and 13 are significantly above the Zeldovich predictions. This conclusion is supported by the internal traverses of Semerjian and Vranos [26] who showed that NO_x was generated very quickly early in the reaction zone and Zeldovich NO_x kinetics could only explain the later slower increase in NO_x. Similar phenomena have been observed in laminar flames and partially explained by the presence of super equilibrium oxygen atoms [32]. However, at the weak mixtures and low temperature of the present work most of the explanations for his "prompt" NO are not satisfactory.

The data scatter in the results of other workers, shown in Figs. 12 and 13 is somewhat disturbing as they indicate that either the results are not very repeatable or that some of the apparently minor differences in stabilizer geometry do have an influence on NO_x. Figure 12 includes data from systems which are predominantly based on grid plate flame stabilizers with a relatively large number of holes. The range of NO_x values is approximately a three fold variation for a given flame temperature. Similarly in Fig. 13, where a range of flame stabilisers is compared the variation in NO_x emissions is large and generally the NO_x values are significantly higher than those in Fig. 12 for grid plates. Clearly the data scatter is too large for the effect of stabilizer geometry to be identified.

Although the premixed combustion systems do not exhibit the ultra low NO_x emissions that were at first anticipated [1,2] they do show substantially lower NO_x emissions than conventional systems, which exhibit NO_x levels above 100 ppm (corrected to a 1-bar test pressure) for turbine entry temperatures 1500–1600 K. Andrews [25] has shown that the jet mixing system can be operated with kerosine injected at the stabilizer to give low NO_x emissions. An example of these results, comparable with the present jet mix flame stabilizer is shown in Fig. 11. This demonstrates that although the NO_x emissions are above the premixed at low temperatures, they are sufficiently low to suggest that rapid mixing flame stabilisers offer a solution to the NO_x problem. This conclusion has been confirmed by tests at practical engine conditions [16]. The efficiency data presented here provide an indication of the optimum primary zone equivalence ratios necessary for such systems to also exhibit low CO and unburnt hydrocarbon emissions at both high and low power operating conditions.

Conclusions

The experimental premixed combustion data on the in-

fluence of flame stabilizer geometry on combustion efficiency and NO_x has identified optimum equivalence ratios for the operation of primary zones with maximum combustion efficiency. These correspond to primary zone temperatures of 1900 K at low inlet temperatures and 1800 K at high inlet temperatures. NO_x emissions at these conditions are 10 and 5 ppm, respectively, and thus the design conditions for operation of a well mixed gas turbine system with low NO_x and low CO and unburnt hydrocarbons have been identified. The flame stabilizer geometry to achieve this desired goal has been identified as a large number of small recirculation zones. Further work is necessary to understand the weak extinction phenomena at these optimum conditions are quite close to weak extinction. The extension of weak extinction limits and the possible increases in combustion efficiency arising from the use of flame stabilizers with higher pressure loss characteristics will be studied in the next phase of this programme. The weak extinction results can be qualitatively explained from a turbulent flame propagation viewpoint [12] and this will form a basis for further theoretical work.

Acknowledgments

We would like to thank the S.R.C. for support of this work, Ruston Gas Turbines for the loan of the Chemitox NO_x analyser and the Iraq Cultural Department for a scholarship to Al Dabbagh. We would also like to thank R.A. Boreham and G. Cole for the construction and operation of the experimental facility. The data in Fig. 2 was obtained by U.D. Sadick.

References

1 Ferri, A., "Reduction of NO Formation by Premixing," Paper A-1, AGARD-CP-125, 1973.

2 Lefebvre, A.H., "Pollution control in continuous combustion systems," *Fifteenth Symposium (International) on Combustion,* The Combustion Institute, Pittsburgh, 1975, pp. 1169–1179.

3 Anderson, D.N., "Effect of Premixing on Nitric Oxide Formation," NASA TMX-68220, 1973.

4 Anderson, D.N., "Effects of Equivalence Ratio and Dwell Time on Exhaust Emissions from an Experimental Premixing Prevaporizing Burner," NASA TMX-71592, 1975.

5 Gleason, G.C., Rogers, D.W., and Bahr, D.W., "Experimental Clean Combustor Program Phase II, Final Report," NASA CR-134971, 1976.

6 Roberts, R., Peduzzi, A., and Vitti, G.E., "Experimental Clean Combustor Program Phase II, Final Report," NASA CR-134969, Nov. 1976.

7 Tacina, R.R., "Degree of Vaporization Using an Air Blast Type Injector for a Premixed-Prevaporized Combustor," NASA TM-78836, 1978.

8 Plee, S.L., and Mellor, A.M., "Review of Flashback Reported in Prevaporizing/Premixing Combustors," *Combustion and Flame,* Vol. 32, 1978, pp. 193–203.

9 Niezwiecki, R.W., and Jones, R.E., "Parametric Test Results of a Swirl Can Combustor," NASA TMX-68247, June 1973.

10 Roffe, G., and Venkataramani, K.S., "Emission Measurements for a Lean Premixed Propane/Air System at Pressures up to 30 Atmospheres," NASA CR-159421, June 1978.

11 Roffe, G., "Effect of Inlet Temperature and Pressure on Emissions from a Premixing Gas Turbine Primary Zone Combustor," NASA CR-2740, Sept. 1976.

12 Andrews, G.E., Bradley, D., and Lwakabamba, S. B., "Turbulence and Turbulent Flame Propagation — A Critical Appraisal," *Combustion and Flame,* Vol. 24, 1975, pp. 285–305.

13 Roffe, G., and Venkataramani, K.S., "Experimental Study of the Effects of Flameholder Geometry on Emissions and Performance of Lean Premixed Combustors," NASA-CR-135424, 1978.

14 Schefer, R.W., and Sawyer, R.F. "Lean Premixed Recirculating Flow Combustion for Control of Oxides of Nitrogen," *Sixteenth Symposium (International) on Combustion,* The Combustion Institute, Pittsburgh, 1978, pp. 119–134.

15 Ganji, A.R., and Sawyer, R.F., "An Experimental Study of the Flow Field and Pollutant Formation in a Two-Dimensional, Premixed, Turbulent Flame," AIAA Paper No. 79-0017, Jan 1979.

16 Bunn, G.E., and Winter, J., "The Evolution of a Low-Emission Combustion System for Aircraft Engine Application," paper presented at the 1979 ASME Gas Turbine Conference, Session 22.

17 Grant, J.R., Holladay, T.E., Boenig, F.H., and Duncan, R.L., "Design and Operation of Low-NO_x Combustors with Medium Heating Value, Coal-Derived Gas," ASME Paper No. 80-GT-14.

18 Anon, "The Thermimax Burner," *Energy Digest,* Mar./Apr. 1977, pp. 40–42.

19 Engineering Sciences Data Unit, "Pressure Losses Across Perforated Plates, Orifice Plates and Cylindrical Tube Orifices in Ducts," ESDU 72010, Oct. 1974.

20 Ward-Smith, A.J. *Pressure Losses in Ducted Flows Part 4,* Butterworths, London, 1971.

21 Environmental Protection Agency, "Control of Air Pollution from Aircraft and Aircraft Engines," *Federal Register,* Part III, March 24, 1978.

22 Carmody, T., "Establishment of the Wake Behind a Disk," ASME *Journal of Basic Engineering,* Vol. 86, 1964, pp. 869–882.

23 Davies, T.W., and Beer, J.M., "Flow in the Wake of Bluff-Body Flame Stabilisers," *Thirteenth Symposium (International) on Combustion,* The Combustion Institute, Pittsburgh, 1972, pp. 631–638.

24 Ballal, D.R., and Lefebvre, A.H., "Weak Extinction Limits of Turbulent Flowing Mixtures," ASME Paper No. 78-GT-144.

25 Andrews, G.E., unpublished work, Lucas Aerospace, Burnley, U.K.

26 Semerjian, H., and Vranos, A., "NO_x Formation in Premixed Turbulent Flames," *Sixteenth Symposium (International) on Combustion,* The Combustion Institute, Pittsburgh, 1978, pp. 169–179.

27 Spadaccini, J.J., "Low Emission Combustors for Gas Turbine Power Plants," *Combustion Science and Technology,* Vol. 9, 1974, pp. 133–136.

28 Sheppard, C.G.W., "A Simple Model for Carbon Monoxide Oxidation in Gas Turbine Combustors," *Combustion Science and Technology,* Vol. 11, 1975, pp. 49–56.

29 de Chair, R.S., Sheppard, C.G.W., and Whittaker, M., "A Note on Carbon Monoxide Oxidation with Particular Reference to Gas Turbine Combustion," *Combustion Science and Technology,* Vol. 12, 1976, pp. 245–247.

30 Jamieson, J.B., "Premixed Primary Zone Studies Using a Multiple-Port Baffle," in *Combustion and Heat Transfer in Gas Turbine Systems,* ed., E.R. Norster, Pergamon, 1971, pp. 123–143.

31 Banes, B., McIntyre, R.W., and Simms, J.A., "Properties of Air and Combustion Products with Kerosine and Hydrogen Fuels," Bristol Siddeley Engines Ltd., - AGARD, 1967.

32 Heberling, P.V., "Prompt NO Measurements at High Pressures," *Sixteenth Symposium (International) on Combustion,* The Combustion Institute, Pittsburgh, 1978, pp. 159–168.

33 Marek, C.J., and Papathakos, L.C., "Exhaust Emissions from a Premixing Prevaporizing Flame Tube Using Liquid Fuel Jet A Fuel," NASA TMX-3383, Apr. 1976.

R. L. Hack
Research Assistant.

G. S. Samuelsen
Associate Professor.
Mem. ASME

Mechanical Engineering,
University of California,
Irvine, Calif.

C. C. Poon
Staff Scientist.

W. D. Bachalo
Senior Scientist.
Mem. ASME

Spectron Development Laboratories,
Costa Mesa, Calif.

An Exploratory Study of Soot Sample Integrity and Probe Perturbation in a Swirl-Stabilized Combustor

In-flame measurements of soot particulate using conventional extractive and nonintrusive optical probes are compared for a swirl-stabilized combustor. Except for large ($\sim 5\mu m$) particulate present in the extracted samples, the soot particle size compares favorably with optically measured values, and the soot particle morphology reflects that formed in gas turbine combustors. Two, nonflame sources for the large particulate are suggested by the optical data: particles formed or elongated during transport subsequent to extraction, and particles attrited from upstream carbon deposits on a solid surface. The extractive probe produces a change in the local particle number density which varies from little change to a 70-fold suppression in reacting flow and a 200-fold increase in cold seeded flow depending on the location within the combustor of the optical sampling volume, the location of the extractive probe relative to the optical sampling volume, and the combustor operating conditions.

Introduction

A primary challenge in the operation of gas turbine engines on broad specification and alternative fuels is the propensity of these fuels to form soot. Approaches under consideration to reduce this soot production include combustor modification, and the use of smoke-suppressant fuel additives. The severe economic penalties associated with retrofit make combustor modification more appropriate for new engines whereas the use of smoke-suppressant fuel additives is more appropriate for existing gas turbine engines. Implementation of either control approach first requires the experimental evidence (1) to identify the causal effects of fuel properties, additive properties, and combustor operating conditions on soot formation, and (2) to evaluate and develop models destined for turbine design.

Experimental studies in progress that address the sooting associated with alternative and broad specification fuels are oriented toward the *gross* soot emission and radiation from simple flames (e.g., [1]), well-stirred reactors (e.g., [2]), and production combustors (e.g., [3]). As the interest focuses on the mechanics of soot formation, so does the need to measure *local* properties of soot such as number density, weight concentration, and particle size distribution. Extractive probes have been and continue to be used (e.g., [3,4]) for these measurements. The use of such techniques is dictated by state-of-the-art and cost. The only viable alternatives are nonintrusive, optical methods which are in their infancy in development.

Two major questions are associated with the use of extractive probes:

- *Representativeness of Sample.* Is the extracted sample representative of the particulate at the probe entrance or do the processes of extraction, transport, and subsequent deposition of the particulate on a filter transform the morphology and number density of the soot?

- *Flow Perturbation.* Does the presence of the probe in the flow perturb the local conditions (e.g., temperature, aerodynamics, chemistry) and thereby produce a condition at the probe entrance that is different from that which occurs in the absence of the probe?

These questions are especially important in flows, such as those that occur in gas turbine combustors, where the aerodynamics includes swirl and flow reversal.

This paper presents data on both the representativeness of the sample and probe perturbation in a swirl-stabilized combustor using nonintrusive optical techniques focused at the entrance of an extractive probe. The optical techniques are on the forefront of technology for point measurements in flows dominated by strong aerodynamics. As such, optical sizing in the present case is limited to particles with diameters in excess of $0.3\mu m$. The net result is that the present results are exploratory, and not exhaustive. However, the results reveal the type of problems introduced by extractive probes, specific questions that must be raised in the interpretation of data from extractive and optical probes, and the type of experiments necessary to develop and test soot measurement methods in order to insure that the data obtained are representative of the events that occur within swirl-stabilized combustors.

Contributed by the Gas Turbine Division and presented at the International Gas Turbine Conference, Houston, Texas, March 8-12, 1981, of THE AMERICAN SOCIETY OF MECHANICAL ENGINEERS. Manuscript received at ASME Headquarters, December 5, 1980. Paper No. 81-GT-27.

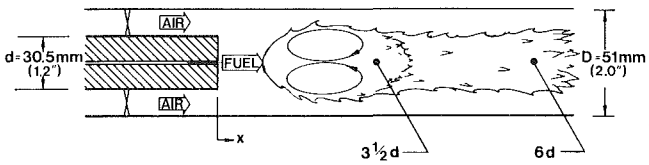

Fig. 1 Combustor configuration

Experiment

Combustor Configuration. The combustor configuration is presented in Fig. 1. The combustor housing is 51mm (2 in.) o.d. quartz tubing. The internal centerbody and annular air jet swirl provide a stabilized recirculating flow concentrated in the center of the combustor. The fuel is introduced through a central jet with a 1.3mm (0.052 in.) diameter. The angle of swirl is 60 deg and the blades are located 57mm (2¼ ins.) upstream of the centerbody face. The principal criteria for the selection of this combustor design were the inclusion of complex (i.e., turbulent, reverse flow) aerodynamics and optical accessibility.

Test Conditions. The test conditions are itemized in Table 1. The range of reference velocities was selected to (1) be representative of those produced in practical combustors, (2) span a range of operating conditions, and (3) bracket effects observed in the probe perturbation studies. The mixture ratios were selected to (1) be representative of those in practical combustors, and (2) in the case of $\phi = 0.37$, produce conditions suitable for good optical measurements. Finally, the sampling locations were selected to represent a point in the wake of the zone of recirculation, and within the zone of recirculation.

The combustor was operated on gaseous ethylene.

Table 1 Test conditions

Reference velocity[1] U_{ref} (m/s)	Overall equivalence ratio[2] ϕ	Sampling location[3] (x/d)
0.65	0.2	6
5.5	0.2, 0.37	6, 3½
7.5	0.2, 0.37	6
15.0	0.2	6

1. cold flow velocity referenced to duct diameter, 51mm (2 in.)
2. actual overall fuel-to-air ratio divided by stoichiometric ratio
3. x,d: Refer to Fig. 1

Extractive Probe. The probe and sample systems used in this study (Fig. 2) are of conventional design. The probe is constructed of stainless steel throughout with a 9.5mm (3/8 in.) outside diameter and a 3.0mm (1/8 in.) i.d. sampling tube. The overall length of the probe is 914mm (36 in.) including a large radius bend in order to clear the combustor exhaust stream. The probe is water cooled to approximately 80°C and has isokinetic pressure ports, a gas sampling port for gas analysis, and an inert gas injection port. The purpose of the latter is to dilute the mixture, quench reactions, and prevent deposition along the walls.

The remainder of the system consists of a heated sample line to prevent condensation leading from the probe to an oven. The oven, heated to 80°C, contains a two stage filter utilizing 47mm Nuclepore membrane filters: 5μm pore size for the primary filter and 0.2μm pore size for the secondary. Nuclepore filters were chosen for their adaptability to scanning electron microscopy (SEM).

Sample analysis proceeded by drying and cooling the filters in an oven and a desiccator, respectively. Sample times were 10 minutes. Size analysis and physical characterization of the particles were conducted utilizing a scanning electron microscope.

The 9.5mm (3/8 in.) probe diameter is the smallest reasonable size to incorporate the necessary ports and provide clearance for sample transport. As a result, the probe to combustor duct diameter is large (3/8 in. to 2 in.). However, this proved beneficial in the present study by enabling the demonstration of blockage. In particular, combustor operating conditions were established for which blockage by the extractive probe dominated the results, and conditions were identified for which blockage did not influence the results.

Optical Probe. Figure 3 provides a schematic diagram of the dual range optical probe. Two techniques, scattering intensity ratioing [5] and particle sizing interferometry [6], are used. For the configuration employed, the scattering intensity ratioing is sensitive to particles in the size range of 0.3 to 1.8μm. The particle sizing interferometry is sensitive to particles in the size range of 2 to 7.5μm.

An argon-ion laser operating in multiline mode serves as the light source for the system. The laser lines are separated with the use of a disperion prism and the two dominant lines, 0.5145μm (green) and 0.4880μm (blue), are directed through separate optical paths.

For scattering intensity ratioing, the blue beam is expanded by a factor of 3.5 to produce the required beam diameter. Because the small particles are typically more numerous and scatter less light, and beam must be focused to the minimum possible diameter which, for the present case, is approximately 50μm.

The beam (green) used for particle sizing interferometry is partitioned into two equal intensity beams with a path-matched beamsplitter. A mirror system is then used to recombine and focus the two beams at a common point in the flow field. Where the green beams cross, an interference fringe pattern of spatially varying light intensity is formed. Superimposed on this is the highly focused blue beam for the scattering intensity ratioing technique.

Light scattered by particles passing through the focused beams is collected by a system of lenses. The scattered light from each of the two wavelengths, 0.5145μm and 0.4880μm, is separated and directed to the appropriate photodetectors. Half of the scattered light is viewed by PMT-3 for interferometric processing. The other half passes through a system of masks which consists of annular ring openings in order to admit the scattered light at only the two scattering angles used. These masks also serve to effectively limit the length of the measurement region. The two photodetectors, PMT-1 and PMT-2, in turn transform these angularly selected rays into electronic signals which are then processed for validation and graphical display.

The interpretation of measurements using these two techniques is based on the analysis of the Mie scattering properties of a homogeneous, isotropic spherical particle. In order to apply these two techniques with confidence, the effects caused by nonspherical scatterers with an uncertain index of refraction require special considerations. For nonspherical scatterers, Hodkinson [7] showed that the forward scatter for a polydisperse system of irregular particles was similar to that of spherical particles of equivalent projected cross-sectional area. Hirleman [5] investigated the scatter from irregularly-shaped particles formed by agglomerated polystyrene spheres and found that the scattering patterns had forward lobes that appeared similar to those of spheres of equivalent diameter. In terms of the intensity ratioing technique, Hirleman also computed the scatter for particles of short aspect ratios and found that the

maximum error due to nonspherical particles was about 40 percent.

The effect due to an uncertain index of refraction was inspected in detail by both Chu and Robinson [8] and Hirleman [5]. Their findings show that, for absorbing particles (as is the case with soot particles), the errror due to an uncertainty in the index of refraction is very small (typically several percent). However, for the nonabsorbing particles, as is the case in the cold flow conditions described below, the error in both techniques can be as much as 25 percent, depending on the actual size of the particles.

Another effect, common to both techniques, which will cause additional error is due to the depth of field. In both techniques, an out-of-focus particle will generally infer a size larger than the sphere of equivalent cross-sectional area from the observed scattered light. Hirleman [5] dealt with this problem and provided solutions. However, in the present situation, out-of-focus particles could not be conveniently optically discriminated using his method. Therefore, the depth of field effect results in a broadening of the size distribution, especially in the large size end. The error in size produced by this effect is less than 30 percent.

In this study, two kinds of sizing conditions were encountered. The first was the cold flow conditions which, as will be seen below, consisted of sizing specified-size particles. Since these particles were nonabsorbing and appeared to be spherical, the combined error according to the above analysis would be 20-30 percent with some broadening of the distribution. The second was the hot flow conditions where soot particles were measured. These particles were expected to be nonspherical but should be absorbing. The combined error would then be 20-30 percent with some broadening of the distribution.

To evaluate the performance of the optical probe, size measurements using specified-size particles were first conducted under cold flow conditions. Two specified-size spherical polystyrene particles were used: 3.3μm (0.12μm SD) and 0.48μm (0.0018μm SD) (Dow Diagnostics, Indianapolis, IN). These two sizes were selected so that each of the two optical sizing techniques could be tested. The test particles were obtained by diluting 300 times the original particle/water mixture using double-filtered (0.2μm filter paper) deionized water. Seeding of these particles was accomplished using a nebulizer located 2m upstream of the centerbody. At this location, it was experimentally determined that pure water droplets produced by the nebulizer would completely evaporate.

To observe the 3.3μm diameter particles, particle sizing interferometry was used. A fringe spacing of 7μm was established thus making the instrument sensitive to particles between 2 to 7.5μm. Measurements were obtained at three axial locations downstream of the centerbody and at a number of flow conditions. Measured mean diameters ranged from 3 to 4μm with a standard deviation near 1μm and a most probable diameter ranging from 2.8 to 3.4μm. Figure 4(*a*) shows measurements obtained at an axial station 6*d* downstream of the centerbody (where *d* is the diameter of the centerbody) resulting in a mean diameter of 3.4μm, a standard deviation of 1.0μm, and a most probable diameter of 3.3μm. The large mean diameter and standard deviation can be accounted for by the broad tail on the large diameter side of the distribution. This tail was determined to be excessively broad for monodispersed particles even though the test

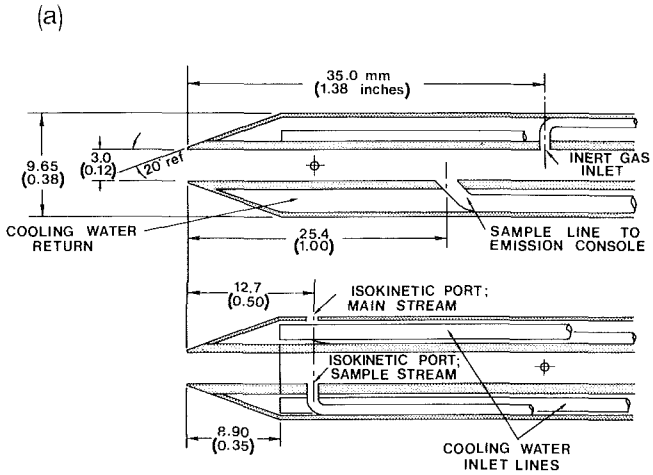

Fig. 2(*a*) Extractive Probe

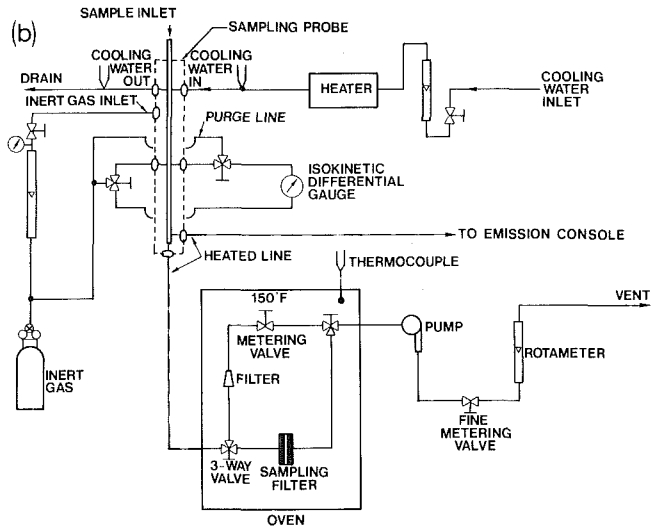

Fig. 2(*b*) Sampling System

Fig. 2 Extractive probe and sampling system

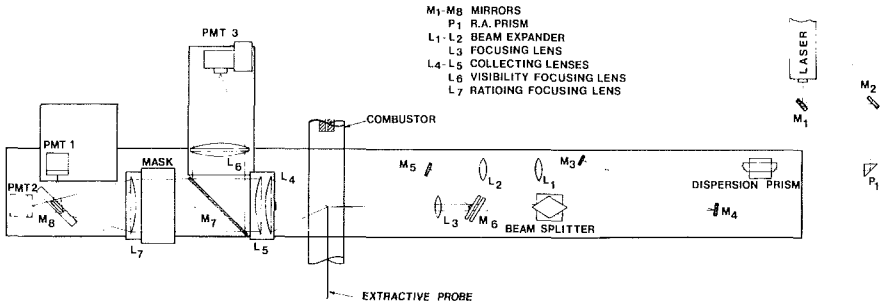

Fig. 3 Optical probe

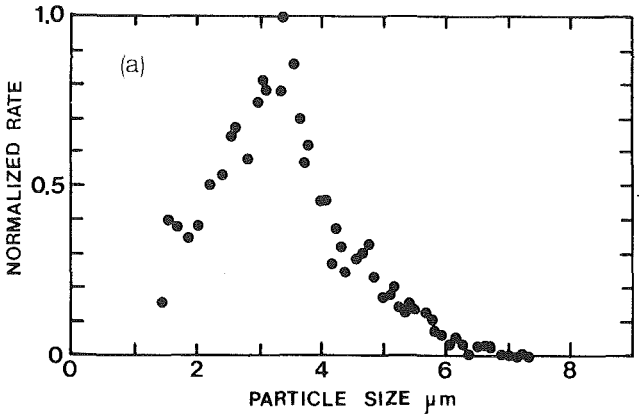

Fig. 4(*a*) Interferometric data (3.3μm particles)

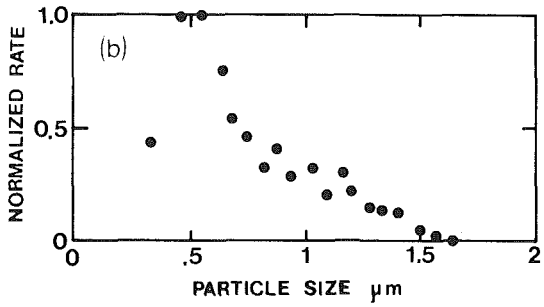

Fig. 4(*b*) Ratioing data (0.48μm particles)

Fig. 4 Optical probe validation – nonreacting flow with seeding (U_{ref} = 7.5mps)

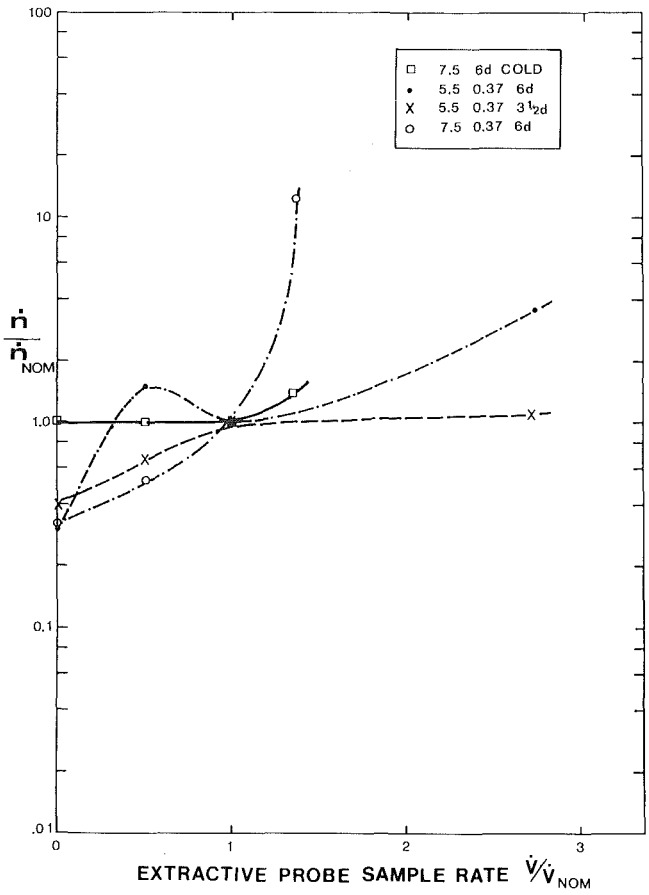

Fig. 5 Extractive probe conditions – effect of sampling flowrate on optically measured data rate

particles were nonabsorbing. Thus the broadening was suspected to be due to effects other than nonspherical particles or an uncertain index of refraction as mentioned before. Probable causes for the broad tail were: finite optical depth of field, particle agglomeration, and the liquid emulsifier (present with the seed particles and with a low vapor pressure) which forms a polydispersed distribution of droplets. Parallel studies of these particles using SEM authenticated the mean size to be 3.3μm with a standard deviation of $\sim$0.2μm.

A similar cold flow study was conducted utilizing 0.48μm diameter particles and the scattering intensity ratioing technique. The two scattering angles selected were 6 and 12 deg, thus making the instrument sensitive to particles between 0.3 and 1.8μm. Figure 4(*b*) shows measurements obtained at an axial station 6d downstream of the centerbody. These measurements were analyzed with the assumption that the most probable diameter of the particles was 0.48μm, thus the study served as a calibration of the instrument. Subsequent SEM studies revealed that these particles had a mean diameter of 0.50μm and a standard deviation of $\lesssim$ 0.05μm. The size distribution measured optically has a broad tail (Fig. 4(*b*)) with a standard deviation of 0.29μm. Again, the finite optical depth of field, particle agglomeration, and the presence of the emulsifier were probably responsible for this effect. Simultaneous sizing measurements employing both techniques during this cold flow condition showed that micron size particles were indeed present, thus providing evidence for the existence of large particles and the occurrence of the broad tail. In soot particle sizing measurements, the size broadening effect would not be significant.

Approach

The approach adopted was to position the optical probe at the entrance of the extractive probe for each of the conditions listed in Table 1. First, the conditions of the extractive probe were varied (Table 2) to change the rate of cooling and dilution experienced by the sample. Simultaneously, optical data were obtained to record the impact on the data rate (i.e., local number density) and particle size distribution within the limits of the optical methods (0.3μm to 7.5μm).

Secondly, the position of the extractive probe was changed relative to the optical probe to assess the perturbation produced by the extractive probe. Beginning at the nominal sampling location, the extractive probe was removed axially in incremental steps while the optical probe remained at the original centerline location. The impact of the probe location on the optical probe measurements was recorded in terms of data rate and particle size distribution. In addition, radial

Table 2 Extractive probe conditions

Reference Velocity, U_{ref}[1] (m/s)	Sample flow rate				N_2 Dilution		
	Nominal[2] (cc/min)	High[3] (cc/min)	< Nominal (cc/min)	Zero (cc/min)	Nominal[4] (cc/min)	< Nominal (cc/min)	Zero (cc/min)
0.65	1700	–[5]	–	–	1200	–	–
5.5	3000	8200	1000	–	530	350	0
7.5	7000	9400	3000	0	2100	950	0
15.0	7300	9400	3100	–	1800	–	0

1. Refer to footnote 1, Table 1
2. Flowrate with isokinetic pressure taps balanced
3. Maximum flowrate that can be achieved
4. Rate established to prevent water condensation for all overall ethylene equivalence ratio of 0.30
5. Runs not conducted

profiles of data rate and particle size distribution were obtained optically with and without the extractive probe in the flame.

The results are presented for the *extractive probe conditions* (Figs. 5-9) and *extractive probe perturbation* (Figs. 10-13), respectively.

Results

A. Extractive Probe Conditions

1. Nonreacting Flow With Seeding. The extractive probe conditions were first tested for the case of nonreacting flow by seeding with 0.48μm polystyrene spheres and recording the effect of sample flow rate on the optically measured data rate at the extractive probe entrance. For a 7.5mps reference velocity, the data rate increased 40 percent at the maximum sample rate (Fig. 5), consistent with theories relating to nonisokinetic effects; namely, the higher flow rate promotes the radial convection of small particles into the sampling volume.

2 Reacting Flow.

Extractive Filter Samples. The extractive probe sampling conditions had a significant impact on soot morphology and number density. As discussed later, the sampling conditions had a relatively small impact on particle size in the range observed optically.

One of two morphologies were observed on the primary (5.0μm pore) filters depending on sample condition: Platelet-like structures (Fig. 6(*a*)) and tightly-packed puff-like structures (Fig. 6(*b*)).

The puff-like structures occurred for higher overall sample transport temperatures and lower cooling rates. For example, the puff-like structures occurred on the primary filter when the N_2 dilution was reduced (Fig. 6(*b*)), when the sample rate was increased, or when the equivalence ratio was increased (Fig. 7). As shown in Fig. 6, this behavior was observed whether the reference velocity was 15mps or 0.65mps.

When small particles were observed, the morphology of the particles on the secondary (0.2μm pore) filter was similar (Fig. 6) to the puff-like structures noted above. In particular, they appeared as 0.5 to 1μm agglomerates of smaller (~.05μm) spherical particles which is consistent with the morphology and size observed in full-scale combustor studies (e.g., [10,11]). The peak size increased as the mixture ratio was enriched (Fig. 7), and as the sampling location was moved closer to the centerbody (3½*d* compared to 6*d*). The number density of particles on the secondary filter also increased sharply as the mixture ratio was enriched (Fig. 7) and as the reference velocity was increased (Fig. 6(*a*)).

At the enriched conditions (ϕ = 0.37), a hybrid of the puff-like structure was observed on the primary filter with zero nitrogen flow (Fig. 8). The sample morphology was akin to a dried mud flat. This is attributed to water condensation on the filter during sampling and subsequent drying of the filter in a desiccator. The water condensation occurred as a result of the sample temperature dropping below the dew point temperature of the mixture, the latter of which was unusually high because of the high concentration of water associated with the high concentration of fuel along the centerline of the combustor.

The addition of nitrogen as a diluent is one approach that can be employed to lower the dew point. The impact of this is shown on the primary filter in Figure 7(*b*). The puff-like structure is clearly discernable though evidence of some moisture remains.

Optical Measurements. The extractive probe results raise two questions typical of extractive probe samples (1) Are the large particles (~5μm) on the primary filter present at the probe entrance, and (2) are the smaller particles observed on the secondary filter present at the probe entrance in the agglomerated size (~1μm) or in the smaller size cut (~.05μm) of the individual particles that make up the agglomerates?

Interferometric Measurements (2-7.5μm). The interferometric size measurement verified that large particles were in fact present at the probe entrance at the enriched conditions (ϕ = 0.37). For example, at 7.5mps, the interferometric measurements (Fig. 9(*a*)) indicate the presence of large particles with a peak size of ~4μm. At this condition, approximately 10 particles per second were observed through the optical probe volume while the SEM picture has approximately 90 particles in the field of view. After adjusting these two values to the same basis, the extractive probe sample had a rate of deposition an order of magnitude higher than the data rate observed optically at the probe entrance. This provides evidence that the 5μm puff-like structures are formed after entering the probe. Further evidence is provided by the optical measurements at ϕ = 0.2 at which no interferometric signals were recorded, yet large puff-like structures (Fig. 6(*b*)) or platelet-like structures (Fig. 6(*a*)) were deposited on the primary filter.

The mechanics of the large particle formation in the sampling system is not firmly established. The present explanation holds to the scenario that the mixture at the sampling volume is comprised of soot particulate formed well upstream (and subsequently deposited on the secondary filter) and fuel undergoing pyrolysis. This fuel is cooled upon entry into the extractive probe. Rapid cooling leads to the platelet-like structures. Less rapid cooling promotes the formation of

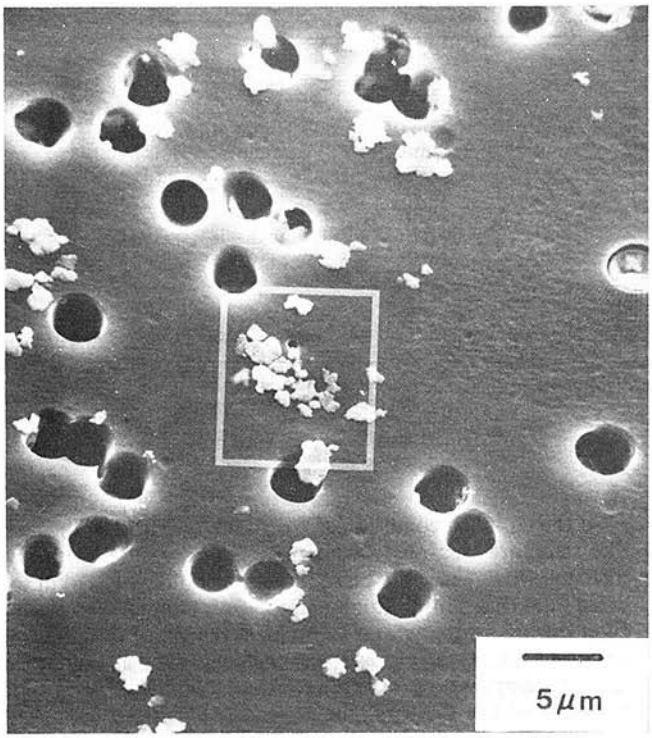

Primary filter – 5μm pore. 0.65 mps

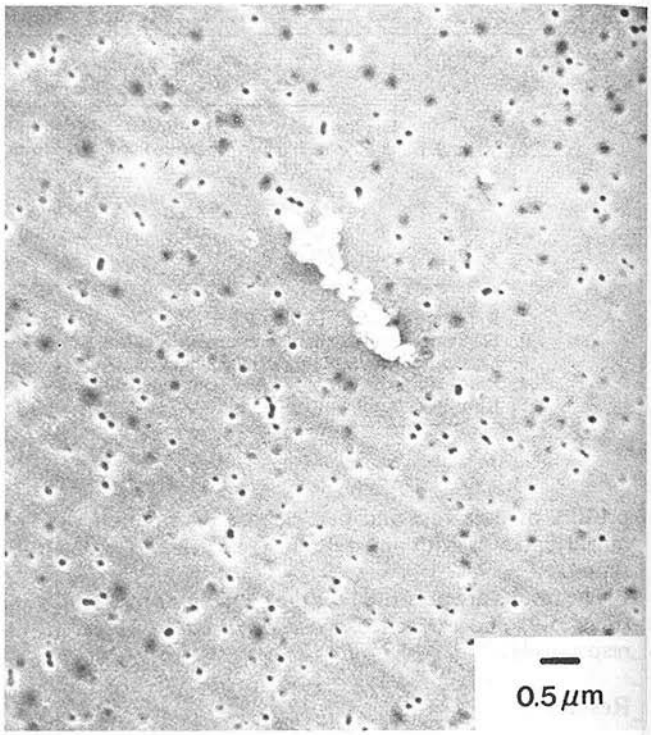

Secondary filter – 0.2μm pore. 0.65 mps

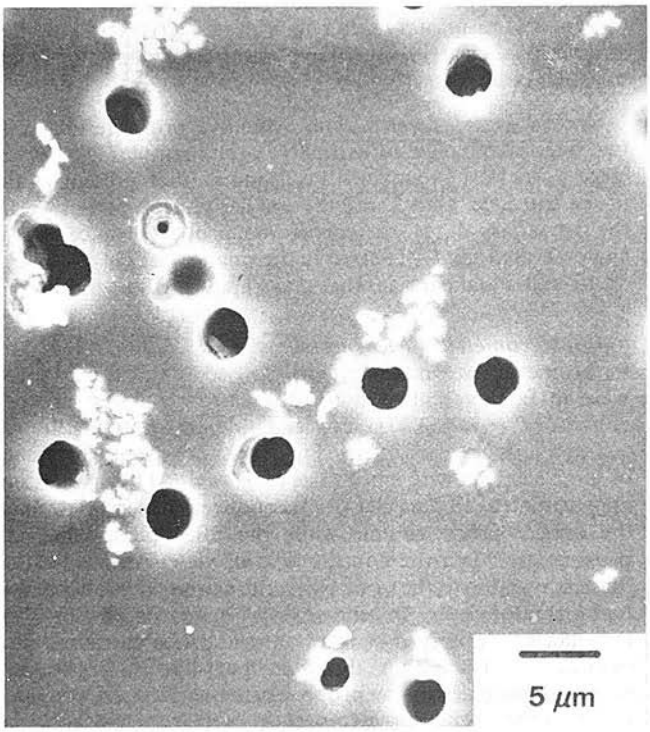

Primary filter – 5μm pore. 15.0 mps

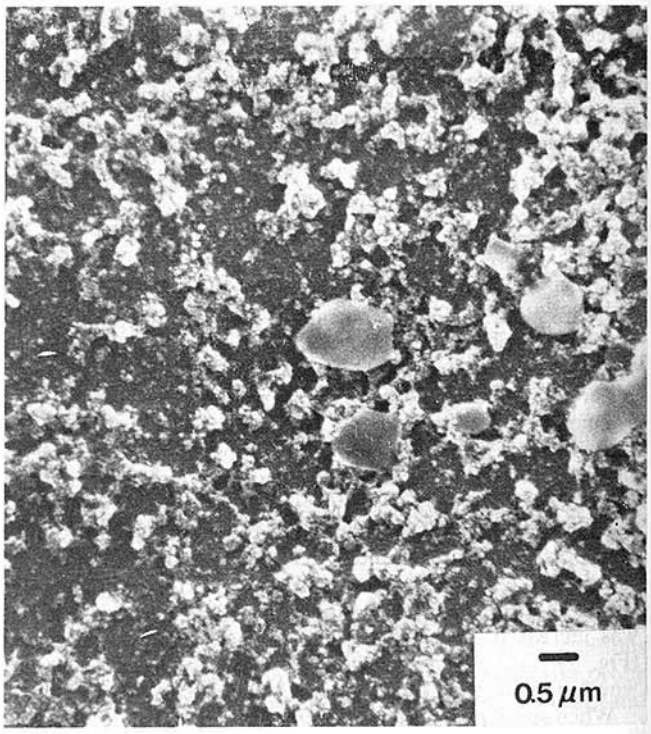

Secondary filter – 0.2μm pore. 15.0 mps

Fig. 6(*a*) Extractive probe conditions – effect of nitrogen dilution on particle morphology ($\phi = 0.2$) nominal nitrogen dilution flow

long chains of aggregated spheriods. Some of the chain structures become sufficiently long to deposit across a 5μm pore of the primary filter. This is then followed by a buildup of soot agglomerate within and finally over the clogged pore. As the resistance to flow through the pore increases, the deposition rate decreases and finally terminates, leaving a puff-like structure with a diameter close to the pore diameter (~5μm). Figure 7(*b*) provides supporting evidence since the puff-like structures are essentially monodispersed and few filter holes are visible.

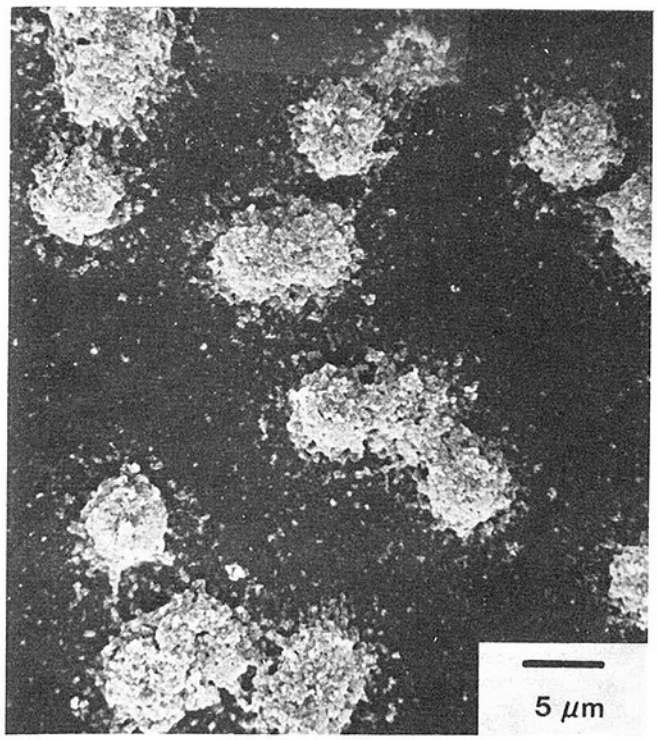

Primary Filter – 5μm pore. 0.65 mps

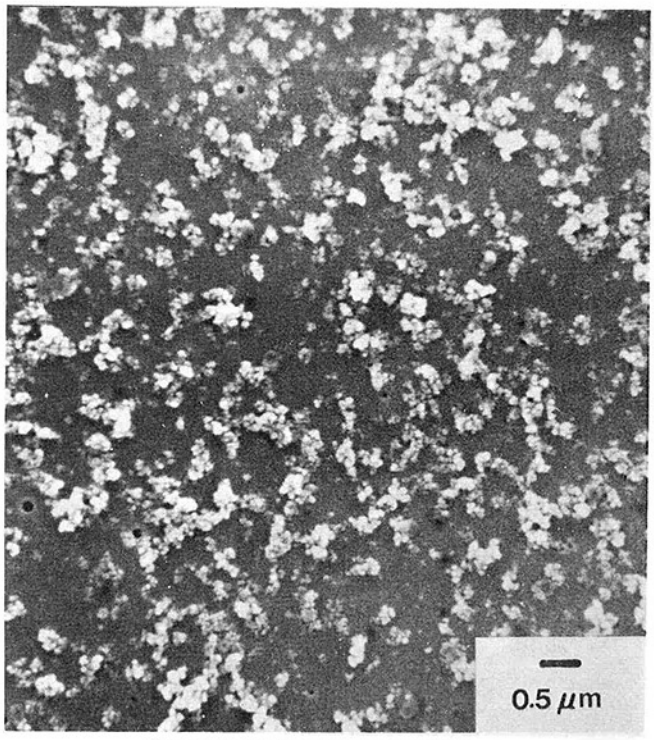

Secondary Filter – 0.2μm pore. 0.65 mps

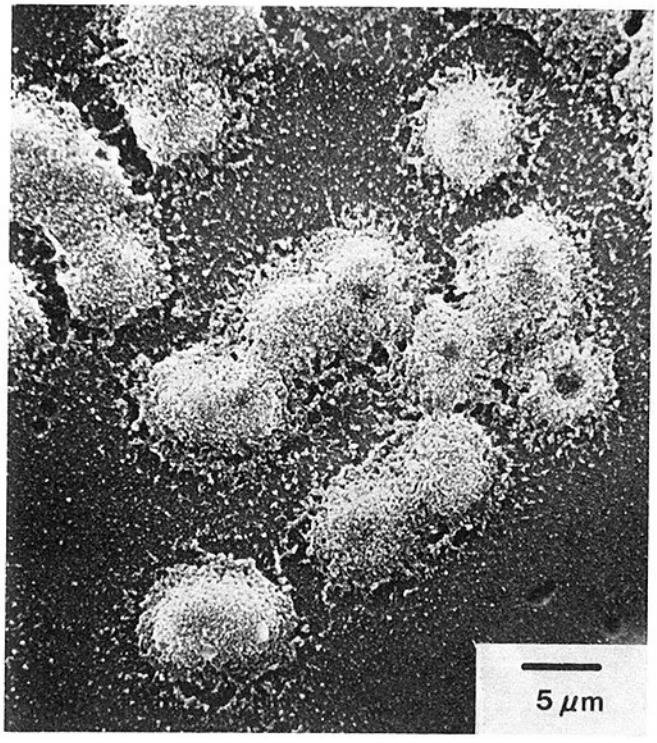

Primary Filter – 5μm pore. 15.0 mps

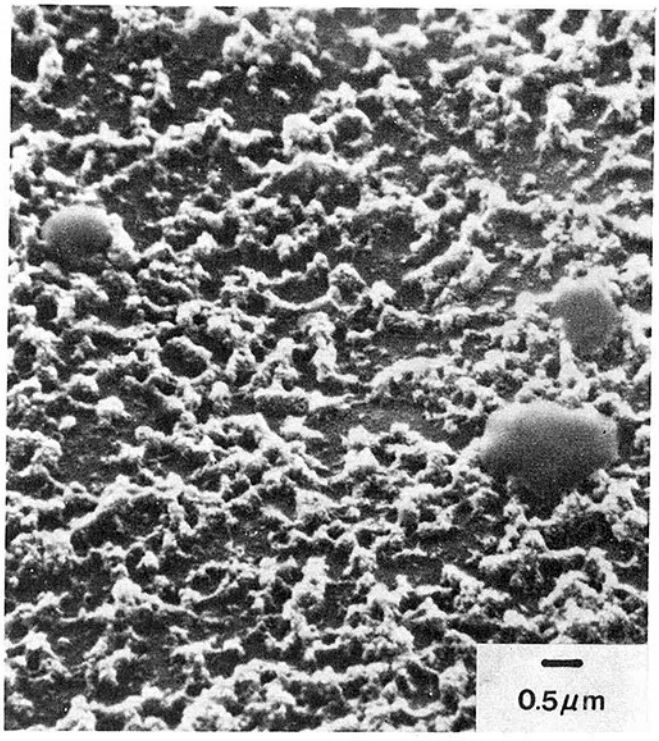

Secondary Filter – 0.2μm pore. 15.0 mps

Fig. 6(*b*) Extractive probe conditions – effect of nitrogen dilution of particle morphology ($\phi = 0.2$) zero nitrogen dilution flow

The $\sim 4\mu m$ particles detected optically at the probe entrance for the enriched ($\phi = 0.37$) condition were suspected of originating from a non-flame source. The measured size distribution (Fig. 9(*a*)) sported a peak size ($\sim 4\mu m$) whereas a monotonically increasing number density as size is reduced would have been anticipated. In the present case, the attrition of deposits off the centerbody was suspected. As a result, an evaluation was conducted during which the interferometric

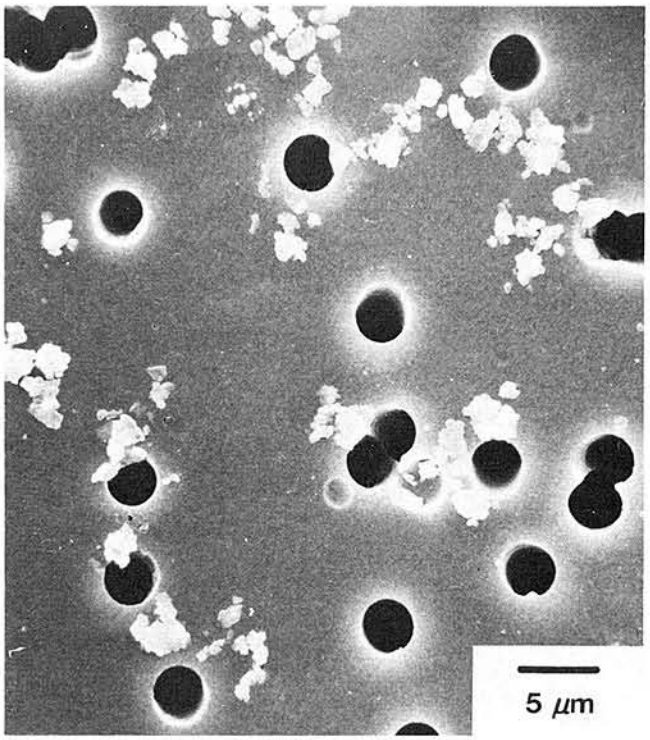

Primary filter-5μm pore

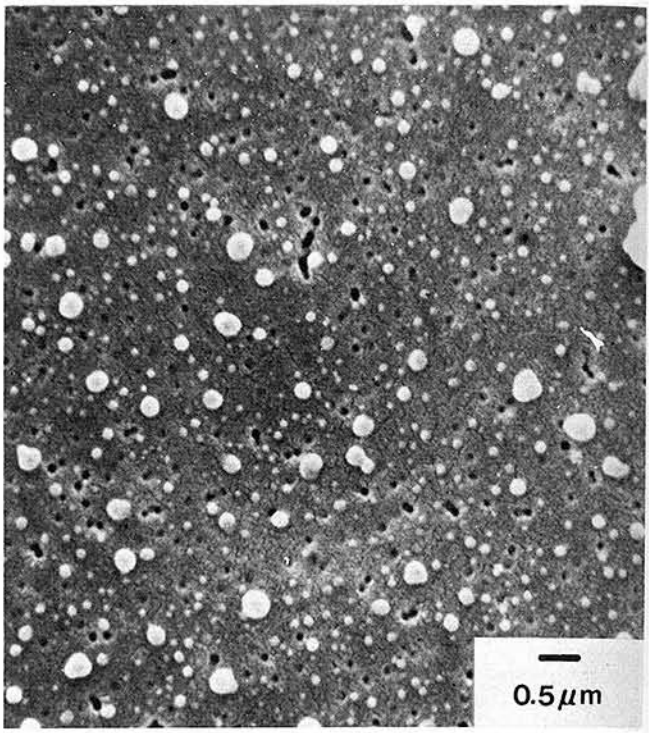

Secondary filter-0.2 μm pore

Fig. 7(a) $\phi = 0.2$

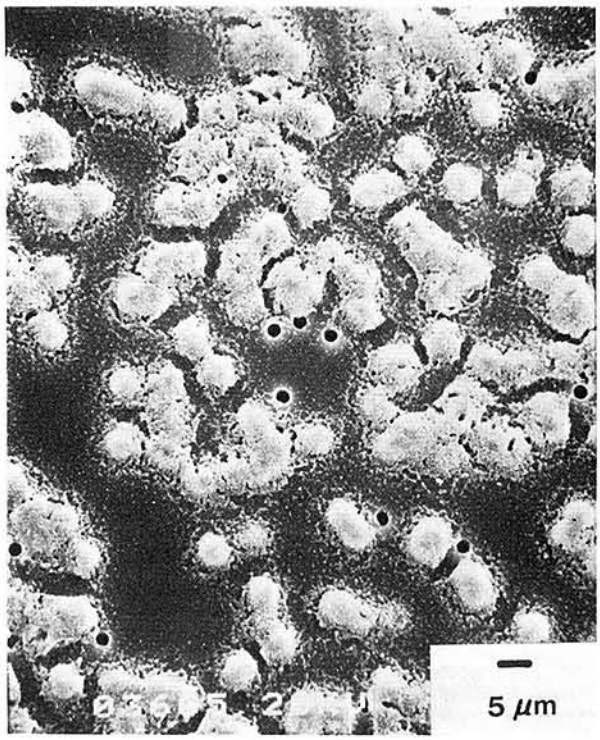

Secondary filter-0.2 μm pore

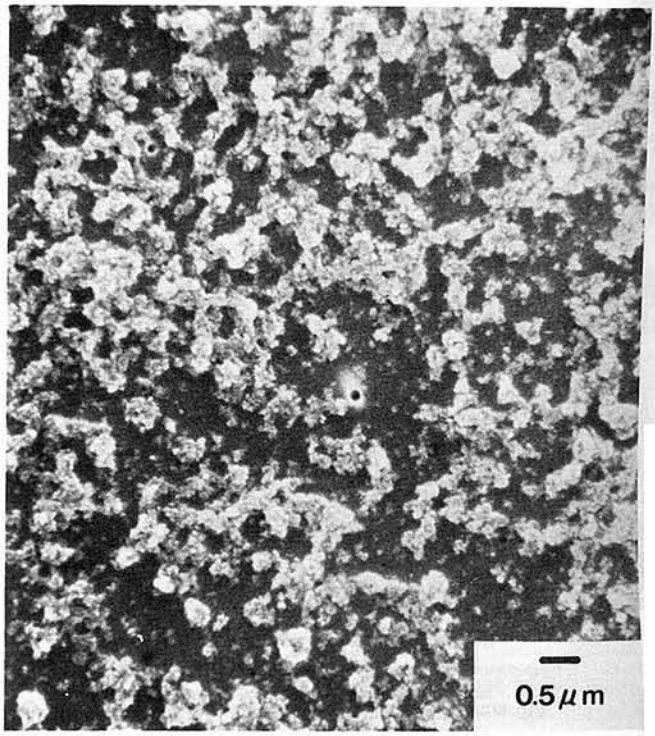

Primary filter-5μm pore

Fig. 7(b) $\phi = 0.37$

Fig. 7 Extractive probe conditions – effect of mixture ratio on number density (U_{ref} = 7.5mps, nominal nitrogen dilution flowrate)

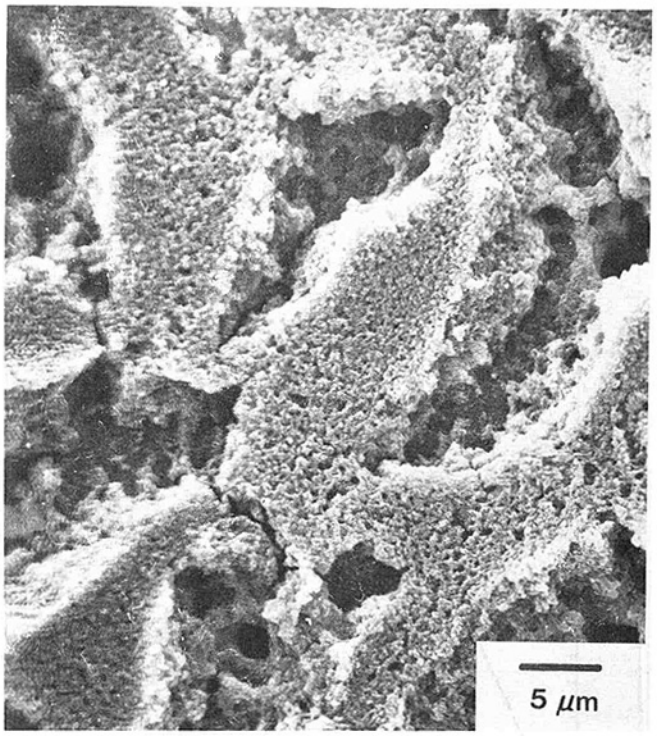

Fig. 8(*a*) Primary filter – 5μm pore

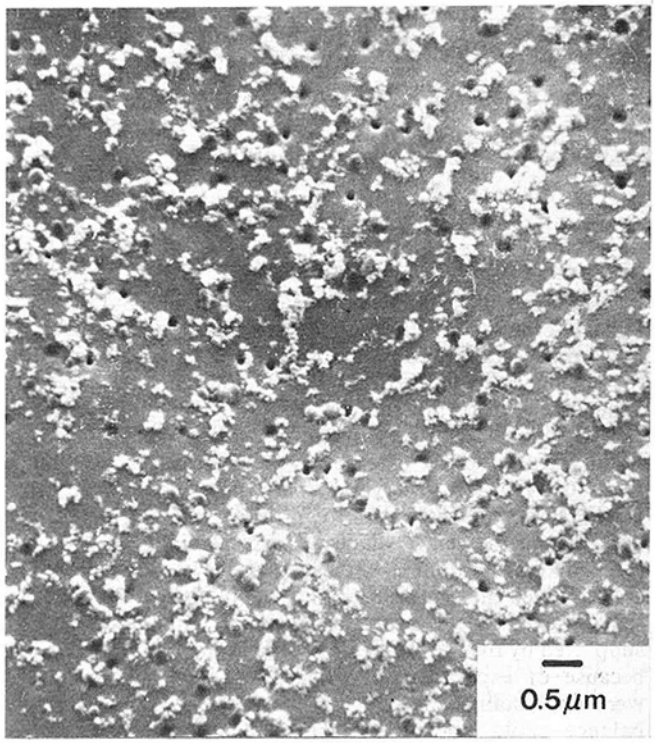

Fig. 8(*b*) Secondary filter – 0.2μm pore

Fig. 8 Extraction probe conditions – effect of water condensation on particle morphology (U_{ref} = 7.5mps, ϕ = 0.37, zero nitrogen flowrate)

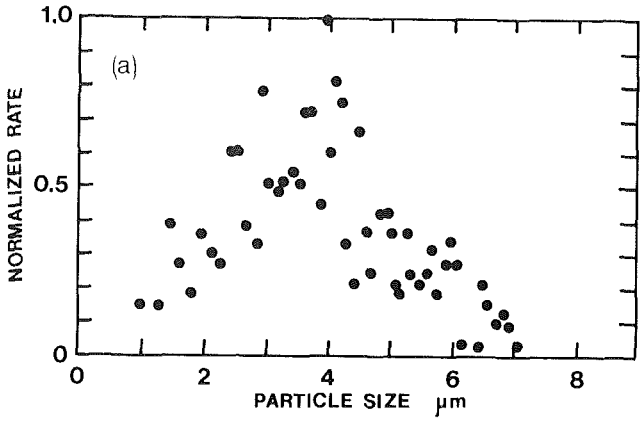


```
TOTAL RAW COUNT=631
TOTAL REDUCED COUNT(MM-2)=631
LINEAR    MEAN=3.9
SURFACE   MEAN=4.1
VOLUME    MEAN=4.3
SAUTER    MEAN=4.7
STANDARD DEV= 1.2

MEAN VELOCITY(M/S)=10.09
RMS  VELOCITY(M/S)=2.43
```

Fig. 9(*a*) Interferometric Data

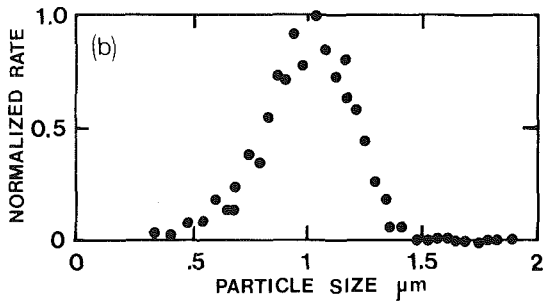


```
TOTAL RAW COUNT= 2585
TOTAL REDUCED COUNT= 169242.6
LINEAR MEAN   = 1
SURFACE MEAN  = 1.02
VOLUME MEAN   = 1.04
SAUTER MEAN   = 1.08
STANDARD DEV = .19

SAMPLE TIME= 22.2
```

Fig. 9(*b*) Ratioing Data

Fig. 9 Extractive probe conditions – representative optical probe sizing data (U_{ref} = 7.5mps, ϕ = 0.37)

data rate was monitored after the centerbody was cleaned. The rate increased in time as the centerbody was conditioned, and finally leveled off to a steady state (albeit low) reading. Although this evidence supports the suspicion, attrited particles from the centerbody have not yet been separately identified on the primary filter. One reason, of course, is the obscuration of attrited particles by the heavy loading of the puff-like structures at ϕ = 0.37.

The interferometric measurements also provide particle velocity. For example, at ϕ = 0.37 (Fig. 7(*b*) and 9), the average velocity of large particles (4μm peak) at the extractive probe entrance was 10.1mps (2.4mps S.D.). Calculation of the probe entrance velocity yielded an entrance velocity (uniform profile) of 15mps. These results suggest that the "isokinetic" setting in this swirling flow produced a flow rate close to but higher than desired.

Ratio Measurements (*~0.8 - 1.8μm*). Although the optical instrument was validated with 0.48μm particles for nonreacting conditions, in the enriched reacting flows (ϕ = 0.37) it was discovered that the presence of a large population of particles in the neighborhood of 1μm masked the observation of smaller particles. Thus, the theoretical dynamic

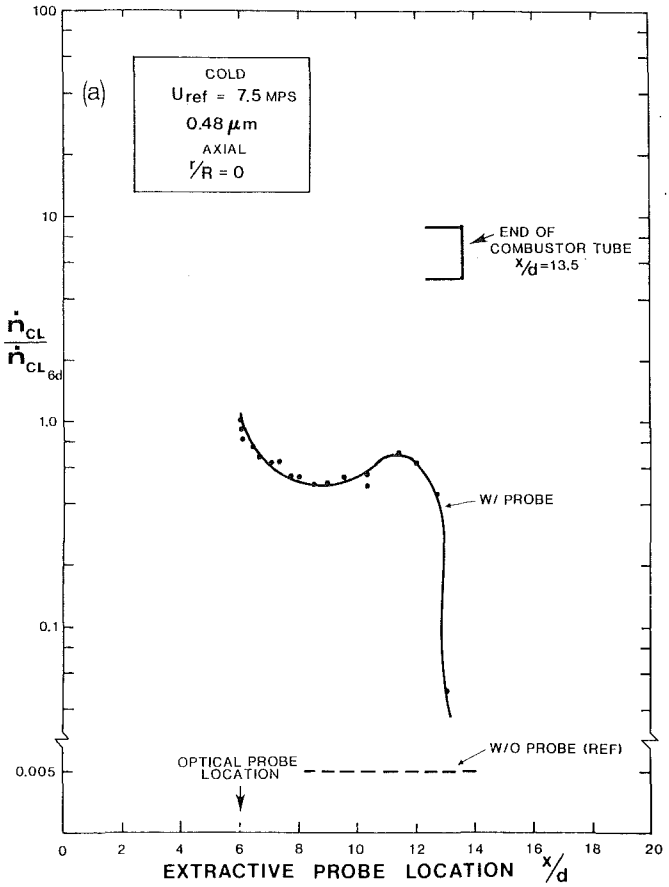

Fig. 10(a) Removal of extractive probe

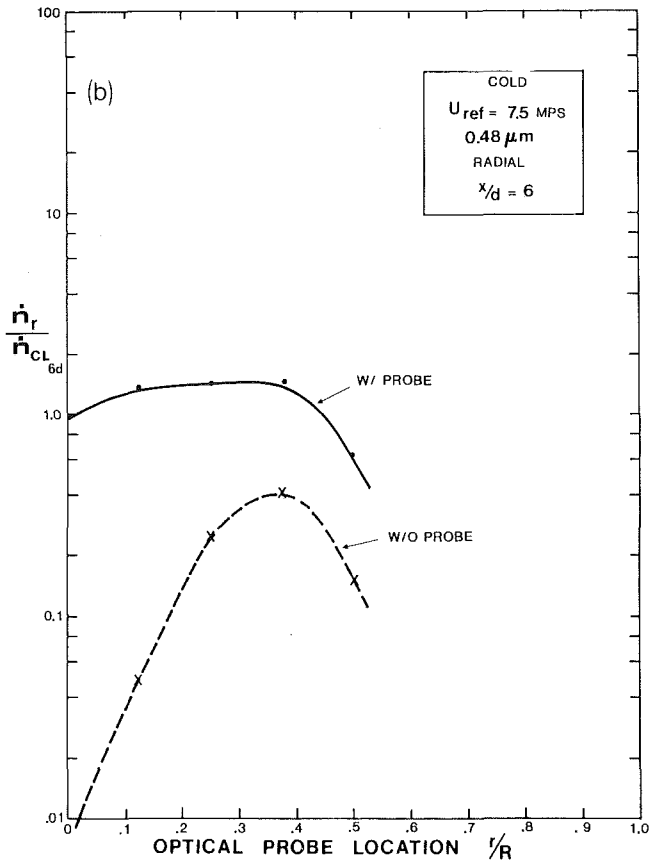

Fig. 10(b) Optical probe radial traverse

Fig. 10 Extractive probe perturbation – nonreacting flow with seeding (U_{ref} = 7.5mps, 0.48μm particles)

range of the ratioing technique (0.3 to 1.8μm) was limited in practice to ~0.8 to 1.8μm.

Despite this limitation, the ratioing measurements indicated that a substantial number of particles entering the extractive probe were of the "agglomerated" 1μm size. For example, ratioing data presented in Figure 9 in combination with the data rate recorded are entirely consistent with the size and number density observed on the SEM sample (Fig. 7(*b*)). The optically measured data rate increased as the mixture ratio was enriched, and as the sampling station was relocated from 6*d* to 3½*d*. This result is again consistent with the SEM data. The effect of extractive probe condition on data rate is shown in Fig. 5. Data rates generally increase for these reacting flows with operating condition and sample volume location controlling the extent of change. Insight into these influences is presented in the extractive probe perturbation results that follow.

B. Extractive Probe Perturbation

1. Nonreacting Flow With Seeding. The extractive probe perturbation study was initiated by seeding a nonreacting flow with 0.48μm polystyrene particles, and recording the optically measured data rate as the extractive probe was removed axially from the optical probe volume.

In the present case, the study was conducted at 7.5mps and at an axial sampling station of $x/d = 6$. As shown in Fig. 10(*a*), the sample rate decreased as the extractive probe was withdrawn, with an overall decrease of more than 200-fold between the with-extractive-probe ("*w*/probe") and without-extractive-probe ("*w*/o probe") conditions. The relatively low sample rate in the absence of the extractive probe is due to the strong, swirl-induced centrifugal force on the particles. When the probe is present, this force is reduced and particles can more freely diffuse radially toward the centerline. The radial diffusion of the particles becomes evident by examining Fig. 10(*b*). Two observations are noteworthy from this figure. First, the without-probe profile exhibits a very small data rate in the center which increases radially. This shows that diffusion is quite small and that very few particles are able to reach the central core of the combustor. However, in the presence of the probe, diffusion is enhanced. This is supported by the flat data rate profile in the figure. Secondly, because of experimental difficulties, radial measurements were not obtained beyond $r/R = 0.5$, thus a particle rate balance could not be performed based on these radial measurements.

2. Reacting Flow. The presence of the extractive probe produced an impact on the optically measured data rate that ranged from a small to a substantial effect depending on the operating conditions. For example, at 5.5mps, $\phi = 0.37$, and at the sampling station $x/d = 6$, the data rate remained relatively constant (Fig. 11) as the extractive probe was separated from the optical probe. In addition, no observable change in the optically measured particle size was recorded. The radial profiles also remain similar for both the with-

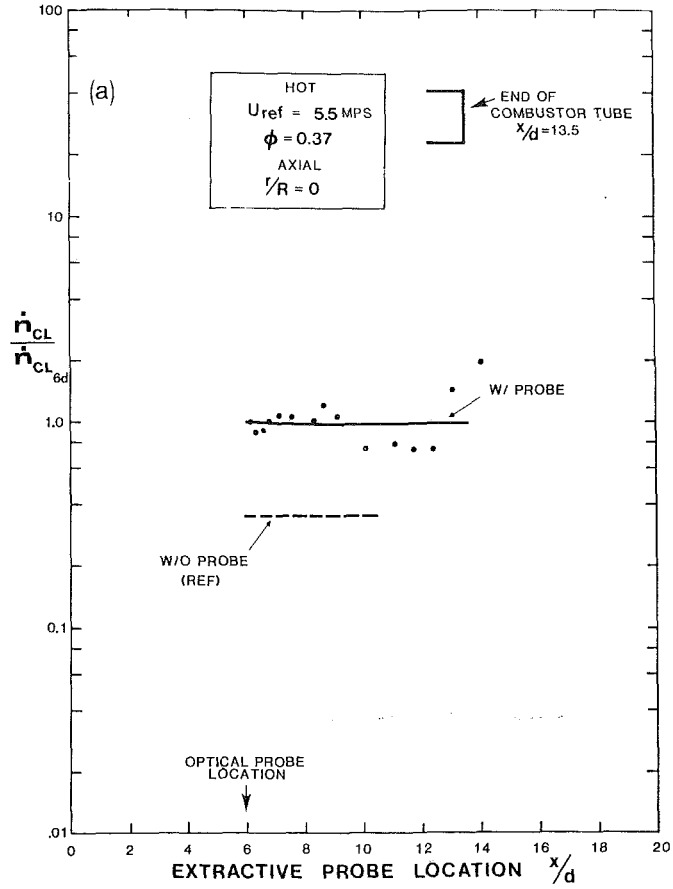

Fig. 11(a) Removal of extractive probe

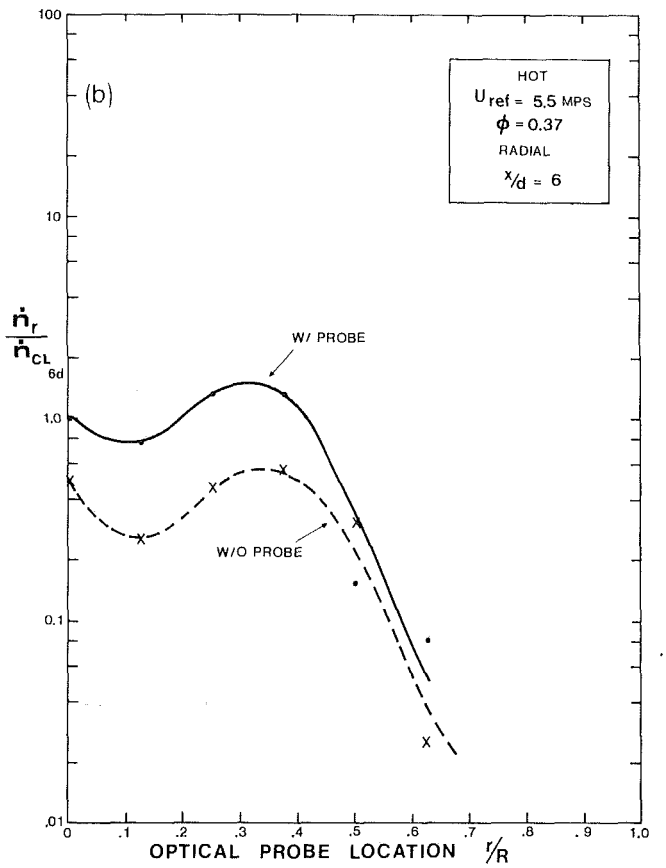

Fig. 11(b) Optical probe radial traverse

Fig. 11 Extractive probe perturbation – reacting flow (U_{ref} = 5.5mps, ϕ = 0.37)

probe and without-probe condition.[1] The lack of change in these measurements is probably due to a relatively small axial and radial gradients in flow properties at this sampling location as a result of the upstream recirculation and mixing.

Closer to the centerbody (x/d = 3½), the results are dramatically different (Fig. 12(*a*)). Here, the sampling station is located within the recirculation zone (refer to Fig. 1). The sample rate increased more than 70-fold as the probe was withdrawn from the optical sampling volume, with the steepest gradient in data rate occuring within 2 centerbody diameters of the sampling station. The change then is likely a result of a substantial perturbation of the local flow field with a concomitant change in mixing, chemistry, and temperature due to the intrusion of a solid, cold body into a zone of reverse flow. It is noteworthy that the effect on data rate levels off at approximately 6 centerbody diameters downstream of the recirculation zone, and the data rate settles to the without-probe condition.

The substantial probe perturbation is further evidenced in the radial profiles (Fig. 12(*b*)). Here, the with-probe profile resembles the previous case (Fig. 11(*b*)). However, the without-probe profile is markedly different, having a distinct maximum data rate on the centerline and decreasing monotonically radially outward.

Increasing the reference velocity from 5.5 to 7.5mps produced an even more dramatic impact even though the sampling volume was located in the wake of the recirculation zone (x/d = 6). Again, the sample rate increased about 40-fold as the probe was removed from the sampling volume (Fig. 13(*a*)). However, for this case there is an appreciable scatter in the measurements. This is attributed to a small but perceptible change in the flame structure, probably due to blockage, as the extractive probe was moved from one location to another. In particular, the flame compressed, and the wake region moved upstream as the extractive probe was moved toward the centerbody. The extractive probe perturbation was therefore not limited just to *local* changes (as in the previous two cases), but extended to dominate flame behavior throughout the combustor. This gross impact on data rate notwithstanding, the change in particle size in the range measured optically was not appreciable. The radial profiles (Fig. 13(*b*)) resemble the last case (5.5mps, ϕ = 0.37, x/d = 3½), showing both the large increase in data rate and large change in the presence of the probe.

The effect of extractive probe sample flowrate on the data rate observed optically at the probe entrance was earlier shown (Fig. 5) to be influenced by combustor operating condition and sample volume location. The extractive probe perturbation results provide some explanation of these trends. At 5.5mps, ϕ = 0.37, and x/d = 6, the perturbation of the extractive probe is minimal and the effect of an increase in sample flowrate is to increase the data rate to the same degree observed in the nonreacting flow tests. At 3½d, the sampling volume is in the recirculation zone. An increase in sample flowrate has no effect on data rate, which indicates that the

[1] The factor of two difference (Fig. 11(*b*)) in data rate at r/R = 0 is not significant and within the reproducibility at ϕ = 0.37. For example, a two-fold change in data rate was observed for small changes (e.g., $\Delta\phi$ = 0.01) in mixture ratio.

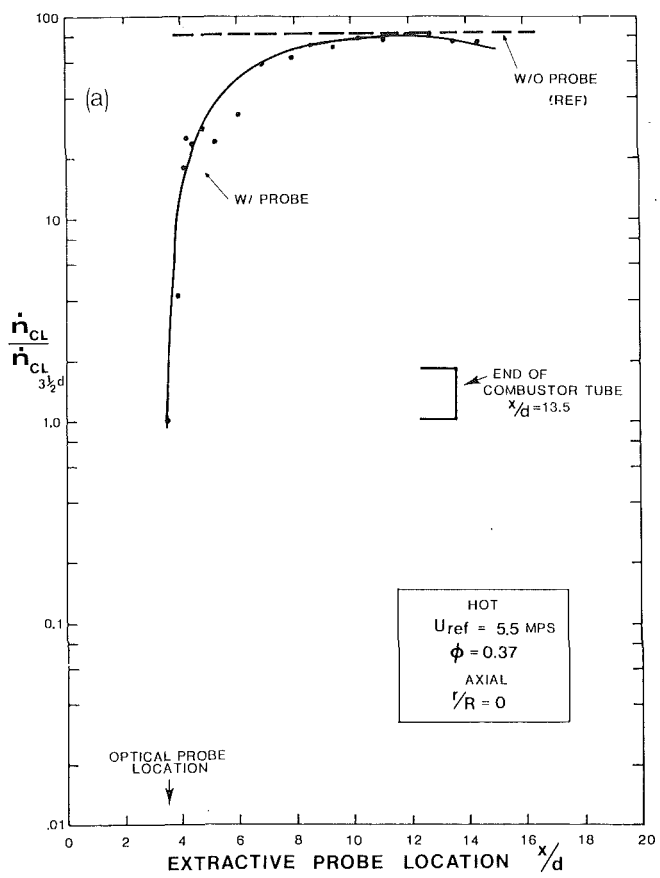

Fig. 12(a) Removal of extractive probe

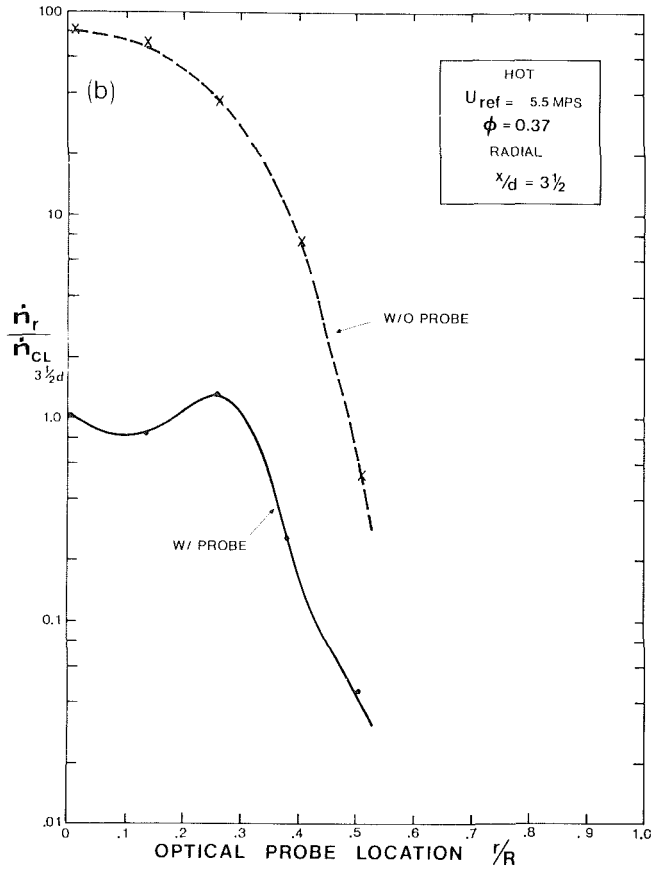

Fig. 12(b) Optical probe radial traverse

Fig. 12 Extractive probe perturbation – reacting flow (U_{ref} = 5.5mps, ϕ = 0.37)

flow aerodynamics fully control the local flow properties. Finally, at 7.5mps, $\phi = 0.37$, and $x/d = 6$, the blockage of the probe dominates and, because the blockage is influenced by sample flowrate, an increase in flowrate was observed to produce a perceptible change in flame structure and, as a result, a substantial change in data rate.

Summary

The present study represents an exploratory investigation into the sample integrity and perturbation associated with extractive probe sampling for soot. The use of nonintrusive optical measurement techniques focused at the entrance of an extractive probe provided a unique and independent measurement of number density (i.e., data rate) and particle size in the range of 0.3μm to 7.5μm for nonreacting flow and ~0.8μm to 7.5μm in the case of reacting flow.

The results pertaining to extractive probe sampling conditions provided new insights as well as reinforcing the traditionally perceived "isokinetic" effect. For example, number density increased with an increase in sample flowrate. However, the entrance velocity calculated from the isokinetically set sample flowrate in this swirl-stabilized flow was found to be 50 percent above the optically measured velocity. In addition, the optical measurements allowed the identification of a non-flame source of particulate – in this case, the attrition of particles off the centerbody.

Changes in nitrogen cooling rate did not affect the optical measurement, but did affect the morphology and number density on the 5μm filter. Higher sample temperatures and lower cooling rates produced a larger chain soot structure that subsequently clogged and built up in the 5μm pores giving the illusion of a monodisperse distribution. For high cooling rates, platelet-like structures were formed, likely as a product of rapidly condensing heavily concentrated fuel pockets extracted in an early stage of pyrolysis.

The effect of the physical presence of the extractive probe varied from no significant impact on data rate and particle size (in the particle size range measured) to a dramatic effect on data rate. The dramatic perturbation occurred when the sampling volume was located in the recirculation zone, or when the reference velocity was increased beyond the value (5.5mps in the present case) above which the blockage produced by the extractive probe becomes significant.

The results reported here are undoubtedly specific to the combustor configuration employed, and the size and design of the extractive probe used. In addition, the results are limited by the small particle size cutoff for the optical technique. As a result, the effect of extractive probe conditions and perturbation on soot particle formation, and on formed soot particles in the size range considered to be heavily populated ($\sim .02\mu m \leq dp \leq 0.3\mu m$) requires an expanded optical capability. This notwithstanding, the present results reveal:

- The type of problems associated with extractive probes
- Questions that must be raised in the interpretation of data from extractive and optical probes
- The type of experiments necessary to develop and test

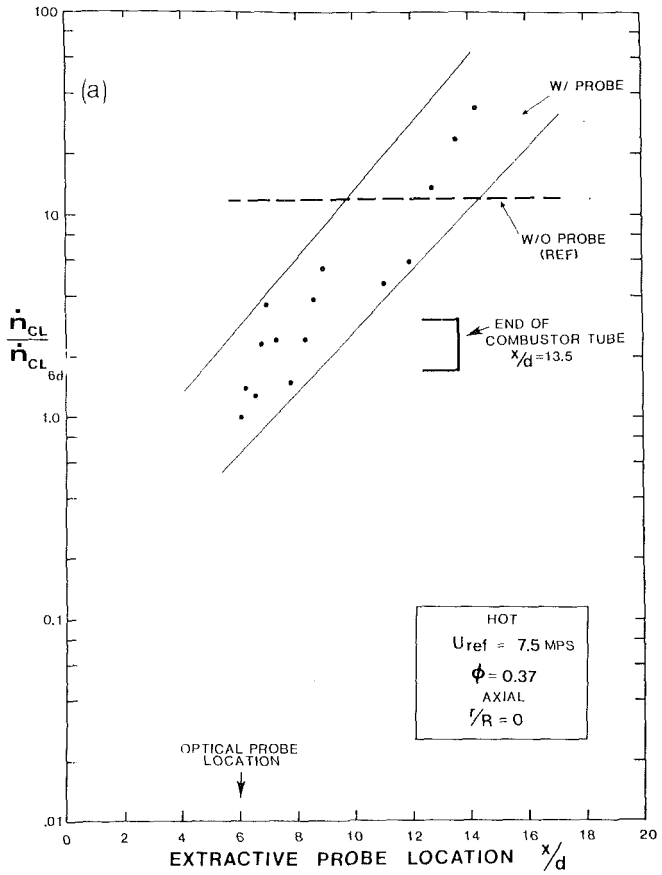

Fig. 13(a) Removal of extractive probe

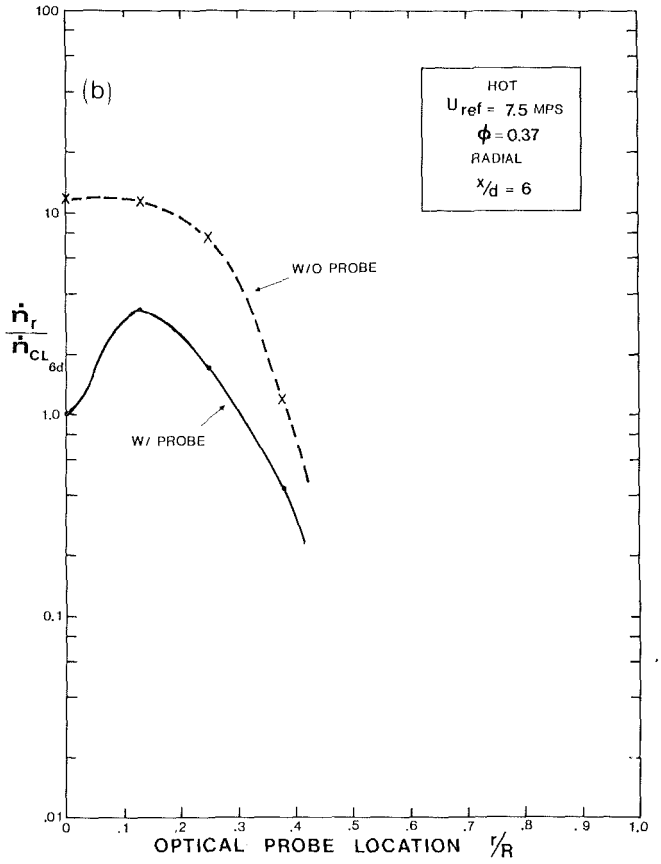

Fig. 13(b) Optical probe radial traverse

Fig. 13 Extractive probe perturbation – reacting flow (U_{ref} = 7.5, ϕ = 0.37)

methods employed to measure soot in gas turbine applications.

Acknowledgment

The results presented were obtained in a soot formation/alternative fuels study in progress at the UCI Combustion Laboratory and supported by the Air Force Engineering and Service Center, Research and Development Directorate, Environics Division (Air Force Contract #FO-8635-79-C-0158) with Captain Harvey Clewell as the project monitor.

References

1 Glassman, I., and Yaccarino, P., "The Temperature Effect in Sooting Diffusion Flames," Eighteenth Symposium (International) on Combustion, The Combustion Institute, 1981.

2 Blazowski, W. S., "Dependence of Soot Production on Fuel Blend Characteristics and Combustion Conditions," ASME Paper 79-GT-155, presented at ASME Gas Turbine Conference, San Diego, Mar. 1979.

3 Schirmer, R. M., "Effect of Fuel Composition on Particulate Emission from Gas Turbine Engines," in *Emissions from Continuous Combustion Systems*, Plenum Press, New York, 1972, p. 189.

4 Clark, V. A., Leonard, J. A., and Mellor, A. M., "Soot Loadings, Radiation Intensities, Gaseous Species Concentrations and Temperatures in a Quasi-Steady Spray Flame," in *Particulate Carbon Formation During Combustion*, Plenum Press, New York, 1981.

5 Hirleman, E. D., "Optical Technique for Particulate Characterization in Combustion Environments: The Multiple Ratio Single Particle Counter," Ph.D. thesis, Purdue University, Aug. 1977.

6 Bachalo, W. D., Hess, C. F., and Hartwell, C. A., "An Instrument for Spray Droplet Size and Velocity Instruments," ASME *Journal of Engineering for Power*, Vol. 102, No. 4, Oct. 1980, p. 798.

7 Hodkinson, J. R., "Light Scattering and Extinction by Irregular Particles Larger than the Wavelength," *Proceedings of Interdisciplinary Conference on Electromagnetic Scattering*, Permagon Press, Oxford, 1963, p. 87.

8 Chu, W. P., and Robinson, D. M., "Scattering from a Moving Spherical Particle by Two Crossed Coherent Plane Waves," *Applied Optics*, Mar. 1977, p. 619.

9 Moses, C. A., and Naegeli, D. W., "Fuel Property Effects on Flame Radiation in Aircraft Turbine Combustors," WSS/CI Paper 80-9, presented at the 1980 Spring Meeting, Western States Section/Combustion Institute, Irvine, Apr. 1980.

10 Sawyer, R. F., "Experimental Studies of Chemical Processes in a Model Gas Turbine Combustor," in *Emissions from Continuous Combustion Systems*, Plenum Press, New York, 1972, p. 243.

11 Fenton, D. L., Luebcke, E. H., and Norstrom, E., "Physical Characterization of Particulate Material from a Turbine Engine," ASME Paper 79-GT-179, presented at the ASME Gas Turbine Conference, San Diego, Mar. 1979.

Akifumi Hori
Managing Director.

Kazuo Takeya
General Manager,
Engineering Division.

Engineering Research Association
for Advanced Gas Turbines,
Tokyo 105, Japan

Outline of Plan for Advanced Reheat Gas Turbine

A new reheat gas turbine system is being developed as a national project by the "Engineering Research Association for Advanced Gas Turbines" of Japan. The machine consists of two axial flow compressors, three turbines, intercooler, combustor and reheater. The pilot plant is expected to go into operation in 1982, and a prototype plant will be set up in 1984. The major objective of this reheat gas turbine is application to a combined cycle power plant, with LNG burning, and the final target of combined cycle thermal efficiency is to be 55 percent (LHV).

Introduction

The Japanese Government started a national project on energy saving in 1978. The main item of this project has included a program to improve the total thermal efficiency of the combined cycle up to 55 percent (LHV) as the final target by developing an advanced gas turbine. Leading Japanese gas turbine manufacturers together with material and ceramic manufacturers jointly set up the "Engineering Research Association for Advanced Gas Turbines" as a gas turbine developing center, and started R & D. In the feasibility study phase, an improvement plan using the conventional simple-cycle gas turbine at higher temperature and a new gas turbine system plant adopting a reheat and intercooling system by changing the basic conception were compared and investigated. As a result, a conclusion has been reached that the reheat gas turbine is most promising when high efficiency is taken as the main object in the combined cycle.

Outline of Reheat Gas Turbine

In developing the reheat gas turbine (pilot plant) at present, the two shafts on the high pressure side and the low pressure side are arranged in tandem. In the HP system, the gas generator is a self-balance type and is rotated at free speed. In the LP system, the LP turbine and the LP compressor are coupled directly to the generator, so that it is driven at a constant speed of 3000 rpm. The cylinder is composed of the HP compressor, combustor, IP turbine, reheater, and LP turbine in one casing, while the LP compressor is separately housed in another casing. The HP system is leading in technology at 55 kg/cm^2 and 1300°C as compared with the conventional gas turbine, but in dimension it is on the same order as the aviation gas turbine. Therefore the design method is applied to the HP turbine blade and nozzle as the technology of jet engines. The LP turbine, driven at 1200°C, has almost the same dimensions as the existing large-size industrial gas turbine. The IP turbine rotor is overhung at the shaft end of the LP turbine rotor. The purpose of the IP turbine is to reduce the inlet gas temperature of the reheater. In designing the reheater, the inlet gas temperature is selected to max 750°C, and the exit gas temperature is selected to max 1200°C. The LP compressor has contributed to improve the part load efficiency together with the matching adjustment of the gas turbine cycle by controlling all the stationary vanes. For the intercooler, instead of adopting an ordinary heat exchanger, an evaporative cooler system by spray water which performs cooling directly by latent heat is utilised. Relative humidity of the cooler exit air is 90 percent. The advantages of the evaporative cooler are: ① power up of the gas turbine, ② enhancement of thermal efficiency, and ③ reduction of NO_x generation in the combustor. Especially, in this project, countermeasures against NO_x are the most important items because the combined cycle power generating plant is taken as a premise.

Overall Performance and Control System

For the reheat gas turbine, a thermal power plant of 1000 MW class using LNG as the fuel is assumed. Therefore, in consideration of the power requirement, it is necessary for the thermal power plant to cover a middle power range next to the nuclear power base load. In such a thermal power plant, daily start and part load operation are required, and great importance must be attached to the part load efficiency. In the planned reheat gas turbine, the air flow can be controlled to less than 50 percent of the rating flow, so that the part load efficiency can be maintained on an incomparably higher level

Contributed by the Gas Turbine Division and presented at the International Gas Turbine Conference, Houston, Texas, March 8-12, 1981, of THE AMERICAN SOCIETY OF MECHANICAL ENGINEERS. Manuscript received at ASME Headquarters, December 5, 1980. Paper No. 81-GT-28.

Table 1 Schedule of National Project (Advanced Gas Turbine)

Fiscal Year (April to March)	1978	1979	1980	1981	1982	1983	1984
Pilot Plant (AGTJ 100A)	Conceptual Design / Basic Design / Detail Drawing			Manufacturing & Assembling / Test Operation			
High Temperature Turbine Developing Unit (HTDU)			Design Manufacturing & Assembling		Test & Research		
Material & Basic Engineering R & D	R & D of Materials Basic Engineering						
Proto Type (Target Combined Cycle Efficiency 55 % (LHV))					Planning & Design	Manufacturing & Assembling	Test Operation

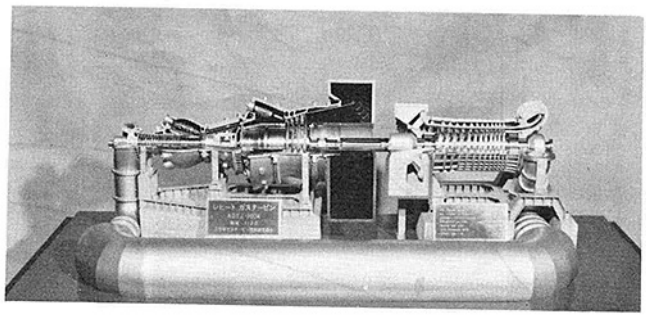

Photo 1 Scale model of reheat gas turbine

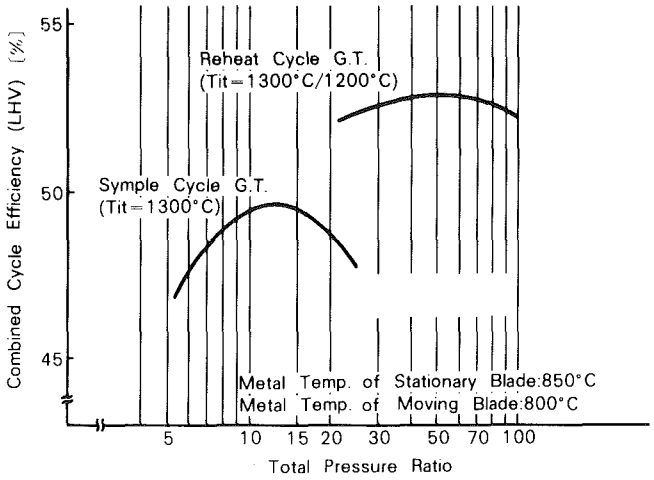

Fig. 1 Total pressure ratio versus efficiency for combined cycle

than that of a combined cycle using a conventional simple-cycle gas turbine.

Bottoming cycle recovery efficiency is important in the combined cycle; in the new system, the gas turbine exhaust temperature is as high as 620°C and the exhaust gas temperature is nearly constant even at part load; therefore, adoption of a reheat type steam turbine of 2400 psi and 1050°F/1050°F has become possible.

Full automatic remote control has been adopted as a control system, as well as a programmable sequencer by minicomputer is used as sequence logic. Load, speed and fuel controls use analog electronics, and the final control uses a EH system by high pressure oil.

Data logging and annunciator are printed out by a data logging system using a minicomputer.

Gas turbine main controls are: ①combustor fuel control, ②reheater fuel control and ③LP compressor stationary vane control; as minor controls, ④intercooler spray water control and ⑤LP compressor blow-off control are used. In the combustor control, the feedback by the constant speed governor attached to the HP shaft is used as the main channel, and the HP turbine inlet temperature limiter, anti-surge limiter, etc. are used as backup. In the reheater fuel control, the LP turbine exhaust temperature is used as the main channel, and the LPT inlet temperature, reheater minimum temperature rise, etc. are used as backup.

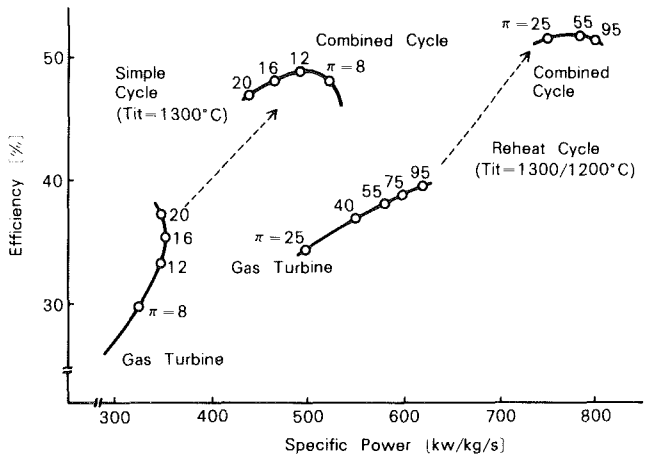

Fig. 2 Specific power versus efficiency

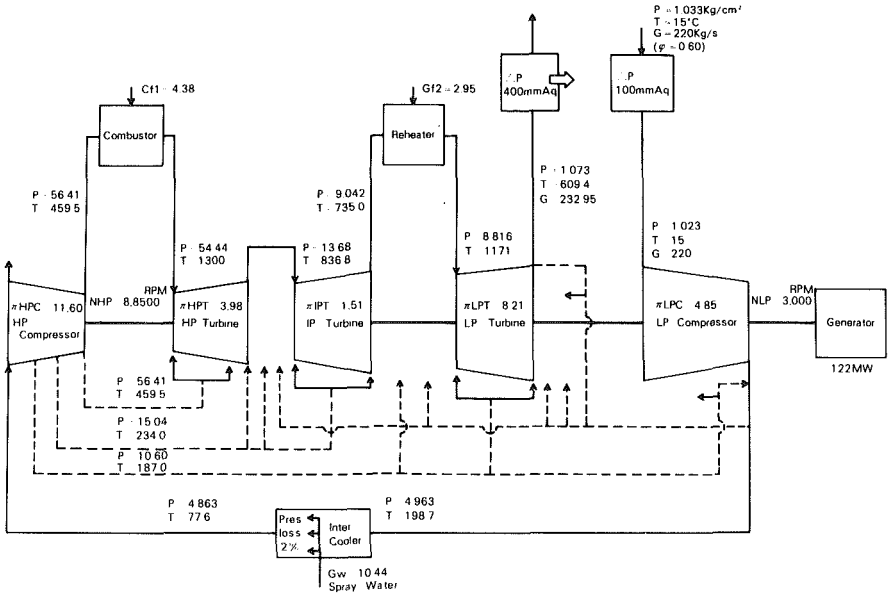

Fig. 3 Heat balance of reheat gas turbine (AGTJ-100A)

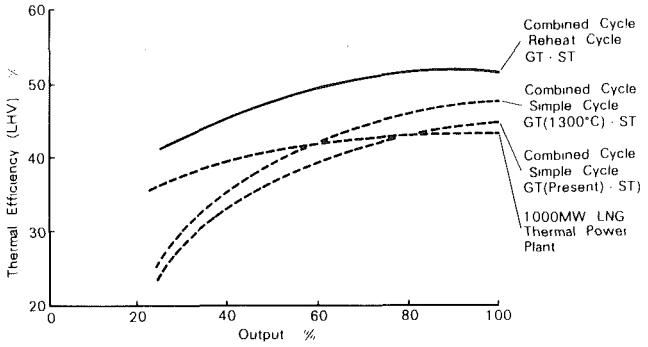

Fig. 4 Partial load efficiency of each power plant

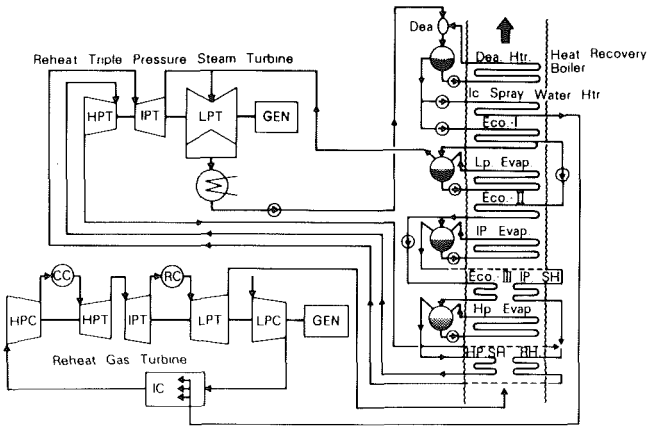

Fig. 5 Schematic diagram of combined plant

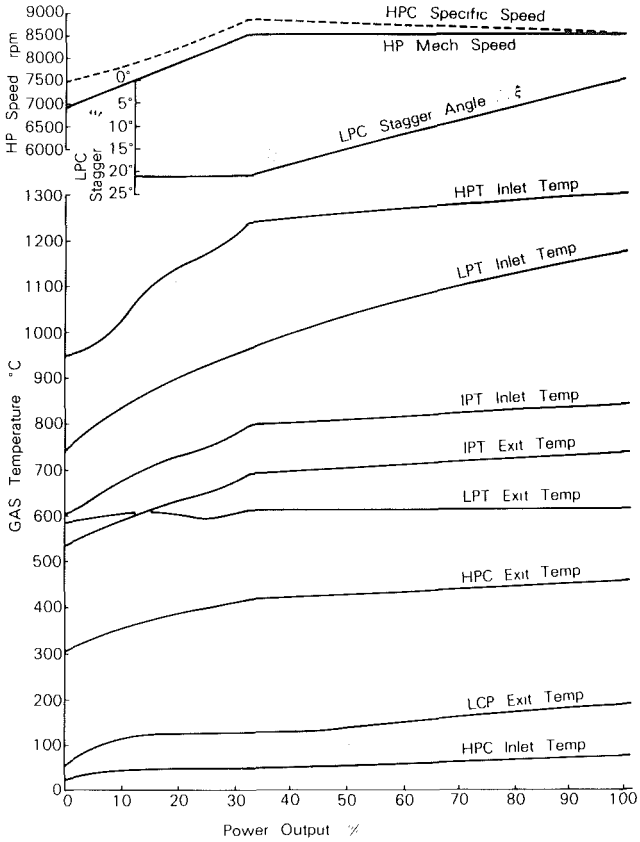

Fig. 6 AGTJ-100A Part load performance

In the LP compressor stationary vane control, the generator output differential is used as feedback.

Furthermore, in Japan, in the generator shutdown test in compliance with government regulations, the transient overspeed is required to be max 110 percent and to be safely set to no-load idle.

As a result of a preliminary dynamic simulation test, a bright prospect was obtained to the effect that the above requirement can be fulfilled by combined use with the LP compressor blow-off valve control.

Supporting Engineering Research

Under this national project, various research and development projects are incorporated to support the

Table 2 Specification of reheat gas turbine (AGTJ-100A)

1 Air Flow		220 Kg/s
2 Gas Turbine Power Output		122 MW
3 Gas Temperature	(HP)	1300°C
	(LP)	1200 °C
4 Total Press Ratio		55
5 Speed	(HP)	8,500 RPM
	(I LP)	3,000 RPM
6 No of Stage	(HP Compressor)	16
	(LP Compressor)	10-All stationary Vane Variable
	(HP Turbine)	2-Cooling Blade
	(IP Turbine)	2
	(LP Turbine)	4-Cooling Blade (1 2 stage)
7 No of Can	(HP Combustor)	10
	(LP Reheater)	12
8 Type of Inter Cooler		Water Spraying Evaporative Cooler

Table 3 Comparison of air inter cooler

Type of Inter Cooler	Evaporative Cooler	Heat Exchanger (Sea Water)	
Water Injection to Combustor	No	No	Yes
NOx Level	Basic (1 0)	(2 6)	(1 0)
Total Power Output for Combined Cycle	Basic (1 0)	(0 88)	(0 95)
Thermal Efficiency for Combined Cycle	Basic (1 0)	(0 992)	(0 965)
Consumption of Clean Water	Basic (1 0)	No	(0 41)

development of two engines for the pilot plant and prototype plant.

Outlines are introduced according to the main items.

①**High Temperature Turbine Developing Unit.** Various performance analysis tests can be conducted at up to 16 kg/cm^2 pressure using the testing facilities by two-stage turbine of almost the same dimensions as the HP turbine.

②**Combustor, Reheater Test Facility.** For conducting various tests of the combustor and reheater, the basic test and the screening test are conducted by the low pressure combustor test facility of max. 3 kg/cm^2, and the confirmation test is conducted by the high pressure combustor test facility of max. 16 kg/cm^2. Furthermore, in the preheater test, the gas condition is simulated by precombustor and water injection.

③**Essential Element Test for High Temperature Blade.** Manufacture engineering fo the full coverage film cooling and transpiration cooling blades, aerodynamic and heat transfer test (two-dimension and three-dimension cascade test), precision casting including directional solidification (DS), and development of super alloy are being planned.

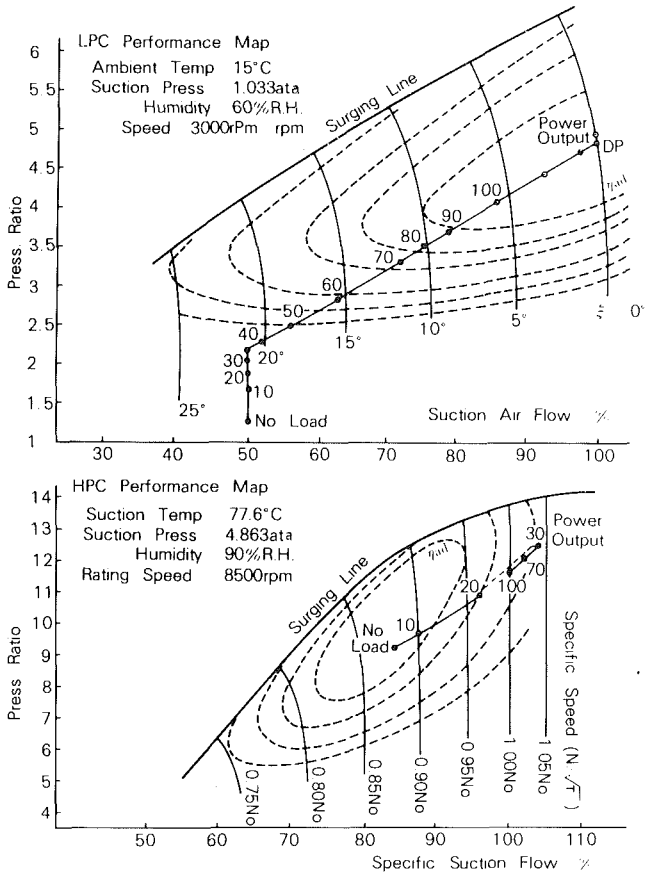

Fig. 7 Part load performance of compressor map

Summary

This report has presented an outline description of the design of the advanced gas turbine used in the Japanese national project. The Research Association will complete almost all the design and will start manufacturing a part of the gas turbine in 1980. In designing and manufacturing this gas turbine, as well as utilizing the existing highest technology, several new designs and technology must be developed. It is hoped that by surmounting these difficulties, the manufacture, operation, and test of the gas turbine will be performed according to the planned schedule.

Acknowledgments

The authors wish to express their appreciation to the Ministry of International Trade & Industry, the Agency of Industrial Science and Technology, and particularly to the Moonlight Project Promotion Office in Japan in charge of the plan and execution of this project.

The authors also express their gratitude to the members of the related national research institutions, including the National Aerospace Laboratory of Science and Technology Agency.

Acknowledgment is made to Mr. Ivan G. Rice, who extended various types of assistance to the publication of this report.

Thermal Expansion Accommodation in a Jet Engine Frame

M.H. Schneider
Senior Engineer,
Exhaust Systems Mechanical Design,
General Electric Co.,
Cincinnati, Ohio 45215

A prime consideration in the design of turbomachinery hot section structural frames is thermal fatigue caused by differential heating of the frame basic structural elements. This paper describes the general thermal deflection pattern of a frame and some design features which can accommodate this relative expansion without excessive stress. Also discussed is a particular combination of design features which provide increased tolerance for thermal expansion while maintaining a large mechanical stiffness as is often required for a high bypass ratio turbofan engine application. This unique combination of frame design features, developed under NASA contract NAS3-20643 to NASA-Lewis Research Center with Mr. Carl C. Ciepluch as the Lewis Project Manager, represents a significant contribution to state of the art frame design.

Frame Description and Design Considerations

A gas turbine engine frame is a static structure which can perform a number of different functions in a given engine configuration. Primarily, frames maintain alignment of the rotor system within the static structure. They also transmit loads across the gas flowpath, provide engine structure spring elements, and help maintain airfoil tip clearances. The frame is vital to the control of airfoil tip clearances by limiting the eccentricity between the rotor and the stator structure and by maintaining roundness in the stator casing. In addition to these primary functions, frames may be required to perform others which could include support of bearings and sumps, aerodynamic turning of the flowpath gas, provision for engine mount and ground handling features, and support of other major engine components, such as inlets, thrust reversers, or centerbodies. Figure 1 illustrates the frame location in a state of the art high bypass ratio turbofan engine. The major structural components of a frame are depicted schematically in Fig. 2. These elements are the inner ring system or hub, the struts, and the outer casing.

The most important consideration in the design of a frame is usually mechanical stiffness. Without an adequate spring constant, the frame could allow excessive rotor deflections under normal loading conditions which produce blade tip rubs and subsequent performance deterioration. Because frames are normally designed to have a large spring rate, they are usually deflection limited rather than stress limited when subjected to mechanical loading. However, the structure must also be designed so as to maintain structural integrity under extreme or ultimate load conditions. These ultimate loads can be produced by events such as rotor seizure or an abnormally high rotor imbalance. Another key consideration in frame design is thermal stress. Without adequate accommodation for thermal expansion in the frame, large thermal stresses may be generated, resulting in premature removal of the frame for repair or replacement. All frames are subject to

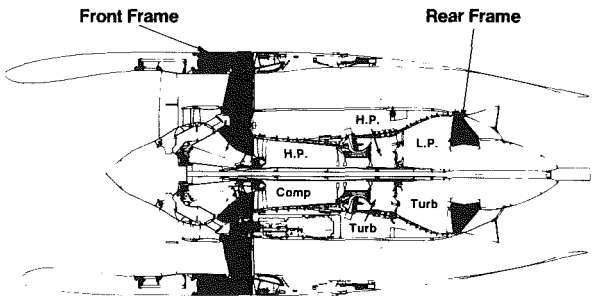

Fig. 1 Engine frame locations

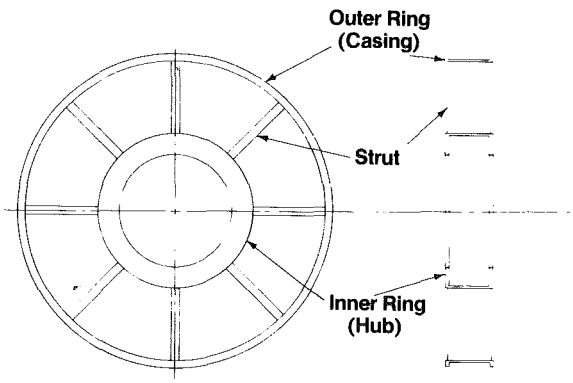

Fig. 2 Frame structural elements

Contributed by the Gas Turbine Division and presented at the Gas Turbine Conference and Products Show, Houston, Texas, March 9-12, 1981 of THE AMERICAN SOCIETY OF MECHANICAL ENGINEERS. Revised manuscript received at ASME Headquarters April 29, 1981.

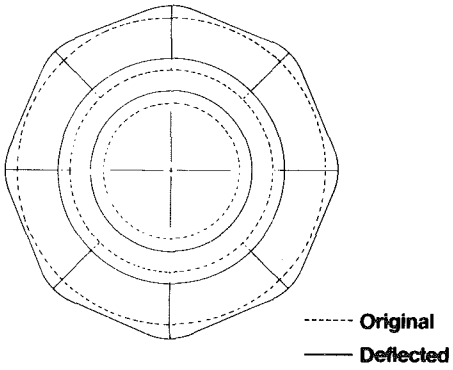

Fig. 3 Thermally induced deflection pattern

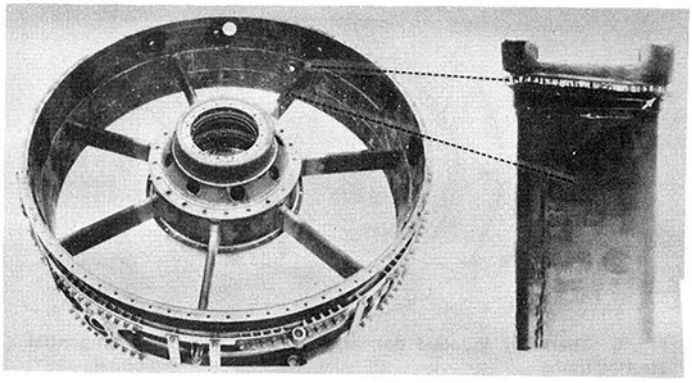

Fig. 4 Fatigue crack in frame at strut casing interface

thermal stresses due to temperature differentials between the major frame components, and the situation becomes more pronounced in the hot section of an engine (i.e., aft of the combustor) where elevated temperature levels occur, both on steady state and transient bases.

Thermal Expansion and Structural Rigidity

Thermal stresses are generated in a frame when there are differences in the thermal growth of the hub, struts, and outer casing. These differences occur due to the various frame components operating at different temperatures and due to any differences in thermal expansion coefficients which can exist if dissimilar materials are used. This mismatch in thermal expansion of the major components of a frame may put the struts in tension or compression and impose radial loads, usually equally spaced, on the hub and on the outer casing. Figure 3 illustrates schematically the deflection pattern resulting from a temperature distribution which puts compression in the struts, radially outward loads on the casing, and radially inward loads on the hub. Although the magnitude of the radial loads imposed on the hub and casing are equal, the casing is subjected to much larger local deflection. For this reason, the maximum thermal stresses usually occur in the casing. This phenomenon takes place because the rigidity of the hub far exceeds that of the casing.

The stress level associated with these relative thermal growths is usually the major factor in determining the life of the frame. The thermal stress, together with any mechanical stresses present, determine the number of thermal cycles that can be tolerated before a crack initiates at the peak stress location. (A thermal cycle may be defined as a period of time within which the thermal stress level passes from some initial value through its entire range of regularly recurring values and back to the initial value.) Analytically predicting the peak stress level in a complex engine frame is a difficult task for a number of reasons. Factors contributing to a tolerance band on the calculated maximum number of thermal cycles permitted include a tolerance on the predicted component metal temperatures, local stress concentrations, and material deviations. Figure 4 shows the type of metal fatique cracks caused by thermal expansion. This figure is photograph of a representative turbine frame after long and severe usage. The cracks appear at the outer casing/strut interface, precisely where the radial loads are imposed under the thermal load condition mentioned previously.

From the previous discussion, the importance of maintaining thermal stress well within the allowable levels becomes obvious. However, an apparent paradox exists in the design considerations or requirements as set forth earlier. On the other hand, stiffness is of paramount importance in frame design. Without adequate stiffness in a frame, the engine system may respond dynamically to a normal rotor imbalance

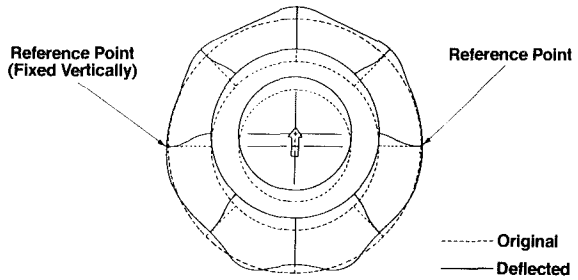

Fig. 5 Mechanically induced deflection pattern due to vertical load applied at the hub

to such a degree that a serious failure could occur. On the other hand, the frame must be designed to accommodate the relative thermal expansions of its components. Without adequate thermal expansion accommodation, the frame may suffer metal fatigue and crack before its service life has been reached. In general, the stiffer the structure, the less capable of accommodating thermal expansion differences. Another means of visualizing this apparent discrepancy in the applicability of the design requirements is illustrated in Fig. 5. This figure shows the frame deflection pattern due to a radial load imposed at the hub. The deflection pattern is the same as that for thermal expansion except that it is asymmetrical about the horizonal centerline. That is, the mechanically induced deflection pattern produced by the load applied as shown in Fig. 5 results in compression in the struts above the horizonal centerline and tension in the struts below the horizonal centerline. The stiffer the frame, the less the deflection for a given mechanical load. However, the stiffer the frame, the more thermal stress for a given thermal load. Thus, the designer must walk a fine line between stiffness and expansion accommodation in the design of an engine frame.

The number of struts in a frame has a major impact on the spring rate of the structure. More struts increase the mechanical stiffness of the frame, but reduce the tolerance to thermal expansion. A relatively large number of struts may be necessary if the frame is required to provide aerodynamic turning of the gas in the flowpath. That is, in order to do an adequate job aerodynamically, the struts would be required to meet a minimum solidity requirement, where solidity is defined as the ratio of the chord of the airfoil shaped strut to the spacing between struts. This, in turn, produces a very stiff structure that does not handle differences in component thermal expansion very well. A remedy to this situation is to design the outer casing to be very "soft." If the outer casing possesses a small moment of inertia about an axis parallel to the engine centerline, then the radial loads imposed by the struts are not restrained to any great degree by the casing, and, therefore, large thermal stresses are not generated. However, this approach does allow large radial deflections at

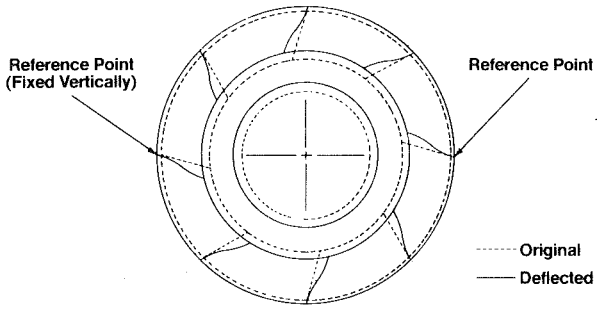

Fig. 6 Thermally induced deflection pattern in a semi tangential strutted frame

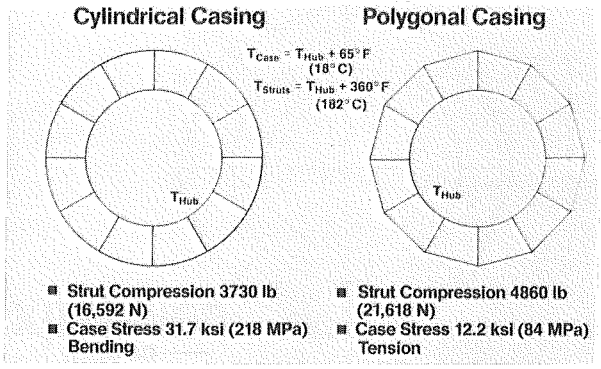

Fig. 8 Frame thermal stress comparison, cylindrical vs. polygonal

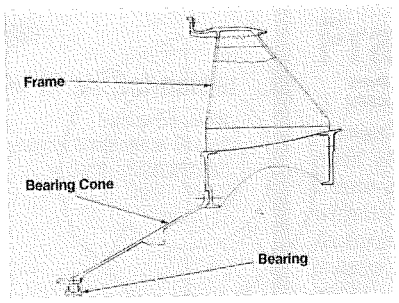

Fig. 7 Frame with long bearing cone

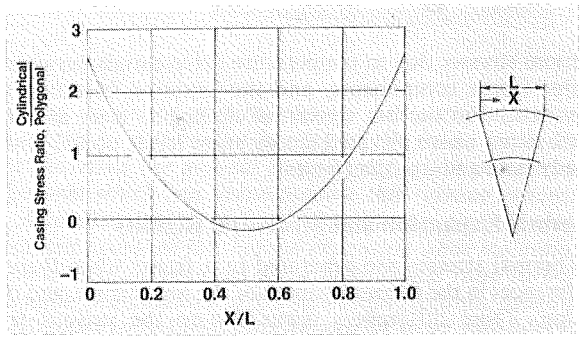

Fig. 9 Frame casing thermal stress distribution

the strut ends and these large deflections are not consistent with one of the aforementioned primary functions of a flame. Specifically, frames help maintain airfoil tip clearances and one means of doing this is to maintain roundness in the casing. Clearly, softening the casing mechanically is not in keeping with this critical frame function.

Another method used successfully for accommodating relative thermal expansion differences in a frame is semitangential or skewed struts. This concept employs struts which lean at an angle from a radial line as measured at the intersection of the strut with the casing. This frame concept is illustrated in Fig. 6 along with its thermally induced deflection pattern. Rotation of the entire frame hub about the engine centerline allows the expansion differences to co-exist without imposing large radial loads on the casing at each strut. Adequate stiffness can usually be supplied with this frame approach as long as there is not a large axial distance between the point of load application, usually a rotor bearing, and the plane of the struts. If a relatively long bearing cone is present, as shown in Fig. 7, then a large overturning moment exists on the frame hub which is reacted by axial loads at each end of each strut. The struts can be viewed as beams pinned at the casing and fixed at the hub, and, therefore, the axial deflection of the struts at the hub is proportional to the strut length to the third power. The structure spring rate is directly proportional to this deflection. It can be seen then that a small increase in strut length, for example, that which results from changing the strut from radial to semitangential, can have a significant impact on the stiffness of the structure. And there is a definite trend in state-of-art gas turbine engine design to utilize as few bearings and associated sump housings as possible. This reduces cost, weight, and complexity, but, with the unsupported rotor length limitation set by such consideration as airfoil tip clearances and critical frequencies, a large axial offset is necessary between the rotor bearings and the frames supporting them. The large overturning moment imposed on a frame in an engine of this type makes the added strut length inherent in a semitangential strutted frame a less desirable method for accommodating thermal expansion differences.

One frame design concept that provides both adequate stiffness and increased tolerance for expansion differences is a polygonal casing. As was described previously, a round casing tends to become chordal between the struts under the imposition of equally spaced radial loads at the struts. A polygonal casing, formed by straight line segments between strut ends, loads up in pure tension or compression when radial loads at the struts are imposed. This is the key to lower thermal stresses under a given thermal load situation. The round casing, because it is more flexible than the polygonal casing, is subjected to large local bending stresses at each strut end. The polygonal casing, though not as flexible radially at the strut end, is subjected to essentially pure tension or compression along the entire length of each polygonal panel. Figure 8 is a comparison of the thermal stresses generated in a cylindrical and a polygonal frame under a typical thermal load condition. The strut compressive load in the polygonal frame is approximately 30 percent larger than that in the cylindrical frame; but, as was stated previously, the casing is normally the limiting component from a thermal stress and therefore fatigue life standpoint due to the relative rigidities of the hub, struts, and casing. Note the casing stress is roughly two and one half times greater in the cyclindrical casing than in the polygonal casing. The cylindrical casing undergoes a local bending stress at the strut end whereas the polygonal casing has a uniform tensile stress distributed over each panel. Figure 9 illustrates the thermal stress distribution in the casing from one strut end to another for both a cylindrical casing and a polygonal casing with equivalent casing and hub radii and with an equal number of struts. It is clear that the polygonal casing is a much more efficient structure due to its greater uniformity in stress distribution. The cylindrical casing gets stressed highly at the struts but does little work between struts. From a stiffness standpoint, the polygonal frame is stiffer than a cylindrical frame. This stiffness advantage is due to less flexibility in the outer casing under the imposition of radial loads at the struts. It can be seen that the

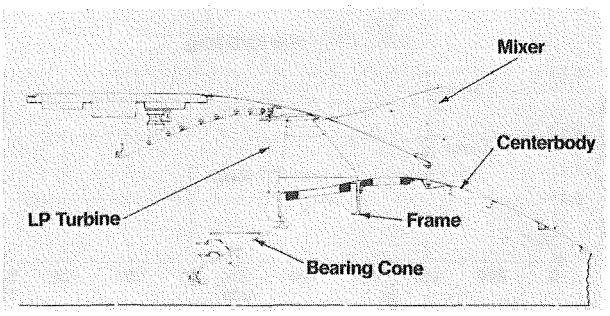

Fig. 10 Turbine rear frame—cross section

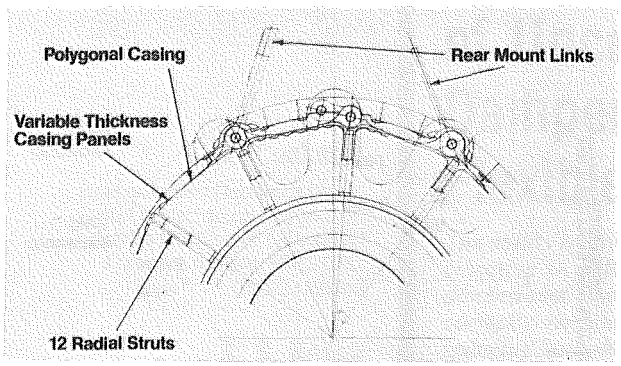

Fig. 11 Turbine rear frame—end view

polygonal casing is a feature which meets both adequate stiffness and low thermal stress requirements.

A Total Frame Concept

The turbine frame concept designed for use on the energy efficient engine currently being developed under NASA contract is shown in cross section in Fig. 10. The relatively long axial length, approximately 10 in. (25.4 cm), from the bearing to the frame indicates the frame must be capable of withstanding a large overturning moment. The rear engine mount is located on the frame, which implies the outer casing must be capable of withstanding large point loads. The overall spring rate requirement for the frame structure, from the bearing to the mount plane, is on the order of 1 million lb per in. (1.75×10^8 N/m). In order to provide the large spring rate, accommodate large point loads at the mounts, and provide adequate thermal expansion accommodations, several design features already mentioned, and some that have not been mentioned, were employed. Specifically, they are: radial struts, polygonal casing, thermal expansion control, and casing strain distribution.

In order to provide the required spring rate from the bearing to the strut plane at the casing, radial struts were employed. The spring constant is defined as the ratio of the vertical load imposed at the bearing to the vertical deflection resulting at the bearing. The long axial length of the bearing sump cone results in a large axial load on each strut when a radial load is applied at the bearing. Thus, the relatively short length on the radial strut, as compared to a semitangential strut configuration, produces a significant stiffness increase in the overall structure. The use of a polygonal casing also enhances the overall frame spring rate. With the outer strut ends less flexible radially due to the polygonal casing panels, the deflection at the bearing due to a load applied at the bearing is reduced from that which would be present if a cylindrical outer casing were used. In this particular instance, the frame is being called upon to provide the rear engine mount points. The polygonal casing is particularly suited to efficiently carrying the large mount loads which are taken

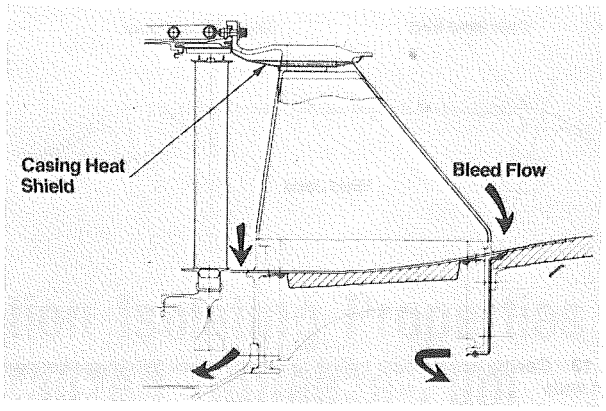

Fig. 12 Frame thermal expansion control features

out at discrete points. With the mount lugs located at strut ends, as shown in Fig. 11, the loads are carried by the frame casing as tension or compression in the polygonal panels. When mounts are incorporated on a cylindrical frame, a large section modulus must be designed into the casing in the vicinity of the mount points to distribute the load around the casing and to withstand the large local bending stresses generated. This cylindrical casing section, usually comprised of radially deep rings, is heavy and may result in a fatigue problem due to large radial temperature gradients in the casing rings themselves. From a thermal fatigue standpoint, the polygonal casing is advantageous because of the lower thermal stresses generated under a given thermal load. Without the large local bending stresses present at the strut ends as in a cylindrical casing, the fatigue life of the polygonal casing is enhanced.

In order to reduce the maximum thermal expansion difference between the frame major components, two thermal expansion control features were incorporated into the design. One feature is a sheet metal heat shield on the outer casing as shown in Fig. 12. This liner serves as a radiation shield and both decelerates the thermal response of the casing during transient operation and effects a lower steady state casing operating temperature. The other feature concerns convectively heating the frame hub with flowpath gas, also shown in Fig. 12. The forward hub ring is heated by means of bleeding flowpath gas radially inward between the last stage of the low pressure turbine and the frame hub. The aft hub ring is heated by bleeding hot gas radially inward between a sheet metal baffle and the aft hub ring. Bleeding the flowpath gas radially inward is possible because the entire cavity inside the frame hub, including the aft centerbody, is vented to ambient at the trailing edge of the centerbody. The relatively large mass comprising the frame hub usually results in a hub thermal response which lags the other frame components and therefore results in large thermal expansion differences during transient operation. Convectively heating the hub accelerates its thermal response and again reduces the thermal expansion differences which can exist during both transient and steady state operation. The hot gas used to heat the hub has an insignificant impact on performance since it is reinjected into the gas stream at the centerbody trailing edge.

The last feature incorporated to enhance thermal expansion accommodation is preferential strain distribution in the casing. This strain distribution is produced by thinning the polygonal panel between struts and leaving the panel thicker at the weldment between the panel and the struts and leaving the panel thicker at the weldment between the panel and the strut end as shown in Fig. 13. Typically, the complex geometry of the strut ends makes them perfect candidates for the use of casting as a fabrication method. However, castings usually possess lower strength than the same material in a

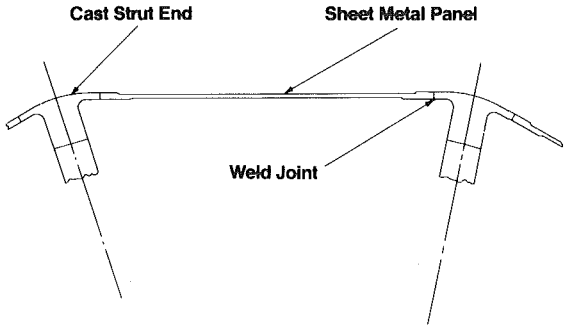

Fig. 13 Casing panel chem milled to reduce stock thickness between strut ends

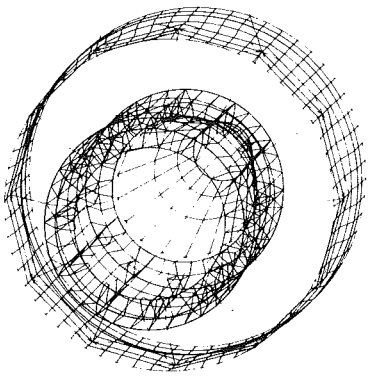

Fig. 14 Turbine frame computer model

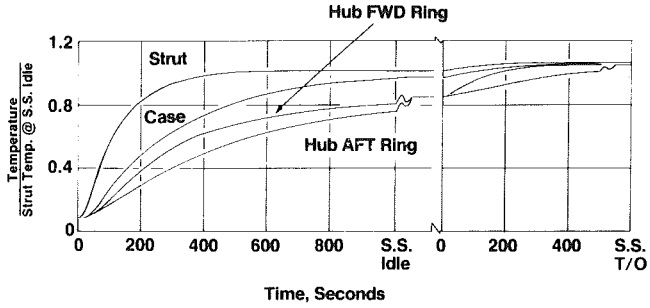

Fig. 15 Turbine frame transient thermal response

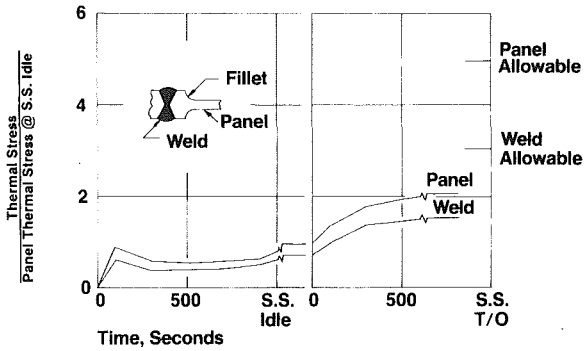

Fig. 16 Frame casing thermal stress

wrought form. By thinning the polygonal panel in the center, more straining takes place in the panel center than at the ends where the welds are located. Expressed another way, the panel will be more highly stressed in the center than at the strut end attachment. The polygonal panel can be made of wrought sheet material and is therefore capable of withstanding the higher strain (or stress) levels. The corresponding strain (or stress) level in the strut end is maintained at a lower level, well within the allowable for the cast material.

Design Approach

Stress and deflection analysis of this frame concept was carried out with the aid of a three-dimensional finite element stress analysis computer program. The computer model generated for the mechanical analysis of the frame is shown in Fig. 14. The sump cone, forward hub ring, aft hub ring, shear cylinder between hub rings, and the polygonal outer casing were modeled with plate elements. The struts were modeled as beams with radially varying cross sections to account for the strut being tapered from the hub to the casing. The straight beams at the top of the model represent the three rear mount links. These beams, pinned at each end, together resist vertical, side, and torque loads imposed on the frame. The model was also fixed axially around the circumference of the casing forward flange.

In order to determine the overall spring rate of the frame structure from the bearing to the mount plane, a unit vertical load was applied at the bearing in the form of a sinusoidally distributed shear load. The net vertical load divided by the resultant vertical deflection at the plane of load application, in this case the bearing location, yields the overall spring rate. The calculated spring rate for this frame was 991,000 lb per in. (1.74×10^8 N/m), approximately the desired value.

The same model was used to determine the thermal stresses generated in the frame. Detailed heat transfer analysis of the frame structure resulted in frame components metal temperature as shown in Fig. 15. This plot represents a typical time history of the metal temperatures from engine start to steady-state idle conditions and from steady-state idle to steady-state takeoff power setting. By inputting component temperatures at a given instant in time, the corresponding thermal stresses can be generated. A plot of the corresponding casing thermal stress versus time is shown in Fig. 16. The thermal stress in the panel includes a stress concentration factor at the fillet in the transition region between the initial and the thinned section of the panel. Likewise, the weld stress includes a stress concentration factor to account for such occurrences as lack of complete weld penetration or slight mismatch between the two ends being joined. The allowable stresses are those which would permit the required number of thermal cycles to be attained without initiation of fatigue cracks. The panel allowable stress and the weld allowable stress are for wrought Inconel 718 and for cast Inconel 718, respectively. As can be seen, the maximum calculated thermal stress is well below the allowable.

Conclusion

The incorporation of either radial struts, a polygonal casing, some means of thermal expansion control (i.e., heat shields or convective heating), or preferential casing strain distribution into a frame design would result in some increase in structural stiffness and/or thermal expansion tolerance. However, the unique combination of all these features permits accommodation of the thermal expansion inherent in a turbine frame structure while maintaining a high stiffness to weight ratio. This results in a lighter weight, longer life design for a given stiffness requirement.

The Vibration Isolating Properties of Uncentralized Squeeze-Film Damper Bearings Supporting a Flexible Rotor

R. A. Cookson
Head of Applied Mechanics Group,
School of Mechanical Engineering,
Cranfield Institute of Technology,
Cranfield, Bedford. MK43 OAL.
United Kingdom

S. S. Kossa
Military Technical College,
Cairo, Egypt

The ability of an uncentralized squeeze-film damper bearing to inhibit the effects of vibration in a flexible rotor-bearing system, has been assessed in terms of non-dimensional system parameters. This analytical approach has shown that a correctly designed squeeze-film damper bearing is a very effective means of reducing both the amplitude of motion of the rotor and the force transmitted to the bearing support structure. However, the analysis has also indicated that a poorly designed squeeze-film damper bearing can produce amplitudes and forces greater than those which would arise if the bearing support remained rigid. An experimental programme has supported the validity of the above analytical technique by showing that the measured motion orbits of the journal and disk centers as the rotor passes through the critical speed, are very similar to those predicted theoretically. Also, the response curves for specific groups of system parameters show very similar trends in practice, to those which result from the analytical approach. Some indication of the ability of a squeeze-film damper bearing to reduce the effect of much greater unbalance than normal is also reported.

Introduction

Most modern gas-turbine engines are fitted with vibration inhibiting devices known as squeeze-film damper bearings. The squeeze-film damper bearing has been shown to be capable of reducing both the vibration amplitudes and transmitted forces associated with rough-running caused by normal unbalance, engine support bounce modes, and proximity to the rotor first flexural (pin-pin) critical speed. In fact, it has been reported by several workers, for example [1], that the fitting of squeeze-film damper bearings to an engine has almost completely removed the effects of a critical speed from the engine running range.

From the early 1960's, the squeeze-film damper bearing, as a damped flexible support for a rotor-bearing system, has been the subject of considerable investigation, for example [2–8], and has found practical application in, among others, the gas-turbine engines of Rolls-Royce [9–10], Pratt and Whitney [11], Rover [12] and General Electric [1].

In its simplest form, the squeeze-film damper consists of a fluid-filled annular cavity surrounding the outer race of a rolling contact bearing. Lubricating oil is usually the fluid employed, presumably because it is readily available at that position within the engine, and the clearance around the outer race of the rolling contact bearing is usually of the order of 0.25 mm. The outer bearing race is prevented from rotating (dogged), but it can orbit around the centre of rotation, while at the same time squeezing a pressure film ahead of it.

There are a number of interesting variations in the design and application of the squeeze-film damper bearing. For example, excessive axial flow of the fluid can be prevented by close fitting endplates or by rubber 'O' rings. However, the most important difference in the design philosophy of squeeze-film damper bearings exists between those where the rotor is allowed to find its own position within the clearance circle, and those where the rotor is held centrally within the clearance circle by a retaining spring. In the former variation, which is the configuration usually employed in aero gas-turbines manufactured in the United Kingdom, the rotor will naturally lie at the bottom of the clearance circle when the turbo-machine is at rest and until sufficient unbalance is generated to lift it off. In the latter configuration, which is that usually employed by aero gas-turbine manufacturers in the U.S., the retaining spring often takes the form of a set of cantilever rods surrounding the rotor in an annular ring (squirrel cage), on which the outer shell of the squeeze-film damper bearing is mounted.

Much of the earlier analysis of squeeze-film damper bearings, for example [2–4], has been based upon the assumption that the steady-state motion of the rotor center will be a circular synchronous orbit around the bearing geometric center. For this condition, it has been shown [13] that it is possible for a flexible rotor, supported by centrally preloaded squeeze-film damper bearings, to pass smoothly through a flexural critical speed. However, the assumption

Contributed by the Gas Turbine Division and presented orally at the Gas Turbine Conference and Products Show, Houston, Texas, March 9–12, 1981, of THE AMERICAN SOCIETY OF MECHANICAL ENGINEERS. Revised manuscript received at ASME Headquarters March 4, 1981.

that the rotor will orbit in a circular synchronous manner only applies to the case where a centralizing spring is used in parallel with the squeeze-film damper bearing or where the rotor is mounted vertically.

The squeeze-film damper bearing which operates without a centralizing spring has the obvious advantage of simplicity with a resulting reduction in both production costs and complexity of assembly. While there is little doubt that this type of squeeze-film damper does function in practice as a vibration inhibitor, it would appear to be possible to produce a poor design which will amplify, rather than attenuate, the exciting force. Unfortunately, there has been very little previous investigation either experimental or analytical, of the uncentralized squeeze-film damper bearing and surprisingly, no previous attempt to evaluate the effectiveness of this type of squeeze-film damper bearing as a function of the relevant system parameters.

It is the purpose of this paper to demonstrate both experimentally and analytically, the ability of an uncentralized squeeze-film damper bearing to reduce the amplitude of vibration and transmitted force, produced by simple unbalance or the proximity of a critical speed.

At the same time, it is hoped to throw some light on the mechanism by which the squeeze-film damper bearing reduces the effects of vibration. For example, by illustrating whether the device removes a critical speed from the engine running range by adding flexibility to the system and hence lowering the critical speed, or alternatively whether it reduces the vibratory amplitudes by damping while leaving the critical speed unchanged.

Theory

Analyzing the simple bearing-rotor system shown in Fig. 1, the following assumptions are made:

(*a*) The rotor is symmetric with part of its mass lumped mid-way between the bearings and the remainder evenly divided and lumped at the bearing stations (implying operation below the second critical speed).
(*b*) The angular speed of rotation is constant.
(*c*) Unbalance can be defined in a single plane.
(*d*) No significant exciting forces are introduced by the rolling contact bearing.
(*e*) There is no gyroscopic effect.

Employing, in this instance, the short bearing approximation, and the π-film model, with atmospheric inlet and end pressures as respresentative of conditions within the squeeze-film bearing, it is possible to derive [14], the following nondimensional form of the equations of motion.

$$\epsilon_B'' = \epsilon_B \psi'^2 + \frac{\bar{W}}{\Omega^2}\cos\psi_B + \frac{1}{2\alpha\Omega^2}\left[\epsilon_D\cos(\psi_D-\psi_B)-\epsilon_B\right] - \frac{2B}{\Omega}\left[\epsilon_B'\psi_B' I_1 \epsilon_B' I_2\right] \quad (1)$$

$$\psi_B' = \frac{1}{\epsilon_B}\left\{-2\epsilon_B'\psi_B' - \frac{\bar{W}}{\Omega^2}\sin\psi_B + \frac{1}{2\alpha\Omega^2}\epsilon_D\sin(\psi_D-\psi_B) - \frac{2B}{\Omega}\left[\epsilon_B\psi_B' I_3 + \epsilon_B' I_1\right]\right\} \quad (2)$$

$$\epsilon_D = \epsilon_D\psi_D'^2 + \frac{\bar{W}}{\Omega^2}\cos\psi_D - \frac{1}{\Omega^2}\left[\epsilon_D - \epsilon_B\cos(\psi_D-\psi_B)\right] - \frac{2\zeta}{\Omega}\epsilon_D' + U\cos(\omega t-\psi_D) \quad (3)$$

$$\psi_D'' = \frac{1}{\epsilon_D}\left[-2\epsilon_D\psi_D' - \frac{\bar{W}}{\Omega^2}\sin\psi_D - \frac{1}{\Omega^2}\epsilon_D\sin(\psi_D-\psi_B) - \frac{2\zeta}{\Omega}\epsilon_D\psi_D' + U\sin(\omega t-\psi_D)\right] \quad (4)$$

where,

$$I_1 = \int_{\theta_1}^{\theta_1+\pi}\frac{\sin\theta\cos\theta}{(1+\epsilon_B\cos\theta)^3}d\theta$$

$$I_2 = \int_{\theta_1}^{\theta_1+\pi}\frac{\cos^2\theta}{(1+\epsilon_B\cos\theta)^3}d\theta \quad (5)$$

$$I_3 = \int_{\theta_1}^{\theta_1+\pi}\frac{\sin^2\theta}{(1+\epsilon_B\cos\theta)^3}d\theta$$

$$\theta_1 = \tan^{-1}\left(\frac{-\dot{\epsilon}_B}{\epsilon_B\dot{\psi}_B}\right)$$

and the nondimensional terms U, B, $\bar{W}$, α, ζ and Ω are defined in the Nomenclature.

The four simultaneous nonlinear differential equations are integrated forward in time until a steady-state solution is reached, if such a solution exists. For the purpose of this

Nomenclature

B = bearing parameter ($\mu RL^3/m_B\omega_c c^3$)
c = radial clearance (housing radius − journal radius)
C_c = critical damping coefficient
C_d = damping coefficient
e = eccentricity between journal center and housing center
e_u = unbalance eccentricity
F_u = unbalance force ($m_D e_u \omega^2$)
G = rotor peak-to-peak amplitude
g = gravitational acceleration
$I_{1,2,3}$ = Integrals defined by equation (5)
L = squeeze-film damper bearing land length
m_B = mass lumped at either of the bearing stations
m_D = mass lumped at the rotor mid-span
R = bearing radius
U = unbalance parameter ($F_u/m_D c\omega^2$)
$W_B = m_B g$
$W_D = m_D g$
W = gravity parameter ($W_D/m_D c\omega_c^2$ or $W_B/m_B c\omega_c^2$)
α = mass ratio (m_B/m_D)
ϵ = eccentricity ratio (e/c)
ζ = damping ratio (C_d/C_c)
θ = angle measured from line of centers (θ_1 = angle from line of centers to start of positive pressure region)
μ = lubricant absolute viscosity
ψ = attitude angle
ω = rotor angular speed (ω_c = pin-pin critical speed)
Ω = speed ratio (ω/ω_c)
$(')$ = $d/d(\omega t)$

Subscripts

B = bearing
d = disk

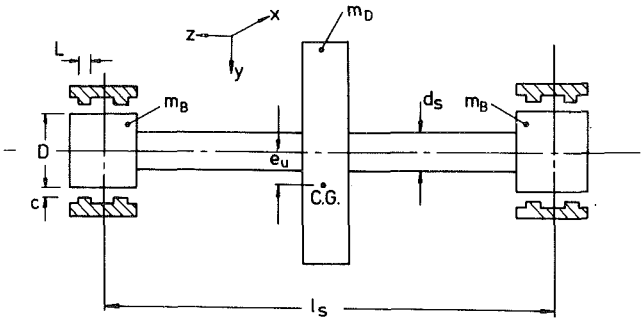

Fig. 1 Simple lumped-mass flexible shaft model with squeeze-film damper bearings

investigation, "steady-state" is defined as the condition where the maximum force transmitted to the bearing support is constant with respect to dimensionless (ωt) within a prescribed accuracy limit, while at the same time the motion orbits converge asymptotically to an approximately steady condition. To reduce the considerable effort required in analysing the motion orbit data, the steady-state orbits of the journal and disk centers are plotted automatically with the aid of a Calcomp Graph Plotter.

Experiment

The flexible rotor, used in the experimental portion of this investigation, consisted of an integral steel disk and shaft. The disk was 0.0503 m (2 in.) thick and 0.127 m (5 in.) in diameter, while the shaft was of constant diameter 0.0381 m (1.5 in.). The disc was located at the mid-span of the shaft which was in turn supported in two rolling-contact bearings. A ball bearing was 0.6096 m (24 in). The outer face of each of the rolling contact bearings was located at the drive shaft end and a roller bearing at the free end. The distance between the centres of the two bearings was located with an interference fit into a cylindrical steel ring, which served as the damper journal. The squeeze-film was located between this journal and an annular ring with a circumferential groove, which was located with a force fit in the massive support pedestal. For the rigid support tests, which were used as a basis for comparison, the damper journal and the squeeze-film outer ring were combined in one solid member, which could also be located with a force fit in the bearing pedestal.

In order to obtain a wide range of values for the bearing and gravity parameters B and $\bar{W}$, a number of interchangeable journals and outer squeeze-film rings of different critical dimensions were used. These dimensions produced squeeze-film radial clearances of 0.0635 mm (0.0025 in.), 0.127 mm (0.0050 in), and 0.1905 mm (0.0075 in.), while the available land lengths were 7.62 mm (0.3 in.) and 15.24 mm (0.6 in.).

A section through a squeeze-film bearing and the bearing pedestal is shown in Fig. 2. Rotation of the journal and the attached outer race of the rolling contact bearing, was prevented by means of a simple plastic loop, which allowed the journal to move freely within the clearance space, but prevented it from rotating.

The rotor was driven by means of a d.c. motor, through a step-up belt drive, to a maximum speed of 17,000 rpm. The rotor was connected to the drive shaft through a P.V.C. connector, which acted as a flexible coupling.

Two types of oil were used during the experiments reported here, namely SAE 30 and turbine oil 3. Hence, two quite different values of the fluid viscosity were obtained. The oil supply pressure to the squeeze-film was kept relatively low at about 14 kN/m^2 (approximately 2 lbf/in^2), just sufficient to maintain an adequate supply of oil to the film, while the end clearances were kept relatively large at about 0.4 mm (approximately 0.015 in.). In this way, it was possible to simulate atmospheric supply and end pressures.

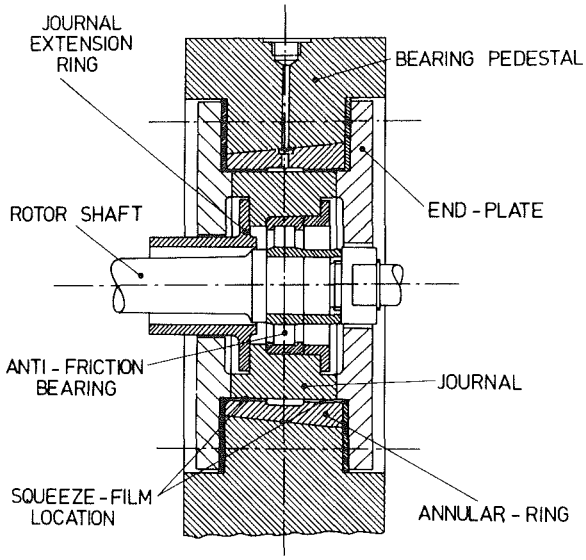

Fig. 2 Bearing pedestal with squeeze-film damper

The motion of the disc centre was detected by two pairs of noncontacting inductive transducers – one pair mounted vertically and the other mounted horizontally. A similar arrangement was employed for detecting the journal motion, but for this case because of space limitations, the axis of the transducers were rotated through 45 deg. The signals from the transducers could be displayed on an X-Y oscilloscope, in order that the complete orbit could be photographed or recorded on a UV oscillograph.

Although the original integral shaft-disk assembly was machine balanced, it was found to have a relatively large residual unbalance. Hence, to facilitate finer balancing, rings with equispaced holes were attached to either side of the disk. Thus, by trial-and-error the residual unbalance was reduced until the peak-to-peak amplitude at the first critical speed was only about 0.05 mm (0.002 in.). Further reduction in this residual unbalance was found to be impossible. However, it was estimated that this residual out-of-balance was less than 4 percent of the added unbalance employed during this investigation. A schematic layout of the apparatus used in this investigation is given in Fig. 3.

Results

A plot of the growth and decay of the journal centre and disk center orbits as the rotor increases speed through the first flexural critical speed, obtained from the proposed analytical treatment, is given in Fig. 4. So that these theoretical orbits can be compared with those obtained experimentally, the system parameters employed in the analysis are very close to those appropriate to the test rig. From sets of orbits such as those shown in Fig. 4, response curves for various combinations of system parameters are computed. A full tabulation of these theoretical results can be found in [15], but Figs. 5 and 6 are examples of the analytical results obtained.

The experimental tests were begun with rigidly supported bearings, that is with no squeeze-film present. The first flexural critical speed for this rigidly supported case was found to be 7248 rpm slightly higher than had been predicted with an available transfer matrix program [16]. Examples of the peak-to-peak amplitudes met with in the rigid support case, are as follows: 0.289 mm (0.0114 in.) for an unbalance of 1.016 gm cm and 0.502 mm (0.0205 in.) for an unbalance of 2.032 gm cm. The response for the rigid support case was

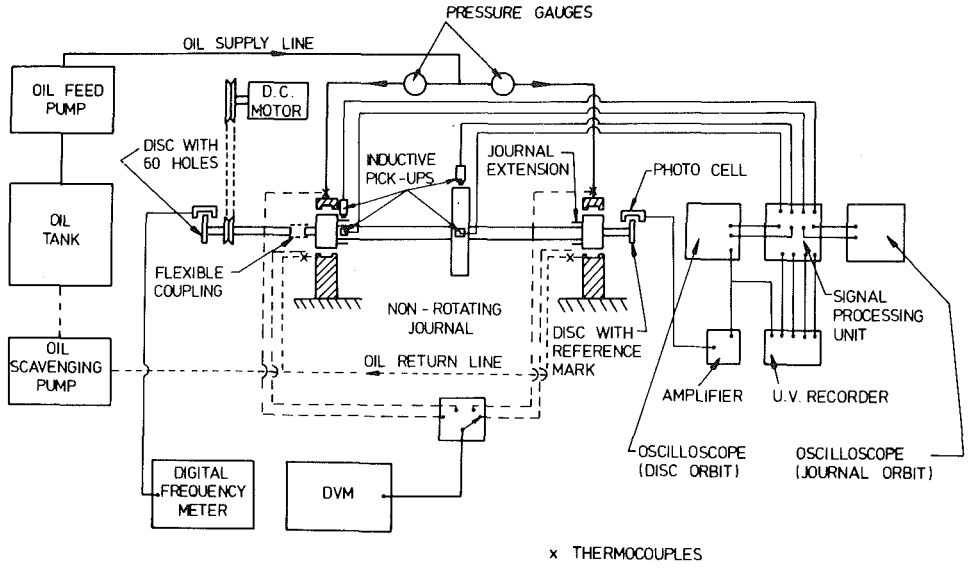

Fig. 3 Schematic lay-out of experimental apparatus

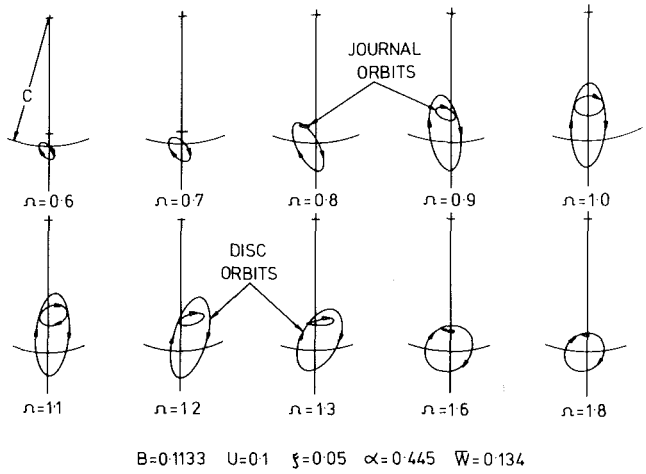

Fig. 4 Variation with speed of the journal and disc orbits determined analytically

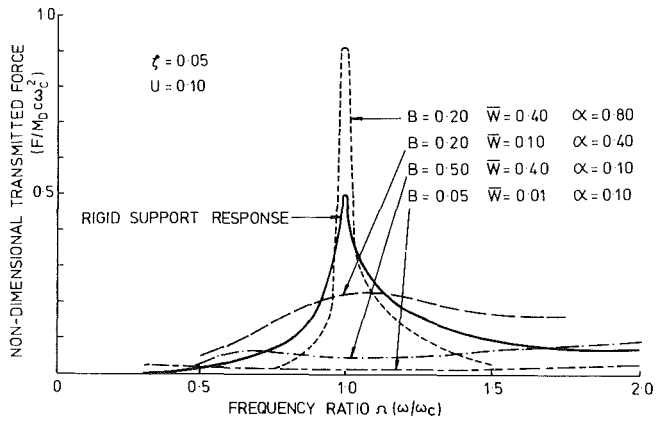

Fig. 6 Theoretical transmitted force curves for a flexible rotor supported by uncentralized squeeze-film damper bearings

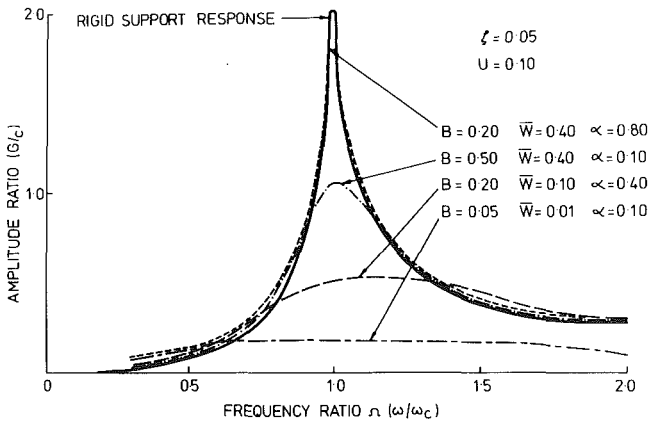

Fig. 5 Theoretical amplitude curves for a flexible rotor supported by uncentralized squeeze-film damper bearings

always accompanied by a sharp resonance peak at the critical speed, for example see Fig. 7(*a*). This would appear to indicate that the system damping was very low. Even for the low unbalances reported here, the disk amplitudes obtained were large and because it was thought inadvisable to risk permanent set of the rotor shaft, or possibly even destruction of the experimental rig, no further rigid bearing tests have so far been carried out.

Experimental tests were now carried out with squeeze-film dampers supporting the rotor. Firstly, a series of disk center orbits as the rotor increases in speed through the first flexural critical speed were obtained. These orbits are shown on the print from a polaroid photograph given in Fig. 8. These orbits can be compared with those shown in Fig. 4.

The total number of response curves, which could be obtained from the possible combinations of system parameters available with the present experimental rig, is obviously too great for inclusion in this report. However, Fig. 9 shows a number of response curves derived for the groups of system parameters listed in Table 1.

All of the reported results in Table 1 were for the case where $U=0.1$, which is considered to be normal unbalance. However, a further programme of work with larger unbalance is in progress and Fig. 10, is an example of the results being obtained. This figure shows journal and disk orbits for unbalances of $U=0.1$, 0.2 and 0.3 applied to the same system. All of these orbits were obtained at a rotor speed of 7058 rpm which is approximately the first flexural critical speed for the rotor system fitted with squeeze-film damper bearings. The

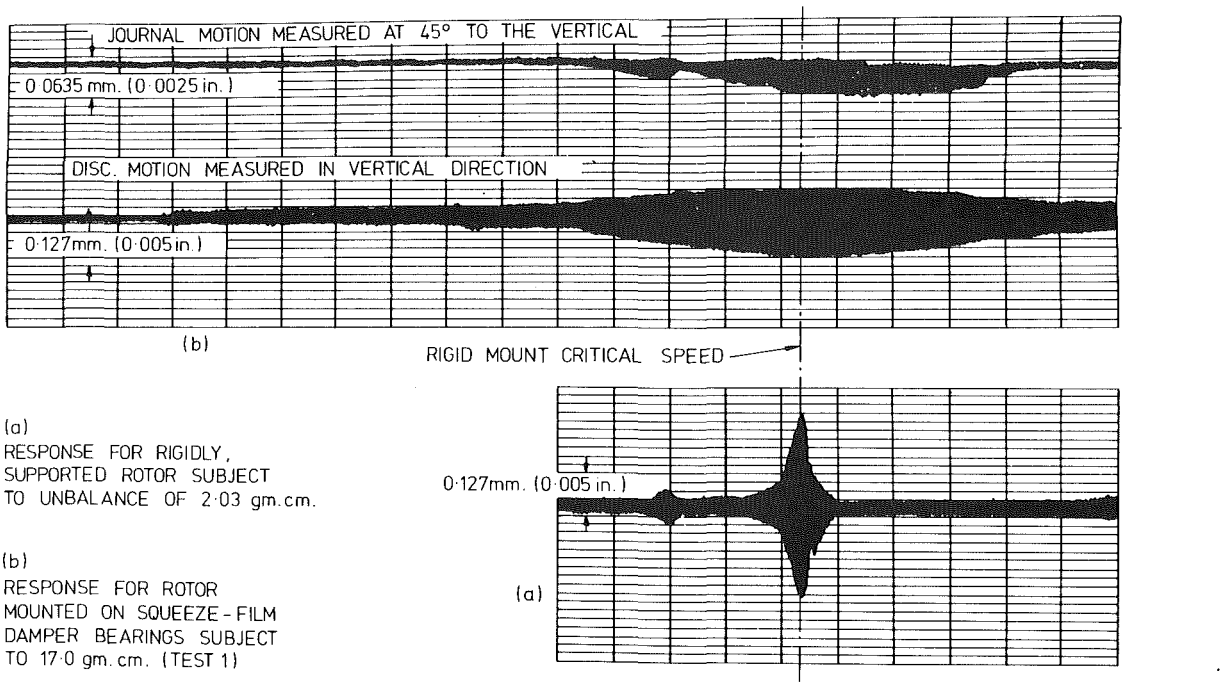

Fig. 7 Measured rotor motions with and without squeeze-film damper bearings

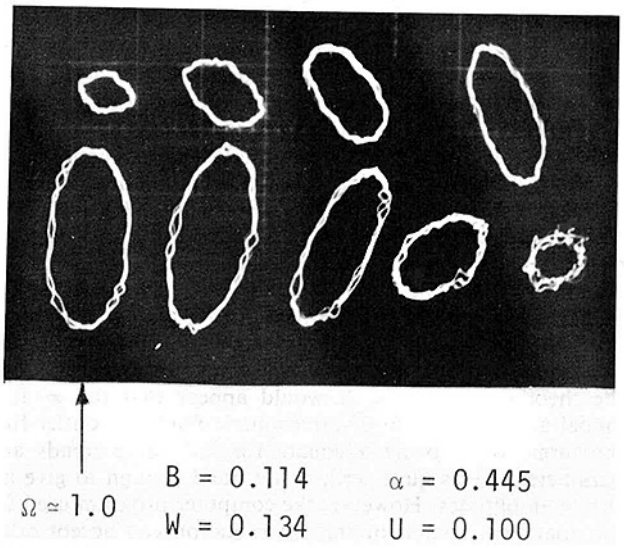

Fig. 8 Variation with speed of experimentally determined rotor orbits

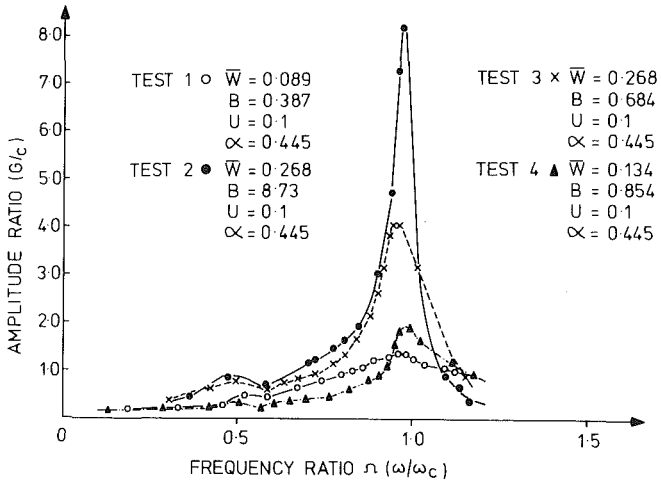

Fig. 9 Experimental amplitude curves for a flexible rotor supported by uncentralized squeeze-film damper bearings

Table 1 Data for the reported tests

Test	c (mm)	L (mm)	Oil Type	Average Viscosity NS/m^2	Unbalance (gm cm)	U	$\bar{W}$	B	α
1	0.1905	7.62	SAE 30	35.98×10^{-2}	17.00	0.1	0.089	0.387	0.445
2	0.0635	7.62	SAE 30	30.10×10^{-2}	5.67	0.1	0.268	8.731	0.445
3	0.0635	7.62	Turbine 3	2.36×10^{-2}	5.67	0.1	0.268	0.684	0.445
4	0.1270	7.62	SAE 30	23.53×10^{-2}	11.33	0.1	0.134	0.854	0.445

measured peak-to-peak amplitudes for $U=0.2$, and 0.3, are 1.114 and 1.234, respectively times that obtained when $U=0.1$.

Discussion

There can be seen to be a close relationship between the theoretically predicted motion orbits shown in Fig. 4, and the measured orbits shown in Fig. 8. Both of these sets of orbits show an interesting trend. The disk orbits in each case begin as extremely small elliptical excursions whose axes have positive slope. Then, as the rotor increases speed, these excursions grow in magnitude and the major axis of the ellipse precesses in the direction of rotation. Near to the rigid mount resonance ($\Omega=1.0$), the major axis is vertical. There is no rapid increase in the amplitude near to the resonance speed, nor rapid decay afterwards. Instead there is a relatively smooth transition until finally the disk orbit is almost cir-

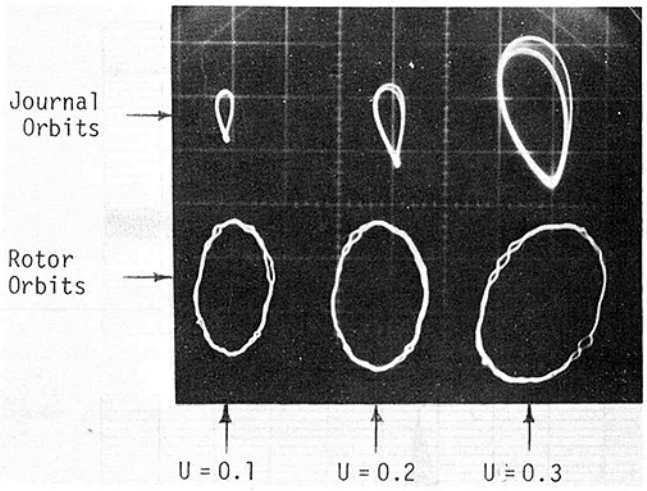

Fig. 10 Experimental disk and journal orbits for varying degrees of unbalance
For journal orbits 1 Division = 0.025 mm (0.001 in.)
For rotor orbits 1 Division = 0.0625 mm (0.0025 in.)

cular. This smooth progression through the critical speed is also shown by the experimental trace in Fig. 7(*b*) and the "peaky" response usually associated with a lightly damped, rigidly mounted system is shown in Fig. 7(*a*).

The typical theoretical response curves, shown in Figs. 5 and 6, clearly illustrate that an uncentralized squeeze-film damper bearing can be designed so as to significantly reduce the effects of vibration. From Fig. 5, it can be seen that the maximum disk amplitude for the case where $B=0.05$, $\bar{W}=0.01$ and $\alpha=0.10$ is only about 8 percent of the amplitude which would be expected if the bearings were rigidly supported. At the same time, the response curve for this set of parameters is extremely flat. With this sort of response it is perhaps not surprising that some past engine designers have suggested that the squeeze-film damper bearing had been instrumental in moving the critical speed to some other part of the engine speed range. In practice, it is unlikely that there would be much flexibility in the choice of value for the mass ratio α. For example, for the experimental tests reported in this paper, the mass ratio if 0.445 and consequently, the response curve in Fig. 5, for parameter values $B=0.20$, $\bar{W}=0.10$, and $\alpha=0.40$ would perhaps be more representative of the experimental equipment employed in the present investigation. Figure 6 illustrates the ratio of the force transmitted to the bearing structure, to the force which would be transmitted if the bearing supports were rigid. The groups of parameters employed in Fig. 6 are the same as those used in Fig. 5, and the trends are broadly the same. However, while the curve for the case of $B=0.05$, $\bar{W}=0.01$ and $\alpha=0.10$, shows a large reduction in the transmitted force, the curve for $B=0.20$, $\bar{W}=0.40$ and $\alpha=0.80$, indicates that the force transmitted to the bearing supports can be much greater than that which would be produced if the bearings were rigidly mounted. Once again the curve for the case where $B=0.20$, $\bar{W}=0.10$ and $\alpha=0.40$, would probably be closest to the conditions experienced with the present experimental equipment, although it should be emphasised here that at this stage in the experimental programme, actual transmitted forces have not been measured.

The U.V. oscillograph traces shown in Fig. 7 are very revealing. Firstly, they show that the disk amplitude experienced with an unbalance of 2.03 gm cm, acting on a system with rigidly mounted bearings is more than twice as great as that experienced by the same system when squeeze-film dampers are fitted and when the unbalance is almost ten times greater. Secondly, Fig. 7 supports the theoretical predictions in showing that the amplitudes growth and decay is smooth and quite unlike the sharp resonance peak associated with the critical speed of a rigidly mounted system. However, the maximum amplitude experienced with squeeze-film damper bearings still occurs approximately at the first pin-pin critical speed. Finally, the journal amplitude shown in Fig. 7, although measured at 45 deg to the vertical axis for convenience, does appear to help in explaining the mechanism by which the squeeze-film damper bearing reduces the rotor amplitude and transmitted force. For in the range where the maximum disk amplitude reduction is being effected, the journal amplitude is greatest. Hence, it would appear that this type of squeeze-film damper bearing operates by allowing room for journal movement to occur instead of disk movement.

The experimental response curves shown in Fig. 9 have the same general form as the predicted curves given in Fig. 5. Also, the trends produced by varying some of the system parameters can be seen to be the same. For example, when the bearing parameter B is large (8.73), the bearing becomes very rigid and a large amplitude is obtained. Then, as the bearing parameter is reduced, the amplitude falls until at $B=0.387$, the response becomes flat and smooth. Similarly, it is observed that the amplitude falls as the gravity parameter is reduced, from $\bar{W}=0.268$ to $\bar{W}=0.089$.

Unfortunately, because the experimental rotor/bearing system employed in this investigation was found to be much more lightly damped than the damping ratio $\zeta=0.05$ used in the theoretical analysis would suggest (in practice it was nearer to 0.005), it has not been possible to determine experimentally the amplitude response for rigidly mounted bearings. However, what can be observed from a comparison of Figs. 5, 7 and 9 is that the relative reduction in the ratio of the disk amplitudes for the case where squeeze-film damper bearings are fitted to those where the bearing supports are rigid, is even greater in practice than was predicted theoretically. At the same time, the absolute values of the amplitudes determined experimentally are greater than those predicted analytically. This difference in absolute amplitudes is thought to be due to the relatively simple film model used in the theoretical analysis. It would appear that the π- film model and assumption of atmospheric inlet and outlet film pressures, while being adequate for indicating trends and parameter effects quite well, is not good enough to give accurate amplitudes. However, the computer program used for the analytical section of this investigation can accept other film models and conditions, and already some success has been achieved in improving the accuracy of the theoretical results [15].

All of the results so far described in this paper, both theoretical and experimental, have been for the case where the unbalance parameter U is equal to 0.1. This value of U is roughly equivalent to the level of unbalance normally encountered in gas-turbine engines and similar machines. An investigation is currently in progress to determine the effect of large unbalances and Fig. 10 is an example of the results so far obtained. This figure gives the disk orbits determined for varying degrees of unbalance, but with all other conditions the same. The level of unbalance represented by $U=0.3$, is quite large, roughly equivalent to the case where a turbomachine sheds a blade and yet the disk excursion is only about 23 percent greater than that experienced with normal unbalance. Of course, the orbits shown in Fig. 10 are steady-state orbits and do not represent the transient conditions experienced with blade-loss. None the less, Fig. 10 is an impressive example of the ability of squeeze-film damper bearings to counteract unbalance.

Conclusions

From the work reported in this paper, it would appear that the vibratory effects of unbalance and sources of excitation in a flexible rotor-bearing system can be significantly reduced by supporting the bearings on squeeze-film dampers of the correct design. By the same token, a poorly designed squeeze-film damper bearing can result in forces, greater than those arising from rigidly mounted bearings, being transmitted into the machine structure.

In general, it is found that the gravity parameter $\bar{W}$ should be less than 0.1, and the bearing parameter should be about 0.1, if the squeeze-film damper bearing is to operate at its greatest efficiency. It is also found that the damper is more effective if the mass ratio α is kept small, but the mass distribution in a rotating machine is usually fixed from other design considerations.

From the close similarity between the predicted motion orbits of the disk and journal centres, and those which were measured experimentally, it would appear that the theoretical model employed in the analytical section of this investigation, is a good representation of the true situation. This confirmation of the proposed analytical treatment is further supported by the conformity between the predicted response curves and those obtained experimentally, plus the correct prediction of the effect of varying the system parameters. An extension of the work reported in this paper has indicated that a closer agreement between the predicted and measured vibratory amplitudes can be obtained by replacing the π-film model with a slightly more sophisticated model in the computer program.

A preliminary investigation into the effects of unbalances larger than the normal unbalance assumed in this work, indicated that squeeze-film damper bearings are capable of dealing with the steady-state effects of quite large unbalances.

Finally, the experimental results presented in this paper, would appear to indicate that the uncentralized squeeze-film does not overcome the effects of vibration in a rotating machine by moving the critical speed to a lower region of the speed range. In fact, from a study of the appropriate disk and journal motion orbits at a critical speed, it would appear that the uncentralized squeeze-film damper is simply a device which allows movement of the journal within the clearance circle to assist in overcoming the effect of the vibratory amplitude of the disk.

References

1 Magge, N., "Philosophy, Design and Evaluation of Soft-mounted Engine Rotor Systems," *Journal of Aircraft*, Vol. 12, No. 4, Apr. 1975, pp. 318–324.

2 White, D. C., "The Dynamics of a Rigid Rotor supported on Squeeze-film Bearings," Inst. Mech. Engrs., *Conference on Vibrations of Rotating Systems*, 213, 1972.

3 Mohan, S., and Hahn, E. J., "Design of Squeeze-film Damper Supports for Rigid Rotors," ASME *Journal Engineering Industry*, Aug. 1974, pp. 976–982.

4 Gunter, E. J., Barrett, L. E., and Allaire, P. E., "Design and Application of Squeeze-film Damper for Turbomachinery Stabilization," Report No. ME-4040-122-75, University of Virginia, 1975.

5 Holmes, R., "The Non-linear Performance of Squeeze-film Bearings," *Journal of Mechanical Engineering Science*, Vol. 14. 1, Feb. 1972.

6 Gunter, E. J., Barrett, L. E. and Allaire, F. E., "Design of Non-linear Squeeze-film Dampers for Aircraft Engines," ASME Paper No. 76-LUB-25, 1976.

7 Humes, B., "The Non-linear Performance of Squeeze-film Bearings." Ph.D. Thesis, University of Sussex, England, 1977.

8 Cunningham, R. E., "Influence of Oil Squeeze-film Damping on Steady-state Response of Flexible Rotor Operating to Super-critical Speeds," NASA Tech Paper 1094, Dec. 1977.

9 "Reduction Noise, more Flexibility Offer—Trent RB 303 Engineering," *Aviation Week and Space Technology*, Vol. 86. 39, Feb 1967.

10 "The Rolls Royce RB 211—Three-Shaft Turbo-Fan, *Aircraft Engineering*, Vol. 40(6), Apr. 1968.

11 Brown, P. F. "Bearings and Dampers for Advanced Jet Engines." SAE Paper No. 700318, 1970.

12 Penny, R. N., "The Development of a Glass Ceramic Regenerator for the Rover 2S/150R Engine," SAE Paper No. 660361, 1966.

13 Rabinowitz, M., and Hahn, E. J., "Steady State Performance of a Squeeze-film Damper Supported Flexible Rotor." ASME Paper No. 77-GT-51.

14 Cookson, R. A., and Kossa, S. S., "The Effectiveness of Squeeze-film Damper Bearings Supporting Flexible Rotors without a Centralising Spring," *Int. Journal of Mechanical Science*, Vol. 22, May 1980, pp. 313/324.

15 Kossa, S. S., "Theoretical and Experimental Investigation of Uncentralised Squeeze-film Damper Bearings," Ph.D. Thesis, Cranfield Institute of Technology, 1980.

16 Bannister, R. H., Personal Communication.

Performance and Air Pollutant Emissions of an Experimental Water/Residual Oil Emulsion Burner in a Commercial Boiler

J. Taylor Beard[1]

R. E. Hall

Industrial Environmental Research Laboratory,
U.S. Environmental Protection Agency,
Research Triangle Park, N.C.

The performance and air pollution emissions of an experimental water/oil emulsion burner are presented. The burner was fired with two residual oils at selected emulsion water fractions. In addition, various stoichiometric ratios and two load conditions were used to determine how operational parameters influenced the results. Particulate mass emissions and particle size distributions are presented. Examples show that, even though particulate mass may decrease, the total amount of fine particulate emissions may increase by using water/oil emulsions. The performance of the boiler is reduced when large fractions of water are used in the emulsion due to latent heat losses. This performance loss may be only slightly recovered by operating at a reduced stoichiometric ratio corresponding to a smoke limit. NO_x and CO emissions data are also presented for various test conditions, but neither were affected significantly by use of water/oil emulsions.

Introduction

The performance and environmental effects of water/oil emulsions fired in special burners have been shown to be influenced by the fuel, equipment design, and operating parameters [1-8]. In order to obtain technical information about oil and water/oil emulsions, the U.S. Environmental Protection Agency's Industrial Environmental Research Laboratory in Research Triangle Park, N.C., has established an ongoing in-house experimental program. The research presented in this paper was conducted as part of that experimental program.

Early reports on burning emulsions of oil and water were that emulsions burn faster, improve combustion, and reduce soot formation in comparison to conventional oil combustion [1]. In the late 1960's, Barrett, et al., [2] of Battelle-Columbus Laboratories performed preliminary tests of water/oil emulsions under contract to the U.S. Public Health Service, one of EPA's predecessors. Scherer and Tranie [3] reported test results in which particulate mass was carefully measured, but few data were obtained for other emissions, and no efficiency data were obtained. Turner and Siegmund showed that emulsions reduce thermally generated NO_x, but do not influence NO_x formed from fuel nitrogen [4]. Also, Dryer has reviewed information on combustion of emulsions from a variety of sources [5,6].

More recently, Hall reported results for commercial boilers comparing the Total and Cottell Reactor water/oil emulsifiers with conventional distillate and residual oil firing at similar stoichiometric ratios [7,8]. He presented four applications where emulsions caused the particulate emissions to be reduced and showed that smoke and CO emissions may be increased or reduced, depending on fuel, equipment, and operation. NO emissions were reduced while firing distillate oil but were not significantly affected when residual oil was fired. The indicated changes in efficiency due to firing emulsions were also found to vary (from an increase of about 1 percent to a reduction of about 7 percent) in comparison to firing only oil, with the excess air being set for a smoke limit in both cases.

Elf Union, a French national petroleum company, in cooperation with SICMA, a European burner manufacturer, has developed various high pressure atomizing emulsion burners. These have been installed for commercial and industrial heating applications and for petroleum waste incineration. In 1971 preliminary tests were conducted in France jointly by Elf Union and one of EPA's predecessors, the U.S. National Air Pollution Control Administration [9]. The results indicated that NO_x emissions were increased with load and did not depend on whether a water/oil emulsion or only oil was fired. However, at high load with high stoichiometric ratios, firing an emulsion resulted in a slight increase of NO. Operation at lower than normal stoichiometric ratios was possible without encountering flame instability or high particulate levels when the emulsion was used. This capability, coupled with the trend of a decrease of NO_x with decreased excess air, pointed to the possibility of some reduction of NO_x by the use of emulsions.

[1] Currently with: Department of Mechanical and Aerospace Engineering, University of Virginia, Charlottesville, Va.

Contributed by the Air Pollution and Control Division of The American Society of Mechanical Engineers and presented at the Winter Annual Meeting. November 16-21, 1980. Chicago, Illinois. Manuscript received at ASME Headquarters July 24, 1980. Revised manuscript received February 7, 1981.

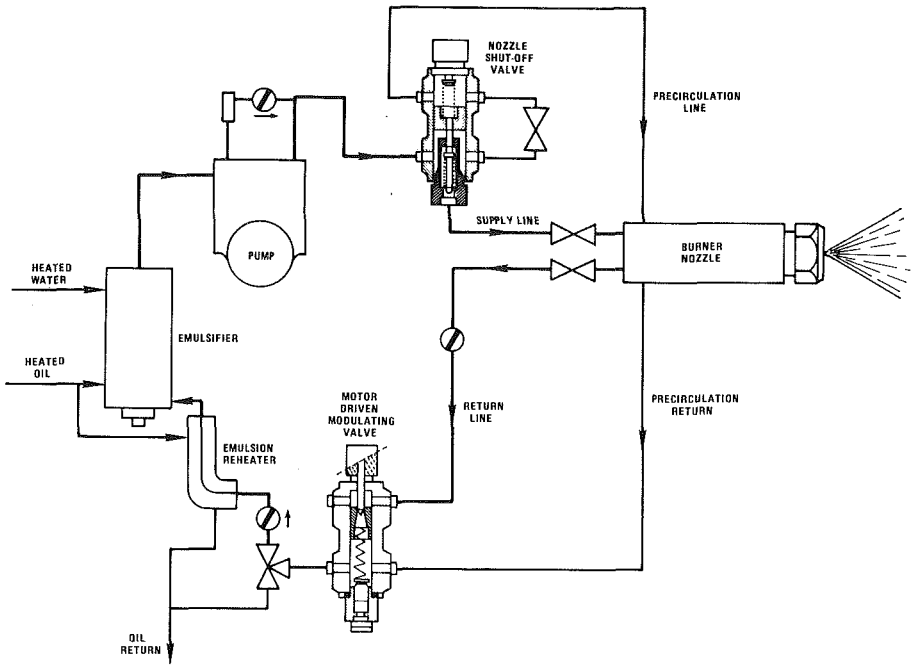

Fig. 1 Elf/SICMA experimental water/oil emulsion burner system

A decision was made to purchase and test an experimental Elf/SICMA emulsion burner modified for variable emulsion and combustion conditions. The objectives were to determine the influence of water fraction, stoichiometric ratio, and oil firing rate on burner performance and on gaseous and particulate emissions.

Burner and Test Description

The experimental Elf/SICMA emulsion burner was designed for return flow modulated firing of both distillate and residual oils. A schematic diagram of the burner system is shown in Fig. 1. The designed oil firing rates were variable from around 0.038 to 0.227 m^3/hr (10 to 60 gph) by the use of different burner nozzles, blast tubes, and air handling components. According to the manufacturer, the emulsion water should be limited to 30 percent of the volume flow rate of a residual oil or 15 percent of a distillate oil. The burner port and air intake were modified for experimentally controlled firing in an available North American packaged Scotch boiler rated at 0.73 MW (2.5×10^6 Btu/hr).

Tests were conducted with a residual fuel oil fired at intermediate (0.045 m^3/hr or 12 gph) and high (0.064 m^3/hr or 17 gph) load conditions. Water fractions in the emulsion were varied from zero to 0.38 kg water/kg fuel in order to determine the influence of the amount of water on performance and pollutant emissions. Combustion air was controlled for stoichiometric ratios between 1.1 and 2.0 in order to determine the characteristics associated with reduced excess air operation. Most of the results were obtained with 21.8° API fuel oil, but some results were obtained with 19.2° API oil. The properties of these oils are presented in Table 1. Unless specified as data obtained from tests with 19.2° API oil, data discussed in this report and shown in the figures were obtained from tests with 21.8° API oil.

Operating Experience

Typical burner testing include a 2 hr warmup period. After each test condition change, at least 30 min of stable combustion were required before data were taken. Approximately 10 min were required for each test where only gaseous and smoke emissions were measured. One hour of sampling was required for total particulate mass and particulate size test. During the test program the unit was operated approximately 500 hrs.

Combustion stability became a problem only at the higher firing rate when using the upper limit of emulsion water regardless of the stoichiometric ratio. This may have been the result of the nozzle being too small for the flow rate of the emulsified fuel or it may have simply been a result of too much water.

Test Measurements

During each typical test run, data were manually recorded for the following physical parameters: fuel flow rate; emulsion water flow rate; various oil and water pressures and temperatures; stack temperature; ambient air temperature; barometric pressure; condenser cooling water temperatures; and orifice pressure differences.

Gaseous emissions were measured with the following continuous analyzers:

Gas	Analyzer
Oxygen (O_2)	Paramagnetic
Carbon Dioxide (CO_2)	Nondispersive Infrared (NDIR)
Carbon Monoxide (CO)	Nondispersive Infrared (NDIR)
Nitric Oxide (NO)	Chemiluminescence
Hydrocarbon (HC)	Flame Ionization

It should be noted that an unheated sampling line was used. Therefore, NO_2 data could not be obtained and hydrocarbon data may be artifically low.

Smoke was measured under steady state operating conditions and a Bacharach smoke spot number was obtained by averaging ten smoke spots taken at 1 minute intervals [10].

Total particulate emissions were determined for selected test conditions using the EPA Method 5 testing procedure. A minimum of two samples were collected at each test condition.

Table 1 Properties of residual fuel oils used

Parameter			
API (deg		21.8	19.2
Carbon (percent)		86.9	86.9
Hydrogen (percent)		12.2	11.85
Nitrogen (percent)		<0.10	<0.10
Ash (percent)		0.04	0.05
Sulfur (percent)		1.02	1.10
Heat of Combustion			
Gross	(Btu/lb)	18,981	18,879*
	(MJ/kg)	44.150	43.912*
Net	(Btu/lb)	17,868	
	(MJ/kg)	41.560	
Density			
311 K			
(100°F)	(g/cm^3)	0.9086	
	(kg/m^3)	908.6	
372 K			
(210°F)	(g/cm^3)	0.8699	0.8858*
	(kg/m^3)	869.9	885.8*
Viscosity (cp or mPa)			
311 K			
(100°F)		80.77	
372 K			
(210°F)		8.99	

*Best estimate.

Particulate size distributions were determined by using the Mark III Andersen Stack Sampler. A minimum of two Andersen samples were obtained at each selected test condition. A microcomputer with an EPA program providing correction coefficients was used to obtain cumulative mass fractions corresponding to aerodynamic particle diameters [11].

In addition, data were obtained for an EPA Level 1 Environmental Assessment [12]. This required the use of a Source Assessment Sampling System (SASS) Train with subsequent data reduction by Battelle-Columbus Laboratories [13]. The analysis included: spark source mass spectroscopy to provide inorganic particulate information; atomic absorption spectroscopy to provide data about the emission of mercury (Hg), arsenic (As), and antimony (Sb); and total chromatographable organic analysis, gravimetric analysis, infrared analysis, and low resolution mass spectroscopic analysis to obtain information about organic emissions.

Performance Evaluation

The relative performance of the boiler at various emulsion test conditions can be evaluated by either measuring the energy released in a steam condenser or computing energy losses to the boiler room and up the stack [14]. Because of a lack of precision in the available test measurments at the

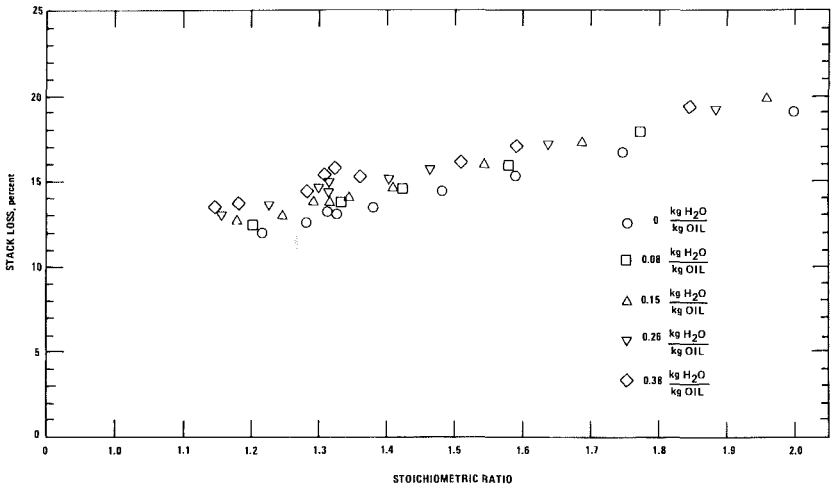

Fig. 2 Stack losses at intermediate firing rate

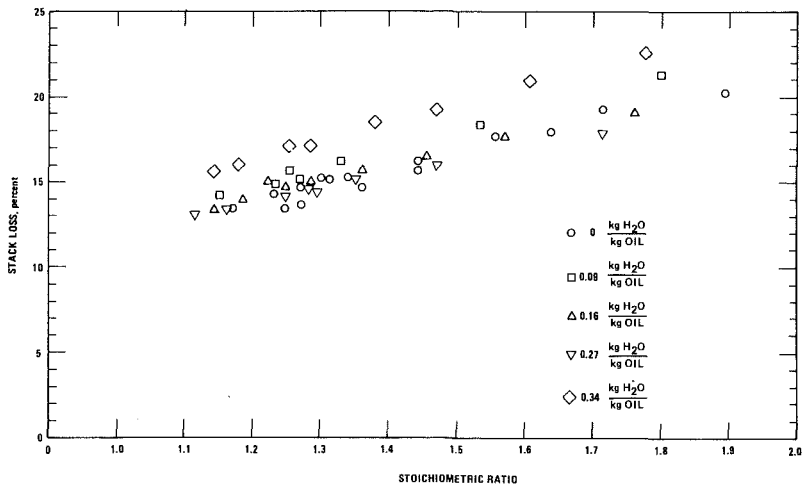

Fig. 3 Stack losses at high firing rate

condenser, the energy loss method was selected. It was assumed that the energy loss to the boiler room did not vary significantly and that stack loss was the major energy loss variable.

Latent and sensible flue gas stack losses were conveniently computed using a programmable calculator. Included were the intermediate calculations to determine the oil and water flow rates, the net stack gas temperature, the amounts of major component flue gases, and the average flue gas specific heat.

The performance results are shown in Figs. 2 and 3 as stack losses corresponding to the intermediate (0.045 m^3/hr or 12 gph) and high (0.064 m^3/hr or 17 gph) oil firing rates, respectively. Although there is some scatter in the data, the results show the expected trend of reduced stack losses associated with reduced stoichiometric ratio. Increased stack losses for increased amounts of emulsion water are caused by the greater latent heat losses. From a combustion efficiency standpoint, it is interesting to note that for the current test program good combustion energy release occurs, and very little energy loss is associated with production of carbon particulate and carbon monoxide.

Particulate Emissions

The averaged total particulate mass emissions are presented in Fig. 4. With one exception, the tests showed less total particulate emissions when an emulsion was fired than when only oil was fired. Although considerable scatter was noticed (up to 22 percent), the averaged results showed an increased total particulate mass emitted only when an emulsion having 0.09 kg water/kg fuel was used at the higher firing rate.

Figure 4 shows that as the amount of emulsion water increased the total particulate emissions generally decreased. The results also indicate that less particulates (on a normalized basis) are emitted at the higher firing rates, except when the unit operates at the upper limit of water in the emulsion. For either firing rate at high values of water in emulsion, the particulates appear to approach a lower limited value (around 42 mg/m^3). This value is only 20 percent higher than the anticipated particulate emissions from the fuel ash alone without any combustibles. Consequently, at the high water emulsion values, the carbon burn-out is very good.

When the burner was fired with the heavier API 19.2° oil in comparison with the API 21.8° oil, total particulate mass emissions were greater at any given water-to-oil ratio. This was probably caused by the poorer atomization quality of the heavier oil. Note that a modest amount of emulsion water had a greater impact on reducing particulate emissions for the heavier oil than for the lighter API 21.8° oil.

The cumulative particulate size distributions are shown for the intermediate and high firing rates in Figs. 5 and 6, respectively. The emulsion causes smaller particulates to be emitted. This is probably due to improved secondary atomization. Figure 5 shows that, at the intermediate flow rate, an increase of the amount of water causes a general reduction in particulate sizes. Although some overlaying of the results is found at the higher firing rate (Fig. 6), the trend is generally established. Both figures also confirm that the average particulate sizes are larger for the heavier API 19.2° oil than for the API 21.8° oil.

It is important to note that the fractions of fine particulates (less than 2.5 μm) from emulsions may be significant. Consider the example of the API 21.8° oil at the higher firing rate. The fraction less than 2.5 μm is 63 percent for the emulsion with 0.34 kg water/kg oil, compared to about 42 percent when firing oil only. From Fig. 4, the total particulate emissions were 46.5 mg/m^3 at the high water emulsion value compared with 70 mg/m^3 with only oil being fired. Therefore, about 29.3 mg/m^3 of particulates smaller than 2.5 μm were emitted with either the high water emulsion or only oil being fired. Thus, the mass of fine particulates remained constant even though the percentage increased when firing an emulsion. On the other hand, when the heavier oil (API 19.2°) was fired at the intermediate rate, more fine particulates were emitted with the emulsion than for firing oil only.

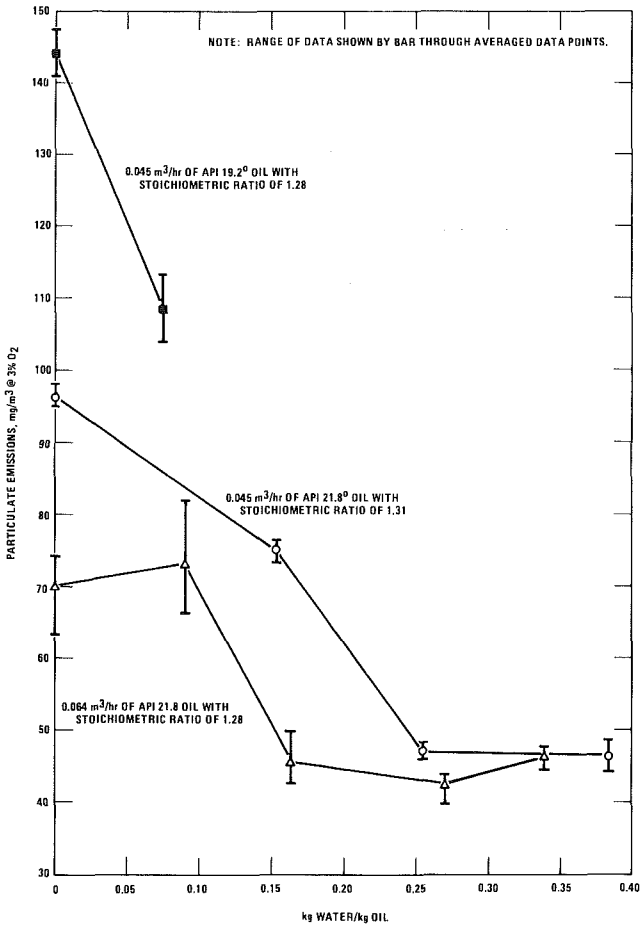

Fig. 4 Particulate emissions from various emulsions

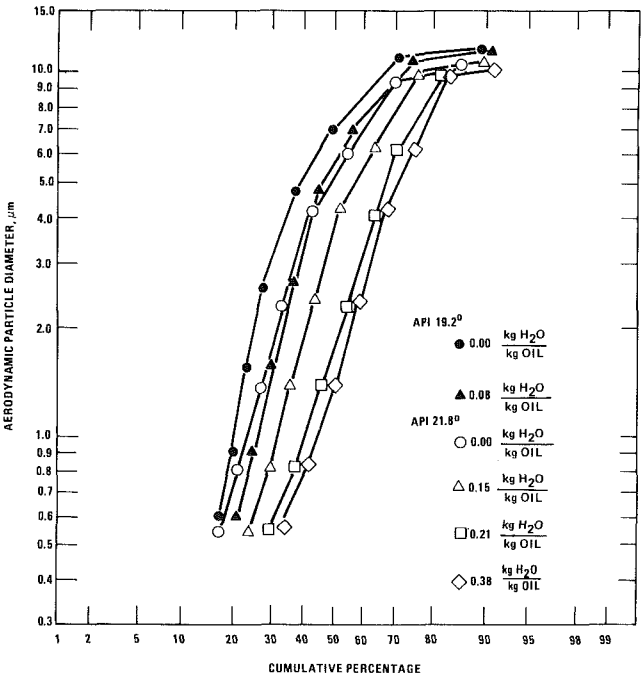

Fig. 5 Particulate size distribution for intermediate firing rate

The data indicate that in all cases considerably more than 99 percent of the particulate emitted was in the inhalable size range (defined as less than 15 μm).

Smoke Emissions

The smoke emissions are presented as Bacharach smoke spot numbers for the intermediate and high firing rates in Figs. 7 and 8, respectively. Both figures show that low smoke is associated with firing only oil. As the water fraction in the emulsion is increased to moderate levels, the smoke increases; and as the water fraction increases to the upper limit, the smoke is generally reduced to below that corresponding to only oil being fired. The influence of reduced stoichiometric ratio is to increase smoke, as is typical for conventional oil burners. For residual oil burners, the useful practice is to operate near a limiting Bacharach smoke number of 3 or 4, depending on the grade of oil being fired. Such a limiting value is recommended as being acceptable from the perspective of both efficiency and emissions [15].

There appears to be a modest advantage for high water fraction emulsions in terms of operation at lower stoichiometric ratios at a smoke limit. However, in consideration of the stack loss results (Figs. 2 and 3), a decrease in efficiency will generally result.

It is interesting to note that as the load is decreased to the intermediate firing rate the smoke emissions increase. This is probably associated with lower furnace temperatures and poorer air/fuel mixing (due to lower air velocities) at the lower firing rate.

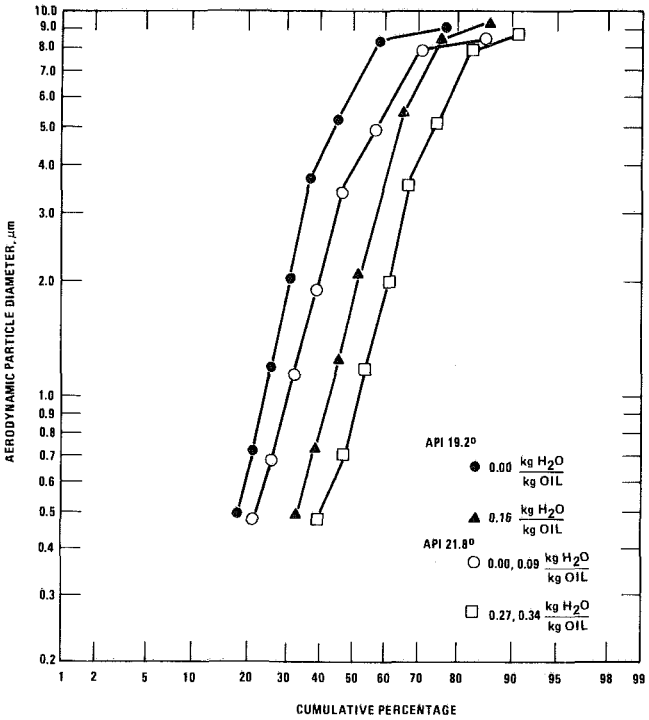

Fig. 6 Particulate size distribution for high firing rate

Nitric Oxide Emissions

The nitric oxide, NO, emissions corresponding to the intermediate and high firing rates are presented in Figs. 9 and 10, respectively. As expected, NO emissions are reduced at lower stoichiometric ratios. They are also higher at the higher firing rate, probably as a result of higher combustion temperatures.

At the intermediate firing rate, the emulsion caused greater NO emissions when the stoichiometric ratio exceeded 1.4. Below a stoichiometric ratio of 1.4, it appears that NO emissions are reduced by firing higher water emulsions.

At the higher firing rate a slight increase in NO emissions is observed for emulsions with 0.16 and 0.27 kg water/kg oil in comparison to firing with only oil. This behavior probably results from an increased combustion temperature associated with better atomization up to these water/oil ratios. However, as the amount of water in the emulsion was increased to 0.34 kg water/kg oil, less NO was emitted than in the case where only oil was fired. This behavior probably results from the latent heat of water at this high rate reducing combustion temperatures, and thus reducing thermal NO formation. This

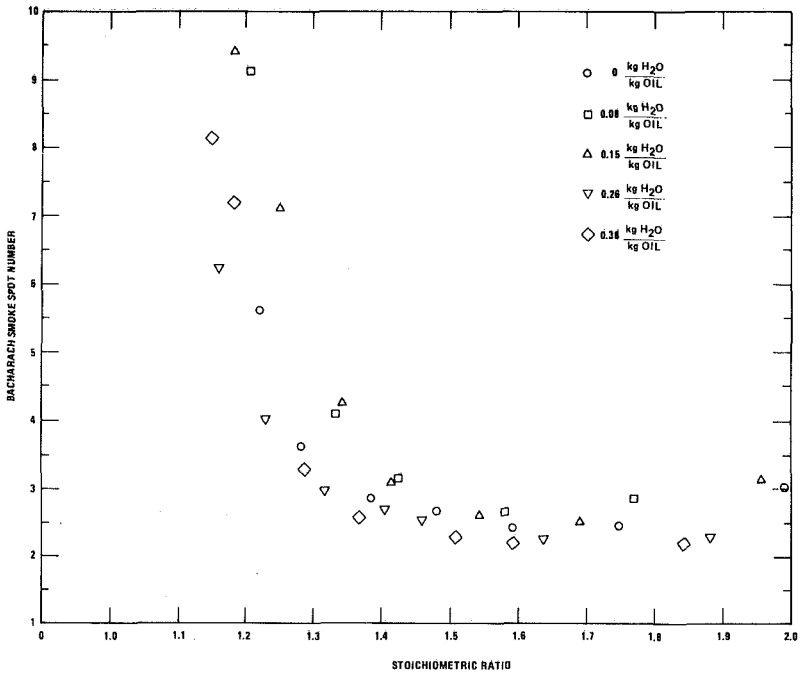

Fig. 7 Smoke at intermediate firing rate

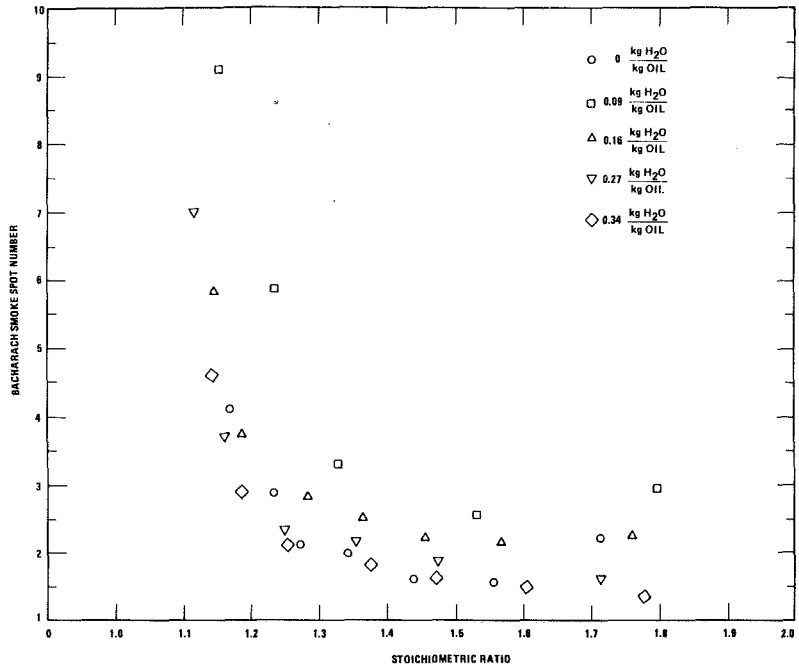

Fig. 8 Smoke at High firing rate

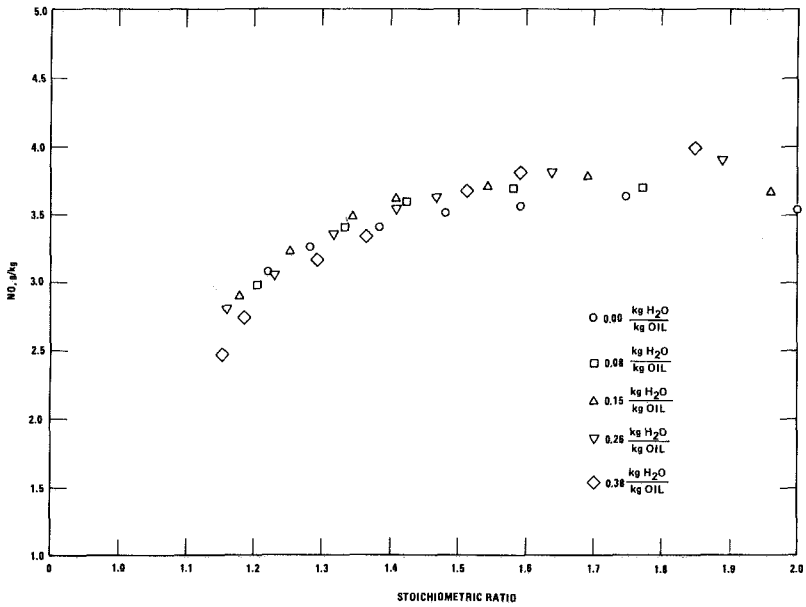

Fig. 9 Nitric oxide emissions at intermediate firing rate

could also explain the similar behavior noted at the intermediate firing rate for stoichiometric ratios below 1.4.

It should be noted that NO emissions are directly related to fuel nitrogen content. The nitrogen content of both fuels used in this study was relatively low for residual fuel oil.

Carbon Monoxide and Hydrocarbon Emissions

Emissions of carbon monoxide, CO, were found to be very low (less than 0.4 g/kg oil, or 30 ppm at 3 percent O_2) for all cases except for low stoichiometric ratios. The measured increase of CO at low stoichiometric ratios, as shown in Figs. 11 and 12, is consistent with accepted combustion theory [15]. Hydrocarbons were measured but were not detected under any conditions. As mentioned previously, this may be due to the unheated sampling line.

Trace Specie Emissions

Samples collected by the Source Assessment Sampling System (SASS) train, while firing the 0.26 kg water/kg oil emulsion at the high firing rate and while firing oil only at the high firing rate, were analyzed for trace species. The samples were analyzed by procedures as specified in reference [12]. Detailed results of the analysis are given in reference [13].

The only significant differences between the two samples occurred in the organic material analyses, as shown in Fig. 13. The general trend is that the fuel oil along emitted about 25 percent more material than the emulsion burner. However, fractions 3 and 4 deviate significantly from this trend. In fraction 3 the trend is completely reversed, with the emulsion burner emitting about twice as much as the fuel oil burner. This is significant since fraction 3 can contain species such as

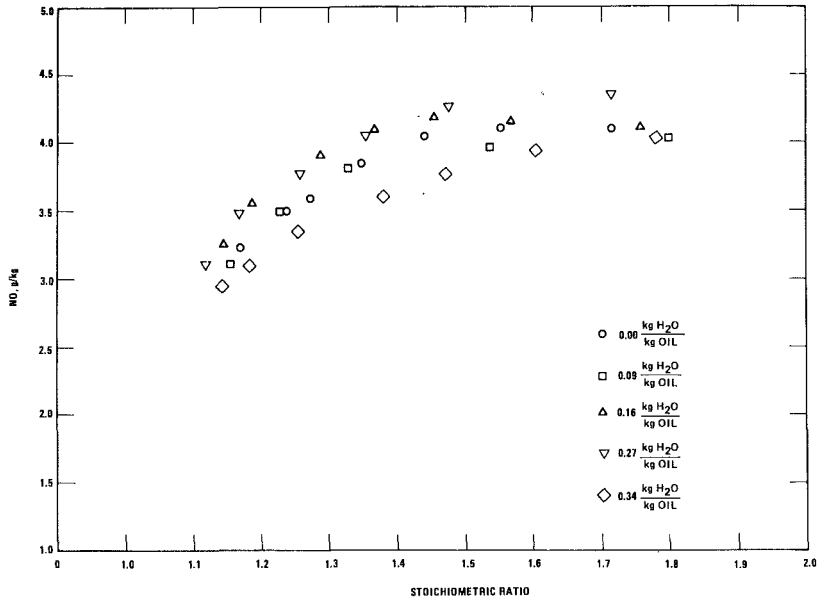

Fig. 10 Nitric oxide emissions at high firing rate

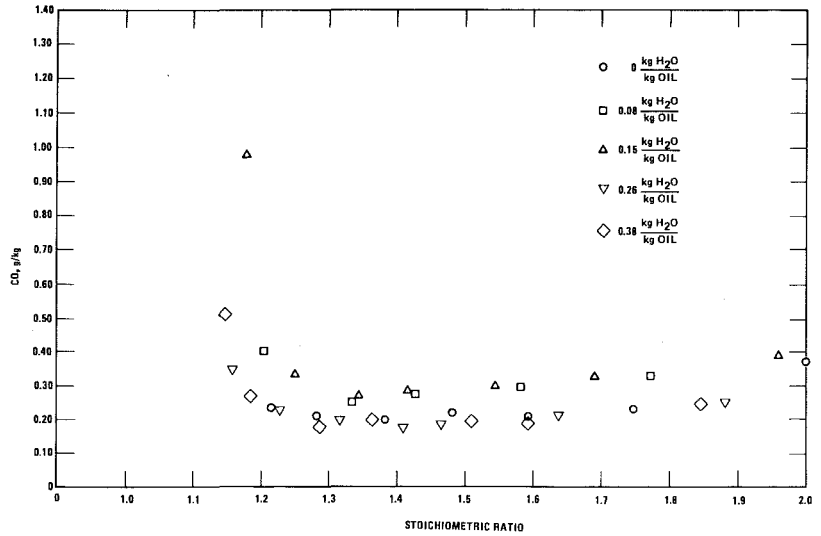

Fig. 11 Carbon monoxide emissions at intermediate firing rate

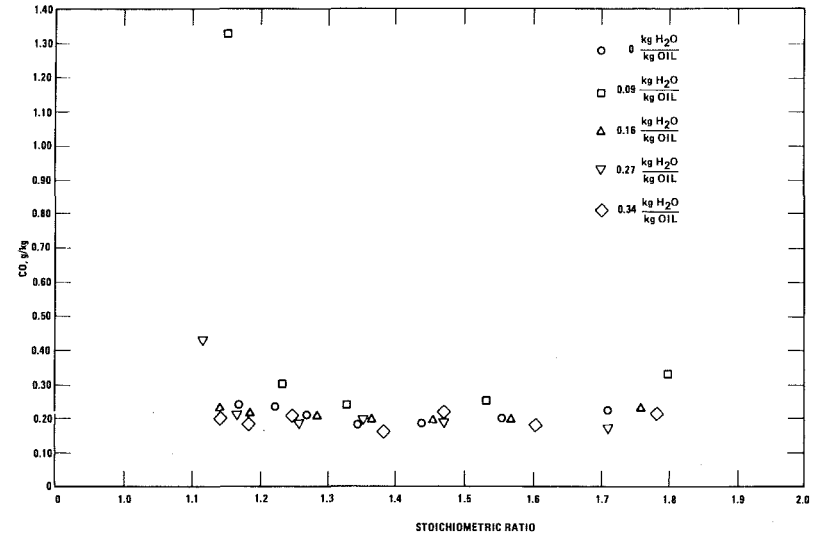

Fig. 12 Carbon monoxide emissions at high firing rate

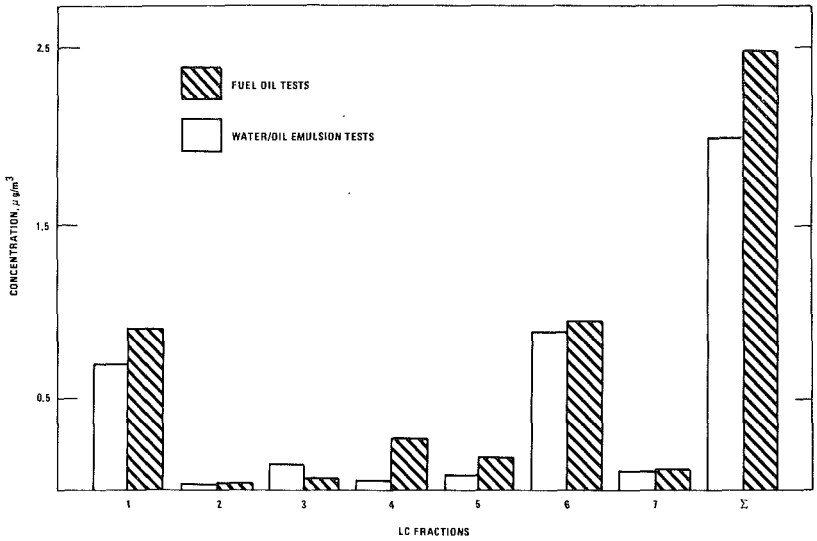

Fig. 13 Comparison of liquid chromotography fraction concentrations at the source

benzo(a)pyrene, which is hazardous in very low concentration. On the other hand, fraction 4 shows that the fuel oil test emitted seven times as much material as the emulsion test. However, this fraction does not contain materials which are hazardous in low concentration.

For these reasons, the total degree of hazard for the emissions from the emulsion fuel is approximately twice that of the fuel oil emissions, as reported in reference [13]. This is due almost entirely to the previously mentioned result that the liquid chromatography fraction 3 concentration for the emulsion is about twice that of the fuel oil test. Since the analysis performed did not isolate specific organic compounds in fraction 3, a more detailed analysis would be necessary in order to reach definite conclusions.

Conclusions

1 As the amount of water in the emulsion is increased, the boiler performance is shown to decrease due to increased latent heat loss. As with other burners, the stack losses are reduced at lower stoichiometric ratios, up to a smoke or particulate emission operational limit. The increased stack losses associated with higher water ratios in the emulsified fuel are not significantly offset by operating at lower stoichiometric ratios.

2 Total particulate mass emissions were generally found to be reduced with the use of water/fuel emulsions in comparison to burner operation with oil only. Also, as more water was added, the average amount of particulate mass emissions was generally reduced, although some small increases were observed at the high firing rate.

3 Particulate size distributions, as measured by the Andersen Stack Sampler, showed reproducible trends of increased fractions of small particulates and reduced fractions of large particulates as the water fraction in the emulsion was increased. In addition, the mass of fine particulates (less than 2.5 μm) emitted may be increased by using water/oil emulsions compared to firing only oil.

4 Total particulate emissions were found to increase by switching from a 21.8° to a heavier 19.2° API residual fuel oil. The average particle size was found to increase with the heavier oil.

5 Except for the highest water/oil ratios, smoke levels increased when emulsions were fired compared to only oil being fired.

6 As with other oil burners, the normalized emissions of NO generally were found to increase with increased load and with increased stoichiometric ratio.

7 There was not a significant change in NO emissions for any emulsion at the intermediate firing rate and for the lowest water/oil emulsion ratio at the high firing rate. However, at the high firing rate NO emissions did increase somewhat with emulsions of 0.16 and 0.27 kg water/kg oil. For the highest water/oil emulsion ratio tested, 0.34 kg water/kg oil, NO emissions were decreased by as much as 8 percent compared to firing oil only.

8 Burner stability became a problem only when firing at the highest water/oil emulsion flow rate. This is probably because the flow exceeded the design capacity of the nozzle, or because there was too much water in the emulsion for good combustion.

Acknowledgments

It is our pleasure to acknowledge the assistance of George R. Gillis, mechanical engineering technician, who ran the tests, performed the sampling, and reduced the data. Thanks are also due to Rachael Barbour and Alf Bjorseth of Battelle-Columbus Laboratories for performing the organic chemical analyses. Georges Boquet and Claude Delatronchette of Elf France in Paris France provided much useful information about the emulsifier. We are also indebted to Ms. Jean Gunn for typing, and re-typing, the manuscript.

References

1 Ivanov, V.M., and Nefedov, P.I., "Experimental Investigation of the Combustion Process of Natural and Emulsified Liquid Fuels," NASA Technical Translations, NASA-TR-F-258, January 1965.

2 Barrett, R.E., et al., "Design, Construction and Preliminary Combustion Trails of a Rig to Evaluate Residual Fuel-Oil/Water Emulsions," Battelle, Columbus, OH. National Air Pollution Control Administration Contract No. PH 86-68-84, Task Order No. 22, July 1970.

3 Scherer, G., and Tranie, L.A., "Pollutant Formation and Destruction in Flames and in Combustion Systems; Pollution Reduction by Combustion of Fuel-Oil Water Emulsion," presented at the Fourteenth International Symposium on Combustion, Pennsylvania State University, Aug. 1972.

4 Turner, D.W., and Siegmund, C.W., "Control of NO_x from Fuel Oil Combustion: Water in Oil Emulsions," presented at the Winter Symposium of the IEC Division of the American Chemical Society, Jan. 1973.

5 Dryer, F.L., "Fundamental Concepts on the Use of Emulsions as Fuels,"

Aerospace and Mechanical Sciences Report No. 1224, Princeton University, Apr. 1975.

6 Dryer, F.L., et al., "Some Preliminary Observations on the Combustion of Heavy Fuels and Water-in-Fuel Emulsions," Aerospace and Mechanical Sciences Report No. 1271, Princeton University, Apr. 1976.

7 Hall, R.E., "The Effect of Water/Distillate Oil Emulsions on Pollutants and Efficiency of Residential and Commercial Heating Systems," APCA Paper No. 75-09.4, presented at 68th Annual Meeting of the Air Pollution Control Association, Boston, MA, June 1975.

8 Hall, R.E., "The Effect of Water/Residual Oil Emulsions on Air Pollutant Emissions and Efficiency of Commercial Boilers," ASME JOURNAL OF ENGINEERING FOR POWER, Vol. 98, No. 4, Oct. 1976, pp. 425–434.

9 Martin, G.B., and Berkau, E.E., "International Trip Report to NAPCA Assistant Commissioner for Science and Technology, Washington, DC, May 20, 1971.

10 "Standard Method of Test for Smoke Density in the Flue Gases from Distillate Fuels," ASTM Designation: D2156-65 (Reapproved 1970), *1970 Annual Book of ASTM Standards,* Part 17, pp. 728–731.

11 Sparks, L.E., "Cascade Impactor Data Reduction with SR-52 and TI-59 Programmable Calculators," EPA-600/7-78-226 (NTIS PB 290710), Industrial Environmental Research Laboratory, U.S. EPA, Research Triangle Park, NC, Nov. 1978.

12 Lentzen, D. E., et al., "IERL-RTP Procedures Manual: Level 1 Environmental Assessment (Second Edition)," EPA-600/7-78-201 (NTIS PB 293795), Research Triangle Institute, Research Triangle Park, NC, Oct. 1978.

13 Barbour, R., and Bjorseth, A., "Analysis of SICMA Water/Oil Emulsion SASS Train Samples," Final Report from Battelle-Columbus Laboratories for EPA Contract No. 68-02-2686, Task Directive 116, February 1980.

14 *Steam, Its Generation and Use,* 38th edition, Babcock and Wilcox, New York, 1972, Chapt. 6.

15 "Guidelines for Burner Adjustments of Commercial Oil-Fired Boilers," EPA-600/2-76-088 (NTIS PB 251919), Battelle-Columbus Laboratories, Columbus, OH, Mar. 1976.

Ronald DiPippo
Mechanical Engineering Department,
Southeastern Massachusetts University,
North Dartmouth, Mass. 02747
Mem. ASME

Eileen A. DiPippo
Power Division,
Stone and Webster Engineering Corp.,
Boston, Mass.

Joseph Kestin
Division of Engineering,
Brown University,
Providence, R.I.
Fellow ASME

H. E. Khalifa
Advanced Energy Conversion Systems,
United Technologies Research Center,
East Hartford, Conn.
Mem. ASME

Compound Hybrid Geothermal-Fossil Power Plants: Thermodynamic Analyses and Site-Specific Applications

In this paper, we extend the analysis of hybrid fossil-geothermal power plants to compound systems which combine the features of the two previously analyzed hybrid plants, the geothermal preheat and the fossil superheat systems. Compound systems of the one- and two-stage type are considered. A complete summary of formulae to assess the performance of the plants is included for completeness. From the viewpoint of thermodynamics, compound hybrid plants are superior to individual all-geothermal and all-fossil plants, and have certain advantages over basic geothermal-preheat and fossil-superheat hybrid plants. The flexibility of compound hybrid systems is illustrated by showing how such plants might be used at several geothermal sites in the western United States.

Introduction

This paper extends the work of the Brown group in hybrid geothermal-fossil power plants to so-called compound hybrid systems. A number of reports and papers have been produced dealing in detail with geothermal-preheat systems [1,2] and fossil-superheat systems [3,4] and describing qualitatively other possible hybrid arrangements [5,6]. A plant of the geothermal-preheat type has been studied from an economic viewpoint [7], and a preliminary design has been prepared for the City of Burbank [8]. Although attention was given to certain types of hybrid plant concepts in the early days of geothermal development [9,10,11], the work of the Brown group is the most systematic treatment consistent with modern thermodynamic principles.

Geothermal-preheat hybrid systems are essentially conventional fossil-fired plants that use geothermal hot water instead of extraction steam for feedwater heating. A simplified flow diagram is shown in Fig. 1. The thermodynamic advantages of this type of arrangement are significant [2]. The reason for the improvement lies in the reduction of losses that are associated with the use of superheated steam extracted from the turbines to provide sensible heating of boiler feedwater in conventional plants [6]. The elimination of bleed steam for the lower-temperature feedwater heaters in favor of geothermnal hot water results in a more favorable match between the two fluids, and thus a reduction in the rate of entropy production. As a side effect, the steam flow through the low-pressure stages of the turbine is enhanced because of the elimination of the lower-pressure extraction points resulting in a greater power output for a given main steam flow.

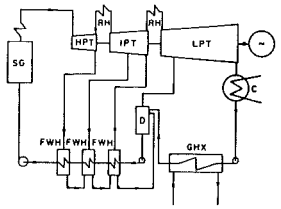

Fig. 1 Geothermal-preheat system. Key: SG = steam generator; HPT, IPT, LPT = high, intermediate, low pressure turbines; RH = reheater; C = condenser; GHX = geothermal heat exchanger; D = deaerator; FWH = feedwater heater

Fossil-superheat hybrid systems, on the other hand, are basically geothermal steam power plants with an added fossil-fired superheater [3,4]. One- and two-stage systems are illustrated schematically in Figs. 2(*a*) and 2(*b*), respectively. The advantages of this type of plant stem mainly from two features. First, the fossil fuel is utilized at a high mean effective temperature, thus improving the plant energy utilization efficiency. Second, the addition of superheat to the geothermal steam (which is typically saturated or only slightly superheated at the turbine inlet) leads to completely dry expansion through the turbine, and a higher machine efficiency according to the Baumann rule [12] that attributes a one percent reduction in turbine efficiency to each one percent of moisture in the turbine exhaust.

Contributed by the Petroleum Division of the American Society of Mechanical Engineers and presented at the Energy Technology Conference & Exhibition, New Orleans, La., February 3-7, 1980. Manuscript received at ASME Headquarters November 29, 1979.

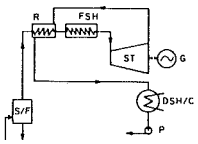

Fig. 2(*a*) One-stage fossil-superheat system. Key: S/F = separator flasher; R = regenerator; FSH = fossil-fired superheater; ST/G = steam turbine/generator; DSH/C = desuperheater/condenser; P = pump

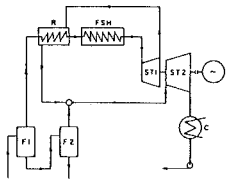

Fig. 2(*b*) Two-stage fossil-superheat system. Key: F1, F2 = flashers; R = regenerator; FSH = fossil-fired superheater; ST1, ST2 = steam turbines; C = condenser

Justification for Compound Hybrid Systems

Neither a geothermal-preheat nor a fossil-superheat system, by itself, is particularly suited to the case where the geothermal fluid emerges from the wellhead as a two-phase mixture of steam and hot water. It is common for example for self-flowing geothermal wells to produce mixtures with a dryness fraction (or quality) of between 5-40 percent at the wellhead. The use of such a mixture for feedwater heating in a geothermal-preheat system would be thermodynamically inefficient because the vapor fraction of the geothermal fluid would suffer the same type of losses as the steam extracted from turbines for feedwater heating in conventional fossil plants. On the other hand, if one attempted to use fossil-superheat systems with this type of resource, one would have to cope with the problem of how to handle the liquid fraction. Since it is impractical to heat, boil and superheat geothermal liquid, one would have to separate the vapor fraction from the liquid, superheat the vapor, and discard the liquid (as in a one-stage system, Fig. 2(*a*)). This procedure would clearly waste a considerable fraction of the available work of the geofluid. Alternatively, one might generate secondary steam by flashing the separated liquid to a lower pressure, at the expense of losses associated with the irreversible liquid-throttling process.

The compound hybrid plants described in this paper may be designed to take full advantage of two-phase geofluids. Furthermore, these designs will be shown to be sufficiently flexible to accommodate a variety of types of resources and a variable market demand for electric power. Finally such plants are excellent energy converters, having better resource utilization efficiencies than current all-geothermal and all-fossil plants.

Physical Descriptions of Compound Hybrid Plants

One-Stage Systems. The simplest compound hybrid plant is shown schematically in Fig. 3. We denote plants of this type as "one-stage" compound plants because there is only one stage of geothermal steam generation. This takes place below the surface by means of a natural flashing process, usually in the wellbore but sometimes (although undesirably) in the reservoir formation.

With reference to Fig. 3, the two-phase geofluid emerges from a number of production wells (PW) and is processed in cyclone separators (S). The separated steam is scrubbed (scubbers not shown) and fed to a superheater (FSH) located in the boiler section of the power house. After leaving the superheater, the steam follows a route which is essentially identical to that of, say, the geothermal steam used at The Geysers geothermal installation in northern California, i.e., through a low-pressure turbine (GT), a condenser (GC), and finally through booster pumps to a number of injection wells (IW).

The liquid fraction of the geofluid is piped from the outlet of the separator (S) to a heat exchanger (BH) in the feedwater heating train of an otherwise more or less conventional Rankine power cycle. The main difference in this case is the elimination of most of the feedwater heaters, which typically

Nomenclature

a_0, a_1 = coefficients in equation (19) for net work
b_0, b_1 = coefficients in equation (20) for a_0
c_0, c_1 = coefficients in equation (21) for a_1
E_g = available work or exergy of geofluid at the wellhead, equation (13)
F = combined figure of merit, equation (1)
F_f = fossil-fuel figure of merit, equation (2)
F_g = geothermal-energy figure of merit, equation (3)
F_0 = overall figure of merit, equations (4,5)
h_a, h_0 = enthalpy of geofluid at the wellhead, and sink
$\dot{m}_a$ = mass flow rate of geofluid at the wellhead per 100 MW plant output
$\dot{m}_1$ = mass flow rate of clean main steam through steam generator SG, Figs. 3 and 4, per unit mass flow of geofluid at the wellhead
Q = heat transfer
R = resource ratio, equation (8)
s_a, s_0 = entropy of geofluid at the wellhead, and sink
T_a = temperature of geofluid at the wellhead
T_0 = temperature of geofluid at the sink; dead-state temperature
W = net work of hybrid power plant
W_f^0 = net lifetime work of an all-fossil plant using to completion the same fossil resource supplying a hybrid plant
W_f^* = net work of a state-of-the-art, all fossil plant, equation (15)
W_g = net work obtained from geothermal steam turbines in hybrid plant
W_g^0 = net lifetime work of an all-geothermal plant using to completion the same geothermal resource supplying a hybrid plant
W_g^* = net work of a state-of-the-art, all-geothermal plant, equation (11)
x_a = dryness fraction or quality of geofluid at the wellhead
Δ = relative depletion parameter, equations (6,7)
$\eta_{\text{eff},f}$ = effective energy conversion efficiency for fossil energy, equation (22)
$\eta_{\text{eff},g}$ = effective energy conversion efficiency for geothermal energy, equation (23)
η_f^* = state-of-the-art, fossil-fuel, cycle efficiency, equation (16)
η_g^* = state-of-the-art, geothermal energy utilization efficiency, equation (12)
ϕ_h = fossil-fuel savings factor for hybrid plant relative to an all-fossil plant of the same output
ψ = work amplification factor, equations (9,10)

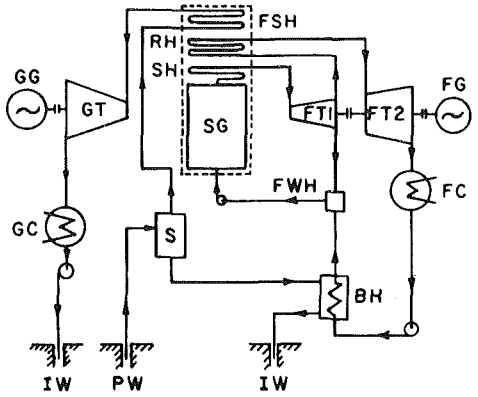

Fig. 3 One-stage compound hybrid system. Key: PW = production well; S = separator; SG, SH, RH, FSH = steam generator and superheaters; FT1, FT2 = fossil turbines; FG = fossil generator; FC = fossil condenser; CP = condensate pump; BH = brine heat exchanger; FWH = feedwater heater; BFP = boiler feed pump; GT = geothermal tubrine; GG = geothermal generator; GC = geothermal condenser; RP = reinjection pump; IW = injection well

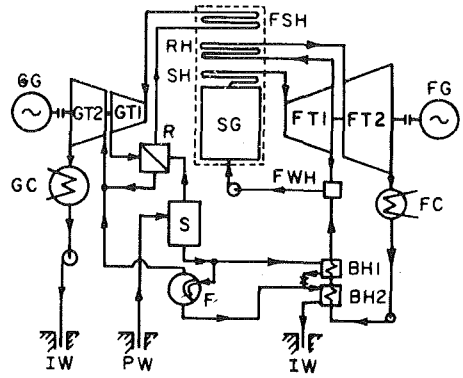

Fig. 4 Two-stage compound hybrid system. Key: same as Fig. 3 except; R = regenerator; F = flash tank

total 5 to 7 in conventional plants, in favor of one, open, deaerating-type heater (FWH) and the brine heat exchanger (BH). The spent brine may be injected either directly using the pressure of the waste liquid (which should be only somewhat less than the separator pressure) or, if necessary, by means of a booster pump.

Two-Stage Systems. In the manner of so-called double-flash geothermal plants, a second stream of geothermal steam may be generated by flashing a fraction of the hot water from the separator (S) before it arrives at the brine heat exchanger (BH). Figure 4 shows a flow diagram for a two-stage system. A flash vessel (F) receives a portion of the separated hot water, where it is throttled to a lower pressure, thereby generating secondary steam and another stream of hot water. The additional steam is mixed with the primary geothermal steam from the first geothermal turbine (GT1) after the primary steam from the turbine exhaust has passed through a steam-steam generator (R). The regenerator is not always feasible. The temperature of the exhaust from the first geothermal turbine must be greater than the wellhead temperature by an amount at least equal to the minimum acceptable temperature difference for the heat exchanger. Under most conditions of operation, a regenerator turns out to be thermodynamically feasible for two-stage systems. (For none of the conditions studied is a regenerator possible for one-stage systems.) The merged streams of geothermal steam then enter a low-pressure turbine (GT2), and generate additional power.

The residual hot water produced at the flash vessel is mixed with the main geothermal hot water leaving the brine heat exchanger (BH1) before entering the lowest temperature feedwater heater (BH2). A small (negligible) loss is encountered at the mixing point because the two fluids are at different pressures and temperatures. Finally, as with one-stage systems, all of the geofluid is eventually reinjected by means of injection wells (IW).

Thermodynamic Analysis

Basic Assumptions and Equations. Definitions of various figures of merit and design parameters for hybrid plants in general have been given elsewhere, and working equations for these terms have been established [1-3,6,13]. Since these performance factors are valid in general, they may be applied to compound hybrid systems. A summary of the most important definitions and working equations is included here for ease of reference. A thorough description and listing of the equations used in the analysis may be found in reference [14].

F = combined figure of merit
$$= W/(W_f^* + W_g^*). \quad (1)$$
F_f = fossil-fuel figure of merit
$$= (W - W_g^*)/W_f^*. \quad (2)$$
F_g = geothermal-energy figure of merit
$$= (W - W_f^*)/W_g^*. \quad (3)$$
F_0 = overall figure of merit
$$= 1 + (F_f - 1)/(1 + R), \text{ for } \Delta < 1 \quad (4)$$
$$= 1 + R(F_g - 1)/(1 + R), \text{ for } \Delta > 1 \quad (5)$$
W = net work of hybrid power plant.
W_f^* = net work of a state-of-the-art, fossil-fueled power plant (typically a supercritical reheat cycle with seven feedwater heaters).
W_g^* = net work of a state-of-the-art, geothermal power plant (typically an optimized double-flash steam plant).
Δ = relative depletion parameter
$$= F_f/F(\psi - 1) \quad (6)$$
$$= 1/F(\psi - F_g). \quad (7)$$
R = resource ratio, i.e., the ratio of the total amount of work W_g^0, that could be extracted from the geothermal resource on which the hybrid plant is built if a state-of-the-art geothermal plant were to be built instead, and a similar work term, W_f^0, for the fossil resource that is committed to the hybrid plant
$$= W_g^0/W_f^0. \quad (8)$$
ψ = work amplification factor
$$= W/W_g^* \quad (9)$$
$$= F(F_g - 1)/(F - 1). \quad (10)$$
$$W_g^* = \eta_g^* E_g. \quad (11)$$
$$\eta_g^* = 0.50 \text{ (fixed)}. \quad (12)$$
E_g = available work (exergy) of the geofluid at the wellhead
$$= h_a - h_0 - T_0(s_a - s_0). \quad (13)$$
h_a, h_0 = geofluid enthalpy at the wellhead and the sink.
s_a, s_0 = geofluid entropy at the wellhead and the sink.
T_0 = absolute temperature of the sink.
$$= 300 \text{ K } (540 \text{ R}). \quad (14)$$
$$W_f^* = \eta_f^*(\Sigma Q_i). \quad (15)$$
$$\eta_f^* = 0.43 \text{ (fixed)} \quad (16)$$
ΣQ_i = sum of all fossil-derived heat to hybrid plant
ϕ_h = fossil-fuel savings factor, i.e., the savings in fossil-fuel (as a fraction) that a hybrid plant is capable of over an all-fossil plant of the same net work output
$$= 1 - (W_f^*/W) \quad (17)$$
$$= F_g/\psi. \quad (18)$$

The analysis incorporates realistic assumptions along with system configurations that simulate practical conditions. The fixed parameters characterizing the plants are listed in Table

1; the ranges of the variable system parameters are given in Table 2. A wide range of geofluid wellhead properties was selected to cover the spectrum that might reasonably be expected at typical liquid-dominated geothermal fields.

Table 1 Fixed system parameters

Conditions	Type of System*	
	One-stage	Two-stage
Fossil side:		
Main steam temperature, °C(°F)	540(1004)	540(1004)
Main steam pressure, MPa (lbf/in^2)	16.5(2400)	16.5(2400)
Extraction pressure, MPa (lbf/in^2)	4.1(595)	4.1(595)
Reheat steam temperature, °C(°F)	540(1004)	540(1004)
Reheat steam pressure, MPa(lbf/in^2)	3.9(565)	3.9(565)
Turbine isentropic efficiency:		
High-pressure turbine, FT1	82 percent	82 percent
Low-pressure turbine, FT2	85 percent	85 percent
Geothermal side:		
Main steam temperature, °C(°F)	510(950)	510(950)
Flash vessel pressure, MPa (lbf/in^2)	–	0.2(29)
Turbine isentropic efficiency	85 percent	85 percent
Regenerator effectiveness	–	80 percent
General:		
Condenser pressure, kPa(in Hg)	5.6(1.9)	5.6(1.9)
Pump isentropic efficiency	80 percent	80 percent
Pressure loss in heat exchangers	10 percent	10 percent

*See Fig. 3 for one-stage systems and Fig. 4 for two-stage systems.

Table 2 Variable system parameters

Conditions	Range of values
Geofluid wellhead temp., °C	150, 200, 250
Geofluid wellhead quality, percent	10, 20, 30, 40
Hot water flash fraction, percent	0*, 25, 50, 75, 100

*One-stage system; see Fig. 3.

A subcritical Rankine cycle was selected for the fossil side of the plant in accordance with a growing trend in the power industry [15]. The extraction pressure was set at 25 percent of the main steam pressure, also in accordance with practice. The temperature of the superheated geothermal steam was held to a conservative 510°C (950°F) instead of the 540°C (1004°F) customarily used for pure steam in order to allow for possible difficulties from impurities that may elude the scrubbers. Corrosion and erosion resistant materials may thus be required for the geothermal steam superheater, resulting in poorer heat transfer characteristics than mild steel.

In the case of two-stage systems, no attempt was made to determine an optimum flash pressure. Instead, a fixed value of 0.2 MPa (29 lbf/in.^{2}) was selected. This pressure being above atmospheric will ensure that the waste hot liquid will flow under its own head from the flash vessel, through the brine heater, and into the injection well. According to the so-called "equal-temperature-split" rule [16], this choice of flash pressure should give nearly optimum results for a wellhead temperature of 200°C (392°F). However, this rule-of-thumb was meant to apply to pure flash systems, not hybrid systems. In any event, earlier studies have shown that considerable latitude exists in the choice of flash point relative to the optimum without seriously affecting the thermodynamic performance of a hybrid plant [4].

Both condensers were chosen to operate at the same pressure, 5.6 kPa (1.9 in Hg), on the assumption that each condenser would be supplied from a common source of cooling water. While somewhat on the low side for present-day geothermal plants, this pressure is consistent with the design values for large central stations served by wet cooling towers. Such operating conditions may be attainable with surface-type condensers in conjunction with any of a number of cooling techniques including wet or wet/dry cooling towers, phased-storage with cooling ponds and/or spray modules [17]. We have allowed for a 10 percent pressure loss in all heat exchangers, including steam generators. The thermodynamic analyses reported in this paper thus should reflect the realities of practical power plant design considerations to a large degree.

It should be noted that the performance of both one- and two-stage plants was determined from a single computer code since the working equations for two-stage systems reduce to those for one-stage systems when the hot water flash fraction r_f is set equal to zero. (r_f is the ratio of mass flow entering the flasher to mass flow of liquid leaving the separator. See Fig. 4.)

For the parametric computer studies the working fluids, i.e., the clean water substance on the fossil side of the plant and the geothermal fluid, have been taken to be pure water substance. That is, the results of the parameteric studies do not reflect the impact of dissolved solids and noncondensable gases that can affect the output of the geothermal side of the plant. However, we incorporated a heuristic correction factor to account roughly for the effect of dissolved solids in the site-specific applications. The properties of water in the liquid and vapor phases were computed according to the fundamental equation of state devised by J.H. Keenan, et al. [18].

Results of Parametric Studies. The complete set of computations are reported elsewhere [14]; owing to space limitations it is possible to show only selected samples here. Table 3 contains a listing of a number of performance and design parameters for a two-stage compound hybrid plant set up with a 50 percent hot water flash fraction. Results are shown there for each combination of wellhead quality and temperature given in Table 2. The calculated terms include: F, the combined figure of merit; F_f, the fossil-fuel figure of merit; F_g, the geothermal figure of merit; W, the net plant output per unit mass of geofluid at the wellhead; ψ, the work amplification factor; $\dot{m}_1$, the mass flow of clean steam on the fossil side per unit mass of geofluid at the wellhead; F_0, the overall figure of merit; and ϕ_h, the fossil-fuel savings factor

Table 3 Performance of two-stage compound systems flash fraction = 50 percent

Wellhead quality		10 %	20%	30%	40%
Wellhead temperature					
	F =	1.040	1.056	1.074	1.095
	F_f =	1.042	1.061	1.085	1.115
	F_g =	1.635	1.583	1.555	1.537
	W =	1.213	1.150	1.087	1.023
150°C(302°F)	ψ =	16.59	11.07	8.08	6.19
	$\dot{m}_1$ =	0.945	0.840	0.735	0.630
	F_0 =	1.039*	1.053	1.050	1.049
	ϕ_h =	9.85	14.29	19.25	24.82
	F =	1.084	1.110	1.138	1.168
	F_f =	1.095	1.131	1.173	1.225
	F_g =	1.716	1.689	1.672	1.661
	W =	1.509	1.045	1.031	1.016
200°C(392°F)	ψ =	9.25	6.96	5.56	4.60
	$\dot{m}_1$ =	0.724	0.644	0.563	0.483
	F_0 =	1.065	1.063	1.061	1.060
	ϕ_h =	18.56	24.26	30.09	36.11
	F =	1.115	1.144	1.174	1.205
	F_f =	1.141	1.187	1.240	1.302
	F_g =	1.621	1.628	1.633	1.637
	W =	0.982	0.995	1.008	1.021
250°C(482°F)	ψ =	6.03	4.99	4.27	3.75
	$\dot{m}_1$ =	0.584	0.519	0.454	0.389
	F_0 =	1.057	1.057	1.058	1.058
	ϕ_h =	26.87	32.62	38.22	43.69

*In this case, $\Delta < 1$; otherwise, $\Delta > 1$.

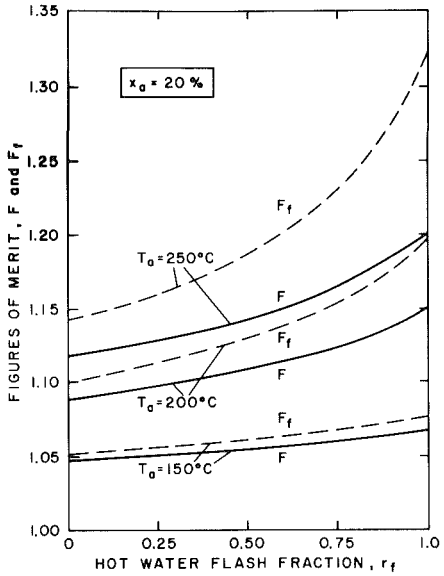

Fig. 5 Figures of merit, F and F_f, versus hot water flash fraction for three different wellhead temperatures and 20 percent wellhead quality

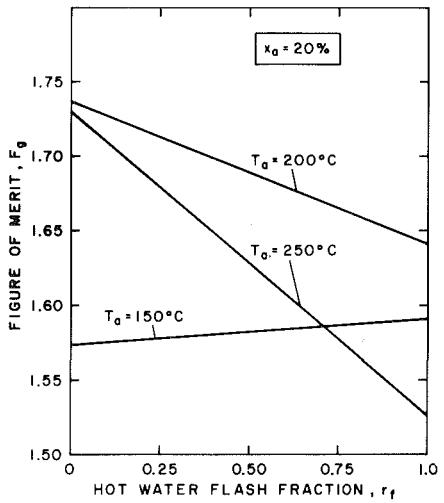

Fig. 6 Figure of merit F_g versus hot water flash fraction for three different wellhead temperatures and 20 percent wellhead quality

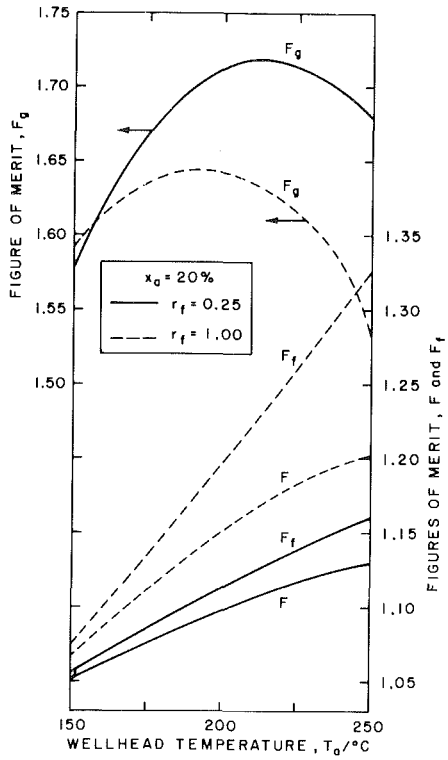

Fig. 7 Figures of merit, F, F_f and F_g, versus wellhead temperature for 25 percent and 100 percent hot water fresh fractions and 20 percent wellhead quality

for the hybrid plant over an all-fossil plant of the same output.

The figures of merit, F and F_f, are shown graphed in Fig. 5 as a function of flash fraction r_f for wellhead fluid temperatures of 150, 200 and 250°C (302, 392 and 482°F) and a wellhead steam fraction of 20 percent. Figure 6 gives similar information for F_g. The values of F and F_f increase with increasing flash fraction, the dependency growing stronger for higher wellhead temperatures. At the lowest temperature studied, F_g depends weakly on r_f; an inverse relation exists between F_g and r_f for higher temperatures, again with the dependency being strongest at the highest temperature. In each case, the figures of merit exceed unity, indicating that the hybrid plant holds a thermodynamic advantage over two, separate state-of-the-art geothermal and fossil power plants receiving the same input as the hybrid plant. This advantage ranges from 53-74 percent from the geothermal viewpoint (i.e., F_g), from 5-33 percent from the fossil viewpoint (i.e., F_f), and from 5-20 percent from a combined viewpoint (i.e., F), for the particular conditions selected for Figs. 5 and 6. Figure 7 shows a cross-plot of the same figures of merit versus wellhead temperature for $r_f = 0.25$ and 1.00, and for $x_a = 20$ percent. The geothermal figure of merit passes through a maximum that depends on the choice of flash fraction, whereas F and F_f increase monotonically with wellhead temperature.

The net work output, W, per unit mass of geofluid at the wellhead depends linearly on flash fraction r_f, and may be correlated using an equation of the form:

$$W(x_a, r_f; T_a) = a_0(x_a; T_a) - a_1(x_a; T_a) \times r_f, \tag{19}$$

where the coefficients a_0 and a_1 turn out to be linear in wellhead quality and may be represented as:

$$a_0(x_a; T_a) = b_0(T_a) - b_1(T_a) \times x_a, \tag{20}$$

$$a_1(x_a; T_a) = c_0(T_a) - c_1(T_a) \times x_a, \tag{21}$$

with numerical values for b_0, b_1, c_0, and c_1 given in Table 4. Interpolation at intermediate wellhead temperatures can be performed by plotting the coefficients b_0, b_1, c_0, and c_1 against temperature to obtain intermediate values. These, together with equations (1-3), allow the net work output to be computed for any desired conditions. Figure 8 illustrates the variation of net work with wellhead temperature for 20 percent wellhead quality and for selected values of flash fraction.

The dependence of the figures of merit and net work on wellhead quality is shown in Fig. 9 for $T_a = 200$°C (392°F) and $r_f = 0.50$.

Site-Specific Applications

We will now apply the concept of the compound hybrid plant to three promising liquid-dominated geothermal resource areas in the western United States. The sites have been chosen to cover a wide range of resource conditions. The plants proposed for the sites are not intended to be "optimal" in any absolute sense, but rather illustrate certain advantageous features of hybrid plants. The geothermal

Table 4 Correlation coefficients b_0, b_1, c_0 and c_1 for net work

Wellhead temperature	Coefficients			
	b_0	b_1	c_0	c_1
150°C (302°F)	1.498	0.853	0.444	0.443
200°C (392°F)	1.465	0.533	0.783	0.780
250°C (482°F)	1.431	0.330	0.923	0.920

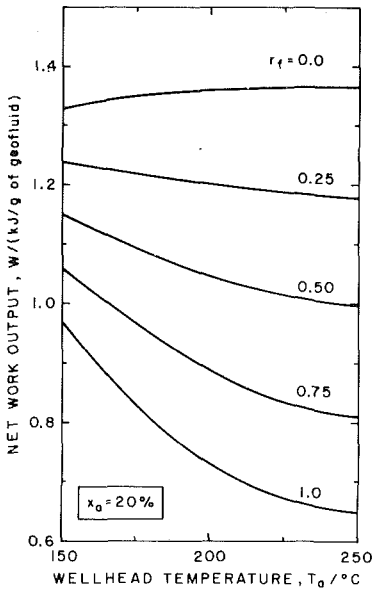

Fig. 8 Net work output per unit mass of geofluid versus wellhead temperature for various hot water flash fractions and 20 percent wellhead quality

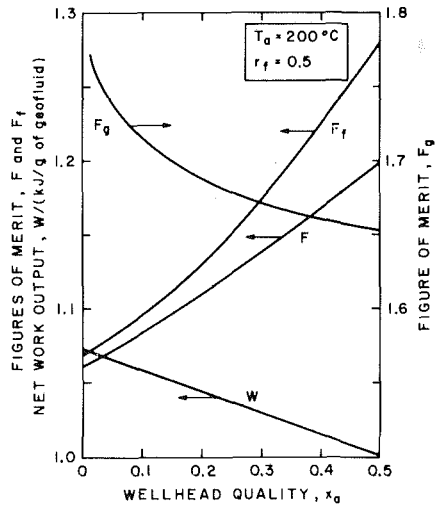

Fig. 9 Figures of merit and net work output versus wellhead quality for 200°C wellhead temperature and 50 percent hot water flash fraction

resources characteristics, the type of plant for each site, and the general objective governing the choice of plant are given in Table 5.

Salton Sea (Niland), California. This resource has the highest temperature and the highest concentration of dissolved solids (TDS) of any geothermal field in the U. S. Owing to the extremely high level of solids, ~ 250,000 ppm or 25 percent, it was necessary to correct the work output terms from our computer calculations that were based on pure water. The net work output from the geothermal turbines was

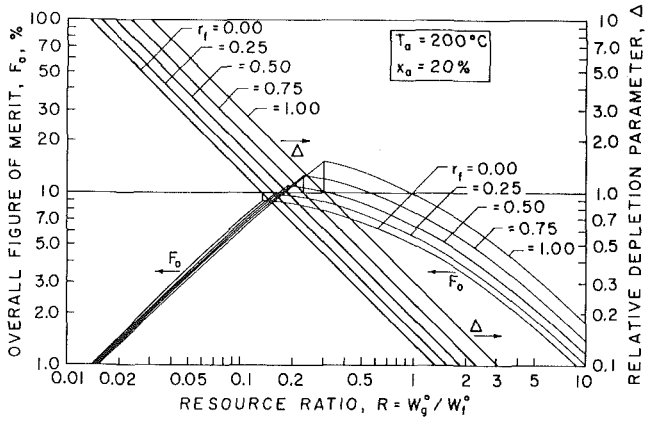

Fig. 10 Overall figure of merit and relative depletion parameter versus resource ratio for 200°C and 20 percent wellhead conditions.

Table 5 Characteristics for site-specific case studies

	Known Geothermal Resources Area (KGRA)		
	Salton Sea	Roosevelt	East Mesa
References	[19-21]	[20-24]	[20,21,25]
Reservoir temp., °C	330	260	180
Wellhead temp., °C	235	187	150
Well flow rate, t/h	159	277	54
Wellhead quality, percent	28	17	6
Dissolved solids, percent	25	< 0.8	< 1
Hybrid plant type	two-stage	two-stage	one-stage
Flash fraction, percent	100	50	0
Objective	High F, F_f	High F_g	High W

reduced by 0.8 percent for each 1 percent of TDS [19], or by a total of 20 percent in this case. A two-stage plant with a 100 percent flash fraction was selected in order to achieve high figures of merit for both fossil-fuel and combined resource usage.

Roosevelt Hot Spring, Utah. Earlier studies commissioned by the City of Burbank, CA showed that this site was advantageous both technically and economically as a location for a hybrid plant of the geothermal-preheat type [8]. A number of coal fields lie in relatively close proximity to the KGRA. The geothermal fluid is relatively hot and reasonably low in dissolved solids. A two-stage plant with a 50 percent flash fraction should yield a high figure of merit for geothermal utilization.

East Mesa, California. This example was selected to illustrate the application of hybrid plants to resources of moderate-to-low temperature and low wellhead quality. The concentration of dissolved solids was taken as less than 1 percent although one well (Mesa 6-1) contains about 2.5 percent TDS. Other wells reveal TDS concentrations that lie below 1 percent. In light of the relatively low wellhead temperature of 150°C (302°F), a one-stage plant was chosen, i.e., a 0 percent flash fraction. This should yield a high value for the net specific work output and result in a minimum geofluid flow rate for a given plant capacity.

Site-Specific Plant Performance. Table 6 lists a number of performance characteristics for each of the compound hybrid plants for the three KGRAs. The mass flow rates of the geofluid and the clean steam, $\dot{m}_a$ and $\dot{m}_1$, and the required number of geothermal wells are given per 100 MW of hybrid plant net capacity, and may be scaled up or down for plants of other sizes. The entry, W_g/W, shows the goethermal contribution to the total plant output, and ranges form 3.5 percent for the East Mesa plant to 47 percent at the Salton Sea. There are two effective efficiencies listed, $\eta_{\text{eff},f}$ and $\eta_{\text{eff},g}$, defined as follows:

Table 6 Hybrid performance for three KGRAs

Characteristic	Known Geothermal Resources Area (KGRA) Salton Sea	Roosevelt	East Mesa
W, kJ/g, geofluid (Btu/lbm)	0.623 (268)	1.080 (464)	1.458 (627)
$\dot{m}_a$, t/100 MW•h (klbm/100 MW•h)	578 (1274)	333 (735)	247 (544)
$\dot{m}_1$, t/100 MW• (klbm/100 MW•h)	140 (310)	240 (530)	289 (636)
No. wells/100 MW	3.6	1.2	4.5
(W_g/W), percent	47.1	15.7	3.5
$\eta_{\text{eff},f}$, percent	58	47	44
$\eta_{\text{eff},g}$, percent	79	84	82
ϕ_h, percent	49	19	7

$$\eta_{\text{eff},f} = F_f \eta_f^*, \tag{22}$$

$$\eta_{\text{eff},g} = F_g \eta_g^*. \tag{23}$$

These may be viewed as effective energy conversion efficiencies for fossil or geothermal energy, allowing for the maximum, presently-attainable utilization efficiency for the other resource. It has been shown [2,26] that these efficiencies are essentially Second Law efficiencies, even in the case of fossil-fuel utilization since the available work (exergy) of a fossil fuel is essentially equal to its standard heat of reaction. Thus for fossil fuels, the so-called First and Second Law efficiencies, while different in concept, are nearly equal numerically. The compound hybrid plants at the selected KGRAs have effective fossil-fuel efficiencies ranging from 44 to 58 percent, and effective geothermal efficiencies of from 79 to 84 percent. The last entry in Table 6 is the percentage savings in fossil fuel when the hybrid plant is built instead of an all-fossil plant of the same net output. The savings amount to 49 percent for the hybrid plant at the Salton Sea, 19 percent for the plant at Roosevelt, and 7 percent for East Mesa.

Optimal Matching of Plant and Resources

We have established the fact that compound hybrid power plants have a thermodynamic advantage over either an all-fossil plant, an all-geothermal plant, or a combination of such plants. When one takes into account the finite nature of the two energy sources supplying a given hybrid plant, it becomes clear that the optimum use will be made of both resources when the plant is so matched to the resources that the two energy supplies are depleted at the same time. Otherwise, the one resource which remains would most likely have to be used in a conventional non-hybrid plant at a lower utilization efficiency. This latter statement is almost certainly true in the case when the fossil fuel supply is depleted first, leaving the geothermal resource to be used on the site. In the other case, the rest of the fossil-fuel could be transported elsewhere for use, and perhaps even to another geothermal site where it might be used in another hybrid plant, but it is probably true that the second site would be less advantageous than the one to which the fossil fuel was committed in the first place.

Therefore, as was shown in our earlier works [2,3], the relative depletion parameter, Δ, should, if possible, be designed equal to unity, ensuring simultaneous depletion of the two resources and the maximum overall figure of merit, F_0. The variation of the relative depletion parameter and of the overall figure of merit were examined as a function of the resource ratio, R, for a family of two-stage compound hybrid plants (i.e., $0 \le r_f \le 1$), utilizing a hypothetical geothermal resource having 200°C (392°F) wellhead temperature and 20 percent wellhead quality. The results are plotted in Fig. 10.

It may be seen that for resource ratios less than about 0.14 there is little to choose among the plants although those with zero flash fractions hold a small advantage over the others. It is in this region where the geothermal resource gives out before the fossil resource, i.e., $\Delta > 1$. On the other hand, for

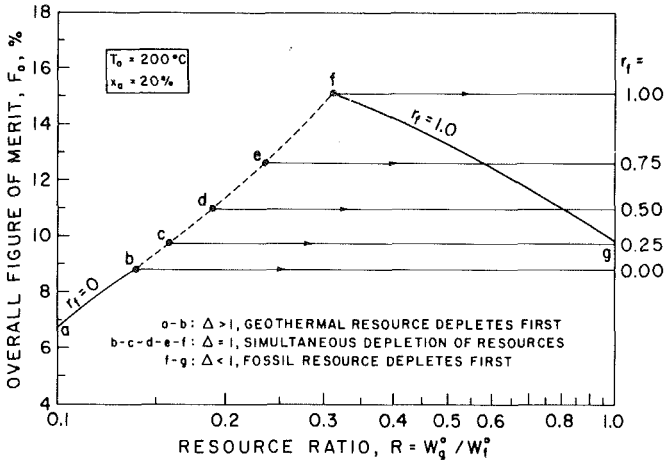

Fig. 11 Overall figure of merit in the neighborhood of the optimum for 200°C and 20 percent wellhead conditions.

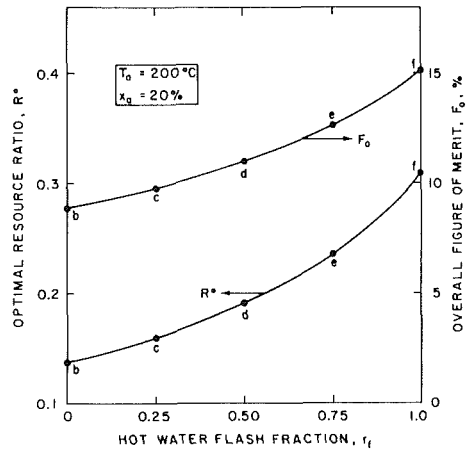

Fig. 12 Optimal resource ratio and overall figure of merit versus hot water flash fraction for 200°C and 20 percent wellhead conditions

values of $R > 0.31$, the advantage lies with plants having $r_f = 1.0$, and the improvement in F_0 is significant in comparison with plants having a lower flash fraction. In these cases, $\Delta < 1$, indicating that the fossil fuel resource is the first to be depleted.

For resource ratios lying between 0.14 and 0.31, it is possible to choose a compound hybrid plant with a particular flash fraction that leads to an optimum overall figure of merit. This selection will be determined by the condition that $\Delta = 1$. Figure 11 gives the upper envelope of the family of curves for F_0, starting with the case of $r_f = 0$, including the locus (broken line) of optimum F_0 values for $r_f = 0.25, 0.50, 0.75$ and continuing with plants having $r_f = 1$. The portion over which $\Delta = 1$ is shown in rectilinear coordinates in Fig. 12 for ease of interpolation.

In practice a designer would likely be confronted with the case of a geothermal resource with a certain assessed electric generation capability of W_g^0 M over, say, a 30-year lifetime (assuming conversion to electricity in a state-of-the-art geothermal power plant). If a fossil resource can be economically committed to a hybrid plant at the geothermal site, then the designer should specify that an amount of fossil resource equivalent to 3.2 W_g^0 (i.e., $W_g^0/0.31$) be purchased to supply a hybrid plant having a hot water flash fraction of 100 percent. For the hypothetical resource under consideration (point f in Fig. 12), this will result in slightly over 15 percent more electrical output over the lifetime of the energy resources than separate utilization of the resources in state-of-the-art geothermal and fossil plants.

There is no thermodynamic advantage to be gained by alloting more fossil fuel than 3.2 W_g^0 since the excess will not

be used at the highest possible effective efficiency. If for other reasons one wishes to assign a greater amount of fossil fuel to the hybrid plant than the optimum value, then the flash fraction should be adjusted downward in accordance with Fig. 11 or 12. For example, if 5 W_g^0 is assigned to the plant, than r_f should be set at 0.56 to achieve an optimal F_0 (corresponding to a gain of about 11.3 percent. Furthermore, if it is not possible to commit at least the equivalent of 3.2 W_g^0 of fossil fuel to the hybrid plant, then the designer should select a plant with a 100 percent flash fraction, and settle for a lower gain than the ultimate. For example, if only 2 W_g^0 of fossil fuel can be obtained, then the fossil fuel will deplete before the geothermal resource ($\Delta = 6.2$, Fig. 10), and the overall gain will be limited to 13.3 percent (Fig. 11). Of course, the designer in such cases might opt to consider hybrid plants of a different generic type such as the gas turbine topping system described elsewhere [6], in an effort to obtain even higher values of the overall figure of merit.

Conclusion

Compound hybrid geothermal-fossil power plants are significantly superior to conventional, individual geothermal and fossil plants in regard to the thermodynamic utilization of the available energy resources. The margin of superiority depends on the particular configuration of the hybrid plant and the characteristics of the geothermal resource. The hybrid plants proposed in this paper use components that are familiar to designers and which are employed in fossil and geothermal power plants now in operation around the world. What is lacking, however, is long-term operating experience with certain of the geothermal elements such as brine heat exchangers, superheaters carrying geothermal steam, piping systems to handle goethermal brines, and reinjection pumps.

Compound hybrid plants are flexible enough to be adapted to a wide range of geothermal resources over a full range of plant capacities. They may be designed to depend more or less upon either of the energy sources to accommodate the availability of the respective "fuels". Since hybrid plants are more efficient than conventional ones, the use of hybrid plants would result in considerable savings in fossil fuels required to generate the same output. Of course, it is obvious that the construction of an all-geothermal plant in lieu of an all-fossil one would also lead to savings in fossil fuel, but a hybrid plant would produce a greater overall savings of the combined resources because of its synergistic characteristics. Thus, the useful lifetime of the non-renewable fossil fuel and of the depletable geothermal resource can be extended by the implementation of the hybrid geothermal-fossil concept in future power plants.

There appear to be several sites in the western United States where hybrid geothermal-fossil plants are technically feasible [13]. The commercial viability of such plants, however, will utimately turn on the economics of each particular proposal. The results of such an assessment will be strongly site-specific and involve importantly the differential cost of transporting the fossil fuel to the proposed site of the hybrid plant (essentially co-incident with the associated geothermal field) in comparison with the cost to ship it to the site of an alternate all-fossil plant designed to provide the same power. It is encouraging that such studies as have been done so far on hybrid plants [7] indicate that reductions of about 10 percent in the busbar cost of electricity may be achievable under certain circumstances.

Acknowledgments

This work was performed with support from DOE/DGE Contract EY-76-S-02-4051.A002 to Brown University.

References

1 DiPippo, R., Kestin, J., and Khalifa, H.E., "Hybrid Fossil-Geothermal Power Plants," Brown Univ. Rep. No. CATMEC/2, DOE/DGE No. C00/4051-3, Feb. 1977.

2 Khalifa, H.E., DiPippo, R., and Kestin, J., "Geothermal Preheating in Fossil-Fired Steam Power Plants," Brown Univ. Rep. No. CATMEC/12, DOE/DGE No. C00/4051-19, Mar. 1978; Also, *Proceedings 13th Intersociety Energy Conversion Engineering Conference,* 1978, Vol. 2, pp. 1068-1073.

3 DiPippo, R., Khalifa, H.E., Correia, R.J., and Kestin, J., "Fossil Superheating in Geothermal Steam Power Plants," Brown Univ. Rep. No. CATMEC/11, DOE/DGE No. C00/4051-18, Mar. 1978; Also *Proceedings 13th Intersociety Energy Conversion Engineering Conference,* 1978, Vol. 2, pp. 1095-1101; Reprinted in *Geothermal Energy Magazine,* Vol. 7, No. 1, Jan. 1979, pp. 17-23.

4 Correia, R.J., "Optimization of Some Hybrid Fossil-Geothermal Energy Conversion Systems," Sc.M. Thesis, Div. of Engineering, Brown University, 1978.

5 Kestin, J., DiPippo, R., and Khalifa, H.E., "Hybrid Geothermal-Fossil Power Plants," *Mechanical Engineering,* 1978, Vol. 100, No. 12, pp. 28-35.

6 Khalifa, H.E., DiPippo, R., and Kestin, J., "Hybrid Fossil-Geothermal Power Plants," *Proceedings 5th Energy Technology Conference,* 1978, pp. 960-970.

7 Thomas, F.J., "Cost Factors Related to Fossil-Geothermal Power Plants," in Minutes of the 6th CATMEC Meeting, July 1977, Brown Univ. Rep. No. CATMEC/5, DOE/DGE No. C00/4051-9; Also, Minutes of the 8th CATMEC Meeting, Feb. 1978, Brown Univ. Rep. No. CATMEC/10, DOE/DGE No. C00/4051-17.

8 City of Burbank, "Site-Specific Analysis of Hybrid Geothermal/Fossil Power Plants," Prepared for ERDA/DGE, Contract E(0-4-1311), Public Service Dept., Burbank, CA, June 1977.

9 Hansen, A., "Thermal Cycles for Geothermal Sites and Turbine Installation at The Geysers Power Plant, California," *Proceeding U.N. Conference on New Sources of Energy,* Vol. 3, Geothermal Energy II, pp. 365-377, Rome, 1961.

10 Armstead, H.C.H., "Geothermal Power for Non-Base Load Purposes," *Geothermics,* Spec. Iss. 2, Vol. 2, 1970, pp. 936-949.

11 James, R., "Power Station Strategy," *Geothermics,* Spec. Iss. 2, Vol. 2, 1970, pp. 1676-1687.

12 Kearton, W.J., *Steam Turbine Theory and Practice,* 7th ed., Pitman & Sons, London, 1958, p. 329.

13 Khalifa, H.E., "Hybrid Fossil-Geothermal Power Plants," Draft of Section 4.3 in a *Sourcebook on the Production of Electricity from Geothermal Energy* (in preparation), Brown Univ. Rep. No. CATMEC/25, DOE/DGE No. C00/4051-33, Sept. 1978, U.S. Government Printing Office, Washington, D.C.

14 DiPippo, R. and Avelar, E.M., "Compound Hybrid Geothermal-Fossil Power Plants," Brown Univ. Rep. No. CATMEC/31, DOE/DGE No. C00/4051-44, June 1978.

15 Quick, S.L., "Large Steam Turbine Technology Trends," *Turbomachinery International,* Vol. 20, No. 3, Apr. 1979, pp. 23-29.

16 Jonsson, V.K., "Geothermal Power Utilization, Present and Future," in *Alternative Energy Sources,* J.P. Hartnett, ed., Academic Press, New York, 1976, pp. 279-324.

17 Robertson, R.C., "Waste Heat Rejection from Geothermal Power Stations," ORNL/TM-6533, Oak Ridge Nat'l Lab., Oak Ridge, TN, Dec. 1978.

18 Keenan, J.H., Keyes, F.G., Hill, P.G., and Moore, J.G., *Steam Tables,* John Wiley & Sons, New York, 1969.

19 Austin, A.L., and Lundberg, A.W., "The LLL Geothermal Energy Program—A Status Report on the Development of the Total-Flow Concept," UCRL-50046-77, Lawrence Livermore Laboratory, University of California, Livermore, CA, Oct. 1978.

20 Phillips, S.L., Tavana, M., Leung, K., and Schwartz, S.R., "Geothermal Energy Databook for the Western United States," (Draft), Nat'l. Geoth. Info. Resource, Lawrence Berkeley Laboratory, Univ. of California, Berkeley, CA, 1979.

21 Williams, F., Cohen, A., Pfundstein, R., and Pond, S., "Site-Specific Analysis of Goethermal Development-Data Files for Prospective Sites," MITRE Tech. Rep. MTR-7586, Vol. III, DGE/4014-1, Metrek Div., The MITRE Corp., McLean, VA, 1977.

22 Butz, J.R., Denver Research Institute, personal communication, June 7, 1979.

23 Lenzer, R.C., Crosby, G.,W., and Berge, C.W., "Geothermal Exploration of Roosevelt KGRA, Utah," Geothermal Resources Council Spec. Short Course No. 6, *Geothermal Resources: Survey of an Emerging Industry,* Houston, TX, GRC, Davis, CA, 1977.

24 Lenzer, R.C., Crosby, G.W., and Berge, C.W., "Recent Development at the Roosevelt Hot Springs KGRA," Geothermal Resource Council Spec. Short Course No. 6, *Geothermal Resources: Survey of an Emerging Industry,* Houston, TX, GRC, Davis, CA, 1977.

25 BuRec, "Geothermal Resource Investigations—East Mesa Test Site," Status Report—April 1977, Bureau of Reclamation, USDOI.

26 Kestin, J., "Available Work in Geothermal Energy,"Brown Univ. Rep. No. CATMEC/20, DOE/DGE No. C00/4051-25, July 1978.

Fan/Foundation Interaction—A Simplified Calculation Procedure

H. M. Chen
Senior Analytical Engineer.

S. B. Malanoski
Supervisor, Engineering Analysis.
Mechanical Technology Inc.,
Latham, N.Y.

This paper presents a simplified analysis procedure to provide initial assessment and guidance on fan rotor dynamics including the foundation interaction. For purposes of early-design decision-making (or trouble-shooting), the interaction of a rotor-bearing dynamic system and a foundation-soil/piling dynamic system is viewed approximately for the vertical, horizontal, and rocking modes of vibration. The equations of motion are written in matrix form and include the pertinent parameters. A numerical example is presented to guide in the interpretation of the analysis; this example considers the unbalance response of the entire system as measured at the bearings.

Introduction

Some serious vibration problems of large fans are due to the interaction of the fan with its foundation. The interaction changes the rotor-bearing critical speeds predicted by the fan manufacturer and also changes the foundation resonance frequencies predicted by the architect-engineer (A-E). When larger-size fans are built, when operation occurs at higher speeds, and when the foundations become relatively less massive, this interaction deserves more attention.

Analytical tools are available for predicting the fan/foundation interaction. Two popular solution methods are the transfer matrix method and the finite-element method. Different modeling techniques may emphasize either the rotor/bearing details or the foundation/soil/piling details. But, in general, these methods require overly complicated modeling and are costly and time-consuming to run and to interpret results. In many instances, this effort may not be justified in the early design stage or for trouble-shooting an existing system. The authors' points of view are that much complexity of the detailed treatments is derived from over-modeling the system to address the interaction problem.

This paper presents a simplified model for predicting the interaction. This procedure is intended to help build a bridge of mutual understanding between the fan manufacturer and the A-E. It is not the intent of the authors to provide a substitute for the detailed methods, but rather to provide this simplified method as a guide in the design-stage decision making and as a trouble-shooting tool. The detailed methods are still recommended for a final design check.

Discussion of Simplified Model

The generation of a simplified model must consider four key elements:

- Rotor
- Bearings
- Pedestals
- Foundation

These are discussed with the rationale and procedure for treatment in the following paragraphs.

Rotor. Fans are usually designed to operate 15-25 percent away from, and usually below, the first rotor-bearing critical speed.[1] Due to a relatively small transverse moment of inertia of the rotor, the second critical speed (conical mode) is normally much higher than the operating speed. It is therefore adequate to represent the rotor by an equivalent mass and an equivalent spring for its lateral vibrations. The equivalent mass (M_R) and spring (K_R) are related to the first natural frequency (N_R in cpm) with rigid bearings by the equation:

$$N_R = \frac{30}{\pi}\sqrt{\frac{K_R}{M_R}} \tag{1}$$

The first rigid bearing natural frequency is readily calculated at the early design stage by formula or critical speed programs. From equation (1), a proper value must be chosen of either K_R of M_R to fix the other. Usually, it is easier to choose M_R as a fraction of the actual rotating mass and then calculate K_R by equation (1).

The fraction is approximately 0.75 and depends upon the ratio of the shaft mass (M_S) and the wheel mass (M_W). As a rule of thumb when considering a large number of fan systems,

$$M_R \simeq M_W + M_S/2 \tag{2}$$

Bearings. Large fans are usually supported and straddled by two journal bearings. One of the bearings also has a thrust-bearing function, but the lateral stiffness and damping of the two bearings are comparable. Thus, a symmetry assumption of the dynamic properties, without missing the major effect of the bearing properties, is possible. Note that the dynamic properties of the bearing properties between the horizontal

Contributed by the Power Division of THE AMERICAN SOCIETY OF MECHANICAL ENGINEERS and presented at the Joint Power Generation Conference, Phoenix, Arizona, September 28–October 2, 1980. Manuscript received at ASME Headquarters June 20, 1980.

[1] This speed, by definition of the Air Movement and Control Assn. (AMCA), is called the installed resonant speed; AMCA Publication 801, Paragraph 3.2.4.

and the vertical modes of the system are one of the sources which couple the two directions. These properties should be retained in the model. The bearing data, as functions of speed, load, and geometry, are obtained from solutions of the lubrication equation (computerized solutions) and used as input for the simplified model.

Pedestals. The pedestals refer to and include the bearing casings and liners,[2] the actual metal pedestals, the sole plate, and/or the concrete piers. Two equivalent mass-spring systems should be modeled, one for the vertical mode and one for the horizontal mode. Generally, only the equivalent spring constants are of major importance to the fan/foundation dynamics. However, if the springs are soft as in the case of the rotor/bearings isolated from the foundation, the equivalent pedestal masses then become important.

The vertical stiffness is usually high. The vertical mass may include the bearing casing and half the metal pedestal where most flexibility is originated.

The horizontal flexibility can be estimated by beam methods, but modified to include shear deformation. The equivalent horizontal mass depends on the flexibility of the concrete pier and the metal pedestal. If most of the horizontal flexibility comes from the pedestal, the horizontal mass may be taken as the mass of the bearing casing plus one-third the pedestal mass. For simplicity, it is also assumed that the inboard and outboard pedestals are the same.

Foundation. The concrete mat is practically a rigid body with six degrees of freedom of motion; but only three of these are of most concern: vertical, horizontal, and rocking. The pitching and the torsional modes are less likely to be excited because the rotor second natural frequency (conical mode) is seldom a problem. However, a simple calculation of these two frequencies may be made to insure that they are not close to the operating speed.

The stiffness and damping of the soil and/or pilings are calculated separately and used as input for the model. The foundation mass and rocking inertia should include the equivalent weights, such as casing, motor, etc. It is, furthermore, assumed that the concrete mat is symmetrical to the rotor axis; therefore, the vertical motion of the mat is not directly coupled with the rocking motion.

With all these considerations, the simplified fan/foundation dynamic system can be represented by the diagram as shown in Fig. 1. Note that the parameter D is the vertical distance measured from the rocking center to approximately the bearing centerline. The concrete pier flexibility is included in the stiffness K_{py}. The value of $M_R e$ is the amount of unbalance on the fan wheel.

[2] This effect may be included in the bearing characteristics as an alternative.

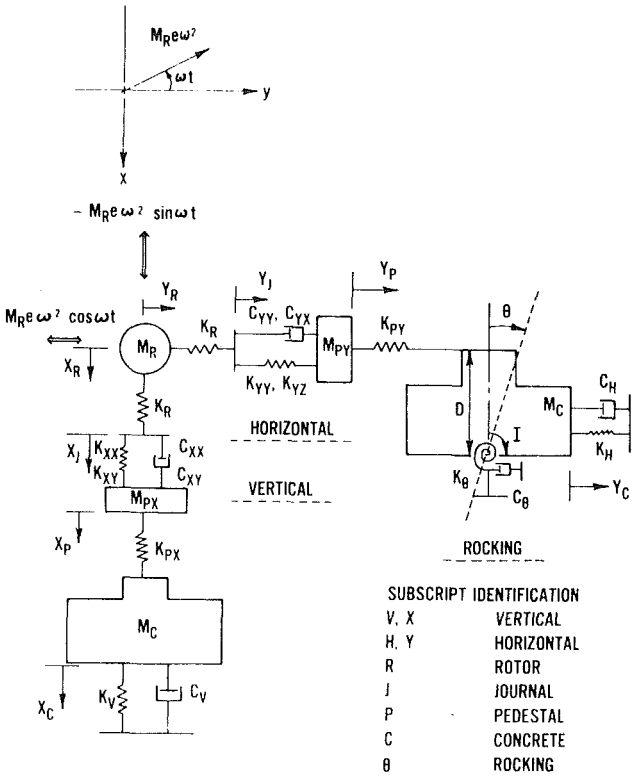

Fig. 1 Simplified mathematical model for fan/foundation system

Analysis

The basic interest in the fan/foundation system of Fig. 1 is unbalance response as measured at the bearings and the concrete mat. Peak responses of the system should be away from the operating speed range. These results will also indicate whether the system is "low-tuned" or "high-tuned."[3] Vibration sensitivity at the bearing casings relative to the unbalance can be determined – specifically, the housing vibration peak-to-peak displacement per oz-in. unbalance at the wheel outer diameter. The unbalance responses are

[3] In the case of a high-tuned design, the fundamental, lateral natural frequency of the foundation is above the operating speed of the fan. In the case of a low-tuned design, the operating speed is above this natural frequency.

Nomenclature

A = complex matrix (see Appendix)
C = damping, double subscript for bearing and subscript for soil, FT/L
D = vertical distance from the rocking center to the bearing centerline, also damping ratio when used with subscript (see Table 2), L
I = foundation rocking moment of inertia, FLT^2
K = stiffness, double subscript for bearing or pedestal, and single subscript for soil or rotor, F/L
M = mass, M
N = natural frequency of equivalent rotor with rigid bearings, cpm
S = laplace transform variable (see Appendix)
X, Y = vertical, horizontal displacement
TF = transfer function (see Appendix)
$\mathbf{U}, \mathbf{V}$ = vectors (see Appendix)
$\mathcal{L}$ = Laplace transform symbol (see Appendix)
e = unbalance mass eccentricity, L
j = $\sqrt{-1}$ (see Appendix)
t = time, T
ω = angular velocity, rad/s
$\bullet$ = differentiation with respect to time, t

Subscripts

C = concrete
H, y = horizontal
J = journal (bearing location on rotor)
P = pedestal
R = rotor
S = shaft
V, x = vertical
W = wheel (fan)
θ = rocking (angular)

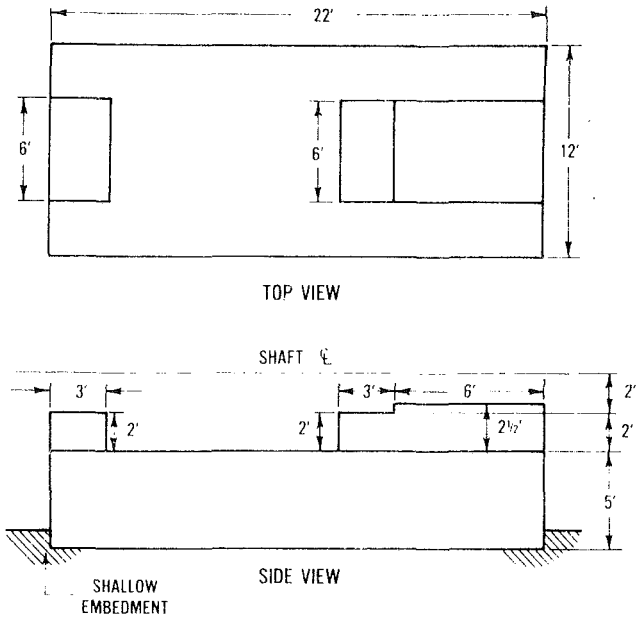

Fig. 2 Dimensions of concrete foundation (Note: 1 ft = 0.3048 m)

calculated using the transfer function method in the frequency domain as shown in Appendix A.

Illustrative Example

Problem Input.

Rotor.

- Wheel Weight = 5000 lb (2.22×10^4 N) with o.d. = 80 in. (2.03 m)
- Shaft Weight = 5000 lb (2.22×10^4 N)
- Rigid-Bearing First Critical, $N_R = 2500$ cpm
- $M_R = 5000 + 5000/_2 = 7500$ lb (3.34×10^4 N)
- $K_{R_8} = (\pi/30\ \ N_R)^{\ 2} M_R = 1.33 \times 10^6$ lb/in. (2.33×10^8 N/m)

Bearings.

- Cylindrical bores with two axial grooves
- Pressure fed with SAE-10-type oil at 150°F (66°C), Viscosity = 1.4×10^{-6} lb-s/in^2 (9.65×10^{-3} Pa•s)
- Diameter = 6 in. (0.152 m)
- Radial Clearance = .004 in. (0.102 mm)
- Length = 12 in. (0.305 m), outboard bearing; 5-¼ in. (0.133 m), two lands, thrust bearing
- Load = 5000 lb (2.22×10^4 N) each
- Dynamic coefficients are listed in Appendix B, [1]; Note: The model uses the sum of the two bearings' coefficients as input, e.g., $K_{xx} = (K_{xx})$ for outboard bearing + (K_{xx}) for thrust bearing.

Pedestals (inboard and outboard).

- Bearing Block = 150 lb (667 N) each
- Metal Pedestal = 300 lb (1334 N) each (flexibility is mainly from metal pedestals)
- Vertical Stiffness $K_{px} = 50 \times 10^6$ lb/in. (8.76×10^9 N/m)
- Horizontal Stiffness $K_{py} = 10 \times 10^6$ lb/in. (1.75×10^9 N/m) (due to shear and bending)
- Vertical Mass $M_{px} = 2(150 + 300/2) = 600$ lb (2.67×10^3 N)
- Horizontal Mass $M_{py} = 2(150 + 300/3) = 500$ lb (2.22×10^3 N)

Foundation. A sketch is given in Fig. 2.

- Concrete weight: 225,000 (1.00×10^6 N). Assumed concrete density: 150 lb/cu ft (2403 kg/m^3)
- Equipment weight including motor and fan casing but excluding rotor: 35,000 lb (1.56×10^5 N)

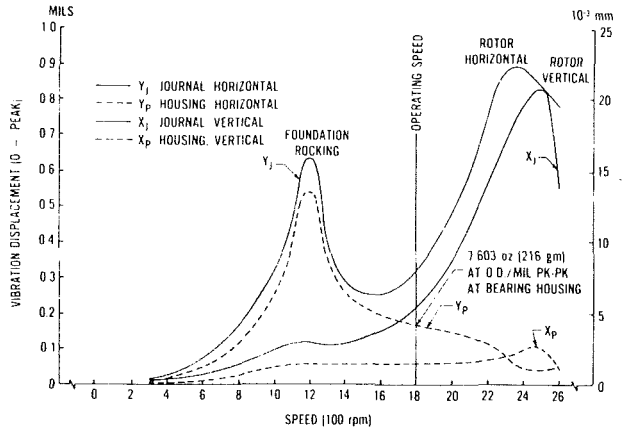

Fig. 3 Example of normal fan/foundation system unbalance responses at bearings

Table 1 Soil dynamic coefficents

K_V	9.17×10^6 lb/in. (1.60×10^9 N/m)
K_H	6.95×10^6 lb/in.) (1.22×10^9 N/m)
K_θ	5.13×10^{10} in. lb/rad (5.80×10^9 m.N/rad)
$C_V\ (D_V = 0.313)$	4.92×10^4 lb/in./s (8.61×10^6 N/m/s)
$C_H\ (D_H = 0.185)$	2.53×10^4 lb/in./s (4.43×10^6 N/m/s)
$C_\theta\ (D_\theta = 0.067)$	5.35×10^7 in.lb/rad/s (6.04×10^6 m.N/rad/s)

Note: Soil properties used in the calculation are:
Shear Modulus = 12,500 psi (8.62×10^7 Pa)
Poisson's Ratio = 0.4
Density = 110 lb/ft^3 (1762 Kg/m^3)
D_V, D_H, D_θ = Damping Ratios
The damping values are halves of the calculated values.

- $M_c = 225{,}000 + 35{,}000 = 260{,}000$ lb (3.47×10^6 N)
- Rocking moment of inertia of concrete about the bottom center: 7.48×10^8 lb-in^2 (2.15×10^6 N•m^2)
- Rocking moment of inertia of equipment masses about the bottom center: 4.54×10^8 lb-in^2 (1.30×10^6 N•m^2)
- Total rocking moment of inertia: $I = 7.48 \times 10^8 + 4.54 \times 10^8 = 1.20 \times 10^9$ lb-in^2 (3.44×10^6 N•m^2)

Note: equipment weight contributes largely to the rocking moment of inertia.

The soil stiffness and damping for vertical, horizontal and rocking modes are listed in Table 1 [2]. Due to the uncertainty of the soil shear modulus, the listed damping values are 50 percent of those actually calculated. Also, the dependency of the stiffness on frequency is ignored. Per [2], these data refer to motion of the foundation as if pivoted at its base. The parameter $D = 5 + 2 + 2 = 9$ ft = 108 in. (2.74 m). Unbalance at wheel, $M_R e = 100$ oz-in. (7.21×10^3 gm.cm).

Results of Analysis. The responses at the bearings, i.e., X_J, Y_J, X_p, and Y_p, are plotted in Fig. 3. It is apparent that the operating speed, 1800 rpm, is removed from the system peak response frequencies. Specifically, it is 33 percent above the rocking peak and 27 percent below the rotor first horizontal critical speed. This system as analyzed indicates a reasonably well-behaved low-tuned design. It should be pointed out that, as indicated in Table 2, the soil damping and stiffness values are functions of the soil shear modulus. If this shear modulus has some uncertainty, a range of values should be considered because this parameter will directly affect the

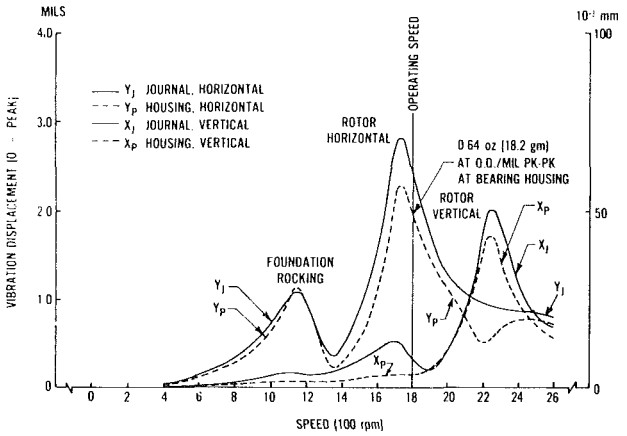

Fig. 4 Example of very flexible pedestals unbalance responses at bearings (Note: ordinate scale change)

amplitude and frequency levels of the foundation rocking mode.

Note that the static horizontal pedestal stiffness at the bearing center is

$$\frac{1}{\frac{1}{K_H}+\frac{D^2}{K_\theta}} = \frac{1}{\frac{1}{6.95\times10^6}+\frac{(9\text{x}12)^2}{5.13\times10^{10}}} = 2.69\times10^6 \text{ lb/in.}, \quad (4.71\times10^8 \text{ N/m})$$

which is less than the total bearing horizontal stiffness at 1800 rpm. Due to the dynamic effect of the concrete mass, the foundation is much stiffer than it appears statically.

If the pedestal anchor bolts or bearings caps are loose or if concrete piers are cracked such that K_{py} and K_{px} are 1/10 of previous values, then the responses become large, as those shown in Fig. 4. (Note the change in ordinate scale.) Now the system is entirely too sensitive.

This example demonstrates both how to use the simplified model and the mass effect of the foundation on the bearing supports. If the pedestal is very flexible, the foundation mass effect will be isolated from the bearing, and the damping in the bearings will become ineffective in controlling the rotor vibration.

Conclusions

A simple mathematical model is contructed for predicting the unbalance response of a large fan seated on an isolated foundation. The model only retains those vibration modes of practical concern and those which are directly excited by the fan rotor unbalance. The retained modes are the rotor lateral (first) modes and the foundation vertical, horizontal, and rocking modes. The bearing dynamic data and the soil and piling dynamic data are available from other sources and are used as input to this model. The simplified model is easy to implement with minimal time and cost, is convenient to use during the fan/foundation system design stage for determining the effect of the critical parameters of the system, and is a valuable diagnostic tool for trouble-shooting existing systems.

The model can be expanded to accommodate nonsymmetry of the bearings, the pedestals, and/or the concrete piers, and to include the offset of the fan axis relative to the foundation center axis. It also can be modified to include the foundation pitching and torsional modes of vibration.

The numerical example presented demonstrates the use of this method and illustrates the foundation-mass effect on rotor response. A fan manufacturer may specify the foundation requirements which should address both stiffness and mass. If only stiffness under the bearings is specified, the dynamic stiffening effect of the foundation would be ignored, and an over-designed or impractical foundation would result. The example also indicates that, no matter how well the foundation is designed, the rotor vibration is uncontrollable if there is considerable flexibility in the pedestals and/or concrete piers. In this case, the bearing casings move easily so that the damping in the bearings is not effectively utilized.

Acknowlegment

Parts of the material presented in this paper result from a consultation contract granted by Green Fan Company, Beacon, N.Y., to Mechanical Technology Incorporated, Latham, N.Y.

References

1 Computer programs CAD-30 and CAD-31 Design of Axial-Grooved, Liquid-Lubricated Journal Bearings by Mechanical Technology Incorporated, Latham, N.Y., 12110.

2 Richart, F., Hall, J., and Woods, R., *Vibration of Soils and Foundations*, Chap. 10, Prentice-Hall, Englewood Cliffs, N.J., 1970.

APPENDIX A

The equations of motions of the simplified Fan/Foundation System are as follows (refer to Fig. 1).

$$M_R\ddot{X}_R + K_R(X_R - X_J) = -M_R e\omega^2 \sin\omega t \tag{1}$$

$$K_R(X_J - X_R) + K_{xx}(X_J - X_p) + C_{xx}(\dot{X}_J - \dot{X}_p) + K_{xy}(Y_J - Y_p) + C_{xy}(\dot{Y}_J - \dot{Y}_p) = 0 \tag{2}$$

$$M_{px}\ddot{X}_p + K_{px}(X_p - X_C) + K_{xx}(X_p - X_J) + C_{xx}(\dot{X}_p - \dot{X}_J) + K_{xy}(Y_p - Y_J) + C_{xy}(\dot{Y}_p - \dot{Y}_J) = 0 \tag{3}$$

$$M_C\ddot{X}_C + K_{px}(X_C - X_p) + K_v X_C + C_v\dot{X}_C = 0 \tag{4}$$

$$M_R\ddot{Y}_R + K_R(Y_R - Y_J) = M_R e\omega^2 \cos\omega t \tag{5}$$

$$K_R(Y_J - Y_R) + K_{yy}(Y_J - Y_p) + C_{yy}(\dot{Y}_J - \dot{Y}_p) + K_{yx}(X_J - X_p) + C_{yx}(\dot{X}_J - \dot{X}_p) = 0 \tag{6}$$

$$M_{py}\ddot{Y}_p + K_{py}(Y_p - Y_C - D\theta) + K_{yy}(Y_p - Y_J) + C_{yy}(\dot{Y}_p - \dot{Y}_J) + K_{yx}(X_p - X_J) + C_{yx}(\dot{X}_p - \dot{X}_J) = 0 \tag{7}$$

$$M_C\ddot{Y}_C + K_H Y_C + C_H\dot{Y}_C + K_{py}(Y_C - D\theta - Y_P) = 0 \tag{8}$$

$$I\ddot{\theta} + K_\theta\theta + C_\theta\dot{\theta} + (D\theta + Y_C - Y_P)K_{py}D = 0 \tag{9}$$

Note: It is normal practice to refer the motion of a mass to its *cg*. However, equations (7-9) of this Appendix assume the base of the foundation as this reference. As outlined in [2], the stiffness and damping values of the horizontal and rocking modes are independently determined. Particularly, in calculating K_θ and C_θ, it is assumed that the foundation pivots about a horizontal axis at its base. Thus, no direct cross-coupling terms between the modes of vibration appear in these equations. Caution should therefore be exercised in using equations (7-9) if the soil dynamic coefficients are obtained from other methods. Accordingly, these particular equations could be rewritten with reference to the foundation *cg*.

Taking Laplace transform of the above equations (1-9) with all initial conditions equal to zero yields the following matrix equation:

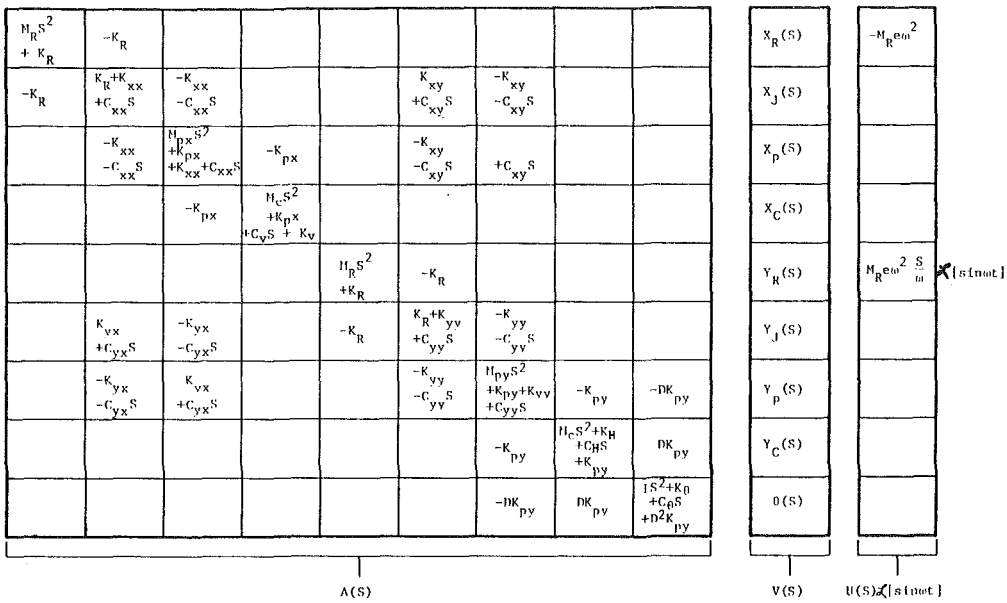

where $\mathcal{L}[\sin\omega t]$ means Laplace transform of the function in the bracket. S is the Laplace transform variable. ω is the rotational frequency. Let the transfer function of the system be:

$$TF(S) = \frac{V(S)}{\mathcal{L}[\sin\omega t]}$$

Then the steady state frequency response of the system is

$$TF(j\omega) = A^{-1}\ (j\omega)\ U\ (j\omega)$$

where

$$j = \sqrt{-1}$$

$A^{-1}\ (j\omega)$ = inverse of the complex matrix $A(j\omega)$

APPENDIX B

Bearing Dynamic Coefficients

Outboard Bearing

Speed	K_{xx}	B_{xx}	K_{xy}	B_{xy}	K_{yx}	B_{yx}	K_{yy}	B_{yy}
100	.974E7	.104E7	.526E7	.213E6	.725E6	.212E6	.175E7	.103E6
200	.542E7	.421E6	.409E7	.946E5	.122E6	.930E5	.157E7	.592E5
300	.391E7	.264E6	.370E7	.609E5	-.202E6	.617E5	.156E7	.460E5
400	.306E7	.201E6	.370E7	.491E5	-.495E6	.497E5	.158E7	.421E5
500	.251E7	.166E6	.381E7	.426E5	-.743E6	.429E5	.161E7	.398E5
600	.224E7	.142E6	.392E7	.349E5	-.836E6	.347E5	.161E7	.346E5
700	.208E7	.125E6	.409E7	.289E5	-.894E6	.285E5	.160E7	.304E5
800	.196E7	.113E6	.430E7	.247E5	-.952E6	.243E5	.161E7	.274E5
900	.187E7	.104E6	.449E7	.215E5	-.100E7	.212E5	.162E7	.250E5
1000	.181E7	.976E5	.472E7	.189E5	-.105E7	.187E5	.162E7	.231E5
1100	.176E7	.930E5	.500E7	.168E5	-.110E7	.166E5	.161E7	.217E5
1200	.173E7	.884E5	.521E7	.150E5	-.114E7	.148E5	.160E7	.203E5
1300	.171E7	.839E5	.540E7	.135E5	-.117E7	.133E5	.159E7	.190E5
1400	.169E7	.803E5	.559E7	.122E5	-.120E7	.121E5	.157E7	.179E5
1500	.168E7	.776E5	.581E7	.112E5	-.123E7	.110E5	.156E7	.171E5
1600	.167E7	.756E5	.607E7	.103E5	-.128E7	.101E5	.155E7	.165E5
1700	.166E7	.743E5	.636E7	.954E4	-.133E7	.937E4	.154E7	.161E5
1800	.165E7	.733E5	.667E7	.890E4	-.139E7	.872E4	.153E7	.157E5
1900	.164E7	.723E5	.697E7	.834E4	-.144E7	.816E4	.152E7	.154E5
2000	.163E7	.710E5	.721E7	.784E4	-.149E7	.767E4	.152E7	.150E5
2100	.162E7	.695E5	.744E7	.740E4	-.153E7	.724E4	.151E7	.147E5
2200	.162E7	.683E5	.767E7	.701E4	-.157E7	.685E4	.151E7	.143E5
2300	.161E7	.672E5	.791E7	.666E4	-.162E7	.649E4	.150E7	.141E5
2400	.161E7	.665E5	.817E7	.634E4	-.167E7	.618E4	.150E7	.138E5
2500	.160E7	.659E5	.845E7	.605E4	-.172E7	.589E4	.150E7	.137E5
2600	.160E7	.656E5	.876E7	.579E4	-.178E7	.563E4	.149E7	.136E5

Thrust Bearing

Speed	K_{xx}	B_{xx}	K_{xy}	B_{xy}	K_{yx}	B_{yx}	K_{yy}	B_{yy}
100	.179E8	.124E7	.696E7	.204E6	.167E7	.204E6	.191E7	.724E5
200	.108E8	.500E6	.550E7	.996E5	.862E6	.992E5	.184E7	.488E5
300	.830E7	.302E6	.494E7	.656E5	.532E6	.654E5	.180E7	.372E5
400	.694E7	.214E6	.462E7	.492E5	.306E6	.492E5	.180E7	.310E5
500	.606E7	.165E6	.444E7	.394E5	.140E6	.396E5	.180E7	.272E5
600	.542E7	.134E6	.432E7	.330E5	.582E4	.332E5	.180E7	.244E5
700	.496E7	.113E6	.424E7	.284E5	-.988E5	.286E5	.181E7	.222E5
800	.458E7	.980E5	.418E7	.250E5	-.199E6	.252E5	.182E7	.208E5
900	.428E7	.864E5	.416E7	.224E5	-.288E6	.226E5	.183E7	.195E5
1000	.404E7	.772E5	.412E7	.202E5	-.358E6	.204E5	.184E7	.182E5
1100	.384E7	.702E5	.410E7	.185E5	-.430E6	.187E5	.185E7	.173E5
1200	.366E7	.646E5	.412E7	.171E5	-.512E6	.173E5	.186E7	.167E5
1300	.350E7	.602E5	.416E7	.160E5	-.600E6	.161E5	.188E7	.163E5
1400	.334E7	.560E5	.414E7	.152E5	-.678E6	.153E5	.190E7	.160E5
1500	.320E7	.520E5	.412E7	.146E5	-.750E6	.146E5	.192E7	.156E5
1600	.306E7	.486E5	.410E7	.140E5	-.818E6	.139E5	.195E7	.152E5
1700	.294E7	.458E5	.410E7	.134E5	-.884E6	.133E5	.197E7	.149E5
1800	.284E7	.434E5	.410E7	.129E5	-.946E6	.128E5	.199E7	.146E5
1900	.276E7	.414E5	.414E7	.124E5	-.101E7	.122E5	.200E7	.143E5
2000	.268E7	.396E5	.416E7	.119E5	-.106E7	.117E5	.202E7	.140E5
2100	.260E7	.382E5	.420E7	.114E5	-.112E7	.112E5	.202E7	.137E5
2200	.254E7	.370E5	.426E7	.109E5	-.117E7	.107E5	.204E7	.134E5
2300	.248E7	.358E5	.432E7	.105E5	-.122E7	.103E5	.204E7	.132E5
2400	.244E7	.350E5	.440E7	.101E5	-.127E7	.986E4	.204E7	.130E5
2500	.240E7	.342E5	.446E7	.964E4	-.132E7	.946E4	.204E7	.127E5
2600	.236E7	.334E5	.454E7	.924E4	-.137E7	.960E4	.204E7	.125E5

Note: K's are in Unit of lb/in. Speed is in Unit of rpm
B's are in Unit of lb/in./sec Multiply lb/in. by 175.1 to obtain N/m.